# Spin polarization as a probe of hot QCD matter formed in ultrarelativistic collisions at the Large Hadron Collider

**A THESIS**

*Submitted in partial fulfilment of the requirements*

*for the award of the degree*

*of*

**DOCTOR OF PHILOSOPHY**

by

**Bhagyarathi Sahoo**




**DEPARTMENT OF PHYSICS**

**INDIAN INSTITUTE OF TECHNOLOGY INDORE**

**July 2026**

# INDIAN INSTITUTE OF TECHNOLOGY INDORE

I hereby certify that the work which is being presented in the thesis entitled **Spin polarization as a probe of hot QCD matter formed in ultrarelativistic collisions at the Large Hadron Collider** in partial fulfillment of the requirements for the award of the degree of **DOCTOR OF PHILOSOPHY** and submitted in the **DEPARTMENT OF PHYSICS, Indian Institute of Technology Indore**, is an authentic record of my own work carried out during the time period from August 2021 to July 2026 under the supervision of **Prof. Raghunath Sahoo, Institute Chair Professor, Department of Physics, Indian Institute of Technology Indore**.

The matter presented in this thesis has not been submitted by me for the award of any other degree of this or any other institute.

Bhagyarathi Sahoo
Date: 06 October 2026

**Signature of the student with date**

**(Bhagyarathi Sahoo)**

---

This is to certify that the above statement made by the candidate is correct to the best of my knowledge.

Raboo 06 oct 2026

**Signature of Thesis Supervisor with date**

**(Prof. Raghunath Sahoo)**

**Mr. Bhagyarathi Sahoo** has successfully given his Ph.D. Oral Examination held on 06 oct 2026

Raboo

**Signature of Thesis Supervisor with date** 06 oct 2026

**(Prof. Raghunath Sahoo)**

*Dedicated to*

*my beloved parents and my younger brother*

# ACKNOWLEDGEMENTS

I begin by humbly thanking the Almighty Lord Jagannath for His constant blessings, grace, and support. I extend sincere thanks to everyone who contributed, both directly and indirectly, to the completion of this thesis. I have made my best effort to acknowledge all deserving individuals; however, I sincerely apologize if anyone has been inadvertently omitted.

First and foremost, I would like to express my deepest gratitude to my thesis supervisor, Prof. Raghunath Sahoo, for giving me the invaluable opportunity to pursue my doctoral research under his guidance. This thesis would not have been possible without his constant encouragement, insightful guidance, and unwavering support throughout my Ph.D. journey. I am sincerely thankful to him for providing an excellent research environment and the freedom to explore diverse aspects of experimental and phenomenological studies in relativistic heavy-ion collisions. I am also grateful for the opportunities and financial support that enabled me to participate in several conferences and academic visits to various institutes in India and abroad during my Ph.D., which enhanced my understanding of the subject. Under his mentorship, I had the opportunity to contribute to two major projects: a review of event-shape analysis published in the reputable journal Physics Reports and a book on non-extensive statistics in high-energy physics. His never-give-up attitude, positive mindset, and encouragement toward interdisciplinary and innovative research have always inspired me. He is always approachable and available for physics discussions, paper resubmissions, as well as any administrative matters. I feel truly blessed and deeply grateful to have such a dynamic mentor and renowned physicist as my thesis supervisor.

I would like to express my sincere gratitude to the eminent scientist Prof. Jane Alam for guiding me in understanding relativistic hydrodynamics during my short research visit to the Variable Energy Cyclotron Centre. His profound understanding of physics and exceptional teaching style have always been a great

source of inspiration and learning for me. I will always cherish and remember his helping nature, kind behavior, humbleness, grounded personality, and humility throughout my life. This thesis would have been almost impossible without the help, support, and guidance of Dr. Captain Rituraj Singh, who served as a senior Research Associate at IIT Indore during my Ph.D. journey and became like an elder brother to me. He played a pivotal role in mentoring me during my Ph.D. and shaping the direction of this thesis. All the phenomenological studies presented in this thesis would simply not have been possible without his invaluable guidance and support. He always treated me like his younger brother and never took offense at my unintentionally rude words. I truly enjoyed the countless hours of physics discussions with him because of his open-minded nature and approachable personality. I look forward to a lifelong mentorship with him and to exploring new avenues of physics together in the future.

The experimental part of this thesis would not have been possible without the Indian participation in the ALICE Collaboration. I gratefully acknowledge the financial support provided by the DAE–DST, Government of India, under the Mega Science Project "Indian Participation in the ALICE Experiment at CERN" for the CERN visit, which also supported my participation in the ALICE Physics Week 2024 and the Quark Matter 2025. I would like to thank all the members of the ALICE Collaboration for providing me with the opportunity to work on one of the world's largest particle accelerator experiments. My sincere gratitude goes to all the members of the Dileptons and Quarkonia Physics Working Group (PWG-DQ) for their valuable comments and suggestions regarding my analysis. In particular, I would like to express my heartfelt thanks to Dr. Luca Micheletti, Dr. Ionut Cristian Arsene, Dr. Maurice Coquet, Dr. Arvind Khuntia, and Dr. Maxime Guilbaud for their constant help and guidance throughout my Ph.D., particularly in software development and physics analysis. I am also thankful to Dr. Laure Marie Massacrier, Dr. Sarah Porteboeuf, Dr. Xiaozhi Bai, Dr. Batoul Diab, Dr. Shreyasi Acharya, Dr. Dhananjaya Thakur, and Dr. Deekshit

Kumar for their valuable comments and suggestions on my analysis work. A special note of thanks is extended to Dr. Maxime Guilbaud and Dr. Nicolas Bize for the fruitful discussions during my service task on $pDCA$ cut optimization for muon tracks. My sincere gratitude also goes to the Analysis Review Committee members, Dr. Luca Micheletti and Dr. Dukhishyam Mallick, for dedicating their valuable time to reviewing my two analysis notes and for providing insightful comments and suggestions. I would further like to thank Lorenzo Mattei, Sara Garetti, Rebecca Cerri, Zhenjun Xiong, Emilie Barreau, Sourav Kanti Giri, and Banajit Barman for the many helpful interactions during my research work.

I would like to wholeheartedly thank my PSPC members, Prof. Safique Ahmed and Dr. Manavendra Mahato, for their continuous guidance and support and for evaluating my progress throughout my Ph.D. journey. I would also like to express my sincere gratitude to all the faculty members of the Department of Physics and the non-teaching staff of IIT Indore for ensuring the smooth functioning of administrative work during my Ph.D. period. I would further like to thank Dr. Amaresh Jaiswal, Dr. Partha Pratim Bhaduri, Dr. Sabyasachi Ghosh, Dr. Santosh Kumar Das, Dr. Biswarup Paul, Dr. Sayantan Sharma, Prof. Saumen Datta, Dr. Sushant Kumar Singh, Dr. Partha Bagchi, and Dr. Arpan Das for the many useful and insightful physics discussions at many conferences.

I sincerely thank Dr. Suman Deb, my first Ph.D. mentor, for introducing me to non-extensive statistics and the PYTHIA model. I am also thankful to Dr. Dushmanta Sahu, who introduced me to the Hadron Resonance Gas (HRG) model and guided me in many phenomenological studies, including experimental data analysis. I have learned a lot from both of them and will remain grateful forever.

I would like to thank Dr. Sushanta Tripathy and Dr. Suraj Prasad for insightful physics discussions during the preparation of the event shape review paper. I am grateful to Dr. Sushanta Tripathy for all his support and help during my visit to CERN. I am truly thankful to Dr. Suraj Prasad and Dr. Neelkamal Mallick for all the technical and coding support they provided during the initial days of

my Ph.D. period. I would like to offer my heartfelt thanks to Dr. Ronald Scaria and Dr. Jayanta Dey, who helped in understanding many aspects of relativistic heavy-ion collisions and cosmic physics. I sincerely thank all my collaborators, Dr. Arvind Khuntia, Dr. Girija Shankar Pradhan, Dr. Kshitish Kumar Pradhan, and Dr. Sourav Dey, for fruitful physics discussions. I would like to offer my heartfelt thanks to Dr. Kamaljeet Singh and Dr. Debadatta Behera for their support and friendship in the last five years. I would like to extend my sincere thanks to my labmates - Kangkan, Aswathy, Rishabha Gupta, Rishabha Tiwari, Vaishakh, Ram, and Aiswarya for their companionship. I also wish to express my deepest appreciation to my former labmates - Ben, Bhavin, Kanika, Preet, Shubham, Hitesh, Vikrant, Sarthak, Udit, Hirak, Pratyay, Surya Prakash, Anushka, Harsit, Purnima, and Parul for the wonderful memories, support, and interactions during my time in the lab. I gratefully acknowledge the financial support provided by the Council of Scientific and Industrial Research (CSIR), Government of India, throughout my Ph.D. program.

I am sincerely thankful to my school, college, and university teachers, seniors, juniors, and friends for their constant guidance and support. It is because of their encouragement and inspiration that I have been able to reach this stage of my academic journey. I would also like to express my heartfelt gratitude to all my well-wishers for their blessings and support throughout the years.

Last but not least, I would like to wholeheartedly thank my parents and my younger brother and sister for their unconditional love, endless support, encouragement, and unwavering faith in me. I am equally grateful to my entire family for always standing by me, and I shall remain forever indebted to them.

This thesis would not have been possible without the collective support of all these individuals and institutions. Thank you all for being a part of this journey.

**Bhagyarathi Sahoo**

# ABSTRACT

Understanding the nature of the fundamental building blocks of matter, quarks and gluons, under extreme conditions of temperature and density, is one of the primary goals of the two largest collider experiments in the world: the Large Hadron Collider (LHC) at CERN and the Relativistic Heavy Ion Collider (RHIC) at Brookhaven National Laboratory. The ALICE experiment at the LHC mainly focuses on investigating the formation and properties of the Quark-Gluon Plasma (QGP), a strongly interacting, deconfined, and locally thermalized state of quarks and gluons that exhibits collective behavior and is expected to be created in ultrarelativistic heavy-ion collisions. To probe this transient state of matter, QGP, several indirect signatures have been proposed, such as the presence of strangeness enhancement, suppression of quarkonia, jet quenching, collective flow, direct photons, and dilepton production. These observables provide strong evidence for the possible formation of QGP in heavy-ion collisions and are commonly referred to as the $1^{st}$-generation probes of the QGP. Some of the most prominent "smoking-gun" signatures of QGP formation, such as quarkonia suppression, jet quenching, and strangeness enhancement, traditionally rely on proton–proton ($pp$) collisions as a baseline system, where the formation of a hot and dense medium is generally not expected. However, recent measurements of high-multiplicity $pp$ collisions at LHC energies have revealed the emergence of several QGP-like features in these small systems. These include an enhanced production of strange hadrons relative to charged pions (strangeness enhancement), as well as the presence of radial and elliptic flow, phenomena that were previously believed to occur exclusively in ultrarelativistic nucleus–nucleus collisions. These findings suggest the possible emergence of QGP-like phenomena in small systems, thereby opening a new research domain to investigate the existence of QGP in such small collision systems. Additionally, these observations challenge the conventional understanding of QGP signatures and the established methodologies used to study

them, particularly for observables such as quarkonia suppression that rely on *pp* collisions as a baseline. Consequently, they highlight the need for a next generation of baseline-independent probes for QGP investigation. In this context, spin polarization phenomena have emerged as a promising avenue for exploring the properties of hot QCD matter. Studying the particle spin polarization in relativistic heavy-ion and hadronic collisions could serve as a $2^{\text{nd}}$-generation probe. This thesis presents a comprehensive investigation of the spin polarization of various hadrons from both experimental and phenomenological perspectives and proposes spin polarization as a promising next-generation probe for QGP studies.

The first part of this thesis presents the experimental analysis of $\mathrm{J}/\psi$ polarization measurements in proton-proton (*pp*) collisions at $\sqrt{s} = 13.6$ TeV and Oxygen–Oxygen (OO) collisions at $\sqrt{s_{\mathrm{NN}}} = 5.36$ TeV, measured via the dimuon decay channel at forward rapidity ($2.5 < y < 4.0$). With the high-statistics Run 3 *pp* data samples, a more precise and differential measurement of the polarization parameters is performed as a function of transverse momentum ($p_{\mathrm{T}}$) in helicity and Collins-Soper reference frames, extending down to zero $p_{\mathrm{T}}$. The light-ion collision data of Run 3 allow the first measurement of $\mathrm{J}/\psi$ polarization parameters as a function of $p_{\mathrm{T}}$ in OO collisions. $\mathrm{J}/\psi$ polarization measurements in hadronic and light-ion collisions can serve as a powerful probe for understanding the production mechanism of quarkonia. Furthermore, quarkonium polarization is sensitive to the environment in which the bound state is produced, offering a unique opportunity to study the effects of the deconfined medium on the evolution of heavy-quark pairs and quarkonium formation. Moreover, in OO collisions, quarkonium polarization may be particularly sensitive to the presence of initial magnetic and vorticity fields. The results obtained in the analyses of *pp* and OO collisions are compared with existing measurements from lower-energy *pp* and Pb–Pb collision systems, respectively. Furthermore, the measurements are confronted with several available theoretical frameworks, including non-relativistic Quantum

Chromodynamics (NRQCD), the Color Singlet Model (CSM), the Improved Color Evaporation Model (ICEM), and the Color Glass Condensate (CGC) + NRQCD approach. Additionally, a Monte Carlo study of J/$\psi$ and $\psi(2S)$ polarization in proton–proton collisions is presented as a function of transverse momentum, charged-particle multiplicity, and rapidity at various center-of-mass energies.

The second part of this thesis explores the phenomenological study of spin alignment of quarkonium states in Pb+Pb collisions at $\sqrt{s_{\rm NN}}$ = 5.02 TeV, calculated at mid-rapidity. The diagonal and off-diagonal elements of the spin density matrix for charmonium [J/$\psi$, $\psi(2S)$] and bottomonium [$\Upsilon(1S)$, $\Upsilon(2S)$] states are explored by calculating the spin projection-dependent eigenenergies, quarkonium wave functions, and decay widths. The dynamics of quarkonium states are described by constructing an effective Hamiltonian including the spin–vorticity and spin–magnetic interactions in a thermal rotating medium with a realistic temperature-dependent complex quarkonium potential. The effect of medium rotation, external magnetic field, medium temperature, and momentum-space anisotropy is systematically studied on the elements of the spin density matrix. Moreover, the spin-dependent dissociation of quarkonium states, governed by their binding energies and sizes, is proposed as a potential mechanism underlying the spin alignment.

Furthermore, the second part of the thesis also investigates the global spin polarization of baryons including $\Lambda$, $\Xi^-$, $\Omega^-$, $\Delta^{++}$ and $\Sigma^{\pm}$, and the spin alignment of vector mesons including $K^{*0}$, $\phi$, and $\rho$ from global quark polarization calculated through partonic elastic scattering within the framework of an effective static potential model. Within this framework, the quark polarization is driven by the Debye screening mass. Hence, any change brought to the Debye screening mass due to external perturbations like a magnetic field and anisotropy, in principle, affects the global quark polarization and hence the spin polarization of hadrons.

The global hyperon spin polarization and the spin alignment of vector mesons are studied in the presence of a strong magnetic field, baryonic chemical potential, and medium anisotropy due to two hadronization mechanisms, i.e., recombination and fragmentation. It is observed that the degree of spin polarization is flavor-dependent for hyperons, while vector meson spin alignment depends on the hadronization mechanisms. In another approach, the global spin polarization of $\Lambda$ hyperons is obtained by determining the lifetime of the vortical QGP fluid and by developing a unified hydrodynamic framework within the ambit of second-order Müller-Israel-Stewart (MIS) based relativistic viscous hydrodynamics. The coupling of the medium viscosity, vorticity, and magnetic field in the hydrodynamic equations is investigated, and the interplay of spin–vorticity and spin–magnetic coupling through the spin polarization observable. Furthermore, the local (or longitudinal) spin polarization of $\Lambda$ hyperons due to thermal vorticity and thermal shear is obtained in an ideal uncharged fluid using hydrodynamic and transport model simulations. These findings advance the understanding of spin polarization phenomena in relativistic heavy-ion collisions by providing deeper insight into the rotational dynamics of quark–gluon plasma.

# ACRONYMS

- **SM**: Standard Model
- **QCD**: Quantum Chromodynamics
- **QED**: Quantum Electrodynamics
- **QGP**: Quark Gluon Plasma
- **RHIC**: Relativistic Heavy Ion Collider
- **LHC**: Large Hadron Collider
- **CEP**: Critical End Point
- **EoS**: Equation of State
- **BGBW**: Boltzmann Gibbs Blast Wave
- **pQCD**: perturbative Quantum Chromodynamics
- **OAM**: Orbital Angular Momentum
- **MIS**: Müller Israel-Stewart
- **BR**: Branching Ratio
- **PDG**: Particle Data Group
- **TMD**: Transverse Momentum Dependent
- **PFF**: Polarizing Fragmentation Function
- **AMPT**: A Multi Phase Transport
- **CERN**: European Organization for Nuclear Research
- **ATLAS**: A Toroidal LHC ApparatuS

- **CMS**: Compact Muon Solenoid
- **LHCb**: Large Hadron Collider beauty
- **ALICE**: A Large Ion Collider Experiment
- **IP**: Interaction Point
- **ZDC**: Zero Degree Calorimeter
- **FIT**: Fast Interaction Trigger
- **FDD**: Forward Diffractive Detector
- **PMTs**: Photo Multiplier Tubes
- **EMCal**: ElectroMagnetic Calorimeter
- **DCal**: Di-jet Calorimeter
- **PHOS**: PHOton Spectrometer
- **MWPC**: Multi Wire Proportional Chamber
- **CPV**: Charged Particle Veto
- **HMPID**: High Momentum Particle Identification Detector
- **RICH**: Ring Imaging Cherenkov
- **TOF**: Time Of Flight
- **MRPC**: Multigap Resistive Plate Chamber
- **TRD**: Transition Radiation Detector
- **TPC**: Time Projection Chamber
- **ITS2**: Inner Tracking System 2

- **MAPS**: Monolithic Active Pixel Sensor
- **MFT**: Muon Forward Tracker
- **MCH**: Muon CHambers
- **MID**: Muon IDentification
- **O$^2$**: Online-Offline
- **AOD**: Analysis Object Data
- **DPL**: Data Processing Layer
- **CTFs**: Compressed Time Frames
- **CCDB**: Conditions and Calibration Database
- **FLP**: First Level Processor
- **TFs**: Time Frames
- **STFs**: Sub Time Frames
- **EPNs**: Event Processing Nodes
- **SoA**: Structure of Arrays
- **NRQCD**: Non Relativistic Quantum Chromodynamics
- **CO**: Color Octet
- **CS**: Color Singlet
- **CSM**: Color Singlet Model
- **ICEM**: Improved Color Evaporation Model
- **CGC**: Color Glass Condensate

- **HE**: Helicity
- **CS**: Collins Soper
- **GJ**: Gottfried Jackson
- **EP**: Event Plane
- **PP**: Production Plane
- **RP**: Reaction Plane
- **LO**: Leading Order
- **NLO**: Next-to-Leading Order
- **RCT**: Run Condition Table
- **CB2**: Double Crystall Ball
- **VWG**: Variable Width Gaussian
- **Pol4Exp**: Polynomial 4 with Exponential
- **MC**: Monte Carlo
- **LDMEs**: Long-Distance Matrix Elements
- **SE**: Schrödinger Equation
- **RDS**: Relativistic Doppler Shift
- **HTL**: Hard Thermal Loop
- **SO**: Second Order
- **ECHO-QGP**: Eulerian Conservative High Order Quark Gluon Plasma
- **EPOS4**: Energy conservation Parallel scatting factOrization Saturation

# PUBLICATIONS

## List of Publications:

**(Publications marked with [*] are included in this thesis)**

1. [*] "Inclusive J/$\psi$ polarization measurement at forward rapidity in proton-proton collisions at $\sqrt{s}$ = 13.6 TeV with ALICE".
   **Bhagyarathi Sahoo**, Raghunath Sahoo.
   Link to Analysis Note: alice-notes.web.cern.ch/node/1691
   Preliminary approved figures: alice-figure.web.cern.ch/node/36516

2. [*] "Inclusive J/$\psi$ polarization measurement at forward rapidity in Oxygen-Oxygen collisions at $\sqrt{s_{\rm NN}}$ = 5.36 TeV with ALICE".
   **Bhagyarathi Sahoo**, Raghunath Sahoo.
   Link to Analysis Note: alice-notes.web.cern.ch/node/1698
   Preliminary approved figures: alice-figure.web.cern.ch/node/36516

3. [*] "Probing Rotational Dynamics of Quark Gluon Plasma via Global Vorticity". **Bhagyarathi Sahoo**, Captain R. Singh, and Raghunath Sahoo.
   Published in: Phys. Lett. B **880**, 140714 (2026).
   DOI: doi:10.1016/j.physletb.2026.140714

4. [*] "Dissociation driven quarkonium spin alignment in Pb–Pb collisions at $\sqrt{s_{\rm NN}}$ = 5.02 TeV".
   **Bhagyarathi Sahoo**, Captain R. Singh, and Raghunath Sahoo.
   Published in: Phys. Rev. D **113**, 054023 (2026).
   DOI: 10.1103/PhysRevD.113.054023

5. [*] "Impact of strong magnetic field, baryon chemical potential, and medium anisotropy on polarization and spin alignment of hadrons".
   **Bhagyarathi Sahoo**, Captain R. Singh and Raghunath Sahoo.

Published in: Eur. Phys. J. C **85**, 580 (2025).

DOI: 10.1140/epjc/s10052-025-14260-4

6. [*] "Estimating Longitudinal Polarization of $\Lambda$ and $\bar{\Lambda}$ Hyperons at Relativistic Energies using Hydrodynamic and Transport models".

   **Bhagyarathi Sahoo**, Captain R. Singh and Raghunath Sahoo.

   Published in: Phys. Scr. **100**, 065310 (2025).

   DOI: 10.1088/1402-4896/add9ef

7. [*] "Polarization measurement of $J/\psi$ and $\psi(2S)$ in proton+proton collisions at the LHC energies using PYTHIA8".

   **Bhagyarathi Sahoo**, Dushmanta Sahu, Suman Deb, Captain R. Singh and Raghunath Sahoo.

   Published in: Phys. Rev. C **109**, 034910 (2024).

   DOI: 10.1103/PhysRevC.109.034910

8. [*] "Impact of vorticity and viscosity on the hydrodynamic evolution of hot QCD medium".

   **Bhagyarathi Sahoo**, Captain R. Singh, Dushmanta Sahu, Raghunath Sahoo and Jan-e Alam.

   Published in: Eur. Phys. J. C **83**, 873 (2023).

   DOI: 10.1140/epjc/s10052-023-12027-3

9. [*]"Spin alignment of Quarkonia: A Possible Probe of a Deconfined QCD matter in Pb–Pb collisions at $\sqrt{s_{\rm NN}} = 5.02$ TeV".

   **Bhagyarathi Sahoo**, Captain R. Singh and Raghunath Sahoo.

   Published in: Eur. Phys. J. C **86**, 880 (2026).

   DOI: doi:10.1140/epjc/s10052-026-16125-w

10. [*] "Global polarization of $\Lambda$ hyperons in hot QCD matter at TeV energies".

    **Bhagyarathi Sahoo**, Captain R. Singh, and Raghunath Sahoo.

    arXiv:2604.13701 (Under Review: Phys. Rev. D)

11. "Rotational susceptibility of a hot and dense hadronic matter".
    **Bhagyarathi Sahoo**, Kshitish Kumar Pradhan, Dushmanta Sahu, and Raghunath Sahoo.
    Published in: Eur. Phys. J. A **62**, 162 (2026).
    DOI: doi:10.1140/epja/s10050-026-01938-w

12. "Effect of magnetic field on the thermodynamic properties of a high-temperature hadron resonance gas with van der Waals interactions".
    **Bhagyarathi Sahoo**, Kshitish Kumar Pradhan, Dushmanta Sahu and Raghunath Sahoo
    Published in: Phys. Rev. D **108**, 074028 (2023).
    DOI: 10.1103/PhysRevD.108.074028

13. "Multiplicity, transverse momentum and pseudorapidity dependence of open-heavy flavored hadron production in proton+proton collisions at $\sqrt{s}$= 13 TeV". **Bhagyarathi Sahoo**, Suman Deb and Raghunath Sahoo
    Published in: Int. J. Mod. Phys. E **33**, 2450055 (2024).
    DOI: 10.1142/S0218301324500551

14. "Event Topology Classifiers at the Large Hadron Collider".
    Suraj Prasad, Sushanta Tripathy, **Bhagyarathi Sahoo** and Raghunath Sahoo.
    Published in: Physics Reports **1181**, 1-75 (2026). [Review article]
    DOI: doi.org/10.1016/j.physrep.2026.04.001

15. "Probing strangeness with event topology classifiers in pp collisions at the LHC with rope hadronization mechanism in PYTHIA".
    Suraj Prasad, **Bhagyarathi Sahoo**, Sushanta Tripathy, Neelkamal Mallick and Raghunath Sahoo
    Published in: Phys. Rev. C **111**, 044902 (2025).
    DOI: 10.1103/PhysRevC.111.044902

16. "Thermodynamics of a rotating hadron resonance gas with van der Waals interaction".
    Kshitish Kumar Pradhan, **Bhagyarathi Sahoo**, Dushmanta Sahu and Raghunath Sahoo
    Published in: Eur. Phys. J. C **84**, 936 (2024).
    DOI: 10.1140/epjc/s10052-024-13283-7

17. 193 Experimental Papers [ALICE] can be found in: INSPIRE HEP

## My Contributions to the Journal Publications:

As the primary analyzer of two experimental physics analyses, I took the lead in all major aspects of the analyses, including formulation of the research problem, development of the corresponding ALICE software analysis framework, design of the analysis strategy and methodology, coding, data and Monte Carlo simulation analysis, interpretation of the results, regular PAG and PWG presentations, preparation of the analysis notes, and making the results approved as ALICE Preliminary in Physics Forum. The analyses are currently being prepared for paper proposals within the ALICE Collaboration.

As the first author in journal publications, I led the majority of the work, including formulation of the research problem, development of the analysis methodology, corresponding coding, physics interpretation of the results, preparation of the first draft of the manuscript, and communication with the journal throughout the revision and publication processes. As a co-author, I contributed to the work by assisting with the formulation of the research problem, verifying the analysis methodology, contributing to coding and Monte Carlo simulation studies, interpreting the results, and revising the manuscript.

## Conference Proceedings:

1. "Quarkonium Polarization Measurement in Hadronic and Nuclear Collisions at Forward Rapidity with ALICE at the LHC".
   **Bhagyarathi Sahoo** (on behalf of the ALICE Collaboration).
   Published in: Springer Proc. Phys. **432**, 1061 (2026).

2. "Spin-Alignment of Vector Mesons in Relativistic Heavy-Ion Collisions".
   **Bhagyarathi Sahoo**, Captain R. Singh and Raghunath Sahoo.
   Published in: Springer Proc. Phys. **432**, 805 (2026).

3. "Can spin alignment of quarkonia be a probe of thermalization in heavy-ion collisions?".
   **Bhagyarathi Sahoo**, Captain R. Singh and Raghunath Sahoo.
   Published in: DAE Symp. Nucl. Phys. **69**, 1063 (2026).

4. "The Liquid-Gas Phase Transition in a Rotating Hadron Resonance Gas".
   Kshitish Kumar Pradhan, **Bhagyarathi Sahoo**, Dushmanta Sahu and Raghunath Sahoo.
   Published in: Springer Proc. Phys. **432**, 1084 (2026).

5. "Polarization: An Emerging $2^{nd}$ Gen. Probe for QGP".
   Captain R. Singh, **Bhagyarathi Sahoo** and Raghunath Sahoo.
   Published in: DAE Symp. Nucl. Phys. **69**, 997 (2026).

6. "QGP as the Most Vortical Fluid and Its Effect on the $\Lambda-$Hyperon Polarization".
   Captain R. Singh, **Bhagyarathi Sahoo** and Raghunath Sahoo.
   Published in: Springer Proc. Phys. **432**, 809 (2026).

7. "Global and local spin polarization of $\Lambda$ hyperons in relativistic heavy ion collisions".

**Bhagyarathi Sahoo**, Captain R. Singh and Raghunath Sahoo.
Published in: J. Subatomic Part. Cosmol. **4**, 100078 (2025).

8. "Quarkonium polarization measurement in hadronic and nuclear collisions at forward rapidity".
**B. Sahoo**, C. R. Singh, S. Deb, D. Sahu, and R. Sahoo, Published in: J. Subatomic Part. Cosmol. **4**, 100098 (2025).

9. "Investigating the local polarization of $\Lambda$ and $\bar{\Lambda}$ hyperons at relativistic energies".
**Bhagyarathi Sahoo**, Captain R. Singh and Raghunath Sahoo.
Published in: DAE Symp. Nucl. Phys. **68**, 1007 (2025).

10. "Exploring the effect of magnetic field on the liquid-gas phase transition in a hadron resonance gas approach with van der Waals interactions".
**Bhagyarathi Sahoo**, Kshitish Kumar Pradhan, Dushmanta Sahu and Raghunath Sahoo.
Published in: DAE Symp. Nucl. Phys. **68**, 863 (2025).

11. "Plausible impact of dissipative forces on QGP evolution in relativistic heavy-ion collisions at the LHC".
Captain R. Singh, **Bhagyarathi Sahoo**, Dushmanta Sahu, Raghunath Sahoo and Jan-e Alam.
Published in: J. Subatomic Part. Cosmol. **4**, 100171 (2025).

12. "Role of Vorticity and Viscosity on the Polarization of $\Lambda$-hyperon at Relativistic Energies".
Captain R. Singh, **Bhagyarathi Sahoo** and Raghunath Sahoo.
Published in: DAE Symp. Nucl. Phys. **68**, 1021 (2025).

13. "Effect of rotation on the liquid-gas phase transition in a hadron resonance gas".

Kshitish Kumar Pradhan, **Bhagyarathi Sahoo**, Dushmanta Sahu and Raghunath Sahoo.

Published in: DAE Symp. Nucl. Phys. **68**, 943 (2025).

14. "Exploring strangeness enhancement in proton-proton collisions at the LHC with event shapes".

    Suraj Prasad, **Bhagyarathi Sahoo**, Sushanta Tripathy, Neelkamal Mallick and Raghunath Sahoo.

    Published in: DAE Symp. Nucl. Phys. **68**, 987 (2025).

15. "Multiplicity, Transverse Momentum and Pseudorapidity Dependence of Freeze-Out Parameters for Open-Charm Hadrons in Hadronic Collisions at LHC Energy".

    **Bhagyarathi Sahoo**, Suman Deb, and Raghunath Sahoo.

    Published in: Springer Proc. Phys. **304**, 882 (2024).

16. "Exploring J/$\psi$ and $\psi(2S)$ polarization dynamics in pp collisions at the LHC energies with PYTHIA8".

    **Bhagyarathi Sahoo**, Suman Deb, Dushmanta Sahu, Captain R. Singh, and Raghunath Sahoo.

    Published in: DAE Symp. Nucl. Phys. **67**, 1035 (2024).

17. "Refractive index of the hadronic medium in the presence of a magnetic field".

    **Bhagyarathi Sahoo**, Kshitish Kumar Pradhan, Dushmanta Sahu, and Raghunath Sahoo.

    Published in: DAE Symp. Nucl. Phys. **67**, 885 (2024).

18. "How do coupled viscosity, vorticity, and magnetic field govern the QGP evolution?".

    Captain R. Singh, **Bhagyarathi Sahoo**, Dushmanta Sahu, Raghunath

Sahoo, and Jan-e Alam.

Published in: DAE Symp. Nucl. Phys. **67**, 985 (2024).

19. "A review on event shape studies in ultra-relativistic collisions at the LHC energies".

    Sushanta Tripathy, Suraj Prasad, Neelkamal Mallick, **Bhagyarathi Sahoo**, and Raghunath Sahoo.

    Published in: DAE Symp. Nucl. Phys. **67**, 1135 (2024).

20. "Insight into the thermodynamic activity of high-multiplicity hadronic collisions at LHC energy".

    **Bhagyarathi Sahoo**, Suman Deb, and Raghunath Sahoo.

    Published in: DAE Symp. Nucl. Phys. **66**, 956 (2023).

## My Contributions to the Conference Proceedings:

As the first author of the conference proceedings papers, I led the majority of the work, including preparing the initial draft of the proceedings, implementing the corresponding code where necessary, and coordinating the manuscript through the revision and publication process. As a co-author of the proceedings papers, I contributed to the work by assisting with the revision of the manuscript.

# Contents


1 Introduction 1

**1.1 The Standard Model** . . . 1

1.1.1 Quantum chromodynamics . . . 2

**1.2 Quark-Gluon Plasma** . . . 5

1.2.1 The QCD phase diagram . . . 6

1.2.2 Heavy ion collisions . . . 7

**1.3 Experimental probes of QGP** . . . 10

1.3.1 Soft probes . . . 11

1.3.2 Hard probes . . . 17

**1.4 Thesis motivation** . . . 21

1.4.1 Spin polarization as a probe for QGP . . . 23

**1.5 Thesis structure** . . . 26

2 Basic concept of spin polarization 31

**2.1 Spin density matrix: an overview** . . . 31

2.1.1 Spin $\frac{1}{2}$ system . . . 32

2.1.2 Spin 1 system . . . 37

2.1.3 Spin $\frac{3}{2}$ system . . . 43

**2.2 Spin polarization: an overview** . . . 45

2.2.1 Types of spin polarization . . . 45

2.2.2 Hyperon spin polarization: an overview . . . 48

2.2.3 Vector meson spin alignment: an overview . . . 54

3 The ALICE Experiment at the LHC 59
**3.1 The Large Hadron Collider** . . . 59
3.1.1 Cross section and luminosity . . . 60
3.1.2 The four giants . . . 62
**3.2 The ALICE detectors** . . . 63
3.2.1 The global detectors . . . 65
3.2.2 The central barrel detectors . . . 66
3.2.3 The muon spectrometer . . . 69
3.2.4 Online-Offline control system and analysis framework . . . 74

4 J/$\psi$ polarization in proton-proton and Oxygen-Oxygen collisions with ALICE 77
**4.1 Quarkonium polarization: an overview** . . . 77
4.1.1 Dilepton decay angular distribution . . . 78
4.1.2 Reference frames . . . 85
4.1.3 Frame invariant parameter . . . 87
4.1.4 J/$\psi$ polarization puzzle . . . 88
**4.2 J/$\psi$ polarization in proton-proton collisions** . . . 90
4.2.1 Data sample selection and analysis cuts . . . 90
4.2.2 Analysis strategy description . . . 97
4.2.3 Signal extraction . . . 98
4.2.4 A $\times\epsilon$ correction . . . 110
4.2.5 Polarization parameter extraction . . . 112
4.2.6 Systematic uncertainties . . . 112
4.2.7 Summary of systematic uncertainties . . . 132
4.2.8 Results . . . 133
4.2.9 Comparison with *pp* measurements at 7 and 8 TeV . . . 135
4.2.10 Comparison with theoretical models . . . 136
**4.3 J/$\psi$ polarization in oxygen-oxygen collisions** . . . 142

4.3.1 Data sample selection and analysis cuts . . . 142
4.3.2 Signal extraction . . . 144
4.3.3 A $\times\epsilon$ correction . . . 151
4.3.4 Polarization parameter extraction . . . 152
4.3.5 Systematic uncertainties . . . 152
4.3.6 Summary of systematic uncertainties . . . 160
4.3.7 Results . . . 161
4.3.8 Comparison with Pb–Pb measurements at 5.02 TeV . . . 162
4.3.9 Comparison with theoretical models . . . 163
4.3.10 Experimental challenges in quarkonia polarization . . . 166

5 $J/\psi$ AND $\psi(2S)$ POLARIZATION IN PROTON-PROTON COLLISIONS FROM MONTE CARLO SIMULATION 167

**5.1 $p_T$ dependence of $\lambda_\theta$, $\lambda_\phi$, and $\lambda_{\theta\phi}$** . . . 169

**5.2 Multiplicity dependence of $\lambda_\theta$, $\lambda_\phi$, $\lambda_{\theta\phi}$** . . . 172

**5.3 Rapidity dependence of $\lambda_\theta$, $\lambda_\phi$, $\lambda_{\theta\phi}$** . . . 174

6 QUARKONIA SPIN ALIGNMENT AS A PROBE OF QGP 177

**6.1 Quarkonia in a thermal rotating medium** . . . 178

6.1.1 Debye mass under a strong magnetic field . . . 185
6.1.2 Debye mass in an anisotropic medium . . . 186

**6.2 Spin alignment of quarkonia due to eigen energies** . . . 187

6.2.1 Diagonal elements of the spin density matrix . . . 189
6.2.2 Off-diagonal elements of the spin density matrix . . . 195

**6.3 Spin alignment of quarkonia due to dissociation mechanisms** 198

6.3.1 Collisional damping . . . 198
6.3.2 Gluonic dissociation . . . 199
6.3.3 Spin alignment of quarkonia . . . 206

7 Spin polarization of hyperons and vector mesons **215**

**7.1 Hydrodynamic medium evolution** . . . 216

7.1.1 Ideal fluid . . . 216

7.1.2 Viscous fluid . . . 217

7.1.3 Rotational viscous fluid . . . 219

7.1.4 Rotational viscous fluid in the presence of a magnetic field 225

**7.2 Global spin polarization of hyperons** . . . 230

7.2.1 Spin polarization due to thermal vorticity and magnetic field 231

7.2.2 Spin polarization due to Debye mass . . . 234

**7.3 Local spin polarization of $\Lambda$ hyperons** . . . 244

7.3.1 Thermal vorticity . . . 244

7.3.2 Thermal shear . . . 247

**7.4 Spin alignment of vector mesons** . . . 254

8 Summary **257**

# Figures

Figure(1.1) Illustration of the color confinement mechanism in QCD. . . . 4

Figure(1.2) Running coupling constant as a function of momentum transfer [1]. . . . . 5

Figure(1.3) Schematic representation of QCD phase diagram in $T - \mu_B$ plane [2]. . . . . 7

Figure(1.4) Schematic evolution of the heavy-ion collisions at LHC energies [2]. . . . . 8

Figure(1.5) Direct photon spectra (top) and direct photon excess $R_\gamma$ (bottom) measured in Pb–Pb collisions at $\sqrt{s_{\rm NN}}$ = 2.76 TeV [8] and $\sqrt{s_{\rm NN}}$ = 200 GeV [9, 10] in the (0-20)% (left) and (20-40) % (right) centrality classes. . . . . 12

Figure(1.6) (Left) The transverse momentum distribution of $\pi^{\pm}$, $K^{\pm}$, p [11], $K^0_S$, and $\Lambda$ [12], and the $\phi$ mesons [13] for (0-5)% and (80-90)% centrality interval in Pb–Pb collisions at $\sqrt{s_{\rm NN}} = 2.76$ TeV. (Right) Blast wave parameters of the kinetic freeze-out parameters $T_{\rm kin}$ and average radial flow velocity $\langle\beta_T\rangle$ obtained from the simultaneous fits to the $\pi^{\pm}$, $K^{\pm}$, p spectra and $v_2$ for the two models in Pb–Pb collisions. . . 14

Figure(1.7) (a,b) Enhancements of multi-strange hadrons as a function of the mean number of participants $\langle N_{\rm part}\rangle$ in AA collisions with pp or p-Be as reference in the rapidity range $|y| < 0.5$ in ALICE (full symbols), RHIC and SPS (open symbols) [17]. (c) Hyperon-to-pion ratios as a function of $\langle N_{\rm part}\rangle$ for A–A and pp collisions at LHC and RHIC energies. The lines represent the thermal model predictions from [18] (full line), and [19] (dashed line). . . . . 15

Figure(1.8) $p_{\rm T}$ dependence of the elliptic flow ($v_2$) for $\pi^{\pm}$, $K^{\pm}$, p+$\bar{p}$, $\phi$, $K^0_S$, $\Lambda$+$\bar{\Lambda}$ in different centrality classes for Pb–Pb collisions at $\sqrt{s_{\rm NN}}$ = 5.02 TeV [20]. . . . . 17

Figure(1.9) (Left) The nuclear modification factor $R_{\rm AA}$ for inclusive J/$\psi$, and $\psi(2S)$ measured in Pb–Pb collisions at $\sqrt{s_{\rm NN}}$ =5.02 TeV as function of $N_{\rm part}$ in the range $2.5 < y < 4.0$ [22]. Prediction from TM-TAMU [23], and SHM [24] are also shown. (Right) The $p_{\rm T}$ dependence of $R_{\rm AA}$ for J/$\psi$, and $\psi(2S)$ measured by ALICE in $2.5 < y < 4.0$ for (0-90)% Pb–Pb collisions [22], are compared with high-p$_{\rm T}$ results in $|y| < 1.6$ and (0–100)% centrality from CMS [25]. Model comparisons are also shown. . . . . 19

Figure(1.10)(Left) Nuclear modification factor $R_{\rm AA}$ for charged hadrons in central Pb–Pb collisions at $\sqrt{s_{\rm NN}} = 5.02$ TeV. (Right) The comparison of $R_{\rm AA}$ for charged hadrons and jets in different LHC experiments [2]. 20

Figure(1.11)$p_{\rm T}$-integrated yield ratios of strange hadrons to pions as a function of average charged-particle multiplicity density $\langle dN_{\rm ch}/d\eta\rangle$ in $pp$, p–Pb, Pb-Pb collisions. Different lines represent the prediction obtained from MC generator [26]. . . . . 22

Figure(1.12)Elliptic flow ($v_2$) of mesons ($\pi^{\pm}$, $K^{\pm}$, $K^0_{\rm S}$) and baryons ($p+\bar{p}$, $\Lambda+\bar{\Lambda}$) in $pp$, p–Pb, Pb-Pb collisions using two-particle correlation method [27]. . . . . 22

Figure(1.13) Illustration of the direction of the orbital angular momentum ($L$) and magnetic field ($B$) in relativistic heavy-ion collisions . . . . . 25

Figure(2.1) Illustration of the $\Lambda$ hyperons decay in its rest frame. . . . . 33

Figure(2.2) Illustration of the different polarization axes. . . . . 46

Figure(2.3) Sketch of the vortical fluid produced in heavy-ion collisions. . . 49

Figure(2.4) Global spin polarization of $\Lambda$ hyperons as function of collision energies [70]. . . . . 49

Figure(2.5) (Left) Illustration of the system created in a non-central heavy-ion collision viewed in the transverse plane. (Right) $\langle cos\theta^{*}\rangle$ of $\Lambda$ and $\bar{\Lambda}$ hyperons as a function of azimuthal angle $\phi$ in Au+Au collisions at $\sqrt{s_{\rm NN}}$ = 200 GeV [55]. . . . . 51

Figure(2.6) The second Fourier sine coefficient of the longitudinal spin polarization $P_{z,s2}$ as a function of centrality (left panel) and transverse momentum $p_{\rm T}$ (right panel) [68]. . . . . 52

Figure(2.7) $\rho_{00}$ for $K^{*0}$, $\phi$ as function of $\langle N_{\rm part}\rangle$ (left)[66] and $\sqrt{s_{\rm NN}}$ (right)[62]. 55

Figure(2.8) $\rho_{00}$ for prompt $D^{*+}$ as a function of $p_{\rm T}$ for two different centralities (left), two different rapidities (middle), and compared with J/$\psi$ (right)[72]. . . . . 57

Figure(2.9) Centrality (left) and $p_{\rm T}$ (right) dependence of $\lambda_\theta$ for J/$\psi$ [71]. . 57

Figure(3.1) Schematic view of the CERN detailed accelerator structure [197]. 60

Figure(3.2) Schematic view of the ALICE detector in Run 3 configuration [203]. . . . . 64

Figure(3.3) Schematic view of the ALICE Muon Spectrometer [217]. . . . . 70

Figure(3.4) Schematic view of the front absorber with its composition [217]. 71

Figure(3.5) Different track types present in the muon spectrometer for Run 3 [218]. 74

Figure(4.1) Sketch of the decay J/$\psi \to \ell^{+}\ell^{-}$. Figure taken from [88] . . . 81

Figure(4.2) Illustration of the coordinate system used for the measurement of the angular variables for two-body decay [88] . . . . . 84

Figure(4.3) Illustration of the angular distribution W($\cos\vartheta$) (left), W($\varphi$) (middle), W($\tilde{\varphi}$) (right) for two extreme and an intermediate values of $\lambda$ parameters [221] . . . . . 86

Figure(4.4) Illustration of the three different definitions of the polarization axis, z, in the helicity (HE), Collins-Soper (CS), and Gottfried-Jackson (GJ) reference frames [157]. . . . . 86

Figure(4.5) (Left) J/$\psi$ polarization parameter $\alpha$ (similar to $\lambda_\theta$) as a function of $p_{\rm T}$ obtained in CDF Collaboration compared to NRQCD and $k_{\rm T}$ factorization model prediction [37]. (Right) $\lambda_\theta$ obtained in ALICE compared with LO-NRQCD, NLO-NRQCD, LO CSM, NLO CSM predictions [93]. . . . . 89

Figure(4.6) Quantities used to describe the multiple scattering with the front absorber. Figure taken from Ref. [224] . . . . . 94

Figure(4.7) $p\times$DCA distribution in $171^o < \theta_{\rm abs} < 177^o$ (left) and $177^o < \theta_{\rm abs} < 178^o$ (right) obtained using LHC22o pass7 dataset [225]. . . . . 95

Figure(4.8) Fit of $p\times$DCA distribution in two diffferent $\theta_{\rm abs}$ with a Gaussian distribution. The distribution is obtained with $p_{\rm T} > 0$ GeV/c [225]. . 96

Figure(4.9) $p_{\rm T}$ integrated signal extraction using CB2+VWG function [229].101

Figure(4.10) Background modulation in like-sign distributions with no $p_{\rm T}$ cut (blue) and with the same $p_{\rm T}$ cut as the trigger (red), for $1 < p_{\rm T} <$ 8 GeV/c [229]. . . . . 103

Figure(4.11) The ratio shown in Fig. 4.10 is fitted with RatioVWG function for $p_{\rm T}$ range $1 < p_{\rm T} < 8$ GeV/c. [229]. . . . . 104

Figure(4.12) $p_{\rm T}$ differential signal extraction using CB2+VWG function for $0 < p_{\rm T} < 1$ GeV/c, $8 < p_{\rm T} < 10$ GeV/c, $10 < p_{\rm T} < 15$ GeV/c, while CB2+RatioVWG is used for $1 < p_{\rm T} < 8$ GeV/c [229]. . . . . 106

Figure(4.13) cos$\theta$ differential signal extraction for $3 < p_{\mathrm{T}} < 4$ GeV/c in Collins-Soper reference frame. The $\cos\theta$ intervals from $-0.8$ to $+0.8$ with a bin width of 0.1 are arranged from left to right and top to bottom. [229]. . . . . 107

Figure(4.14) cos$\theta$ differential signal extraction for $3 < p_{\mathrm{T}} < 4$ GeV/c in helicity frame. The $\cos\theta$ intervals from $-0.8$ to $+0.8$ with a bin width of 0.1 are arranged from left to right and top to bottom [229]. . . . . 108

Figure(4.15) Raw angular distribution as a function of cos$\theta$ (top), $\phi$ (middle), and $\tilde{\phi}$ (bottom) in CS (left) and HE (right) for $0 < p_{\mathrm{T}} < 15$ GeV/c [229]. . . . . 109

Figure(4.16) Acceptance $\times$ Efficiency (A $\times\epsilon$ ) as a function of cos$\theta$ (top), $\phi$ (middle), and $\tilde{\phi}$ (bottom) in Collins-Soper (left) and helicity (right) for $0 < p_{\mathrm{T}} < 15$ GeV/c [229]. . . . . 111

Figure(4.17) $\lambda_\theta$ polarization parameter extraction for $p_{\mathrm{T}}$ bin $0 < p_{\mathrm{T}} < 15$ GeV/c in the Collins-Soper (red) and helicity (blue) frames [229]. . . 113

Figure(4.18) $\lambda_\phi$ polarization parameter extraction for $p_{\mathrm{T}}$ bin $0 < p_{\mathrm{T}} < 15$ GeV/c in the Collins-Soper (red) and helicity (blue) frames [229]. . . 114

Figure(4.19) $\lambda_{\theta\phi}$ polarization parameter extraction for $p_{\mathrm{T}}$ bin $0 < p_{\mathrm{T}} < 15$ GeV/c in the Collins-Soper (red) and helicity (blue) frames [229]. . . 115

Figure(4.20) A representative plot for the systematic variation of $\lambda_\theta$ polarization due to different trials in the Collins-Soper frame for $1 < p_{\mathrm{T}} < 2$ GeV/c [229]. . . . . 117

Figure(4.21) Systematic variation of $\lambda_\theta$ due to different trials in CS and HE frame. The top (bottom) three rows correspond to the CS (HE) frame [229]. . . . . 118

Figure(4.22) Systematic variation of $\lambda_\phi$ due to different trials in CS and HE frame. The top (bottom) three rows correspond to the CS (HE) frame [229]. . . . . 119

Figure(4.23) Systematic variation of $\lambda_{\theta\phi}$ due to different trials in CS and HE. The top (bottom) three rows correspond to the CS (HE) frame [229]. 120

Figure(4.24) Comparison of $\lambda_\theta$, $\lambda_\phi$, and $\lambda_{\theta\phi}$ obtained from 1D-fit and 2D-simultaneous fit as a function of $p_{\mathrm{T}}$ in Collins-Soper and helicity frame [229]. . . . . 122

Figure(4.25) 2D-fit of the angular distribution due to CB2+VWG functions in Collins-Soper frame [229]. . . . . 123

Figure(4.26) 2D-fit of the angular distribution due to CB2+VWG functions in helicity frame [229]. . . . . 124

Figure(4.27) Comparison of the $\lambda_\theta$, $\lambda_\phi$, and $\lambda_{\theta\phi}$ due to two different MC productions (LHC25c3 and LHC25c3b) as a function of $p_{\mathrm{T}}$ in Collins-Soper and helicity frame [229]. . . . . 125

Figure(4.28) $\lambda_\theta$, $\lambda_\phi$, and $\lambda_{\theta\phi}$ due to input MC shape of polarization parameter [229]. . . . . 127

Figure(4.29) $J/\psi$ $p_T$ (left panel) and rapidity $y$ (right panel) distributions obtained from generated MC by applying a weight to the original distributions [229]. . . . . 127

Figure(4.30) Polarization parameters due to input $p_{\mathrm{T}}$ shape [229]. . . . . 128

Figure(4.31) Polarization parameters due to input $y$ shape [229]. . . . . 128

Figure(4.32) Schematic of the MCH used for tracking efficiency calculation 129

Figure(4.33) Comparison of the tracking efficiency evaluated in data and MC. . . . . 130

Figure(4.34) Polarization parameters due to tracking efficiency evaluated in data and Monte Carlo [229]. . . . . 131

Figure(4.35) J/$\psi$ polarization parameters as a function of transverse momentum in $pp$ collisions at $\sqrt{s} = 13.6$ TeV in Collins-Soper and helicity frames [229]. . . . . 133

Figure(4.36) Comparison of inclusive J/$\psi$ polarization at $\sqrt{s}$ = 13.6 TeV, with previous existing measurement at $\sqrt{s}$ = 7 and 8 TeVin $pp$ collisions [229]. . . . . 135
Figure(4.37) Comparison of inclusive J/$\psi$ polarization parameters in $pp$ collisions at $\sqrt{s}$ = 13.6 TeV with different NRQCD model predictions [229]. 136
Figure(4.38) Comparison of inclusive J/$\psi$ polarization parameters in $pp$ collisions at $\sqrt{s}$ = 13.6 TeV with ICEM and CGC+NRQCD model predictions [229]. . . . . 138
Figure(4.39) Frame invariant parameter $\tilde{\lambda}$ as a function of $p_{\mathrm{T}}$ in Collins-Soper and helicity frame. The error bars include the contributions of the systematic and statistical uncertainties [229]. . . . . 140
Figure(4.40) $p_{\mathrm{T}}$-integrated tail parameters extraction with LHC25i4 MC sample using CB2 and NA60 function [233]. . . . . 146
Figure(4.41) $p_{\mathrm{T}}$-integrated tail parameter extraction in Data with CB2 (Signal) and VWG (background) functions [233]. . . . . 146
Figure(4.42) cos$\theta$ differential signal extraction for $4 < p_{\mathrm{T}} < 6$ GeV/c in Collins-Soper frame. The $\cos\theta$ intervals from $-1.0$ to $+1.0$ with a bin width of 0.2 are arranged from left to right and top to bottom. [233]. 148
Figure(4.43) cos$\theta$ differential signal extraction for $4 < p_{\mathrm{T}} < 6$ GeV/c in helicity frame. The $\cos\theta$ intervals from $-1.0$ to $+1.0$ with a bin width of 0.1 are arranged from left to right and top to bottom. [233]. . . . . 149
Figure(4.44) Raw angular distribution as a function of cos$\theta$ (top), $\phi$ (middle), and $\tilde{\phi}$ (bottom) in CS (left) and HE (right) for $0 < p_{\mathrm{T}} < 10$ GeV/c [233]. . . . . 150
Figure(4.45) Acceptance $\times$ Efficiency (A$\times\epsilon$) as a function of cos$\theta$ (top), $\phi$ (middle), and $\tilde{\phi}$ (bottom) in Collins-Soper (left) and helicity (right) frame for $0 < p_{\mathrm{T}} < 10$ GeV/c [233]. . . . . 151
Figure(4.46) $\lambda_\theta$ (top), $\lambda_\phi$ (middle), $\lambda_{\theta\phi}$ (bottom) polarization parameters extraction for $p_{\mathrm{T}}$ bin $0 < p_{\mathrm{T}} < 10$ GeV/c in Collins-Soper frame [233] 153

Figure(4.47) $\lambda_\theta$ (top), $\lambda_\phi$ (middle), $\lambda_{\theta\phi}$ (bottom) polarization parameters extraction for $p_{\mathrm{T}}$ bin $0 < p_{\mathrm{T}} < 10$ GeV/c in helicity frame [233]. . . 153
Figure(4.48) Systematic variation of $\lambda_\theta$ due to different trials in CS frame [233].154
Figure(4.49) Systematic variation of $\lambda_\theta$ due to different trials in helicity [233].154
Figure(4.50) Systematic variation of $\lambda_\phi$ due to different trials in CS [233]. . 155
Figure(4.51) Systematic variation of $\lambda_\phi$ due to different trials in helicity [233].155
Figure(4.52) Systematic variation of $\lambda_{\theta\phi}$ due to different trials in CS [233]. 156
Figure(4.53) Systematic variation of $\lambda_{\theta\phi}$ due to different trials in helicity [233].156
Figure(4.54) Variation in the polarization parameters as a function of transverse momentum due to the 1D vs 2D fit [233]. . . . . 157
Figure(4.55) 2D-fit of the angular distribution due to CB2+VWG functions in Collins-Soper frame [233]. . . . . 158
Figure(4.56) 2D-fit of the angular distribution due to CB2+VWG functions in helicity frame [229]. . . . . 158
Figure(4.57) Variation in the polarization parameters as a function of transverse momentum due to the data-driven tail parameter vs MC tail parameter [233]. . . . . 159
Figure(4.58) Inclusive J/$\psi$ polarization parameters as a function of transverse momentum for OO collisions at $\sqrt{s_{\mathrm{NN}}} = 5.36$ TeV in Collins-Soper and helicity frame [233]. . . . . 161
Figure(4.59) Comparison of inclusive J/$\psi$ polarization parameters in OO collisions at $\sqrt{s_{\mathrm{NN}}} = 5.36$ TeV with Pb–Pb collisions at $\sqrt{s_{\mathrm{NN}}} = 5.02$ TeV [233]. . . . . 162
Figure(4.60) Comparison of inclusive J/$\psi$ polarization parameters in OO collisions at $\sqrt{s_{\mathrm{NN}}} = 5.36$ TeV with different NRQCD model predictions [233]. . . . . 163
Figure(4.61) Frame invariant parameter $\tilde{\lambda}$ as a function of $p_{\mathrm{T}}$ in Collins-Soper and helicity frame. The error bars include the contributions of the systematic and statistical uncertainties [233]. . . . . 164

Figure(4.62)The comparison of $00^{th}$ elements of the spin density matrix, $\rho_{00}$ obtained from $\lambda_\theta$ parameter for OO and Pb-Pb collisions . . . . . 165

Figure(5.1) The cosine of the polar angle (upper panel) and the azimuthal angle (lower panel) distribution in $pp$ collisions for $J/\psi$ and $\psi$(2S) at $\sqrt{s}$ = 13 TeV in helicity (left panel) and Collins-Soper (right panel) reference frame [157]. . . . . 168

Figure(5.2) The $J/\psi$ and $\psi$(2S) polarization parameters as a function of transverse momentum for $pp$ collisions at $\sqrt{s}$ = 7, 8, and 13 TeV using PYTHIA8. The obtained results are compared with the $J/\psi$ polarization measurement in $pp$ collisions from ALICE at $\sqrt{s}$ = 7, 8 TeV, LHCb at $\sqrt{s}$ = 7 TeV, and the NLO-NRQCD model predictions in color singlet (CS) and color singlet + color octet (CS+CO) states at $\sqrt{s}$ = 7 TeV in both helicity and Collins-Soper reference frames [157].170

Figure(5.3) Polarization of $J/\psi$ (left) and $\psi$(2S) (right) as a function of transverse momentum obtained from PYTHIA8 compared with the LHCb experimental data in $pp$ collisions at $\sqrt{s}$ = 7 TeV in the rapidity interval $2.5 < y < 4.0$ in the helicity frame. The MC simulation results are compared with NLO CSM from [93] and NLO NRQCD calculation from (1) [93], (2) [97], and (3) [94, 98] [157]. . . . . 171

Figure(5.4) The $J/\psi$ and $\psi$(2S) polarization parameters as a function of charged-particle multiplicity for $pp$ collisions at $\sqrt{s}$ = 7, 8, and 13 TeV using PYTHIA8 in both helicity and Collins-Soper reference frames [157]. . . . . 173

Figure(5.5) The $J/\psi$ and $\psi$(2S) polarization parameters as a function of rapidity for $pp$ collisions at $\sqrt{s}$ = 7, 8, and 13 TeV using PYTHIA8 in both helicity and Collins-Soper reference frames [157]. . . . . 175

Figure(6.1) The effective temperature ($T_{\rm eff}$) as a function of $p_{\rm T}$ for J/$\psi$, $\psi$(2S), $\Upsilon$(1S), and $\Upsilon$(2S) states calculated at medium temperature $T$ = 0.400 GeV [161]. . . . . 182

Figure(6.2) The energy eigenvalue as a function of $p_{\rm T}$ for J/$\psi$ (upper left), $\psi$(2S) (upper right), $\Upsilon$(1S) (lower left), and $\Upsilon$(2S) (lower right) obtained at $C$ = 1.0 fm using $T$ = 0.175 GeV [163]. . . . . 184

Figure(6.3) The spin alignment observable $\rho_{00}$ as a function of $p_{\rm T}$ for J/$\psi$ (upper left), $\psi$(2S) (upper right), $\Upsilon$(1S) (lower left), and $\Upsilon$(2S) (lower right) in Pb+Pb collisions at $\sqrt{s_{\rm NN}}$ = 5.02 TeV calculated at mid-rapidity for different values of the circulation parameter, $C$ [163]. . . 190

Figure(6.4) The spin alignment observable $\rho_{00}$ as a function of $p_{\rm T}$ for J/$\psi$ (upper panel) and $\psi$(2S) (lower panel) in Pb+Pb collisions at $\sqrt{s_{\rm NN}}$ = 5.02 TeV calculated at mid-rapidity for different values of the circulation parameter, $C$ [163]. . . . . 193

Figure(6.5) The off-diagonal elements of the spin density matrix, such as, Re[$\rho_{1,-1}$] (top), Re[$\rho_{-1,0}$] (middle), and Re[$\rho_{1,0}$] (bottom) as a functions of $p_{\rm T}$ (left), $T$ (middle), $C$(right) for Pb+Pb collisions at $\sqrt{s_{\rm NN}}$ = 5.02 TeV calculated at mid-rapidity [163]. . . . . 197

Figure(6.6) The total decay width $\Gamma_{\rm D}$ as a function of transverse momentum ($p_{\rm T}$) for J/$\psi$ (upper left), $\psi$(2S) (upper right), $\Upsilon$(1S) (lower left), and $\Upsilon$(2S) (lower right) in Pb–Pb collisions at $\sqrt{s_{\rm NN}}$ = 5.02 TeV. Results are presented for three different temperatures, such as $T$ = 0.400 GeV (red dotted dashed line), $T$ = 0.300 GeV (blue dashed line), and $T$ = 0.175 GeV (green solid line), with the circulation parameter $C$ = 0 fm [161]. . . . . 202

Figure(6.7) The total decay width $\Gamma_D$ as a function of transverse momentum ($p_T$) for J/$\psi$ (upper), and $\psi$(2S) (lower) in Pb–Pb collisions at $\sqrt{s_{NN}}$ = 5.02 TeV for three different spin projections $m_j$ = 1 (red dotted dashed line), $m_j$ = 1 (blue dashed line), $m_j$ = 1 (green solid line) states with the circulation parameter $C$ = 1 fm. The upper (lower) left and right panels present the J/$\psi$ ($\psi$(2S)) decay width for two different temperatures: $T$ = 0.400 GeV and 0.175 GeV, respectively [161]. . . 204

Figure(6.8) The total decay width $\Gamma_D$ as a function of transverse momentum ($p_T$) for $\Upsilon$(1S) (upper), and $\Upsilon$(2S) (lower) in Pb–Pb collisions at $\sqrt{s_{NN}}$ = 5.02 TeV for three different spin projections $m_j$ = 1 (red dotted dashed line), $m_j$ = 1 (blue dashed line), $m_j$ = 1 (green solid line) states with the circulation parameter $C$ = 1 fm. The upper (lower) left and right panels present the $\Upsilon$(1S) ($\Upsilon$(2S)) decay width for two different temperatures: $T$ = 0.400 GeV and 0.175 GeV, respectively [161]. . . 205

Figure(6.9) The spin alignment observable $\rho_{00}$ as a function of charged particle multiplicity ($\langle dN_{ch}/d\eta \rangle$) for J/$\psi$ (upper left), $\psi$(2S) (upper right), $\Upsilon$(1S) (lower left), and $\Upsilon$(2S) (lower right) in Pb–Pb collisions at $\sqrt{s_{NN}}$ = 5.02 TeV integrated in the transverse momentum range 1< $p_T$ < 30 GeV/c for different values of the circulation parameter, $C$ [161]. . . . . 208

Figure(6.10) The spin alignment observable $\rho_{00}$ as a function of transverse momentum ($p_T$) for J/$\psi$(1S) (left panel) and $\psi$(2S) (right panel) in Pb–Pb collisions at $\sqrt{s_{NN}}$ = 5.02 TeV for various values of the circulation parameter, $C$, in two extreme multiplicity classes[161]. . . . . 212

Figure(6.11) The spin alignment observable $\rho_{00}$ as a function of transverse momentum ($p_T$) for $\Upsilon$(1S) (left panel) and $\Upsilon$(2S) (right panel) in Pb–Pb collisions at $\sqrt{s_{NN}}$ = 5.02 TeV for various values of the circulation parameter, $C$, in two extreme multiplicity classes [161]. . . . . 213

Figure(7.1) Temperature T (left), viscous term $\Phi$ (middle) and vorticity $\omega$ (right) as a function of time $\tau$ with the initial conditions: T = 0.35 GeV, $\tau_0$ = 0.2 fm, $\omega_0$ = 5.0 fm$^{-1}$. For $T_{Ideal}$; $\omega = 0$ and $\Phi = 0$. For $T_{SO}$; $\omega = 0$ but $\Phi \neq 0$. For $T^{\omega}_{SO}$; $\omega \neq 0$ but $\Phi = 0$. In $\Phi$ plot, $\omega = 0$ and in $\omega$ plot, $\Phi = 0$ [270]. The notations used in this figure are the same as in Ref. [270]. . . . . 223

Figure(7.2) Temperature T (left), viscous term $\Phi$ (middle) and vorticity $\omega$ (right) as a function of time $\tau$ with the same initial conditions as Fig. 7.1 [164]. . . . . 224

Figure(7.3) The temperature (T), and vorticity ($\omega$) are plotted as a function of time $\tau$ in the left and right panel, respectively, with the initial conditions: **T = 0.35 GeV, $\tau_0$ = 0.3 fm, $\omega_0$ = 5.0 fm$^{-1}$, $\Phi_0$ = 0.053 GeV$^4$**. In temperature plot, For $T_{Ideal}$; $\omega = 0$, $\Phi = 0$, $B = 0$. For $T_{SO}$; $\omega = 0$, $\Phi \neq 0$, $B = 0$. For $T^{\omega}_{SO}$; $\omega \neq 0$, $\Phi = 0$, $B = 0$. For $T^{\omega}_{SO-\Phi}$; $\omega \neq 0$, $\Phi \neq 0$, $B = 0$. For $T^{\omega+B(\tau)}_{SO}$; $\omega \neq 0$, $\Phi \neq 0$, and magnetic field is changing with time, B($\tau$). For $T^{\omega+B}_{SO}$; $\omega \neq 0$, $\Phi \neq 0$, and magnetic field is constant. In $\omega$ plot have the same meaning of notations as temperature plot [164]. . . . . 227

Figure(7.4) (Left) The global vorticity $\Omega$ as a function of collision centrality for $\Lambda$, $\Xi^-$, $\bar{\Xi}^+$, $\Omega^-$, and $\bar{\Omega}^+$ obtained in Pb+Pb collisions at mid-rapidity ($|y| < 0.5$) for $\sqrt{s_{NN}}$ = 2.76 TeV. (Right) $\Omega$ as a function of center of mass energies $\sqrt{s_{NN}}$ for $\Lambda$, and $\bar{\Lambda}$ obtained in Au+Au and Pb+Pb collisions at mid-rapidity ($|y| < 0.5$) for 30-40% and 20-40% centrality classes, respectively [280]. . . . . 229

Figure(7.5) The global spin polarization of $\Lambda$ hyperons as a function of transverse momentum ($p_{\rm T}$) for a rotating viscous medium with a time-varying magnetic field (magenta), and without a magnetic field (blue) [164]. The theoretical results are compared with the ALICE experimental measurement in Pb+Pb collisions at $\sqrt{s_{\rm NN}}$ = 2.76 and 5.02 TeV at (15-50)% collision centrality [69]. . . . . 233

Figure(7.6) The variation of Debye mass ($m_D$) as a function of magnetic field ($eB$) (left panel), baryon chemical potential ($\mu_B$) (middle panel), and anisotropic parameter ($\xi$) (right panel) for three different values of temperatures, i.e T = 200 MeV, T=250 MeV, and T = 300 MeV [159]. 237

Figure(7.7) The variation of $\Lambda$ hyperon polarization ($P_\Lambda$) as a function of transverse momentum ($p_{\rm T}$) due to recombination (solid line) and the fragmentation (dashed line) process of hadronization in the presence of a magnetic field ($eB$) (left panel), baryon chemical potential ($\mu_B$) (middle panel), and anisotropic parameter ($\xi$) (right panel) at temperature T = 200 MeV [159]. . . . . 238

Figure(7.8) The variation of baryon polarization as a function of transverse momentum ($p_{\rm T}$) in the recombination (solid line) and fragmentation (dashed line) processes of hadronization due to the magnetic field ($eB$) (left panel), baryon chemical potential ($\mu_B$) (middle panel), and anisotropic parameter ($\xi$) (right panel) at temperature T = 200 MeV [159]. . . . . 239

Figure(7.9) The variation of hyperon polarization as a function of transverse momentum due to magnetic field (left panel), baryon chemical potential (middle panel), and anisotropic parameter (right panel) at temperature T = 200 MeV [159]. The results are compared with STAR measurements taken from Refs. [54, 59]. The statistical and systematic uncertainties of the experimental data points are within the marker size. . . . . 243

Figure(7.10) The upper left panel shows the longitudinal component of $\Lambda$ and $\bar{\Lambda}$ polarization ($P_z$) as a function of azimuthal angle ($\phi$) obtained from ECHO-QGP model simulation for $\sqrt{s_{\rm NN}} = 5.02$ TeV and $\sqrt{s_{\rm NN}} =$ 200 GeV in Pb+Pb and Au+Au collisions, respectively [160]. The upper right panel shows $P_z$ as a function of $\phi$ obtained from ECHO-QGP, EPOS4, AMPT model simulation for $\sqrt{s_{\rm NN}} = 5.02$ TeV in Pb+Pb collisions [160]. The lower left and right panel shows $P_z$ as a function of collision centrality and transverse momentum ($p_{\rm T}$) obtained from ECHO-QGP, EPOS4, and AMPT model. . . . . 253

Figure(7.11) The upper panel shows the variation of spin alignment of the $\phi$ vector meson as a function of transverse momentum due to the magnetic field (left panel) and the anisotropic parameter (right panel) at temperature T = 200 MeV [159]. The lower panel shows the variation of spin alignment of $\phi$, $K^{*0}$, and $\rho$ vector mesons. The results are compared with STAR measurements taken from Ref. [62]. . . . . 256

Figure(1) cos$\theta$ differential signal extraction for J/$\psi$ using CB2+RatioVWG function for $1 < p_{\rm T} < 4$ GeV/c in Collins-Soper reference frame [229]. 276

Figure(2) cos$\theta$ differential signal extraction for J/$\psi$ using CB2+RatioVWG function for $4 < p_{\rm T} < 8$ GeV/c in Collins-Soper reference frame [229]. 277

Figure(3) cos$\theta$ differential signal extraction for J/$\psi$ using CB2+VDW function for $0 < p_{\rm T} < 1$ GeV/c (top two rows), and $8 < p_{\rm T} < 15$ GeV/c (bottom four rows) in Collins-Soper reference frame [229]. . . 278

Figure(4) cos$\theta$ differential signal extraction for J/$\psi$ using CB2+RatioVWG function for $1 < p_{\rm T} < 4$ GeV/c in helicity reference frame [229]. . . . 279

Figure(5) cos$\theta$ differential signal extraction for J/$\psi$ using CB2+RatioVWG function for $4 < p_{\rm T} < 8$ GeV/c in helicity reference frame [229]. . . . 280

Figure(6) cos$\theta$ differential signal extraction for J/$\psi$ using CB2+VWG function for $0 < p_{\mathrm{T}} < 1$ GeV/c (top two rows), and $8 < p_{\mathrm{T}} < 15$ GeV/c (bottom four rows) in helicity reference frame [229]. . . . . 281
Figure(7) J/$\psi$ mass as a function of $\cos\theta$ (top), $|\phi|$ (middle), and $\tilde{\phi}$ (bottom) in Collins-Soper (left) and helicity (right) frames for $0 < p_{\mathrm{T}} < 15$ GeV/c [229]. . . . . 282
Figure(8) J/$\psi$ width as a function of $\cos\theta$ (top), $|\phi|$ (middle), and $\tilde{\phi}$ (bottom) in Collins-Soper (left) and helicity (right) frames for $0 < p_{\mathrm{T}} < 15$ GeV/c [229]. . . . . 283
Figure(9) J/$\psi$ raw yield as a function of cos$\theta$ in CS and HE frame. . . . 284
Figure(10) J/$\psi$ raw yield as a function of $\phi$ in CS and HE frame. . . . . 285
Figure(11) J/$\psi$ raw yield as a function of $\tilde{\phi}$ in CS and HE frame. . . . . 286
Figure(12) cos$\theta$ differential signal extraction for $2 < p_{\mathrm{T}} < 4$ GeV/c in CS [233]. . . . . 287
Figure(13) cos$\theta$ differential signal extraction for $2 < p_{\mathrm{T}} < 4$ GeV/c in HE [233]. . . . . 287
Figure(14) cos$\theta$ differential signal extraction for $6 < p_{\mathrm{T}} < 10$ GeV/c in CS [233]. . . . . 288
Figure(15) cos$\theta$ differential signal extraction for $6 < p_{\mathrm{T}} < 10$ GeV/c in HE [233]. . . . . 288
Figure(16) $\phi$ differential signal extraction for $2 < p_{\mathrm{T}} < 4$ GeV/c in CS [233]. 289
Figure(17) $\phi$ differential signal extraction for $2 < p_{\mathrm{T}} < 4$ GeV/c in HE [233]. 289
Figure(18) $\phi$ differential signal extraction for $4 < p_{\mathrm{T}} < 6$ GeV/c in CS [233]. 290
Figure(19) $\phi$ differential signal extraction for $4 < p_{\mathrm{T}} < 6$ GeV/c in HE [233]. 290
Figure(20) $\phi$ differential signal extraction for $6 < p_{\mathrm{T}} < 10$ GeV/c in CS [233]. 291
Figure(21) $\phi$ differential signal extraction for $6 < p_{\mathrm{T}} < 10$ GeV/c in HE [233]. 291
Figure(22) $\tilde{\phi}$ differential signal extraction for $2 < p_{\mathrm{T}} < 4$ GeV/c in CS [233]. 292
Figure(23) $\tilde{\phi}$ differential signal extraction for $2 < p_{\mathrm{T}} < 4$ GeV/c in HE [233]. 292
Figure(24) $\tilde{\phi}$ differential signal extraction for $4 < p_{\mathrm{T}} < 6$ GeV/c in CS [233]. 293

Figure(25) $\tilde{\phi}$ differential signal extraction for $4 < p_{\mathrm{T}} < 6$ GeV/c in HE [233].293
Figure(26) $\tilde{\phi}$ differential signal extraction for $6 < p_{\mathrm{T}} < 10$ GeV/c in CS [233].294
Figure(27) $\tilde{\phi}$ differential signal extraction for $6 < p_{\mathrm{T}} < 10$ GeV/c in HE [233].294
Figure(28) J/$\psi$ mass as a function of $\cos\theta$ (top), $|\phi|$ (middle), and $\tilde{\phi}$ (bottom) in Collins-Soper (left) and helicity (right) frames for $0 < p_{\mathrm{T}} <$ 15 GeV/c [233]. . . . . 295
Figure(29) J/$\psi$ width as a function of $\cos\theta$ (top), $|\phi|$ (middle), and $\tilde{\phi}$ (bottom) in Collins-Soper (left) and helicity (right) frames for $0 < p_{\mathrm{T}} <$ 10 GeV/c [233]. . . . . 296
Figure(30) J/$\psi$ raw yield as a function of cos$\theta$, $\phi$, and $\tilde{\phi}$ in CS and HE frame.297

# Tables

Table4.1 $p_{\mathrm{T}}$ differential CB2 tail parameters obtained from the LHC24 pass1. . . . . 105
Table4.2 Summary of systematic uncertainties on $\lambda_\theta$ for Collins-Soper frame. . . . . 132
Table4.3 Summary of systematic uncertainties on $\lambda_\theta$ for helicity frame.132
Table4.4 $\lambda_\theta$, $\lambda_\phi$, and $\lambda_{\theta\phi}$ as a function of $p_{\mathrm{T}}$ in the Collins–Soper frame. Uncertainties are quoted as statistical and systematic, respectively. . . . . 134
Table4.5 $\lambda_\theta$, $\lambda_\phi$, and $\lambda_{\theta\phi}$ as a function of $p_{\mathrm{T}}$ in the helicity frame. Uncertainties are quoted as statistical and systematic, respectively. 134
Table4.6 Significance (expressed in $\sigma$) of $\lambda_\theta$, $\lambda_\phi$ and $\lambda_{\theta\phi}$ with respect to the no-polarization hypothesis in the Collins–Soper (CS) and helicity (HE) frames. . . . . 134

Table4.7 $p_{\mathrm{T}}$ integrated CB2 tail parameters obtained from LHC25i4. 145
Table4.8 $p_{\mathrm{T}}$ integrated NA60 tail parameters obtained from LHC25i4. 146
Table4.9 $p_{\mathrm{T}}$ integrated CB2 tail parameters obtained from data. . . 147
Table4.10 Summary of systematic uncertainties on $\lambda_\theta$ for Collins-Soper frame. . . . . 160
Table4.11 Summary of systematic uncertainties on $\lambda_\theta$ for helicity frame. 160
Table4.12 $\lambda_\theta$, $\lambda_\phi$, and $\lambda_{\theta\phi}$ as a function of $p_{\mathrm{T}}$ in the Collins–Soper frame. Uncertainties are quoted as statistical and systematic, respectively. . . . . 160
Table4.13 $\lambda_\theta$, $\lambda_\phi$, and $\lambda_{\theta\phi}$ as a function of $p_{\mathrm{T}}$ in the helicity frame. Uncertainties are quoted as statistical and systematic, respectively. 160

Table6.1 The $\langle \frac{dN_{\mathrm{ch}}}{d\eta} \rangle$ values measured for Pb+Pb collisions at $\sqrt{s_{\mathrm{NN}}} =$ 5.02 TeV in $|\eta| < 0.5$ for 11 centrality classes are taken from ALICE experimental data [263]. . . . . 209

# Chapter 1

## Introduction

## 1.1 The Standard Model

The Standard Model (SM) is a gauge theory based on the symmetry group $\mathrm{SU}(3)_C \otimes \mathrm{SU}(2)_L \otimes \mathrm{U}(1)_Y$, which describes the strong, electromagnetic, and weak interactions among the elementary particles of the Universe. In the SM, the fundamental constituents of matter are semi-integer spin particles, known as *fermions*, which interact through the exchange of integer-spin gauge *bosons*–the mediators of the fundamental forces of nature. Fermions are organized into three generations: quarks (u, d), (c, s), (t, b), and leptons ($e^-$, $\nu_e$), ($\mu^-$, $\nu_\mu$), ($\tau^-$, $\nu_\tau$), each accompanied by their respective antiparticles. The spin 1 gauge bosons correspond to specific interactions: eight massless gluons ($g$) for the strong force, a massless photon ($\gamma$) for electromagnetism, and three massive bosons, $W^\pm$ and $Z$, for the weak force. The SM is one of the greatest achievements of modern physics, providing an elegant and successful framework for describing the fundamental particles and their interactions. Its success culminated in the discovery of the Higgs boson in 2012, completing the particle content of the theory and validating the mechanism responsible for the generation of particle masses. This thesis focuses on strongly interacting matter under extreme conditions, and henceforth will discuss only the strong interaction section of the SM and related physics.

### 1.1.1 Quantum chromodynamics

Quantum chromodynamics (QCD), the theory of strong interaction, is a non-Abelian gauge field theory that describes the interactions of quarks and gluons via their color quantum numbers. Based on the SU(3) symmetry group, the QCD Lagrangian can be written as

$$\mathcal{L}_{\rm QCD} = -\frac{1}{4} G^{\mu\nu}_a G^a_{\mu\nu} + \sum_f \bar{q}_f \left(i\gamma^\mu D_\mu - m_f\right) q_f, \tag{1.1}$$

where $G^{\mu\nu}_a$ is the gluon field tensor, $q_f$ denotes the quark field, $\gamma^\mu$ represent the Dirac matrices, and $m_f$ is the quark mass, while $a$ and $f$ are gluon color and quark flavor indices. Similar to Quantum Electrodynamics (QED) case, the QCD Lagrangian is demanded to be also invariant under *local* $\mathrm{SU}(3)_C$ transformations, which introduces the covariant derivative $D^\mu \equiv \partial^\mu + i g_s \frac{\lambda^a}{2} G^\mu_a$, where $\lambda^a$ ($a = 1$, 2, ..8) denote the generators of the fundamental representations of the $\mathrm{SU}(3)_C$, and $G^\mu_a$ represent the gluon fields. The gluon field tensor can be decomposed as;

$$G^{\mu\nu}_a = \partial^\mu G^\nu_a - \partial^\nu G^\mu_a - g_s \sum_{b,c=1}^{8} f_{abc} G^{\mu b} G^{\nu c} \tag{1.2}$$

where $f_{abc}$ is the structure constant of $\mathrm{SU}(3)_C$.

Expanding Eq. 1.1, the QCD Lagrangian can be decomposed into several parts

$$\begin{aligned}
\mathcal{L}_{\rm QCD} = & -\frac{1}{4}(\partial^\mu G^\nu_a - \partial^\nu G^\mu_a)(\partial_\mu G^a_\nu - \partial_\nu G^a_\mu) + \sum_f \bar{q}^\alpha_f \left(i\gamma^\mu \partial_\mu - m_f\right) q^\alpha_f \\
& - g_s\, G^\mu_a \sum_f \bar{q}^\alpha_f \gamma_\mu \left(\frac{\lambda^a}{2}\right)_{\alpha\beta} q^\beta_f \\
& + \frac{g_s}{2} f^{abc} (\partial^\mu G^\nu_a - \partial^\nu G^\mu_a) G^b_\mu G^c_\nu - \frac{g_s^2}{4} f^{abc} f_{ade} G^\mu_b G^\nu_c G^d_\mu G^e_\nu
\end{aligned} \tag{1.3}$$

The first line of Eq. 1.3 contains the correct (quadratic) kinetic terms for the different fields, which give rise to their corresponding propagator. The second line of Eq. 1.3 contains the color interaction between quarks and gluons. The third line of Eq. 1.3 carries several important features of the non-Abelian $\mathrm{SU}(3)_C$

color gauge group. The term $G_a^{\mu\nu}G^a_{\mu\nu}$ generates cubic and quartic gluon self-interactions, which are the first and second terms of the third line of Eq. 1.3, respectively. The strength of the interactions is given in terms of a single universal coupling $g_s$, which also appears in the coupling between quarks and gluons. Thus, all interactions are given in terms of a universal coupling $g_s$ that is known as the *strong coupling constant*. It is also written in terms of $\alpha_s = \frac{g_s^2}{4\pi}$.

Unlike QED, where the gauge bosons do not interact with one another, the gauge fields in QCD exhibit self-interactions because the gluons themselves carry color charge, representing one of its most important and distinctive features. This gives rise to a few interesting aspects of QCD, including color confinement and asymptotic freedom, which are discussed below;

1. **Color Confinement**: At large distances (or low momentum scales), a single quark or gluon cannot be isolated from a hadron. Thus, the quarks or gluons are always bound within the color-neutral state of the hadron. In nature, no single quark or gluon is observed. This property of QCD matter is called *color confinement*.

   The QCD vacuum potential between partons (quarks and gluons) is defined as

   $$V_{\mathrm{QCD}}(r) = -\frac{4}{3}\frac{\alpha_s}{r} + \sigma r \tag{1.4}$$

   where $\alpha_s$ is the strong coupling constant and $\sigma$ is the string tension. In Eq. 1.4, the first term describes the short-distance Coulomb-like interaction, whereas the second term gives rise to a linearly increasing confining potential at large distances. Unlike QED, where the electric field strength decreases as the separation between charged particles increases, the color field in QCD becomes increasingly stronger as two color charges are pulled apart. Beyond a certain separation, the energy stored in the color flux tube connecting the charges becomes sufficiently large to produce a quark–antiquark pair from the vacuum. As a result, the formation of new color-

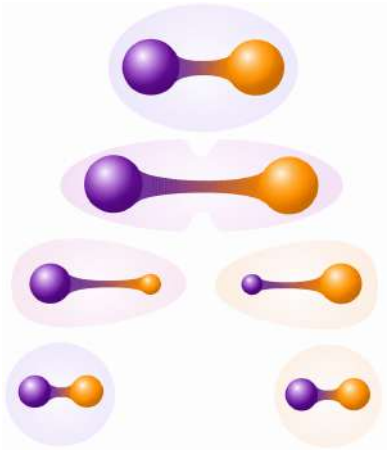


Figure 1.1: Illustration of the color confinement mechanism in QCD.

neutral hadrons is energetically favored over the existence of isolated color charges, as illustrated in Fig. 1.1.

2. **Asymptotic freedom:** At short distances (or high momentum scales), the strong interaction between quarks and gluons becomes relatively weaker. This phenomenon is called *asymptotic freedom*. It means that within a proton or pion, say, the quarks rattle around without interacting much. The strong coupling constant $\alpha_s$ is not truly a constant but depends on the momentum transfer scale ($Q$) involved in the interaction between partons, i.e., $\alpha_s \equiv \alpha_s(Q^2)$. This scale dependence is referred to as the *running coupling constant*, and the corresponding running coupling is given by [1]

$$\alpha_s(Q^2) = \frac{12\pi}{(11N_c - 2N_f)\ln\left(\frac{Q^2}{\Lambda^2_{\rm QCD}}\right)} \tag{1.5}$$

Here, $N_c$, and $N_f$ represent the number of colors and quark flavors, respectively. $\Lambda_{\rm QCD}$ represent the non-perturbative QCD scale parameter. Equation 1.5 indicates that the running coupling constant decreases and approaches zero asymptotically, with increasing momentum transfer ($Q^2$), as illustrated in Fig. 1.2. Consequently, the partons become relatively free from the nucleonic boundary at higher energies.

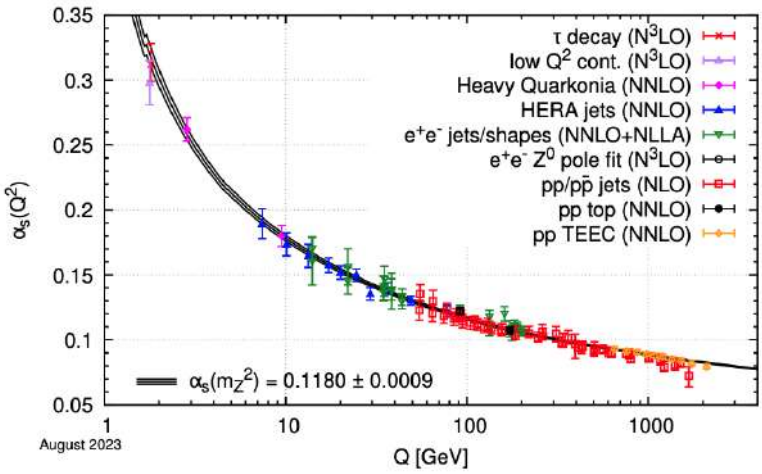



Figure 1.2: Running coupling constant as a function of momentum transfer [1].

## 1.2 Quark-Gluon Plasma

The color confinement property of the strong interaction is responsible for binding quarks and gluons into color-neutral hadrons such as protons, neutrons, and pions. However, according to QCD and cosmological models of the early Universe, this picture was not valid during the first few microseconds after the Big Bang. At that time, the temperature and energy density of the Universe were extremely high, preventing the formation of bound hadronic states. Under such extreme conditions, nuclear matter undergoes a phase transition to a deconfined state of strongly interacting matter exhibiting collective behavior known as the *Quark–Gluon Plasma* (QGP). In this phase, quarks and gluons are no longer confined inside individual hadrons and are free to move within the deconfined region. The study of QGP provides a unique opportunity to investigate the properties of QCD matter at high temperature and density, as well as to gain insight into the evolution of the early Universe.

In the laboratory, the QGP can be created for a very short time by colliding heavy nuclei at ultra-relativistic energies. Such collisions are performed at facilities including the Relativistic Heavy Ion Collider (RHIC) and the Large Hadron

Collider (LHC). The hot and dense medium formed in these collisions rapidly expands and cools, eventually undergoing hadronization to produce the final-state particles, which are detected by various detectors in experiments. Understanding the properties and dynamics of QGP has become one of the central research goals of modern high-energy nuclear physics.

### 1.2.1 The QCD phase diagram

Studying the phase structure of QCD matter under extreme conditions is an active area of research in contemporary high-energy physics from both experimental and theoretical aspects and is usually characterized by temperature ($T$) and baryochemical potential ($\mu_B$). The latter quantity corresponds to the energy required to increase the baryon number of the system by one unit at fixed volume and entropy, and is proportional to the net baryon density of the system. A conceptual representation of the QCD phase diagram is illustrated in Fig. 1.3, where the region explored by LHC experiments and lower collision energy experiments is shown. The points shown in Fig. 1.3 represent the chemical freeze-out parameters, $T_{\rm chem}$ and $\mu_{\rm B,ch}$, extracted from hadron yield measurements at LHC energies (blue) and at lower collision energies (red). In the region where lattice QCD calculations are available, indicated by the green band, the confinement (or crossover) temperature is found to be consistent with $T_{\rm chem}$ within uncertainties. This observation suggests that chemical freeze-out occurs at, or shortly after, the hadronization of the deconfined medium. At large $\mu_{\rm B}$, a well-known technical issue of lattice QCD calculations, commonly referred to as the *fermion sign problem* [3], prevents direct first-principle evaluations of thermodynamic observables. Consequently, one must rely on approximate techniques, such as Taylor expansions and analytic continuation methods, to investigate this region of the QCD phase diagram [4, 5]. These studies suggest the existence of a first-order phase transition at high baryon densities, which is expected to terminate at a

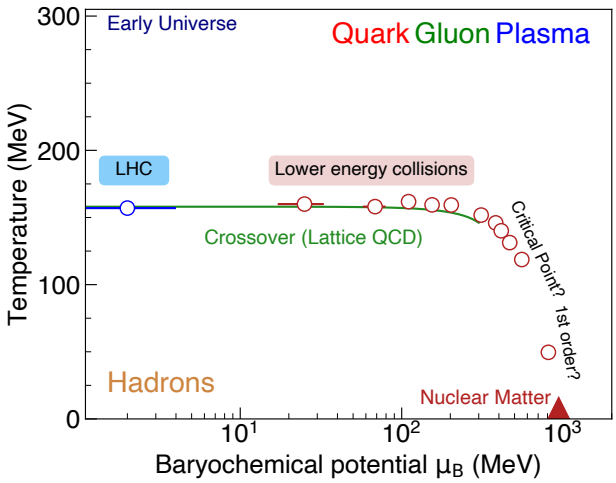



Figure 1.3: Schematic representation of QCD phase diagram in $T - \mu_B$ plane [2].

Critical End Point (CEP) as $\mu_B$ decreases [6, 7]. Thus, exploring this region of the phase diagram is of considerable importance for understanding the properties of strongly interacting matter under extreme conditions.

### 1.2.2 Heavy ion collisions

Ultra-relativistic heavy-ion collisions provide a unique environment for studying strongly interacting QCD matter under extreme conditions of temperature and energy density, where the formation of the QGP is expected. These collisions create an extended strongly interacting medium with a spatial size significantly larger than the characteristic scale of the strong interaction ($\sim$ 1 fm) and a lifetime sufficiently long for collective phenomena to develop, enabling detailed investigations of the properties and evolution of deconfined QCD matter. Figure 1.4 illustrates a schematic space–time evolution of a heavy-ion collision. A nucleus–nucleus collision is characterized by the impact parameter ($b$), defined as the transverse distance between the centers of the two colliding nuclei. The impact parameter serves as a measure of the collision centrality and is commonly used to classify collisions into the following categories:

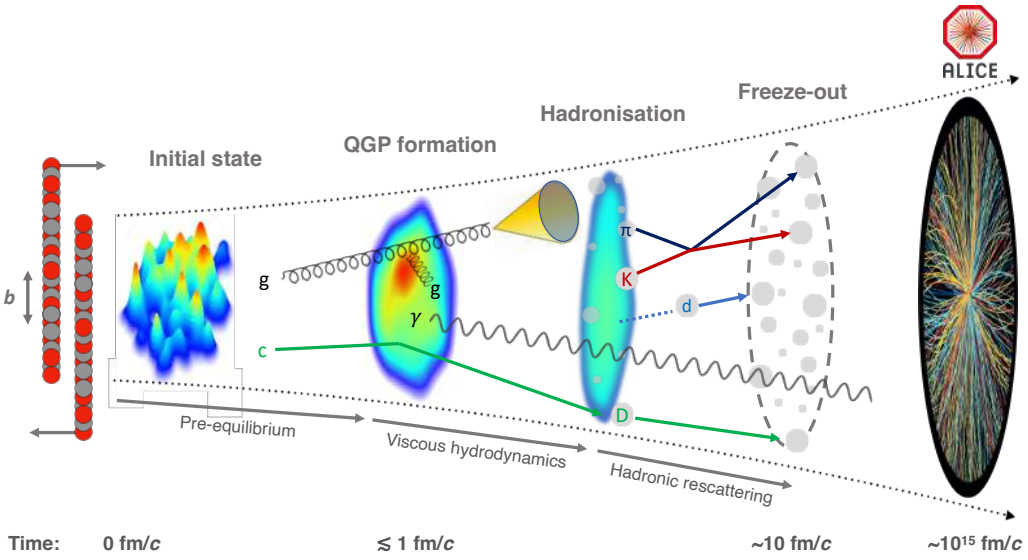



Figure 1.4: Schematic evolution of the heavy-ion collisions at LHC energies [2].

- *Peripheral collisions*: These correspond to large values of the impact parameter, where only a small fraction of the total nucleons participate in the collision. Consequently, the overlap region is relatively small, leading to lower particle production and referred to as a low charged-particle multiplicity class.

- *Central collisions*: These occur at small impact parameters, where a large number of nucleons participate in the collision. The resulting overlap region is relatively larger, producing a hot and dense medium with high particle yields and referred to as a high charged-particle multiplicity class.

In heavy-ion collision experiments, those nucleons that participate in the collisions are called *participants*, and those nucleons that do not participate in the collisions are called *spectators*. The centrality of the collision is determined by the number of binary collisions $N_{\text{coll}}$ and the number of participating nucleons $N_{\text{part}}$. These quantities can not be directly measured in an experiment, but can be estimated using phenomenological models like the *Glauber model*. Notably, these quantities

play a crucial role in determining the initial geometry of the collision and strongly influence the subsequent space–time evolution and dynamics of the produced medium. Although the entire evolution of the produced matter traverses various phases, it is broadly classified into three phases as shown in Fig. 1.4, which are discussed below:

- **Pre-equilibrium phase** $(0 < \tau \lesssim \tau_0 \approx 1)$ fm/(c)): This stage begins immediately after the collision ($\tau = 0$) and is characterized by the production of highly energetic partons through hard-scattering processes. Such processes involve large momentum transfers ($Q^2$), for which the strong coupling constant ($\alpha_s$) becomes sufficiently small, allowing the use of perturbative QCD calculations. During this phase, the produced partons undergo multiple scatterings and interactions, driving the system toward local thermal equilibrium. The time at which thermalization is achieved is commonly referred to as the thermalization time ($\tau_0$).

- **QGP phase** ($\tau_0 < \tau \leq \tau_{\rm ch} \approx$ a few fm/c): After local thermal equilibrium is achieved, the hot and dense strongly interacting medium undergoes rapid expansion driven by the large pressure gradients between the medium and the surrounding vacuum. This stage is commonly described within the framework of relativistic viscous hydrodynamics, whose governing equations will be discussed in Chapter 5. As the system expands, its temperature and energy density decrease. When the temperature approaches the critical temperature, commonly referred to as the chemical freeze-out temperature ($T_{\rm ch}$), the deconfined quarks and gluons begin to hadronize, leading to the formation of hadrons. The corresponding time at which hadronization occurs is known as the chemical freeze-out time ($\tau_{\rm ch}$). On the other hand, chemical freeze-out is defined as the stage when the relative abundances of different particle species are fixed. The interval between the thermalization time, $\tau_0$, and the chemical freeze-out time, $\tau_{\rm ch}$, is known as the *QGP*

*lifetime*. The evolution and duration of this deconfined phase are strongly governed by the properties of the medium, such as its viscosity, vorticity, electromagnetic fields, equation of state (EoS), etc.

- **Hadronic phase** ($\tau_{\rm ch} < \tau \leq \tau_f \approx 10$ fm/c): The formation of new hadrons via hadronization occurs through two primary mechanisms: *fragmentation* and *coalescence* (or recombination). In the fragmentation process, high-$p_{\rm T}$ partons hadronize by producing high-$p_{\rm T}$ hadrons, whereas in the coalescence mechanism, nearby low-$p_{\rm T}$ quarks combine to form hadrons. Up to the hadronization stage, the constituent partons undergo both elastic and inelastic interactions. After hadronization, inelastic hadronic interactions gradually cease, fixing the relative abundances of different particle species at chemical freeze-out. However, elastic scatterings continue to redistribute momentum among the hadrons. The stage at which these elastic interactions also cease is known as the *kinetic freeze-out*.

- **Free streaming** ($\tau \geq 10$ fm): After kinetic freeze-out, the mean free path is greater than the system size, and the momentum spectra of the particles get frozen. The particle undergoes free-streaming and is detected by the detectors.

## 1.3 Experimental probes of QGP

The strongly interacting QGP produced in ultra-relativistic heavy-ion collisions is a transient state of matter with an extremely short lifetime, surviving for only a few fm/c. Therefore, the direct observation of this deconfined state of matter is not possible. Nevertheless, a wide range of experimental observables is sensitive to its formation and evolution, providing valuable information about the properties of the medium created in heavy-ion collisions. Owing to the diverse physical processes involved, QGP observables are commonly categorized into *soft*

and *hard* probes. In the following sections, the main experimental signatures of QGP formation and the corresponding measurements will be discussed, with particular emphasis on results obtained at the LHC and RHIC energies.

### 1.3.1 Soft probes

The vast majority of particles produced in heavy-ion collisions originate from soft processes. For example, in Au–Au collisions at RHIC, approximately 99.5% of the produced particles have transverse momenta $p_{\mathrm{T}} \leq 1$ GeV/c. The yields of these low-$p_{\mathrm{T}}$ particles are generally observed to scale approximately with the number of participating nucleons in the collision. In the following sections, several key soft probes of the hot and dense medium are discussed, including direct photon production, particle spectra, anisotropic flow, and strangeness enhancement.

#### 1.3.1.1 Direct photons

Direct photons are among the most powerful probes for investigating the medium formed in heavy-ion collisions. They are defined as photons that do not originate from the decays of hadrons and are produced throughout the entire evolution of the collision. Owing to their electromagnetic nature, direct photons barely interact with the surrounding medium and therefore escape largely unaffected, carrying information from the stage at which they were produced. In particular, thermal photons emitted by the QGP and the subsequently formed hadronic matter provide valuable insight into the temperature, thermodynamic properties, and space–time evolution of the medium. These thermal photons predominantly contribute to the low-$p_{\mathrm{T}}$ ($p_{\mathrm{T}} \leq 4$ GeV/c) region of the direct-photon spectrum. Figure 1.5 depicts the measurement of the direct photon spectrum in Pb–Pb and Au–Au collisions at $\sqrt{s_{\mathrm{NN}}} = 2.76$ TeV [8] and $\sqrt{s_{\mathrm{NN}}} = 200$ GeV [9, 10], respectively, in the (0-20)% (left) and (20-40)% (right) centrality classes. The hydrodynamical model calculations for Pb–Pb collisions were found to be con-

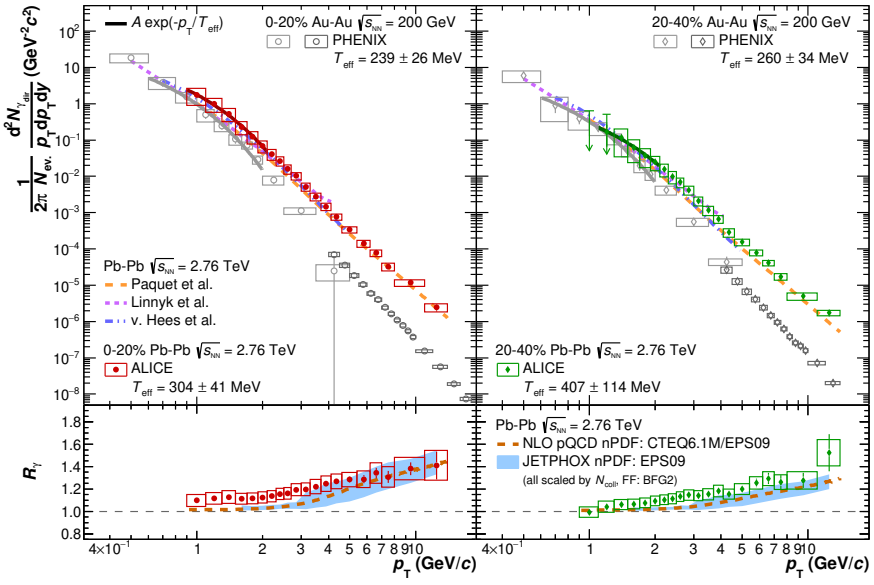



Figure 1.5: Direct photon spectra (top) and direct photon excess $R_\gamma$ (bottom) measured in Pb–Pb collisions at $\sqrt{s_{\rm NN}} = 2.76$ TeV [8] and $\sqrt{s_{\rm NN}} = 200$ GeV [9, 10] in the (0-20)% (left) and (20-40) % (right) centrality classes.

sistent with data. The region that is dominated by thermal direct photons is fitted by an exponential function ($f(p_{\rm T}) \propto \exp(-p_{\rm T}/T_{\rm eff})$) to obtain the effective temperature $T_{\rm eff}$. For central and semi-central Pb–Pb collisions, the fits lead to $T_{\rm eff} = 304 \pm 41$ MeV and $T_{\rm eff} = 407 \pm 114$ MeV, respectively. Comparing these values with Au–Au collisions reported in Fig. 1.5, an increase in the effective temperature is found from RHIC to LHC energies.

#### 1.3.1.2 Particle spectra

The *transverse momentum spectra* of the identified hadrons serve as an important probe of the thermal and collective properties of the medium created in heavy-ion collisions. The $p_{\rm T}$-spectra of produced particles by a system in thermal equilibrium follow a Boltzmann-Gibbs type of distribution;

$$\frac{d^2N}{dp_{\rm T}dy} \propto \exp\left(\frac{-\sqrt{m^2+p_{\rm T}^2}}{T}\right), \tag{1.6}$$

where $T$ is the inverse slope parameter, and is obtained from the fit of the transverse momentum distribution of the various hadrons. It is referred to as the effective temperature of the system, which carries contributions from both the random thermal motion and the collective radial flow, and is related to the kinetic freeze-out temperature $T_{\rm kin}$ via the relation

$$T = T_{\rm kin} + \frac{1}{2} m \langle v_T \rangle^2 \tag{1.7}$$

Where $\langle v_T \rangle$ is the average radial transverse flow velocity arising due to the pressure gradients generated by the compression and/or the heating of the nuclear matter in the collision. The collective radial expansion of the medium imparts a mass-dependent boost to the produced particles, resulting in a flattening of the $p_{\rm T}$ spectra, particularly in the low-$p_{\rm T}$ regions. This effect is clearly visible in the left panel of Fig. 1.6, where the $p_{\rm T}$ spectra measured in the most central (0–5)% Pb–Pb collisions are significantly flatter than those observed in peripheral (80–90)% collisions at $\sqrt{s_{\rm NN}} = 2.76$ TeV. The flatter spectral shapes in central collisions indicate the presence of stronger collective radial flow arising from the larger pressure gradients developed in the system.

To quantify the collective hydrodynamic expansion of the system, the identified hadron $p_{\rm T}$ spectra are commonly analyzed using the Boltzmann-Gibbs Blast-Wave (BG-BW) model. The corresponding fits to Pb–Pb collision data at $\sqrt{s_{\rm NN}} =$ 2.76 and 5.02 TeV provide estimates of the kinetic freeze-out temperature, $T_{\rm kin}$, and the average radial flow velocity, $\langle \beta_{\rm T} \rangle$, and are presented in the right panel of Fig. 1.6, illustrating the interplay between the thermal motion and collective expansion of the medium at kinetic freeze-out.

#### 1.3.1.3 Strangeness enhancement

Enhanced production of particles with strangeness in heavy-ion collisions with respect to *pp* collisions, known as *strangeness enhancement*, is originally proposed as an indirect signature of the formation of QGP [14–16]. Before the collisions, the

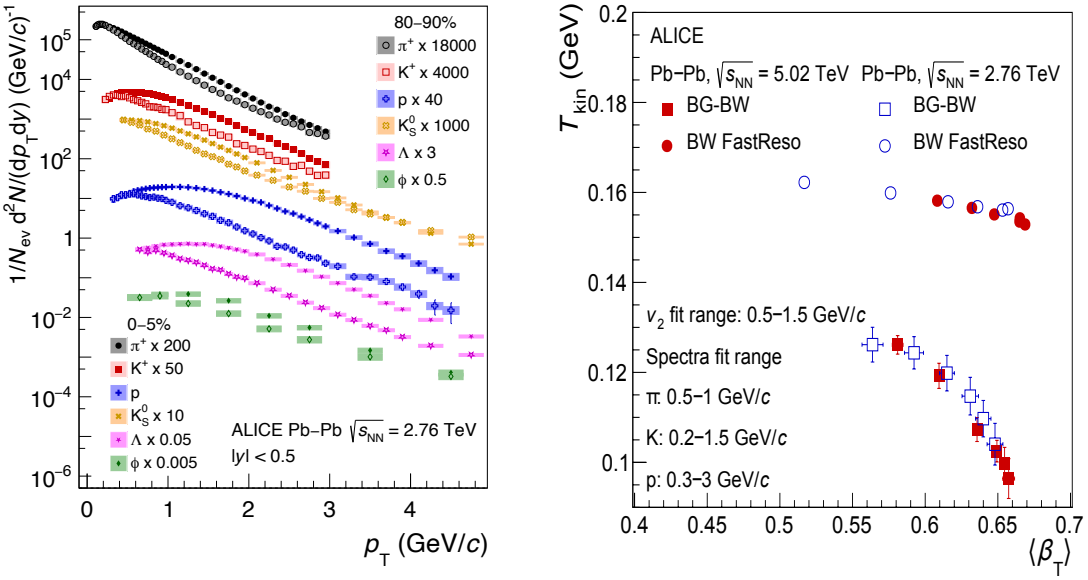



Figure 1.6: (Left) The transverse momentum distribution of $\pi^{\pm}$, $K^{\pm}$, p [11], $K^0_S$, and $\Lambda$ [12], and the $\phi$ mesons [13] for (0-5)% and (80-90)% centrality interval in Pb–Pb collisions at $\sqrt{s_{\rm NN}} = 2.76$ TeV. (Right) Blast wave parameters of the kinetic freeze-out parameters $T_{\rm kin}$ and average radial flow velocity $\langle\beta_T\rangle$ obtained from the simultaneous fits to the $\pi^{\pm}$, $K^{\pm}$, p spectra and $v_2$ for the two models in Pb–Pb collisions.

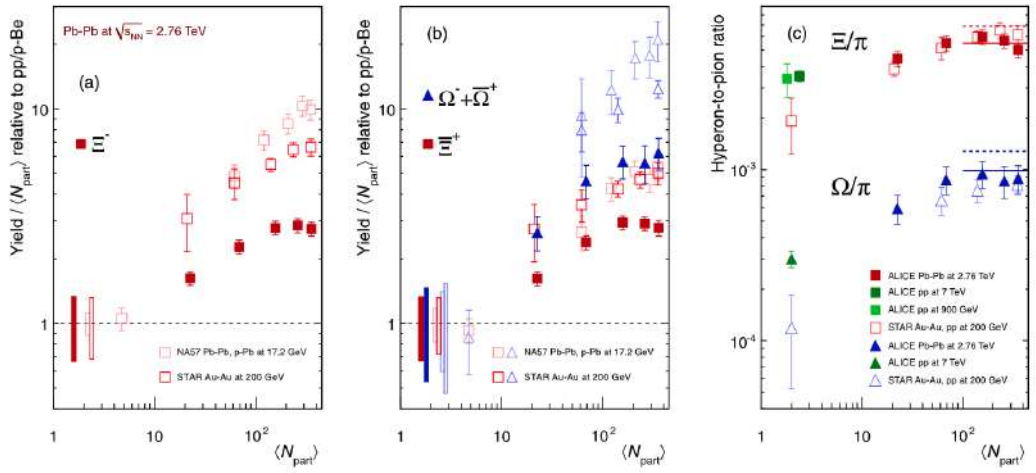



Figure 1.7: (a,b) Enhancements of multi-strange hadrons as a function of the mean number of participants $\langle N_{\text{part}} \rangle$ in AA collisions with pp or p-Be as reference in the rapidity range $|y| < 0.5$ in ALICE (full symbols), RHIC and SPS (open symbols) [17]. (c) Hyperon-to-pion ratios as a function of $\langle N_{\text{part}} \rangle$ for A–A and pp collisions at LHC and RHIC energies. The lines represent the thermal model predictions from [18] (full line), and [19] (dashed line).

colliding nuclear matter contained only up and down quarks, and strange quarks were not present as valence quarks. In the early state after the collision, the strange quarks are produced via hard perturbative processes via flavor creation ($q\bar{q} \to s\bar{s}$), gluon fusion ($gg \to s\bar{s}$), and flavor excitation ($gs \to gs$, $qs \to qs$). These processes are responsible for the strange particle production with higher transverse momenta after the subsequent hadronization. In general, in a system that goes through the QGP phase, the temperature of the QGP phase is much greater than the strange quark mass $m_s$, i.e., $T \gg m_s$; thus, an abundance of thermal production of strange quarks can occur in the medium. Hence, when comparing the production of strange or multi-strange hadrons, a system with QGP should show an enhancement feature larger than unity compared to the scenario without a QGP. This phenomenon is experimentally observed at SPS, RHIC, and LHC energies, and illustrated in Figure 1.7. Interestingly, the enhancement factor

depends upon the strangeness content of the particles, i.e., particles with more strangeness quantum number show higher enhancement compared to particles with less strangeness quantum number.

#### 1.3.1.4 Anisotropic flow

Anisotropic flow is one of the major contributors to the collectivity of the system in heavy-ion collisions. It is mostly driven by the collision geometry of the overlap region and the subsequent pressure gradients generated during the evolution of the medium. The azimuthal anisotropies in the particle production are a key signature of collective motion and provide strong evidence for the rapid thermalization of the system. Measurements of anisotropic flow therefore offer valuable insight into the initial conditions, transport properties, and hydrodynamic evolution of the QGP. The anisotropic flow of the system can be quantified by the coefficients of the Fourier expansion of the azimuthal distribution of particles in the final state, given as follows.

$$\frac{dN}{d\phi} \propto 1 + 2\sum_{i=1}^{\infty} v_n \cos[n(\phi - \psi_n)] \tag{1.8}$$

Here, $v_n$ and $\psi_n$ are the $n^{\text{th}}$ order anisotropic flow coefficients and reaction plane angles, respectively. The *reaction plane* is defined as the plane determined by the impact parameter vector and the beam axis. In Eq. 1.8, $v_1$, $v_2$, $v_3$, and $v_4$, are called *directed, elliptic, triangular*, and *quadriangular flow*, respectively. These Fourier coefficients can be obtained using the formula

$$v_n = \langle \cos[n(\phi - \psi_n)] \rangle \tag{1.9}$$

where the $\langle\rangle$ denotes the average over all particles, summed over all the events. The *directed flow* ($v_1$) characterizes the collective sideward motion of particles relative to the reaction plane and is generally small in symmetric collisions at LHC energies. In non-central collisions, the elliptic shape of the overlap region gives rise to a sizable *elliptic flow* ($v_2$). Higher-order flow coefficients, such as

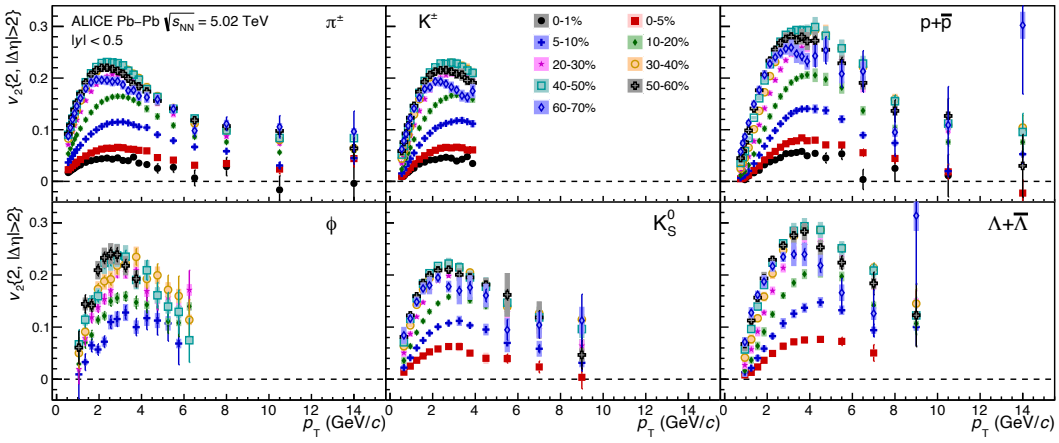



Figure 1.8: $p_{\mathrm{T}}$ dependence of the elliptic flow ($v_2$) for $\pi^{\pm}$, $K^{\pm}$, p+$\bar{p}$, $\phi$, $K^0_S$, $\Lambda+\bar{\Lambda}$ in different centrality classes for Pb–Pb collisions at $\sqrt{s_{\mathrm{NN}}} = 5.02$ TeV [20].

triangular flow ($v_3$) and quadriangular flow ($v_4$), originate primarily from event-by-event fluctuations in the initial geometry and provide important information on the transport properties and thermalization dynamics of the medium. To have an estimate of the flow coefficients in Pb–Pb collisions, the elliptic flow $v_2$ of the light hadrons is shown as a function of $p_{\mathrm{T}}$ in Fig. 1.8 for various centrality classes. Interestingly, the elliptic flow increases with centrality up to (40-50)% for all the species. This is due to the eccentricity of the overlap region increasing with centrality, causing an almost linear increase in $v_2$. However, for peripheral collisions (i.e., (50-60)%, or (60-70)%), the $v_2$ is smaller than that of previous centrality, suggesting the system formed has a relatively shorter lifetime.

### 1.3.2 Hard probes

Hard probes are produced in processes involving large momentum transfer and are therefore generated at very early stages of the collision. Their production cross sections are relatively small and can generally be calculated using perturbative Quantum Chromodynamics (pQCD), owing to the small value of the strong coupling constant at high momentum scales. In heavy-ion collisions, the production

yield of hard probes is expected to scale with the number of binary nucleon–nucleon collisions, making them valuable tools for investigating the properties of the hot and dense medium formed in the collision. In the following sections, several key hard probes of the hot and dense medium are discussed, including quarkonium suppression and jet quenching.

#### 1.3.2.1 Quarkonium suppression

Quarkonia are bound states of a heavy quark and its corresponding anti-quark. Depending on the quark flavor, they are classified as *charmonia* ($c\bar{c}$) and *bottomonia* ($b\bar{b}$). Owing to their large masses and early production in hard-scattering processes, quarkonia serve as important probes of the QGP and provide valuable insight into its properties in heavy-ion collisions. It was recognized that the binding of heavy quark pairs can be significantly modified when quarkonia are immersed in a deconfined medium. The high density of free color charge in the QGP leads to the screening of the QCD potential of quarkonia, eventually leading to the dissociation of the quarkonium state in the medium. This phenomenon is known as *quarkonium suppression* and is considered one of the *smoking gun signatures* for the QGP signal [21]. The degree of suppression depends strongly on both the temperature of the medium and the binding energy of the quarkonium state. Consequently, weakly bound excited states are expected to dissociate at lower temperatures than the more tightly bound ground states. This hierarchical melting pattern is commonly referred to as *sequential suppression*. Experimentally, the dissociation of quarkonium states is quantified through the nuclear modification factor, $R_{\mathrm{AA}}$, which is defined as

$$R_{\mathrm{AA}} = \frac{\left(\frac{d^2N}{dydp_{\mathrm{T}}}\right)_{\mathrm{AA}}}{\langle N_{\mathrm{coll}}\rangle \left(\frac{d^2N}{dydp_{\mathrm{T}}}\right)_{pp}} \tag{1.10}$$

The observable $R_{\mathrm{AA}}$ has several important features. A unity value of $R_{\mathrm{AA}}$ represents that heavy-ion collisions are just a linear superposition of $pp$ collisions. If

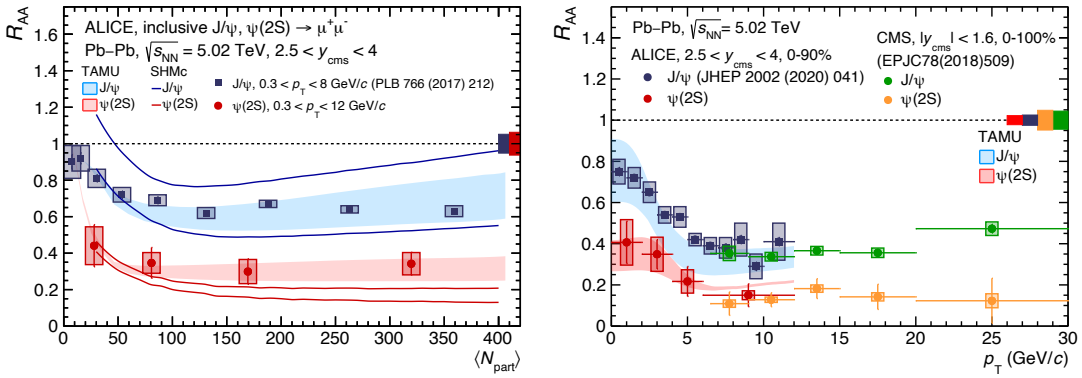



Figure 1.9: (Left) The nuclear modification factor $R_{\rm AA}$ for inclusive J/$\psi$, and $\psi(2S)$ measured in Pb–Pb collisions at $\sqrt{s_{\rm NN}}$ =5.02 TeV as function of $N_{\rm part}$ in the range $2.5 < y < 4.0$ [22]. Prediction from TM-TAMU [23], and SHM [24] are also shown. (Right) The $p_{\rm T}$ dependence of $R_{\rm AA}$ for J/$\psi$, and $\psi(2S)$ measured by ALICE in $2.5 < y < 4.0$ for (0-90)% Pb–Pb collisions [22], are compared with high-p$_{\rm T}$ results in $|y| < 1.6$ and (0–100)% centrality from CMS [25]. Model comparisons are also shown.

$R_{\rm AA}$ <1 indicates a possible hint of medium formation in heavy-ion collisions, as a results particles yield reduces due to medium effects.

The left panel of Fig. 1.9 presents the nuclear modification factor, $R_{\rm AA}$, for inclusive J/$\psi$ and $\psi$(2S) production in Pb–Pb collisions at $\sqrt{s_{\rm NN}}$ = 5.02 TeV. The observed suppression pattern is consistent with the sequential suppression scenario, and no significant centrality dependence is observed for the $\psi$(2S) within the Run 2 uncertainties. The right panel shows a $p_{\rm T}$ dependence of $R_{\rm AA}$ for J/$\psi$, and $\psi(2S)$. The relatively weaker suppression at low-$p_{\rm T}$ can be understood as a direct consequence of the recombination process of charm and anticharm quarks. At higher transverse momenta, both J/$\psi$ and $\psi(2S)$ show a strong suppression up to $p_{\rm T}$ = 30 GeV/c, and agree with measurements reported by the CMS experiment at mid-rapidity.

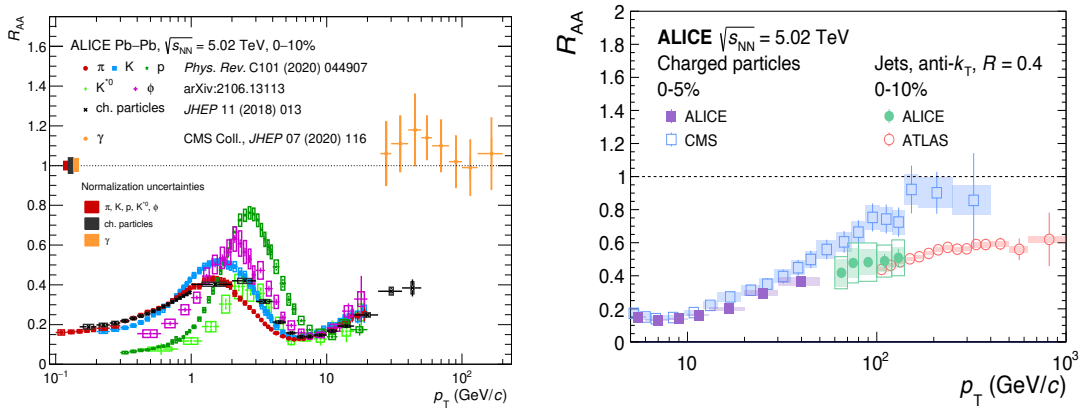



Figure 1.10: (Left) Nuclear modification factor $R_{\mathrm{AA}}$ for charged hadrons in central Pb–Pb collisions at $\sqrt{s_{\mathrm{NN}}} = 5.02$ TeV. (Right) The comparison of $R_{\mathrm{AA}}$ for charged hadrons and jets in different LHC experiments [2].

#### 1.3.2.2 Jet quenching

Energetic, highly virtual partons produced in hard-scattering nuclear collisions undergo fragmentation and hadronization, giving rise to collimated sprays of particles known as jets. These jets interact with the surrounding QGP medium, and their properties and structure get modified while traversing through the medium. The in-medium modification of the jet shower is referred to as *jet quenching*. It has several distinct observable consequences and serves as a multi-messenger for investigating the QGP structure and dynamics. The jets lose energy via *radiative* and *collisional* processes before undergoing hadronization, and their yield is reduced due to the medium interaction. Radiative energy loss is expected to be the dominant mechanism responsible for the suppression of inclusive particle production at high-$p_{\mathrm{T}}$. Similar to quarkonium suppression, the jet quenching is also measured using the same nuclear modification factor $R_{\mathrm{AA}}$. The left panel of Fig. 1.10 shows the $R_{\mathrm{AA}}$ as a function of $p_{\mathrm{T}}$ for light-flavor mesons, protons, and isolated photons in Pb–Pb collisions at $\sqrt{s_{\mathrm{NN}}} = 5.02$ TeV. The measured values of $R_{AA} < 1$ for light-flavor mesons and protons demonstrate the strong

suppression of high-$p_{\mathrm{T}}$ particles due to parton energy loss in the QGP. The right panel of Fig. 1.10 shows that similar suppression patterns are observed by the CMS and ATLAS experiments, further confirming the jet-quenching phenomenon in heavy-ion collisions.

The conventional observables discussed above, encompassing both soft and hard probes of the QGP, may be collectively regarded as the *first-generation probes* of the deconfined medium.

## 1.4 Thesis motivation

As discussed so far, studies related to QGP and heavy-ion collisions provide a unique opportunity to investigate QCD in both its perturbative and non-perturbative regimes. Experimental signatures of QGP formation in heavy-ion collisions, such as strangeness enhancement, jet quenching, and quarkonium suppression, are traditionally established through comparisons with *pp* collisions, which serve as the baseline reference system. Historically, the formation of a QGP in *pp* collisions was considered highly unlikely due to the small system size, and it lacked the necessary conditions for achieving local thermal equilibrium. However, the recent measurements at the LHC have revealed several features in high-multiplicity *pp* collisions that resemble those observed in heavy-ion collisions, including strangeness enhancement and collective flow, as shown in Figs 1.11 and 1.12, respectively [26–30].

Figure 1.11 depicts an alternative way of measuring the strangeness enhancement, complementary to the approach shown in panels (a) and (b) of Fig. 1.7. Instead of comparing strange-hadron yields to those measured in a reference collision system, the enhancement is quantified through the ratio of strange to non-strange particle production. As shown in Fig. 1.11, a pronounced increase in the strange-to-non-strange particle ratio is observed with increasing charged-particle multiplicity in *pp* collisions. Remarkably, this behavior closely resembles that observed in p–Pb

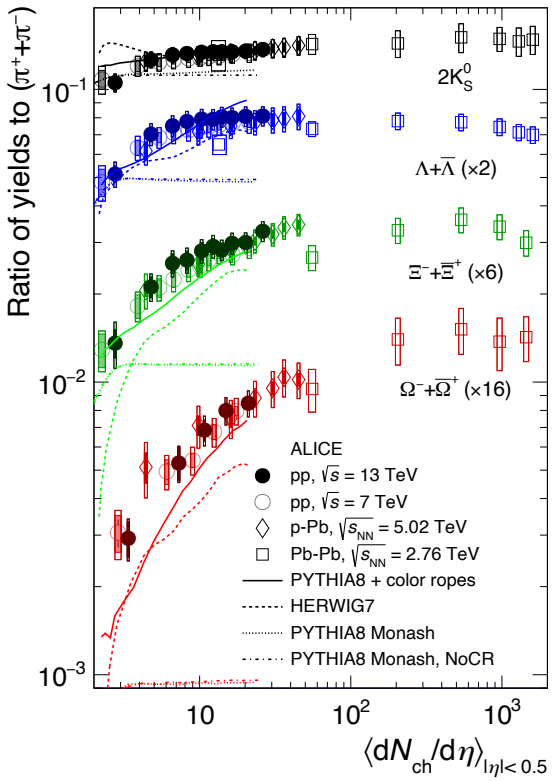



Figure 1.11: $p_{\mathrm{T}}$-integrated yield ratios of strange hadrons to pions as a function of average charged-particle multiplicity density $\langle dN_{\mathrm{ch}}/d\eta \rangle$ in $pp$, p–Pb, Pb-Pb collisions. Different lines represent the prediction obtained from MC generator [26].

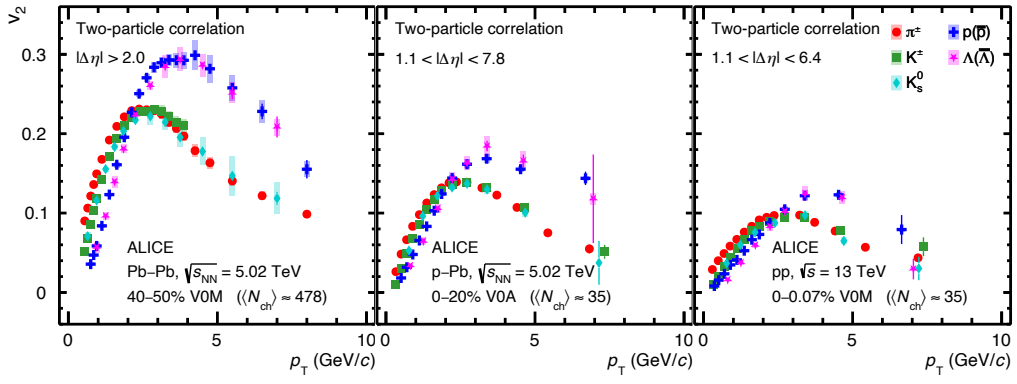



Figure 1.12: Elliptic flow ($v_2$) of mesons ($\pi^{\pm}$, $K^{\pm}$, $K^0_{\mathrm{S}}$) and baryons ($p+\bar{p}$, $\Lambda+\bar{\Lambda}$) in $pp$, p–Pb, Pb-Pb collisions using two-particle correlation method [27].

and Pb–Pb collisions, suggesting the presence of strangeness enhancement even in small collision systems. Furthermore, the right panel of Fig. 1.12 shows a finite value of elliptic flow $v_2$ for mesons and ($\pi^{\pm}$, $K^{\pm}$, $K^0_S$) and baryons ($p+\bar{p}$, $\Lambda+\bar{\Lambda}$) in high multiplicity *pp* collisions. Such collective behavior was traditionally believed in p–Pb (middle panel of Fig. 1.12) and Pb–Pb (right panel of Fig. 1.12) collisions. The observation of a non-zero $v_2$ in high-multiplicity *pp* events therefore provides intriguing evidence for collective dynamics and may indicate the presence of medium-like effects, including possible hydrodynamic behavior, even in small collision systems. At the same time, alternative studies suggest that such phenomena may also originate from other QCD mechanisms unrelated to QGP formation [31, 32]. For instance, different Monte Carlo predictions shown in Fig. 1.11 qualitatively explain the strangeness enhancement feature in *pp* collisions. These observations challenge the conventional interpretation of the existing first-generation QGP probes and the methodologies traditionally used to establish QGP formation. Consequently, they motivate the search for next-generation observables or probes that are independent of baseline assumptions and can provide complementary insights into the properties of strongly interacting matter. In this context, particle spin polarization has emerged as a promising observable, offering a potentially *baseline-independent* and sensitive probe for investigating the properties and dynamics of hot QCD matter.

### 1.4.1 Spin polarization as a probe for QGP

Recent measurements of hyperon spin polarization and vector-meson spin alignment at RHIC and LHC energies have stimulated extensive investigations into the global, local, and transverse spin polarization of hadrons produced in relativistic heavy-ion and hadronic collisions [33–73]. Substantial theoretical progress has been made in understanding the spin polarization phenomena of various hadrons produced in relativistic heavy-ion and hadronic collisions [74–164]. Several mech-

anisms have been proposed in the literature to explain the observed spin polarization of various hadrons in relativistic heavy-ion collisions. Among these, the vorticity field generated in non-central heavy-ion collisions plays a particularly significant role. Various potential sources have been proposed to explain the generation of such a large vorticity in the medium. Among them, the dominant contribution is generally believed to originate from the large initial orbital angular momentum (OAM) carried by the colliding nuclei in peripheral collisions. The total OAM deposited at the collision point is given by $L \simeq bA\sqrt{s_{\rm NN}}/2$, where $b$ denotes the impact parameter, $A$ is the atomic mass number of the colliding nuclei, and $\sqrt{s_{\rm NN}}$ is the center-of-mass energy per nucleon pair. For Au–Au collisions at $\sqrt{s_{\rm NN}} = 200$ GeV, the total OAM is estimated to be of the order of $10^5 - 10^6\,\hbar$, depending on the impact parameter. A fraction of the total initial OAM of the system is transferred to the produced partonic medium, although the exact fraction remains unknown. If a small fraction (of the order of 1%) of this OAM is transferred to the partonic medium, it exerts a huge torque on the system, generating velocity gradients and shear flow within the medium, which subsequently develop into a vortical fluid motion characterized by a non-zero vorticity field of the order $10^{22}$ s$^{-1}$. A pictorial representation of the direction of the OAM, which is along the same direction as the vorticity field, in heavy-ion collisions is shown in Fig. 1.13. The vorticity of the medium can induce quark polarization through spin–orbit coupling. Subsequently, this polarization is transferred to the hadrons formed during the hadronization process [79, 80]. The vorticity field can decay with time and affect the hydrodynamic evolution of the medium. A detailed study on the impact of vorticity on hydrodynamic medium evolution and $\Lambda$ hyperons' spin polarization is presented in Chapter 7.

On the other hand, in addition to the vorticity field, a large magnetic field ( $\sim m_\pi^2 \sim 10^{18}$ G) is also produced in non-central heavy-ion collisions due to the motion of the charged spectators [165]. The magnetic field can interact with the electric charge, and the spin of the quarks leads to quark polarization, and hence

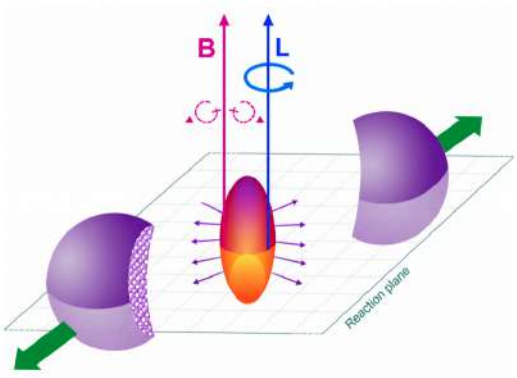



Figure 1.13: Illustration of the direction of the orbital angular momentum ($L$) and magnetic field ($B$) in relativistic heavy-ion collisions

contributes to the final hadron polarization. Interestingly, in relativistic heavy-ion collisions, the magnetic field has the same direction as the direction of OAM, as indicated in Fig. 1.13. Another source of polarization is the inhomogeneous expansion of the medium, resulting in an anisotropic flow in the transverse plane. The anisotropic flow coefficients induce a local spin polarization of the final-state hadrons [55, 118]. Further, the local correlations or fluctuations of the strong vector meson force field could also lead to polarization of vector mesons [131, 152]. Particle production mechanisms can also contribute to the spin polarization of hadrons in hadronic and nuclear collisions. Additionally, the baryon chemical potential, momentum-space anisotropy, thermal shear, temperature gradients, and gradients of the baryon chemical potential all of which may contribute to the observed polarization signals in heavy-ion collisions. Therefore, determining the contribution of each possible source of spin polarization in ultra-relativistic collisions is a complex phenomenon that requires comprehensive theoretical studies quantifying the impact of all these mechanisms separately.

Motivated by these developments, this thesis presents the spin polarization of various baryons and the spin alignment of vector mesons, including light-flavor, charmonium, and bottomonium states, in heavy-ion and hadronic collisions from

both experimental and phenomenological perspectives. The corresponding results and discussions are presented in the following chapters.

## 1.5 Thesis structure

This thesis is organized into eight chapters, the contents of which are summarized below:

- **Chapter 1** provides an introduction to the Standard Model of particle physics, followed by a discussion of the theory of strong interactions, Quantum Chromodynamics. Particular emphasis is placed on two fundamental properties of QCD, namely color confinement and asymptotic freedom. The chapter further introduces the Quark–Gluon Plasma, the primordial state of strongly interacting matter, and discusses its formation and evolution in ultra-relativistic heavy-ion collisions. Experimental signatures of the QGP are classified into two broad categories: soft probes and hard probes. The corresponding experimental evidence is reviewed, with special emphasis on spin polarization as an emerging and novel probe of hot QCD matter.

- **Chapter 2** provides an introduction to the fundamental concepts of spin polarization and spin density matrix of various spin systems. It connects the angular distribution of the decay daughter with the elements of the spin density matrix and polarization. It presents both theoretical and experimental perspectives on the global and local spin polarization of hyperons and the spin alignment of vector mesons in relativistic heavy-ion collisions. In this context, this chapter discusses the different physics mechanisms responsible for spin polarization of various hyperons and spin alignment of vector mesons, with particular attention to heavy-flavor particles.

- **Chapter 3** describes the experimental apparatus of the ALICE experiment during Run 3 of the LHC. The chapter begins with a brief introduction to

the LHC, followed by an overview of ALICE. The main detector systems, including the global detectors, central barrel detectors, and forward detectors, are discussed. Particular emphasis is placed on the muon spectrometer, which plays a central role in the analyses presented in this thesis, as the reconstruction and identification of J/$\psi$ are performed through its dimuon decay channel.

- **Chapter 4** presents the experimental analysis of (J/$\psi$) polarization in proton–proton ($pp$) and Oxygen–Oxygen (OO) collisions, measured via the dimuon decay channel at forward rapidity ($2.5 < y < 4.0$). The chapter begins with an overview of the theoretical and experimental aspects of quarkonium production and polarization. It then describes in detail the analysis methodology, including the data samples, Monte Carlo simulations, event and track selection criteria, extraction of the polarization parameters, and evaluation of systematic uncertainties. The polarization results obtained in $pp$ collisions at $\sqrt{s} = 13.6$ TeV are compared with previous measurements at $\sqrt{s} = 7$ and 8 TeV, while the results from OO collisions at $\sqrt{s_{\rm NN}} = 5.36$ TeV are compared with the existing measurements in Pb–Pb collisions at $\sqrt{s_{\rm NN}} = 5.02$ TeV. In addition, the experimental findings are confronted with several theoretical predictions. The results presented in this chapter have been approved by the ALICE collaboration as preliminary results. This chapter is based on the following ALICE analysis note:

  1. "*Inclusive* J/$\psi$ *polarization measurement at forward rapidity in proton-proton collisions at* $\sqrt{s}$ *= 13.6 TeV with ALICE*".
     **Bhagyarathi Sahoo**, Raghunath Sahoo.
     Analysis Note: alice-notes.web.cern.ch/node/1691 [**AN-1691**]
     Preliminary approved figures: alice-figure.web.cern.ch/node/36516
  2. "*Inclusive* J/$\psi$ *polarization measurement at forward rapidity in Oxygen–Oxygen collisions at* $\sqrt{s_{\rm NN}}$ *= 5.36 TeV with ALICE*".

**Bhagyarathi Sahoo**, Raghunath Sahoo.
Analysis Note: alice-notes.web.cern.ch/node/1698 [**AN-1698**]
Preliminary approved figures: alice-figure.web.cern.ch/node/36516

The chapter concludes with a discussion of the experimental challenges in quarkonium polarization measurements in hadronic and nuclear collisions.

- **Chapter 5** presents the study of the transverse momentum, charged-particle multiplicity, and rapidity dependence of the polarization parameters for J/$\psi$ and $\psi(2S)$ in proton–proton collisions, obtained from Monte Carlo simulations at various center-of-mass energies. This chapter is based on the following publications:

  1. "*Polarization measurement of* J/$\psi$ *and* $\psi(2S)$ *in proton+proton collisions at the LHC energies using PYTHIA8*".
     **Bhagyarathi Sahoo**, Dushmanta Sahu, Suman Deb, Captain R. Singh and Raghunath Sahoo.
     Published in: Phys. Rev. C **109**, 034910 (2024).

  Finally, the chapter provides an outlook on the ongoing and future ALICE experimental efforts in this direction.

- **Chapter 6** explores the phenomenological study of spin alignment of quarkonia in Pb+Pb collisions at $\sqrt{s_{\rm NN}} = 5.02$ TeV. This covers the estimation of the diagonal and off-diagonal elements of the spin density matrix for various quarkonium states by calculating the spin projection-dependent eigenenergies, quarkonium wave function, and decay width. An effective Hamiltonian is constructed by including the spin–vorticity and spin–magnetic interactions in a rotating thermal medium with a realistic temperature-dependent complex heavy-quark potential to describe the dynamics of quarkonium states. The effect of medium rotation, external magnetic field, medium

temperature, and momentum-space anisotropy is systematically studied on the elements of the spin density matrix. Moreover, the spin-dependent dissociation of quarkonium states, governed by their binding energies and sizes, is proposed as a potential mechanism underlying the spin alignment. This chapter is based on the following publications:

1. "*Spin alignment of Quarkonia: A Possible Probe of a Deconfined QCD matter in Pb–Pb collisions at* $\sqrt{s_{\rm NN}} = 5.02\ TeV$".
   **Bhagyarathi Sahoo**, Captain R. Singh and Raghunath Sahoo.
   Published in: Eur. Phys. J. C **86**, 880 (2026).

2. "*Dissociation driven quarkonium spin alignment in Pb–Pb collisions at* $\sqrt{s_{\rm NN}} = 5.02\ TeV$".
   **Bhagyarathi Sahoo**, Captain R. Singh, and Raghunath Sahoo.
   Published in: Phys. Rev. D **113**, 054023 (2026).

- **Chapter 7** investigates the global spin polarization of baryons including $\Lambda$, $\Xi^-$, $\Omega^-$, $\Delta^{++}$ and $\Sigma^{\pm}$, and spin alignment of vector mesons $K^{*0}$, $\phi$, and $\rho$ from global quark polarization calculated through partonic elastic scattering within the framework of an effective static potential model. Within this framework, the quark polarization is driven by the Debye screening mass. Hence, any change brought to the Debye screening mass due to external perturbations like a magnetic field and anisotropy affects the global quark polarization and hence the effect of these parameters on the spin polarization of hadrons. In another approach, the global spin polarization of $\Lambda$ hyperons is obtained by determining the lifetime of the vortical QGP fluid and by developing a unified hydrodynamic framework within the ambit of second-order Müller-Israel-Stewart (MIS) based relativistic viscous hydrodynamics. The medium viscosity, vorticity, and magnetic field are coupled in the hydrodynamic equations, and the interplay of spin–vorticity

and spin–magnetic coupling is investigated through the spin polarization observable. This chapter also presents a novel method for the extraction of the global vorticity produced in relativistic heavy-ion collisions. Furthermore, the local spin polarization of $\Lambda$ hyperons due to thermal vorticity and thermal shear is obtained in an ideal uncharged fluid using hydrodynamic and transport models. This chapter is based on the following publications:

1. "*Impact of vorticity and viscosity on the hydrodynamic evolution of hot QCD medium*". **Bhagyarathi Sahoo**, Captain R. Singh, Dushmanta Sahu, Raghunath Sahoo and Jan-e Alam.
   Published in: Eur. Phys. J. C **83**, 873 (2023).
2. "*Probing rotational dynamics of quark gluon plasma via global vorticity*". **Bhagyarathi Sahoo**, Captain R. Singh, and Raghunath Sahoo.
   Published in: Phys. Lett. B **880**, 140714 (2026).
3. "*Global polarization of $\Lambda$ hyperons in hot QCD matter at TeV energies*". **Bhagyarathi Sahoo**, Captain R. Singh, and Raghunath Sahoo. arXiv:2604.13701 (Under Review: Phys. Rev. D)
4. "*Impact of strong magnetic field, baryon chemical potential, and medium anisotropy on polarization and spin alignment of hadrons*".
   **Bhagyarathi Sahoo**, Captain R. Singh and Raghunath Sahoo.
   Published in: Eur. Phys. J. C **85**, 580 (2025).
5. "*Estimating Longitudinal Polarization of $\Lambda$ and $\bar{\Lambda}$ Hyperons at Relativistic Energies using Hydrodynamic and Transport models*".
   **Bhagyarathi Sahoo**, Captain R. Singh and Raghunath Sahoo.
   Published in: Phys. Scr. **100**, 065310 (2025).

- Finally, the important findings and conclusions drawn from this thesis are summarized in Chapter 8.

# Chapter 2

## Basic concept of spin polarization

Since this thesis is devoted to the study of spin polarization from both experimental and phenomenological perspectives, it is important to introduce the fundamental concepts of the spin density matrix and the methods used to quantify polarization in relativistic heavy-ion collisions. Therefore, this chapter presents the essential framework of the spin density matrix and particle polarization.

### 2.1 Spin density matrix: an overview

Consider an ensemble of particles with spin quantum number $S$. The normalized spin states are denoted by $|\psi_i\rangle$, from which the spin density operator is defined

$$\rho = \sum_i \mathcal{P}_i |\psi_i\rangle\langle\psi_i|, \tag{2.1}$$

where $\mathcal{P}_i$ is the probability of the spin state $|\psi_i\rangle$. A few important properties of the spin density operator are listed below:

- $\rho$ is Hermitian, $\rho = \rho^\dagger$
- The trace of $\rho$ is 1, $\mathrm{Tr}(\rho) = \sum_j \langle\psi_j| \rho |\psi_j\rangle = \sum_i \mathcal{P}_i = 1$
- $\rho$ is a positive-semidefinite operator, i.e., for any state $|\phi\rangle$, one obtains $\langle\phi|\rho|\phi\rangle = \sum_i \mathcal{P}_i \left|\langle\phi|\psi_i\rangle\right|^2 \geqslant 0$

For a particle with spin $S$, the spin space has dimension $(2S+1)$. Consequently, the spin density operator is represented by a $(2S+1)\times(2S+1)$ matrix containing $2(2S+1)^2$ real parameters. Imposing the Hermiticity and unit-trace conditions reduces the number of independent real parameters to $4S(S+1)$, while the positive-semidefinite condition further constrains them.

If the particle is unpolarized, the spin density matrix $\rho$ has a simple form

$$\rho = \frac{1}{2S+1}\text{diag}\,(1,1,\cdots,1). \tag{2.2}$$

Any deviation from Eq. 2.2 indicates the degree of spin alignment or polarization. To illustrate this, a few examples are considered. The discussion begins with spin $\frac{1}{2}$ particles and is subsequently extended to spin 1 and spin $\frac{3}{2}$ particles.

### 2.1.1 Spin $\frac{1}{2}$ system

The first example is a spin $\frac{1}{2}$ particle, whose spin density matrix is a 2×2 Hermitian matrix characterized by three independent real parameters. The spin density matrix for a spin $\frac{1}{2}$ system can be written as;

$$\rho = \frac{1}{2}(1 + \overrightarrow{\mathscr{P}}\cdot\boldsymbol{\sigma}), \tag{2.3}$$

where $\overrightarrow{\mathscr{P}}$ is a unit three-vector serving as the polarization vector and $\boldsymbol{\sigma} = (\sigma_1,\sigma_2,\sigma_3)$ are Pauli matrices, which have the form,

$$\sigma_1 = \begin{pmatrix} 0 & 1 \\ 1 & 0 \end{pmatrix}, \qquad \sigma_2 = \begin{pmatrix} 0 & -i \\ i & 0 \end{pmatrix}, \qquad \sigma_3 = \begin{pmatrix} 1 & 0 \\ 0 & -1 \end{pmatrix}. \tag{2.4}$$

In Eq. 2.3, the three real independent parameters are denoted by $\mathscr{P}_1$, $\mathscr{P}_2$, $\mathscr{P}_3$, and Eq. 2.3 can be further expanded as;

$$\rho = \begin{pmatrix} \rho_{\frac{1}{2},\frac{1}{2}} & \rho_{\frac{1}{2},-\frac{1}{2}} \\ \rho_{-\frac{1}{2},\frac{1}{2}} & \rho_{-\frac{1}{2},-\frac{1}{2}} \end{pmatrix} = \frac{1}{2}\begin{pmatrix} 1+\mathscr{P}_3 & \mathscr{P}_1 - i\mathscr{P}_2 \\ \mathscr{P}_1 + i\mathscr{P}_2 & 1-\mathscr{P}_3 \end{pmatrix}. \tag{2.5}$$

The polarization vector can be obtained using the formula

$$\overrightarrow{\mathscr{P}} = \frac{\text{Tr}(\rho\boldsymbol{\sigma})}{\text{Tr}(\rho)}. \tag{2.6}$$

On the other hand, from Eq. 2.6, the component of polarization vector are given as,

$$\begin{aligned}
\mathscr{P}_1 &= \frac{\rho_{\frac{1}{2},-\frac{1}{2}} + \rho_{-\frac{1}{2},\frac{1}{2}}}{\rho_{\frac{1}{2},\frac{1}{2}} + \rho_{-\frac{1}{2},-\frac{1}{2}}} = \frac{2\,\mathrm{Re}[\rho_{\frac{1}{2},-\frac{1}{2}}]}{\mathrm{Tr}(\rho)}, \\
\mathscr{P}_2 &= i\frac{\rho_{\frac{1}{2},-\frac{1}{2}} - \rho_{-\frac{1}{2},\frac{1}{2}}}{\rho_{\frac{1}{2},\frac{1}{2}} + \rho_{-\frac{1}{2},-\frac{1}{2}}} = \frac{2\,\mathrm{Im}[\rho_{\frac{1}{2},-\frac{1}{2}}]}{\mathrm{Tr}(\rho)}, \\
\mathscr{P}_3 &= \frac{\rho_{\frac{1}{2},\frac{1}{2}} - \rho_{-\frac{1}{2},-\frac{1}{2}}}{\rho_{\frac{1}{2},\frac{1}{2}} + \rho_{-\frac{1}{2},-\frac{1}{2}}} = \frac{\mathrm{Tr}(\rho\sigma_z)}{\mathrm{Tr}(\rho)}.
\end{aligned} \tag{2.7}$$

Notably, one can obtain the above Eq. 2.7 by comparing the coefficients of the spin density matrix from Eq. 2.5. Therefore, the polarization of spin $\frac{1}{2}$ particles can be computed through their spin density matrix as defined in Eq. 2.6.

To understand the spin polarization phenomena explicitly, an example of the $\Lambda$ hyperon is considered, which is a spin $\frac{1}{2}$ particle. Its polarization can be measured through its parity-violating weak decay [38, 166]:

$$\Lambda \rightarrow \mathrm{p} \quad + \pi^-, \quad (\sim 63.9\%) \tag{2.8}$$

with a branching ratio (BR) of 63.9%

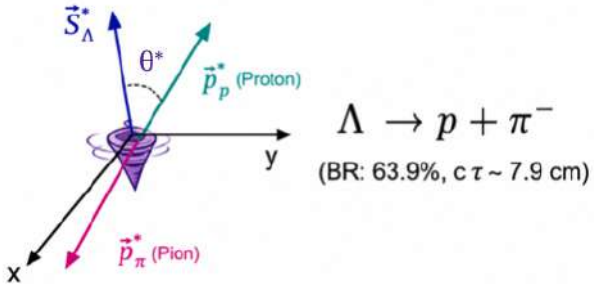



Figure 2.1: Illustration of the $\Lambda$ hyperons decay in its rest frame.

Experimentally, the global spin polarization of the $\Lambda$ hyperon is determined by measuring the angular distribution of the daughter proton along the direction of the orbital angular momentum in the $\Lambda$ hyperon's rest frame. For completeness, the corresponding angular distribution is briefly derived below.

In the rest frame of the $\Lambda$ hyperons, the initial state and final state total angular momentum $J$ and $J_z$ should be conserved. Consider a $\Lambda$ hyperon in $J = \frac{1}{2}$, and $J_z = \frac{1}{2}$, the final state has

$$J = L \pm S = \frac{1}{2} \,,$$
$$J_z = L_z \pm S_z = \frac{1}{2} \,. \tag{2.9}$$

The total angular momentum conservation demands two possible values of L, which are discussed below

- L = 0 (S-wave):
  Initial state parity, $P_i = (-1)^L P(\Lambda) = 1$
  Final state parity, $P_f = (-1)^L P(\pi) P(p)$ = -1
  Since $P_i \neq P_f$, parity is violated.

- L = 1 (P-wave):
  Initial state parity = $(-1)^L P(\Lambda)$ = -1
  Final state parity = $(-1)^L P(\pi) P(p)$ = -1
  Since $P_i = P_f$, parity is conserved.

Given that, $\Lambda$ hyperon has spin parity $\mathrm{J}^P(\Lambda) = \left(\frac{1}{2}\right)^+$, proton has spin parity $\mathrm{J}^P(p) = \left(\frac{1}{2}\right)^+$, pion has spin parity $\mathrm{J}^P(\pi^-) = 0^-$.
Thus, the weak decay of $\Lambda$ hyperons can violate parity conservation, and the final state is not described by a purely $L = 0$ state or $L = 1$ state, but rather a linear combination of S-wave and P-wave with amplitudes $A$ and $B$, respectively. Thus, the total wave function can be described as;

$$|\Psi\rangle = A\,|L = 0\rangle + B\,|L = 1\rangle \,, \tag{2.10}$$

Writing Eq. 2.10 in terms of the spherical harmonics, one obtains

$$|\Psi\rangle = A \begin{pmatrix} Y_{00} \\ 0 \end{pmatrix} + B \begin{pmatrix} -\sqrt{\frac{1}{3}} Y_{10} \\ \sqrt{\frac{2}{3}} Y_{11} \end{pmatrix} . \tag{2.11}$$

The total probability density can be written as;

$$|\Psi|^2 = \langle\Psi|\Psi\rangle = A^\dagger A Y_{00}^\dagger Y_{00} + \frac{1}{3}B^\dagger B Y_{10}^\dagger Y_{10} - \frac{2\ \mathrm{Re}(\mathrm{AB}^\dagger)}{\sqrt{3}} Y_{00} Y_{10} + \frac{2\mathrm{B}^\dagger\mathrm{B}}{3} Y_{11}^\dagger Y_{11}, \tag{2.12}$$

The definitions of spherical harmonics are given by;

$$Y_{00} = \frac{1}{\sqrt{4\pi}},\ \ Y_{1,0} = \frac{1}{2}\sqrt{\frac{3}{\pi}}\cos\theta,\ \ \mathrm{Y}_{1,1} = -\frac{1}{2}\sqrt{\frac{3}{2\pi}}\mathrm{e}^{\mathrm{i}\phi}\sin\theta,\ \ \mathrm{Y}_{1,-1} = \frac{1}{2}\sqrt{\frac{3}{2\pi}}\mathrm{e}^{-\mathrm{i}\phi}\sin\theta, \tag{2.13}$$

Using Eq. 2.13 in Eq. 2.12, one obtains;

$$|\Psi|^2 = (|A|^2 + |B|^2)\frac{1}{4\pi}\left[1 - \frac{2\ \mathrm{Re}(\mathrm{AB}^\dagger)}{|A|^2 + |B|^2}\ \cos\theta^*\right]. \tag{2.14}$$

The term $(|A|^2 + |B|^2)$ in Eq. 2.14 corresponds to the total decay rate, while the term inside the square brackets determines its angular dependence and hence represents the differential decay rate. The angular distribution of the daughter proton can be obtained from the decay probability density. For a mixed initial state, the decay probability density is given by;

$$|\Psi|^2 = \sum_n a_n |\Phi_n|^2 = \mathrm{Tr}(\rho)\ , \tag{2.15}$$

If the initial state is described by $\rho_{\mathrm{initial}}$, then the final state is described by

$$\rho_{\mathrm{final}} = \hat{T}\rho_{\mathrm{initial}}\hat{T}^\dagger\ , \tag{2.16}$$

where $\hat{T}$ is the transition (or decay) operator, which converts the initial $\Lambda$ state into the final proton-pion state, such that;

$$\hat{T}_{ij}\ |i\rangle_{\mathrm{initial}} = |j\rangle_{\mathrm{final}}\ \ , \tag{2.17}$$

The decay probability density can be written as;

$$|\Psi|^2 = \mathrm{Tr}(\rho_{\mathrm{final}}) = \mathrm{Tr}(\hat{\mathrm{T}}\rho_{\mathrm{initial}}\hat{\mathrm{T}}^\dagger), \tag{2.18}$$

Now, the transition amplitudes are calculated using the relation

$$T_{fi} = \langle f|\hat{T}|i\rangle, \tag{2.19}$$

In the $\Lambda$ hyperon weak decay, the transition matrix can be built as;

$$T = \frac{1}{\sqrt{4\pi}} \begin{pmatrix} A - B\cos\theta & -B\sin\theta\, e^{-i\phi} \\ -B\sin\theta\, e^{i\phi} & A + B\cos\theta \end{pmatrix}, \tag{2.20}$$

The above Eq. 2.20 can be written in the compact form;

$$T = \frac{1}{\sqrt{4\pi}} (A - B\,\boldsymbol{\sigma}\cdot\hat{\mathbf{p}}). \tag{2.21}$$

where, $\hat{\mathbf{p}}$ is the direction of proton momentum in $\Lambda$ hyperon rest frame.

For a given decay amplitude $T$, the differential decay rate is given by;

$$dW \propto |\Psi|^2\, d\Omega, \tag{2.22}$$

Thus, the angular distribution of the decay proton can be

$$\begin{aligned} \frac{dN}{d\Omega} = \mathrm{Tr}[\hat{T}\rho\hat{T}^\dagger] &= \frac{1}{2(4\pi)}\mathrm{Tr}\left[(\mathrm{A} - \mathrm{B}\,\boldsymbol{\sigma}\cdot\hat{\mathbf{p}})\,(1 + \overrightarrow{\mathscr{P}}\cdot\boldsymbol{\sigma})\,\left(\mathrm{A}^\dagger - \mathrm{B}^\dagger\,(\boldsymbol{\sigma}\cdot\hat{\mathrm{p}})^\dagger\right)\right] \\ &= \frac{1}{4\pi}\left[(|A|^2 + |B|^2) - 2\,\mathrm{Re}(\mathrm{AB}^\dagger)\,\overrightarrow{\mathscr{P}}\cdot\hat{\mathbf{p}}\right] \\ &= \frac{(|A|^2 + |B|^2)}{4\pi}\left[1 - \frac{2\,\mathrm{Re}(\mathrm{AB}^\dagger)}{(|A|^2 + |B|^2)}\overrightarrow{\mathscr{P}}\cdot\hat{\mathbf{p}}\right]. \end{aligned} \tag{2.23}$$

To obtain the above Eq. 2.23, the standard Pauli matrix identities are used;

$$(\boldsymbol{\sigma}\cdot\boldsymbol{a})\,(\boldsymbol{\sigma}\cdot\boldsymbol{b}) = \mathbf{a}\cdot\mathbf{b} + i\,\boldsymbol{\sigma}\cdot(\boldsymbol{a}\times\boldsymbol{b}), \quad \mathrm{Tr}(\sigma_\mathrm{i}) = 0, \quad \mathrm{Tr}(\sigma_\mathrm{i}\sigma_\mathrm{j}) = 2\delta_\mathrm{ij} \tag{2.24}$$

Using the above relation, one can obtain,

$$\mathrm{Tr}\,[\boldsymbol{\sigma}\cdot\hat{\mathbf{p}}] = 0, \quad \mathrm{Tr}\left[\overrightarrow{\mathscr{P}}\cdot\boldsymbol{\sigma}\right] = 0, \quad \mathrm{Tr}\left[(\boldsymbol{\sigma}\cdot\hat{\mathbf{p}})\,(\boldsymbol{\sigma}\cdot\overrightarrow{\mathscr{P}})\right] = 2(\overrightarrow{\mathscr{P}}\cdot\hat{\mathbf{p}}). \tag{2.25}$$

The interference term in Eq. 2.23 produces the familiar decay asymmetry. For $\Lambda$ hyperons, Eq. 2.23 can be written as;

$$\frac{dN}{d\Omega} \;\propto\; (1 + \alpha_\Lambda \overrightarrow{\mathscr{P}}_\Lambda\cdot\hat{\mathbf{p}}) \;\propto\; (1 + \alpha_\Lambda \mathscr{P}_\Lambda \cos\theta^*), \tag{2.26}$$

where,

$\alpha_\Lambda = \dfrac{-2\,\mathrm{Re}(\mathrm{AB}^\dagger)}{|A|^2 + |B|^2}$ is the $\Lambda$ hyperon decay parameter, with value $\alpha_\Lambda = 0.750 \pm 0.009$

In experimental analyses, Eq. 2.26 is used to determine the hyperon spin polarization by fitting the measured corrected angular distribution, with the decay parameter adopted from the Particle Data Group (PDG).

### 2.1.2 Spin 1 system

The second example is a spin 1 particle, whose spin density matrix is a 3×3 Hermitian matrix characterized by eight independent real parameters, given by;

$$\rho = \begin{pmatrix} \rho_{1,1} & \rho_{1,0} & \rho_{1,-1} \\ \rho_{0,1} & \rho_{00} & \rho_{0,-1} \\ \rho_{-1,1} & \rho_{-1,0} & \rho_{-1,-1} \end{pmatrix} = \begin{pmatrix} \rho_{1,1} & \rho^*_{0,1} & \rho^*_{-1,1} \\ \rho_{0,1} & \rho_{00} & \rho^*_{-1,0} \\ \rho_{-1,1} & \rho_{-1,0} & \rho_{-1,-1} \end{pmatrix}. \tag{2.27}$$

The spin density matrix shown in Eq. 2.27 can be decomposed into vector and tensor components and rewritten as;

$$\rho = \frac{1}{3}\left(1 + \frac{3}{2}\mathscr{P}_i S_i + 3\mathscr{T}_{ij} S_{ij}\right), \tag{2.28}$$

where, $S_i$ (i = 1, 2, 3 or $x$ , $y$, $z$) are the three spin matrices with their corresponding coefficients $\mathscr{P}_i$ representing the three components of the spin polarization vector $\overrightarrow{\mathscr{P}}$. The spin polarization vector $\overrightarrow{\mathscr{P}}$ can be determined from the spin density matrix using the relation [116]

$$\overrightarrow{\mathscr{P}} = \frac{1}{S}\frac{\mathrm{Tr}(\rho\hat{\mathbf{S}})}{\mathrm{Tr}(\rho)}, \tag{2.29}$$

where $S = 1$ and the spin operators for vector mesons, $\hat{\mathbf{S}} = (\hat{S}_1, \hat{S}_2, \hat{S}_3)$, are defined by

$$\hat{S}_1 = \frac{1}{\sqrt{2}}\begin{pmatrix} 0 & 1 & 0 \\ 1 & 0 & 1 \\ 0 & 1 & 0 \end{pmatrix}, \quad \hat{S}_2 = \frac{1}{\sqrt{2}}\begin{pmatrix} 0 & -i & 0 \\ i & 0 & -i \\ 0 & i & 0 \end{pmatrix}, \quad \hat{S}_3 = \begin{pmatrix} 1 & 0 & 0 \\ 0 & 0 & 0 \\ 0 & 0 & -1 \end{pmatrix}. \tag{2.30}$$

The polarization vector $\overrightarrow{\mathscr{P}} = (\mathscr{P}_1, \mathscr{P}_2, \mathscr{P}_3)$, can be obtained using Eq. 2.29, which are expressed as follows;

$$\begin{aligned} \mathscr{P}_1 &= \sqrt{2}\frac{1}{\mathrm{Tr}(\rho)}\mathrm{Re}(\rho_{-1,0} + \rho_{1,0}), \\ \mathscr{P}_2 &= \sqrt{2}\frac{1}{\mathrm{Tr}(\rho)}\mathrm{Im}(\rho_{-1,0} + \rho_{1,0}), \\ \mathscr{P}_3 &= \frac{1}{\mathrm{Tr}(\rho)}\left(\rho_{11} - \rho_{-1,-1}\right). \end{aligned} \tag{2.31}$$

In Eq. 2.28, $S_{ij} = S_{ji}$ are five traceless matrices with corresponding coefficients $\mathscr{T}_{ij} = \mathscr{T}_{ji}$ form a traceless rank-2 tensor, and can be expressed as;

$$S_{ij} = \frac{1}{2}(S_i S_j + S_j S_i) - \frac{2}{3}\mathbf{1}\delta_{ij} \tag{2.32}$$

The coefficients $\mathscr{T}_{ij}$ can be extracted using the relation $\mathscr{T}_{ij} = \mathrm{Tr}(\rho \mathbf{S}_{ij})$ (since S=1, and Tr($\rho$) =1),

$$\begin{aligned} \mathscr{T}_{12} &= \mathrm{Im}(\rho_{-1,1}), \\ \mathscr{T}_{23} &= \frac{1}{\sqrt{2}}\mathrm{Im}(\rho_{1,0} - \rho_{-1,0}), \\ \mathscr{T}_{31} &= \frac{1}{\sqrt{2}}\mathrm{Re}(\rho_{1,0} - \rho_{-1,0}). \end{aligned} \tag{2.33}$$

However, it is not possible to extract $\mathscr{T}_{11}$, $\mathscr{T}_{22}$, $\mathscr{T}_{33}$ in the same way since $\mathrm{Tr}(\mathbf{S}_{\mathrm{ii}}\mathbf{S}_{\mathrm{jj}}) \neq 0$. They can only be determined directly from $\rho_{-1,1}$, $\rho_{1,1} + \rho_{-1,-1}$, and traceless condition for $\mathscr{T}_{ij}$. The results read

$$\begin{aligned} \mathscr{T}_{11} &= \frac{1}{2}\left(\rho_{00} - \frac{1}{3}\right) + \mathrm{Re}(\rho_{-1,1}), \\ \mathscr{T}_{22} &= \frac{1}{2}\left(\rho_{00} - \frac{1}{3}\right) - \mathrm{Re}(\rho_{-1,1}), \\ \mathscr{T}_{33} &= -\left(\rho_{00} - \frac{1}{3}\right). \end{aligned} \tag{2.34}$$

In the following section, the spin alignment of spin 1 vector mesons is studied from the daughters' angular distribution for two distinct decay modes: (i) decays into two spin 0 pseudoscalar mesons and (ii) decays into two spin $\frac{1}{2}$ fermion particles.

(i) As a first example, the strong decays of the vector mesons $K^{*0}$ and $\phi$ into two spin 0 particles are considered. The dominant decay channels are:

$$\begin{aligned} K^{*0} &\to K^+ + \pi^-, \quad (\sim 100\%), \\ \phi &\to K^+ + K^-, \quad (\sim 49\%), \\ \rho &\to \pi^+ + \pi^-, \quad (\sim 100\%). \end{aligned} \tag{2.35}$$

The polarization of $K^{*0}$, $\phi$, and $\rho$ can be measured through these decays [40]. Notably, the parity is conserved in strong decays, so the final states must be in the P-wave with $L = 1$. In the following section, $K^{*0}$ is taken as an example, however, all discussions apply to $\phi$, and $\rho$ equally. The decay amplitude can be described by the $\mathscr{S}$ matrix

$$\langle K^+, \pi^- | \mathscr{S} | K^{*0}; S_z \rangle = Y_{1,S_z}(\theta, \phi) \tag{2.36}$$

where $S_z = -1, 0, 1$ are three spin projection of spin 1 particle. In Eq. 2.36, $\theta$, and $\phi$ denote the polar and azimuthal angle of one decay daughter, and $Y_{1,S_z}(\theta, \phi)$ denote the spherical harmonic functions of $L = 1$. The angular distribution of $K^+$ or $\pi^-$ for a specific initial spin state $|1, S_z\rangle$ of $K^{*0}$ is

$$\frac{dN}{d\Omega} = \left| \langle K^+, \pi^- | \mathscr{S} | K^{*0}; S_z \rangle \right|^2 = |Y_{1,S_z}(\theta, \phi)|^2 . \tag{2.37}$$

Consider an ensemble of $K^{*0}$ at rest having the probability $\mathcal{P}_i$ in the spin state $|\psi_i\rangle$. Then the spin density operator $\rho$ is given by Eq. (2.1). The angular distribution for the decay daughter can be written as

$$\begin{aligned} \frac{dN}{d\Omega} &= \sum_i \mathcal{P}_i \left| \langle K^+, \pi^- | \mathscr{S} | \psi_i \rangle \right|^2 = \sum_i \mathcal{P}_i \langle K^+, \pi^- | \mathscr{S} | \psi_i \rangle \langle \psi_i | \mathscr{S}^\dagger | K^+, \pi^- \rangle \\ &= \langle K^+, \pi^- | \mathscr{S} \rho \mathscr{S}^\dagger | K^+, \pi^- \rangle . \end{aligned} \tag{2.38}$$

Inserting a completeness relation $\sum_{S_z} |K^{*0}; S_z\rangle\langle K^{*0}; S_z| = 1$ into Eq. 2.38, one can obtain Eq. (10) of Ref. [167], which is given by;

$$\begin{aligned} &\frac{dN}{d\Omega} = \sum_{S_{z1}, S_{z2}} \langle K^+, \pi^- | \mathscr{S} | K^{*0}; S_{z1} \rangle \langle K^{*0}; S_{z1} | \rho | K^{*0}; S_{z2} \rangle \langle K^{*0}; S_{z2} | \mathscr{S}^\dagger | K^+, \pi^- \rangle \\ &= \sum_{S_{z1}, S_{z2}} \rho_{S_{z1}, S_{z2}} Y_{1,S_{z1}}(\theta, \phi) Y^*_{1,S_{z2}}(\theta, \phi) \\ &= \frac{3}{8\pi} \Big[ (1 - \rho_{00}) + (3\rho_{00} - 1) \cos^2\theta - 2\mathrm{Re}\rho_{1,-1} \sin^2\theta \cos(2\phi) - 2\mathrm{Im}\rho_{1,-1} \sin^2\theta \\ &\sin(2\phi) + \sqrt{2}\mathrm{Re}(\rho_{-1,0} - \rho_{1,0}) \sin(2\theta) \cos\phi + \sqrt{2}\mathrm{Im}(\rho_{-1,0} - \rho_{1,0}) \sin(2\theta) \sin\phi \Big] , \end{aligned} \tag{2.39}$$

where $\rho_{S_{z1},S_{z2}} \equiv \langle K^{*0}; S_{z1}|\rho|K^{*0}; S_{z2}\rangle$ denote the spin density matrix elements for $K^{*0}$.

(ii) As a second example, the electromagnetic decays of quarkonium states, for example J/$\psi$ and $\Upsilon(1S)$, decaying into two spin $\frac{1}{2}$ particles are considered. The decay channels are:

$$\begin{aligned} \mathrm{J}/\psi &\to \mu^+ + \mu^-(\ e^+ + e^-), \quad (\sim 5.9\%), \\ \Upsilon(1\mathrm{S}) &\to \mu^+ + \mu^-(\ e^+ + e^-), \quad (\sim 2.5\%), \end{aligned} \tag{2.40}$$

Parity is also conserved in electromagnetic decays, so the final states must be in the P-wave with $L = 1$. As an example, the decay of J/$\psi \to \mu^+\mu^-$ is considered; however, all discussions apply to all quarkonium states decaying to $\mu^+\mu^-$ (or $\mathrm{e}^+e^-$) channel. Following a similar procedure as above,

$$\begin{aligned} \frac{dN}{d\Omega} &= \sum_{S_{z1},S_{z2}} \langle \mu^+,\mu^-|\mathscr{S}|\mathrm{J}/\psi; S_{z1}\rangle\langle \mathrm{J}/\psi; S_{z1}|\rho|\mathrm{J}/\psi; S_{z2}\rangle\langle \mathrm{J}/\psi; S_{z2}|\mathscr{S}^\dagger|\mu^+,\mu^-\rangle \\ &= \sum_{S_{z1},S_{z2}} \rho_{S_{z1},S_{z2}} Y_{1,S_{z1}}(\theta,\phi) Y^*_{1,S_{z2}}(\theta,\phi) \\ &= \frac{3}{16\pi}\Big[(1+\rho_{00}) + (1-3\rho_{00})\cos^2\theta + 2\mathrm{Re}\rho_{1,-1}\sin^2\theta\cos(2\phi) + 2\mathrm{Im}\rho_{1,-1}\sin^2\theta \\ &\sin(2\phi) - \sqrt{2}\mathrm{Re}(\rho_{-1,0}-\rho_{1,0})\sin(2\theta)\cos\phi - \sqrt{2}\mathrm{Im}(\rho_{-1,0}+\rho_{1,0})\sin(2\theta)\sin\phi\Big], \end{aligned} \tag{2.41}$$

where $\rho_{S_{z1},S_{z2}} \equiv \langle \mathrm{J}/\psi; S_{z1}|\rho|\mathrm{J}/\psi; S_{z2}\rangle$ denote the spin density matrix elements for J/$\psi$.

On the other hand, the above angular distribution Eq. 2.41 can be written in terms of a set of different polarization parameters, $\lambda_\theta$, $\lambda_\phi$, and $\lambda_{\theta\phi}$ as follows;

$$\begin{aligned} \frac{dN}{d\Omega} \quad &\propto \frac{1}{(3+\lambda_\theta)}\,(1 + \lambda_\theta\cos^2\theta + \lambda_\phi\sin^2\theta\cos 2\phi + \lambda_{\theta\phi}\sin 2\theta\cos\phi \\ &+ \lambda^\perp_\phi\sin^2\theta\sin 2\phi + \lambda^\perp_{\theta\phi}\sin 2\theta\sin\phi) \end{aligned} \tag{2.42}$$

The detailed derivation of Eq. 2.42 can be found in Chapter 4. By comparing the coefficients of the angular terms in Eqs. (2.41) and (2.42), the spin density

matrix elements can be expressed in terms of the $\lambda$-polarization parameters as

$$\rho_{00} = \frac{1-\lambda_\theta}{3+\lambda_\theta}, \tag{2.43}$$

$$\mathrm{Re}\,\rho_{1,-1} = \frac{2\lambda_\phi}{3+\lambda_\theta}, \tag{2.44}$$

$$\mathrm{Im}\,\rho_{1,-1} = -\frac{2\lambda_\phi^\perp}{3+\lambda_\theta}, \tag{2.45}$$

$$\mathrm{Re}(\rho_{-1,0}-\rho_{1,0}) = -\frac{2\sqrt{2}\,\lambda_{\theta\phi}}{3+\lambda_\theta}, \tag{2.46}$$

$$\mathrm{Im}(\rho_{-1,0}+\rho_{1,0}) = -\frac{2\sqrt{2}\,\lambda_{\theta\phi}^\perp}{3+\lambda_\theta}. \tag{2.47}$$

Using the Hermiticity condition, $\rho_{m',m} = \rho^\dagger_{m,m'}$ and the parity relation, $\rho_{10} = -\rho_{-1,0}$, the individual off-diagonal matrix elements become

$$\rho_{-1,0} = -\frac{\sqrt{2}}{3+\lambda_\theta}\left(\lambda_{\theta\phi} + i\lambda_{\theta\phi}^\perp\right), \tag{2.48}$$

$$\rho_{1,0} = \frac{\sqrt{2}}{3+\lambda_\theta}\left(\lambda_{\theta\phi} - i\lambda_{\theta\phi}^\perp\right), \tag{2.49}$$

$$\rho_{1,-1} = \frac{2}{3+\lambda_\theta}\left(\lambda_\phi - i\lambda_\phi^\perp\right). \tag{2.50}$$

Hence, the spin density matrix can be written as

$$\rho = \frac{1}{3+\lambda_\theta}\begin{pmatrix} 1+\lambda_\theta & \sqrt{2}\left(\lambda_{\theta\phi} - i\lambda_{\theta\phi}^\perp\right) & 2\left(\lambda_\phi - i\lambda_\phi^\perp\right) \\ \sqrt{2}\left(\lambda_{\theta\phi} + i\lambda_{\theta\phi}^\perp\right) & 1-\lambda_\theta & -\sqrt{2}\left(\lambda_{\theta\phi} - i\lambda_{\theta\phi}^\perp\right) \\ 2\left(\lambda_\phi + i\lambda_\phi^\perp\right) & -\sqrt{2}\left(\lambda_{\theta\phi} + i\lambda_{\theta\phi}^\perp\right) & 1+\lambda_\theta \end{pmatrix}. \tag{2.51}$$

Therefore, the spin density matrix elements and the polarization parameters, $\lambda_\theta$, $\lambda_\phi$, $\lambda_{\theta\phi}$, $\lambda_\phi^\perp$, and $\lambda_{\theta\phi}^\perp$, constitute two equivalent parameterizations of the spin state of a vector meson. Since they are related through one-to-one transformations, they encode the same physical information, and either set can be uniquely reconstructed from the other. Throughout this thesis, both parameterizations are employed, as appropriate, to characterize the spin polarization (or spin alignment) of vector mesons.

Note that $\frac{dN}{d\Omega}$ is automatically normalized to 1.

$$\int d\Omega \, \frac{dN}{d\Omega} = 1 \tag{2.52}$$

If the parent particle is unpolarized, $\rho_{S_{z1},S_{z2}} = \frac{1}{3}\delta_{S_{z1},S_{z2}}$, then $\frac{dN}{d\Omega} = \frac{1}{4\pi}$. In principle, if one measures $\frac{dN}{d\Omega}$ in experiments, one can determine five real parameters out of eight in the spin density matrix for vector mesons according to Eq. 2.39, and Eq. 2.41,

$$\rho_{00}, \quad \mathrm{Re}\rho_{1,-1}, \quad \mathrm{Im}\rho_{1,-1}, \quad \mathrm{Re}(\rho_{-1,0} - \rho_{1,0}), \quad \mathrm{Im}(\rho_{-1,0} - \rho_{1,0}). \tag{2.53}$$

Note that the above five parameters do not correspond to elements of the spin density matrix appears in the polarization vector defined in Eq. 2.31. Thus, the polarization $\overrightarrow{\mathscr{P}}$ of vector mesons can not be measured from $\frac{dN}{d\Omega}$ in strong decays, where the parity is conserved. This is in contrast to the weak decay of $\Lambda$ hyperons, where the parity violation allows the polarization to be extracted from the decay angular distribution. This constitutes one of the fundamental differences between polarization measurements for spin $\frac{1}{2}$ and spin 1 particles. Accordingly, these phenomena are referred to as *spin polarization* and *spin alignment*, respectively. When the azimuthal angle $\phi$ in Eq. 2.39 is integrated out, one obtains the polar angle distribution as;

$$\frac{dN}{d\cos\theta} = \int_0^{2\pi} d\phi \frac{dN}{d\Omega} = \frac{3}{4}\left[(1-\rho_{00}) + (3\rho_{00}-1)\cos^2\theta\right]. \tag{2.54}$$

The above expression describes the angular distribution of the daughter pseudoscalar meson from the decay of a vector meson in its rest frame. Similarly, when the azimuthal angle $\phi$ in Eq. 2.41 is integrated out, one obtains the polar angle distribution

$$\frac{dN}{d\cos\theta} = \int_0^{2\pi} d\phi \frac{dN}{d\Omega} = \frac{3}{4}\left[(1+\rho_{00}) + (1-3\rho_{00})\cos^2\theta\right]. \tag{2.55}$$

The above expression describes the angular distribution of the daughter dilepton in the vector meson's rest frame.

In both cases, one can measure $\rho_{00}$ experimentally from the acceptance- and efficiency-corrected polar angle distribution of the daughter particle. Any deviation from $\frac{1}{3}$ for $\rho_{00}$ indicates the degree of vector meson spin alignment. These types of measurements have been performed in the STAR and ALICE experiments [62, 66, 72].

### 2.1.3 Spin $\frac{3}{2}$ system

The third example is a spin $\frac{3}{2}$ particle, whose spin density matrix is a 4×4 Hermitian matrix characterized by fifteen independent real parameters. The polarization vector $\overrightarrow{\mathscr{P}} = (\mathscr{P}_1, \mathscr{P}_2, \mathscr{P}_3)$ for $\Delta^{++}$ can be determined from Eq. 2.29 with $S = \frac{3}{2}$ and the spin operators for spin $\frac{3}{2}$ particles being defined by

$$\hat{S}_1 = \frac{1}{2}\begin{pmatrix} 0 & \sqrt{3} & 0 & 0 \\ \sqrt{3} & 0 & 2 & 0 \\ 0 & 2 & 0 & \sqrt{3} \\ 0 & 0 & \sqrt{3} & 0 \end{pmatrix}, \quad \hat{S}_2 = \frac{i}{2}\begin{pmatrix} 0 & -\sqrt{3} & 0 & 0 \\ \sqrt{3} & 0 & -2 & 0 \\ 0 & 2 & 0 & -\sqrt{3} \\ 0 & 0 & \sqrt{3} & 0 \end{pmatrix}, \quad \hat{S}_3 = \begin{pmatrix} \frac{3}{2} & 0 & 0 & 0 \\ 0 & \frac{1}{2} & 0 & 0 \\ 0 & 0 & -\frac{1}{2} & 0 \\ 0 & 0 & 0 & -\frac{3}{2} \end{pmatrix}, \tag{2.56}$$

whose result is

$$\begin{aligned} \mathscr{P}_1 &= \frac{1}{\mathrm{Tr}(\rho)}\left[\frac{2}{\sqrt{3}}\left(\mathrm{Re}\rho_{-\frac{3}{2},-\frac{1}{2}} + \mathrm{Re}\rho_{\frac{1}{2},\frac{3}{2}}\right) + \frac{4}{3}\mathrm{Re}\rho_{-\frac{1}{2},\frac{1}{2}}\right], \\ \mathscr{P}_2 &= \frac{1}{\mathrm{Tr}(\rho)}\left[\frac{2}{\sqrt{3}}\left(\mathrm{Im}\rho_{-\frac{3}{2},-\frac{1}{2}} + \mathrm{Im}\rho_{\frac{1}{2},\frac{3}{2}}\right) + \frac{4}{3}\mathrm{Im}\rho_{-\frac{1}{2},\frac{1}{2}}\right], \\ \mathscr{P}_3 &= \frac{1}{\mathrm{Tr}(\rho)}\left[\frac{1}{3}\left(\rho_{\frac{1}{2},\frac{1}{2}} - \rho_{-\frac{1}{2},-\frac{1}{2}}\right) + \rho_{\frac{3}{2},\frac{3}{2}} - \rho_{-\frac{3}{2},-\frac{3}{2}}\right]. \end{aligned} \tag{2.57}$$

The polarization vector for $\Delta^{++}$ can be obtained from Eq. 2.29, and the result is given by Eq. 2.57. To understand the spin polarization through angular distribution, an example of the decuplet baryon $\Delta^{++}$ is considered, which decays into

$$\Delta^{++} \to p^+ + \pi^+, \quad (\sim 100\%) \tag{2.58}$$

This is a strong decay. The spin-parity of $\Delta^{++}$ is $(\frac{3}{2})^+$, while those of the proton and pion are $(1/2)^+$ and $0^-$ respectively. By parity conservation in the strong

decay, the angular distribution of the proton must be in the P-wave state with $L = 1$. The angular distribution for the decay daughter can be written as

$$\begin{aligned}\frac{dN}{d\Omega} &= \sum_{S_z^{\rm p}} \langle \hat{\mathbf{p}}, S_z^{\rm p}; \pi^+ | \mathscr{S} \rho \mathscr{S}^\dagger | \hat{\mathbf{p}}, S_z^{\rm p}; \pi^+ \rangle \\ &= \sum_{S_{z1}, S_{z2}} \rho_{S_{z1}, S_{z2}} \sum_{S_z^{\rm p}} f(S_z^{\rm p}, S_{z1}) f^*(S_z^{\rm p}, S_{z2}), \end{aligned} \tag{2.59}$$

where the final state of the proton and pion is denoted as $|\hat{\mathbf{p}}, S_z^{\rm p}; \pi^+\rangle$ with $\hat{\mathbf{p}}$ being the proton's momentum direction and $S_z^{\rm p}$ denoting the proton's spin state along the $z$-direction. In deriving the second line of Eq. 2.59, a complete set of spin states of $\Delta^{++}$ is inserted into the first line of Eq. 2.59;

$$\sum_{S_z} \left| \Delta^{++}, S_z \right\rangle \left\langle \Delta^{++}, S_z \right| = 1 \tag{2.60}$$

where $S_z$ denotes the spin state along the z-direction. In Eq. 2.59, $f(S_z^{\rm p}, S_z)$ is the decay amplitude given by;

$$f(S_z^{\rm p}, S_z) = \langle \hat{\mathbf{p}}, S_z^{\rm p}; \pi^+ | \mathscr{S} | \Delta^{++}, S_z \rangle = \langle \hat{\mathbf{p}}, S_z^{\rm p}; \pi^+ | \frac{3}{2}, S_z \rangle_{\rm f}, \tag{2.61}$$

and $\rho_{S_{z1}, S_{z2}}$ are the spin density matrix elements for $\Delta^{++}$ given by;

$$\rho_{S_{z1}, S_{z2}} \equiv \langle \Delta^{++}, S_{z1} | \rho | \Delta^{++}, S_{z2} \rangle. \tag{2.62}$$

The summation over $S_{z1}$ and $S_{z2}$ in Eq. 2.59 is made for all spin states of $\Delta^{++}$ with $S_{z1}, S_{z2} = \pm\frac{1}{2}, \pm\frac{3}{2}$. The final form of the angular distribution is given by;

$$\begin{aligned}\frac{dN}{d\Omega} = \frac{3}{8\pi} \Bigg\{ &\left[ 1 - \frac{2}{3} \left( \rho_{-\frac{1}{2}, -\frac{1}{2}} + \rho_{\frac{1}{2}\frac{1}{2}} \right) \right] - \left[ 1 - 2 \left( \rho_{-\frac{1}{2}, -\frac{1}{2}} + \rho_{\frac{1}{2}, \frac{1}{2}} \right) \right] \cos^2\theta \\ &+ \frac{2}{\sqrt{3}} \left( {\rm Re}\rho_{-\frac{3}{2}, -\frac{1}{2}} - {\rm Re}\rho_{\frac{1}{2}, \frac{3}{2}} \right) \sin(2\theta) \cos\phi + \frac{2}{\sqrt{3}} \left( {\rm Im}\rho_{-\frac{3}{2}, -\frac{1}{2}} - {\rm Im}\rho_{\frac{1}{2}, \frac{3}{2}} \right) \sin(2\theta) \sin\phi \\ &- \frac{2}{\sqrt{3}} \left( {\rm Re}\rho_{-\frac{3}{2}, \frac{1}{2}} + {\rm Re}\rho_{-\frac{1}{2}, \frac{3}{2}} \right) \sin^2\theta \cos(2\phi) - \frac{2}{\sqrt{3}} \left( {\rm Im}\rho_{-\frac{3}{2}, \frac{1}{2}} + {\rm Im}\rho_{-\frac{1}{2}, \frac{3}{2}} \right) \sin^2\theta \sin(2\phi) \Bigg\}, \end{aligned} \tag{2.63}$$

The above angular distribution defined in Eq. 2.63 involves only five parameters out of fifteen independent ones; the rest of the ten parameters cannot be determined by the daughter particle's momentum distribution alone. The parameters appearing in the polarization vector $\overrightarrow{\mathscr{P}}$ of Eq. 2.57 are independent of those in the angular distribution Eq. 2.63. This is the feature of the parity-conserved decay of $\Delta^{++}$, same as in the strong decay of $K^{*0}$ in Eq. 2.35.

## 2.2 Spin polarization: an overview

Over the last few decades, considerable efforts have been made to understand different aspects of spin polarization of various hadrons in relativistic heavy-ion collisions. Despite the spin polarization phenomena manifesting in several forms, the underlying physics remains the same. Spin polarization observables quantify the degree to which particle spins are aligned along a preferred direction. In relativistic heavy-ion collisions, various types of spin polarization have been studied, which are listed below.

### 2.2.1 Types of spin polarization

The spin polarization observables are classified into different categories according to the choice of the quantization axis. Figure 2.2 presents the schematic illustration of the different polarization axes commonly used in these studies. For illustration in Fig. 2.2, $\Lambda$ hyperons are used as an example; however, the same definitions and discussions apply equally to all hyperons.

1. **Global polarization ($\overrightarrow{\mathscr{P}} \parallel \overrightarrow{L}$):** It is measured along the direction of orbital (or total) angular momentum $\overrightarrow{L}$. It originates from spin-orbit interaction. A detailed discussion of global spin polarization is given in Sec. 2.2.2.1.

2. **Local (or Longitudinal) polarization ($\overrightarrow{\mathscr{P}} \parallel \overrightarrow{p}_{beam}$):** It is measured along the direction of beam momentum $\overrightarrow{p}_{\rm beam}$. It originates from the in-

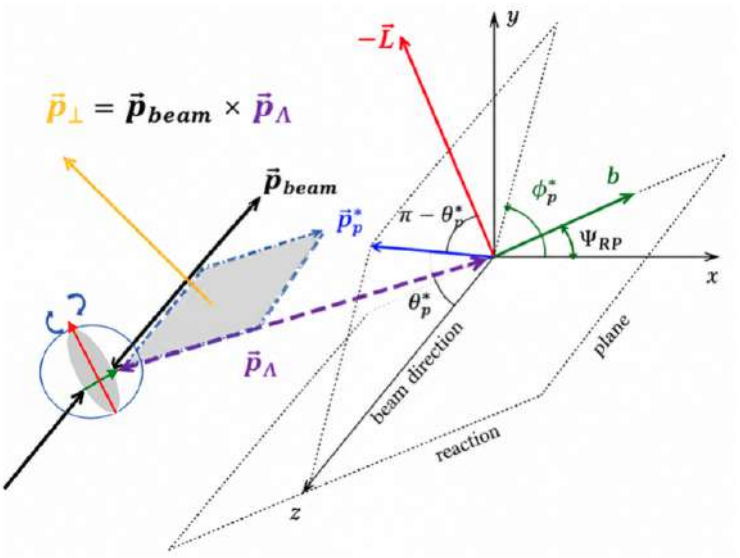



Figure 2.2: Illustration of the different polarization axes.

homogeneous expansion of the fireball. A detailed discussion on local spin polarization is given in Sec. 2.2.2.2.

3. **Transverse polarization ($\overrightarrow{\mathscr{P}} \parallel (\overrightarrow{p}_{\rm beam} \times \overrightarrow{p}_\Lambda)$):** It is measured along the direction perpendicular to the plane defined by the beam momentum $\overrightarrow{p}_{\rm beam}$ and the momentum of the $\Lambda$ hyperon $\overrightarrow{p}_\Lambda$, commonly referred to as the *production plane*. It is primarily originates from the non-perturbative elements in the factorization expansion of the cross section, and can be explained through the transverse momentum dependent (TMD) polarizing fragmentation function (PFF) [73].

4. **Circular polarization:** It can be measured along the same axis as the transverse polarization. It originates from the non-uniform expansion of the fireball, which gives the circular structure of the transverse vorticity around the $z$ direction, which depends on the longitudinal coordinates [119]. This transverse vorticity generates a local polarization in the medium called *circular* polarization.

5. **Toroidal polarization:** It can be measured along the same axis as the transverse polarization. Vortex rings are developed in a cylindrically symmetric flow of fluid with the longitudinal velocity depending on the radius. Such flow results in the formation of toroidal vorticity structures, i.e., the vortex rings, which carry information about this early stage of the collision [168–171]. A new observable called *Ring observable* is proposed to quantify the ring structure, which can be measured through the global spin polarization of hyperons. Such a type of polarization is called *Toroidal polarization*. This could provide compelling evidence for the thermalization of the smallest droplet of the QGP.

6. **Helicity polarization** ($\overrightarrow{\mathscr{P}} \parallel \overrightarrow{p}_{\Lambda}$): It is measured along the direction of the momentum of the $\Lambda$ hyperons. It is induced by both vorticity and helicity charge in non-central heavy-ion collisions [172–174].

7. **Polarization from jet through fluid:** It is measured along the direction normal to the $\Lambda$ ($\bar{\Lambda}$) production plane inside a jet. Transverse polarization inside jets gives direct access to the PFF in jet fragmentation [65].

8. **Polarization correlations:** It is a recently proposed spin observable that probes the correlation between the spins of hadron pairs produced in relativistic collisions. It is suggested to originate from spin-correlated virtual quark–antiquark pairs in the QCD vacuum, whose correlations are partially preserved during hadronization and transferred to the final-state hadrons [175]. Remarkably, the same mechanism has also been shown to qualitatively explain the unexpectedly large spin alignment of $\phi$ vector mesons observed in heavy-ion collisions [176]. These measurements open a new avenue for investigating the role of QCD vacuum fluctuations as well as correlations and fluctuations of spin in the hadronization process.

9. **Vector meson spin alignment:** It is conventionally measured with re-

spect to the direction of the orbital (or total) angular momentum, $\vec{L}$, of the collision system, although other quantization axes, such as the helicity and Collins–Soper frames, are also commonly used. It is quantified through the spin density matrix element $\rho_{00}$ and the $\lambda_\theta, \lambda_\phi, \lambda_{\theta\phi}$ parameters. The spin alignment is expected to arise from the interplay of spin–orbit coupling, thermal vorticity, magnetic fields, and hadronization dynamics in the quark–gluon plasma. A detailed discussion of vector meson spin alignment is presented in Sec. 2.2.3.

### 2.2.2 Hyperon spin polarization: an overview

Understanding the role of orbital angular momentum (OAM) and its implications on various observables in relativistic heavy-ion collisions has attracted significant attention over the past two decades [52, 79, 80, 84]. A substantial fraction of initial created OAM is thought to be deposited in the deconfined phase of QCD matter, where the shear in the initial velocity distribution of the participants manifests a non-zero vorticity component. This vorticity can lead to the spin polarization of hadrons. It is believed that the transverse component of the vorticity field is responsible for the global spin polarization, while the longitudinal component of the vorticity field accounts for the local polarization. The following section presents a brief overview of the hyperons' spin polarization from both experimental and theoretical points of view.

#### 2.2.2.1 Global spin polarization of hyperons

The global spin polarization originates from spin-orbit coupling, as it is measured along the direction of OAM [79, 101]. In this context, the observed global spin polarization in relativistic heavy-ion collisions is considered a direct manifestation of the vortical dynamics of the QGP as shown in Fig. 2.3. Following the landmark measurement of $\Lambda$ hyperons spin polarization by the STAR experiment [52],

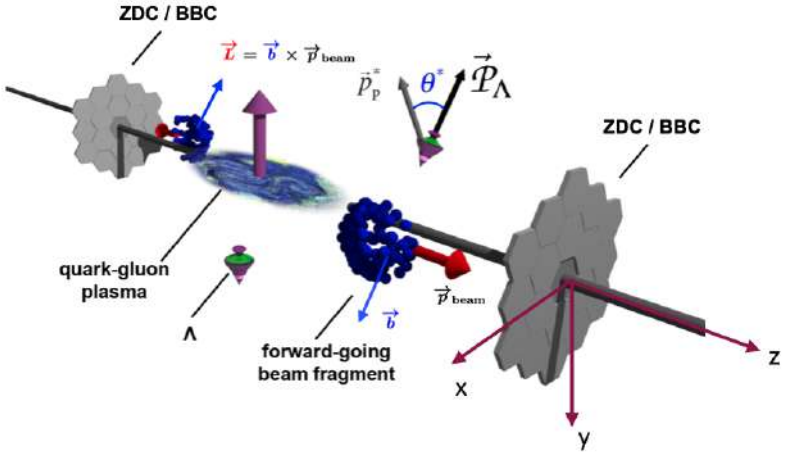



Figure 2.3: Sketch of the vortical fluid produced in heavy-ion collisions.

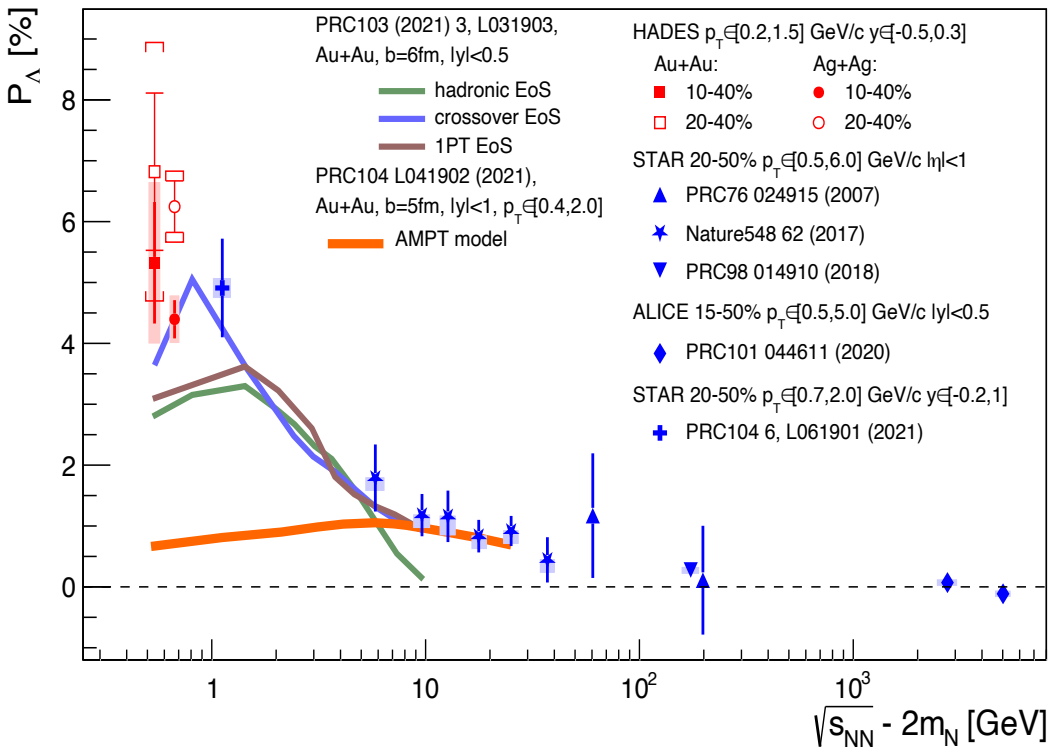



Figure 2.4: Global spin polarization of Λ hyperons as function of collision energies [70].

a broad range of theoretical and phenomenological studies have further advanced this field [110, 115, 126, 127, 135, 138, 145, 149, 154, 177]. Figure 2.4 shows the global spin polarization of Λ hyperons measured across a broad range of center of mass energies from different experiments, which indicates that global spin polarization decreases as a function of collision energy. This observation is particularly important to understand the effect of medium dynamics on the spin polarization observable. For instance, at HADES energies, where QGP formation is considered highly unlikely, the measured polarization is relatively large (approximately 8%, within uncertainties), whereas at LHC energies, the polarization is significantly smaller. This energy dependence suggests that the degree of spin polarization is sensitive to the underlying medium formed in the collision, and thus may serve as a useful probe for distinguishing between QGP and non-QGP environments. The hyperon polarization is primarily sensitive to the average polarization of constituent quarks. Various hydrodynamic and transport model calculations of the global spin polarization of Λ hyperons exhibit qualitative agreement with measurements at RHIC and HADES energies [115, 126, 127, 135, 138, 145, 149, 154, 177]. These frameworks employ a thermally equilibrated treatment of spin degrees of freedom and use thermal vorticity as the primary source to describe such spin polarization phenomena. Collectively, these studies characterize the medium as the most vortical fluid with the least viscosity produced in relativistic heavy-ion collisions under extreme temperature and density. In theoretical studies, multiple sources contributing to spin polarization have been identified. Alongside the vorticity field, electromagnetic fields, shear viscosity, gradients of temperature and baryon chemical potential, medium anisotropy, as well as chromo-electric and chromo-magnetic fields, play important roles in shaping the spin polarization of hyperons [117, 124, 159, 178]. It requires the formulation of a modern hybrid relativistic viscous spin-magnetohydrodynamic approach, where hydrodynamic fields and their leading and higher-order gradients are consistently incorporated, and spin is treated as an explicit dynamical degree of freedom for the evolution

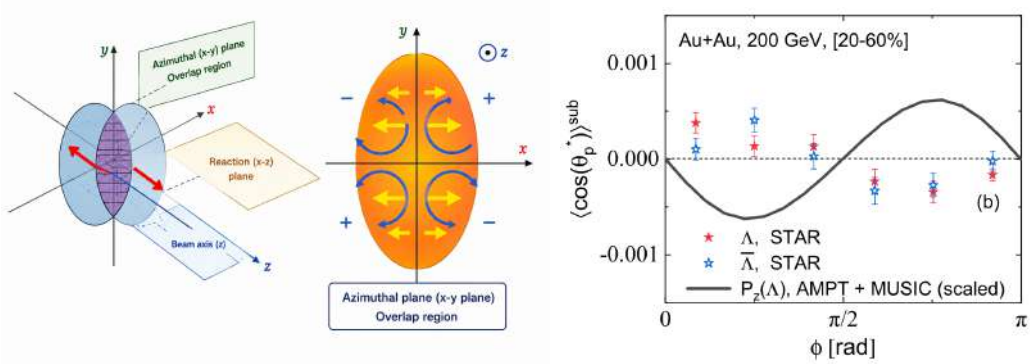



Figure 2.5: (Left) Illustration of the system created in a non-central heavy-ion collision viewed in the transverse plane. (Right) $\langle cos\theta^* \rangle$ of $\Lambda$ and $\bar{\Lambda}$ hyperons as a function of azimuthal angle $\phi$ in Au+Au collisions at $\sqrt{s_{\rm NN}} = 200$ GeV [55].

of the medium. In addition to $\Lambda$ hyperons, the averaged global spin polarization measurement of $\Omega$ and $\Xi$ hyperons is obtained using the polarization transfer method in the STAR collaboration [59]. This result hints at a possible hierarchy in the global spin polarization, i.e., $P_\Lambda < P_\Xi < P_\Omega$ [59]. The large systematic and statistical uncertainties raise a question as to whether the difference in spin polarization of various hadrons is due to the mass, lifetime, strangeness quantum number, differential freeze-out, and/or any localized effects, etc. Motivated by this comprehensive set of measurements and various contributing mechanisms, a quantitative and systematic assessment of their individual contribution to the global spin polarization of various hyperons is studied in Chapter 7.

#### 2.2.2.2 Local spin polarization of hyperons

Besides global spin polarization, the local (or longitudinal) spin polarization of $\Lambda$-hyperons along the beam direction is observed in experiments [55, 61, 68]. The longitudinal polarization arises due to the inhomogeneous expansion of the fireball. Specifically, in non-central heavy-ion collisions, anisotropic flow in the transverse plane forms a quadrupole pattern of longitudinal vorticity along the beam direction (z-axis), leaving particles longitudinally polarized [103, 108, 118,

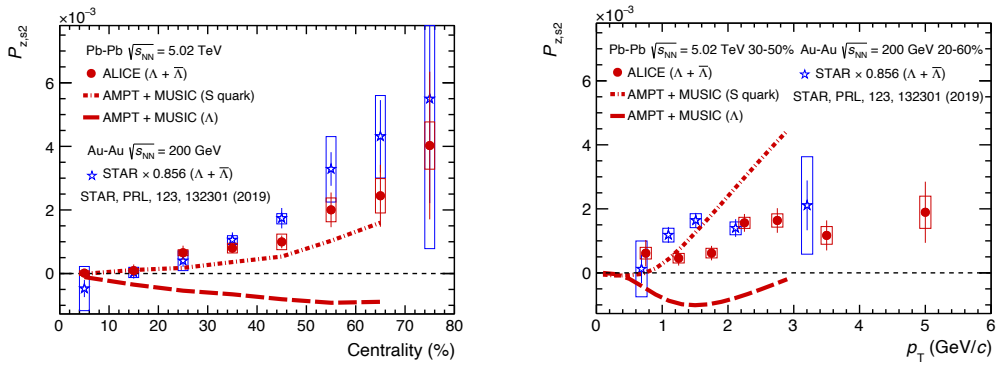



Figure 2.6: The second Fourier sine coefficient of the longitudinal spin polarization $P_{z,s2}$ as a function of centrality (left panel) and transverse momentum $p_{\mathrm{T}}$ (right panel) [68].

119, 126]. Unlike the polarization along OAM, the longitudinal polarization ($P_z$) is sensitive only to transverse expansion dynamics [118]. It does not decrease rapidly with increasing center-of-mass energy; thus, it is detectable even at LHC energies. Furthermore, it is sustained in the Bjorken longitudinal boost invariance scenario and does not require identifying the orientation of the reaction plane. However, the topology of the colliding ions plays a crucial role in determining the longitudinal polarization of the particles.

The experimental measurement of longitudinal polarization of $\Lambda$ ($\bar{\Lambda}$) with the azimuthal angle ($\phi$) relative to the second-order event plane ($\Psi_2$) by the STAR Collaboration [55] shows an opposite trend compared to the theoretical predictions as shown in the right panel of Fig. 2.5. [118]. This discrepancy between theoretical models and experimental data is commonly referred to as a "spin sign puzzle." The reason for the opposite signs of longitudinal polarization across various hydrodynamic models remains uncertain. In some studies, it has been attempted to explain this by adding a thermal shear term at local equilibrium into the spin polarization vector [178–183]. Further, a multi-phase transport model (AMPT) based study was also able to address this polarization sign issue by considering

the quadrupole structure of longitudinal vorticity [119]. Moreover, there have been several additional efforts to address this issue. For instance, by substituting the thermal vorticity in the spin polarization equation (Eq. 7.60) with projected thermal vorticity or T-vorticity, the longitudinal component of polarization flips its sign and aligns with experimental observations [184, 185]. Recent studies suggest that the emergence of longitudinal polarization is due to a combination of shear-induced tensor, thermal vorticity, and fluid acceleration [186]. They argued that while the shear-induced term accounts for the correct angular dependence of longitudinal polarization, its overall impact might be nullified by thermal vorticity and fluid acceleration. A few attempts have been made to resolve this spin sign puzzle by incorporating a spin tensor component into the orbital angular momentum [187–190]. The spin sign puzzle has been attempted to be solved by considering the gradient of chemical potential [191] and spin potential [192]. A chiral kinetic approach with AMPT initial conditions also predicts the same $P_z$ modulation as experimental data [193].

The centrality and transverse momentum ($p_{\mathrm{T}}$) dependence of longitudinal polarization observed at the RHIC and LHC energies are shown in Fig. 2.6. The hydrodynamic model MUSIC with AMPT initial conditions is used to estimate the centrality and $p_{\mathrm{T}}$ dependence of longitudinal polarization of $\Lambda$-hyperons by incorporating both thermal shear and thermal vorticity. It predicts that thermal vorticity dominates when the hyperon mass is taken as the spin-carrying mass, whereas thermal shear dominates when the strange quark mass is used instead. The latter scenario reproduces the experimentally observed positive longitudinal polarization, suggesting that $\Lambda$ hyperons inherit the spin polarization of strange quarks. A simple boost-invariant blast wave hydrodynamic model with kinematic vorticity and a few freeze-out parameters explains the centrality and $p_{\mathrm{T}}$ dependence of longitudinal polarization measured by the STAR Collaboration [55]. It is important to note that in both cases, the effect of hadronic interactions on $\Lambda$ hyperons' spin polarization is not considered. Therefore, the particle spin polar-

ization dynamics depend on the assumptions used in the model to calculate the polarization observable. So, it is crucial to validate the longitudinal polarization data with other hydrodynamic and transport models that consider hadronic scattering. Motivated by this study, the longitudinal spin polarization of $\Lambda$ hyperons using hydrodynamic and transport models is explored in Chapter 7.

### 2.2.3 Vector meson spin alignment: an overview

Unlike the spin polarization of hyperons, the corresponding phenomenon for spin 1 particles, often referred to as the "twin effect" of hyperon polarization, is the spin alignment of vector mesons. Spin alignment is described by a $3 \times 3$ Hermitian spin density matrix, $\rho_{m,m'}$, where $m$ and $m'$ denote the spin projections of the vector meson along the chosen quantization axis. The diagonal elements, $\rho_{11}$, $\rho_{00}$, and $\rho_{-1-1}$, represent the probabilities of finding the vector meson in the spin states $+1$, 0, and $-1$, respectively. Out of these three diagonal elements, $\rho_{00}$ is independent, and it can be experimentally determined from the angular distributions of two-body decays into either pseudoscalar mesons (e.g., $\phi \to K^+K^-$) or spin $\frac{1}{2}$ fermions (e.g., J/$\psi \to \mu^+\mu^-$ or $e^+e^-$), as discussed in Sec. 2.1.2. In the absence of spin alignment, the three spin states ($m = +1,\ 0,\ -1$) are equally populated, corresponding to $\rho_{00} = \frac{1}{3}$. Therefore, the deviation of $\rho_{00}$ from $\frac{1}{3}$, i.e., $\rho_{00} - \frac{1}{3}$, quantifies the degree of spin alignment of the vector meson. A value of $\rho_{00} < \frac{1}{3}$ indicates a preferential population of the transverse spin states, whereas $\rho_{00} > \frac{1}{3}$ corresponds to a preferential population of the longitudinal spin state with respect to the chosen quantization axis. A precise determination of $\rho_{00}$, together with the associated polarization parameters in different polarization frames, provides valuable insights into the spin dynamics of vector mesons and the influence of the surrounding medium in relativistic heavy-ion collisions. The spin alignment is commonly studied in the helicity, Collins–Soper, event-plane, production-plane, and random-plane reference frames. In the following, a review

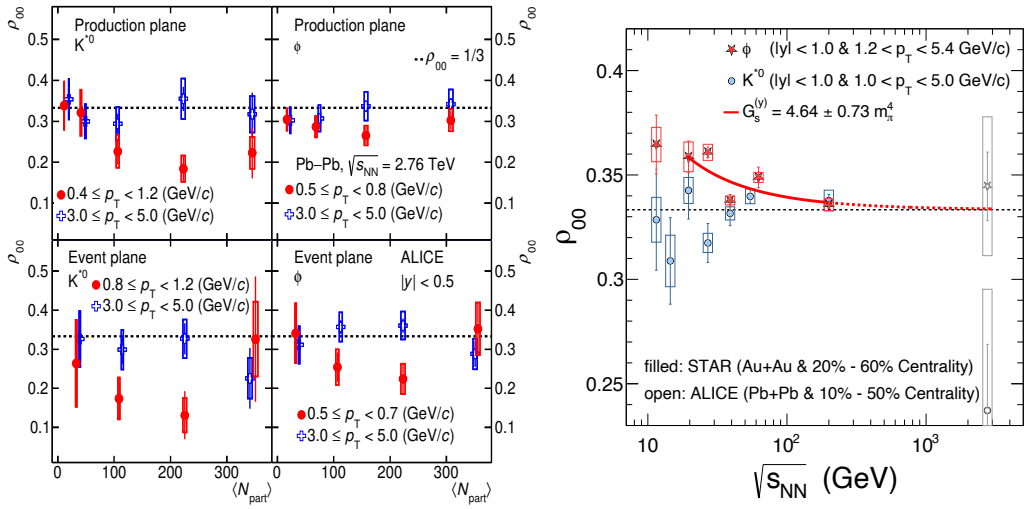



Figure 2.7: $\rho_{00}$ for $K^{*0}$, $\phi$ as function of $\langle N_{\rm part}\rangle$ (left)[66] and $\sqrt{s_{\rm NN}}$ (right)[62].

of the experimental observations and theoretical developments related to the spin alignment of light- and heavy-flavor vector mesons is presented.

#### 2.2.3.1 Spin alignment of light-flavor vector mesons

The first evidence of spin alignment of light-flavor vector mesons ($K^{*0}$ and $\phi$) in heavy-ion collisions was reported by the ALICE [66], and subsequently by the STAR at RHIC energies [62]. The right panel of Fig. 2.7 presents the measured values of the spin density matrix element $\rho_{00}$ for $K^{*0}$ and $\phi$ in heavy-ion collisions at RHIC and LHC energies. The $\rho_{00}$ is found to be below $\frac{1}{3}$ for $\phi$ mesons at the LHC, while it is observed to be above $\frac{1}{3}$ at RHIC. The magnitude of the measured spin alignment of light-flavor vector mesons at both RHIC and LHC energies is significantly larger than that expected from the global $\Lambda$ polarization in the non-relativistic thermodynamic limit, assuming vorticity to be the sole source of polarization [66, 116]. As the spin alignment of vector mesons arises from contributions of both constituent quarks and antiquarks, the resulting spin alignment is expected to scale quadratically with medium vorticity [117]. These unexpected observations have stimulated extensive theoretical efforts to under-

stand the underlying mechanisms responsible for vector meson spin alignment. In particular, the spin alignment of vector mesons probes the local spin correlations and fluctuations of quark–antiquark pairs [156], fluctuations of quark polarization in turbulent color fields due to locally fluctuating axial charge currents [194], and local spin correlation induced by the color fields in the glasma phase [195] show that these mechanisms could lead to large vector meson spin alignment.

In Refs. [80, 117], hadronization through the quark coalescence mechanism is predicted to result in $\rho_{00} < \frac{1}{3}$. However, the predicted deviation from the unpolarized value of $\frac{1}{3}$ is considerably smaller than that observed experimentally. In contrast, the positive deviation, $\rho_{00} > \frac{1}{3}$, measured for $\phi$ mesons at RHIC energies can be qualitatively explained by models that incorporate fluctuations of the $\phi$-meson field [131, 152, 153]. Within this framework, strange and antistrange quarks become polarized through their interaction with the $\phi$-meson field generated by the current of pseudoscalar bosons during the formation of the $\phi$ meson. Consequently, the local spin correlations and fluctuations induced by the vector meson field lead to $\rho_{00} > \frac{1}{3}$ for $\phi$ mesons produced via the coalescence of polarized strange and antistrange quarks. Furthermore, recent calculations based on the holographic approach predict a significant spin alignment of flavorless vector mesons arising from modifications of their spectral functions in different spin channels in the presence of a thermal medium [155]. These calculations are also in qualitative agreement with the observed spin alignment of $\phi$ mesons at RHIC energies. Despite the progress made by various theoretical approaches, a unified theoretical framework capable of consistently describing the spin alignment of light-flavor vector mesons across different collision energies and hadron species has not yet been established. Consequently, further theoretical developments are required to achieve a comprehensive understanding of the underlying mechanisms responsible for vector meson spin alignment. In view of these experimental observations and the current theoretical challenges, the spin alignment of the $K^{*0}$, $\phi$, and $\rho$ vector mesons is investigated in Chapter 7.

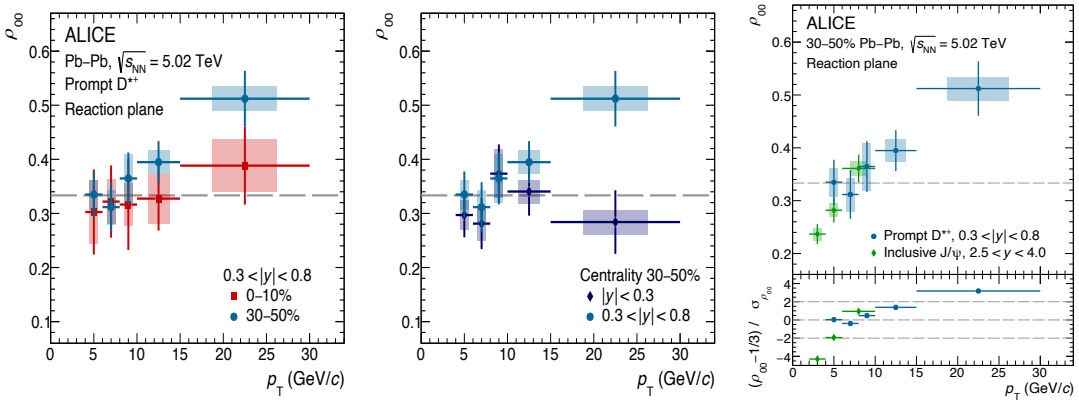



Figure 2.8: $\rho_{00}$ for prompt $D^{*+}$ as a function of $p_{\mathrm{T}}$ for two different centralities (left), two different rapidities (middle), and compared with J/$\psi$ (right)[72].

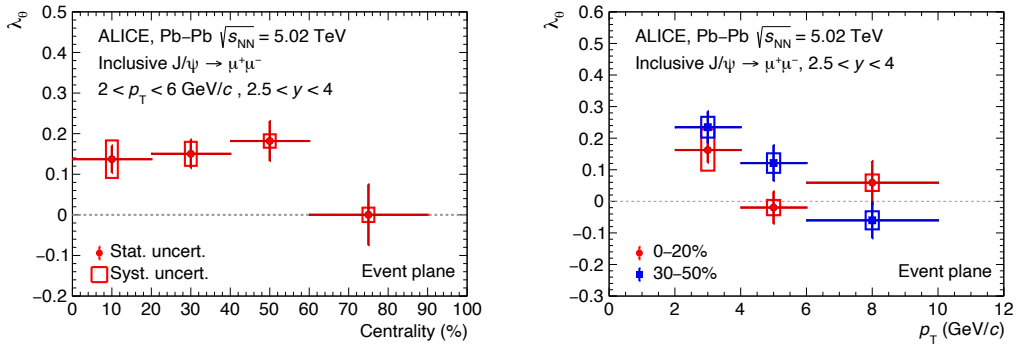



Figure 2.9: Centrality (left) and $p_{\mathrm{T}}$ (right) dependence of $\lambda_\theta$ for J/$\psi$ [71].

### 2.2.3.2 Spin alignment of heavy-flavor vector mesons

Unlike light-flavor hadrons, which are predominantly formed in the later stages of heavy-ion collision evolution, heavy-flavor hadrons are expected to be more sensitive to the system's early-time dynamics. This is because charm quarks are primarily produced in the initial hard partonic scatterings, with a characteristic production time of $\mathcal{O}(0.1$ fm/$c)$, which is considerably shorter than the QGP formation time of $\mathcal{O}(1$ fm/$c)$ [2]. Consequently, charm quarks experience the intense magnetic field and large fluid vorticity that exist immediately after the collision, when these fields attain their maximum strength [196]. Furthermore,

charm quarks with high-$p_{\mathrm{T}}$ are expected to preserve a larger fraction of their initial polarization owing to their shorter interaction time with the medium constituents. However, the degree of polarization retention also depends on the corresponding spin-relaxation time [162]. The ALICE Collaboration has performed the first measurement of the spin alignment of prompt open-charm hadrons ($D^{*+}$) at midrapidity ($|y| < 0.8$) in Pb–Pb collisions at $\sqrt{s_{\mathrm{NN}}} = 5.02$ TeV, as shown in Fig. 2.8. The measurement of the spin density matrix element $\rho_{00}$ for prompt $D^{*+}$ mesons in Pb–Pb collisions provides important input for theoretical models describing the spin alignment of charm hadrons in the hot and dense medium. Such measurements offer valuable insights into the propagation of charm quarks in the presence of strong magnetic fields and large vorticity generated during the early stages of heavy-ion collisions. Furthermore, measurements at high-$p_{\mathrm{T}}$ are particularly important for understanding the transfer of charm-quark polarization to the final-state hadrons when hadronization is dominated by the quark fragmentation mechanism. Furthermore, the ALICE collaboration has recently reported the first evidence of a significant spin alignment of inclusive J/$\psi$ mesons in Pb–Pb collisions at $\sqrt{s_{\mathrm{NN}}} = 5.02$ TeV [68]. The measurement was performed at low-$p_{\mathrm{T}}$ and forward rapidity, and the corresponding results are shown in Fig. 2.9. The observed spin alignment is qualitatively consistent with theoretical predictions based on the holographic approach presented in Ref. [155]. Motivated by the experimental observations and the absence of a unified theoretical description for vector mesons, the spin alignment of the J/$\psi$ meson from an experimental perspective is presented in Chapter 5. Further, a theoretical study of the spin alignment of the J/$\psi$, $\psi(2S)$, $\Upsilon(1S)$, and $\Upsilon(2S)$ vector mesons is presented in Chapter 6.

# Chapter 3

## The ALICE Experiment at the LHC

### 3.1 The Large Hadron Collider

At the France-Switzerland border, the European Organization for Nuclear Research (CERN) houses the Large Hadron Collider (LHC), which is the highest-energy particle or ion accelerator in the world. The LHC tunnel is around 27 km in circumference, situated underground between 50 to 175 meters. Inside the accelerator, two beams of particles are guided in separate vacuum pipes, in opposite directions, and are guided by strong magnetic fields provided by superconducting magnets; hence, the magnets are kept at very low temperatures of about 1.85 K with liquid helium. Before particles start circulating inside the LHC, the particles pass through a chain of pre-accelerators (Figure 3.1), gaining more energy in each step until reaching a center-of-mass energy at the TeV scale. These particles, grouped into bunches, consist of protons (extracted from hydrogen gas), oxygen, neon, xenon, or lead ions. The beam size and trajectory are controlled with quadrupole and dipole magnets, respectively. The two beams, accelerated at very high speeds, cross at four different points, around which are located the different CERN experiments: ATLAS, LHCb, CMS, and ALICE.

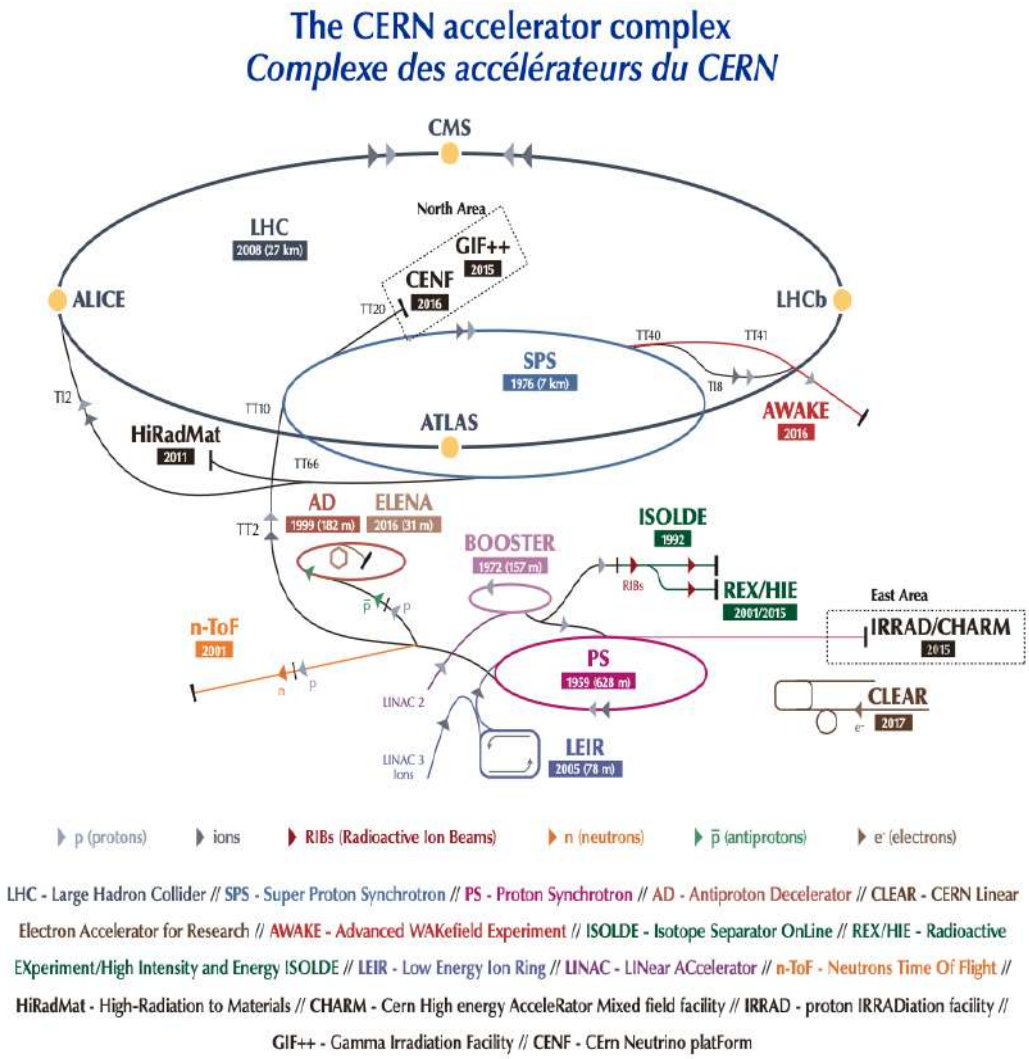



Figure 3.1: Schematic view of the CERN detailed accelerator structure [197].

### 3.1.1 Cross section and luminosity

High-energy collisions at the LHC are inherently probabilistic, and the probability of occurrence of a given interaction is quantified by the cross section $\sigma$. The cross section is an intrinsic property of the underlying physical interaction and has the dimensions of area. At low energies, it can be interpreted classically as the effective transverse overlap between the colliding particles, analogous to the interaction of two hard spheres.

The number of inelastic collisions occurring per unit time at a given interaction point is denoted by $\frac{dR}{dt}$ and is referred to as the *collision rate*. To characterize collisions between two bunches, the luminosity measurements are an essential parameter and must be determined. The instantaneous luminosity, $\mathcal{L}$, quantifies the rate of inelastic interactions and is expressed in units of $\mathrm{cm}^{-2}\mathrm{s}^{-1}$. It can be calculated theoretically using the following expression:

$$\mathcal{L} = \frac{1}{\sigma}\frac{dR}{dt} \tag{3.1}$$

where $\sigma$ is the inelastic collision cross-section of a given process and $\frac{dR}{dt}$ is the number of collisions per unit of time. Luminosity is one of the key parameters of particle accelerators, which quantifies the capability of the accelerator to produce a large number of interactions or collisions per unit time.

One can also define the integrated luminosity $\mathcal{L}_{\mathrm{int}}$ which quantifies the number of events observed during a given data-taking period:

$$\mathcal{L}_{\mathrm{int}} = \int \mathcal{L}\, dt = \int \frac{1}{\sigma}\frac{dR}{dt}\, dt \tag{3.2}$$

In the case of a circular accelerator like the LHC, the luminosity at a given interaction point can also be calculated using the relation [1];

$$\mathcal{L} = f_{\mathrm{coll}}\frac{N_1 N_2}{4\pi\sigma_x\sigma_y}\mathcal{F} \tag{3.3}$$

where $N_1$ and $N_2$ are the number of particles per bunch in the two beams. $\sigma_x$ and $\sigma_y$ characterize the transverse size of the colliding beams at the interaction point. $\mathcal{F}$ is a factor of order 1 that takes into account inefficient geometric overlapping of the beams due to a crossing angle between the colliding beams, finite bunch length, and beam focus. $f_{\mathrm{coll}}$ is the frequency of bunch crossings, which is linked to the number of bunches per beam $n_b$ by $f_{\mathrm{coll}} = n_b f_0$, where $f_0$ is the revolution frequency of the LHC, which is 11.223 kHz. To achieve high luminosity, it is necessary to maximize the number of colliding bunches, increase the collision

frequency, and optimize the geometric overlap of the beams at the interaction point.

During Run 3, the LHC operates at an instantaneous luminosity of about $2 \times 10^{34}$ cm$^{-2}$s$^{-1}$. The High-Luminosity LHC (HL-LHC) upgrade [198] aims to increase this value up to approximately $5 \times 10^{34}$ cm$^{-2}$s$^{-1}$ for the ATLAS and CMS experiments. In contrast, ALICE and LHCb operate at lower luminosities, as their detectors and beam conditions are optimized for specific physics goals and are not designed to accommodate such high interaction rates. This upgrade is expected to deliver an integrated luminosity of about 250 fb$^{-1}$ per year. The HL-LHC program is planned to be implemented during Long Shutdown 3 (LS3), scheduled for the late 2020s.

On the other hand, at the LHC and RHIC experiments, rare events (or exotic particles) are characterized by small production cross sections, $\sigma$. Consequently, a large number of events is required to study such measurements with sufficient statistical precision. During Run 3, this rate increased compared to Run 2 to gather more events, which will help in the study of rare candidates and reach up to 50 kHz for Pb–Pb collisions.

### 3.1.2 The four giants

The four major experiments surrounding the collision points of the LHC accelerator, as displayed in Figure 3.1, are the following:

- **A Toroidal LHC ApparatuS (ATLAS):** ATLAS [199] is a general-purpose detector at the LHC, designed to study the SM physics and beyond, including the Higgs boson and supersymmetric particles. ATLAS also contributes to the heavy-ion and QGP studies. The detector comprises several subsystems arranged around the interaction point, enabling precise measurements of particle trajectories, momentum, and energy. A large magnet provides a magnetic field of about 2 T, bending the paths of charged parti-

cles for accurate momentum determination. ATLAS has a pseudorapidity coverage of $|\eta| < 2.5$, with muon measurements accessible down to $p_{\mathrm{T}} \sim 3$ GeV/$c$. ATLAS has very high $p_{\mathrm{T}}$ measurement capabilities up to a few hundred GeV/c.

- **Compact Muon Solenoid (CMS):** The CMS detector [200] is a multi-purpose experiment at the LHC with similar physics goals as ATLAS. The detector is built around a large superconducting solenoid, forming a cylindrical coil that generates a magnetic field of about 4 T. CMS covers a pseudorapidity range of $|\eta| < 2.5$, with muon measurements accessible down to transverse momenta of about $p_{\mathrm{T}} \sim 1.2$–$3.5$ GeV/$c$.

- **LHC beauty (LHCb):**The LHCb [201] is a single-arm forward spectrometer detector that is primarily dedicated to heavy-flavor physics, with a particular focus on the decays of $b$-hadrons, and the study of matter-antimatter asymmetry. The detector includes a dipole magnet with a bending power of about 4 T·m and covers a pseudorapidity range of $2 < \eta < 5$. The LHCb can operate in a fixed-target mode by injecting noble gases (such as He, Ne, and Ar) into the LHC beam pipe at the interaction point.

- **A Large Ion Collider Experiment (ALICE):** The ALICE [202] detector is mostly dedicated to QGP studies. The upgraded ALICE detector in Run 3 configuration is shown in Figure 3.2. This experiment will be further detailed in the next section.

## 3.2 The ALICE detectors

The ALICE detector is designed to study QGP produced in heavy-ion collisions at the LHC. It is located approximately 56 m underground and has dimensions of about 26 m in length, 16 m in height, and 16 m in width, with a total weight of

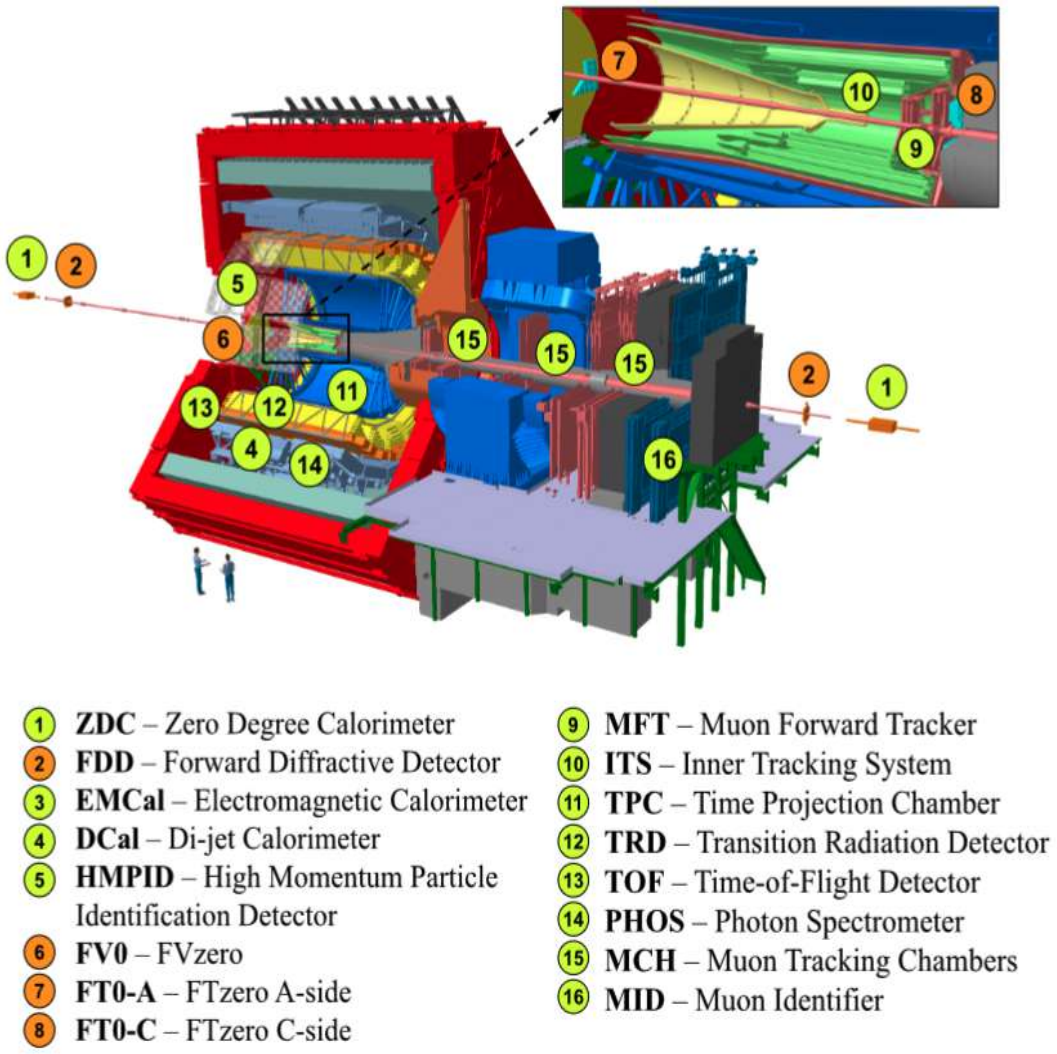



Figure 3.2: Schematic view of the ALICE detector in Run 3 configuration [203].

around 10,000 tonnes. The detector comprises 16 subdetectors, which are broadly categorized into global detectors, central barrel detectors, and the muon spectrometer. A detailed description of these detectors is provided below. Quarkonium measurements can be performed down to $p_{\mathrm{T}} = 0$ GeV/c. These measurements are carried out in the dielectron decay channel at midrapidity ($|\eta| < 0.9$) and in the dimuon decay channel at forward rapidity ($-4 < \eta < -2.5$).

### 3.2.1 The global detectors

The global detectors are located around the interaction point (IP) and provide global measurements such as collision centrality, collision time, and particle multiplicity. Examples of global detectors include the Zero Degree Calorimeter (ZDC) and the Fast Interaction Trigger (FIT).

#### 3.2.1.1 The Zero Degree Calorimeter (ZDC):

The Zero Degree Calorimeter (ZDC) [204] consists of two hadronic and two electromagnetic calorimeters installed on both sides of the interaction point (IP). The hadronic calorimeters, located at $z = \pm 112.5$ m, are the farthest detectors from the IP and measure the energy of spectator nucleons. The electromagnetic calorimeters, positioned closer to the IP at about 7 m in the forward region, detect the energy of photons at forward rapidity. The ZDCs are based on Cherenkov light detection and are composed of quartz fibers read out by photomultiplier tubes (PMTs). Charged particles traversing the quartz at velocities exceeding the speed of light in the medium produce Cherenkov radiation, which is collected and converted into an amplified signal by the PMTs. These calorimeters enable the determination of global event properties, such as collision centrality and the reaction plane.

#### 3.2.1.2 The Fast Interaction Trigger (FIT):

The FIT detector [205] consists of five distinct detector stations grouped into three sub-detectors (FT0, FV0, FDD) installed on both sides (A and C side), ranging from -19.5 m to 17 m from the IP. It is mainly used for triggering event selection, to estimate collision time information, collision centrality, and particle multiplicity determination.

**The FT-zero (FT0) detector**: The FT0 detector consists of two detectors, namely, FT0+A and FT0+C. These two are located on opposite sides of the

IP. Both FT0+A and FT0+C are composed of 12 Cherenkov counters. These counters are made of quartz fibers, connected to PMTs. These counters use a similar detection method as explained for the ZDC detector using Cherenkov light. This detector provides a precise collision time with 25 ps resolution and determines a vertex position for the collisions.

**The FV-zero+ (FV0+) detector**: The FV0+ detector is made up of two scintillator counter arrays, namely FV0+A and FV0+C, placed on the opposite sides of the IP. Each scintillator array is segmented into four rings in the radial direction, and further, each of these rings is divided into eight sections in the azimuthal direction. Hence, both of these arrays are divided into 32 counters. When a particle hits a counter, the light produced is transmitted to PMTs through optical fibers. This detector discriminates the beam-beam interaction from the beam-gas background interactions, thus providing a minimum bias trigger. Additionally, it provides the beam luminosity, charged particle multiplicity, and azimuthal distributions.

**The Forward Diffractive Detector (FDD)**: The FDD is composed of two sub-detectors placed on opposite sides of the IP. Each array consists of eight rectangular scintillator pads. When a particle hits a counter, such as V0+, it emits light that is carried by optical fibers to the PMTs. This detector provides measurements of diffractive cross-sections and centrality, selections of ultra-peripheral collisions, and monitoring of the beam quality.

### 3.2.2 The central barrel detectors

The central barrel detectors are used for particle identification and tractography of charged particles and photons. The details of the central barrel detectors are presented in the following section.

#### 3.2.2.1 The ElectroMagnetic Calorimeter - Di-jet Calorimeter (EMCal - DCal):

The EMCal [206] is located at a distance of 4.28 m from the IP, covering an azimuthal angle of $\Delta\phi = 110°$ and a pseudorapidity range of $|\eta| < 0.7$. It is a layered Pb–scintillator sampling calorimeter. The DCal [207] was later installed to extend the physics capabilities of the EMCal, particularly for the study of back-to-back correlations. It covers an azimuthal angle of $\Delta\phi = 70°$ within the same pseudorapidity range. These electromagnetic calorimeters enable the identification of photons and neutral mesons via their photonic decay channels.

#### 3.2.2.2 The PHOton Spectrometer (PHOS):

The PHOS [208] is located at a distance of 4.6 m from the IP, covering an azimuthal angle of $\Delta\phi = 70°$ and a pseudorapidity range of $|\eta| < 0.12$. It is a high-resolution electromagnetic calorimeter composed of dense lead–tungstate scintillating crystals. A Multi-Wire Proportional Chamber (MWPC), installed in front of the calorimeter, serves as a Charged Particle Veto (CPV). PHOS enables the measurement of photons and neutral mesons via their photonic decay channels, facilitating studies of jet quenching, particularly at high $p_{\mathrm{T}}$.

#### 3.2.2.3 The High Momentum Particle Identification Detector (HMPID):

The HMPID [209] is located at a distance of 4.9 m from the IP, covering an azimuthal angle of $\Delta\phi = 58°$ and a pseudorapidity range of $|\eta| \leq 0.6$. It is based on Ring Imaging Cherenkov (RICH) technology and consists of seven modules designed to measure the Cherenkov emission angle for particle identification. The HMPID complements the capabilities of other central barrel detectors, such as the ITS, TPC, and TOF, enabling $\pi/K$ separation up to 3 GeV/$c$ and $K/p$ separation up to 5 GeV/$c$.

#### 3.2.2.4 The Time Of Flight detector (TOF):

The TOF detector [210] is located at a radial distance of 3.7 m from the interaction point (IP), covering a pseudorapidity range of $|\eta| \leq 0.9$. It consists of a cylindrical array with an active area of about 141 $m^2$, segmented into 18 sectors and based on Multigap Resistive Plate Chamber (MRPC) technology. The TOF measures the time at which particles reach the detector with a resolution better than 50 ps. Combined with the collision time provided by FT0, this allows the determination of particle velocity. The detector enables particle identification of protons up to $p_T < 4$ GeV/$c$, and pions and kaons up to $p_T < 2.5$ GeV/$c$.

#### 3.2.2.5 The Transition Radiation Detector (TRD):

The TRD [211] is a cylindrical detector, approximately 7 m in length and diameter, surrounding the TPC. It covers the full azimuthal angle and operates within the pseudorapidity range $|\eta| \leq 0.84$, with a radial extension from about 2.9 m to 3.68 m from the IP. Each TRD readout chamber consists of an MWPC with an amplification and a drift region, filled with an Xe–$CO_2$ gas mixture, and a radiator. High-energy electrons traversing the radiator produce transition radiation, enabling the detector to distinguish electrons from pions for transverse momenta $p_T \gtrsim 1$ GeV/$c$. In addition, the TRD provides tracking information, complementing the capabilities of other central barrel detectors.

#### 3.2.2.6 The Time Projection Chamber (TPC):

The TPC [212] is a cylindrical detector with a volume of about 90 $m^3$, filled with a Ne–$CO_2$–$N_2$ gas mixture. It covers the full azimuthal angle and a pseudorapidity range of $|\eta| \leq 0.9$. Charged particles traversing the detector ionize the gas, producing electron–ion pairs. Under an applied electric field, the liberated electrons drift towards the endplates, where they are collected by readout chambers, enabling tracking, momentum measurement, and particle identification. The con-

tinuous readout chambers of the upgraded TPC [213] in Run 3 significantly reduce the ion backflow and the associated space-charge effects. This allows operation at interaction rates of up to 50 kHz in Pb–Pb collisions.

#### 3.2.2.7 The Inner Tracking System 2 (ITS2)

The ITS2 is the innermost detector of the ALICE central barrel. It provides precise determination of the primary vertex and reconstruction of secondary vertices from heavy-flavor hadron decays. In addition, it enables tracking down to low-$p_{\mathrm{T}}$ and improves the momentum and angular resolution of tracks reconstructed in the TPC. The ITS2 [214] consists of seven cylindrical layers, covering the full azimuthal angle and a pseudorapidity range of $|\eta| \leq 1.3$, with radial positions from 2.2 cm to 40 cm around the IP. It is based on ALPIDE chips employing Monolithic Active Pixel Sensor (MAPS) technology, providing excellent spatial resolution. Thanks to its reduced distance from the IP, the ITS2 achieves significantly improved pointing resolution compared to the ITS used in Run 1 and Run 2.

### 3.2.3 The muon spectrometer

The muon spectrometer [215] is the primary detector used in the analysis presented in the next chapter. It is designed to study quarkonium states ($\mathrm{J}/\psi$, $\psi(2\mathrm{S})$, $\Upsilon(1\mathrm{S})$, $\Upsilon(2\mathrm{S})$, $\Upsilon(3\mathrm{S})$), low-mass vector mesons ($\rho$, $\omega$, $\phi$), open heavy-flavor hadrons ($D$ and $B$ mesons), and gauge bosons ($\mathrm{W}^{\pm}$, and $\mathrm{Z}^{0}$) at forward pseudorapidity ($-4 < \eta < -2.5$) via their muonic decay channels. These measurements are performed in various collision systems, including $pp$, p–O, p–Pb, O–O, Ne–Ne, Xe–Xe, and Pb–Pb collisions. The spectrometer covers the full azimuthal angle. A schematic view of the muon spectrometer is shown in Fig. 3.3. It consists of a dipole magnet, tracking stations, trigger chambers, and absorbers. However, the presence of the front absorber between the interaction point (IP) and

the spectrometer introduces significant multiple scattering of the muon tracks, leading to a degradation of the tracking resolution. As a consequence, certain physics measurements are limited, in particular the separation of open charm and beauty contributions. To overcome these limitations in Run 3, the Muon Forward Tracker (MFT) [216] has been installed between the IP and the front absorber, providing precise vertexing capabilities and improving the separation of heavy-flavor sources.

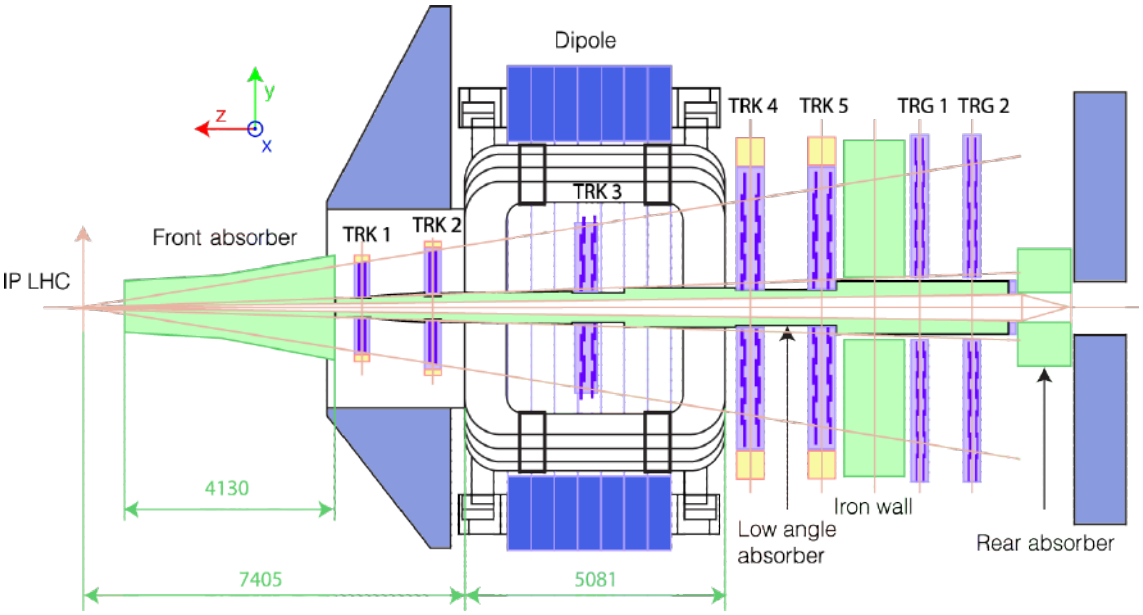



Figure 3.3: Schematic view of the ALICE Muon Spectrometer [217].

#### 3.2.3.1 The absorbers:

The front absorber (shown in Figure 3.4) is designed to reduce the contamination of hadrons and of low-momentum muons, mainly coming from pion and kaon decays. It is 4.13 m long and located inside the solenoid magnet, at 90 cm from the IP. The design of the absorber is optimized to limit multiple scattering effects, which can degrade the momentum and invariant mass resolution. To achieve this, low-$Z$ materials such as carbon are used in the region closest to the IP, followed

by concrete. On the other hand, high-$Z$ materials, including lead (Pb) and Tungsten (W), are employed on the absorber's end side. The absorber is designed to suppress low-energy photons and secondary particles produced within the front absorber. To further protect the spectrometer from beam–gas interactions and secondaries at high rapidities, a low-angle absorber is installed around the beam pipe, composed of dense materials such as lead (Pb), Tungsten (W), and steel. In addition, an iron wall of about 1.2 m thickness is placed between the tracking and trigger chambers to absorb the remaining hadronic background, allowing only muons with momenta above approximately 4 GeV/$c$ to pass through. Finally, a rear absorber, about 1.1 m thick and located downstream of the trigger chambers, reduces contamination from beam–gas interactions reaching the detector.

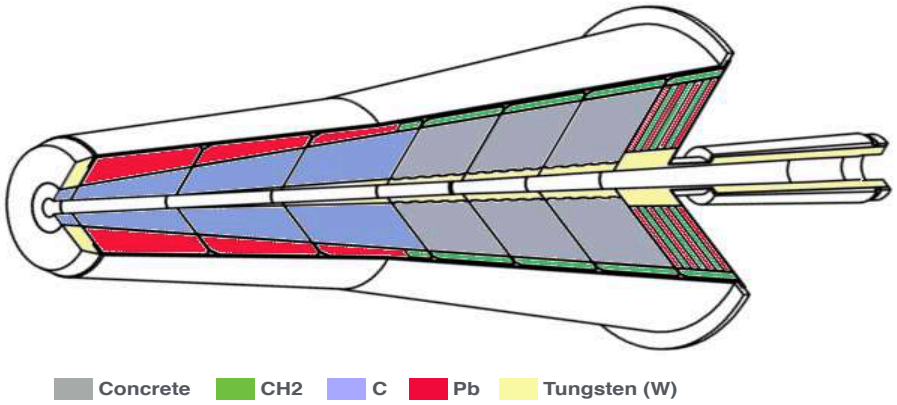



Figure 3.4: Schematic view of the front absorber with its composition [217].

#### 3.2.3.2 The dipole magnet:

The dipole magnet, with dimensions of approximately 5 m in length, 6.6 m in width, and 8.6 m in height, is located 7 m from IP. It generates an integral magnetic field of about 3 T·m, oriented perpendicular to the beam axis. This magnetic field bends the trajectories of charged particles (e.g., muons); by measuring the curvature of their paths, both their momentum and the sign of their

electric charge can be determined.

#### 3.2.3.3 The Muon CHambers (MCH):

The Muon CHambers form the tracking system of the Muon spectrometer, with 5 stations, each composed of 2 chambers, located between 5.2 m and 14.4 m from the IP. The chambers are designed to minimize multiple scattering of muons and are constructed using low-$Z$ materials, such as carbon fiber. Each chamber is a cathode pad chamber featuring a central anode wire sandwiched between two cathode planes, providing high granularity. The chambers are filled with a gas mixture of Argon (80

#### 3.2.3.4 The Muon IDentification (MID):

It is located 16 m away from the IP, behind the iron wall filter. It consists of two stations, each composed of two planes of resistive plates. These plates are made of electrodes separated by a gap of 2 mm filled with gas. When a charged particle traverses the detector, it initiates an avalanche of secondary electrons. The time of response when a muon passes through these chambers is about 2 ns. However, the readout time window is about 25 ns.

#### 3.2.3.5 The Muon Forward Tracker (MFT):

As mentioned, during the LS2, a new detector has been installed around 40 cm from the IP and is located between the IP and the front absorber, covering the pseudorapidity region of -3.6 $< \eta <$ -2.5. The first goal of this detector is to improve the muon pointing resolution. On the other hand, this detector provides a precise determination of secondary vertexing capabilities and allows the separation of prompt and non-prompt quarkonia and muons produced from open heavy-flavor hadrons in general. The detailed layout of the MFT can be found in Refs. [216, 218, 219]

Thus, the forward tracks can be made up by combining information coming from 3 different detectors, including MFT, MCH, and MID. In Run 3, different nomenclature for different track types is adopted, which are listed below and shown in Fig 3.5:

1. **Global muon track**: tracks constructed by matching MCH, MID, and MFT information. These tracks will be used in prompt and non-prompt separation of quarkonium states.

2. **Global forward track**: tracks constructed by matching MCH and MFT information.

3. **Muon Standalone track**: tracks constructed by matching MCH and MID. This track definition is similar to the previous Run 1 and Run 2 measurements. A similar physics analysis to Run 1 and Run 2 can be performed with more precise and differential measurements using these forward muon tracks in Run 3. My analysis, presented in Chapter 3, utilizes these tracks.

4. **MCH Standalone track**: these are MCH tracks for which a match couldn't be found in MID. These can be used to study soft muons or muons with $\eta > 3.6$.

5. **MFT Standalone track**: these are MFT tracks for which a match couldn't be found in MCH and MID. These can be used for multiplicity analyses and underlying event characterization.

The exact algorithm for track reconstruction and matching for the aforementioned tracks is presented in Ref. [218, 219].

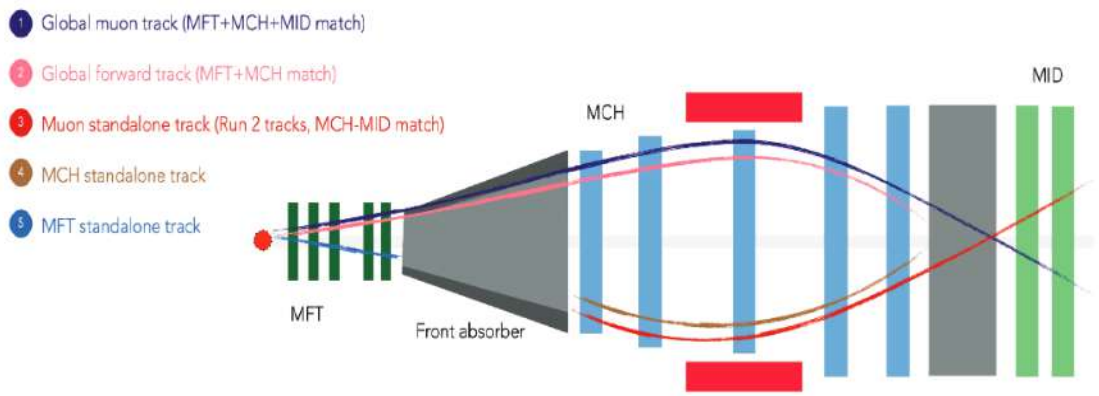



Figure 3.5: Different track types present in the muon spectrometer for Run 3 [218].

### 3.2.4 Online-Offline control system and analysis framework

A new computing system, $O^2$ (Online-Offline), is developed during LS2 to accommodate the requirements for Run 3 and Run 4, such as continuous readout and increased luminosity. The data processing chain transforms raw detector data into Analysis Object Data (AOD), which is used for physics analyses. The computing system operates through two data-driven workflows: synchronous and asynchronous. In the synchronous workflow, continuous raw data from the detectors is first received by the First Level Processor (FLP) nodes, where an initial data compression is performed. The data are then partitioned into Sub-Time Frames (STFs) and sent to the Event Processing Nodes (EPNs), where they are merged into complete Time Frames (TFs). At this stage, a total compression factor of approximately 35 is achieved. This is followed by the asynchronous workflow, in which full data reconstruction and final calibrations are performed using inputs from the Conditions and Calibration Database (CCDB). These processes are carried out on EPNs and on distributed computing infrastructures such as the Worldwide LHC Computing Grid. The processed data are then stored in

permanent formats, including Compressed Time Frames (CTFs) and AODs. The asynchronous processing stage produces Analysis Object Data (AOD) files, which are stored in ROOT trees, enabling efficient bulk reading and writing. In the Run 3 continuous readout scheme, collision vertices are associated with tracks via indexing, while collision- and track-related quantities are stored in separate tables. This structure follows a structure-of-arrays (SoA) format, optimized to exploit modern hardware architectures. Consequently, the Run 3 data model consists of a collection of flat tables organized in a relational, database-like structure, where connections are established through indices. This design allows for flexible data operations, such as joins, grouping, filtering, and combining multiple tables. Data analysis within the $O^2$ framework is organized into workflows composed of modular and flexible Data Processing Layer (DPL) tasks. Users implement analysis tasks in `C++`, specifying input data tables and producing outputs tailored to their needs, ranging from intermediate tables to final results for storage. The pipeline-based processing enables the reuse of common tasks across analyses, including table readers, writers, calibration modules, and quality selection routines.

# Chapter 4

## J/$\psi$ polarization in proton-proton and Oxygen-Oxygen collisions with ALICE

Based on:

1. "Inclusive J/$\psi$ polarization measurement at forward rapidity in proton-proton collisions at $\sqrt{s} = 13.6$ TeV", **B. Sahoo**, and R. Sahoo.
   Analysis Note: alice-notes.web.cern.ch/node/1691
   Preliminary approved Figures: alice-figure.web.cern.ch/node/36516

2. "Inclusive J/$\psi$ polarization measurement at forward rapidity in Oxygen-Oxygen collisions at $\sqrt{s_{\rm NN}} = 5.36$ TeV". **B. Sahoo**, and R. Sahoo.
   Analysis Note: alice-notes.web.cern.ch/node/1698
   Preliminary approved Figures: alice-figure.web.cern.ch/node/36516

## 4.1 Quarkonium polarization: an overview

Polarization is one of the most important observables in the study of quarkonia. Polarization is an observable that measures the degree of alignment of the total angular momentum of a particle with respect to a chosen axis, defined as the polarization or quantization axis. It is theoretically regarded as a powerful

probe to understand the long-standing problem of the mechanism of quarkonium production in elementary collisions. On the other hand, quarkonium polarization may be sensitive to the environment in which the bound state is produced, offering a unique opportunity to study the effects of the deconfined medium on the evolution of heavy-quark pairs and quarkonium formation. The interpretation of polarization measurements has been important but difficult in the past because of the complexities of its theoretical description and the limited accuracy of early experimental data. However, in recent years, substantial progress has been made in theoretical approaches, particularly within the framework of Non-Relativistic QCD (NRQCD), Improved Color Evaporation Model (ICEM), and the Color Glass Condensate (CGC) effective theory. This motivates us to perform precise and more differential measurements of the J/$\psi$ polarization in the high-luminosity Run 3 era of LHC operation. This chapter begins with an overview of the fundamental concepts of quarkonium polarization, emphasizing both the theoretical framework underlying this observable and providing the key experimental results obtained through this study. The experimental results presented in this thesis are divided into two parts. In the first part, the measurement of (J/$\psi$) polarization in proton–proton ($pp$) collisions using the high-statistics Run 3 data collected by the ALICE experiment is reported. The second part presents the first measurement of (J/$\psi$) polarization in Oxygen–Oxygen (OO) collisions, utilizing the light-ion collision data recorded at the LHC.

### 4.1.1 Dilepton decay angular distribution

Vector quarkonium states, including J/$\psi$, $\psi(2S)$, and $\Upsilon$(nS), predominantly decay electromagnetically into pairs of charged leptons. The reconstruction of the dilepton decay channels provides the cleanest and most precise method for measuring quarkonium production and polarization, benefiting from relatively well-controlled backgrounds and a theoretically well-established decay mechanism.

## 4.1 Quarkonium polarization: an overview

The polarization, or spin alignment, of vector quarkonia can be inferred from the angular distributions of the decay leptons. In the following sections, the formalism and experimental techniques used to extract quarkonium polarization from dilepton angular distributions are discussed. For example, the J/$\psi$ meson is considered as the decaying particle throughout this discussion. Nevertheless, the results derived here are general and apply to any vector state with quantum numbers $J^{PC} = 1^{--}$.

The total angular momentum operator, **J**, is given by the vector sum of the orbital angular momentum, **L**, and the spin angular momentum, **S**

$$\mathbf{J} = \mathbf{L} + \mathbf{S} \ , \tag{4.1}$$

According to the theory of angular momentum addition, the maximum allowed value for **J** varies between |**L** - **S**| and |**L** + **S**|. If the eigenvalues of the operators $\mathbf{L}^2$, $\mathbf{S}^2$, and $\mathbf{J}^2$ are characterized by the quantum numbers $l$, $s$ and $j$, then the total angular momentum **J**, can take eigenvalues in the range

$$|l - s| \ \leq \ j \ \leq \ |l + s|. \tag{4.2}$$

In general, the total angular momentum state is characterized by the quantum numbers $j$ and $j_z$, where $j_z$ denotes the projection of **J** along the chosen quantization axis ($z$-axis). Such a state is represented by the ket $|j, j_z\rangle$. Vector mesons, such as the J/$\psi$ and $\Upsilon(1S)$, are characterized by spin $s = 1$ and orbital angular momentum $l = 0$. Consequently, the total angular momentum is $j = 1$, while the magnetic quantum number can assume the values $j_z = +1,\ 0,\ -1$. Therefore, a generic vector-meson state $|\mathcal{V}\rangle$ can be expressed as a linear superposition of the three spin projection eigenstates,

$$|\mathcal{V}\rangle = b_{+1}|1, +1\rangle + b_0|1, 0\rangle + b_{-1}|1, -1\rangle, \tag{4.3}$$

where $b_{+1}$, $b_0$, and $b_{-1}$ are complex coefficients of the linear combinations, representing the probability amplitudes of the corresponding spin projection states.

The relative populations of these sub-states, determined by $|b_{+1}|^2$, $|b_0|^2$, and $|b_{-1}|^2$, define the polarization of the vector meson. In particular, if $b_0 = 0$ and $|b_{+1} + b_{-1}| = 1$, then the particle is transversely polarized, while if $b_0 = 1$ and $|b_{+1} = b_{-1}| = 0$, then the particle is longitudinally polarized.

The coefficients $b_{+1}$, $b_0$, and $b_{-1}$ cannot be measured directly in experiments. However, the polarization of a vector meson can be inferred from the angular distributions of its decay products. In particular, for two-body dilepton decays, such as $\mathrm{J}/\psi \to \ell^+\ell^-$ and/or $\Upsilon(1S) \to \ell^+\ell^-$, the shape of the angular distribution carries information about the polarization of the parent particle. An isotropic angular distribution corresponds to an unpolarized state, whereas any anisotropy indicates the presence of polarization. The relationship between the polarization amplitudes $b_{+1}$, $b_0$, and $b_{-1}$ and the angular distribution of the decay leptons can be derived from first principles. The following section presents the formalism based on the approach developed in Ref. [88], adapted to the present discussion. Consider the situation illustrated in Fig. 4.1. A quarkonium state (shown here for the $\mathrm{J}/\psi$) moving along the $z$-axis decays into a dilepton pair, $\ell^+\ell^-$. In the quarkonium rest frame, the two leptons are emitted back-to-back, thereby defining a new reference axis, denoted by $z'$.

The derivation proceeds through the following steps:

1. Before the decay, the quarkonium state is characterized by a total angular momentum $J = 1$ and its projection $m$ along the chosen polarization axis ($z$-axis). The state can therefore be written as $|Q\bar{Q} = \mathrm{J}/\psi;\ J = 1, m\rangle$.

2. After the decay, angular momentum conservation requires that the dilepton system retains the same angular momentum projection along the $z$-axis. The final state can thus be expressed as $|\ell^+\ell^-;\ J = 1, l = m\rangle$, where $l$ denotes the projection of the dilepton angular momentum along the $z$-axis.

3. If the dilepton state is described with respect to the decay axis $z'$, defined by the direction of the outgoing leptons in the quarkonium rest frame, it

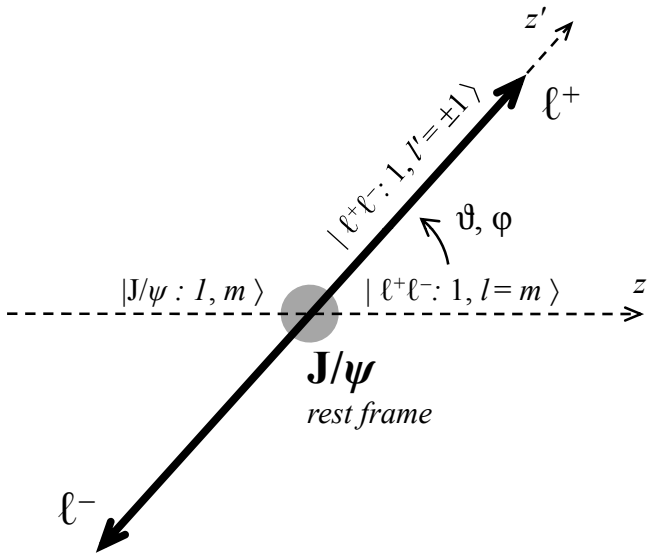



Figure 4.1: Sketch of the decay $J/\psi \to \ell^+\ell^-$. Figure taken from [88]

is represented by $|\ell^+\ell^-;\, J = 1, l' = \pm 1\rangle$. The condition $l' = \pm 1$ follows from helicity conservation in the decay process $Q\bar{Q} \to \gamma^* \to \ell^+\ell^-$, assuming massless leptons. Consequently, the dilepton pair carries the same angular momentum projection along the $z'$-axis as the intermediate virtual photon. Although electrons and muons are not strictly massless, this approximation is well justified because their masses ($m_e \approx 0.51$ MeV/$c^2$ and $m_\mu \approx 105$ MeV/$c^2$) are negligible compared to the mass of the lightest quarkonium state, $m_{J/\psi} \approx 3.096$ GeV/$c^2$.

The objective is to express the dilepton state $|\ell^+\ell^-;\, J = 1, l' = \pm 1\rangle$ defined with respect to the $z'$-axis as a superposition of the angular momentum eigenstates $|\ell^+\ell^-;\, J = 1, l\rangle$, with $l = 0, \pm 1$ defined with respect to the $z$-axis. This transformation between the two quantization axes is achieved using the rotation operator, following the standard formalism of angular momentum theory. Let $R(\alpha, \beta, \gamma)$ denote the rotation operator that transforms a reference frame $(x, y, z)$ into a rotated frame $(x', y', z')$, where $\alpha$, $\beta$, and $\gamma$ are the Euler angles. Throughout this discussion, positive rotations are defined according to the right-hand rule. Under

such a rotation, an eigenstate $|J, M'\rangle$ of the angular momentum component $J_{z'}$ can be expressed as a linear combination of the eigenstates $|J, M\rangle$ of $J_z$ according to

$$|J, M'\rangle = \sum_{M=-J}^{+J} \mathcal{D}^{J}_{MM'}(R)\,|J, M\rangle \tag{4.4}$$

where $\mathcal{D}^{J}_{MM'}$ is the complex rotation matrix, and it can be expressed in terms of the reduced matrix elements $d^{J}_{MM'}(\beta)$

$$\begin{aligned}\mathcal{D}^{J}_{MM'}(\alpha,\beta,\gamma) &= \langle J, M|e^{-i\alpha J_x}e^{-i\beta J_y}e^{-i\gamma J_z}|J, M'\rangle \\ &= e^{-iM\alpha}\langle J, M|e^{-i\beta J_y}|J, M'\rangle e^{-iM'\gamma} \\ &= e^{-iM\alpha}d^{J}_{MM'}(\beta)e^{-iM'\gamma}\end{aligned} \tag{4.5}$$

Using the Condon–Shortley phase convention [220], the elements of the reduced rotation matrix are real-valued and can be written as

$$d^{J}_{MM'}(\beta) = \sum_{t=\max(0,M-M')}^{\min(J+M,J-M')} (-1)^t\,\mathcal{K}(t)\left(\cos\frac{\beta}{2}\right)^{2J+M-M'-2t}\left(\sin\frac{\beta}{2}\right)^{2t-M+M'} \tag{4.6}$$

with

$$\mathcal{K}(t) = \frac{\sqrt{(J+M)!\,(J-M)!\,(J+M')!\,(J-M')!}}{(J+M-t)!\,(J-M'-t)!\,t!\,(t-M+M')!} \tag{4.7}$$

For J = 1, it takes the form

$$d^{1}(\beta) = \begin{pmatrix} \frac{1}{2}(1+\cos\beta) & -\frac{1}{\sqrt{2}}\sin\beta & \frac{1}{2}(1-\cos\beta) \\ \frac{1}{\sqrt{2}}\sin\beta & \cos\beta & -\frac{1}{\sqrt{2}}\sin\beta \\ \frac{1}{2}(1-\cos\beta) & \frac{1}{\sqrt{2}}\sin\beta & \frac{1}{2}(1+\cos\beta) \end{pmatrix} \tag{4.8}$$

The rotation relevant to the dilepton decay geometry maps the polarization $z$-axis onto the dilepton $z'$-axis. Such a transformation can be parametrized by the Euler angles $\beta = \vartheta$ and $\alpha = -\gamma = \varphi$. Under this rotation, the dilepton angular momentum state is represented as a linear combination of the $J_z$ eigenstates,

$$|\ell^+\ell^-; 1, l'\rangle = \sum_{l=0,\pm1} \mathcal{D}^{1}_{ll'}(\varphi,\vartheta,-\varphi)\,|\ell^+\ell^-; 1, l\rangle\,. \tag{4.9}$$

To compute the amplitude of the process $\mathrm{J}/\psi(m) \to \ell^+\ell^-(l')$, one must evaluate the matrix element between the initial quarkonium state and the final dilepton state by applying the transition operator $\mathcal{B}$:

$$B_{ml'} \;=\; \sum_{l=0,\pm1} \mathcal{D}^{1*}_{ll'}(\varphi,\vartheta,-\varphi)\,\langle \ell^+\ell^-;1,l \,|\, \mathcal{B} \,|\, \mathrm{J}/\psi;1,m\rangle \tag{4.10}$$

Since the third component of angular momentum is conserved in the transition, using the condition $\langle \ell^+\ell^-;1,l \,|\, \mathcal{B} \,|\, \mathrm{J}/\psi;1,m\rangle = B\,\delta_{ml}$, Eq. 4.10, reduces to:

$$B_{ml'} = \; B\,\mathcal{D}^{1*}_{ml'}(\varphi,\vartheta,-\varphi)\,, \tag{4.11}$$

The amplitude for $\mathrm{J}/\psi \to \ell^+\ell^-(l')$, considering all possible $m$ values in the initial states is obtained substituting $|\,\mathrm{J}/\psi;1,m\rangle$ with Eq. 4.3,

$$B_{l'} \;=\; \sum_{m=-1,+1} b_m B\,\mathcal{D}^{1*}_{ml'}(\varphi,\vartheta,-\varphi) \;=\; \sum_{m=-1,+1} a_m\,\mathcal{D}^{1*}_{ml'}(\varphi,\vartheta,-\varphi) \tag{4.12}$$

The transition probability is obtained by squaring $B_{l'}$ and summing over the unobserved spin alignments ($l' = \pm1$) of the dilepton system. Substituting the matrix element $\mathcal{D}^{1*}_{ml'}$, one obtain;

$$\begin{aligned} W(\cos\vartheta,\varphi) \;\propto\; \sum_{l'=\pm1} |B_{l'}|^2 \;\propto\; \frac{\mathcal{N}}{(3+\lambda_\vartheta)}\,(1 + \lambda_\vartheta\cos^2\vartheta + \;\lambda_\varphi \sin^2\vartheta\cos 2\varphi \\ + \lambda_{\vartheta\varphi}\sin 2\vartheta\cos\varphi + \;\lambda^\perp_\varphi \sin^2\vartheta \sin 2\varphi \;+\; \lambda^\perp_{\vartheta\varphi}\sin 2\vartheta\sin\varphi) \end{aligned} \tag{4.13}$$

with $\mathcal{N} = |a_0|^2 + |a_{+1}|^2 + |a_{-1}|^2$ and

$$\begin{aligned} \lambda_\vartheta &= \frac{\mathcal{N} - 3|a_0|^2}{\mathcal{N} + |a_0|^2}\,, \\ \lambda_\varphi &= \frac{2\,\mathrm{Re}[a^{(i)*}_{+1} a_{-1}]}{\mathcal{N} + |a_0|^2}\,, \\ \lambda_{\vartheta\varphi} &= \frac{\sqrt{2}\,\mathrm{Re}[a^{(i)*}_0 (a_{+1} - a_{-1})]}{\mathcal{N} + |a_0|^2}\,, \\ \lambda^\perp_\varphi &= \frac{-2\,\mathrm{Im}[a^*_{+1} a_{-1}]}{\mathcal{N} + |a_0|^2}\,, \\ \lambda^\perp_{\vartheta\varphi} &= \frac{-\sqrt{2}\,\mathrm{Im}[a^*_0 (a_{+1} + a_{-1})]}{\mathcal{N} + |a_0|^2}\,. \end{aligned} \tag{4.14}$$

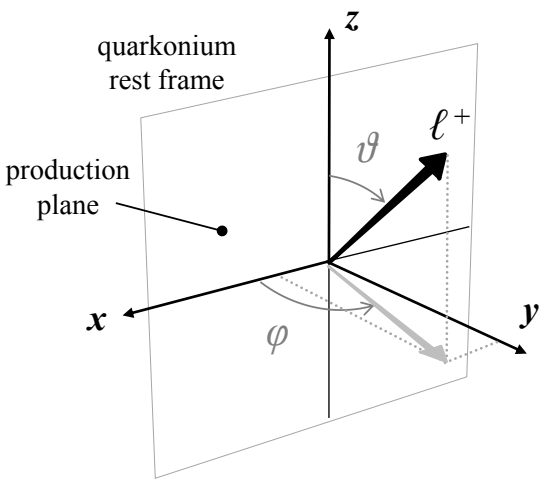



Figure 4.2: Illustration of the coordinate system used for the measurement of the angular variables for two-body decay [88]

The last two terms in Eq. 4.13, i.e., $\lambda_{\varphi}^{\perp} \sin^2\vartheta \sin 2\varphi$ and $\lambda_{\vartheta\varphi}^{\perp} \sin 2\vartheta \sin\varphi$, introduce an asymmetry of the distribution with respect to the $(x, z)$ plane. From an experimental perspective, it is called the *production plane*, defined as the plane containing the direction of colliding hadrons and the momentum of the decaying particles. Nevertheless, in hadronic collisions, the asymmetry can be observed only by considering the $z$-axis parton momentum and not the hadron one. This means the last two terms in Eq. 4.13 can not be observed because they vanish when averaging over multiple parton collisions. With this simplification, the experimentally accessible angular distribution is:

$$\boxed{W(\vartheta,\varphi) \propto \frac{1}{3+\lambda_{\vartheta}} \left(1 + \lambda_{\vartheta}\cos^2\vartheta + \lambda_{\varphi}\sin^2\vartheta\cos 2\varphi + \lambda_{\vartheta\varphi}\sin 2\vartheta\cos\varphi\right)} \quad (4.15)$$

Alternative to the above two-dimensional (2D) angular distribution, which is a function of $\cos\vartheta$ and $\varphi$, the one-dimensional (1D) distribution can be obtained by integrating out Eq. 4.15 with respective angular variables, and obtain;

$$W(\vartheta) \propto \frac{1}{3+\lambda_{\vartheta}} \left(1 + \lambda_{\vartheta}\cos^2\vartheta\right) \quad (4.16)$$

$$W(\varphi) \propto 1 + \frac{2\lambda_{\varphi}}{3+\lambda_{\vartheta}}\cos 2\varphi \quad (4.17)$$

From these angular shapes, $\lambda_\vartheta$ and $\lambda_\varphi$ parameters can be extracted in two separate steps. The $\lambda_{\vartheta\varphi}$ term of Eq. 4.15 vanishes in both cos$\vartheta$ and $\varphi$ integration and it can be obtained by defining $\tilde{\varphi}$ variables, and defined as:

$$\tilde{\varphi} = \begin{cases} \varphi - \frac{3}{4}\pi & \text{if} \quad \cos\vartheta > 0 \\ \varphi - \frac{1}{4}\pi & \text{if} \quad \cos\vartheta < 0 \end{cases} \tag{4.18}$$

and the corresponding angular distribution takes the form:

$$W(\tilde{\varphi}) \propto 1 + \frac{\sqrt{2}\lambda_{\vartheta\varphi}}{3+\lambda_\vartheta}\cos 2\tilde{\varphi} \tag{4.19}$$

From Eq. 4.14, it is evident that the polarization parameters are directly determined by the coefficients appearing in Eq. 4.3. Indeed, Eq. 4.12 implies that ($a_m = b_m\ B$), establishing a direct correspondence between the spin-state amplitudes and the observable angular-distribution parameters. Consequently, the degree of spin alignment can be extracted experimentally by fitting the dilepton angular distribution. To illustrate the physical meaning of the polarization parameters from the angular distributions themselves, we consider two extreme and an intermediate case of $\lambda$ parameters, shown in Fig. 4.3. In particular, if

- $\lambda_\vartheta = 1$, $\lambda_\varphi$ =0 , $\lambda_{\vartheta\varphi} = 0$, corresponds to pure transverse polarization. This is obtained by substituting $a_{0,\pm1}$ =0, and $a_{\pm1} = 1$ in Eq. 4.14.
- $\lambda_\vartheta$ = -1, $\lambda_\varphi$ =0, $\lambda_{\vartheta\varphi}$ = 0, corresponds to pure longitudinal polarization. This is obtained by substituting $a_0 = 1$, and $a_\pm = 0$ in Eq. 4.14.
- $\lambda_\vartheta = 0$, $\lambda_\varphi$ =0, $\lambda_{\vartheta\varphi} = 0$ for zero polarization.

### 4.1.2 Reference frames

There are three different conventions to define the polarization reference frames (definition of the z-axis), which are illustrated in Fig. 4.4.

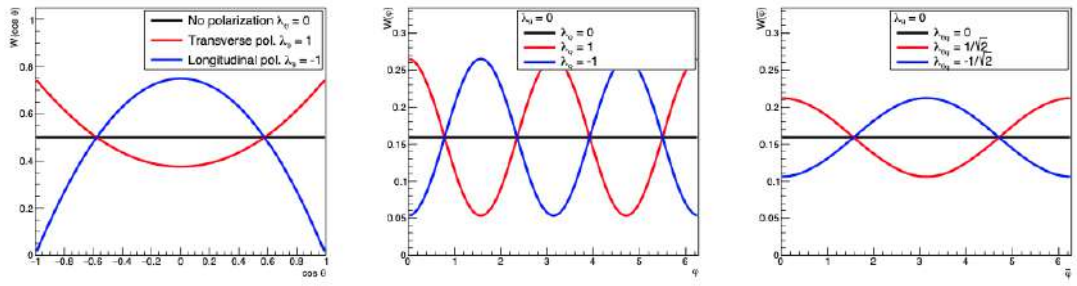



Figure 4.3: Illustration of the angular distribution W(cos$\vartheta$) (left), W($\varphi$) (middle), W($\tilde{\varphi}$) (right) for two extreme and an intermediate values of $\lambda$ parameters [221]

- **Helicity**: In the direction of quarkonia (J/$\psi$ or $\psi$(2S)) momentum in the center-of-mass frame of the colliding beams.
- **Collins-Soper**: The bisector of the angle between the momentum of one beam and the successive direction of the other beam [222].
- **Gottfried-Jackson**: The direction of the momentum of one of the colliding beams [223].

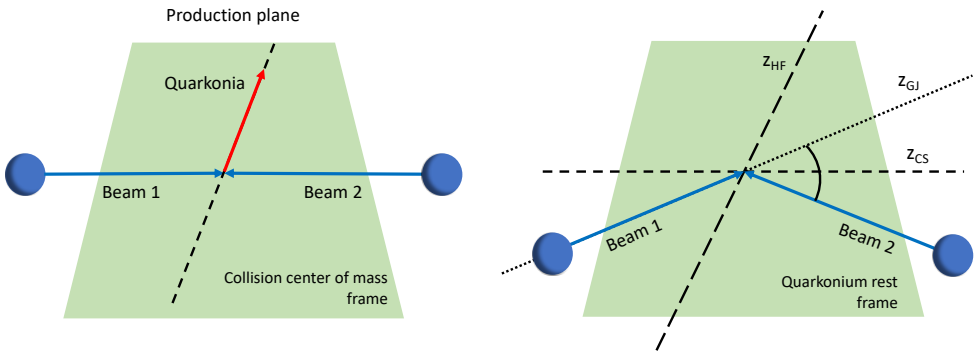



Figure 4.4: Illustration of the three different definitions of the polarization axis, z, in the helicity (HE), Collins-Soper (CS), and Gottfried-Jackson (GJ) reference frames [157].

### 4.1.3 Frame invariant parameter

As discussed above, all possible *experimentally definable* polarization axes in inclusive measurements lie within the production plane (defined in Fig. 4.2). We can, therefore, parametrize the transformation from an observation frame to another by one angle describing a rotation about the $y$ axis. Instead of rotating the angular momentum state vectors, we can apply a purely geometrical transformation directly to the observable angular distribution. The rotation matrix

$$R_y(\delta) = \begin{pmatrix} \cos\delta & 0 & -\sin\delta \\ 0 & 1 & 0 \\ \sin\delta & 0 & \cos\delta \end{pmatrix} \tag{4.20}$$

where $\delta$ is the angle between two different frames of reference. In the spherical coordinate system, the unit vector which indicates the decay lepton direction is $\hat{r} = (\sin\vartheta\cos\varphi, \sin\vartheta\sin\varphi, \cos\vartheta)$. Thus, the change in coordinate system is achieved by expressing the direction of the old frame as a function of the new coordinates in the new frame ($\hat{r}'$):

$$\hat{r} = R_y^{-1}(\delta)\hat{r}' \tag{4.21}$$

In particular,

$$\cos\vartheta \;=\; -\sin\delta\sin\vartheta'\cos\varphi' \;+\; \cos\delta\cos\vartheta' \,. \tag{4.22}$$

Substituting Eq. 4.22, into Eq. 4.15, we obtain the angular distribution in the rotated frame:

$$W'(\cos\vartheta', \varphi') \propto \frac{1}{3+\lambda'_\vartheta}(1 + \lambda'_\vartheta\cos^2\vartheta' \lambda'_\varphi \sin^2\vartheta'\cos 2\varphi' + \lambda'_{\vartheta\varphi}\sin 2\vartheta'\cos\varphi') \tag{4.23}$$

where

$$\begin{aligned} \lambda'_\vartheta &= \frac{\lambda_\vartheta - 3\Lambda}{1+\Lambda}\,, \quad \lambda'_\varphi = \frac{\lambda_\varphi + \Lambda}{1+\Lambda}\,, \\ \lambda'_{\vartheta\varphi} &= \frac{\lambda_{\vartheta\varphi}\cos 2\delta - \frac{1}{2}(\lambda_\vartheta - \lambda_\varphi)\sin 2\delta}{1+\Lambda}\,, \\ \text{with} \quad \Lambda &= \frac{1}{2}(\lambda_\vartheta - \lambda_\varphi)\sin^2\delta - \frac{1}{2}\lambda_{\vartheta\varphi}\sin 2\delta\,. \end{aligned} \tag{4.24}$$

Since the magnitude of the "polar anisotropy", $\lambda_\vartheta$, never exceeds 1 in any frame, we deduce the frame-independent inequalities by imposing the rotational invariance properties:

$$|\lambda_\varphi| \leq \frac{1}{2}(1+\lambda_\vartheta), \quad |\lambda_{\vartheta\varphi}| \leq \frac{1}{2}(1-\lambda_\varphi),$$
$$\text{and, for } \lambda_\varphi \leq -1/3, \quad (2\lambda_\varphi+1)^2 + 2\lambda_{\vartheta\varphi}^2 \leq 1. \tag{4.25}$$

which imply the bounds $|\lambda_\varphi| \leq 1$ and $|\lambda_{\vartheta\varphi}| \leq 1$.

These relations imply the existence of a frame-invariant quantity:

$$\tilde{\lambda} \equiv \mathcal{F}_{c_1,c_2,c_3} = \frac{\lambda_\vartheta + 3\lambda_\varphi}{1-\lambda_\varphi} \tag{4.26}$$

$\tilde{\lambda}$ is called the *frame invariant parameter* and is widely used in quarkonium polarization analysis. It is used to validate the consistency in the polarization measurement between different frames of reference.

With the theoretical foundations of quarkonium polarization established, we now proceed to its experimental measurement.

### 4.1.4 J/$\psi$ polarization puzzle

Over the past few decades, the quarkonium polarization has been very challenging because of the disagreement between the experimental measurements and the theoretical predictions. The left panel of Fig. 4.5 presents the polarization parameter $\alpha$ (similar to $\lambda_\theta$) for J/$\psi$ measured at Tevatron using data collected in $p\bar{p}$ collisions. The CDF Collaboration measured the J/$\psi$ polarization as a function of $p_{\mathrm{T}}$ at $\sqrt{s} = 1.96$ TeV for mid-rapidity ($|y| < 0.6$), as shown in the left-side plot of Fig. 4.5. This figure indicates a disagreement between the experimental data and the theoretical prediction. In particular, models such as NRQCD and $k_{\mathrm{T}}$ factorization predict a transverse and strong longitudinal polarization, respectively. While the experimental data show close to zero (or very small longitudinal) polarization within uncertainty. This disagreement between data and

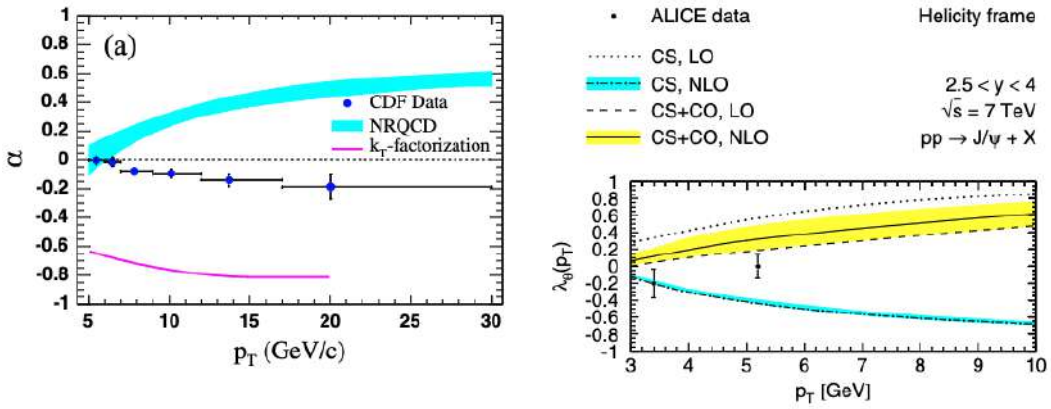



Figure 4.5: (Left) J/$\psi$ polarization parameter $\alpha$ (similar to $\lambda_\theta$) as a function of $p_{\mathrm{T}}$ obtained in CDF Collaboration compared to NRQCD and $k_{\mathrm{T}}$ factorization model prediction [37]. (Right) $\lambda_\theta$ obtained in ALICE compared with LO-NRQCD, NLO-NRQCD, LO CSM, NLO CSM predictions [93].

the theoretical model even exists at higher collision energy at $\sqrt{s} = 7$ TeV, which is evident from the right panel of Fig. 4.5. The NRQCD and Color Singlet (CS) Model, including the NLO contribution, could not explain the ALICE data [53]. This is commonly called the J/$\psi$ *polarization puzzle*.

Additionally, J/$\psi$ polarization has been widely investigated in *pp* collisions. In particular, at RHIC, the PHENIX [43, 57] and STAR [56] have measured J/$\psi$ polarization at $\sqrt{s} = 200$ and 510 GeV. At LHC, ALICE [45, 53], CMS [46, 64], and LHCb [48] have measured J/$\psi$ polarization at $\sqrt{s} = 7$, 8, 13 TeV. Higher resonances, such as $\psi(2S)$, and $\Upsilon(nS)$ polarization are also measured in *pp* collisions at several experiments [47, 49, 51]. Motivated by these experimental measurements along with the theoretical challenges, this thesis presents the inclusive J/$\psi$ polarization measurements in two distinct collision systems, namely proton–proton (*pp*) and oxygen–oxygen (OO) collisions, using the high-statistics Run 3 data. The first section is devoted to the measurement of J/$\psi$ polarization in *pp* collisions, whereas the second section presents the first measurement of J/$\psi$ polarization in OO collisions.

## 4.2 $J/\psi$ polarization in proton-proton collisions

This section presents the inclusive $J/\psi$ polarization measurement in proton-proton collisions at $\sqrt{s} = 13.6$ TeV using the high-luminosity Run 3 data of the upgraded ALICE detector. This analysis is performed using the dimuon decay channel at forward rapidity ($2.5 < y < 4.0$) in the transverse momentum range $0 < p_{\mathrm{T}} < 15$ GeV/c. The significantly higher statistics allow precise and more differential measurements of polarization parameters $\lambda_\vartheta$, $\lambda_\varphi$, and $\lambda_{\vartheta\varphi}$ across transverse momentum bins compared to Run 1 and Run 2 measurements. The details of the dataset, MC sample, event, and track selection criteria are given below.

### 4.2.1 Data sample selection and analysis cuts

#### 4.2.1.1 Data sample selection

This analysis is performed using the skimmed dataset obtained during the period 2024. The data are acquired in continuous readout, so no hardware trigger is issued at the muon level. The data sample periods used in this analysis are: **LHC24 pass1 skimmed**. The latest reconstruction pass is adopted for this analysis. This analysis is performed by using all the GOOD Run periods with QC flags checked on the Run Condition Table (RCT) and following the centrally produced **CBT muon** criteria. They are defined as:

1. FT0, ITS, MCH, MID detectors as Good or Limited Acceptance and MC reproducible

2. TPC as Good or Limited Acceptance and MC reproducible or Bad PID

The list of the run numbers, grouped by data-taking periods, can be found in https://alimonitor.cern.ch/hyperloop/view-dataset/1494.

Since a completely new analysis framework (called the $O^2$ *framework*) has been developed for Run 3, the analysis procedure is described in the following steps:

1. **Muon skimming**: To optimize the resources, the so-called streaming procedure is applied with the analysis task called *tablemaker*. This task is used to select muon candidates using the AO2D produced from ppfilter and write only the necessary information at collision and track level that is necessary for the analysis. The output of this task produces a reduced dataset with a significant decrease in size of the dataset.

2. **Dimuon creation**: The analysis task called *tablereader* is used to build the dimuon observables using the reduced dataset produced from tablemaker. Further selection can be applied at the level of the track/pair.

#### 4.2.1.2 Monte Carlo sample

The MC sample **LHC25c3** (anchored to the LHC24 pass1 dataset) is used for this analysis. In this production, 1 J/$\psi$ + 1 $\psi$(2S) are generated at forward rapidity and injected into a minimum bias (MB) pp event in every 5 events. The details about runlists used in the dataset can be found at alimonitor.cern.ch/hyperloop/view-dataset/1837. The details about the MC production can be found in the JIRA tickets its.cern.ch/jira/browse/O2-5853.
In addition, another MC production **LHC25c3b** (anchored to the LHC24 pass1 dataset) is also used for this analysis. These two MC productions (LHC25c3 vs. LHC25c3b) differ from each other in the reconstruction pass (old vs. new package tag). The impact of these two MC productions on the polarization parameter is investigated. The details about runlists used in the dataset can be found at alimonitor.cern.ch/hyperloop/view-dataset/2208. The details about the MC production can be found in the JIRA tickets its.cern.ch/jira/browse/O2-5853.

#### 4.2.1.3 Event selection

The standard event selection cut **eventStandardSel8** is used in this analysis. Minimum bias events are selected with **Sel8** conditions, and a selection on the primary vertex position is applied to ensure good vertex reconstruction efficiency and compatibility with the Monte Carlo description. The applied cuts are listed below:

- **eventStandardNoINT7**: This includes the vertex position between ± 10 cm with respect to the nominal interaction point ($|\mathrm{Vtx_z}| < 10$ cm)
- **Sel8**: It ensures that the event passes the minimum-bias trigger.

  The **Sel8** condition is composed of several composite cuts, such that
  **Sel8 = TriggerTVX+NoITSROFrameBorder+NoTimeFrameBorder**

  1. **TriggerTVX**: This cut passes events through the minimum-bias trigger.
  2. **NoITSROFrameBorder**: This cut removes the events close to the ITS readout-frame border to prevent timing mismatches.
  3. **NoTimeFrameBorder**: This cut rejects the events with vertices at the edges of the Time-Frame to avoid border effects.

#### 4.2.1.4 Track selection cuts

In this analysis, standalone muons are used, which satisfy the MCH-MID match requirement (**Track type 3**). To select a pure sample of muons, a set of cuts is applied at the single-track level and dimuon level:

1. On single muon: **muonQualityCuts**
   (a) Radial transverse position of the muon tracks at the end of the absorber ($R_{\mathrm{abs}}$) cut: 17.6 cm $< R_{\mathrm{abs}} <$ 89.5 cm, to remove tracks crossing the thicker part of the absorber

(b) Pseudorapidity cut: -4.0 $< \eta <$ -2.5, to reject tracks at the edges of the spectrometer

(c) Transverse momentum cut: $p_{\mathrm{T}} > 0.7$ GeV/c, to have similar $p_{\mathrm{T}}$ cut as applied in the offline trigger

(d) $pDCA$ cut: 0 GeV·cm/c $< pDCA <$ 594 GeV·cm/c for 17.6 cm $< R_{\mathrm{abs}} <$ 26.5 cm, to remove tracks not pointing to the interaction vertex

(e) $pDCA$ cut: 0 GeV·cm/c $< pDCA <$ 324 GeV·cm/c for 26.5 cm $< R_{\mathrm{abs}} <$ 89.5 cm

(f) $0 < \chi^2 < 10^6$, and $0 < \chi^2_{\mathrm{matchMCHMID}} < 10^6$

Before moving ahead, the following section presents a detailed discussion on the $pDCA$ cut optimization for forward muon tracks in Run 3 analysis, which was carried out as part of the ALICE service task [225].

During the track reconstruction process, the extrapolation of reconstructed parameters of muon tracks to the primary vertex is incorrect for background tracks due to the Coulomb Multiple Scattering (CMS) between the tracks and material in the front absorber of the muon spectrometer, as depicted in Fig. 4.6. These background tracks are produced far away from the primary vertex. This incorrect extrapolation introduces some correlation between the track kinematic variables. So, based on the behavior of CMS, we need to develop a cut that removes the beam-induced background. This beam-induced background is located at higher $p$ and higher $p \times$DCA values, which can be seen in the left panel of Fig. 4.7. The behavior of the beam-induced background is different from that of other sources. A combination cut of momentum ($p$) and Distance of Closest Approach (DCA), i.e., $p \times$ DCA, is the most efficient and powerful cut to remove the beam-induced background.

With CMS, the Root Mean Square (RMS) of the scattering angle $\theta_{\mathrm{RMS}}$ as

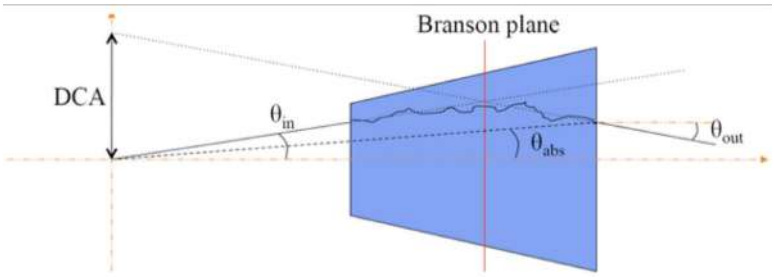



Figure 4.6: Quantities used to describe the multiple scattering with the front absorber. Figure taken from Ref. [224]

a function of the incident particle momentum is given by [225];

$$\theta_{\mathrm{RMS}} = \frac{13.6\ \mathrm{MeV}}{p\ \beta c} \mathrm{z}\sqrt{\mathrm{x/X}}\ [1 + 0.038\ \ln(\mathrm{x/X_0})]\,, \tag{4.27}$$

Where p, $\beta c$, and z are the momentum, velocity, and charge number of the incident particle, and $\mathrm{x/X_0}$ is the thickness of the scattering medium in radiation length. The value of $\mathrm{x/X_0}$ is usually taken as 60 and $\beta \simeq 1$ in high-energy muon tracks. From Eq. (4.27), one can easily write;

$$\theta_{\mathrm{RMS}} \times p = \text{constant} \tag{4.28}$$

With the small-angle approximation, for tracks produced close to the primary vertex, one can write

$$\mathrm{DCA} \propto \theta_{\mathrm{scattering}} \tag{4.29}$$

where $\theta_{\mathrm{scattering}}$ is the scattering angle for tracks inside the front absorber. Then, Eq. 4.29 can be written as;

$$\sigma(p \times \mathrm{DCA}) \equiv p \times \mathrm{DCA_{RMS}} = \text{constant} \tag{4.30}$$

From Eq. (4.30), one can conclude that the tracks produced at or close to the primary vertex have a momentum times the RMS distribution of DCA [defined as $\sigma(p \times \mathrm{DCA})$] that is constant, which means $\sigma(p \times \mathrm{DCA})$ does not

depend on any other variables. According to this property, the $p \times$ DCA distribution of muons is expected to be different for different sources, and it could be used to reject the beam-induced background in the inclusive muon spectrum.

According to Eq. (4.27), the value of $\sigma(p \times \text{DCA})$ defined in Eq. (4.30) depends on the property of the scattering medium. The front absorber of the muon spectrometer is made up of two different materials as shown in Fig. 3.4. The farthest region from the interaction point (IP) (i.e., $171^o < \theta_{\text{abs}} < 177^o$) is made up of high-Z material (such as Pb, Tungsten), and the closest region to the IP (i.e., $177^o < \theta_{\text{abs}} < 178^o$) is made up of low-Z material (such as carbon followed by concrete). Therefore, the extraction of $\sigma(p \times \text{DCA})$ in the data should be presented for the two $\theta_{\text{abs}}$ independently, as shown in Fig. 4.8.

Furthermore, the extracted value of $\sigma(p \times \text{DCA})$ for these two regions is reported in Ref. [225]. The effect of different $\sigma(p \times \text{DCA})$ cuts on the $p \times \text{DCA}$ vs. $p$ distribution is shown explicitly. Finally, the effect of $p \times$ DCA cuts on J/$\psi$ and $\Upsilon(nS)$ signal extraction is discussed in detail [225].

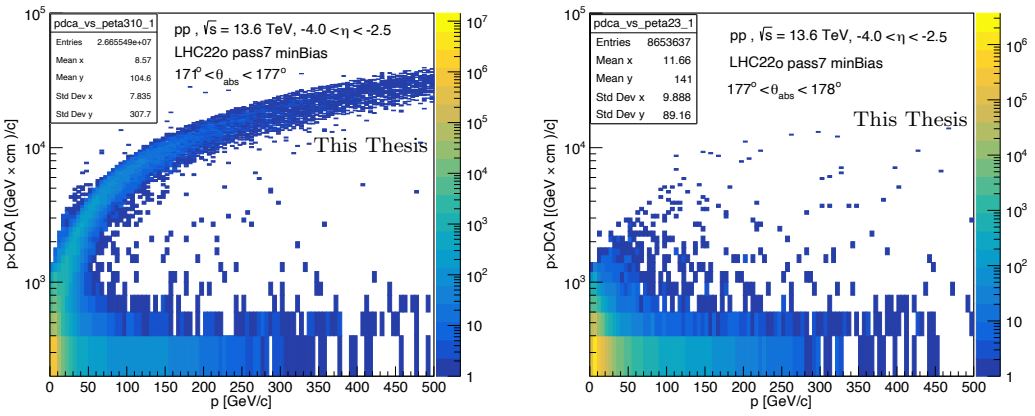



Figure 4.7: $p \times$DCA distribution in $171^o < \theta_{\text{abs}} < 177^o$ (left) and $177^o < \theta_{\text{abs}} < 178^o$ (right) obtained using LHC22o pass7 dataset [225].

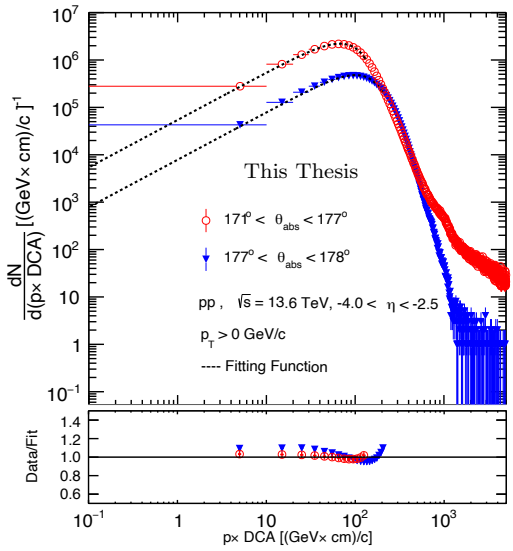



Figure 4.8: Fit of $p\times$DCA distribution in two diffferent $\theta_{\rm abs}$ with a Gaussian distribution. The distribution is obtained with $p_{\rm T} > 0$ GeV/c [225].

2. On dimuon pairs: **muonLowPt210SigmaPDCA**

   (a) $p_{\rm T}^{\mu} > 0.7$ GeV/c

   (b) $2.5 < y < 4.0$

   (c) $0 < p_T < 15$ GeV/c

#### 4.2.1.5 Data sample used for background studies

In the skimmed dataset created for muon analysis with fDimuon ($p_T^{\mu} > 0.7$ GeV/c and $M_{\mu^+\mu^-} > 1.8$ GeV/c$^2$), software trigger selections in pp collisions create a modulation in the background of dimuon invariant mass spectra [226]. This modulation is due to the streaming procedure applied in Run 3. This will be explained in more detail in Sec. 4.2.3.1. To account for this modulation, the signal extraction as a function of $p_{\rm T}$ also requires the minimum-bias sample to build the mixed event. It is used to build the mixed-event, like-sign dimuon distribution, which is used to model the shape of the combinatorial background. Each event

is mixed with other events, and this ensures that there are enough statistics for a good extraction of the background shapes, as shown in Sec. 4.2.3.1. The sample is LHC24 pass1 MinBias (alimonitor.cern.ch/hyperloop/view-dataset/1662). The run list includes the same quality requirements as the skimmed sample. The same event selection and muon selections as the skimmed sample are also applied to the MB.

### 4.2.2 Analysis strategy description

This analysis uses the standard correction method to extract the polarization parameters:

1. **Binning definitions**: After the event and track selection cuts, the whole data sample is split into bins of $p_{\mathrm{T}}$ intervals. Then, for each $p_{\mathrm{T}}$ bin, the sample is divided into bins of $cos\vartheta$, $\varphi$ and $\tilde{\varphi}$ for helicity and Collins-Soper frames. The unlike-sign dimuon invariant mass distributions corresponding to each angular bin are built.

2. **Signal extraction**: The raw yield of J/$\psi$ in each bin of $\cos\vartheta$, $\varphi$, and $\tilde{\varphi}$ is obtained by fitting the dimuon invariant mass distribution with the double Crystal Ball (CB2) function for the signal and Variable Width Gaussian (VWG) or Polynomial 4 with Exponential (Pol4Exp) to describe the background.

3. $A \times \epsilon$ **corrections**: The raw angular distributions are corrected by the acceptance and efficiency ($A \times \epsilon$) of the detector with a Monte Carlo simulation to take into account the detector coverage and its inefficiencies.

4. **Extraction of the polarization parameters**: The corrected angular distributions $W(\cos\vartheta), W(\varphi)$, and $W(\tilde{\varphi})$ are fitted with the theoretical expected functions defined in Eqs. 4.16, 4.17, and 4.19 to determine the three polarization parameters $\lambda_\vartheta$, $\lambda_\varphi$, and $\lambda_{\vartheta\varphi}$ for each $p_{\mathrm{T}}$ bin.

5. **Construct frame-invariant parameters**: The frame-invariant quantity $\tilde{\lambda}$ will also be computed using $\lambda_\vartheta$, $\lambda_\varphi$, and $\lambda_{\vartheta\varphi}$ to exclude a possible bias in the analysis procedure in both frames.

### 4.2.3 Signal extraction

The procedure adopted for this analysis involves fitting the opposite-sign dimuon invariant mass distribution with different combinations of functions describing the signal and background contributions. The use of multiple functional forms in the signal extraction is intended to ensure the stability of the results and to assess possible systematic uncertainties associated with the choice of fitting functions.

- **Double Crystal Ball (CB2)**: A double Crystal Ball function has a Gaussian core with power-law tails on either side. The tail structure arises in the invariant mass distribution because of the multiple Coulomb scattering of muons in the front absorber, residual misalignment, fluctuations in energy loss, and radiative decays, etc.

  The functions adopted here are listed below [227].

$$f(x; N, \mu, \sigma, \alpha_L, n_L, \alpha_R, n_R) = N \cdot \begin{cases} \exp\left(-\frac{(x-\mu)^2}{2\sigma^2}\right), & \text{for } \alpha_R > \frac{(x-\mu)}{\sigma} > -\alpha_L \\ A \cdot \left(B - \frac{(x-\mu)}{\sigma}\right)^{-n_L}, & \text{for } \frac{(x-\mu)}{\sigma} \leq -\alpha_L \\ C \cdot \left(D + \frac{(x-\mu)}{\sigma}\right)^{-n_R}, & \text{for } \frac{(x-\mu)}{\sigma} \geq -\alpha_R \end{cases} \tag{4.31}$$

$$A = \left(\frac{n_L}{|\alpha_L|}\right)^{n_L} \exp\left(-\frac{|\alpha_L^2|}{2}\right)$$

$$B = \frac{n_L}{|\alpha_L|} - |\alpha_L|$$

$$C = \left(\frac{n_R}{|\alpha_R|}\right)^{n_R} \exp\left(-\frac{|\alpha_R^2|}{2}\right)$$

$$D = \frac{n_R}{|\alpha_R|} - |\alpha_R|$$

Here $N$ is the normalization factor, $\mu$ and $\sigma$ are the mean and width of the Gaussian distribution, and $\alpha_L, n_L, (\alpha_R, n_R)$ represent tail parameters on the left (right) side.

The mentioned phenomenological functions are used for the signals (J/$\psi$ and $\psi(2S)$) and the residual background functions; several fits are performed, changing the fitting range and the tails of the signal function. The $\psi(2S)$ mass and width are bound to the J/$\psi$ and ones according to the following equations:

$$m_{\psi(2S)} = m^{FIT}_{\mathrm{J}/\psi} + \Delta m^{PDG} \tag{4.32}$$

where

$$\Delta m^{PDG} = m^{PDG}_{\psi(2S)} - m^{PDG}_{\mathrm{J}/\psi} \tag{4.33}$$

$$\sigma_{\psi(2S)} = \sigma^{FIT}_{\mathrm{J}/\psi} \times \frac{\sigma^{INT}_{\psi(2S)}}{\sigma^{INT}_{\mathrm{J}/\psi}} \tag{4.34}$$

where $m^{PDG}_{\psi(2S)}$, and $m^{PDG}_{\mathrm{J}/\psi}$ are the $\psi(2S)$ and J/$\psi$ mass taken from the PDG, respectively.

In Run 3, the ratio of mass resolution between $\psi(2S)$ and J/$\psi$ is obtained from the $p_{\mathrm{T}}$- and $y$-integrated spectrum both in the data sample and in MC simulations anchored to the sample itself. The extraction of this factor from the data, using different fit ranges and background functions, gives [226]

$$\left(\frac{\sigma^{INT}_{\psi(2S)}}{\sigma^{INT}_{\mathrm{J}/\psi}}\right)_{\mathrm{Data}} = 1.11 \pm 0.06\ (\mathrm{sys.}, 5\%) \tag{4.35}$$

The extraction of the $\sigma^{INT}_{\psi(2S)}/\sigma^{INT}_{\mathrm{J}/\psi}$ can also be obtained from MC using the average of different productions anchored to the 2024 data [226].

$$\left(\frac{\sigma^{INT}_{\psi(2S)}}{\sigma^{INT}_{\mathrm{J}/\psi}}\right)_{\mathrm{MC}} = 1.08 \pm 0.01\ (\mathrm{sys.}, 1\%) \tag{4.36}$$

The ratio obtained from MC is found to be compatible with the one extracted from the data. In Run 2, this ratio is taken from MC and found to be 1.05 (since $\sigma_{\mathrm{J}/\psi} = 69.6 \pm 0.2$ MeV and $\sigma_{\psi(2S)} = 72.8 \pm 3.9$ MeV) [228]. For the moment,

the analysis is performed by considering $\sigma^{INT}_{\psi(2S)}/\sigma^{INT}_{\mathrm{J}/\psi} = 1.05$. A systematic study with 5% variation on $\sigma^{INT}_{\psi(2S)}/\sigma^{INT}_{\mathrm{J}/\psi}$ with respect to Run 3 value is performed in Ref. [229], the effect is found to be neglesible.

The background in the mass region under study is predominantly composed of uncorrelated $\mu^+\mu^-$ pairs and by semileptonic decays of charmed hadrons, and in general, it can be described by adopting phenomenological functions. The two shapes used for background fits are a Variable Width Gaussian (VWG) and the product of a fourth-degree polynomial function times an exponential function.

- **Variable Width Gaussian (VWG)**: a Gaussian with a mass-dependent width is defined as follows:

$$f(x; N, \mu, A, B) = N \cdot \exp\left(-\frac{(x-\mu)^2}{2\sigma^2_{VDW}}\right) \tag{4.37}$$

with

$$\sigma_{VDW} = A + B \cdot \frac{(x-\mu)}{\mu} \tag{4.38}$$

- **Polynomial4 with Exponential (Pol4Exp)**

$$f(x; N, p_0, p_1, p_2, p_3, p_4, p_5) = N \cdot \left(p_0 + p_1 x + p_2 x^2 + p_3 x^3 + p_4 x^4\right) \cdot \exp\left(-p_5 x\right) \tag{4.39}$$

Before going into the analysis details, $p_{\mathrm{T}}$, cos$\theta$, $\phi$, and $\tilde{\phi}$ bins used for this study are listed below:

- $p_{\mathrm{T}}$ bins: [0, 1], (1, 2], (2, 3], (3, 4], (4, 5], (5, 6], (6, 8], (8, 10], and (10, 15] GeV/c (Total 9 bins)

- cos$\theta$ bins: [-1, -0.8], (-0.8, -0.7], (-0.7, -0.6], (-0.6, -0.5], (-0.5, -0.4],(-0.4, -0.3],(-0.3, -0.2], (-0.2, -0.1],(-0.1, 0],[0, +0.1], (+0.1, +0.2], (+0.2, +0.3], (+0.3, +0.4], (+0.4, +0.5],(+0.5, +0.6],(+0.6, +0.7], (+0.7, +0.8], and (+0.8, 1.0] (Total 18 bins)

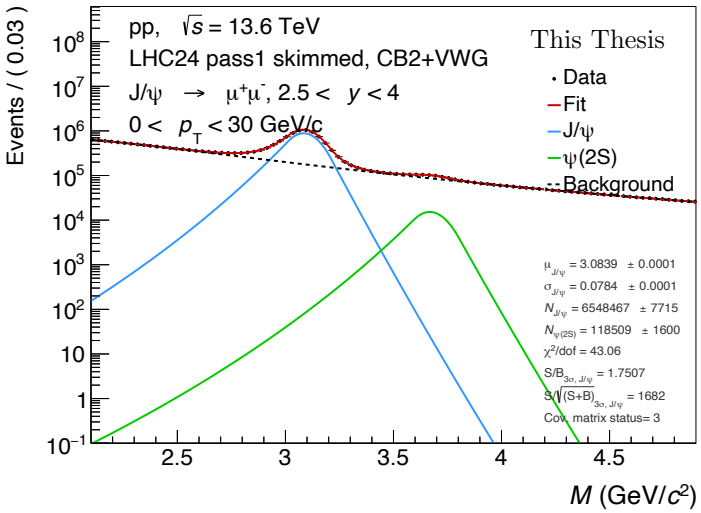



Figure 4.9: $p_{\mathrm{T}}$ integrated signal extraction using CB2+VWG function [229].

- $\phi$ bins: [0,0.628),(0.628, 0.942],(0.942, 1.256],(1.256, 1.57],(1.57, 1884],(1.884, 2.198],(2.198, 2.512], and (2.512, 3.14] (Total 8 bins)
- $\tilde{\phi}$ bins: 0 to $2\pi$ with equal bin width 0.314 (Total 20 bins)

The binning has to be chosen as narrow as possible, with enough statistics per (cos$\theta$, $\phi$) range to fit the invariant mass spectrum.

#### 4.2.3.1 $\mathrm{p_T}$ differential signal extraction and background modulation

$\mathrm{p_T}$ differential signal extraction is more challenging because the shape of the invariant mass spectrum is altered by the single-muon $p_{\mathrm{T}}$ cut ($p_T^{\mu} > 0.7$ GeV/c) introduced by the software trigger in the skimming procedure. The analysis of the like-sign distribution of dimuons in mixed events from the minimum-bias sample, with an additional single-muon $p_{\mathrm{T}}$ cut to mimic the skimming, gives an estimation of the background shape. A more detailed discussion of the background modulation is discussed in the $\Psi(2S)/J/\psi$ ratio analysis in Run 3 [226]. In this note, it has been shown that choosing either the mixed-event, like-sign or opposite-sign

dimuon distribution gives equivalent outcomes, so it does not matter which one is used to parametrize the background. This modulation is similar to a bump-like structure, which evolves with $p_{\mathrm{T}}$. The shape of the modulation for the $p_{\mathrm{T}}$ bin considered is shown in Fig. 4.10. For ranges within $p_{\mathrm{T}} < 0.5$ GeV/c and $p_{\mathrm{T}} > 8$ GeV/c, the impact of the modulation can be neglected. In the momentum range $0.5 < p_{\mathrm{T}} < 1$ GeV/c, the fact that the modulation is at the left edge of the mass range makes the fit converge even without taking this modulation into account. For ranges within $1 < p_{\mathrm{T}} < 8$ GeV/c, the modulation affects the shape inside the mass fit range, and it has to be parametrized to improve the quality of the fit. In summary, the possible approaches to parametrize this modulation in the background are discussed below [226].

1. The ratio is computed between the mixed-event, like-sign dimuon spectrum in the MB sample without any single-muon $p_{\mathrm{T}}$ cut and the one with the $p_{\mathrm{T}}$ cut at 0.7 GeV/c.

2. The ratio of the two spectra is fitted with a first VWG function plus a constant term [VWG1+, C], and the parameters are stored.

3. The background distribution for the final signal extraction from the same-event, opposite-sign, skimmed sample is defined as a function traditionally used for background parametrization, for example, another VWG ($\mathrm{VWG_2}$) or a Pol4Exp, divided by the previously extracted $\mathrm{VWG_1}$+C, which is fully fixed to take into account the bump-like structure. Therefore, the two options used to fit the background are:

$$\mathrm{a_1}(\mathcal{N}_{\mathrm{bkg}}) = \mathcal{N}_{\mathrm{bkg}} \cdot \mathrm{RatioVWG(free\ numerator)} = \mathcal{N}_{\mathrm{bkg}} \cdot \frac{\mathrm{VWG_2(free)}}{\mathrm{[VWG_1 + C](fixed)}} \tag{4.40}$$

$$\mathrm{a_2}(\mathcal{N}_{\mathrm{bkg}}) = \mathcal{N}_{\mathrm{bkg}} \cdot \mathrm{RatioPol4Exp(free\ numerator)} = \mathcal{N}_{\mathrm{bkg}} \cdot \frac{\mathrm{Pol4Exp(free)}}{\mathrm{[VWG1 + C](fixed)}} \tag{4.41}$$

Thus, the modulation is observed to be within the invariant-mass fit range (2 $< M_{\mu^+\mu^-} <$ 5 GeV/c$^2$) for the $p_{\rm T}$ ranges between 1 and 8 GeV/c, for which the RatioVWG and/or RatioPol4Exp function is used to parametrize the background. However, for all the other cases, it is either outside the range or at the edge; therefore, a simple VWG or Pol4Exp is used for a background description.

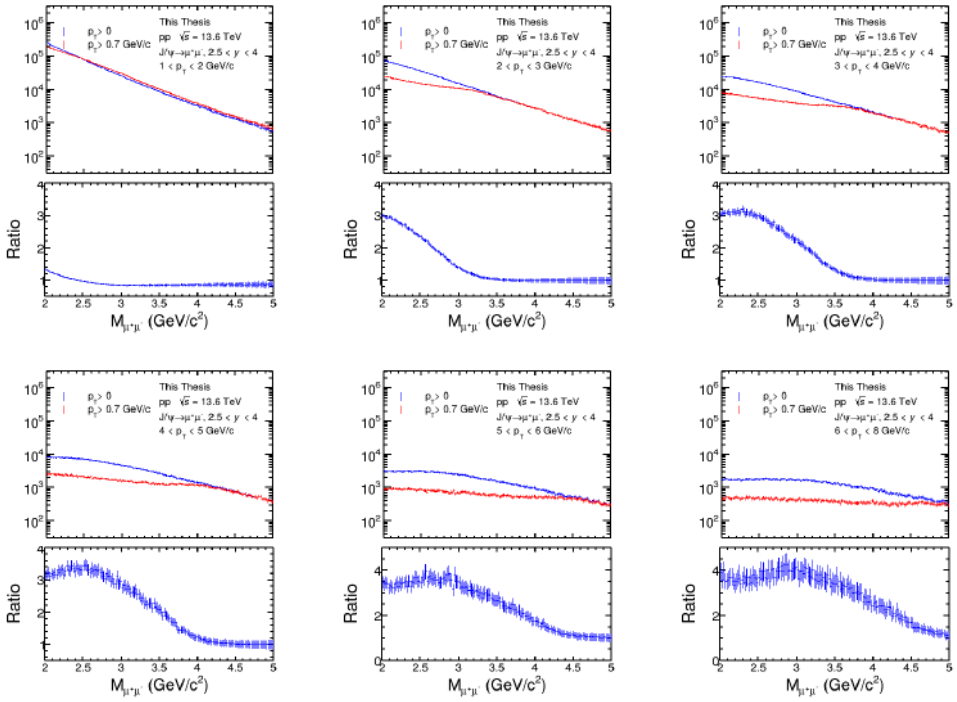



Figure 4.10: Background modulation in like-sign distributions with no $p_{\rm T}$ cut (blue) and with the same $p_{\rm T}$ cut as the trigger (red), for $1 < p_{\rm T} < 8$ GeV/c [229].

#### 4.2.3.2 Tail parameters extraction

For the moment, the CB2 tail parameters have been extracted from the data. The detailed description of the tail parameters is defined below.

- **Using raw data**: For raw data, two CB2 functions have been fitted with the reconstructed J/$\psi$ and $\psi(2S)$ signal along with the VWG (0$<$ $p_{\rm T}$ $<$ 1

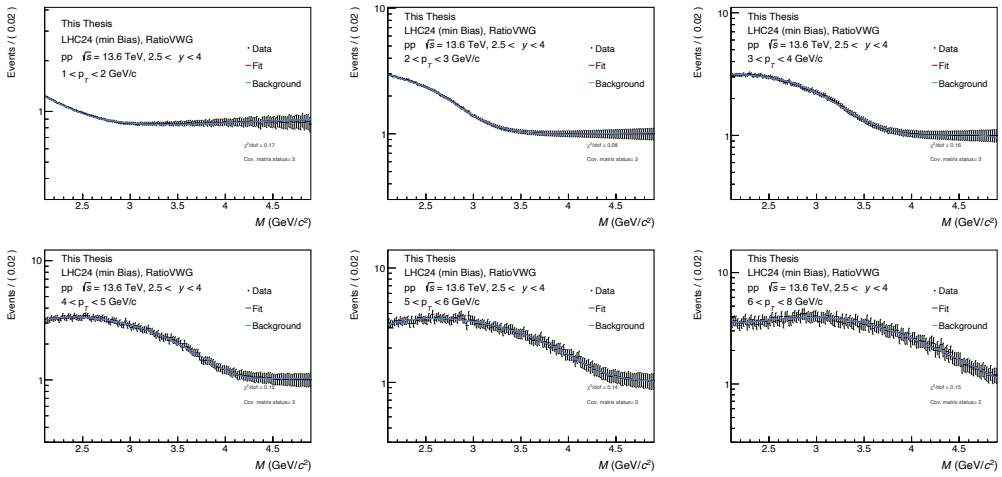



Figure 4.11: The ratio shown in Fig. 4.10 is fitted with RatioVWG function for $p_{\mathrm{T}}$ range $1 < p_{\mathrm{T}} < 8$ GeV/c. [229].

GeV/c, and $8 < p_{\mathrm{T}} < 15$ GeV/c) and RatioVWG ($1 < p_{\mathrm{T}} < 8$ GeV/c) function have been fitted to the residual background. While fitting the $p_{\mathrm{T}}$ differential dimuon invariant mass spectrum, we keep the mass and width of J/$\psi$ free, and all the tail parameters of J/$\psi$ are free, as shown in Fig.4.12. Fig.4.12 shows the J/$\psi$ signal extraction using CB2 function for signal and VWG function for background in the transverse momentum range $0 < p_{\mathrm{T}} <$ 1 GeV/c (left), $8 < p_{\mathrm{T}} < 10$ GeV/c (middle), $10 < p_{\mathrm{T}} < 15$ GeV/c (right), while RatioVWG is used for background in the transverse momentum range $1 < p_{\mathrm{T}} < 8$ GeV/c to properly take into account the background modulation. The $p_{\mathrm{T}}$ differential tail parameters are reported in Table 4.1.

However, while extracting the signal for the $\cos\theta$, $\phi$, $\tilde{\phi}$ differential dimuon invariant mass fit, we use the $p_{\mathrm{T}}$ differential tail parameters obtained from data as a first step to proceed. If the fit does not converge, we try to keep a few tail parameters free or tune the range by range.

- **Using MC sample**: Notably, it is worth mentioning that the present available MC simulations in pp collisions (LHC25c3 and LHC25c3b) can not

| $p_{\mathrm{T}}$ (GeV/c) | $\alpha_L$ | $n_L$ | $\alpha_R$ | $n_R$ |
|---|---|---|---|---|
| $0 < p_{\mathrm{T}} < 1$ | 0.89 ± 0.01 | 10.15 ± 1.16 | 2.02 ± 0.04 | 20.80 ± 13.04 |
| $1 < p_{\mathrm{T}} < 2$ | 0.89 ± 0.01 | 3.55 ± 0.02 | 1.98 ± 0.02 | 1.79 ± 1.61 |
| $2 < p_{\mathrm{T}} < 3$ | 1.03 ± 0.01 | 15.4 ± 0.08 | 2.04 ± 0.04 | 50.8 ± 10.13 |
| $3 < p_{\mathrm{T}} < 4$ | 0.98 ± 0.01 | 4.29 ± 0.23 | 1.73 ± 0.02 | 50.5 ± 12.31 |
| $4 < p_{\mathrm{T}} < 5$ | 1.0 ± 0.01 | 3.4 ± 0.2 | 1.57 ± 0.02 | 7.07 ± 1.0 |
| $5 < p_{\mathrm{T}} < 6$ | 0.97 ± 0.01 | 7.7 ± 1.01 | 1.52 ± 0.02 | 6.61 ± 0.96 |
| $6 < p_{\mathrm{T}} < 8$ | 0.90 ± 0.01 | 15.4 ± 0.85 | 1.31 ± 0.03 | 13.54 ± 3.13 |
| $8 < p_{\mathrm{T}} < 10$ | 0.93 ± 0.03 | 5.36 ± 0.96 | 1.19 ± 0.03 | 9.05 ± 1.86 |
| $10 < p_{\mathrm{T}} < 15$ | 0.98 ± 0.03 | 3.52 ± 0.61 | 1.05 ± 0.03 | 7.37 ± 1.52 |

Table 4.1: $p_{\mathrm{T}}$ differential CB2 tail parameters obtained from the LHC24 pass1.

reproduce the signal shapes of the data sample, despite LHC25c3 containing some realistic effects such as MID efficiency. This is explicitly discussed in the $\psi(2S)/J/\psi$ ratio analysis note in Appendix 6 [226]. This is because the current MC simulation is not fully realistic. Therefore, the tail parameter obtained from the MC simulation is not reliable for describing the signal shape.

#### 4.2.3.3 Angular differential signal extraction

Following the same signal-extraction procedure, the J/$\psi$ yield is extracted in different $\cos\theta$, $\phi$, and $\tilde{\phi}$ bins for each $p_{\mathrm{T}}$ interval. As an example, Fig. 4.13, and Fig. 4.14 show the signal extraction in different $\cos\theta$ bins for $3 < p_{\mathrm{T}} < 4$ GeV/$c$ in Collins-Soper and helicity frame, respectively. The corresponding results for the remaining $p_{\mathrm{T}}$ intervals are provided in Appendix A.1, from Fig. 1 to Fig. 6. The resulting raw angular distributions as functions of $\cos\theta$ (top), $\phi$ (middle), and $\tilde{\phi}$ (bottom) in the Collins–Soper (left) and helicity (right) frames are presented in Fig. 4.15 for $0 < p_{\mathrm{T}} < 15$ GeV/$c$.

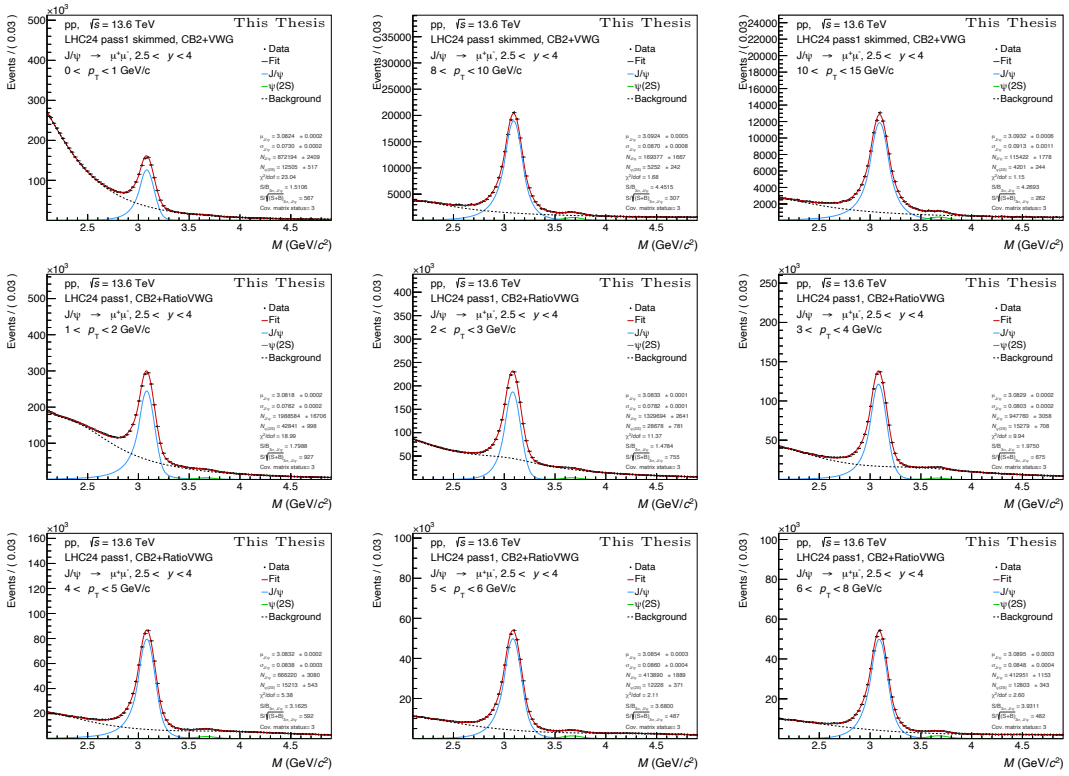



Figure 4.12: $p_{\mathrm{T}}$ differential signal extraction using CB2+VWG function for $0 < p_{\mathrm{T}} < 1$ GeV/c, $8 < p_{\mathrm{T}} < 10$ GeV/c, $10 < p_{\mathrm{T}} < 15$ GeV/c, while CB2+RatioVWG is used for $1 < p_{\mathrm{T}} < 8$ GeV/c [229].

The fitting parameters such as J/$\psi$ mass ($m_{\mathrm{J}/\psi}$) and width ($\sigma_{\mathrm{J}/\psi}$) for different $\cos\theta$, $\phi$, and $\tilde{\phi}$ bins in different transverse momentum ranges are shown in Appendix A.1, from Fig. 7 to Fig. 8, respectively. Furthermore, the $\cos\theta$, $\phi$, and $\tilde{\phi}$ differential J/$\psi$ raw angular distributions corresponding to all fitting ranges and fitting functions are shown in Appendix A.1 from Fig. 9 to Fig. 11. The extracted raw-yield distributions are consistent within statistical uncertainties, indicating that the signal extraction is stable against variations in the fitting procedure.

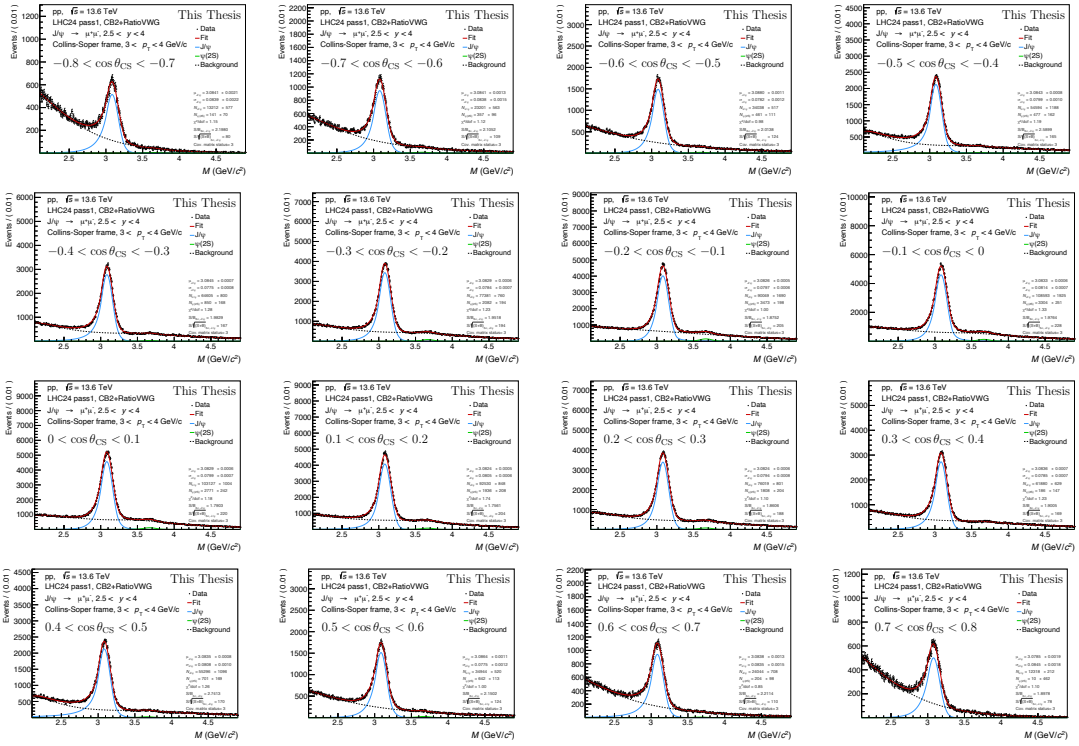



Figure 4.13: $\cos\theta$ differential signal extraction for $3 < p_{\mathrm{T}} < 4$ GeV/c in Collins-Soper reference frame. The $\cos\theta$ intervals from $-0.8$ to $+0.8$ with a bin width of 0.1 are arranged from left to right and top to bottom. [229].

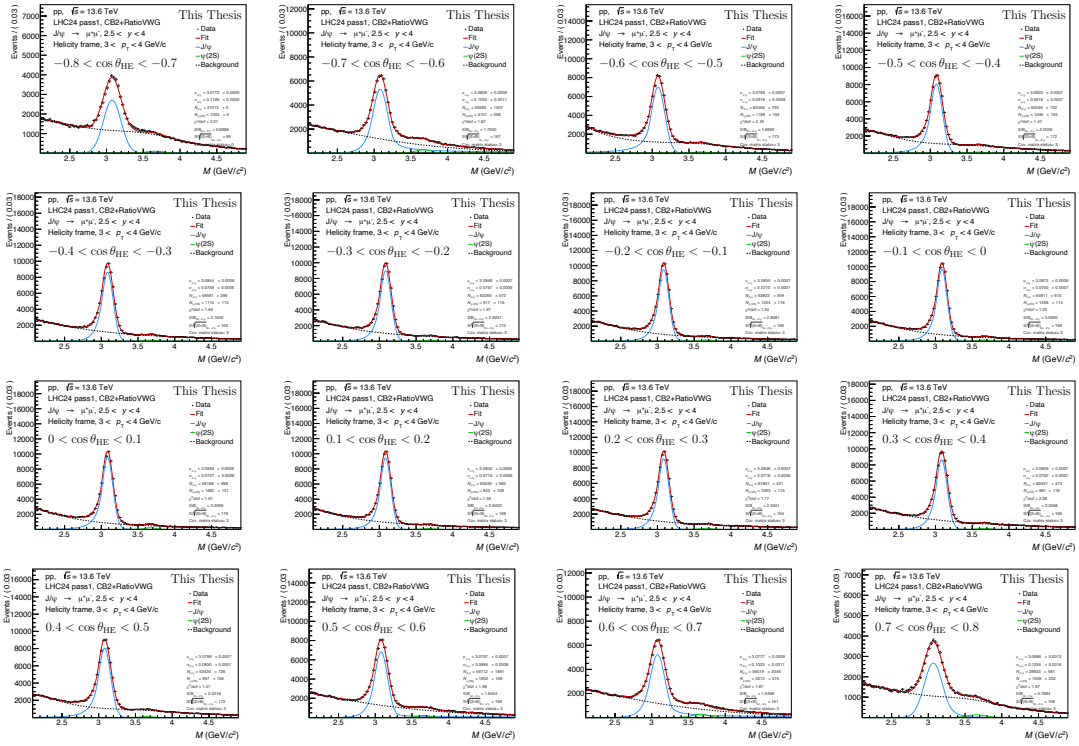



Figure 4.14: $\cos\theta$ differential signal extraction for $3 < p_{\mathrm{T}} < 4$ GeV/c in helicity frame. The $\cos\theta$ intervals from $-0.8$ to $+0.8$ with a bin width of 0.1 are arranged from left to right and top to bottom [229].

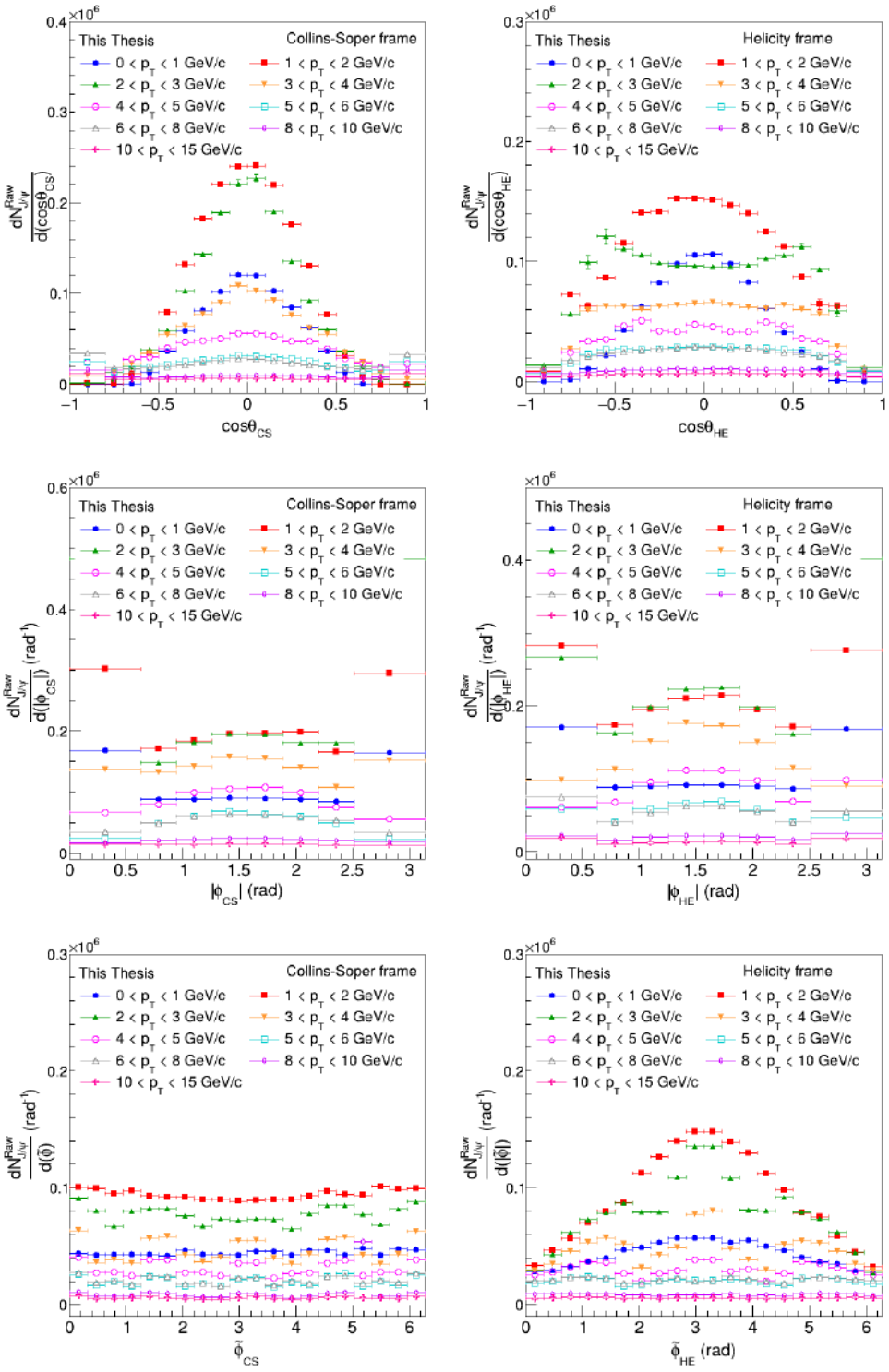



Figure 4.15: Raw angular distribution as a function of cos$\theta$ (top), $\phi$ (middle), and $\tilde{\phi}$ (bottom) in CS (left) and HE (right) for $0 < p_{\mathrm{T}} < 15$ GeV/c [229].

### 4.2.4 A $\times\epsilon$ correction

The acceptance $\times$ efficiency (A$\times\epsilon$) is evaluated using the injected Monte-Carlo productions. The details about the MC production used in this study are discussed in Sec. 4.2.1. The A$\times\epsilon$ for J/$\psi$ is defined as the ratio of the number of reconstructed J/$\psi$ to the number of generated J/$\psi$. In this context, the particles produced by the event generator (without any detector effects) are referred to as the "generated" particles. These particles are the input for the GEANT4 detector simulation and the track and signal reconstruction algorithms. The tracks which are identified by the reconstruction algorithms and which pass the track and kinematic selection cuts are referred to as "reconstructed" tracks. The rapidity-integrated and angular differential acceptance and efficiency are defined as,

$$A \times \epsilon(p_T, \cos\theta, \phi) = \frac{\mathrm{N}^{\mathrm{rec}}_{\mathrm{J}/\psi}(\mathrm{p_T}, \cos\theta, \phi)}{\mathrm{N}^{\mathrm{gen}}_{\mathrm{J}/\psi}(\mathrm{p_T}, \cos\theta, \phi)} \tag{4.42}$$

For a given $p_{\mathrm{T}}$ interval, we estimate the A$\times\epsilon$ in each angular bins, i.e, in cos$\theta$, $\phi$, and $\tilde{\phi}$ bins at forward rapidity. It is noteworthy to mention that in these productions J/$\psi$ is generated flat in the angular variables. This hypothesis, which corresponds to the assumption of no initial polarization, can be considered true until the binning is sufficiently narrow to assume the distribution of generated J/$\psi$ is flat inside each bin.

Figure 4.16 shows the A$\times\epsilon$ distribution as a function of cos$\theta$ (top), $\phi$ (middle), and $\tilde{\phi}$ (bottom) in Collins-Soper (left) and helicity (right) for $0 < p_{\mathrm{T}} < 15$ GeV/c. The angular differential A $\times\epsilon$ is symmetric, and the shape of the A$\times\epsilon$ distribution changes as a function of $p_{\mathrm{T}}$ and angular variables.

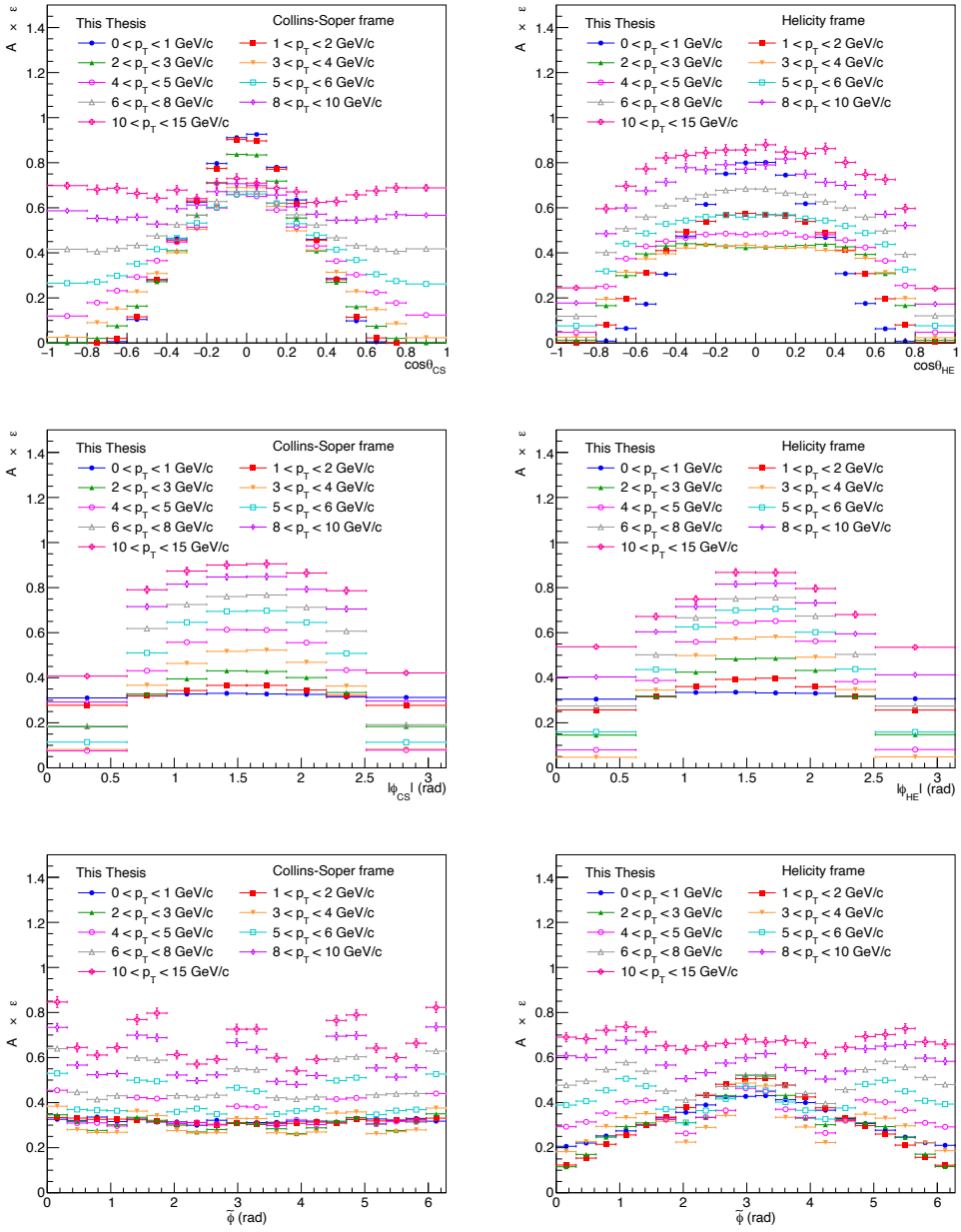



Figure 4.16: Acceptance × Efficiency (A $\times\epsilon$ ) as a function of cos$\theta$ (top), $\phi$ (middle), and $\tilde{\phi}$ (bottom) in Collins-Soper (left) and helicity (right) for $0 < p_{\mathrm{T}} < 15$ GeV/c [229].

### 4.2.5 Polarization parameter extraction

Once the A×$\epsilon$ is obtained from the MC, the raw cos$\theta$ angular distribution is corrected using the following relation;

$$N^{corr}(p_T, \cos\theta, \phi) = \frac{N^{raw}(p_T, \cos\theta, \phi)}{A \times \epsilon(p_T, \cos\theta, \phi)} \tag{4.43}$$

Similarly, the $\phi$ and $\tilde{\phi}$ distributions are corrected using the corresponding raw and A×$\epsilon$ distributions. Furthermore, we perform a 1D fit to the corrected angular distributions of cos$\theta$, $\phi$, and $\tilde{\phi}$ for each $p_T$ bins using the Eqs. 4.16, 4.17, 4.19 and obtain the polarization parameters $\lambda_\theta$, $\lambda_\phi$, and $\lambda_{\theta\phi}$ as a function of $p_T$. Figure 4.17 to Fig. 4.19 shows the 1D fit of cos$\theta$, $\phi$, and $\tilde{\phi}$ corrected angular distribution to obtain the polarization parameters $\lambda_\theta$, $\lambda_\phi$, and $\lambda_{\theta\phi}$ in the transverse momentum range $0 < p_T < 15$ GeV/c in Collins-Soper and helicity frame.

### 4.2.6 Systematic uncertainties

Different sources of systematic uncertainties are evaluated on the polarization parameters:

1. Signal extraction
    - 1D fit approach
    - 2D fit approach
2. Different MC production (LHC25c3 vs LHC25c3b)
3. Input MC shapes (Iterative approach)
    - Input polarization parameter
    - Input $p_T$ shapes
    - Input $y$ shapes
4. Tracking efficiency

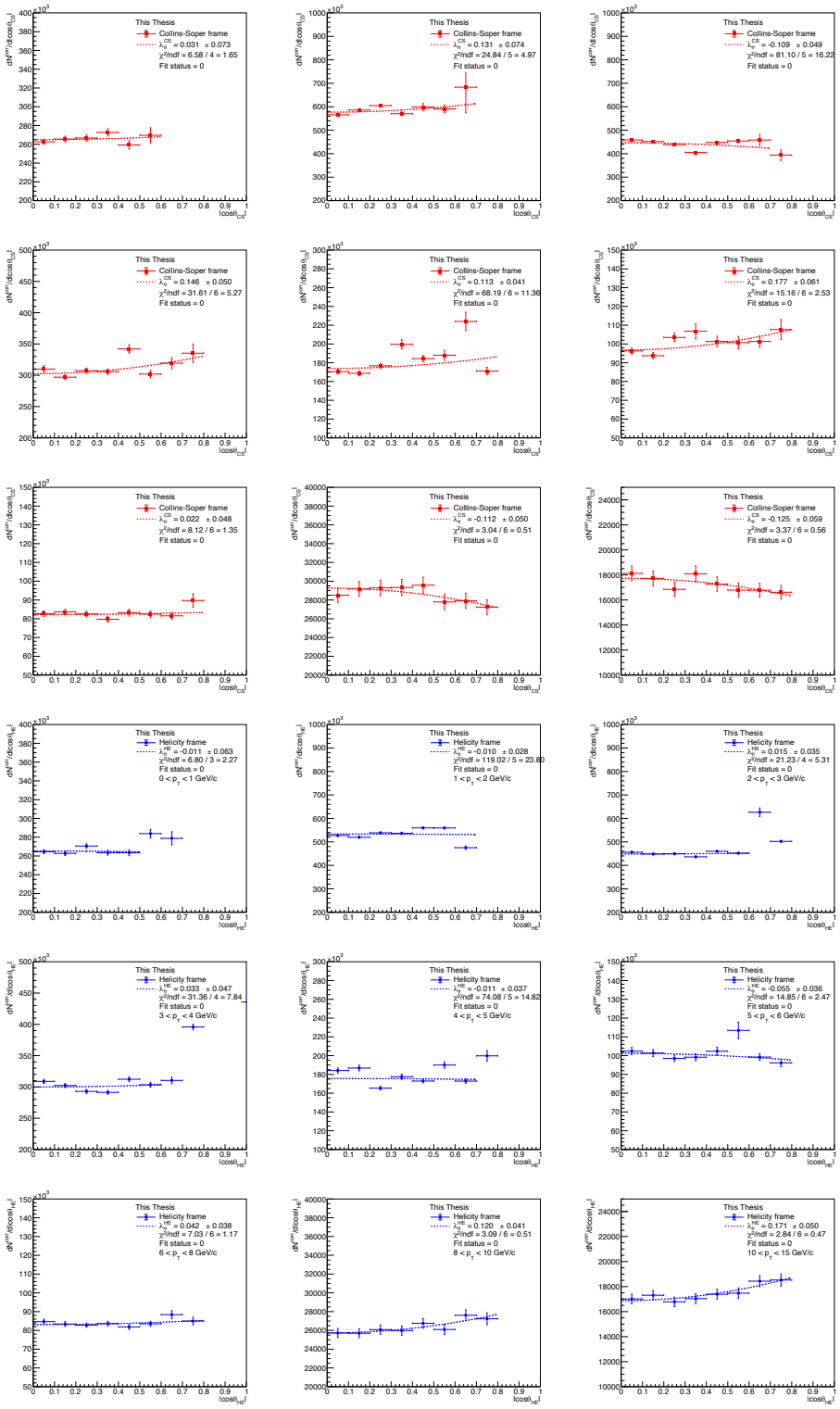



Figure 4.17: $\lambda_\theta$ polarization parameter extraction for $p_{\mathrm{T}}$ bin $0 < p_{\mathrm{T}} < 15$ GeV/c in the Collins-Soper (red) and helicity (blue) frames [229].

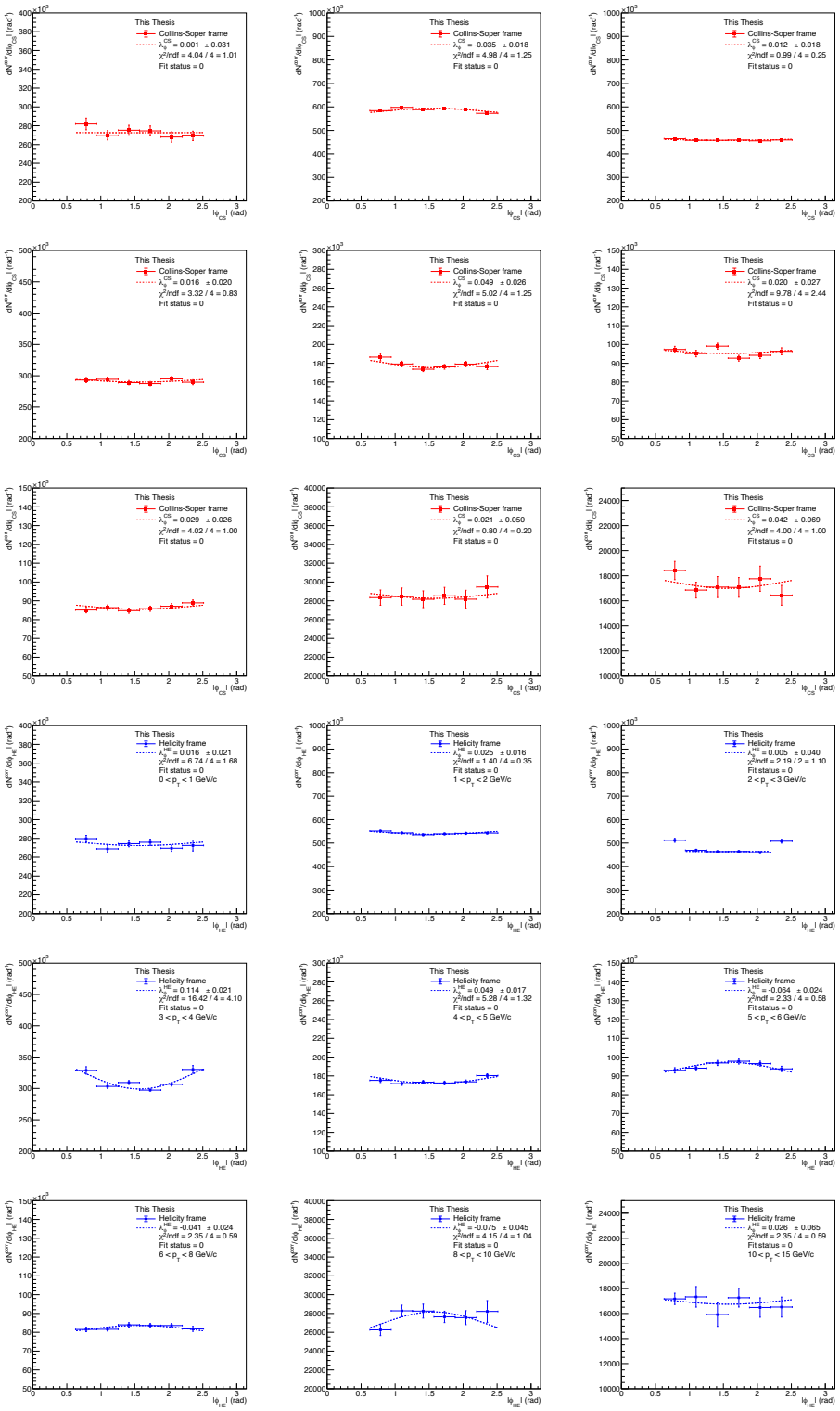



Figure 4.18: $\lambda_\phi$ polarization parameter extraction for $p_{\mathrm{T}}$ bin $0 < p_{\mathrm{T}} < 15$ GeV/c in the Collins-Soper (red) and helicity (blue) frames [229].

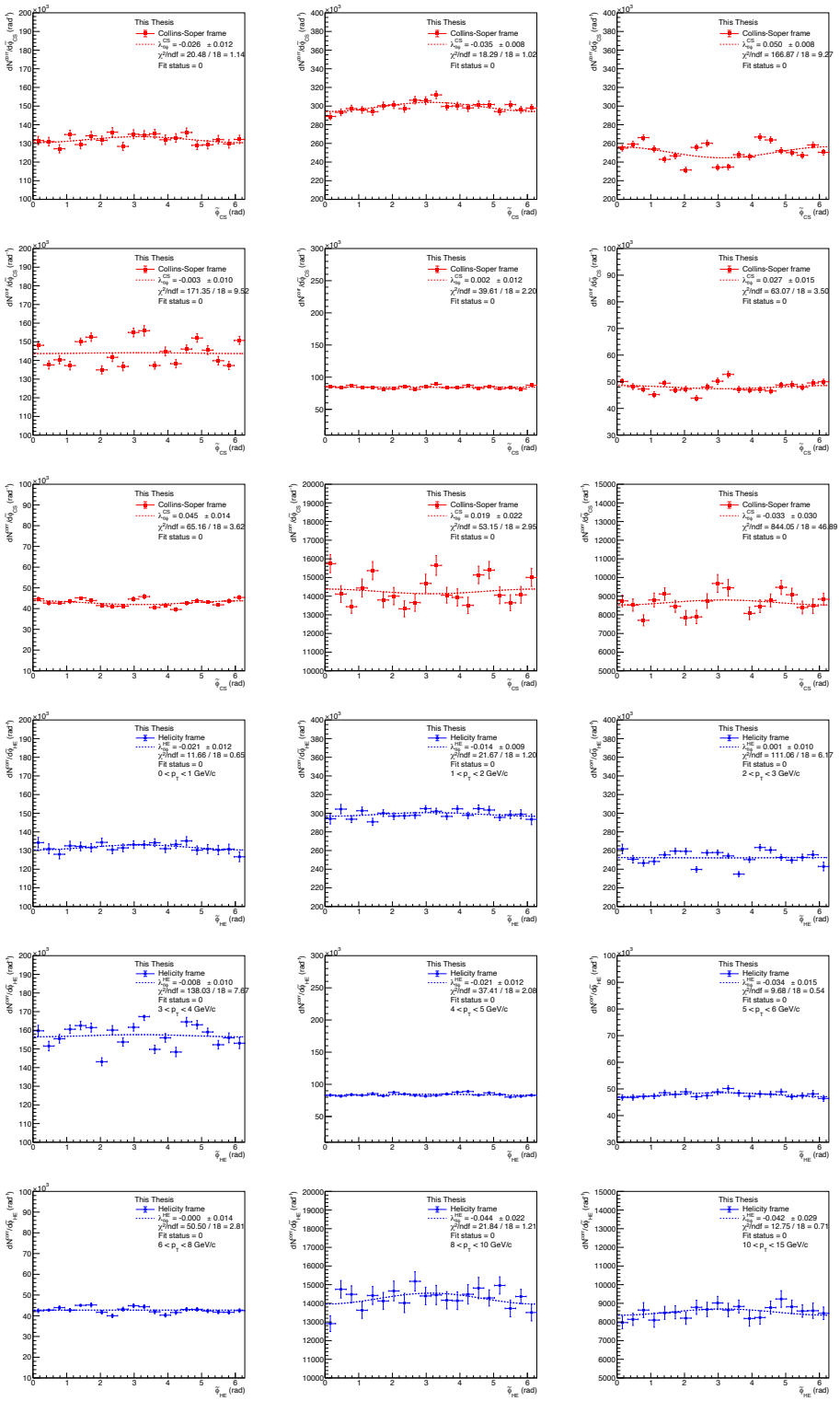



Figure 4.19: $\lambda_{\theta\phi}$ polarization parameter extraction for $p_{\mathrm{T}}$ bin $0 < p_{\mathrm{T}} < 15$ GeV/c in the Collins-Soper (red) and helicity (blue) frames [229].

#### 4.2.6.1 Systematic uncertainty due to signal extraction

The number of J/$\psi$ is obtained using different shapes to describe the signal and the background, in details:

1. Signal: Crystal Ball (CB2)
2. Background: Variable Width Gaussian (VWG), Ratio of Variable Width Gaussian (RatioVWG), an exponential times a four-degree polynomial function (POL4EXP), and a RatioPol4Exp

The systematic uncertainty is obtained by varying the fitting ranges of the dimuon invariant mass distribution. The variation in the dimuon invariant mass fitting ranges is listed below.
Fitting Ranges:

- $2.1 < M_{\mu^+\mu^-} < 4.9\ GeV/c^2$
- $2.2 < M_{\mu^+\mu^-} < 4.8\ GeV/c^2$
- $2.3 < M_{\mu^+\mu^-} < 4.7\ GeV/c^2$

The NA60 function is not used for signal extraction in *pp* collisions because its MC signal shape does not adequately reproduce the data, and its large number of tail parameters prevents a reliable data-driven determination of the tails [226]. However, the use of an alternative background function (RatioPol4Exp) in the systematic uncertainty evaluation of $\lambda_\theta$ (Fig. 4.21) results in larger systematic uncertainties in low-$p_{\rm T}$ bins.
Using these variations, we study the RMS of the polarization parameters. The evaluation of $\lambda_\theta$, $\lambda_\phi$, and $\lambda_{\theta\phi}$ is related to the shape of the corrected J/$\psi$ distribution, and it does not depend on the normalization of the spectrum. The mean, statistical uncertainity and the systematic uncertainity on $\lambda_\theta$, $\lambda_\phi$, and $\lambda_{\theta\phi}$ polarization parameters are calculated using the following formula:

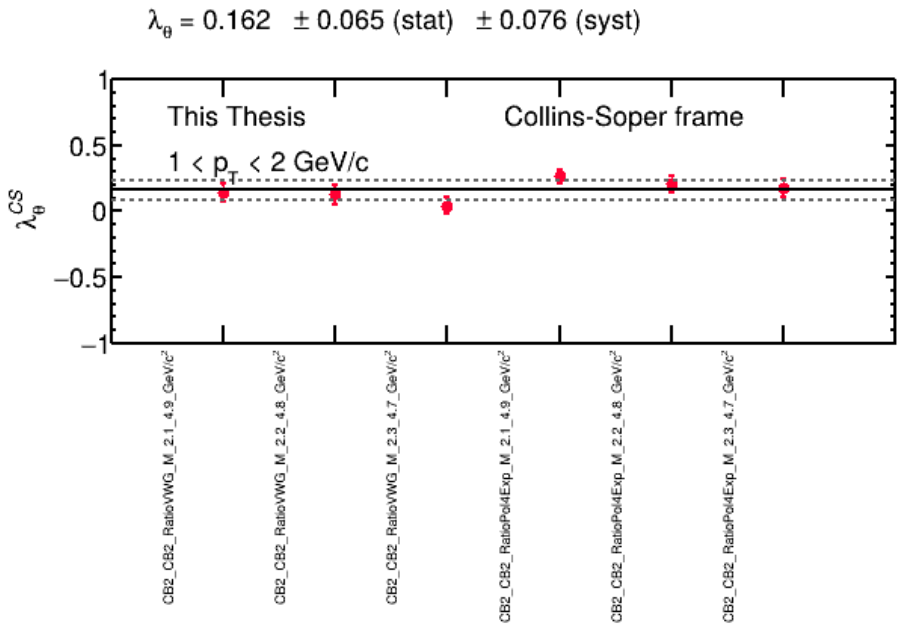



Figure 4.20: A representative plot for the systematic variation of $\lambda_\theta$ polarization due to different trials in the Collins-Soper frame for $1 < p_{\mathrm{T}} < 2$ GeV/c [229].

$$\bar{\lambda} = \frac{\sum_j \lambda^j}{N}, \qquad \sigma_{\bar{\lambda}}^{stat} = \frac{\sum_j \sigma_\lambda^j}{N}, \qquad \sigma_{\bar{\lambda}}^{syst} = \sqrt{\frac{\sum_j |\lambda^j - \bar{\lambda}|^2}{N-1}} \tag{4.44}$$

#### 4.2.6.2 Systematic variations of polarization parameters

Figure 4.20 shows the systematic variations in the $\lambda_\theta$ polarization parameter arising from 1D fit of different signal-extraction trials in the Collins–Soper frame for $1 < p_{\mathrm{T}} < 2$ GeV/$c$ [229]. This figure serves as a representative example; the corresponding results for all other $p_{\mathrm{T}}$ bins, the $\lambda_\theta$, $\lambda_\phi$, and $\lambda_{\theta\phi}$ parameters, and the helicity frame are presented in Figs. 4.21 to Figs. 4.23. For each $p_{\mathrm{T}}$ bin, the baseline measurements are obtained using three variations of the fitting range and two background functions. The dashed lines indicate the systematic uncertainties estimated from the RMS of the trial variations.

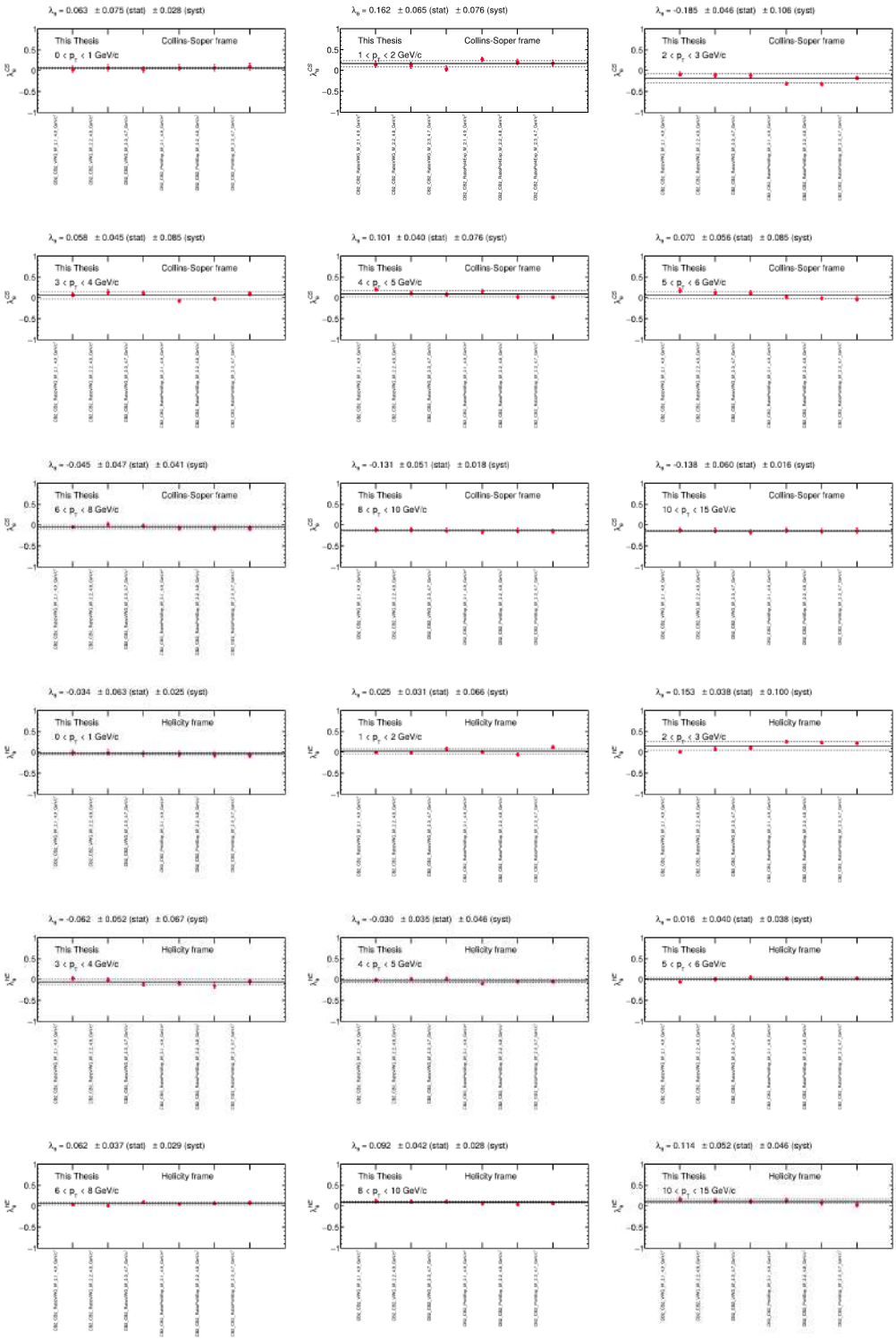



Figure 4.21: Systematic variation of $\lambda_\theta$ due to different trials in CS and HE frame. The top (bottom) three rows correspond to the CS (HE) frame [229].

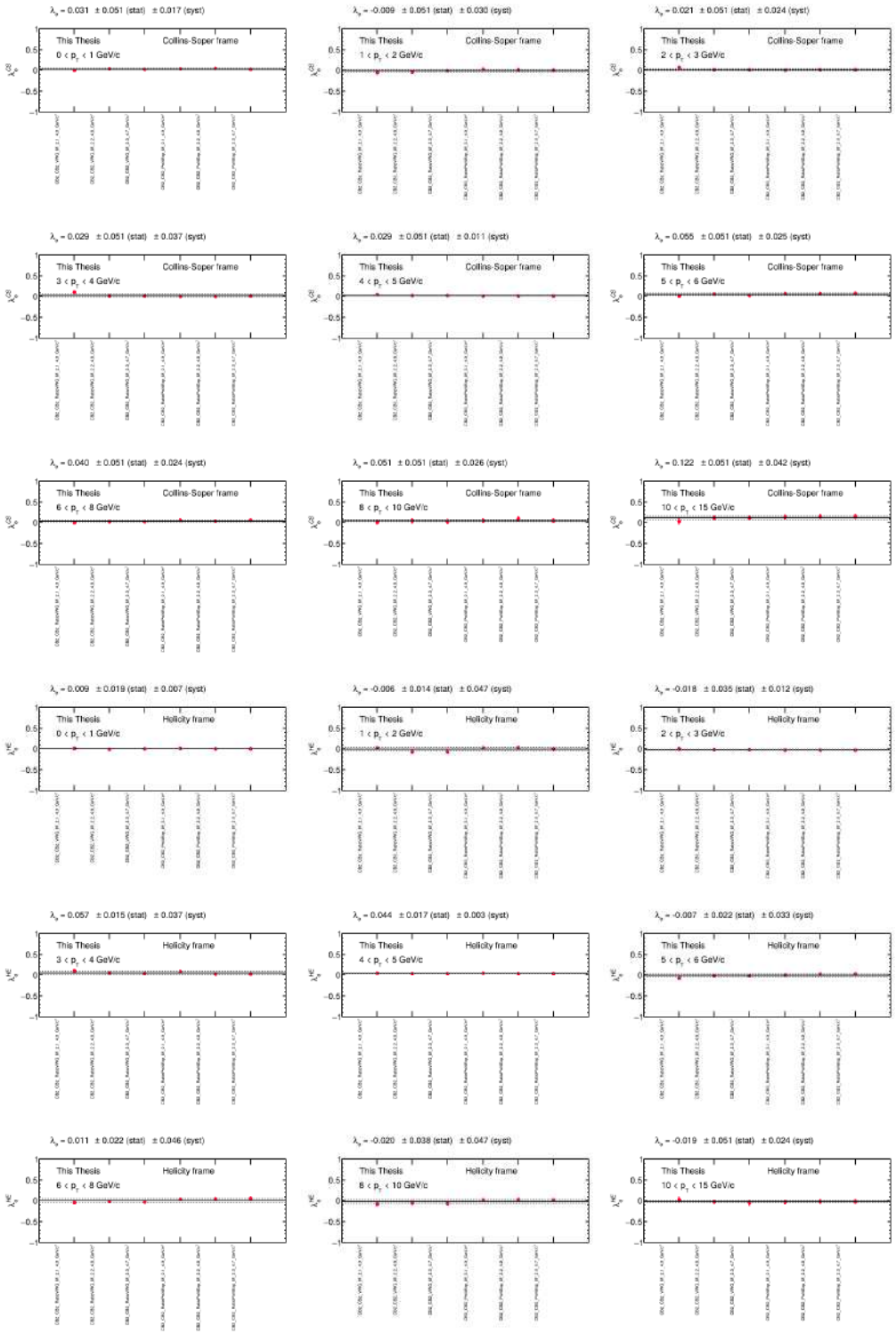



Figure 4.22: Systematic variation of $\lambda_\phi$ due to different trials in CS and HE frame. The top (bottom) three rows correspond to the CS (HE) frame [229].

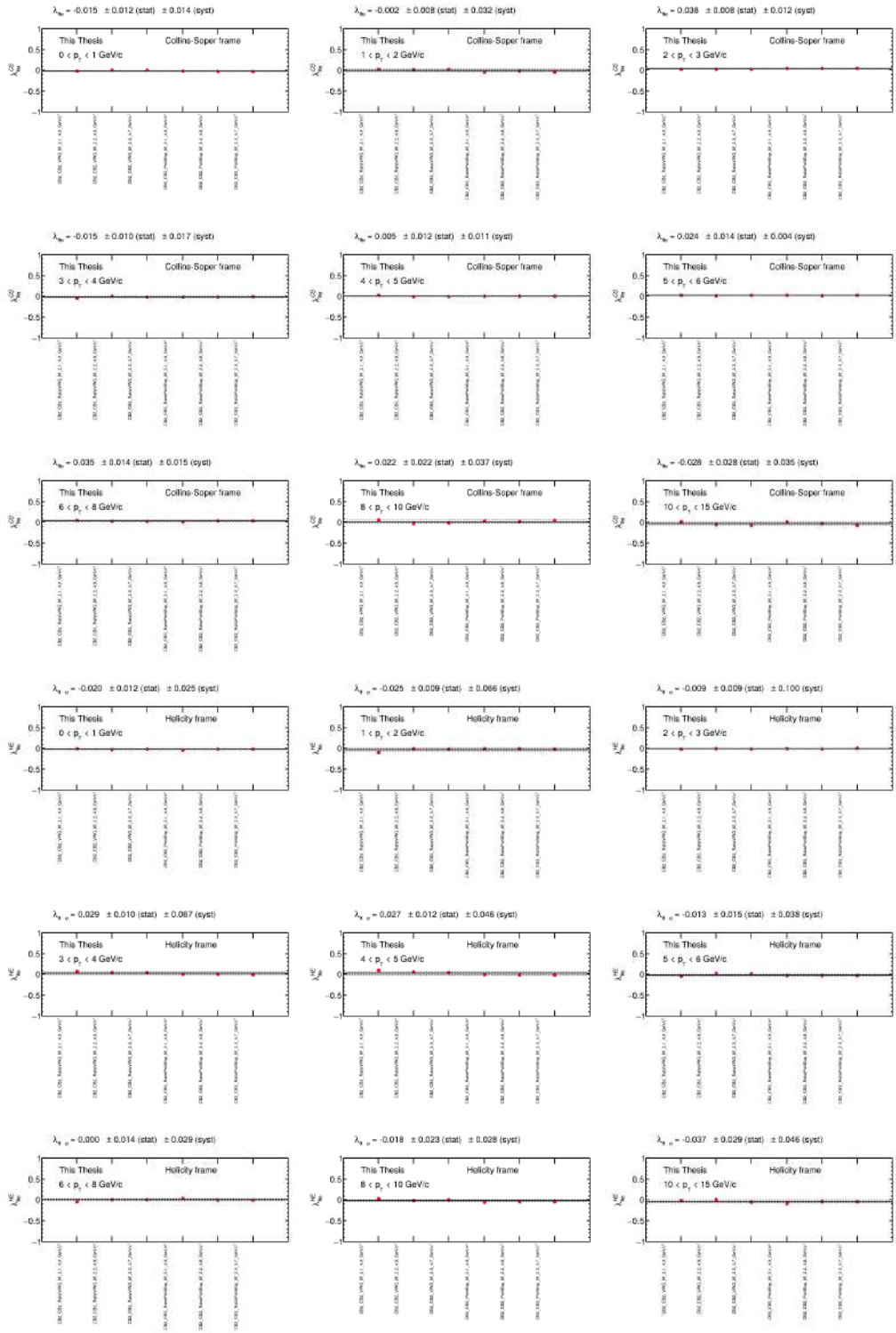



Figure 4.23: Systematic variation of $\lambda_{\theta\phi}$ due to different trials in CS and HE. The top (bottom) three rows correspond to the CS (HE) frame [229].

#### 4.2.6.3 2D fit approach

An additional systematic uncertainty is associated with the choice of fitting strategy used to extract the polarization parameters. Besides the baseline 1D-fit approach, a two-dimensional (2D) simultaneous fit is performed to extract $\lambda_\vartheta$, $\lambda_\varphi$, and $\lambda_{\vartheta\varphi}$ simultaneously, thereby accounting for the full angular distribution and reducing potential biases. To evaluate the impact of the fitting method, the polarization parameters obtained from the 1D and 2D approaches were compared in each $p_{\mathrm{T}}$ interval. Figure 4.24 shows this comparison in the Collins–Soper and helicity frames, while examples of the 2D fits are provided in Figs. 4.25 and 4.26. Half of the difference between the 1D and 2D results is assigned as a systematic uncertainty, with the 1D approach retained as the baseline method.

#### 4.2.6.4 Impact of two different MC productions on polarization

The polarization parameters $\lambda_\vartheta$, $\lambda_\varphi$, and $\lambda_{\vartheta\varphi}$ due to two different MC productions (LHC25c3 and LHC25c3b) are compared and shown in Fig. 4.27. The two MC productions differ in the reconstruction pass employed and in the treatment of real detector effects. Half of the difference between the two Monte Carlo productions is assigned as a systematic uncertainty, with the 1D approach retained as the baseline method.

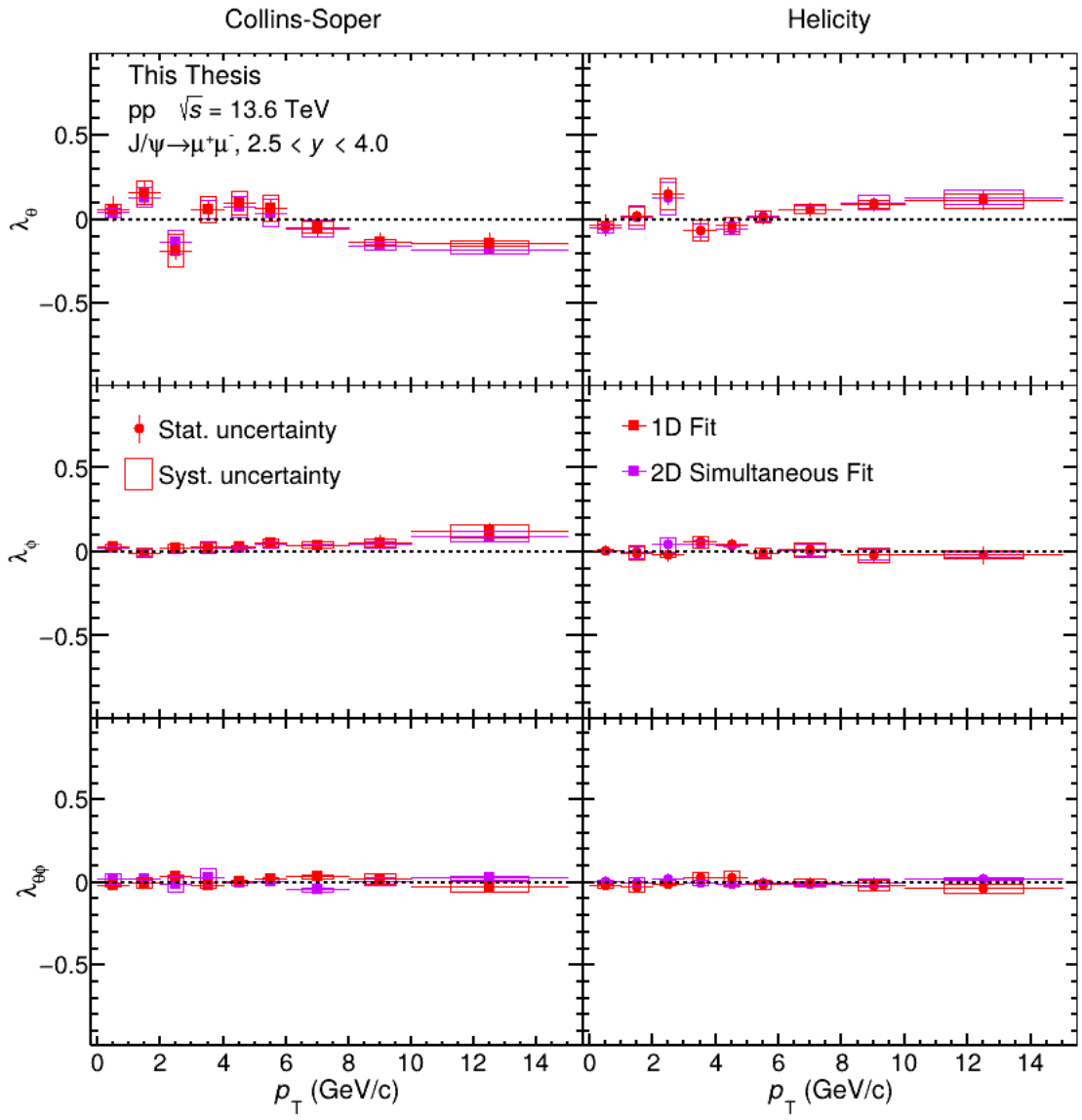



Figure 4.24: Comparison of $\lambda_\theta$, $\lambda_\phi$, and $\lambda_{\theta\phi}$ obtained from 1D-fit and 2D-simultaneous fit as a function of $p_{\mathrm{T}}$ in Collins-Soper and helicity frame [229].

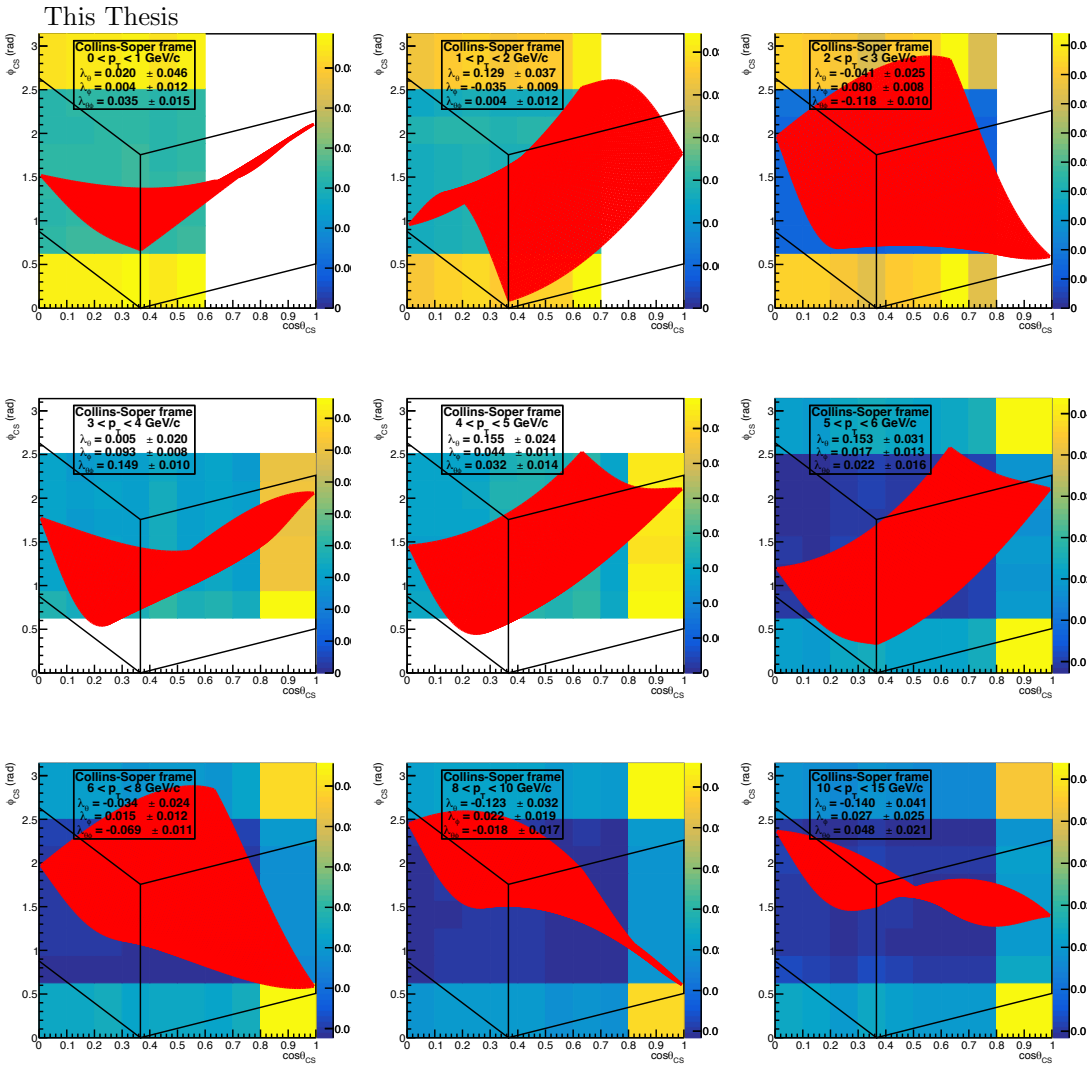



Figure 4.25: 2D-fit of the angular distribution due to CB2+VWG functions in Collins-Soper frame [229].

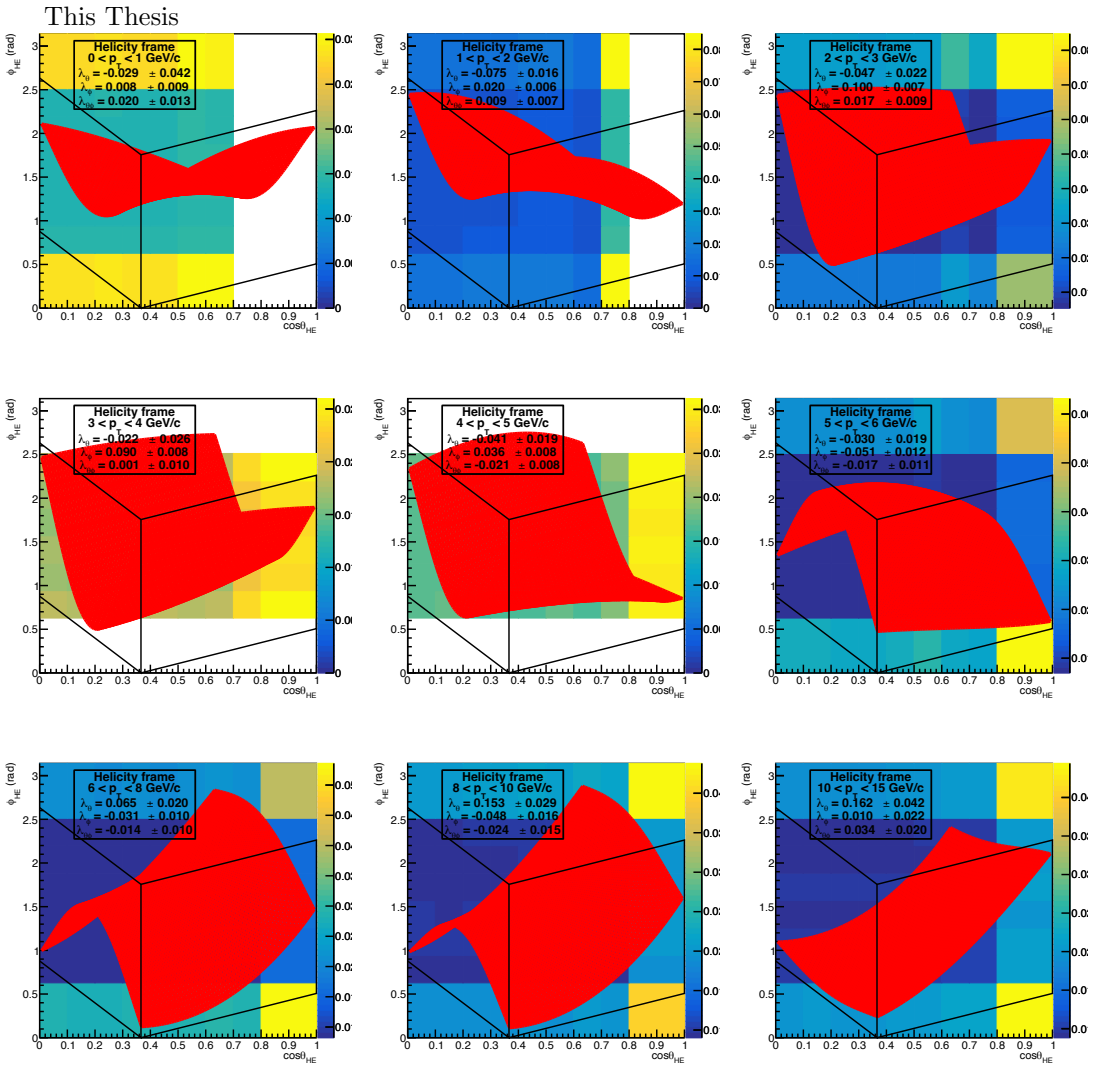



Figure 4.26: 2D-fit of the angular distribution due to CB2+VWG functions in helicity frame [229].

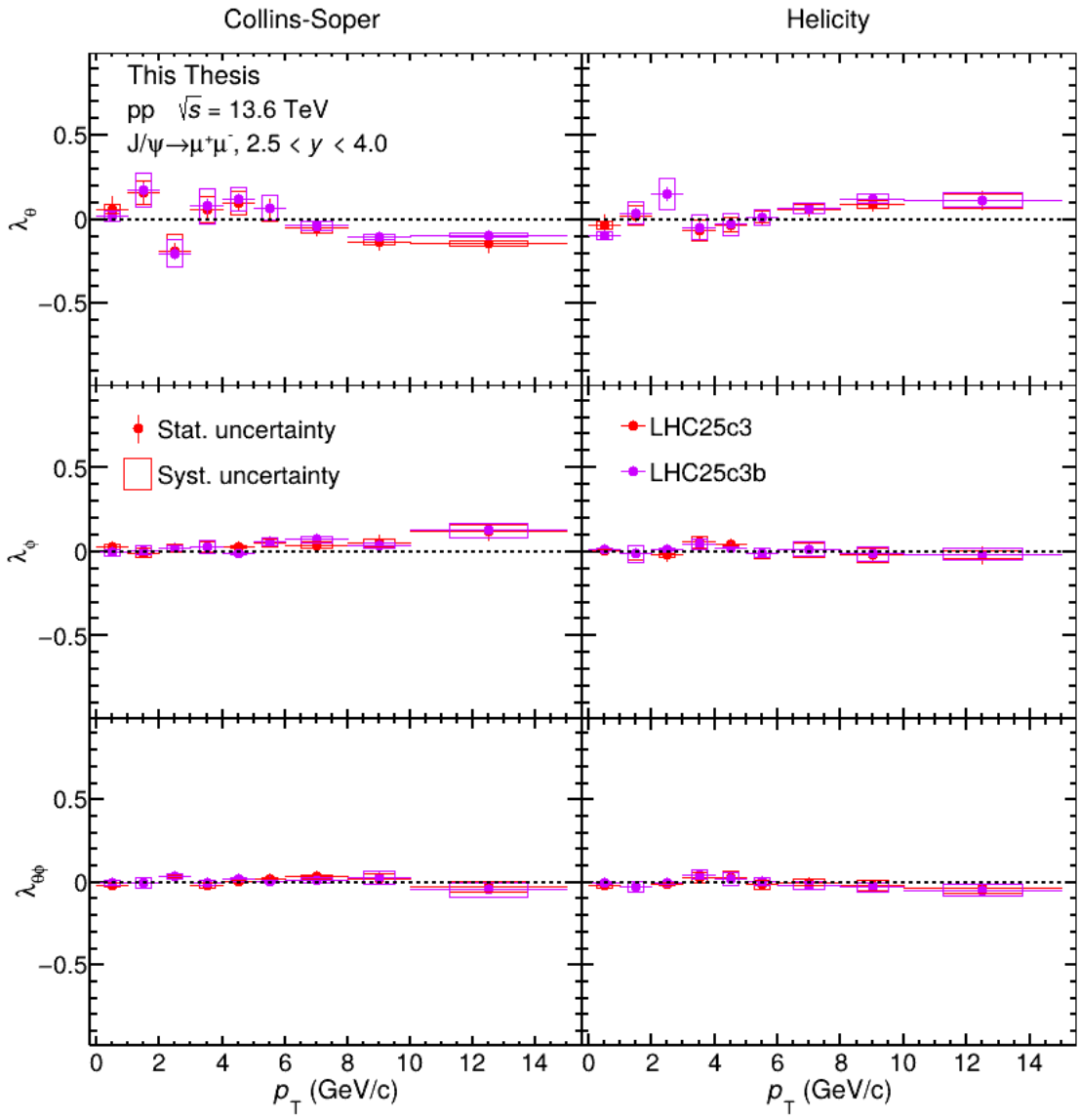



Figure 4.27: Comparison of the $\lambda_\theta$, $\lambda_\phi$, and $\lambda_{\theta\phi}$ due to two different MC productions (LHC25c3 and LHC25c3b) as a function of $p_T$ in Collins-Soper and helicity frame [229].

#### 4.2.6.5 Systematic uncertainty due to input MC shape

Systematic uncertainty due to input MC shape has three different sources, including (i) input polarization parameter, (ii) input $p_{\mathrm{T}}$ shape, and (iii) input $y$ shape.

**Systematic uncertainty due to input polarization parameters**

This systematic uncertainty is evaluated by performing an iterative procedure to tune the $A \times \epsilon$ according to the measured polarization. The default Monte Carlo simulations are employed where J/$\psi$ mesons are initially generated under the assumption of no inherent polarization. This hypothesis can no longer be valid for the extreme cos$\theta$ and $\phi$ values, where a large binning is used [230, 231]. This is because the detector's acceptance and efficiency are not uniformly distributed and are sensitive to the polarization of the parent particle. To evaluate the impact of the input polarization assumption, an iterative MC reweighting procedure is employed. Starting from an unpolarized MC sample, the extracted polarization parameters are used to reweight the angular distributions and derive updated efficiency corrections. The procedure is repeated until convergence is reached. In this analysis, five iterations are performed (Fig. 4.28), with the difference between the fourth and fifth iterations found to be within the statistical uncertainties. The absolute half-difference between the first and fifth iterations is taken as the systematic uncertainty associated with the input polarization.

**Systematic uncertainty due to input $p_{\mathrm{T}}$ and $y$ shape**

The systematic uncertainty associated with the input $p_{\mathrm{T}}$ shape is evaluated by varying the generated $p_{\mathrm{T}}$ distribution, as shown in Fig. 4.29. A weighted $p_{\mathrm{T}}$ distribution is obtained from the ratio of the acceptance-corrected data spectrum to the generated MC spectrum, and the resulting weights are applied to the MC sample to derive new $A \times \epsilon$ corrections. Two additional variations that account

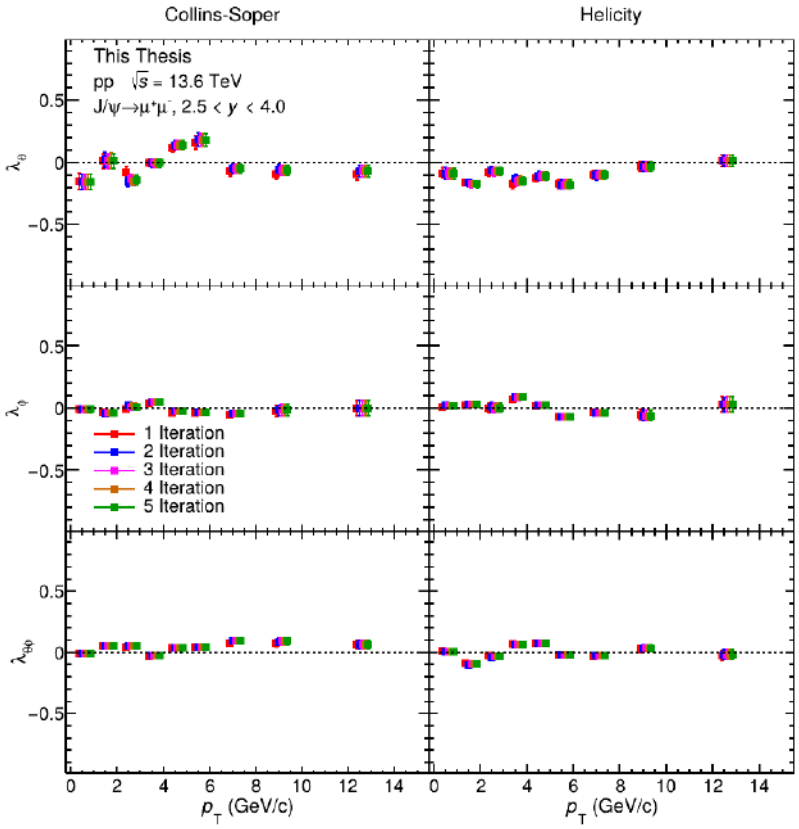



Figure 4.28: $\lambda_\theta$, $\lambda_\phi$, and $\lambda_{\theta\phi}$ due to input MC shape of polarization parameter [229].

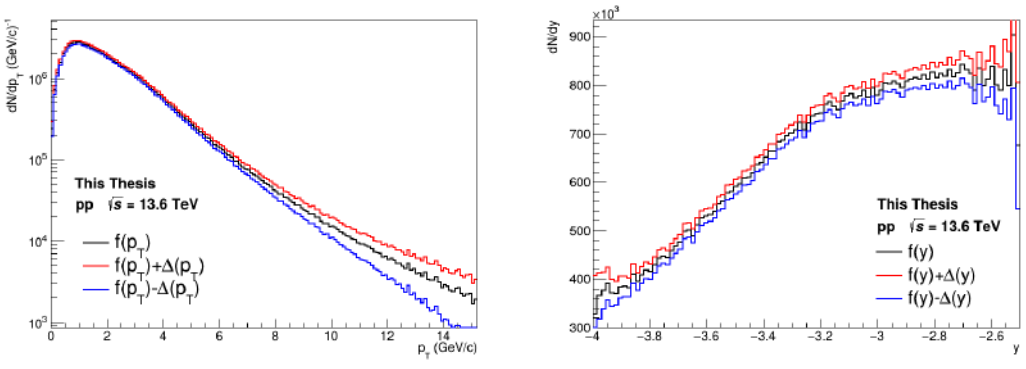



Figure 4.29: $J/\psi$ $p_T$ (left panel) and rapidity $y$ (right panel) distributions obtained from generated MC by applying a weight to the original distributions [229].

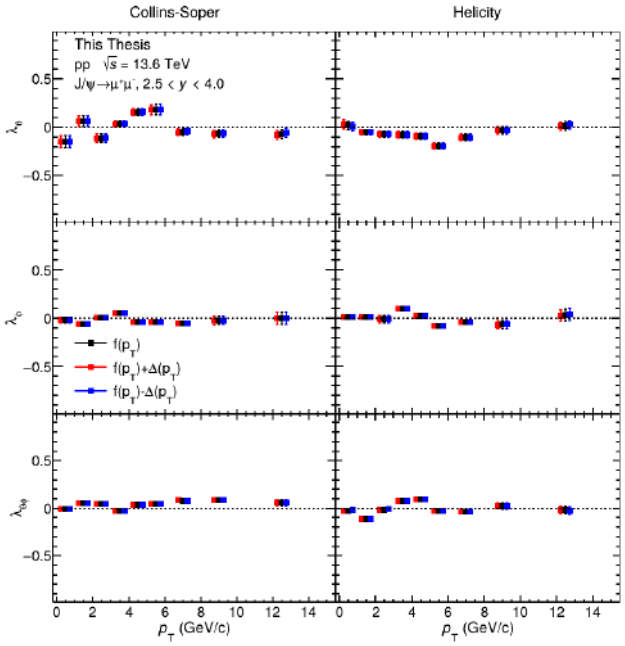



Figure 4.30: Polarization parameters due to input $p_{\mathrm{T}}$ shape [229].

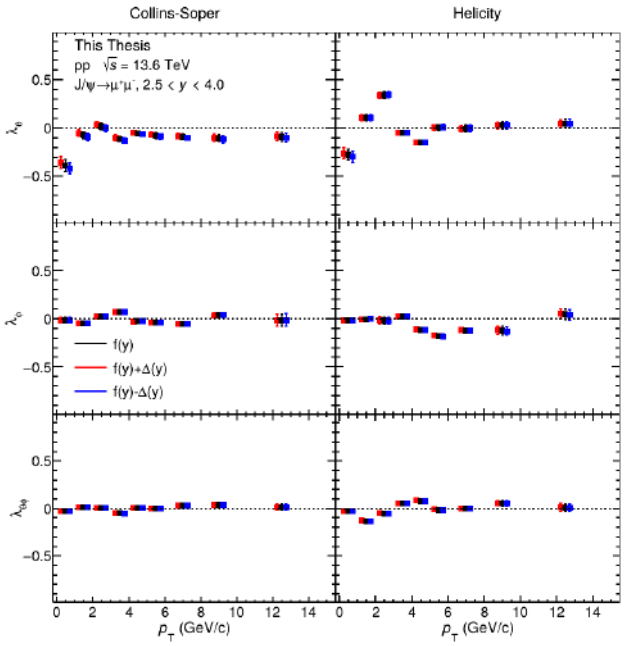



Figure 4.31: Polarization parameters due to input $y$ shape [229].

for the statistical uncertainty in the data are also considered. The polarization parameters obtained with these modified corrections are shown in Fig. 4.30. The absolute half-difference between the results from the two variations is assigned as the systematic uncertainty due to the input $p_{\mathrm{T}}$ shape. A similar procedure is applied to the systematic uncertainty due to the MC input rapidity shape; the variation in polarization parameters due to different input rapidity shapes is shown in Fig. 4.31.

The quadratic sum of these three sources is used as the total systematic uncertainty due to the input MC shape.

#### 4.2.6.6 Systematic uncertainty due to Tracking Efficiency

The calculation of the tracking efficiency for the Muon Chambers (MCH) is performed following Ref [232]. In Fig. 4.32, a schematic of the MCH is shown.

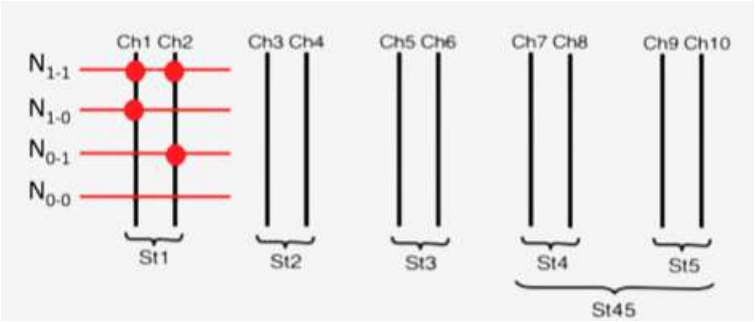



Figure 4.32: Schematic of the MCH used for tracking efficiency calculation

First of all, the efficiency is computed per chamber using Eq. 4.45

$$\epsilon_i = \frac{N_{ij}}{N_{0j} + N_{ij}} \tag{4.45}$$

Secondly, the tracking efficiency is evaluated per station using Eqs. 4.46 and 4.47

$$\epsilon_{\mathrm{St.}(1,2,3)} = 1 - (1 - \epsilon_i)(1 - \epsilon_j) \tag{4.46}$$

$$\epsilon_{\text{St.}(45)} = \prod_{i=7}^{i=10} \epsilon_i + \sum_{i=7}^{i=10} \left( (1 - \epsilon_i) \prod_{j=7, i \neq j}^{j=10} \epsilon_j \right) \tag{4.47}$$

Finally, the total tracking efficiency is calculated using the following formula;

$$\epsilon_{trk} = \epsilon_{\text{St.}(1)} \cdot \epsilon_{\text{St.}(2)} \cdot \epsilon_{\text{St.}(3)} \cdot \epsilon_{\text{St.}(45)} \tag{4.48}$$

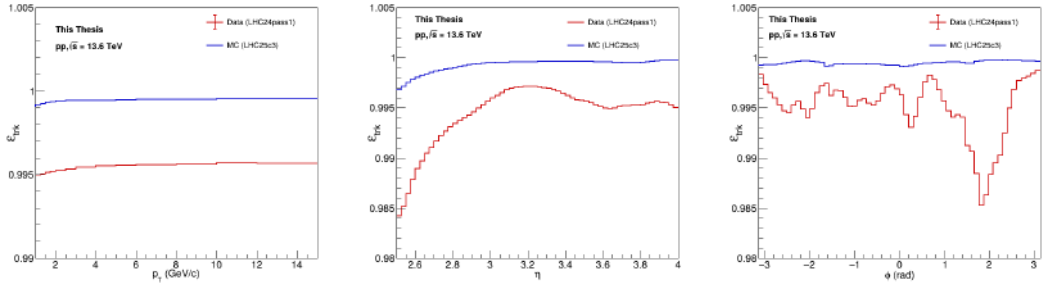



Figure 4.33: Comparison of the tracking efficiency evaluated in data and MC.

The procedure is repeated for data and Monte Carlo, and results are compared as a function of $p_{\mathrm{T}}$, $\eta$, and $\varphi$ of the single tracks, as shown in Fig. 4.33. To evaluate the impact of the tracking efficiency on the evaluation of the polarization parameters, the following test is performed. According to the tracking efficiency shown in Fig. 4.33, we assign a weight to every single muon, and then we re-weight every dimuon with the inverse of the product of the single muon efficiencies:

$$w = \frac{1}{\epsilon_{\mu_1} \epsilon_{\mu_2}} \tag{4.49}$$

This approach should be used to perform the efficiency correction, considering only the tracking effect. We apply the weights corresponding to data and MC to each MC event and obtain new $A \times \epsilon$ terms for Data and MC, denoted as *Data correction* and *MC correction*, as shown in Fig. 4.34. With the new $A \times \epsilon$, we correct the raw angular distribution, and following a similar method as before, we calculate $\lambda_\vartheta$, $\lambda_\varphi$, and $\lambda_{\vartheta\varphi}$ polarization parameters due to Data and MC correction. The absolute half difference of $\lambda_\vartheta$, $\lambda_\varphi$, and $\lambda_{\vartheta\varphi}$ parameters due to

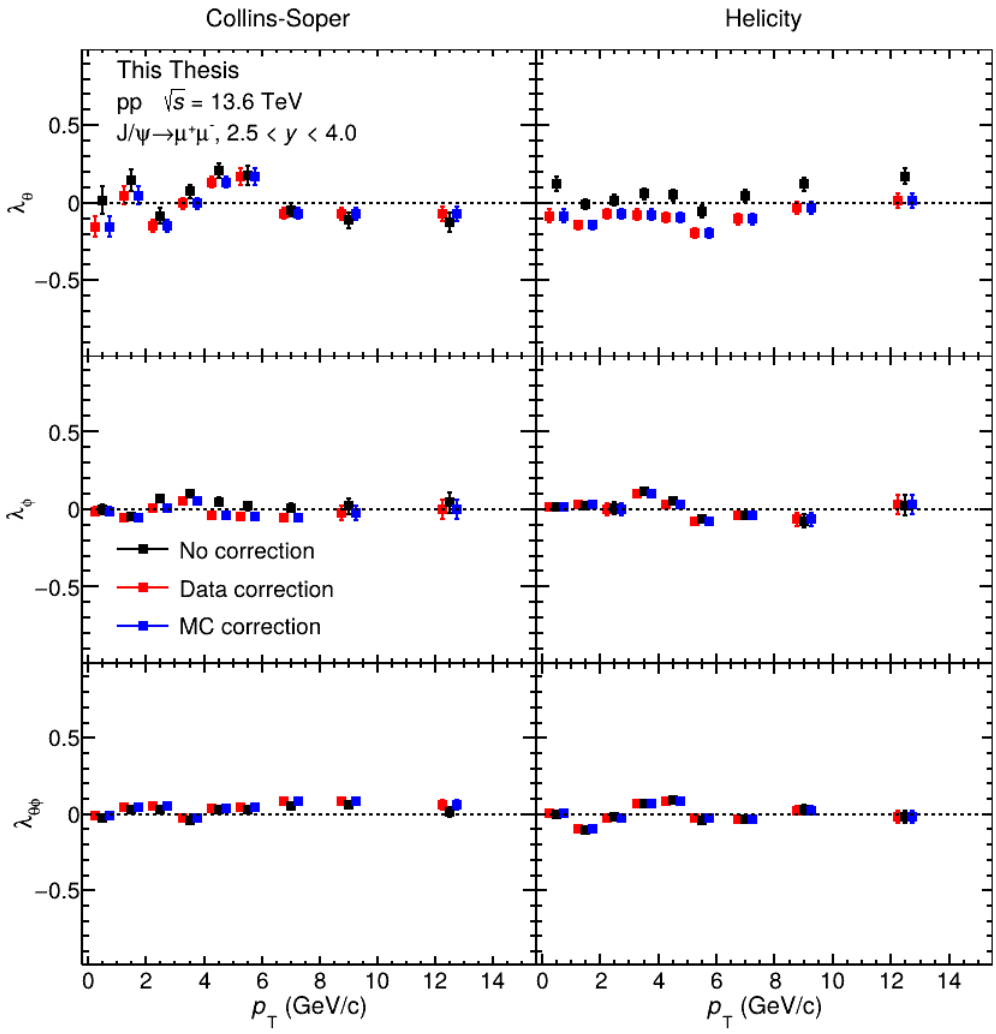



Figure 4.34: Polarization parameters due to tracking efficiency evaluated in data and Monte Carlo [229].

Data correction and MC correction is taken as systematic uncertainty due to the tracking efficiency. Notably, it is observed that the systematic uncertainty due to tracking efficiency in polarization analysis is observed to be neglesible, which is consistent with previous analysis [230]

### 4.2.7 Summary of systematic uncertainties

The summary of the systematic uncertainties in Collins-Soper and helicity frames is reported in the following Tables 4.2 and Tables 4.3, respectively.

Table 4.2: Summary of systematic uncertainties on $\lambda_\theta$ for Collins-Soper frame.

| $p_T$ (GeV/$c$) | Tot Syst. | Sig. Extr. | 1D vs 2D | MC pass | Input Shape | Trk Eff. |
|---|---|---|---|---|---|---|
| 0–1 | 0.0443 | 0.0257 | 0.0099 | 0.0202 | 0.0002 | 9.7e-06 |
| 1–2 | 0.0752 | 0.0690 | 0.0143 | 0.0072 | 0.0001 | 6.5e-06 |
| 2–3 | 0.1032 | 0.0966 | 0.0255 | 0.0026 | 0.0010 | 1.6e-05 |
| 3–4 | 0.0791 | 0.0776 | 0.0004 | 0.0115 | 0.0014 | 1.1e-05 |
| 4–5 | 0.0726 | 0.0689 | 0.0128 | 0.0099 | 0.0014 | 2.8e-06 |
| 5–6 | 0.0805 | 0.0773 | 0.0148 | 0.0008 | 0.0012 | 1.1e-06 |
| 6–8 | 0.0410 | 0.0372 | 0.0043 | 0.0052 | 0.0046 | 1.6e-06 |
| 8–10 | 0.0324 | 0.0162 | 0.0113 | 0.0151 | 0.0044 | 2.9e-06 |
| 10–15 | 0.0393 | 0.0142 | 0.0213 | 0.0236 | 0.0110 | 3.2e-07 |

Table 4.3: Summary of systematic uncertainties on $\lambda_\theta$ for helicity frame.

| $p_T$ (GeV/$c$) | Tot Syst. | Sig. Extr. | 1D vs 2D | MC pass | Input Shape | Trk Eff. |
|---|---|---|---|---|---|---|
| 0–1 | 0.0429 | 0.0231 | 0.0078 | 0.0296 | 0.0134 | 0.0006 |
| 1–2 | 0.0616 | 0.0605 | 0.0071 | 0.0081 | 0.0001 | 3.1e-05 |
| 2–3 | 0.0932 | 0.0911 | 0.0125 | 0.0084 | 1.7e-05 | 1.6e-05 |
| 3–4 | 0.0636 | 0.0616 | 0.0006 | 0.0087 | 5.0e-05 | 7.8e-07 |
| 4–5 | 0.0443 | 0.0420 | 0.0118 | 0.0024 | 0.0001 | 6.7e-06 |
| 5–6 | 0.0346 | 0.0344 | 0.0029 | 0.0018 | 6.4e-05 | 2.2e-07 |
| 6–8 | 0.0271 | 0.0267 | 0.0016 | 0.0037 | 3.7e-05 | 2.5e-05 |
| 8–10 | 0.0312 | 0.0257 | 0.0048 | 0.0168 | 0.0002 | 2.5e-05 |
| 10–15 | 0.0441 | 0.0424 | 0.0096 | 0.0019 | 0.0071 | 7.1e-05 |

### 4.2.8 Results

Figure 4.35 presents the inclusive J/$\psi$ polarization in $pp$ collisions at $\sqrt{s}$ = 13.6 TeV in the Collins–Soper and helicity frames at forward rapidity.

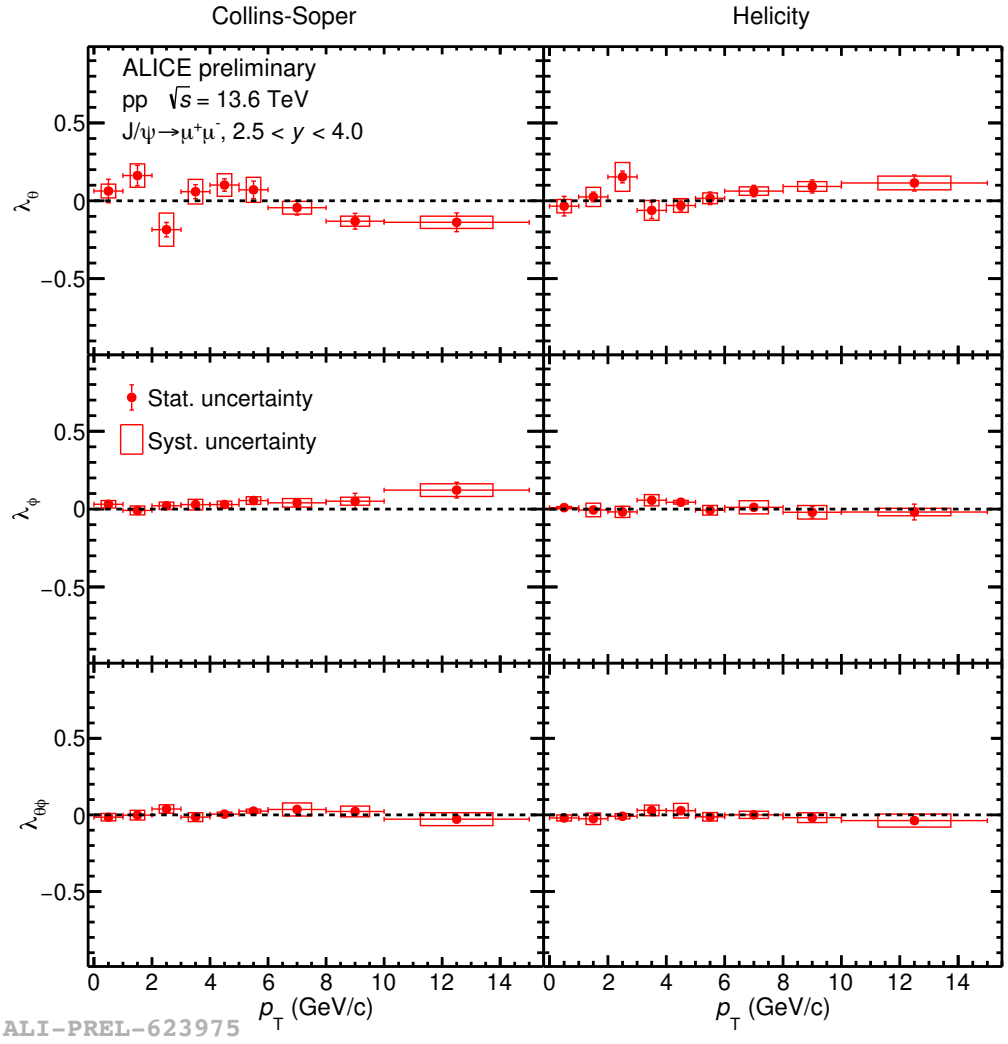



Figure 4.35: J/$\psi$ polarization parameters as a function of transverse momentum in $pp$ collisions at $\sqrt{s}$ = 13.6 TeV in Collins-Soper and helicity frames [229].

The final values of $\lambda_\theta$, $\lambda_\phi$ and $\lambda_{\theta\phi}$ with uncertainties in Collins-Soper, and helicity are quoted in Tables 4.4, and 4.5, respectively. The significance of $\lambda_\theta$, $\lambda_\phi$ and $\lambda_{\theta\phi}$ with respect to no polarization hypothesis are quoted in Table 4.6.

Table 4.4: $\lambda_\theta$, $\lambda_\phi$, and $\lambda_{\theta\phi}$ as a function of $p_{\mathrm{T}}$ in the Collins–Soper frame. Uncertainties are quoted as statistical and systematic, respectively.

| $p_{\mathrm{T}}$ (GeV/$c$) | $\lambda_\theta$ | $\lambda_\phi$ | $\lambda_{\theta\phi}$ |
|---|---|---|---|
| 0–1 | $0.063 \pm 0.075 \pm 0.044$ | $0.031 \pm 0.026 \pm 0.024$ | $-0.015 \pm 0.012 \pm 0.024$ |
| 1–2 | $0.162 \pm 0.065 \pm 0.075$ | $-0.009 \pm 0.018 \pm 0.029$ | $-0.002 \pm 0.008 \pm 0.032$ |
| 2–3 | $-0.185 \pm 0.045 \pm 0.103$ | $0.021 \pm 0.018 \pm 0.024$ | $0.038 \pm 0.008 \pm 0.027$ |
| 3–4 | $0.058 \pm 0.045 \pm 0.079$ | $0.029 \pm 0.019 \pm 0.034$ | $-0.015 \pm 0.010 \pm 0.029$ |
| 4–5 | $0.101 \pm 0.040 \pm 0.073$ | $0.029 \pm 0.023 \pm 0.022$ | $0.005 \pm 0.012 \pm 0.013$ |
| 5–6 | $0.070 \pm 0.056 \pm 0.080$ | $0.055 \pm 0.027 \pm 0.024$ | $0.024 \pm 0.014 \pm 0.013$ |
| 6–8 | $-0.045 \pm 0.047 \pm 0.041$ | $0.040 \pm 0.026 \pm 0.027$ | $0.035 \pm 0.014 \pm 0.043$ |
| 8–10 | $-0.131 \pm 0.051 \pm 0.032$ | $0.051 \pm 0.051 \pm 0.026$ | $0.022 \pm 0.022 \pm 0.035$ |
| 10–15 | $-0.138 \pm 0.060 \pm 0.039$ | $0.122 \pm 0.050 \pm 0.041$ | $-0.028 \pm 0.028 \pm 0.042$ |

Table 4.5: $\lambda_\theta$, $\lambda_\phi$, and $\lambda_{\theta\phi}$ as a function of $p_{\mathrm{T}}$ in the helicity frame. Uncertainties are quoted as statistical and systematic, respectively.

| $p_{\mathrm{T}}$ (GeV/$c$) | $\lambda_\theta$ | $\lambda_\phi$ | $\lambda_{\theta\phi}$ |
|---|---|---|---|
| 0–1 | $-0.034 \pm 0.063 \pm 0.043$ | $0.009 \pm 0.019 \pm 0.007$ | $-0.020 \pm 0.012 \pm 0.020$ |
| 1–2 | $0.025 \pm 0.031 \pm 0.062$ | $-0.006 \pm 0.014 \pm 0.043$ | $-0.025 \pm 0.009 \pm 0.038$ |
| 2–3 | $0.153 \pm 0.038 \pm 0.093$ | $-0.018 \pm 0.035 \pm 0.035$ | $-0.009 \pm 0.009 \pm 0.018$ |
| 3–4 | $-0.062 \pm 0.052 \pm 0.064$ | $0.057 \pm 0.015 \pm 0.036$ | $0.029 \pm 0.010 \pm 0.035$ |
| 4–5 | $-0.030 \pm 0.035 \pm 0.044$ | $0.044 \pm 0.017 \pm 0.012$ | $0.027 \pm 0.012 \pm 0.048$ |
| 5–6 | $0.016 \pm 0.040 \pm 0.035$ | $-0.007 \pm 0.022 \pm 0.031$ | $-0.013 \pm 0.015 \pm 0.028$ |
| 6–8 | $0.062 \pm 0.037 \pm 0.027$ | $0.011 \pm 0.022 \pm 0.042$ | $0.000 \pm 0.014 \pm 0.024$ |
| 8–10 | $0.092 \pm 0.042 \pm 0.031$ | $-0.020 \pm 0.038 \pm 0.043$ | $-0.018 \pm 0.023 \pm 0.032$ |
| 10–15 | $0.114 \pm 0.052 \pm 0.044$ | $-0.019 \pm 0.051 \pm 0.024$ | $-0.037 \pm 0.029 \pm 0.042$ |

Table 4.6: Significance (expressed in $\sigma$) of $\lambda_\theta$, $\lambda_\phi$ and $\lambda_{\theta\phi}$ with respect to the no-polarization hypothesis in the Collins–Soper (CS) and helicity (HE) frames.

| | CS | | | HE | | |
|---|---|---|---|---|---|---|
| $p_{\mathrm{T}}$ (GeV/$c$) | $\lambda_\theta$ | $\lambda_\phi$ | $\lambda_{\theta\phi}$ | $\lambda_\theta$ | $\lambda_\phi$ | $\lambda_{\theta\phi}$ |
| 0–1 | 0.72 | 0.88 | 0.56 | 0.45 | 0.46 | 0.87 |
| 1–2 | 1.63 | 0.25 | 0.06 | 0.36 | 0.12 | 0.66 |
| 2–3 | 1.60 | 0.71 | 1.34 | 1.53 | 0.36 | 0.45 |
| 3–4 | 0.64 | 0.74 | 0.48 | 0.75 | 1.45 | 0.81 |
| 4–5 | 1.22 | 0.92 | 0.27 | 0.53 | 2.10 | 0.56 |
| 5–6 | 0.72 | 1.51 | 1.25 | 0.30 | 0.20 | 0.40 |
| 6–8 | 0.71 | 1.06 | 0.79 | 1.36 | 0.24 | 0.01 |
| 8–10 | 2.18 | 0.89 | 0.54 | 1.76 | 0.35 | 0.46 |
| 10–15 | 1.92 | 1.88 | 0.55 | 1.68 | 0.34 | 0.72 |

### 4.2.9 Comparison with *pp* measurements at 7 and 8 TeV

Figure 4.36 shows a comparison of the inclusive J/$\psi$ polarization measured at $\sqrt{s}$ = 13.6 TeV with previous ALICE and LHCb measurements at $\sqrt{s}$ = 7 and 8 TeV in *pp* collisions, for both the Collins-Soper and helicity frames at forward rapidity. The results at 13.6 TeV are found to be consistent with the earlier measurements within the experimental uncertainties.

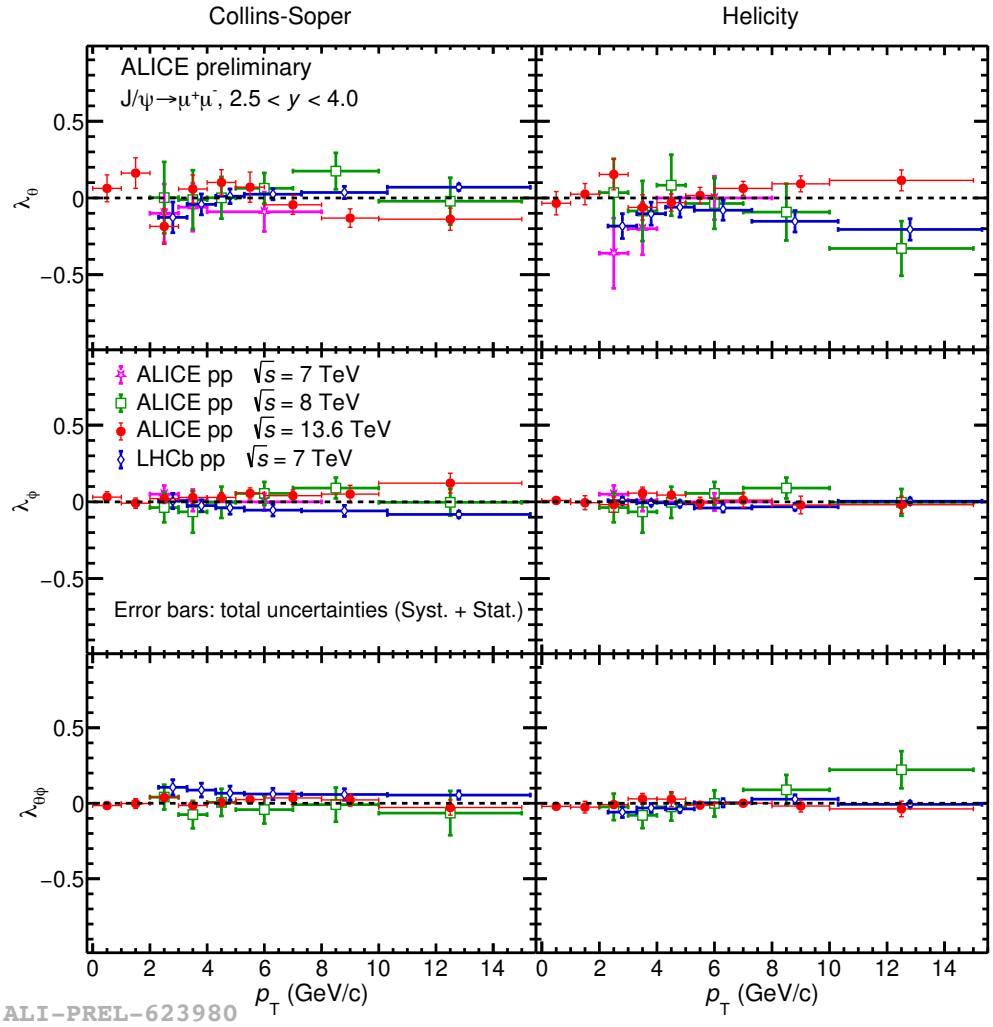



Figure 4.36: Comparison of inclusive J/$\psi$ polarization at $\sqrt{s}$ = 13.6 TeV, with previous existing measurement at $\sqrt{s}$ = 7 and 8 TeVin *pp* collisions [229].

### 4.2.10 Comparison with theoretical models

#### Comparison with different NRQCD models

Figure 4.37 presents a comparison of the measured inclusive J/$\psi$ polarization parameters as a function of transverse momentum $p_{\mathrm{T}}$ in $pp$ collisions with various NRQCD predictions, including the color singlet and color octet contributions.

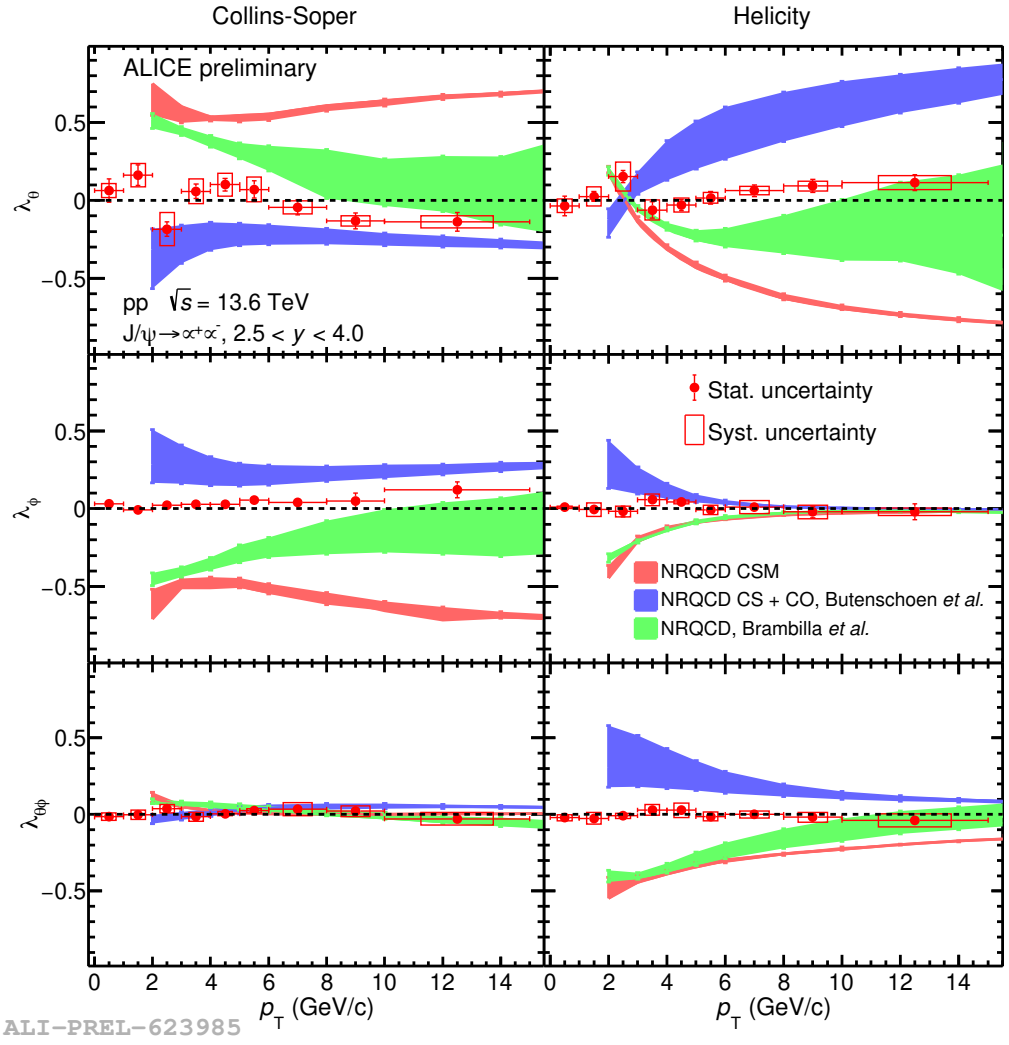



Figure 4.37: Comparison of inclusive J/$\psi$ polarization parameters in $pp$ collisions at $\sqrt{s} = 13.6$ TeV with different NRQCD model predictions [229].

The measurements are compared with NLO CSM [93] and several NLO NRQCD calculations [93, 94, 97, 98], which differ in the experimental data sets used to determine the long-distance matrix elements.

### Comparison with ICEM and CGC+NRQCD models

Figure 4.38 compares the measured J/$\psi$ polarization parameters as a function of $p_{\mathrm{T}}$ in $pp$ collisions with predictions from the Improved Color Evaporation Model (ICEM)and CGC-based NRQCD calculations. Below, we define a few important features of the compared theoretical models:

- **Color Singlet Model (CSM)**: It describes quarkonium production by assuming that a heavy quark-antiquark pair is produced directly in a color-singlet state with the same quantum numbers as the observed quarkonium. The production cross section can be factorized into a short-distance part, calculable using perturbative QCD, and a long-distance factor that is proportional to the quarkonium wave function at the origin. While the CSM successfully captures several features of quarkonium production, it underestimates the measured yields at high transverse momentum. In addition, the CSM, even with both LO and NLO calculations, fails to adequately describe the experimentally measured J/$\psi$ polarization in hadronic collisions.

- **Nonrelativistic QCD (NRQCD)[CS+CO]**: It is the most widely used effective field theory for describing heavy quarkonium production and decay. It is based on the factorization of the quarkonium production process into short-distance and long-distance contributions. The short-distance coefficients, corresponding to the production of a heavy quark-antiquark ($\mathrm{Q}\bar{\mathrm{Q}}$) pair, are calculable using perturbative QCD (pQCD), while the long-distance matrix elements (LDMEs) describe the non-perturbative transition of the $\mathrm{Q}\bar{\mathrm{Q}}$ pair into a physical quarkonium state. A key feature of NRQCD is the inclusion of both *color-singlet* (CS) and *color-octet* (CO) production

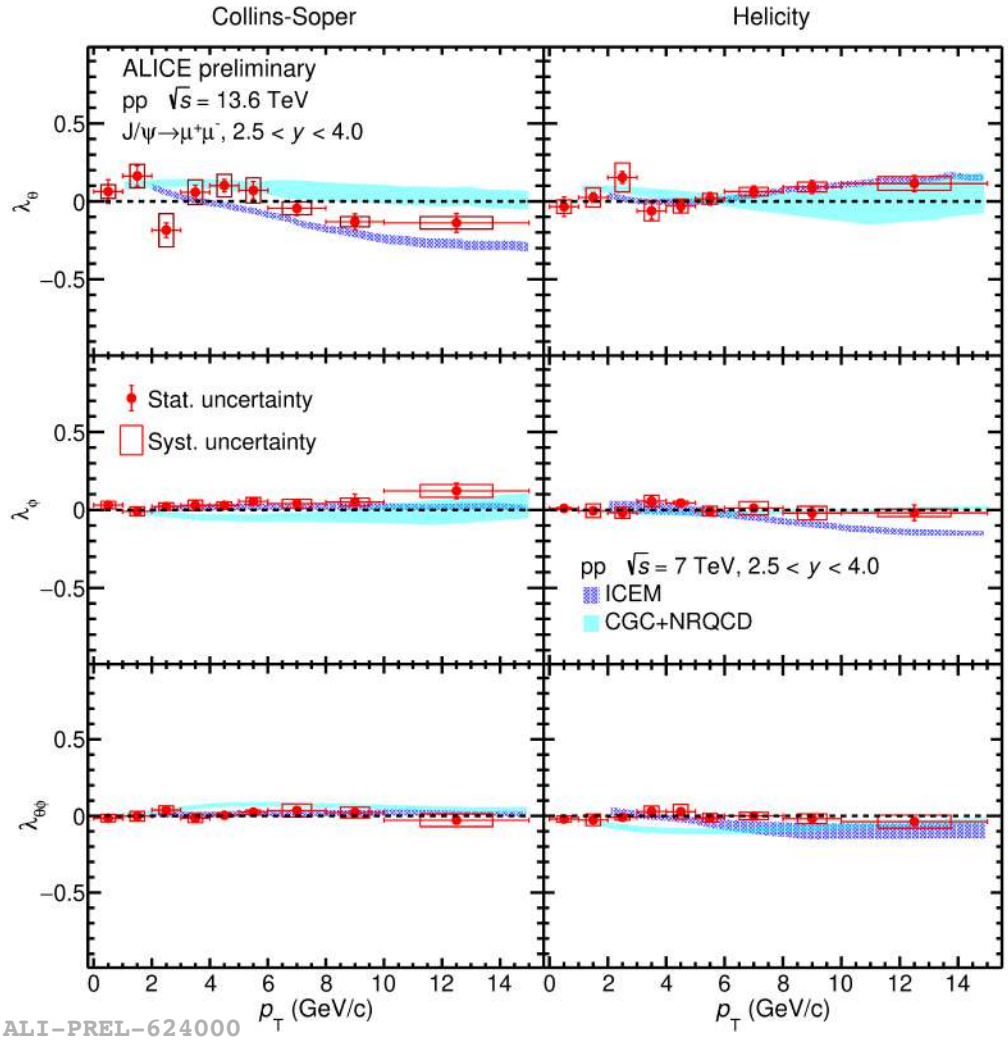



Figure 4.38: Comparison of inclusive J/$\psi$ polarization parameters in $pp$ collisions at $\sqrt{s} = 13.6$ TeV with ICEM and CGC+NRQCD model predictions [229].

channels. As mentioned above, in the color-singlet mechanism, the $Q\bar{Q}$ pair is produced directly with the same quantum numbers as the final quarkonium state, whereas in the color-octet mechanism, the pair is produced in a colored state and subsequently evolves into quarkonium through the emission of soft gluons. The inclusion of color-octet contributions enables NRQCD to explain the large quarkonium production cross sections observed at high transverse momentum, which could not be adequately described by the CSM alone. Consequently, NRQCD provides a comprehensive framework for studying quarkonium production in high-energy hadronic collisions. However, despite their success in describing quarkonium production cross sections, both the CSM and NRQCD (CS+CO) frameworks fail to provide a satisfactory quantitative description of the measured (J/$\psi$) polarization in *pp* collisions, as shown in Fig. 4.37.

- **Improved Color Evaporation Model (ICEM)**: It is an extension of the Color Evaporation Model (CEM) that incorporates the kinematic constraints of the produced quarkonium state. In the ICEM, the production cross section is calculated by integrating the heavy quark-antiquark pair mass spectrum over a restricted invariant mass range between the quarkonium mass and the open heavy flavor threshold. Unlike the conventional CEM, the ICEM accounts for the momentum relationship between the intermediate $Q\bar{Q}$ pair and the final quarkonium, leading to improved predictions for transverse momentum spectra and polarization observables. This improvement provides a more realistic description of quarkonium transverse momentum distributions and polarization while maintaining the simplicity of the original CEM.

- **Color Glass Condensate (CGC) + Nonrelativistic QCD (NRQCD)**: This framework combines the effective description of high-density gluon fields at small Bjorken-$x$ provided by the CGC with the quarkonium produc-

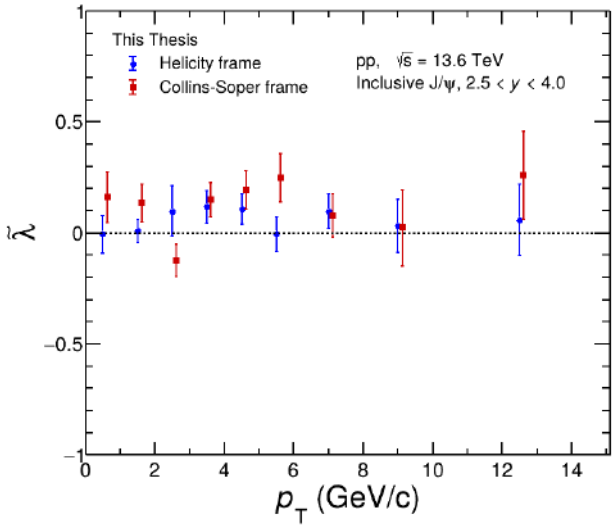



Figure 4.39: Frame invariant parameter $\tilde{\lambda}$ as a function of $p_{\mathrm{T}}$ in Collins-Soper and helicity frame. The error bars include the contributions of the systematic and statistical uncertainties [229].

tion mechanism of NRQCD. In this approach, the CGC formalism describes the initial-state gluon saturation effects that dominate at high collision energies, while NRQCD factorizes the hadronization of the produced heavy quark-antiquark pair into short-distance coefficients and universal LDMEs. The CGC+NRQCD framework has been successful in describing quarkonium production, particularly at low transverse momentum and forward rapidity, where gluon saturation effects are expected to be significant. It also provides a better description of $J/\psi$ polarization measurements for $p_{\mathrm{T}} \leq 15$ GeV/c relative to the existing NLO calculations within the collinear factorization framework. It therefore provides a unified theoretical framework for studying both perturbative production dynamics and non-perturbative quarkonium formation in high-energy hadronic collisions.

To validate the consistency of polarization measurements in the Collins–Soper and helicity frames, the frame-invariant parameter defined in Eq. 4.26 is shown

in Fig. 4.39. The results from both reference frames are qualitatively consistent within the quoted statistical and systematic uncertainties, apart from a few $p_{\mathrm{T}}$ bins. This partial agreement suggests that the analysis procedure does not introduce significant bias, even though some sources of uncertainty may be correlated between the Collins–Soper and helicity frame measurements.

*In summary, this section presents the analysis details of the experimental measurement of* J/$\psi$ *polarization parameters at forward rapidity in pp collisions at* $\sqrt{s}$ = *13.6 TeV. With the high-statistics Run 3 data collected at the LHC energies, a more precise and differential measurement of* $\lambda_\theta, \lambda_\phi,$ *and* $\lambda_{\theta\phi}$ *parameters is performed by the ALICE Collaboration in hadronic collisions with respect to the existing measurements at LHC energies. For the first time, the* J/$\psi$ *polarization parameters are obtained down to zero* $p_{\mathrm{T}}$*. Despite a few decades after the discovery of* J/$\psi$*, its polarization measurement in hadronic collisions through NRQCD and CSM models is still challenging. However, improved theoretical models such as ICEM and CGC+NRQCD qualitatively predict the experimental data.*

Following a similar analysis strategy, the next section discusses the J/$\psi$ polarization measurement in oxygen-oxygen collisions.

## 4.3 $J/\psi$ polarization in oxygen-oxygen collisions

This section presents the first measurement of inclusive $J/\psi$ polarization in oxygen-oxygen collisions at $\sqrt{s_{NN}} = 5.36$ TeV using the light-ion Run 3 data of the upgraded ALICE detector. This analysis is performed using the dimuon decay channel at forward rapidity ($2.5 < y < 4.0$) in the transverse momentum range $0 < p_T < 10$ GeV/c for (0-100)%. The unexpectedly large integrated luminosity accumulated in OO collisions provides a unique opportunity to perform a variety of physics measurements at forward rapidity using dimuon tracks. Among these, it enables a differential study of the $J/\psi$ polarization parameters $\lambda_\vartheta$, $\lambda_\varphi$, and $\lambda_{\vartheta\varphi}$ across different transverse-momentum intervals.

The study of $J/\psi$ polarization in OO collisions is of particular interest. In peripheral nuclear collisions, the polarization of $J/\psi$ may carry information about the initial OAM and the magnetic field generated during the early stages of the collision. In addition, both cold nuclear matter effects and hot medium effects can influence the observed $J/\psi$ polarization. As in *pp* collisions, polarization measurements also provide valuable insight into the underlying $J/\psi$ production mechanism. Since the OO collision has a system size that lies between *pp* and Pb–Pb collisions, measurements of $J/\psi$ polarization in OO collisions offer a unique opportunity to investigate the system-size dependence of the polarization parameters. With these motivations, the following section presents the $J/\psi$ polarization measurement in OO collisions. The details of the dataset, MC samples, and the event and track selection criteria are described below.

### 4.3.1 Data sample selection and analysis cuts

#### 4.3.1.1 Data samples

This analysis is performed using the **LHC25ae pass2** with the standard association dataset obtained during the period 2025. The data are acquired in

continuous readout, so no hardware trigger is applied at the muon level. The latest reconstruction pass is adopted for this analysis. This analysis is performed using all the GOOD Run periods with QC flags checked on RCT. The RunList follows the standard **CBT muon** criteria as used for pp collisions.
**RunList**: 564356, 564359, 564373, 564374, 564387, 564400, 564414, 564430, 564445

#### 4.3.1.2 Monte Carlo sample

The MC sample **LHC25i4** (anchored tothe LHC25ae pass2 dataset) is used for this analysis. In this production, 1 J/$\psi$ + 1 $\psi$(2S) are generated at forward rapidity and injected into a minimum bias (MB) pp event in every 5 events. The details about runlists used in the dataset can be found at alimonitor.cern.ch/hyperloop/view-dataset/2527. The details about the MC production can be found in the JIRA tickets its.cern.ch/jira/browse/O2-6324

#### 4.3.1.3 Event selection

The event selection cut **eventSel8** is used in this analysis. Minimum bias events are selected with **Sel8** conditions, which are composed of the following selection cuts: **Sel8** = TriggerTVX + NoITSROFrameBorder + NoTimeFrameBorder The physical meaning of these selection cuts is defined in Sec. 4.2.

#### 4.3.1.4 Track selection

Similar to the *pp* analysis, the standalone muons are used, which satisfy the MCH-MID match requirement. To select a pure sample of muons, a set of cuts is applied at the single-track level and dimuon level:

1. On a single muon
   (a) Radial transverse position of the muon tracks at the end of the absorber ($R_{\rm abs}$) cut: 17.6 cm $< R_{\rm abs} <$ 89.5 cm.

(b) Pseudorapidity cut: -4.0 $< \eta <$ -2.5

(c) Transverse momentum cut: $p_{\mathrm{T}}^{\mu} > 0$ GeV/c

(d) $pDCA$ cut: 0 GeV·$cm/c$ $< pDCA <$ 594 GeV·cm/c for 17.6 cm $< R_{\mathrm{abs}} <$ 26.5 cm

(e) $pDCA$ cut: 0 GeV·$cm/c$ $< pDCA <$ 324 GeV·cm/c for 26.5 cm $< R_{\mathrm{abs}} <$ 89.5 cm

(f) $0 < \chi^2 < 10^6$, $0 < \chi^2_{\mathrm{matchMCHMID}} < 10^6$

2. On dimuon pairs

(a) $2.5 < y < 4.0$

(b) $0 < p_T <$ 10 GeV/c

(c) FT0C Centrality: (0-100) %

### 4.3.2 Signal extraction

We follow the same signal-extraction strategy in OO collisions as in *pp* collisions. However, in OO collisions, the nominal fit employs a CB2 function for the signal and a VWG function for the background. Unlike in *pp* collisions, no background modulation is observed in the dimuon mass spectrum, since no single-muon $p_{\mathrm{T}}$ threshold is applied in the software trigger. In OO collisions, we consider the NA60 function as another fitting function for the signal, which is defined below.

#### 4.3.2.1 NA60

The NA60 function is a modified Gaussian with asymmetric, parameterized tails that accurately models the detector resolution and radiative effects in dimuon invariant-mass spectra. Because of its flexible left/right deformation, the NA60 function provides a highly reliable description of the J/$\psi$ peak, making it one

of the most robust choices for signal extraction in heavy-ion and fixed-target experiments. The functions adopted here are listed below [227].

$$t = \frac{x-\mu}{\sigma}, \qquad \sigma < 0 \Rightarrow t \to -t.$$

$$f(x) = \begin{cases} \exp\left[-\frac{1}{2}\left(\frac{t}{T_L(t)}\right)^2\right], & t \leq \alpha_{\mathrm{L}}, \\ \exp\left(-\frac{t^2}{2}\right), & \alpha_{\mathrm{L}} < t < \alpha_{\mathrm{R}}, \\ \exp\left[-\frac{1}{2}\left(\frac{t}{T_R(t)}\right)^2\right], & t \geq \alpha_{\mathrm{R}}, \end{cases}$$

$$T_L(t) = 1 + p_1^{\mathrm{L}}\left(\alpha_{\mathrm{L}} - t\right)^{p_2^{\mathrm{L}} - p_3^{\mathrm{L}}\sqrt{\alpha_{\mathrm{L}} - t}},$$

$$T_R(t) = 1 + p_1^{\mathrm{R}}\left(t - \alpha_{\mathrm{R}}\right)^{p_2^{\mathrm{R}} - p_3^{\mathrm{R}}\sqrt{t - \alpha_{\mathrm{R}}}}.$$

#### 4.3.2.2 Tail parameters extraction

Two sets of $p_{\mathrm{T}}$-integrated tail parameters are used in this analysis. One set is obtained from MC and the other from data, as described below.

**Using MC data**

The reconstructed $p_{\mathrm{T}}$-integrated $J/\psi$ spectrum obtained from the MC sample is fitted with the CB2 and NA60 functions, keeping mass, width, and all the tail parameters free, as shown in the left and right panels of Fig. 4.40. The tail parameters for the CB2 and NA60 functions are reported in Tables. 4.7 and 4.8, respectively. Notably, this one set of $p_{\mathrm{T}}$-integrated tail parameters are used each $p_{\mathrm{T}}$, cos$\theta$, $\phi$, $\tilde{\phi}$ differential bins.

| $p_{\mathrm{T}}$ (GeV/c) | $\alpha_L$ | $n_L$ | $\alpha_R$ | $n_R$ |
|---|---|---|---|---|
| $0 < p_{\mathrm{T}} < 20$ | 0.99 ± 0.004 | 2.69 ± 0.018 | 2.15 ± 0.015 | 6.84 ± 0.28 |

Table 4.7: $p_{\mathrm{T}}$ integrated CB2 tail parameters obtained from LHC25i4.

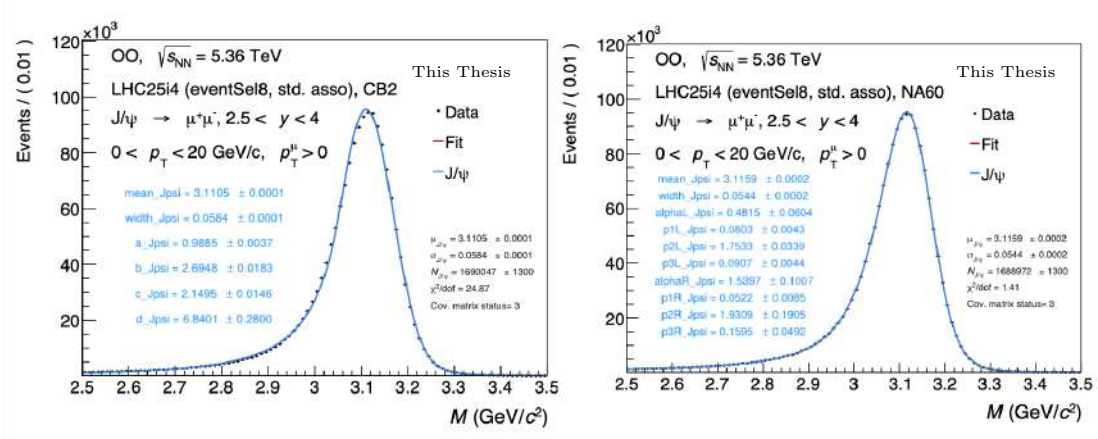



Figure 4.40: $p_{\mathrm{T}}$-integrated tail parameters extraction with LHC25i4 MC sample using CB2 and NA60 function [233].

| $p_{\mathrm{T}}$ (GeV/c) | $\alpha_L$ | $p_{1L}$ | $p_{2L}$ | $p_{3L}$ | $\alpha_R$ | $p_{1R}$ | $p_{2R}$ | $p_{3R}$ |
|---|---|---|---|---|---|---|---|---|
| $0 < p_{\mathrm{T}} < 20$ | 0.48 ± 0.06 | 0.08 ± 0.004 | 1.75 ± 0.034 | 0.09 ± 0.004 | 1.54 ± 0.101 | 0.05 ± 0.008 | 1.93 ± 0.19 | 0.16 ± 0.049 |

Table 4.8: $p_{\mathrm{T}}$ integrated NA60 tail parameters obtained from LHC25i4.

### Using raw data

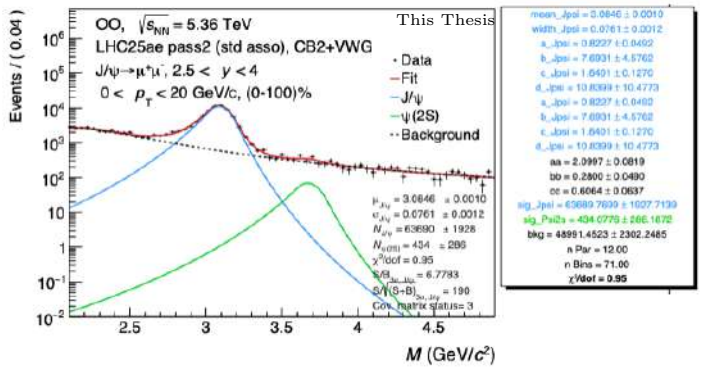



Figure 4.41: $p_{\mathrm{T}}$-integrated tail parameter extraction in Data with CB2 (Signal) and VWG (background) functions [233].

Two CB2 functions have been fitted to the reconstructed $J/\psi$ and $\psi(2S)$ signal,

and the VWG function has been fitted to the residual background. While fitting the $p_{\mathrm{T}}$-integrated dimuon mass spectrum, we keep the mass and width of $J/\psi$ free and all the tail parameters of $J/\psi$ free, as shown in Fig. 4.41. The tail parameters for the CB2 function are reported in Table. 4.9. $p_{\mathrm{T}}$-integrated tail parameters obtained from data are used each $p_{\mathrm{T}}$, cos$\theta$, $\phi$, $\tilde{\phi}$ differential bins.

| $p_{\mathrm{T}}$ (GeV/c) | $\alpha_L$ | $n_L$ | $\alpha_R$ | $n_R$ |
|---|---|---|---|---|
| $0 < p_{\mathrm{T}} < 20$ | 0.823 ± 0.05 | 7.693 ± 4.58 | 1.64 ± 0.13 | 10.84 ± 10.48 |

Table 4.9: $p_{\mathrm{T}}$ integrated CB2 tail parameters obtained from data.

Before going into the analysis details, the $p_{\mathrm{T}}$, cos$\theta$, $\phi$, and $\tilde{\phi}$ bins used for this study are listed below:

- $p_{\mathrm{T}}$ bins: [0, 2], (2, 4], (4, 6], (6, 10] GeV/c (Total 4 bins)
- cos$\theta$ bins: [-1,+1] with equal bin width 0.2 (Total 10 bins)
- $\phi$ bins: [0, $\pi$] with equal bin width 0.314 (Total 10 bins)
- $\tilde{\phi}$ bins: [0, 2$\pi$] with equal bin width 0.628 (Total 10 bins)

We extract the J/$\psi$ yield is extracted in different cos$\,\theta$, $\phi$, and $\tilde{\phi}$ bins for each $p_{\mathrm{T}}$ interval. As an example, Fig. 4.42, and Fig. 4.43 shows the signal extraction in different cos$\,\theta$ bins for $4 < p_{\mathrm{T}} < 6$ GeV/$c$ in Collins-Soper and helicity frame, respectively. The corresponding results for the remaining $p_{\mathrm{T}}$ intervals are provided in Appendix B.1 (Fig. 12) to Appendix B.3 (Fig. 27). The resulting raw angular distributions as functions of cos$\,\theta$ (top), $\phi$ (middle), and $\tilde{\phi}$ (bottom) in the Collins–Soper (left) and helicity (right) frames are presented in Fig. 4.44 for $0 < p_{\mathrm{T}} < 10$ GeV/$c$. The fitting parameters such as J/$\psi$ mass ($m_{\mathrm{J}/\psi}$) and width ($\sigma_{\mathrm{J}/\psi}$) for different cos$\,\theta$, $\phi$, and $\tilde{\phi}$ bins in different transverse momentum ranges are shown in Appendix B.3, from Fig. 28 to Fig. 29, respectively. Additionally, the cos$\,\theta$, $\phi$, and $\tilde{\phi}$ differential J/$\psi$ raw angular distributions corresponding to all

fitting ranges and fitting functions are shown in Fig. 30 of Appendix B.3. The extracted raw-yield distributions are consistent within statistical uncertainties, indicating that the signal extraction is stable against variations in the fitting procedure.

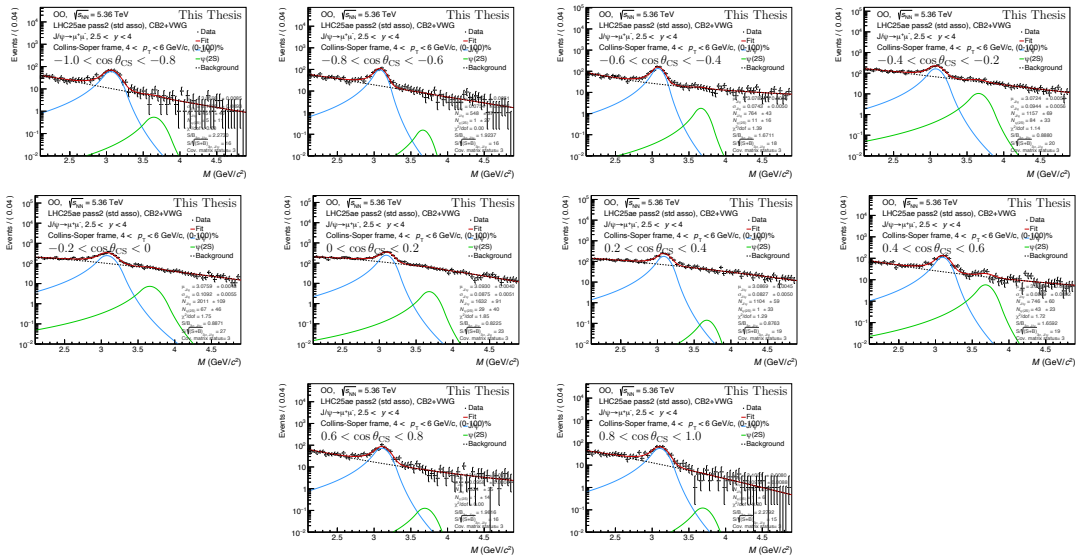



Figure 4.42: $\cos\theta$ differential signal extraction for $4 < p_{\mathrm{T}} < 6$ GeV/c in Collins-Soper frame. The $\cos\theta$ intervals from $-1.0$ to $+1.0$ with a bin width of 0.2 are arranged from left to right and top to bottom. [233].

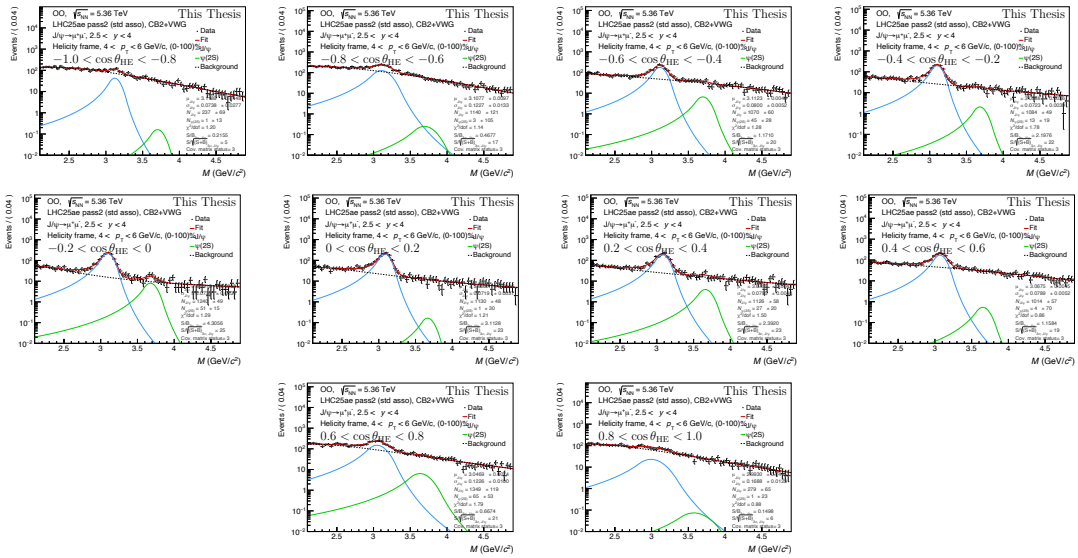



Figure 4.43: $\cos\theta$ differential signal extraction for $4 < p_{\mathrm{T}} < 6$ GeV/c in helicity frame. The $\cos\theta$ intervals from $-1.0$ to $+1.0$ with a bin width of 0.1 are arranged from left to right and top to bottom. [233].

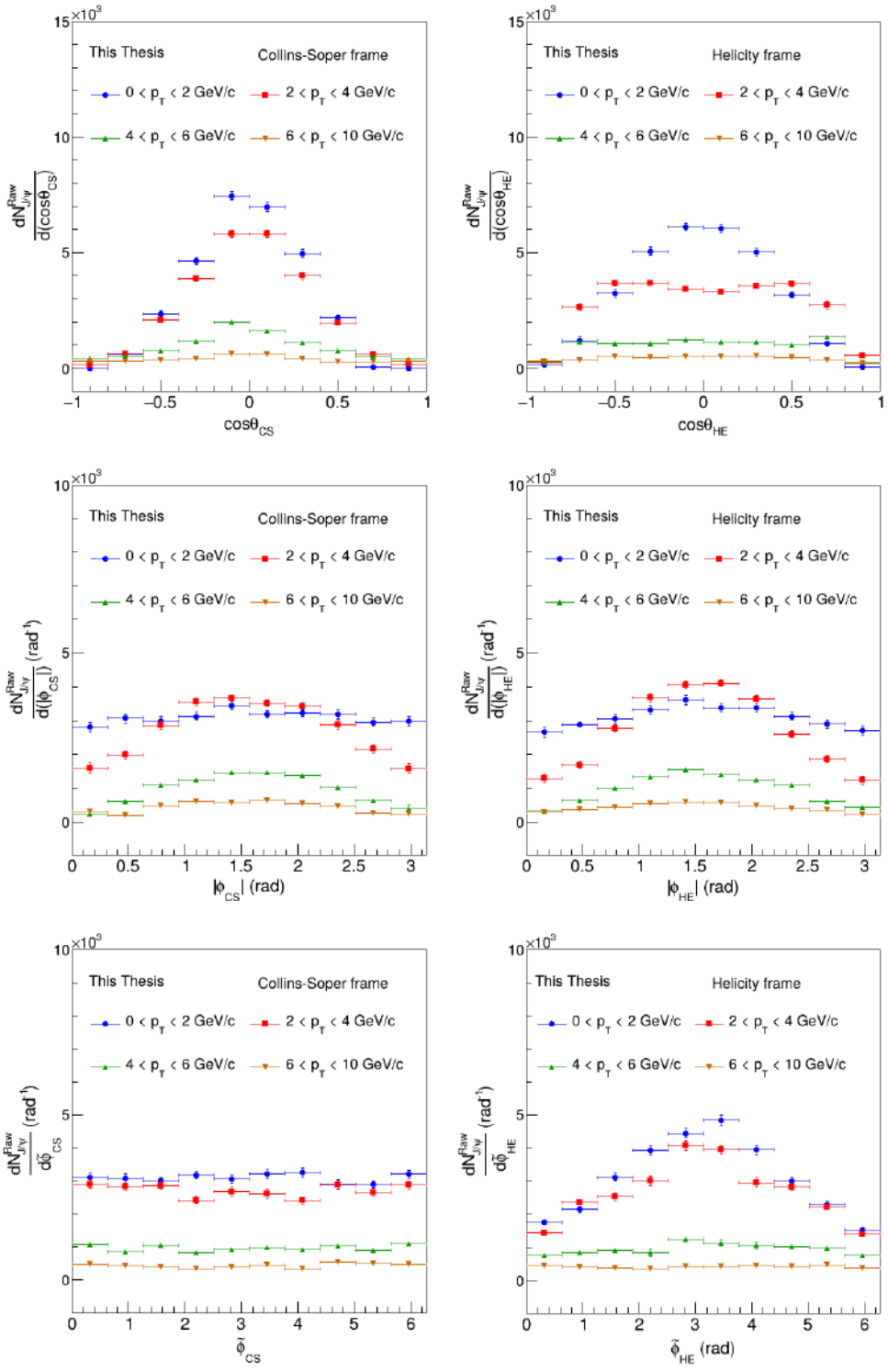



Figure 4.44: Raw angular distribution as a function of cos$\theta$ (top), $\phi$ (middle), and $\tilde{\phi}$ (bottom) in CS (left) and HE (right) for $0 < p_{\mathrm{T}} < 10$ GeV/c [233].

### 4.3.3 A $\times\epsilon$ correction

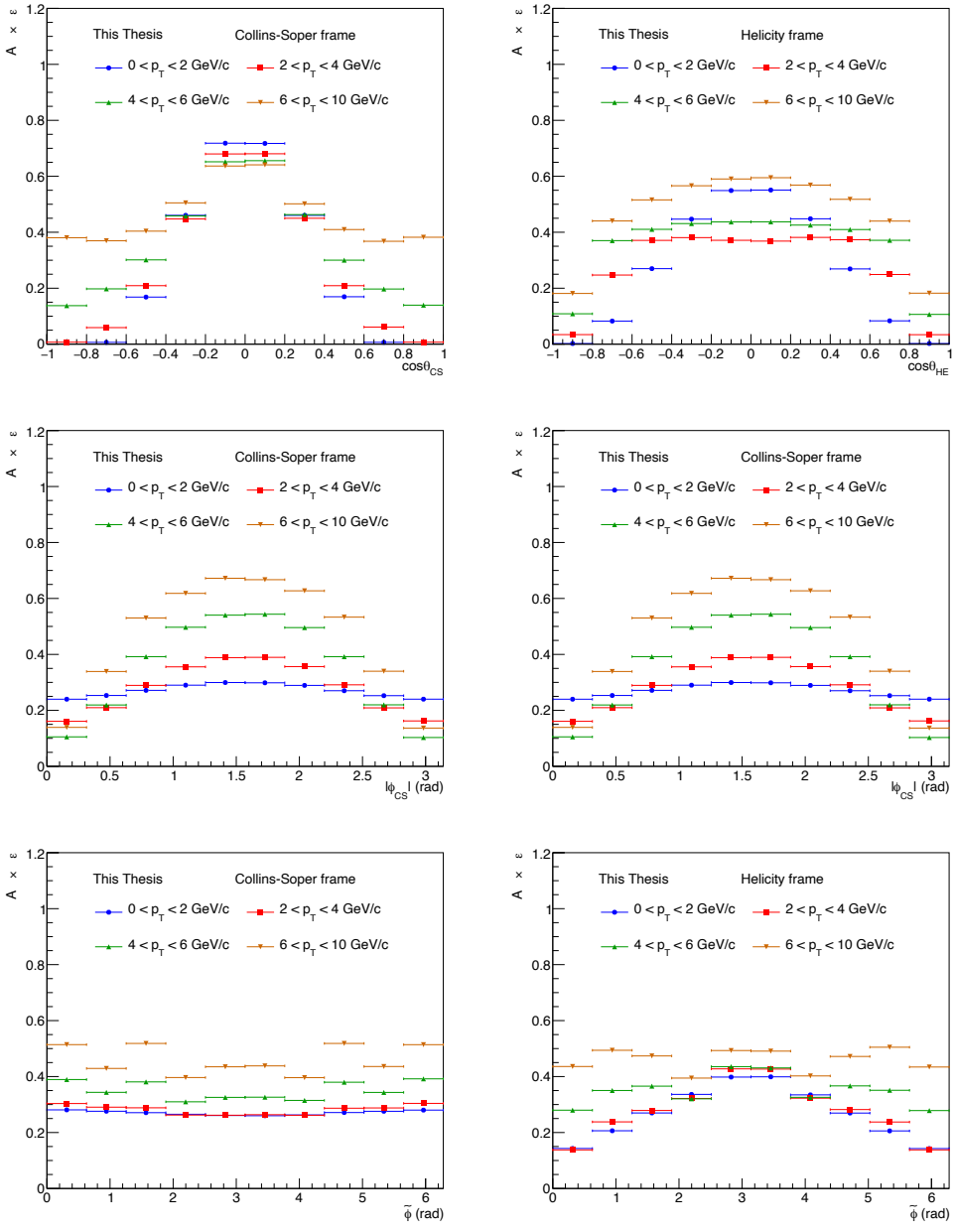



Figure 4.45: Acceptance $\times$ Efficiency (A$\times\epsilon$) as a function of cos$\theta$ (top), $\phi$ (middle), and $\tilde{\phi}$ (bottom) in Collins-Soper (left) and helicity (right) frame for 0 $< p_{\mathrm{T}} <$ 10 GeV/c [233].

Following a similar method as the *pp* analysis, the angular differential acceptance and efficiency are defined as,

$$A \times \epsilon(p_T, cos\theta, \phi) = \frac{N^{rec}_{J/\psi}(p_T, cos\theta, \phi)}{N^{gen}_{J/\psi}(p_T, cos\theta, \phi)} \tag{4.50}$$

Figure 4.45 shows the A×$\epsilon$ distribution as a function of cos$\theta$ (top), $\phi$ (middle), and $\tilde{\phi}$ (bottom) in Collins-Soper (left) and helicity (right) for $0 < p_T < 10$ GeV/c.

### 4.3.4 Polarization parameter extraction

Once the A×$\epsilon$ is obtained from the MC, the raw cos$\theta$ angular distribution is corrected using the following relation;

$$\mathrm{N^{corr}(p_T, cos\theta, \phi)} = \frac{\mathrm{N^{raw}(p_T, cos\theta, \phi)}}{\mathrm{A} \times \epsilon(\mathrm{p_T}, \mathrm{cos\theta}, \phi)} \tag{4.51}$$

Furthermore, a 1D fit to the corrected angular distributions of cos$\theta$, $\phi$, and $\tilde{\phi}$ is performed for each $p_T$ bins using the Eqs. 4.16, 4.17, 4.19 and obtain the polarization parameters $\lambda_\theta$, $\lambda_\phi$, and $\lambda_{\theta\phi}$ as a function of $p_T$. Figure 4.46, and Fig. 4.47 shows the 1D fit to the corrected angular distribution of of cos$\theta$ (top), $\phi$ (middle), and $\tilde{\phi}$ (bottom) to obtain the polarization parameters $\lambda_\theta$, $\lambda_\phi$, and $\lambda_{\theta\phi}$ in the transverse momentum range $0 < p_T < 10$ GeV/c in Collins-Soper and helicity frame, respectively.

### 4.3.5 Systematic uncertanities

The systematic uncertainties in OO collisions are evaluated following the same procedure as in *pp* collisions. However, additional sources of systematic uncertainty are considered in OO collisions, including the choice of the NA60 function for signal fitting and the use of MC-derived tail parameters. Figure 4.48 to Fig. 4.53 shows the systematic variations of $\lambda_\theta$, $\lambda_\phi$, and $\lambda_{\theta\phi}$ parameters due to different trials in 1D fit in Collins-Soper and helicity frame.

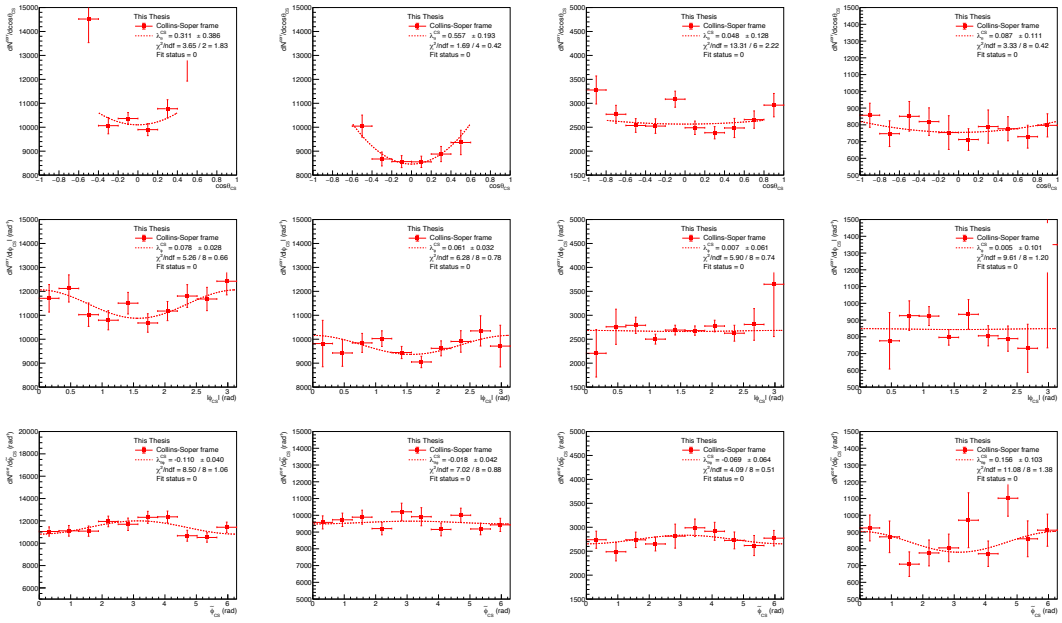


Figure 4.46: $\lambda_\theta$ (top), $\lambda_\phi$ (middle), $\lambda_{\theta\phi}$ (bottom) polarization parameters extraction for $p_{\mathrm{T}}$ bin $0 < p_{\mathrm{T}} < 10$ GeV/c in Collins-Soper frame [233]

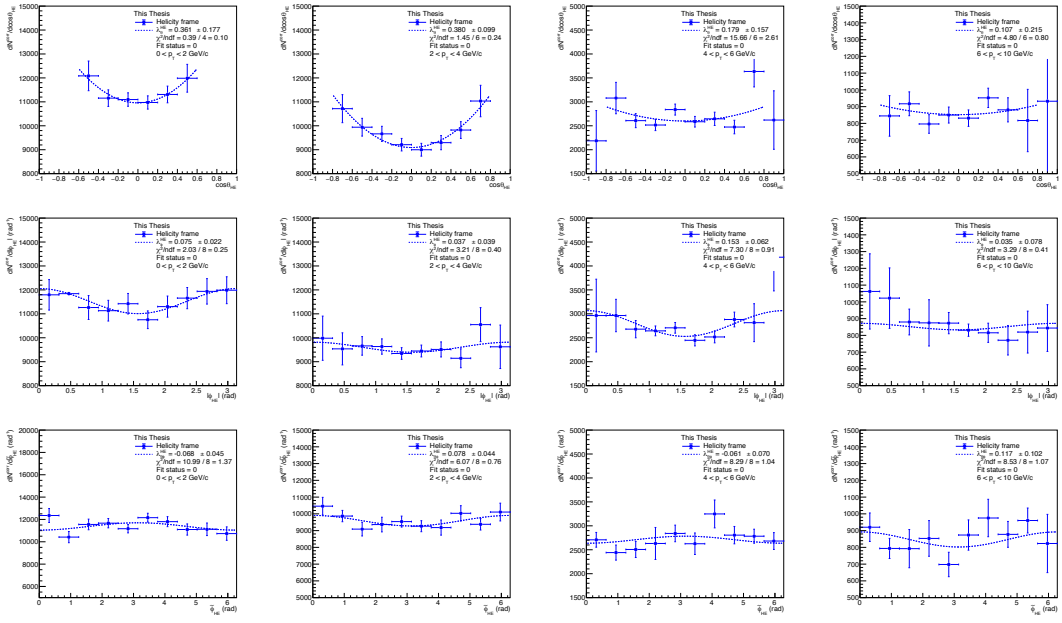


Figure 4.47: $\lambda_\theta$ (top), $\lambda_\phi$ (middle), $\lambda_{\theta\phi}$ (bottom) polarization parameters extraction for $p_{\mathrm{T}}$ bin $0 < p_{\mathrm{T}} < 10$ GeV/c in helicity frame [233].

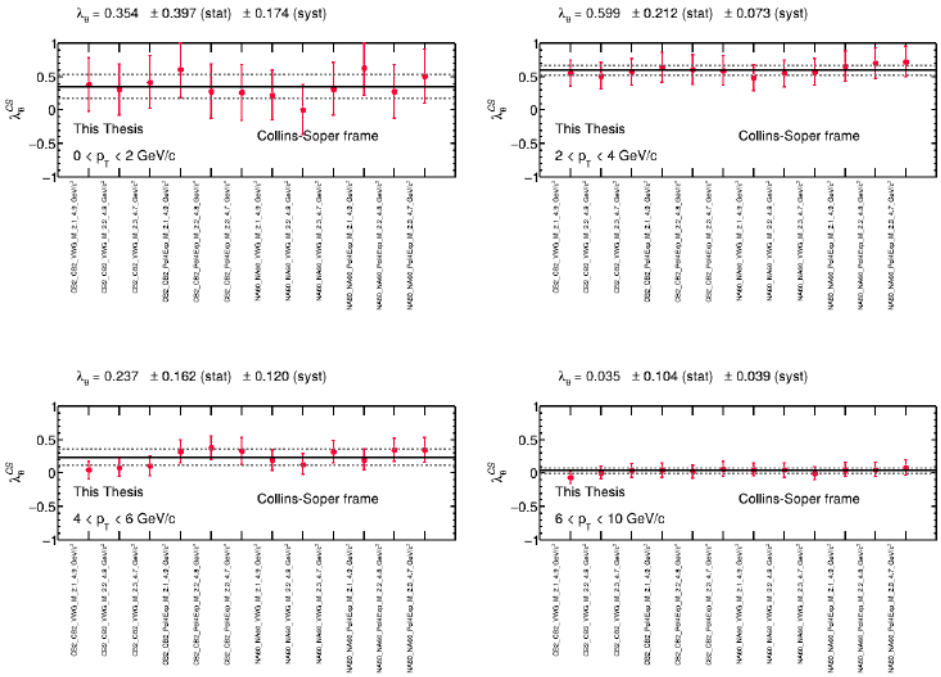



Figure 4.48: Systematic variation of $\lambda_\theta$ due to different trials in CS frame [233].

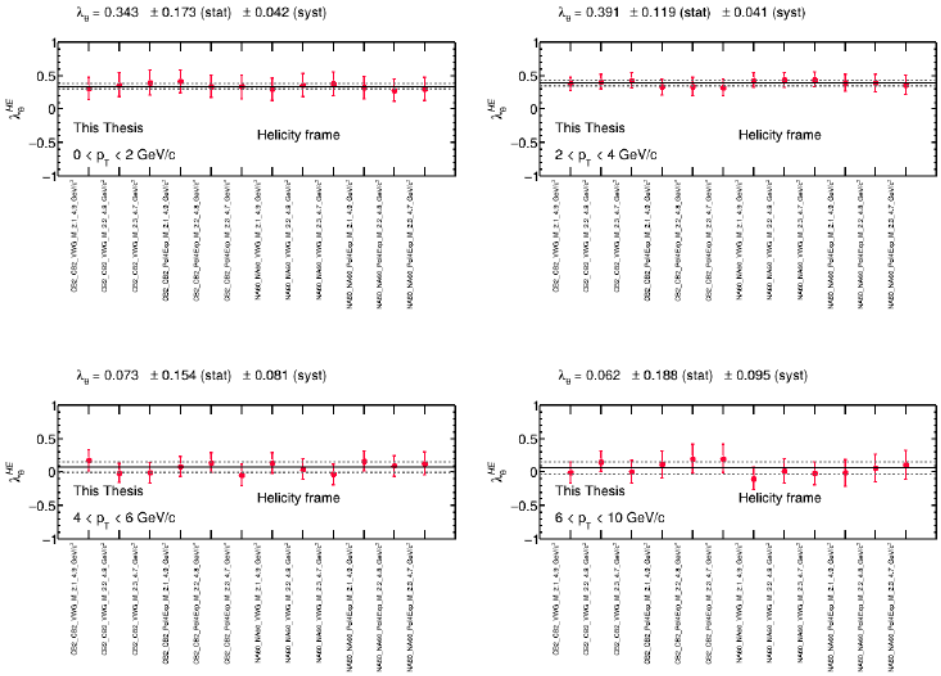



Figure 4.49: Systematic variation of $\lambda_\theta$ due to different trials in helicity [233].

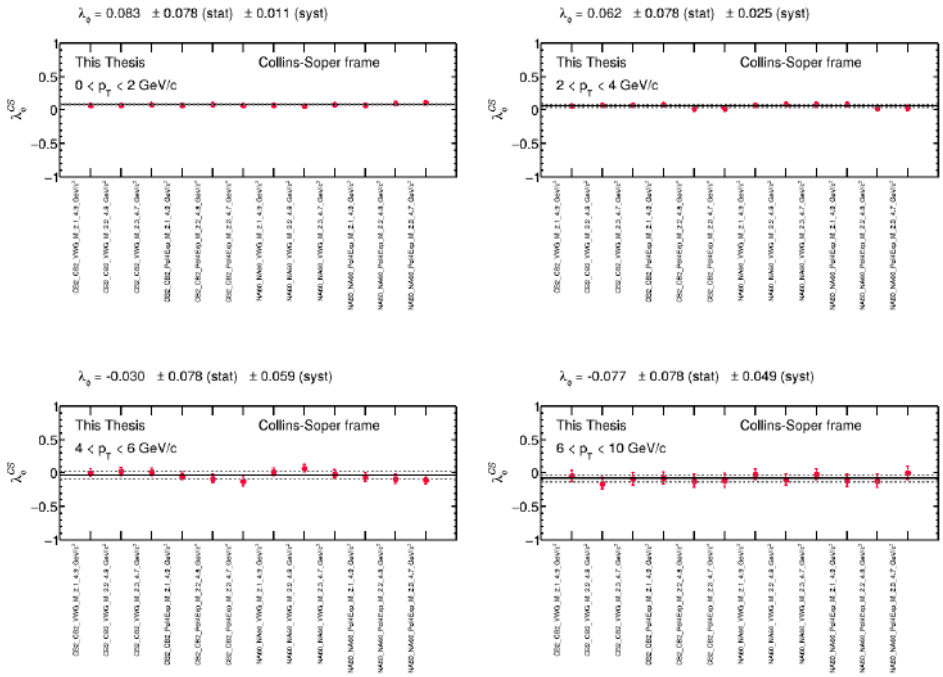



Figure 4.50: Systematic variation of $\lambda_\phi$ due to different trials in CS [233].

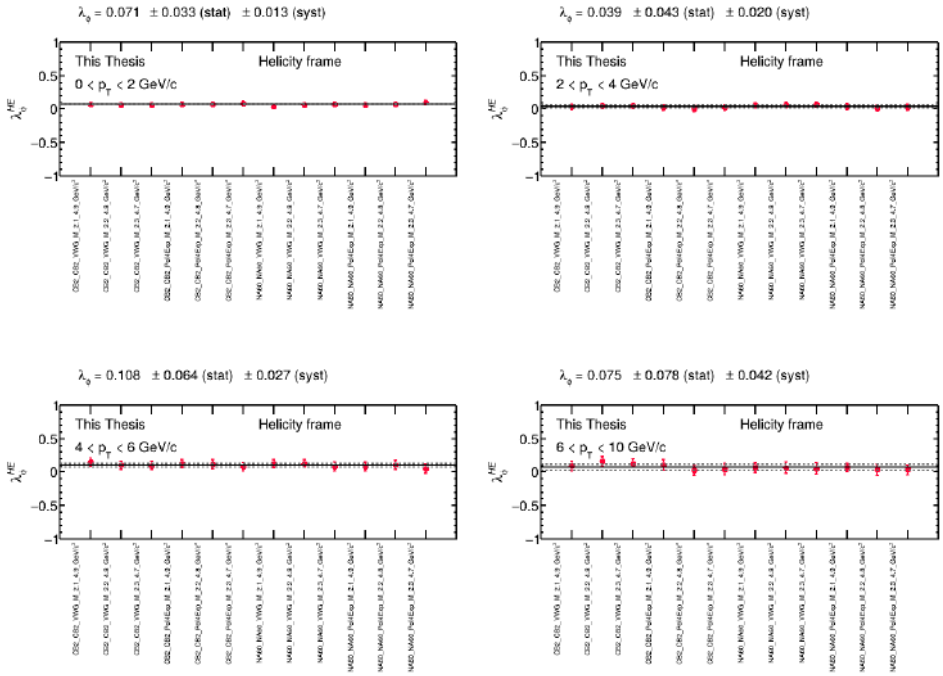



Figure 4.51: Systematic variation of $\lambda_\phi$ due to different trials in helicity [233].

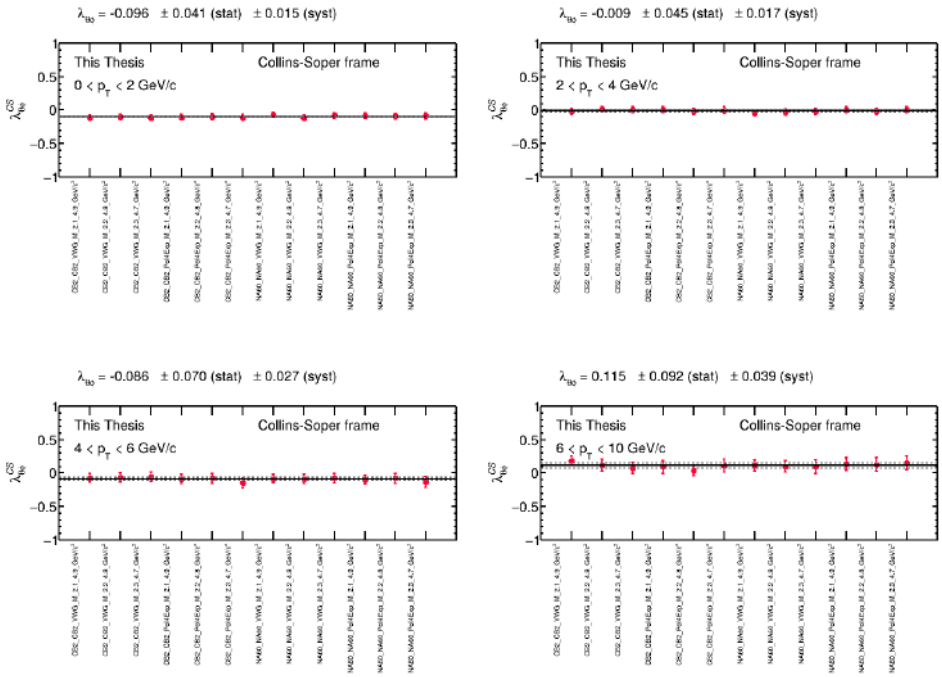



Figure 4.52: Systematic variation of $\lambda_{\theta\phi}$ due to different trials in CS [233].

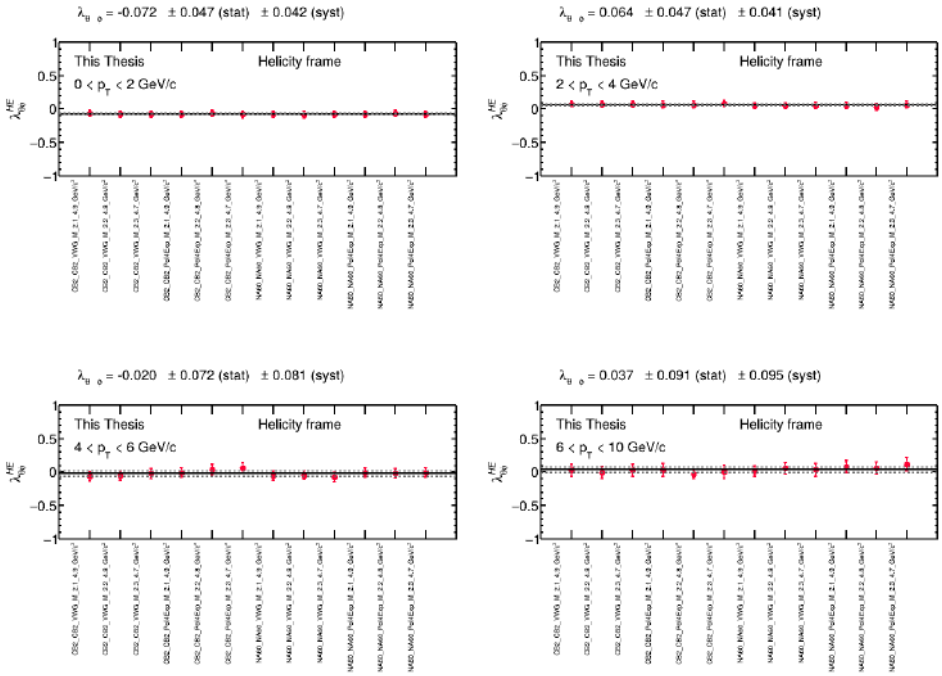



Figure 4.53: Systematic variation of $\lambda_{\theta\phi}$ due to different trials in helicity [233].

#### 4.3.5.1 Systematic uncertainty due to 1D vs 2D fit

Figure 4.54 illustrates the difference in the extracted J/$\psi$ polarization parameters obtained using the 1D-fit and 2D-fit methods. A few examples of the 2D fits in Collins-Soper and helicity are provided in Figs. 4.55 and 4.56. Half of this difference is assigned as a systematic uncertainty and included in the total systematic uncertainty, with the 1D approach retained as the baseline method.

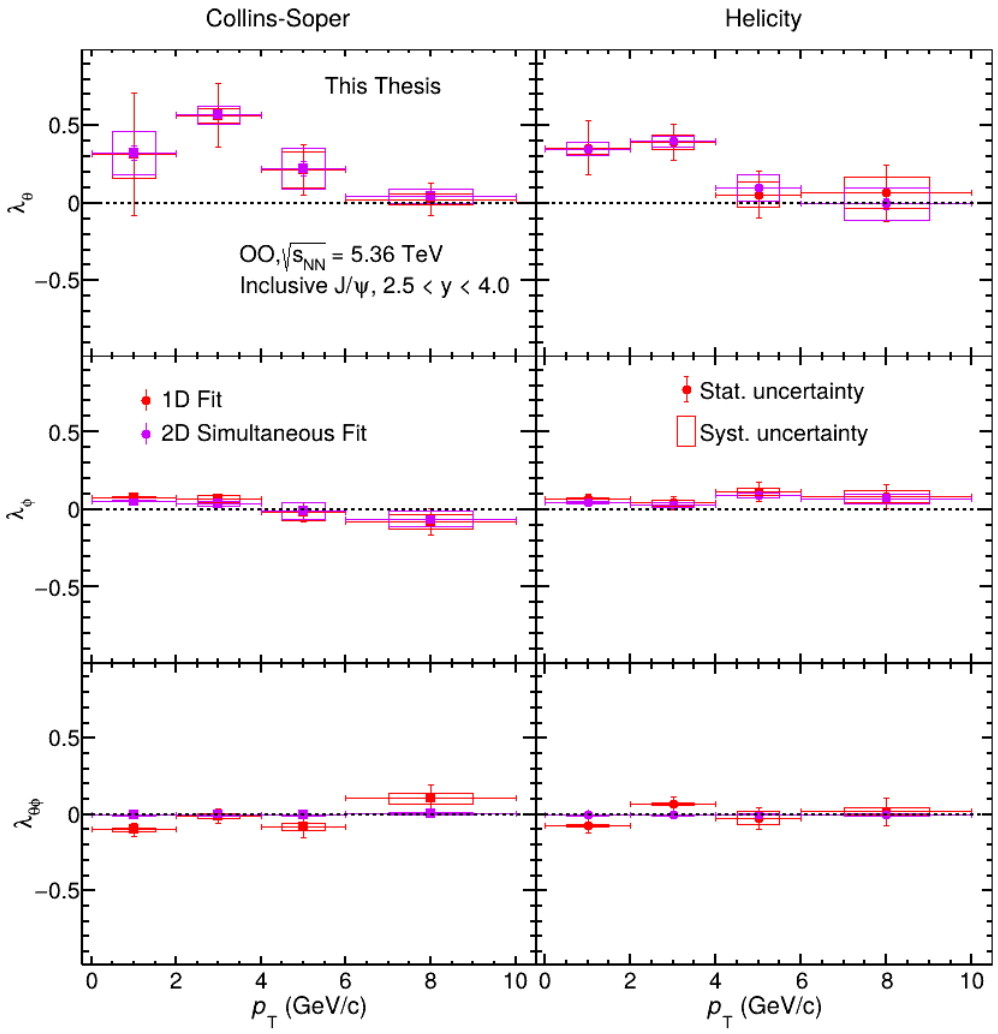



Figure 4.54: Variation in the polarization parameters as a function of transverse momentum due to the 1D vs 2D fit [233].

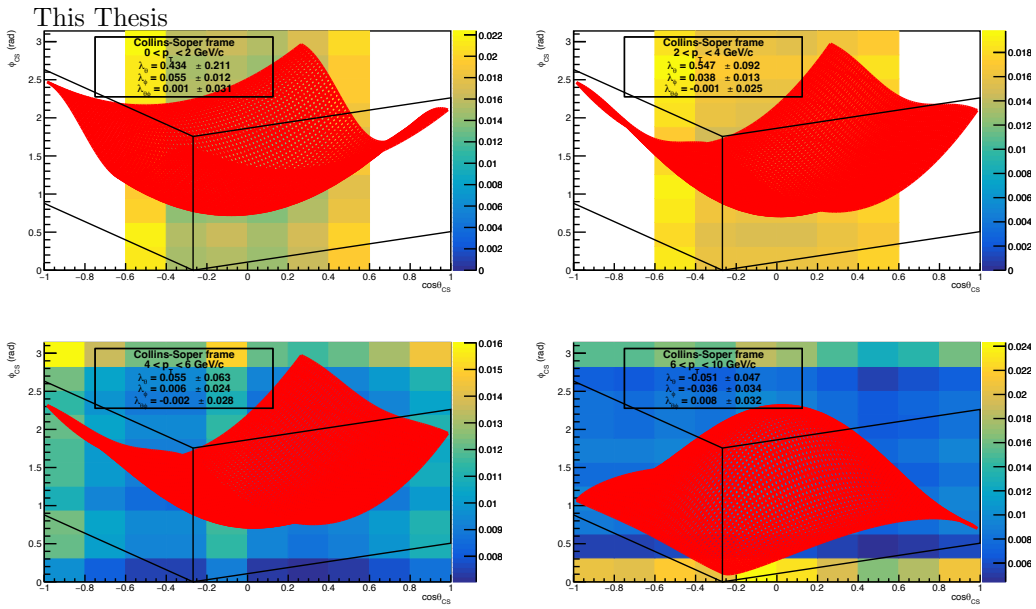



Figure 4.55: 2D-fit of the angular distribution due to CB2+VWG functions in Collins-Soper frame [233].

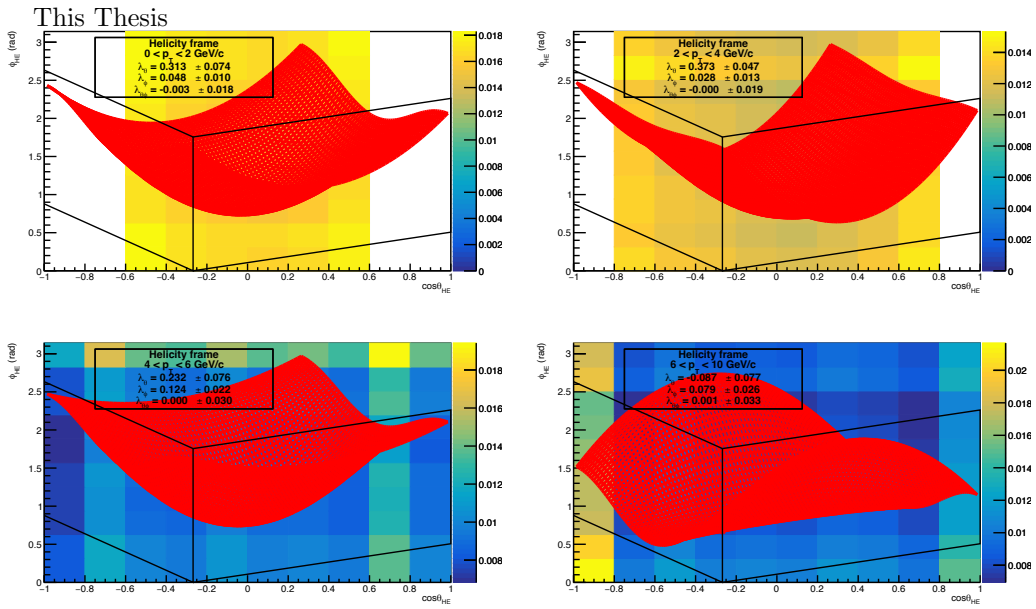



Figure 4.56: 2D-fit of the angular distribution due to CB2+VWG functions in helicity frame [229].

#### 4.3.5.2 Systematic uncertainty due to Data vs MC fit

Figure 4.57 illustrates the difference in the extracted J/$\psi$ polarization parameters obtained using data-driven and MC tail parameters. Half of this difference is assigned as a systematic uncertainty and included in the total systematic uncertainty.

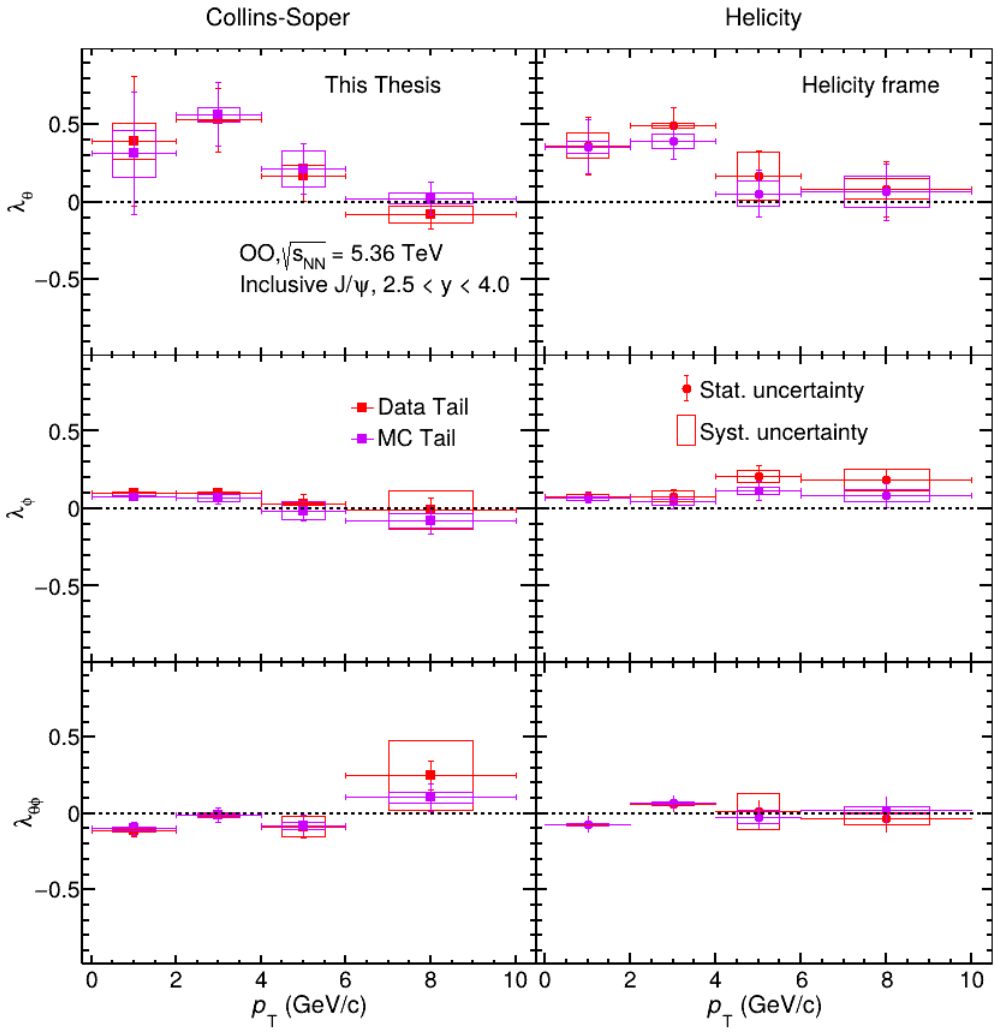



Figure 4.57: Variation in the polarization parameters as a function of transverse momentum due to the data-driven tail parameter vs MC tail parameter [233].

### 4.3.6 Summary of systematic uncertainties

The summary of the systematic uncertainties in Collins-Soper and helicity frames is reported in the following Tables 4.10 and Tables 4.11, respectively.

Table 4.10: Summary of systematic uncertainties on $\lambda_\theta$ for Collins-Soper frame.

| $p_T$ (GeV/$c$) | Total Syst. | Sig. Extr. | 1D vs 2D | Data vs MC Tail | cos$\theta$ Fit Range | Input Shape |
|---|---|---|---|---|---|---|
| 0–2 | 0.157 | 0.152 | 0.007 | 0.040 | 0.0 | 0.002 |
| 2–4 | 0.240 | 0.045 | 0.001 | 0.018 | 0.233 | 0.024 |
| 4–6 | 0.123 | 0.105 | 0.004 | 0.022 | 0.0 | 0.015 |
| 6–10 | 0.070 | 0.036 | 0.011 | 0.051 | 0.0 | 0.027 |

Table 4.11: Summary of systematic uncertainties on $\lambda_\theta$ for helicity frame.

| $p_T$ (GeV/$c$) | Total Syst. | Sig. Extr. | 1D vs 2D | Data vs MC Tail | cos$\theta$ fit Range | Input Shape |
|---|---|---|---|---|---|---|
| 0–2 | 0.0624 | 0.037 | 0.004 | 0.003 | 0.0 | 0.050 |
| 2–4 | 0.093 | 0.045 | 0.003 | 0.05 | 0.037 | 0.052 |
| 4–6 | 0.108 | 0.079 | 0.022 | 0.06 | 0.0 | 0.038 |
| 6–10 | 0.108 | 0.101 | 0.035 | 0.01 | 0.0 | 0.003 |

Table 4.12: $\lambda_\theta$, $\lambda_\phi$, and $\lambda_{\theta\phi}$ as a function of $p_T$ in the Collins–Soper frame. Uncertainties are quoted as statistical and systematic, respectively.

| $p_T$ (GeV/$c$) | $\lambda_\theta$ | $\lambda_\phi$ | $\lambda_{\theta\phi}$ |
|---|---|---|---|
| 0–2 | $0.314 \pm 0.396 \pm 0.157$ | $0.079 \pm 0.029 \pm 0.016$ | $-0.100 \pm 0.041 \pm 0.054$ |
| 2–4 | $0.567 \pm 0.207 \pm 0.240$ | $0.065 \pm 0.034 \pm 0.032$ | $-0.010 \pm 0.044 \pm 0.018$ |
| 4–6 | $0.216 \pm 0.161 \pm 0.123$ | $-0.014 \pm 0.062 \pm 0.059$ | $-0.081 \pm 0.069 \pm 0.049$ |
| 6–10 | $0.025 \pm 0.102 \pm 0.070$ | $-0.078 \pm 0.087 \pm 0.056$ | $0.105 \pm 0.089 \pm 0.133$ |

Table 4.13: $\lambda_\theta$, $\lambda_\phi$, and $\lambda_{\theta\phi}$ as a function of $p_T$ in the helicity frame. Uncertainties are quoted as statistical and systematic, respectively.

| $p_T$ (GeV/$c$) | $\lambda_\theta$ | $\lambda_\phi$ | $\lambda_{\theta\phi}$ |
|---|---|---|---|
| 0–2 | $0.356 \pm 0.174 \pm 0.062$ | $0.068 \pm 0.032 \pm 0.017$ | $-0.073 \pm 0.047 \pm 0.051$ |
| 2–4 | $0.394 \pm 0.115 \pm 0.092$ | $0.043 \pm 0.042 \pm 0.038$ | $0.067 \pm 0.047 \pm 0.046$ |
| 4–6 | $0.055 \pm 0.152 \pm 0.108$ | $0.115 \pm 0.063 \pm 0.058$ | $-0.024 \pm 0.072 \pm 0.049$ |
| 6–10 | $0.065 \pm 0.181 \pm 0.108$ | $0.084 \pm 0.079 \pm 0.065$ | $0.020 \pm 0.089 \pm 0.038$ |

### 4.3.7 Results

Figure 4.58 presents the first measurement of inclusive J/$\psi$ polarization in OO collisions at $\sqrt{s_{\rm NN}} = 5.36$ TeV in the Collins–Soper and helicity frames at forward rapidity. The $\lambda_\phi$ and $\lambda_{\theta\phi}$ parameters are consistent with zero within 1 $\sigma$, while $\lambda_\theta$ deviates from zero by up to 2.6 $\sigma$ (CS) and 1.8 $\sigma$ (HE) for $2 < p_{\rm T} < 4$ GeV/$c$.

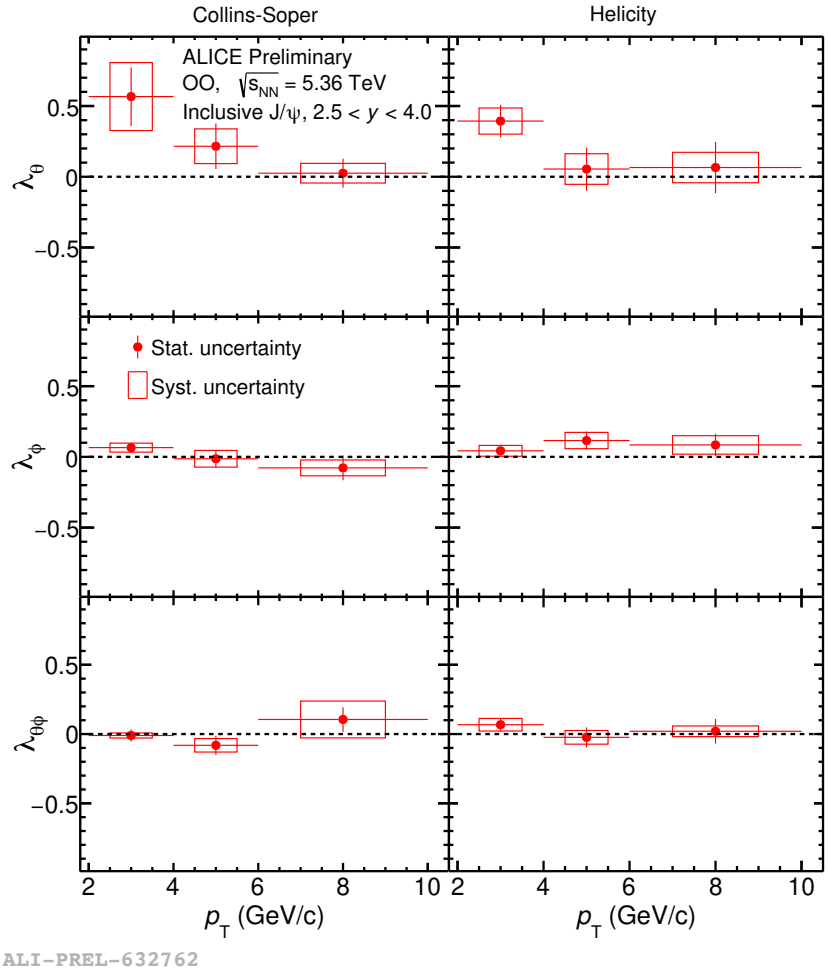



Figure 4.58: Inclusive J/$\psi$ polarization parameters as a function of transverse momentum for OO collisions at $\sqrt{s_{\rm NN}} = 5.36$ TeV in Collins-Soper and helicity frame [233].

### 4.3.8 Comparison with Pb–Pb measurements at 5.02 TeV

Figure 4.59 presents a comparison between the measured inclusive J/$\psi$ polarization parameters in OO collisions and the corresponding measurements in Pb–Pb collisions at $\sqrt{s_{\rm NN}}$ = 5.02 TeV. The $\lambda_\phi$ and $\lambda_{\theta\phi}$ are qualitatively consistent between the two measurements within uncertainties, while $\lambda_\theta$ exhibits a system-size dependence. Further theoretical studies are needed to understand this difference.

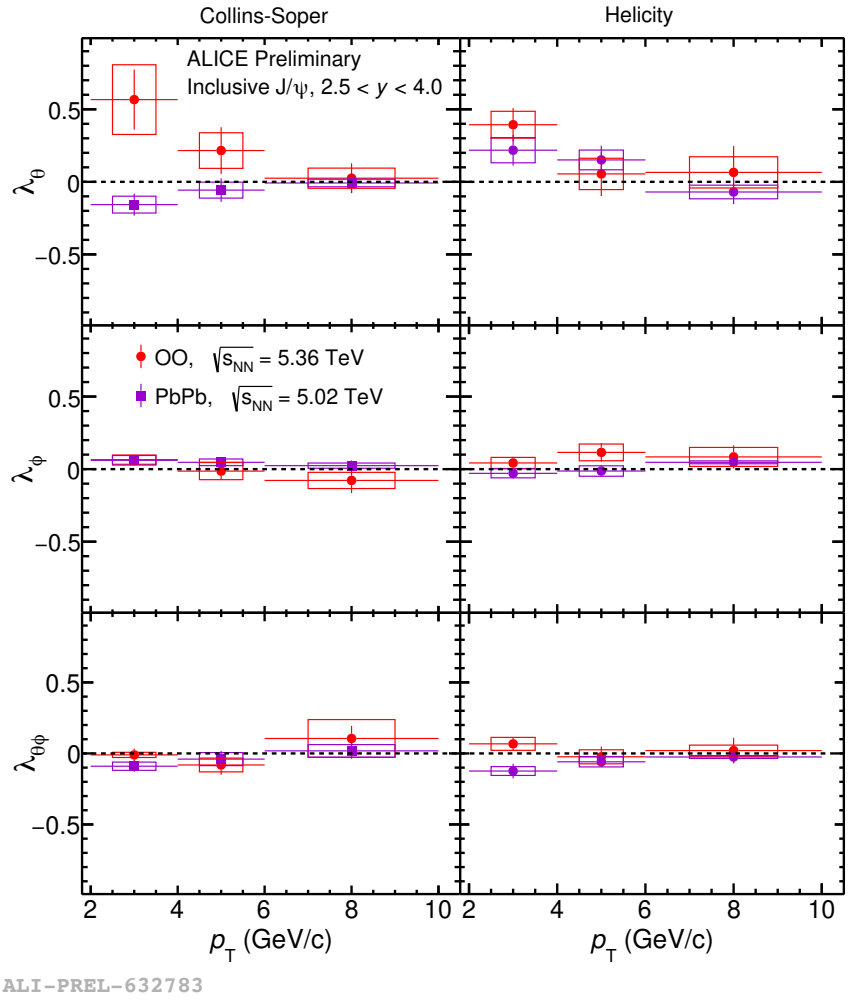



Figure 4.59: Comparison of inclusive J/$\psi$ polarization parameters in OO collisions at $\sqrt{s_{\rm NN}}$ = 5.36 TeV with Pb–Pb collisions at $\sqrt{s_{\rm NN}}$ = 5.02 TeV [233].

### 4.3.9 Comparison with theoretical models

Figure 4.60 compares the measured J/$\psi$ polarization parameters as a function of $p_{\mathrm{T}}$ in OO collisions with predictions from various NRQCD calculations.

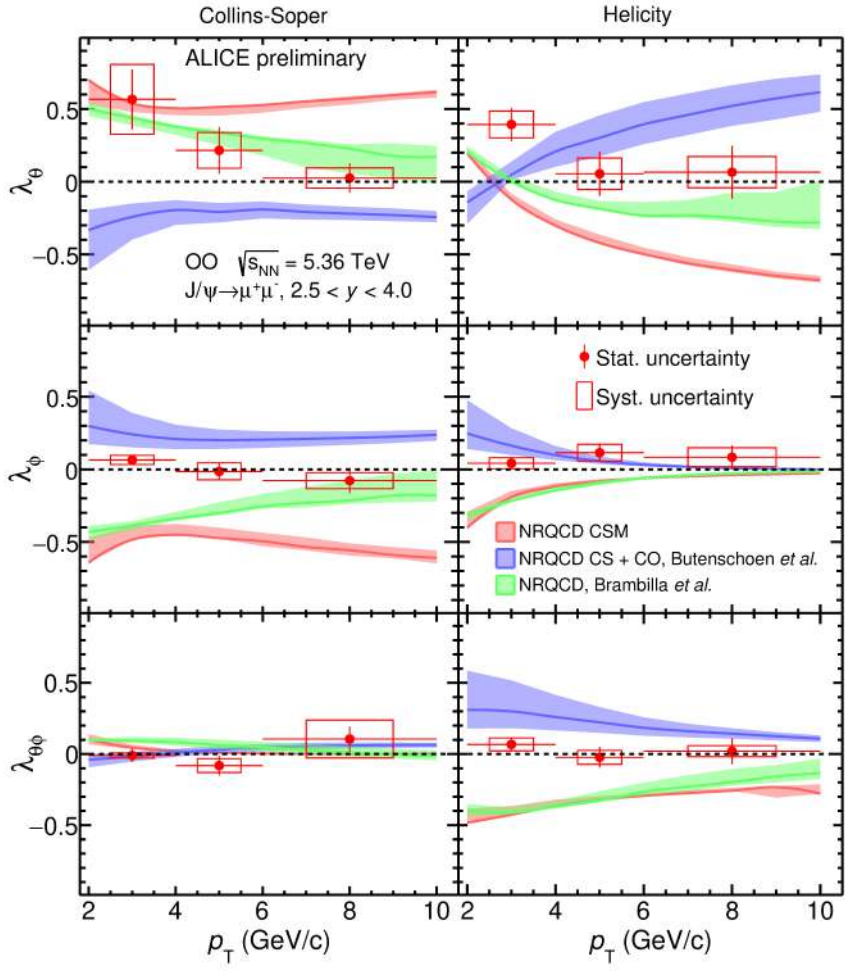



Figure 4.60: Comparison of inclusive J/$\psi$ polarization parameters in OO collisions at $\sqrt{s_{\mathrm{NN}}} = 5.36$ TeV with different NRQCD model predictions [233].

The calculations were performed for OO collisions at $\sqrt{s_{\mathrm{NN}}} = 5.36$ TeV in the forward-rapidity interval $2.5 < y < 4.0$, using the nCTEQ nuclear parton distribution function to account for nuclear modifications of the partonic structure.

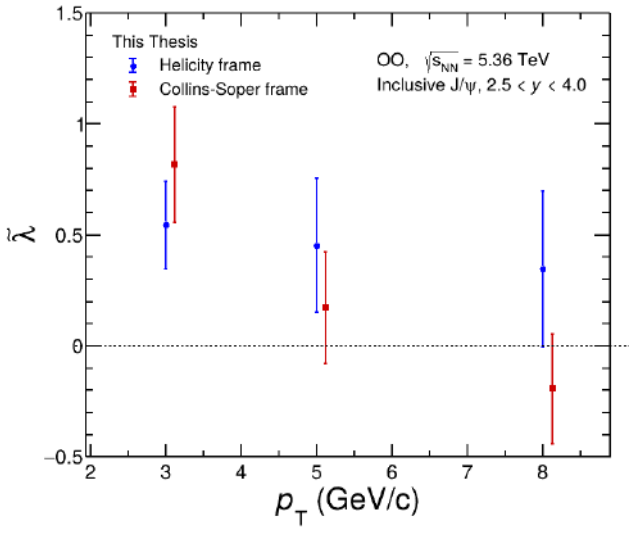



Figure 4.61: Frame invariant parameter $\tilde{\lambda}$ as a function of $p_{\mathrm{T}}$ in Collins-Soper and helicity frame. The error bars include the contributions of the systematic and statistical uncertainties [233].

Specifically, the nCTEQ15HQ_FullNuc_16_8 set was used, corresponding to an oxygen nucleus with mass number $A = 16$ and atomic number $Z = 8$. All medium effects, at least for unpolarized quarkonium production, are effectively reproduced by these nuclear PDF sets, as the cold nuclear matter effects are included in the model. It is important to note that the NRQCD calculations considered for OO collisions do not include QGP medium effects. Consequently, the observed differences between the experimental data and the model predictions could potentially be attributed, at least in part, to modifications of the J/$\psi$ polarization induced by the QGP medium.

To verify the consistency of the results obtained in the Collins–Soper and helicity frames, the frame-invariant parameter defined in Eq. 4.26 is presented in Fig. 4.61. The measurements from the two reference frames are found to be qualitatively consistent within the uncertainties, which include both statistical and systematic contributions. This observed agreement suggests the absence of significant biases

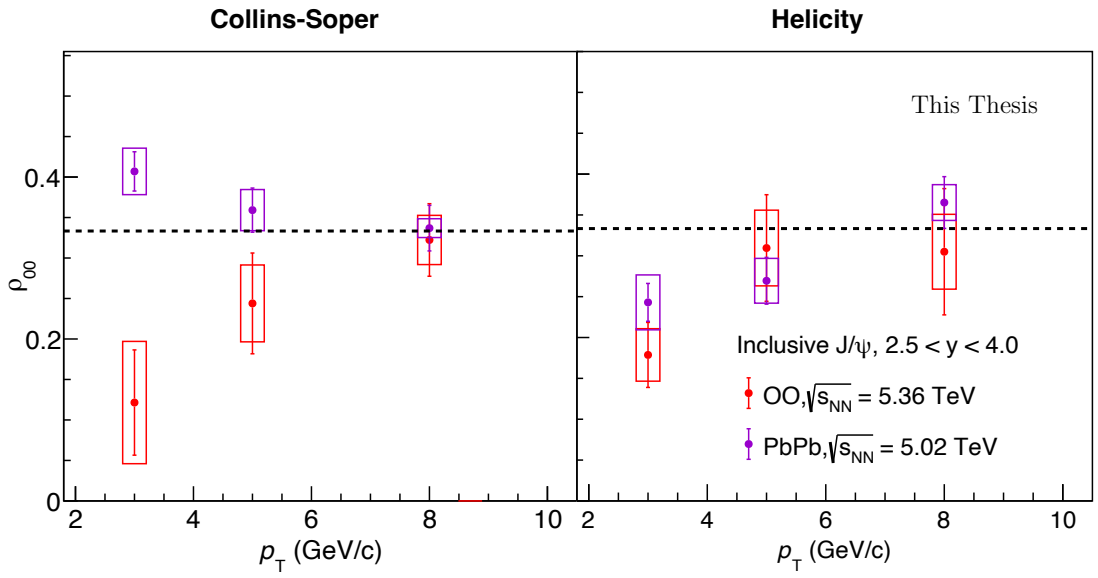



Figure 4.62: The comparison of $00^{\text{th}}$ elements of the spin density matrix, $\rho_{00}$ obtained from $\lambda_\theta$ parameter for OO and Pb-Pb collisions

.

in the analysis, considering that some uncertainty sources may be correlated between the Collins–Soper and helicity frames.

On the other hand, as discussed in the beginning of this chapter, the $\lambda$ polarization parameters, which quantify the anisotropy of the decay distribution, can be directly related to the elements of the spin density matrix $\rho$. The parameter $\rho_{00}$, which quantifies the probability of the vector meson being in a spin-zero projection along the quantization axis, is connected to the polar anisotropy parameter $\lambda_\theta$ by the relation,

$$\rho_{00} = \frac{1 - \lambda_\theta}{3 + \lambda_\theta} \tag{4.52}$$

Figure 4.62 shows the comparison of $\rho_{00}$ obtained from $\lambda_\theta$ parameter for OO collisions at $\sqrt{s_{\text{NN}}} = 5.36$ TeV and Pb-Pb at $\sqrt{s_{\text{NN}}} = 5.02$ TeV collisions. The devi-

ation of $\rho_{00}$ from the baseline value $\frac{1}{3}$ indicates the presence of a spin-alignment feature in light-ion and nuclear collisions at low $p_{\mathrm{T}}$.

### 4.3.10 Experimental challenges in quarkonia polarization

The experimental measurement of quarkonium polarization through the angular distribution of its decay products is highly challenging for several reasons:

- Such measurements require a high-statistics data sample because the extraction of polarization parameters involves a multi-differential analysis in several kinematic variables.
- The signal is contaminated by combinatorial backgrounds, making an accurate signal extraction essential to avoid biases in the measured angular distributions.
- A precise determination of the polarization parameters requires an accurate correction for detector acceptance and reconstruction efficiency, as well as the subtraction of kinematic correlations introduced by the detector response.
- Feed-down contributions from higher quarkonium states, such as $\chi_c$, $\chi_b$, and excited $\psi$ or $\Upsilon$ states, can modify the observed polarization of the inclusive quarkonium sample and complicate its interpretation.
- The measured polarization depends on the choice of polarization frame. Therefore, measurements in multiple reference frames and frame-invariant quantities are necessary to validate the results.
- The limited statistical precision, particularly in narrow intervals of charged-particle multiplicity and rapidity, makes it difficult to measure the dependence of the polarization parameters on these variables.

# Chapter 5

## J/$\psi$ and $\psi(2S)$ polarization in proton-proton collisions from Monte Carlo Simulation

Based on:

1. "Polarization measurement of $J/\psi$ and $\psi(2S)$ in proton+proton collisions at the LHC energies using PYTHIA8", **B. Sahoo**, D. Sahu, S. Deb, C. R. Singh and R. Sahoo, Phys. Rev. C **109**, 034910 (2024).

---

This chapter presents a Monte Carlo study of spin polarization of $J/\psi$ and $\psi$(2S) in proton-proton collisions. Unlike the standard analysis procedure discussed previously in Chapter 4, an alternative approach based on the averaged dimuon angular distribution is adopted. The polarization parameters $\lambda_\theta$, $\lambda_\phi$ and $\lambda_{\theta\phi}$ are then extracted using Eq. (5.1), Eq. (5.2), and Eq. (5.3), respectively. This method provides an alternative to the conventional extraction of polarization parameters through a single or multi-parameter fit of Eq. (4.15) to the dimuon angular distribution. The relevant averaged angular distributions are given by;

$$\langle \cos^2\theta \rangle = \frac{1+\frac{3}{5}\lambda_\theta}{3+\lambda_\theta} \tag{5.1}$$

$$\langle \cos 2\phi \rangle = \frac{\lambda_\phi}{3+\lambda_\theta} \tag{5.2}$$

$$\langle \sin 2\theta \cos\phi \rangle = \frac{4}{5}\frac{\lambda_{\theta\phi}}{3+\lambda_\theta} \tag{5.3}$$

The upper and lower panel of Fig. 5.1 shows the polar and azimuthal angu-

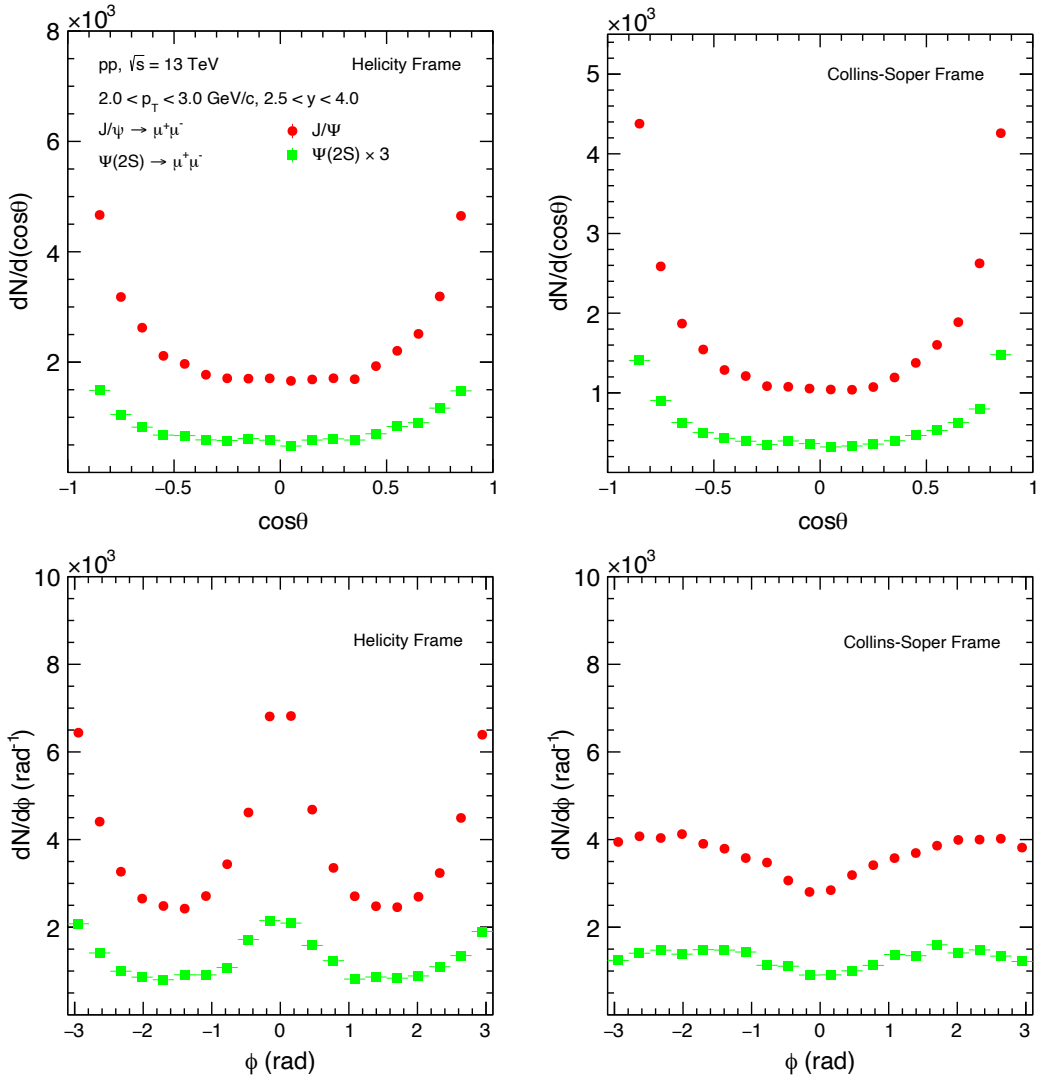



Figure 5.1: The cosine of the polar angle (upper panel) and the azimuthal angle (lower panel) distribution in $pp$ collisions for $J/\psi$ and $\psi$(2S) at $\sqrt{s} = 13$ TeV in helicity (left panel) and Collins-Soper (right panel) reference frame [157].

lar distributions of dimuons (corresponding to $J/\psi$ and $\psi$(2S)) obtained from the PYTHIA8 simulation of $pp$ collisions at $\sqrt{s} = 13$ TeV in helicity (left) and Collins-Soper (right) frames, respectively. In this study, PYTHIA version 8.303 is used. For simplicity, it is referred to as PYTHIA 8 throughout the following text

and figures. These distributions are evaluated in the range $2.0 < p_{\mathrm{T}} < 3.0$ GeV/c and $2.5 < y < 4.0$. The observed anisotropy in the angular distribution shown in Fig. 5.1, for both reference frames, motivates the extraction of the anisotropy parameters $\lambda_\theta$, $\lambda_\phi$, and $\lambda_{\theta\phi}$. This anisotropic behavior in PYTHIA8 simulations may arise, among other factors, from the inclusion of multiple scattering effects built into the model. Furthermore, this chapter primarily focuses on the dependence of the polarization parameters ($\lambda_\theta$, $\lambda_\phi$, and $\lambda_{\theta\phi}$) on transverse momentum, charged-particle multiplicity, and rapidity, which are discussed in Sections 5.1, 5.2, and 5.3, respectively.

## 5.1 $p_{\mathrm{T}}$ dependence of $\lambda_\theta$, $\lambda_\phi$, and $\lambda_{\theta\phi}$

The $p_{\mathrm{T}}$ dependence of the polarization parameters of $J/\psi$ and $\psi(2S)$ is studied in $pp$ collisions using PYTHIA8. The results at $\sqrt{s} = 7, 8$, and 13 TeV, obtained in the helicity and Collins–Soper frames, are shown in Fig. 5.2. The PYTHIA8 results for $J/\psi$ are compared with experimental measurements from LHCb at $\sqrt{s}$ = 7 TeV [48] and ALICE at $\sqrt{s} = 7$ and 8 TeV [45, 53], as well as with NRQCD predictions (CS and CS+CO with NLO corrections) [93]. The analysis uses a $p_{\mathrm{T}}$ range and a dimuon rapidity interval $2.5 < y < 4.0$ consistent with ALICE measurements. From Fig. 5.2, $\lambda_\theta$ indicates longitudinal polarization at low-$p_{\mathrm{T}}$ and transverse polarization at high-$p_{\mathrm{T}}$ in both frames for $J/\psi$ and $\psi(2S)$. This trend is consistent with ALICE measurements at $\sqrt{s} = 7$ TeV in the helicity frame [53]. A decrease in longitudinal polarization with increasing $p_{\mathrm{T}}$ is observed. Similar low-$p_{\mathrm{T}}$ longitudinal behavior in the Collins–Soper frame is reported by HERA-B [42], while LO NRQCD calculations predict strong transverse polarization at high-$p_{\mathrm{T}}$ [74, 75, 77, 78]. At low-$p_{\mathrm{T}}$, $\psi(2S)$ exhibits weaker longitudinal polarization than $J/\psi$, while its polarization increases at higher $p_{\mathrm{T}}$. This behavior may be attributed to the more favorable formation of $J/\psi$ from $c\bar{c}$ pairs at low-$p_{\mathrm{T}}$, leading to a reduced $\psi(2S)$ yield and consequently affecting its polarization. No

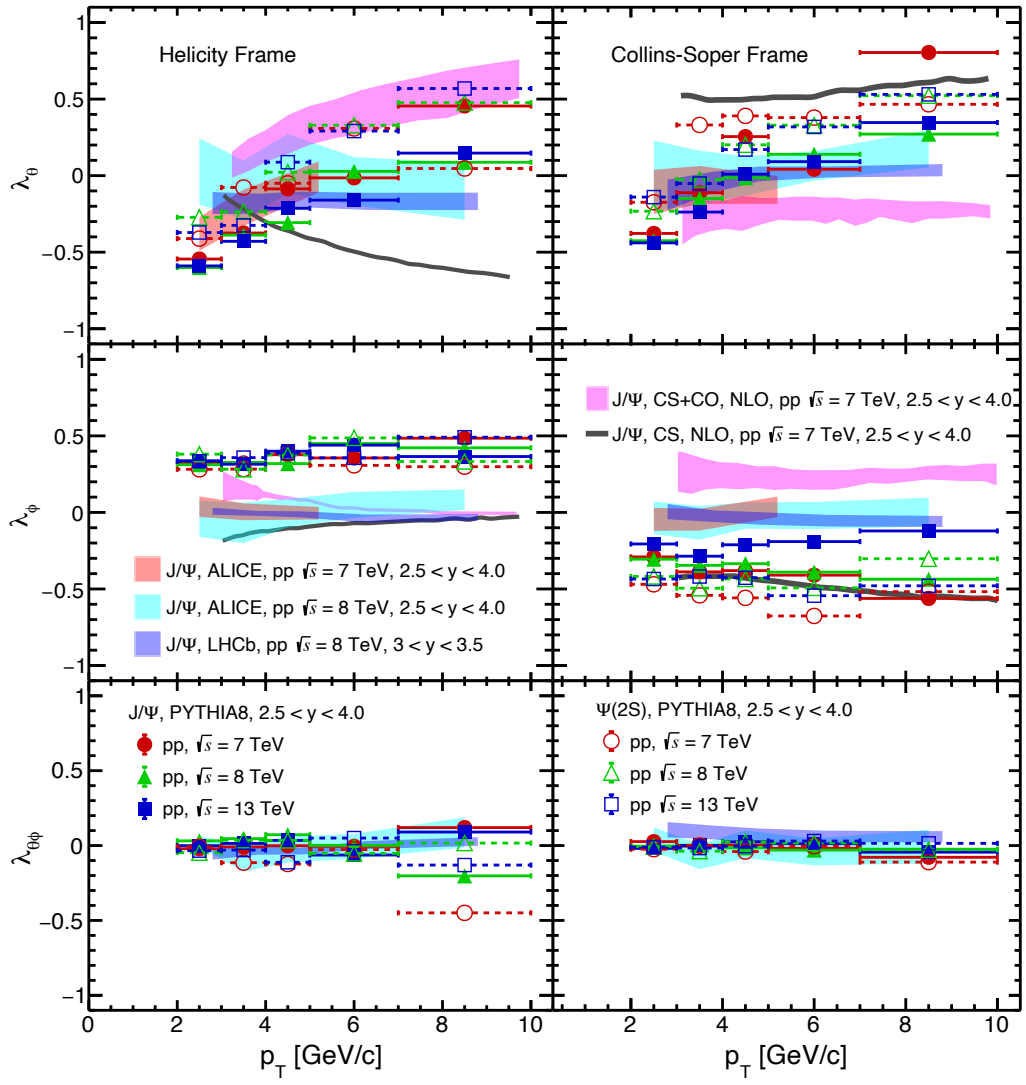



Figure 5.2: The $J/\psi$ and $\psi$(2S) polarization parameters as a function of transverse momentum for $pp$ collisions at $\sqrt{s}$ = 7, 8, and 13 TeV using PYTHIA8. The obtained results are compared with the $J/\psi$ polarization measurement in $pp$ collisions from ALICE at $\sqrt{s}$ = 7, 8 TeV, LHCb at $\sqrt{s}$ = 7 TeV, and the NLO-NRQCD model predictions in color singlet (CS) and color singlet + color octet (CS+CO) states at $\sqrt{s} = 7$ TeV in both helicity and Collins-Soper reference frames [157].

significant dependence on the center-of-mass energy is observed for quarkonium polarization in PYTHIA8 in either reference frame. The parameter $\lambda_\phi$ indicates transverse polarization in the helicity frame and longitudinal polarization in the Collins–Soper frame, reflecting differences in the azimuthal angular distributions. Non-zero values of $\lambda_\theta$ and $\lambda_\phi$ imply unequal populations of spin states, resulting in anisotropic decay distributions. PYTHIA8 tends to predict larger $\lambda_\phi$ values compared to experimental data. In contrast, $\lambda_{\theta\phi}$ remains close to zero for both $J/\psi$ and $\psi(2S)$, consistent with LHC observations shown in Fig. 5.2.

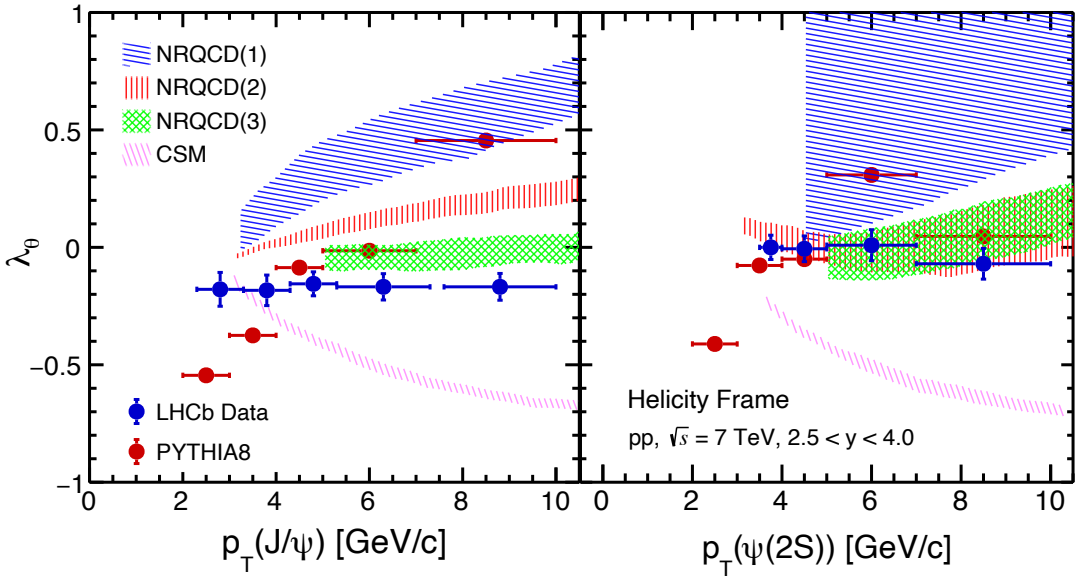



Figure 5.3: Polarization of $J/\psi$ (left) and $\psi$(2S) (right) as a function of transverse momentum obtained from PYTHIA8 compared with the LHCb experimental data in $pp$ collisions at $\sqrt{s} = 7$ TeV in the rapidity interval $2.5 < y < 4.0$ in the helicity frame. The MC simulation results are compared with NLO CSM from [93] and NLO NRQCD calculation from (1) [93], (2) [97], and (3) [94, 98] [157].

Figure 5.3 presents the rapidity-integrated ($2.5 < y < 4.0$) $p_{\mathrm{T}}$ dependence of the angular parameter $\lambda_\theta$ for $J/\psi$ and $\psi(2S)$ in the helicity frame, compared with NLO CSM and various NLO NRQCD calculations [93, 94, 97, 98]. The CSM

predictions show clear disagreement with both experimental data and PYTHIA8 results for $J/\psi$ and $\psi(2S)$. For $J/\psi$, NRQCD calculations [94, 98] provide qualitative agreement with data, while the increasing trend of $\lambda_\theta$ with $p_{\mathrm{T}}$ from PYTHIA8 is partially consistent with NRQCD predictions [93, 97]. For $\psi(2S)$, both LHCb data and PYTHIA8 favor NRQCD results from Refs. [94, 98] and [97] at low-$p_{\mathrm{T}}$. The observed differences between $J/\psi$ and $\psi(2S)$ polarization in PYTHIA8 may arise from their mass difference. Additionally, experimental $J/\psi$ polarization includes contributions from feed-down decays of higher charmonium states, whereas $\psi(2S)$ remains largely unaffected by such contributions.

The charmonium polarization in $pp$ collisions is based on a few basic principles, such as: 1) helicity conservation in the dilepton decays; 2) rotational covariance of angular momentum eigenstates; and 3) conservation of parity and its violation, which govern the polarization of charmonium states [88, 147]. As PYTHIA8 considers LO NRQCD mechanisms for quarkonia production, it can be anticipated that the finite polarization of charmonium states is due to the QCD processes involved in PYTHIA8. The observed difference between the experimental data and PYTHIA8 predictions may arise from the interplay between these fundamental processes and additional mechanisms contributing to charmonium polarization in realistic collision environments.

## 5.2 Multiplicity dependence of $\lambda_\theta$, $\lambda_\phi$, $\lambda_{\theta\phi}$

The charged particle multiplicity dependence of charmonia polarization provides insight into the role of particle density in $pp$ collisions. Figure 5.4 shows the charged-particle multiplicity dependence of the polarization parameters for $J/\psi$ and $\psi(2S)$ at $\sqrt{s} = 7, 8$, and 13 TeV, using multiplicity classes from Ref. [234]. The experimental study of particle multiplicity dependence on $J/\psi$ polarization in $pp$ collisions with ALICE is underway. However, CMS has reported particle multi-

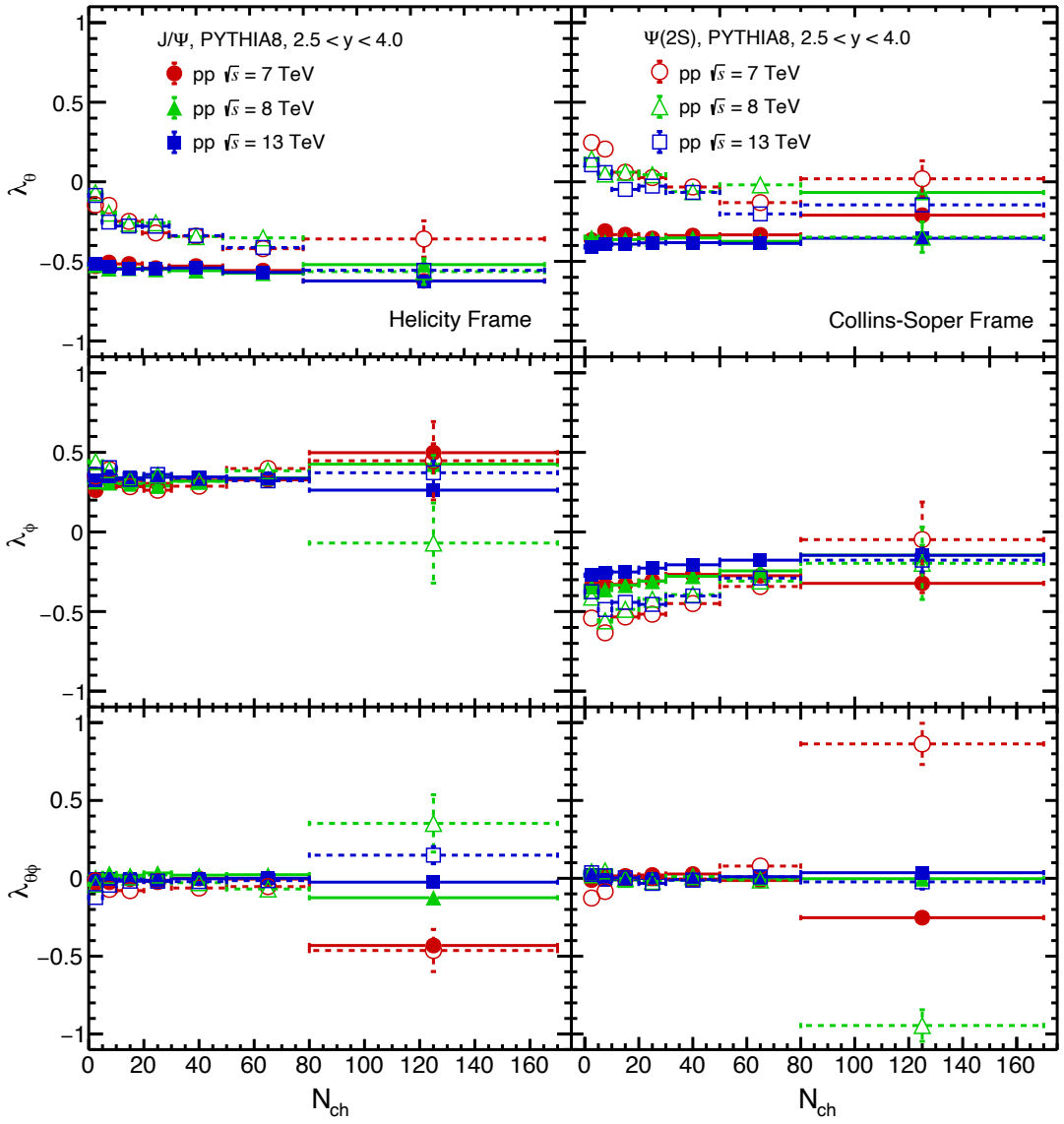



Figure 5.4: The $J/\psi$ and $\psi$(2S) polarization parameters as a function of charged-particle multiplicity for $pp$ collisions at $\sqrt{s}$ = 7, 8, and 13 TeV using PYTHIA8 in both helicity and Collins-Soper reference frames [157].

plicity dependence of polarization for three $\Upsilon(nS)$ states at 7 TeV [51], while theoretical predictions for $J/\psi$ are available from the CGC+NRQCD framework [139] in $pp$ and $p$-Pb collisions at $\sqrt{s}$ = 13 and $\sqrt{s_{\rm NN}}$ = 8.16 TeV, respectively. From

Fig. 5.4, $\lambda_\theta$ indicates an increasing longitudinal polarization with multiplicity for $\psi(2S)$, whereas it remains nearly constant for $J/\psi$ in both frames. The parameter $\lambda_\phi$ shows transverse (helicity) and longitudinal (Collins–Soper) polarization for both states across all multiplicities. The parameter $\lambda_{\theta\phi}$ is negligible at low multiplicity but becomes finite at higher multiplicities. Overall, the polarization shows only a weak dependence on the collision energy.

## 5.3 Rapidity dependence of $\lambda_\theta$, $\lambda_\phi$, $\lambda_{\theta\phi}$

This section presents the rapidity dependence of the polarization parameters for $J/\psi$ and $\psi(2S)$ in $pp$ collisions at $\sqrt{s} = 7, 8$, and 13 TeV. The $p_{\mathrm{T}}$-integrated results are evaluated over $2.5 < y < 4.0$ with a bin width of 0.3 is shown in Fig. 5.5. The binning choice is consistent with LHCb measurements at $\sqrt{s} =$ 7 TeV [48]; the overall polarization remains small. In the helicity frame, $J/\psi$ exhibits stronger longitudinal polarization than $\psi(2S)$, while in the Collins–Soper frame, $J/\psi$ remains longitudinally polarized and $\psi(2S)$ shows transverse polarization. No clear rapidity dependence of $\lambda_\theta$ is observed in either frame. Similar to $p_{\mathrm{T}}$ and charged-particle multiplicity dependence, the parameter $\lambda_\phi$ is positive (helicity) and negative (Collins–Soper) for both states, whereas $\lambda_{\theta\phi}$ remains close to zero across all rapidities, energies, and frames.

In summary, the $p_{\mathrm{T}}$-dependence of the polarization parameters may help us to understand the dynamics of particle production. While the charged-particle multiplicity dependence study of quarkonium polarization would be an interesting topic to investigate the medium effect, it may serve as a benchmark for heavy-ion collisions as well. Similarly, the rapidity dependence of polarization studies may reveal the phase-space analysis of the particles produced in ultra-relativistic collisions.

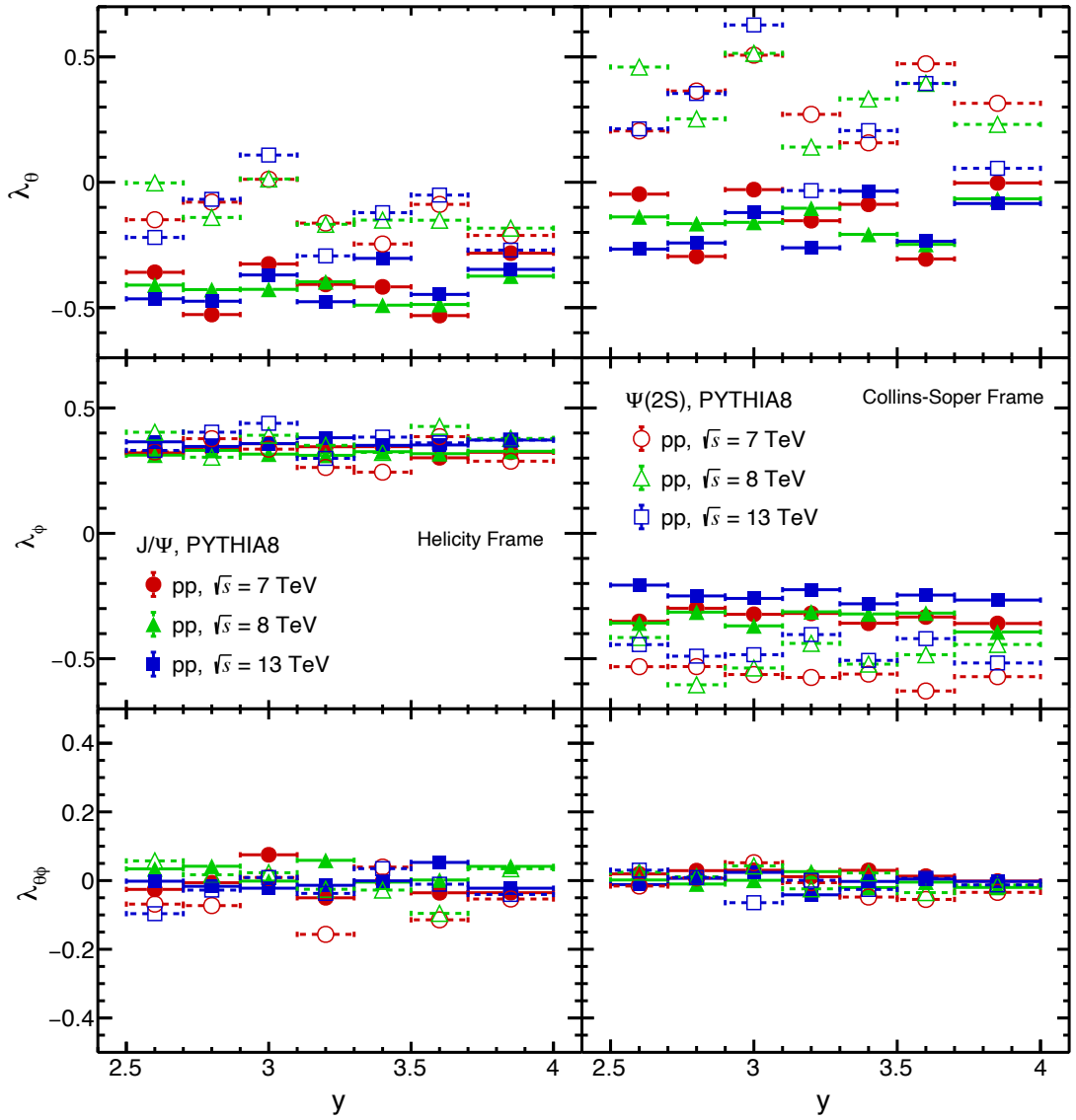



Figure 5.5: The $J/\psi$ and $\psi$(2S) polarization parameters as a function of rapidity for $pp$ collisions at $\sqrt{s}$ = 7, 8, and 13 TeV using PYTHIA8 in both helicity and Collins-Soper reference frames [157].

It is noteworthy to mention that the polarization results obtained in both experimental analyses and Monte Carlo studies consider only the production of $J/\psi$ and $\psi$(2S), without taking the feed-down from higher excited states. The investi-

gation of charmonia polarization by taking the feed-down from higher resonances would be an interesting topic to investigate in the near future. The charged particle multiplicity and rapidity differential measurement of J/$\psi$ polarization using the high-statistics Run 3 data in *pp* collisions with the ALICE experiment is an ongoing effort. Looking ahead, the proposed ALICE 3 detector, with its significantly extended kinematic acceptance for the muon spectrometer, will enable more precise and differential measurements of the rapidity dependence of quarkonium polarization parameters, providing new opportunities to further constrain quarkonium production mechanisms. On the other hand, the newly built Muon Forward Tracker detector in the Run 3 and Run 4 setup of ALICE 2, in conjunction with the muon spectrometer, has better vertexing and precise measurement capabilities, helping us to separate prompt and non-prompt charmonium states at forward rapidity. Investigation of the prompt and non-prompt spin polarization of quarkonium states in the experimental analysis would be an intriguing subject to test in the near future.

# Chapter 6

## Quarkonia spin alignment as a probe of QGP

Based on:

1. "Spin alignment of Quarkonia: A Possible Probe of a Deconfined QCD matter in Pb–Pb collisions at $\sqrt{s_{\rm NN}} = 5.02$ TeV", **B. Sahoo**, C. R. Singh, and R. Sahoo, Eur. Phys. J. C **86**, 880 (2026).

2. "Dissociation driven quarkonium spin alignment in Pb–Pb collisions at $\sqrt{s_{\rm NN}} = 5.02$ TeV", **B. Sahoo**, C. R. Singh, and R. Sahoo. Phys. Rev. D **113**, 054023 (2026).

---

This chapter investigates the spin alignment of charmonium states, such as J/$\psi$ and $\psi(2S)$, as well as bottomonium states, including $\Upsilon(1S)$ and $\Upsilon(2S)$, in Pb+Pb collisions at $\sqrt{s_{\rm NN}} = 5.02$ TeV at mid-rapidity from a theoretical perspective. In this framework, quarkonium states are treated as quantum systems described by wavefunctions, with their real-time evolution governed by the Schrödinger Equation (SE) using a temperature-dependent complex heavy-quark potential. This approach has been extensively employed to study the evolution, production, and suppression of quarkonium states in heavy-ion and small collision systems across various center-of-mass energies [235–240]. Building on this formalism, we examine the spin alignment of quarkonium states by incorporating spin–vorticity and spin–magnetic field interactions in a thermal rotating medium. Before ad-

dressing the spin alignment mechanism within the QGP, we first analyze how the quarkonium Hamiltonian is modified in the presence of vorticity, temperature, and magnetic fields.

## 6.1 Quarkonia in a thermal rotating medium

The Hamiltonian of a charged particle with charge $q$, mass $m$, and spin $S$, moving in a rotating medium with angular velocity $\omega$ and subjected to a magnetic field $B$, can be expressed as [241–243];

$$\mathcal{H} = \frac{1}{2m}\left(\boldsymbol{p} - q\boldsymbol{A} - m\boldsymbol{\omega}\times\mathbf{r}\right)^2 - \frac{m}{2}(\boldsymbol{\omega}\times\mathbf{r})^2 - \boldsymbol{\mu}\cdot\mathbf{B} - \boldsymbol{\omega}\cdot\mathbf{S} + V(\boldsymbol{r}) \tag{6.1}$$

Here, the $\boldsymbol{\omega}\cdot\mathbf{S}$ term arises from the coupling between the rotation of the system and the spin of the particle, while the term $\boldsymbol{\mu}\cdot\mathbf{B}$ results from the coupling between the magnetic field and the spin magnetic dipole moment. $\boldsymbol{A} = -\frac{1}{2}(\mathbf{r}\times\mathbf{B})$ denotes the magnetic vector potential, and $\boldsymbol{\mu}$ stands for the magnetic moment associated with the spin of a particle with charge $q$ and mass $m$. The magnetic moment is defined as $\boldsymbol{\mu} = g\frac{q}{2m}\boldsymbol{S}$, where $g$ is the Land'e $g$-factor.

Now, for a two-body system like quarkonia, Eq. 6.1 can be written as;

$$\mathcal{H} = \sum_{i=1,2}\left[\frac{1}{2m_i}(\boldsymbol{p}_i - q_i\boldsymbol{A_i} - m_i\boldsymbol{\omega}_i\times\mathbf{r}_i)^2 - \frac{m_i}{2}(\boldsymbol{\omega_i}\times\mathbf{r}_i)^2 - \boldsymbol{\mu_i}\cdot\mathbf{B_i} - \boldsymbol{\omega_i}\cdot\mathbf{S_i}\right] + V(|\mathbf{r_1} - \mathbf{r_2}|) \tag{6.2}$$

The index $i$ runs over 1 and 2, representing the heavy quark and antiquark, respectively. Employing the standard reduction procedure of a two-body system to an effective one-body description in the center of mass frame and introducing the corresponding reduced coordinate system, the dynamics of the quarkonia can

be expressed through the following relation,

$$\begin{cases} \mathbf{P} = \mathbf{p_1} + \mathbf{p_2}, & \mathbf{p} = m_\mu \left( \dfrac{\mathbf{p_1}}{m_1} - \dfrac{\mathbf{p_2}}{m_2} \right) \\ m_\mu = \dfrac{m_1\, m_2}{m_1 + m_2}, & \\ \mathbf{r_1} = \mathbf{R} + \dfrac{m_2}{m_1 + m_2}\mathbf{r}, & \mathbf{r_2} = \mathbf{R} - \dfrac{m_1}{m_1 + m_2}\mathbf{r} \end{cases} \tag{6.3}$$

where $m_\mu = m_q/2$ represents the reduced mass in the center-of-mass frame of the heavy-quark pair, with the charm quark mass $m_c = 1.27$ GeV and bottom quark mass $m_b = 4.18$ GeV. We assume that the quark and anti-quark pair forming the quarkonium states exist within the same vortical and magnetic fields. Thus, one obtains $\boldsymbol{\omega}_1 = \boldsymbol{\omega}_2 = \boldsymbol{\omega}$ and $\boldsymbol{B}_1 = \boldsymbol{B}_2 = \boldsymbol{B}$, and following this, the Hamiltonian can be rewritten as

$$\begin{aligned} \mathcal{H} = \frac{P^2}{2M} + \frac{p^2}{2m_\mu} - \mathbf{P}\cdot(\boldsymbol{\omega}\times\mathbf{R}) - \mathbf{p}\cdot(\boldsymbol{\omega}\times\mathbf{r}) \\ - (\boldsymbol{\mu_1} + \boldsymbol{\mu_2})\cdot\mathbf{B} - \boldsymbol{\omega}\cdot(\mathbf{S}_1 + \mathbf{S}_2) + V(|\mathbf{r}|) \end{aligned} \tag{6.4}$$

In the reduced coordinate, the above Eq. 6.4 reduces to

$$\mathcal{H} = \frac{p^2}{2m_\mu} - \mathbf{p}\cdot(\boldsymbol{\omega}\times\mathbf{r}) - (\boldsymbol{\mu_1} + \boldsymbol{\mu_2})\cdot\mathbf{B} - \boldsymbol{\omega}\cdot(\mathbf{S}_1 + \mathbf{S}_2) + V(|\mathbf{r}|) \tag{6.5}$$

Assuming the magnetic field $\boldsymbol{B}$ and the rotation $\boldsymbol{\omega}$ along the $z$ direction, such that $\boldsymbol{B} = B\hat{z}$ and $\boldsymbol{\omega} = \omega\hat{z}$, the Eq. 6.5, can be written as;

$$\mathcal{H} = \frac{p^2}{2m_\mu} - \mathbf{p}\cdot(\boldsymbol{\omega}\times\mathbf{r}) - \frac{qB}{2m}(S_{1z} - S_{2z}) - \omega(S_{1z} + S_{2z}) + V(|\mathbf{r}|) \tag{6.6}$$

Writing $\mathbf{p} = -i\boldsymbol{\nabla}$, $\mathcal{H} = i\frac{\partial}{\partial t}$, $L_z = -i\frac{\partial}{\partial\phi}$, $S_{1z} + S_{2z} = S_z$, Eq. 6.6 reduces to

$$i\frac{\partial}{\partial t} = -\frac{1}{2m_\mu}\boldsymbol{\nabla}^2 - \omega(L_z + S_z) - \frac{qB}{2m}(S_{1z} - S_{2z}) + V(|\mathbf{r}|) \tag{6.7}$$

Expressing the Laplacian operator in spherical coordinates and following the variable separation method, the radial part of the Schrödinger equation becomes;

$$\begin{aligned} \frac{1}{r^2}\frac{d}{dr}\left(r^2\frac{dR(r)}{dr}\right) + 2m_\mu\Bigg[(E - V(r)) - \frac{l(l+1)}{2m_\mu r^2} \\ -\omega(L_z + S_z) - \frac{qB}{m_\mu}(S_{1z} - S_{2z})\Bigg] R(r) = 0 \end{aligned} \tag{6.8}$$

To solve the Schrödinger equation in the presence of rotation, we define $\omega$ in terms of the conserved circulation $C$,

$$C = \oint \mathbf{v} \cdot \mathbf{dl} \tag{6.9}$$

Applying the fundamental Stokes' theorem, the line integral can be converted into a surface integral. Thus, Eq. 6.9 can be written as;

$$C = \oint \boldsymbol{\nabla} \times \mathbf{v} \cdot \mathbf{dS} = 2\omega\pi r^2 \tag{6.10}$$

where, $\boldsymbol{\omega} = \frac{1}{2}\boldsymbol{\nabla} \times \mathbf{v}$ is the non-relativistic vorticity. Here, we assume the rotation to be classical and can be related to the hydrodynamic vorticity, such as the thermal vorticity, temperature vorticity, and enthalpy vorticity, etc.
Substituting the value of $C$ in Eq. 6.8, we obtain

$$\frac{1}{r^2}\frac{d}{dr}\left(r^2\frac{dR(r)}{dr}\right) + 2m_\mu\left[(E - V(r)) - \frac{l(l+1)}{2m_\mu r^2} - \frac{m_j C}{2\pi r^2} - \frac{qB}{m_\mu}\right]R(r) = 0 \tag{6.11}$$

The color singlet potential for $c-\bar{c}$ bound state in the QGP as follows [244];

$$\begin{aligned} V(r,m_D) = {} & \frac{\sigma}{m_D}(1 - e^{-m_D\, r}) - \alpha_{\text{eff}}\left(m_D + \frac{e^{-m_D\, r}}{r}\right) \\ & - i\alpha_{\text{eff}} T_{\text{eff}} \int_0^\infty \frac{2\, z\, dz}{(1+z^2)^2}\left(1 - \frac{\sin(m_D\, r\, z)}{m_D\, r\, z}\right) \end{aligned} \tag{6.12}$$

Where the first and second terms on the right-hand side of Eq. 6.12 are the string term and the Coulombic term, respectively. The third term on the right-hand side is the imaginary part of the heavy-quark potential, which accounts for the collisional or Landau damping of the low-frequency gauge fields that mediate interactions between quark-antiquark pairs. In the above Eq. 6.12 :

- $\sigma$ is the string tension constant between $c\bar{c}$ bound state, and is given as $\sigma = 0.192$ GeV$^2$.

- $T_{\rm eff}$ denotes the effective temperature of quarkonia in the medium arising from the relativistic Doppler shift (RDS). Owing to their large mass and velocity, quarkonium states do not fully thermalize with the surrounding partonic medium; hence, their rest-frame temperature is effectively described by the RDS resulting from their relative motion with respect to the medium. As a result, $T_{\rm eff}$ is quantified in terms of the relative velocity $v_r$ between the quarkonium states and the local fluid cell of the medium. The velocities of the medium and the quarkonium states are denoted by $v_m$ and $v_{Q(nl)}$, respectively. The latter is related to the quarkonium transverse momentum ($p_{\rm T}$) given as $v_{Q(nl)} = p_{\rm T}/E_{\rm T}$, where $E_{\rm T} = \sqrt{p_{\rm T}^2 + M_{Q(nl)}^2}$ and $M_{Q(nl)}$ is the mass of the quarkonium states. The medium thermal velocity $v_m$ is obtained using the Maxwell-Jüttner distribution [237]. The RDS effect leads to an angle-dependent effective temperature experienced by the quarkonium, which is given as [235–237];

$$T_{\rm eff}(\tau, b, p_{\rm T}) = \frac{T(\tau, b)\sqrt{1 - |v_r|^2}}{1 - |v_r|\cos\theta}, \tag{6.13}$$

where, $\theta$ denotes the angle between $v_m$ and $v_{Q(nl)}$. The medium temperature $T(\tau, b)$ is obtained from the solution of coupled differential Eqs. (7.34), (7.33), and (7.12). To obtain an isotropic (angle-independent) representation of the effective temperature, Eq. (6.13) is averaged over the solid angle, yielding the mean effective temperature as;

$$T_{\rm eff}(\tau, b, p_{\rm T}) = T(\tau, b)\frac{\sqrt{1 - |v_r|^2}}{2|v_r|}\ln\left(\frac{1 + |v_r|}{1 - |v_r|}\right) \tag{6.14}$$

The effective temperature of quarkonia encapsulates the modification of the local thermal environment perceived by the moving quarkonium in a relativistically expanding medium. It is important to note that Eq. **??** is valid under the limit $v_r \ll 1$. For a more detailed discussion on effective temperature, see Refs [235–237].

To have a quantitative understanding of the $T_{\rm eff}$, Fig. 6.1 presents $T_{\rm eff}$ at

$T = 400$ MeV as a function of $p_{\mathrm{T}}$ for various quarkonium states. The initial rise of $T_{\mathrm{eff}}$ for $p_{\mathrm{T}} \lesssim M_{Q(nl)}$ originates from an effective blue-shift when the quarkonium velocity is much smaller than the medium flow velocity ($v_Q \ll v_m$), leading to a higher apparent temperature due to their relative motion. In contrast, for $p_{\mathrm{T}} \gg M_{Q(nl)}$ ($v_Q \gg v_m$), the kinematic red-shift dominates, reducing the slope of the thermal spectrum and consequently decreasing $T_{\mathrm{eff}}$ for both charmonium and bottomonium states. This behavior reflects the interplay between quarkonium kinematics and the medium flow.

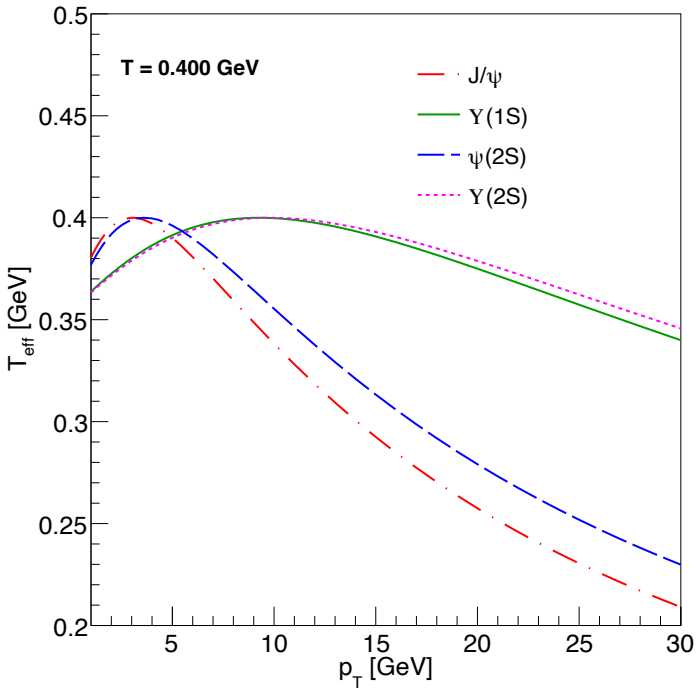



Figure 6.1: The effective temperature ($T_{\mathrm{eff}}$) as a function of $p_{\mathrm{T}}$ for J/$\psi$, $\psi$(2S), $\Upsilon$(1S), and $\Upsilon$(2S) states calculated at medium temperature $T = 0.400$ GeV [161].

- $m_{\mathrm{D}}$ is the Debye mass. Debye mass is a property of the gauge bosons, calculated from the pole of the dressed gauge boson propagator. In QCD, the temporal component of the gluon self-energy tensor at the static limit

gives the Debye mass. In the deconfined medium, it has contributions from both the gluons and quarks degrees of freedom, and is expressed as;

$$m_D(T) = T_{\text{eff}}\sqrt{4\pi\alpha_s^T\left(\frac{N_c}{3}+\frac{N_f}{6}\right)} \tag{6.15}$$

Here, $N_c = 3$, $N_f = 3$, and $\alpha_s^T$ is the strong coupling constant at the hard scale obtained under the Hard Thermal Loop (HTL) limit. In general, the leading order strong running coupling constant $\alpha_s$ is defined as;

$$\alpha_s(\Lambda^2) = \frac{1}{b_1 \ln\left(\frac{\Lambda^2}{\Lambda^2_{\overline{MS}}}\right)} \tag{6.16}$$

where $b_1 = \frac{11N_c-2N_f}{12\pi}$, $\Lambda_{\overline{MS}} = 0.176$ GeV, and $\Lambda$ is renormalization scale. The $\alpha_s^T$ is obtained by scaling at the HTL limit ($\Lambda = 2\pi T$), i.e. $\alpha_s^T = \alpha_s(2\pi T)$. The Eq. (6.16) reflects that the $\alpha_s^T$ depends on medium temperature. At a particular temperature, say $T = 400$ MeV, $\alpha_s^T \simeq 0.26$. Likewise, the coupling constant at the soft scale, $\alpha_s^s$, and ultra-soft scale $\alpha_s^u$ are determined by evaluating the running coupling at the characteristic scales associated with heavy-quark dynamics; $\alpha_s^s = \alpha_s(m_q\alpha_s/2)$ and $\alpha_s^u = \alpha_s(m_q\alpha_s^2/2)$. Here, $m_q$ is the mass of the charm/bottom quark.

In the presence of a magnetic field, the magnetic field-dependent contribution to the Debye mass arises from the quark loop only since gluons do not interact with the magnetic field. Similarly, for an anisotropic QGP case, the anisotropic Debye mass can be factorized into the isotropic Debye mass and an anisotropic contribution in a parametrized way [245–250]. The mathematical expression of Debye mass in the presence of a magnetic field and anisotropy is given in subsections 6.1.1 and 6.1.2, respectively.

- $\alpha_{\text{eff}}$ represents the effective coupling constant and is defined in terms of soft-scale coupling as $\alpha_{\text{eff}} = \frac{4}{3}\alpha_s^s$. For the chosen set of parameters, we obtain $\alpha_s^s \simeq 0.33$ for bottom quark, and $\alpha_s^s \simeq 0.5$ for charm quark, which fixes the numerical value of $\alpha_{\text{eff}}$, respectively.

We solve Eq. 6.11 numerically by taking a $10^4$-point, logarithmically spaced finite spatial grid. The quarkonium wave functions and corresponding energy eigenvalues are obtained using a temperature-dependent potential as defined in Eq. 6.12. Figure 6.2 shows the energy eigenvalues for J/$\psi$, $\psi(2S)$, $\Upsilon(1S)$, and $\Upsilon(2S)$ states are obtained as a function of $p_{\mathrm{T}}$ for three different spin projection quantum number $m_j$ values at C = 1.0 fm and $T$ = 0.175 GeV.

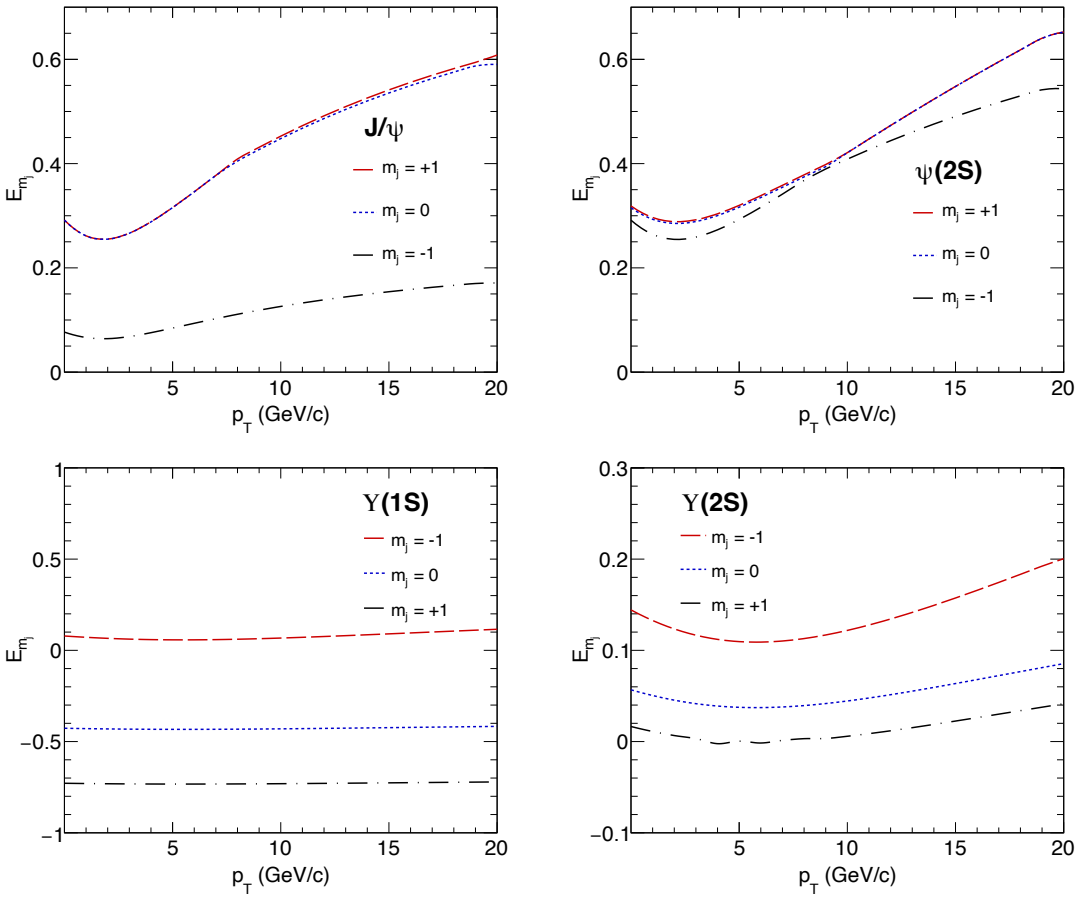



Figure 6.2: The energy eigenvalue as a function of $p_{\mathrm{T}}$ for J/$\psi$ (upper left), $\psi$(2S) (upper right), $\Upsilon$(1S) (lower left), and $\Upsilon$(2S) (lower right) obtained at $C$ = 1.0 fm using $T$ = 0.175 GeV [163].

Figure 6.2 indicates that the energy eigenvalue strongly depends on $m_j$. Particularly, for J/$\psi$ resonance, for $m_j$ = -1, the energy eigenvalue decreases considerably

as compared to $m_j = 0$. While for $m_j = 1$, the energy eigenvalue slightly increases with respect to $m_j = 0$ at higher $p_{\rm T}$. However, for $\Upsilon(1S)$ and $\Upsilon(2S)$, a clear splitting of the energy eigenvalues is observed for three different spin projections because of the spin-vorticity coupling. We found the rotation in the medium leads to the decrease (increase) of the eigen energy depending on the value of $m_j$ = 1 ($m_j$ = -1) as compared to the irrotational case, i.e., $m_j = 0$. The upper and lower panel of Fig. 6.2 shows that the medium modification alters eigenenergy differently for different quarkonium states, and thus it is natural to expect that the degree of spin alignment will be different for different quarkonium states. The relativistic corrections to the potential model are neglected during the evolution of quarkonium states due to the large mass of charm and bottom quarks. As Eq. 6.12 indicates, the energy eigenvalues and quarkonium wave function depend on the Debye mass. Hence, in principle, any change in the Debye mass will change the eigenvalues and wave function. In this study, we consider two physical scenarios: first, we discuss the Debye mass in the presence of an external magnetic field, and then the Debye mass in the presence of momentum-space anisotropy.

### 6.1.1 Debye mass under a strong magnetic field

The magnetic field generated in non-central heavy-ion collisions is expected to decay rapidly and thus primarily influence the partonic phase at early times of the system's evolution. Such fields tend to align charged particles, inducing quark polarization. Since quarks carry fractional electric charge, the magnetic field can modify their orientation within the QGP medium. Consequently, in the presence of a strong magnetic field, the total Debye mass for partons in the static limit can be obtained from the temporal component of the one-loop vacuum self-energy diagram and is given by [251–254];

$$m_D^2(T, eB) = 4\pi\alpha_s(\Lambda^2, |eB|)\left[T^2\frac{N_c}{3} + \sum_f \frac{|q_f eB|}{4\pi^2}\right] \tag{6.17}$$

Here, $\alpha_s(\Lambda^2, |eB|)$ is the running coupling constant, which depends on the magnetic field and temperature. It can be written as [253],

$$\alpha_s(\Lambda^2, |eB|) = \frac{g_s^2}{4\pi} = \frac{\alpha_s(\Lambda^2)}{1 + b_1\alpha_s(\Lambda^2)\ln\left(\frac{\Lambda^2}{\Lambda^2+|eB|}\right)} \tag{6.18}$$

with $\alpha_s(\Lambda^2)$ is defined in Eq. 6.16.

### 6.1.2 Debye mass in an anisotropic medium

Momentum-space anisotropy arises from the collision geometry, which leads to different expansion of the fireball in the longitudinal and transverse directions. This anisotropy consequently modifies the effective mass of the medium. The resulting effect on the Debye mass is given by [245–250];

$$m_D(T, \xi) = m_D(T)\left[f_1(\xi)\cos^2\theta + f_2(\xi)\right]^{-\frac{1}{4}} \tag{6.19}$$

The parameter $\xi$ measures the degree of momentum-space anisotropy, defined as;

$$\xi = \frac{1}{2}\frac{<\mathbf{k}_\perp^2>}{<k_z^2>} - 1 \tag{6.20}$$

where $k_z \equiv \mathbf{k}\cdot\mathbf{n}, \mathbf{k}_\perp \equiv \mathbf{k} - \mathbf{n}(\mathbf{k}\cdot\mathbf{n})$ correspond to the particle momenta along and perpendicular to the direction of anisotropy, and $\theta$ is the angle between the particle momentum ($\mathbf{k}$) and the direction of anisotropy ($\mathbf{n}$). Here, we assume a classical picture in which the direction of anisotropy is along the direction of the particle. The $f_1(\xi)$ and $f_2(\xi)$ are parameterized[1] in such a way that Eq. 6.19 remains always true for small and large values of $\xi$,

$$f_1(\xi) = \frac{9\xi(1+\xi)^{\frac{3}{2}}}{2\sqrt{3+\xi}(3+\xi^2)}\frac{\pi^2(\sqrt{2}-(1+\xi)^{\frac{1}{8}}) + 16(\sqrt{3+\xi}-\sqrt{2}))}{(\sqrt{6}-\sqrt{3})\pi^2 - 16(\sqrt{6}-3)} \tag{6.21}$$

$$f_2(\xi) = \xi\left(\frac{16}{\pi^2} - \frac{\sqrt{2}(\frac{16}{\pi^2}-1) + (1+\xi)^{\frac{1}{8}}}{\sqrt{3+\xi}}\right)\left(1 - \frac{(1+\xi)^{\frac{3}{2}}}{1+\frac{\xi^2}{3}}\right) + f_1(\xi) + 1 \tag{6.22}$$

[1]Here, it is worth mentioning that the parametrization of the anisotropic Debye mass for arbitrary $\xi$ is obtained by constructing a model for the real part of short-range heavy quark-antiquark potential [247].

Using the above formalism, we evaluate quarkonium spin alignment via two approaches. First, we compute spin-projection-dependent eigenenergies by solving the SE and determine the spin alignment observable $\rho_{00}$ for various quarkonium states (see Sec. 6.2). Second, using the obtained eigenenergies and wavefunctions, we estimate the quarkonium decay width arising from collisional damping and gluon dissociation mechanisms, and obtain the spin alignment observable $\rho_{00}$ for various quarkonium states (see Sec. 6.3).

## 6.2 Spin alignment of quarkonia due to eigen energies

The spin density operator can be written as

$$\hat{\rho} = \frac{e^{-\beta \hat{H}}}{Z}, \quad \beta = \frac{1}{T}. \tag{6.23}$$

Here, $\hat{H}$ is the Hamiltonian operator, and Z is the normalization factor corresponding to the spin density matrix, and $\mathrm{Z} = \mathrm{Tr}(\rho)$. In general, Eq. 6.23 is the canonical density operator (or density matrix) employed for describing a statistical thermodynamic equilibrium system. Motivated by the physics mechanism for the experimental measurement of J/$\psi$ polarization [63], we aim to investigate the anisotropic coefficients in a thermal rotating system. The spin density matrix in a rotating frame with angles $\theta_r$ and $\phi_r$ can be transformed as;

$$\hat{\rho}^r(\theta_r, \phi_r) = U(\theta_r, \phi_r)\ \hat{\rho}\ U(\theta_r, \phi_r)^{-1} \tag{6.24}$$

where

$$U(\theta_r, \phi_r) = D(\alpha, \beta, \gamma) = \exp\left(\frac{-iJ_x\alpha}{\hbar}\right) \exp\left(\frac{-iJ_y\beta}{\hbar}\right) \exp\left(\frac{-iJ_z\gamma}{\hbar}\right) \tag{6.25}$$

Taking $\alpha = \phi_r, \beta = \theta_r$, and $\gamma = 0$, Eq. 6.25 can be written as,

$$D^j_{m,m'}(\phi_r, \theta_r) = \langle j, m | D(\phi_r, \theta_r, 0) | j, m' \rangle \tag{6.26}$$

with

$$D^{j}_{m,m'}(\phi_r,\theta_r) = e^{-im\phi_r} d^{j}_{m,m'}(\theta_r) \tag{6.27}$$

$$\left[D^{j}_{m,m'}(\phi_r,\theta_r)\right]^{-1} = e^{im\phi_r}\left[d^{j}_{m,m'}(\theta_r)\right]^{-1} \tag{6.28}$$

For j = 1, one obtains;

$$d^{1}(\theta_r) = \begin{pmatrix} \frac{1}{2}(1+\cos\theta_r) & -\frac{1}{\sqrt{2}}\sin\theta_r & \frac{1}{2}(1-\cos\theta_r) \\ \frac{1}{\sqrt{2}}\sin\theta_r & \cos\theta_r & -\frac{1}{\sqrt{2}}\sin\theta_r \\ \frac{1}{2}(1-\cos\theta_r) & \frac{1}{\sqrt{2}}\sin\theta_r & \frac{1}{2}(1+\cos\theta_r) \end{pmatrix} \tag{6.29}$$

We can expand the right-hand side of Eq. 6.24,

$$\hat{\rho}^{r}_{m,m'}(\theta_r,\phi_r) = \sum_{m'',m'''} \langle j,m|D|j,m''\rangle\langle j,m''|\hat{\rho}|j,m'''\rangle\langle j,m'''|D^{-1}|j,m'\rangle \tag{6.30}$$

$$= \sum_{m'',m'''} e^{-im\phi_r} d^{j}_{m,m''}(\theta_r)\langle j,m''|\hat{\rho}|j,m'''\rangle e^{im'''\phi_r}\left[d^{j}_{m''',m'}(\theta_r)\right]^{-1}$$

$$= \sum_{m'',m'''} e^{i(m'''-m)\phi_r} d^{j}_{m,m''}(\theta_r)\rho_{m'',m'''}\left[d^{j}_{m''',m'}(\theta_r)\right]^{-1} \tag{6.31}$$

and

$$\rho_{m'',m'''} = \langle j,m''|\hat{\rho}|j,m'''\rangle = \frac{1}{Z}e^{-\beta E_{m'''}}\delta_{m'',m'''} \tag{6.32}$$

Employing the above-developed formalism, the diagonal and off-diagonal elements of the spin density matrix are estimated for quarkonium states in a rotating, magnetized, and anisotropic medium. Notably, the energy eigenvalues used to calculate the spin alignment factor depend on the medium temperature, rotation, magnetic field, and anisotropy parameter. The values of $\theta_r$ and $\phi_r$ used in Eq. 6.31 are taken from Ref. [255], where these parameters are determined by solving a system of equations in the Collins-Soper frame for J/$\psi$ and $\Upsilon$ states with respective ranges $4 < p_{\mathrm{T}} < 6$ GeV/c and $p_{\mathrm{T}} > 15$ GeV/c. The value of $\theta_r = 1.75 \pm 0.10$ rad for J/$\psi$ and $\theta_r = 1.58 \pm 0.10$ rad for $\Upsilon$ states. The off-diagonal elements are obtained using $\phi_r = 0$.

With the aforementioned formalism, we first examine the impact of medium rotation, quantified by the circulation parameter $C$, on the diagonal spin density matrix element $\rho_{00}$ for various quarkonium states. We then study the effects of medium temperature ($T$), external magnetic field ($eB$), and momentum-space anisotropy ($\xi$) on $\rho_{00}$. Finally, selected off-diagonal elements of the spin density matrix are analyzed to provide a comprehensive understanding of spin–vorticity coupling in relativistic heavy-ion collisions.

### 6.2.1 Diagonal elements of the spin density matrix

Using Eq. 6.31, one can obtain the $00^{\text{th}}$ diagonal elements of the spin−density matrix in a rotating frame, $\rho^r_{00}$, and is expressed as follows;

$$\rho^r_{00} = \frac{1}{Z}\left[\cos^2\theta_r e^{-\beta E_0} + \frac{1}{2}\sin^2\theta_r\left(e^{-\beta E_1} + e^{-\beta E_{-1}}\right)\right] \tag{6.33}$$

Figure 6.3 presents the $00^{\text{th}}$ element of the spin density matrix, $\rho_{00}$[2] as a function of $p_{\text{T}}$ for different values of the circulation parameter $C$ at $T = 0.175$ GeV. The black dashed line in Fig. 6.3 and subsequent figures corresponds to a thermal irrotational medium ($C = 0$), for which $\rho_{00} = 1/3$. This value serves as the baseline for spin alignment studies, and any deviation from $\rho_{00} = 1/3$ indicates preferential spin alignment. The upper and lower panels of Fig. 6.3 display the spin alignment of J/$\psi$ (left), $\psi$(2S) (right), $\Upsilon$(1S) (left), and $\Upsilon$(2S) (right) as functions of $p_{\text{T}}$, respectively. The $p_{\text{T}}$ dependence of $\rho_{00}$ is incorporated through the effective temperature $T_{\text{eff}}$, which characterizes the quarkonium temperature in the medium. The $T_{\text{eff}}$ originates from the relativistic Doppler shift, increasing up to $p_{\text{T}} \sim 3$ GeV/$c$ and decreasing thereafter with increasing $p_{\text{T}}$. It is used to determine the energy eigenvalues, which are subsequently employed in the calculation of quarkonium spin alignment. As a result, the spin alignment observable

[2]Throughout this study, we use $\rho^r_{00}$ interchangeably with $\rho_{00}$ for simplicity. Thus, $\rho_{00}$ refers to the $00^{\text{th}}$ element of the spin density matrix in the rotating frame

$\rho_{00}$ for J/$\psi$ initially decreases with $p_{\rm T}$ up to $\sim$ 3 GeV/$c$, as shown in the upper left panel of Fig. 6.3, and subsequently increases for $p_{\rm T} \gtrsim 4$ GeV/$c$. For a fixed $p_{\rm T}$, $\rho_{00}$ increases with increasing circulation parameter $C$, which encodes the vorticity information of the medium.

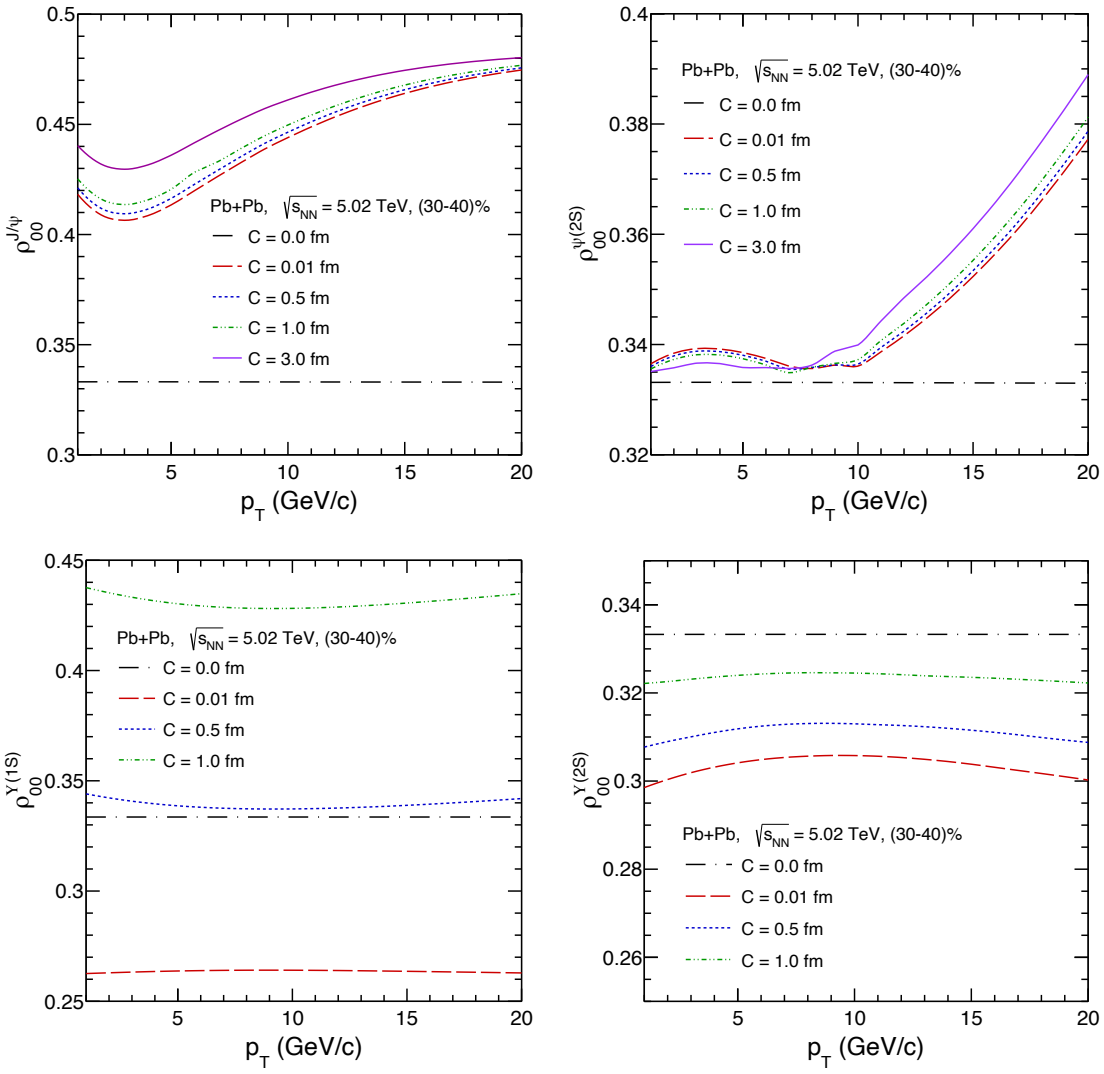



Figure 6.3: The spin alignment observable $\rho_{00}$ as a function of $p_{\rm T}$ for J/$\psi$ (upper left), $\psi$(2S) (upper right), $\Upsilon$(1S) (lower left), and $\Upsilon$(2S) (lower right) in Pb+Pb collisions at $\sqrt{s_{\rm NN}} = 5.02$ TeV calculated at mid-rapidity for different values of the circulation parameter, $C$ [163].

The coupling between quarkonium spin and medium vorticity enhances quarkonium stability by reducing its eigenenergy in the medium. The influence of vorticity remains small for $\omega \leq 0.16$ fm$^{-1}$ (corresponding to $C = 1$ fm and $r = 1$ fm); however, with increasing vorticity or $C$, $\rho_{00}^{J/\psi}$ increases while preserving its overall $p_{\mathrm{T}}$ dependence. The upper right panel of Fig. 6.3 shows that $\rho_{00}$ for $\psi$(2S) increases slightly at low $p_{\mathrm{T}} \leq 2$ GeV/$c$. In this region, the $\psi$(2S) is expected to move more slowly relative to the surrounding medium, leading to a reduced effective temperature $T_{\mathrm{eff}}$ and consequently a lower eigenenergy, which enhances $\rho_{00}$. In the intermediate momentum range, $2 < p_{\mathrm{T}} < 9$ GeV/$c$, the $\psi$(2S) interacts more coherently with the medium, resulting in an increase in $T_{\mathrm{eff}}$ and eigenenergy, thereby reducing $\rho_{00}$. Since $\psi$(2S) is an excited state with comparatively higher eigenenergy, it is less stable and less susceptible to polarization in the medium, yielding weaker spin alignment than J/$\psi$. Unlike J/$\psi$, the $\psi$(2S) state exhibits a decrease in $\rho_{00}$ with increasing circulation parameter $C$ for $p_{\mathrm{T}} \lesssim 9$ GeV/$c$, reflecting the interplay between medium vorticity and $T_{\mathrm{eff}}$. However, for $p_{\mathrm{T}} > 9$ GeV/$c$, the spin alignment trend of $\psi$(2S) becomes similar to that of J/$\psi$, although the deviation of $\rho_{00}$ from the baseline value remains small.

The lower panels of Fig. 6.3 show the spin alignment of $\Upsilon$(1S) (left) and $\Upsilon$(2S) (right) for different values of the circulation parameter $C$ at mid-rapidity. Owing to its large mass and strong binding, the $\Upsilon$(1S) state possesses relatively small eigenenergies, leading to sizable spin polarization for both small and large values of $C$ (e.g., $C = 0.01$ fm and 1.0 fm). In contrast, around $C = 0.5$ fm, the polarization becomes negligible with $\rho_{00} \approx 1/3$. The weak dependence of $\rho_{00}$ on $p_{\mathrm{T}}$ indicates the high stability of the $\Upsilon$(1S) state, for which variations in eigenenergy induced by $T_{\mathrm{eff}}$ at $T = 0.175$ GeV remain minimal. On the other hand, the $\Upsilon$(2S) state exhibits a noticeable $p_{\mathrm{T}}$ dependence of $\rho_{00}$, following a behavior similar to that of $\psi$(2S) for $p_{\mathrm{T}} < 9$ GeV/$c$. However, due to its larger mass, the relevant $p_{\mathrm{T}}$ range for $\Upsilon$(2S) extends up to $p_{\mathrm{T}} \gtrsim 20$ GeV/$c$. The magnitude of spin alignment for $\Upsilon$(2S) is found to decrease with increasing circulation parameter $C$. It is im-

portant to note that $\rho_{00}$ exhibits stronger sensitivity to the circulation parameter $C$ for the $\Upsilon$(1S) state than for $\Upsilon$(2S). For instance, in the case of $\Upsilon$(1S), the deviation of $\rho_{00}$ from the baseline value 1/3 is negative at $C = 0.01$ fm ($\rho_{00} < 1/3$), while it becomes positive at $C = 1.0$ fm ($\rho_{00} > 1/3$). This behavior suggests a flip in the angular distribution anisotropy induced by medium vorticity. Since $\rho_{00}$ is directly related to the polarization parameter $\lambda_\theta$, such a transition corresponds to a change from transverse to longitudinal spin polarization. The vorticity at which this transition occurs is expected to be sensitive to the temperature and equilibration time of the quark-gluon plasma. Therefore, the spin alignment of the $\Upsilon$(1S) state may serve as a sensitive probe of system thermalization and could potentially provide information on the equilibration time. In contrast, for the $\Upsilon$(2S) state, the deviation of $\rho_{00}$ from the baseline value remains negative for all considered values of $C$. Nevertheless, $\rho_{00}$ gradually approaches 1/3 with increasing $C$, suggesting that at sufficiently large vorticity the $\Upsilon$(2S) state may exhibit behavior similar to that of $\Upsilon$(1S).

Besides vorticity, strong magnetic fields and momentum-space anisotropy generated in heavy-ion collisions are also expected to influence the spin alignment of vector mesons [159]. Since heavy quarks (charm and/or beauty) are primarily produced at the early stage of heavy-ion collisions, the initially generated magnetic field and anisotropy are anticipated to polarize the heavy quarks. Hence, heavy quarks can be considered a crucial probe to study the spin dynamics and magnetic field effect in ultra-relativistic heavy-ion collisions. In Fig. 6.4, we investigate the initial state dynamics, such as the effect of rotation, magnetic field, and anisotropy on the spin alignment observables. The interplay of coupling of spin with rotation ($\boldsymbol{\omega} \cdot \mathbf{S}$) and magnetic field ($\boldsymbol{\mu} \cdot \mathbf{B}$, where $\boldsymbol{\mu} = g\frac{q}{2m}\boldsymbol{S}$), is examined through the spin density matrix element $\rho_{00}$.

The upper left panel of Fig. 6.4 presents $\rho_{00}$ as a function of the magnetic field $eB$ at $C = 1.0$ fm in Pb+Pb collisions at $\sqrt{s_{\rm NN}} = 5.02$ TeV at mid-rapidity for the 1S and 2S quarkonium states. The results show a slight decrease in the

spin alignment of J/$\psi$ with increasing magnetic field, whereas the spin alignment of $\psi$(2S) remains nearly unchanged. For $\Upsilon$(1S), the magnetic field has only a marginal effect, with $\rho_{00}$ remaining almost constant. Similarly, the $\Upsilon$(2S) state is found to be largely insensitive to the magnetic field, with $\rho_{00}$ fluctuating close to the unpolarized baseline value of 1/3. The upper right panel of Fig. 6.4 presents

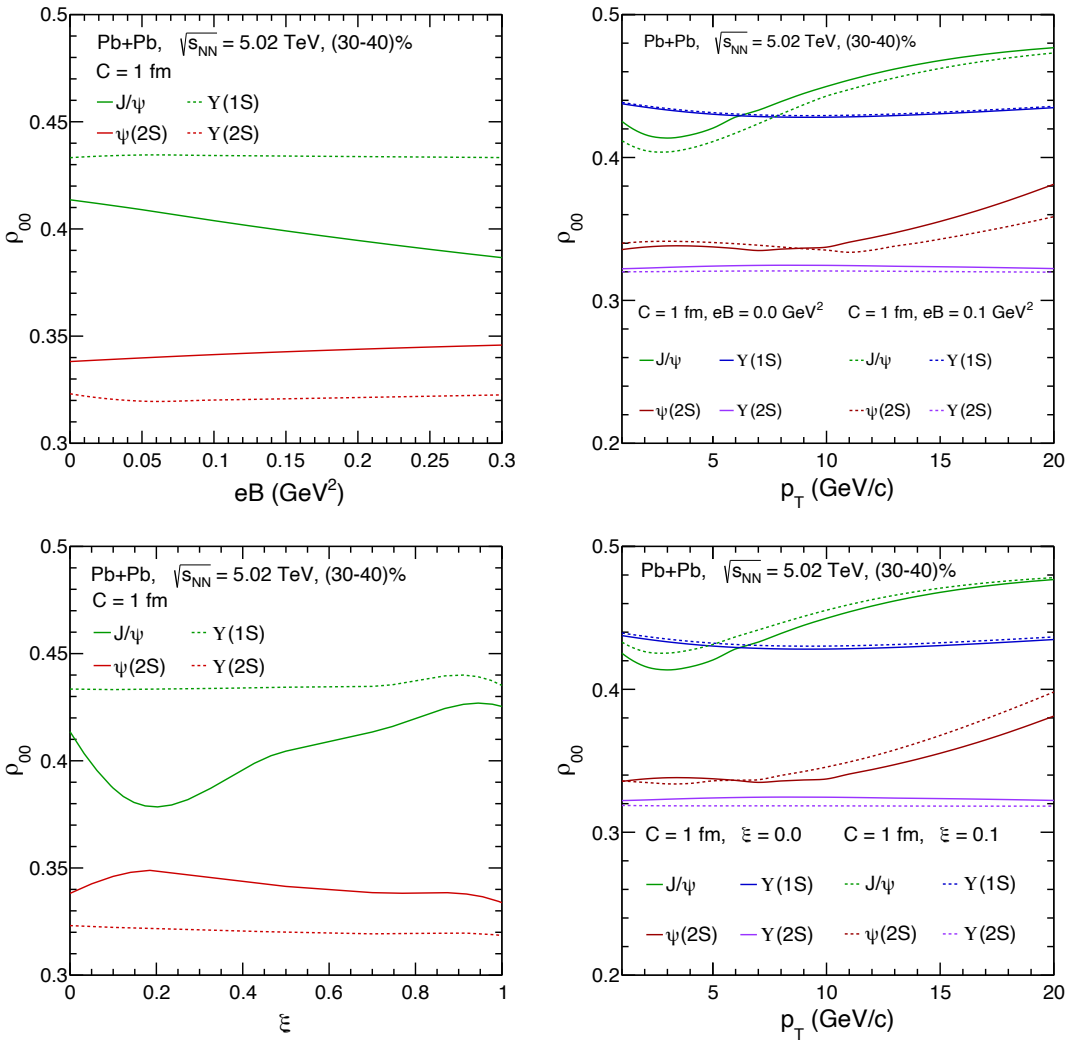



Figure 6.4: The spin alignment observable $\rho_{00}$ as a function of $p_{\mathrm{T}}$ for J/$\psi$ (upper panel) and $\psi$(2S) (lower panel) in Pb+Pb collisions at $\sqrt{s_{\mathrm{NN}}}$ = 5.02 TeV calculated at mid-rapidity for different values of the circulation parameter, $C$ [163].

$\rho_{00}$ as a function of $p_{\mathrm{T}}$ at $C$ = 1.0 fm for the same collision system and energy,

illustrating the influence of the magnetic field on the spin alignment of different quarkonium states. The solid lines correspond to the presence of a magnetic field, $eB = 0.1$ GeV$^2$, while the dashed lines represent the case without a magnetic field. For J/$\psi$, the magnetic field reduces the degree of spin alignment, quantified by the deviation of $\rho_{00}$ from 1/3, over the entire $p_{\rm T}$ range. In contrast, for $\psi$(2S), the deviation from 1/3 slightly increases at lower $p_{\rm T}$. Interestingly, the magnetic field enhances the absolute spin alignment, $|\rho_{00} - 1/3|$, for both $\Upsilon$(1S) and $\Upsilon$(2S), but in opposite directions: $\rho_{00} > 1/3$ for $\Upsilon$(1S), whereas $\rho_{00} < 1/3$ for $\Upsilon$(2S). This behavior suggests that the magnetic-field effect on spin alignment depends sensitively on the binding energy of the quarkonium state. It is also important to note that the timescales associated with quarkonium coupling to medium vorticity and to the magnetic field may differ. Therefore, a quantitative estimate of the relaxation time governing quarkonium spin alignment with local flow gradients is essential for a more complete understanding.

The lower left panel of Fig. 6.4 presents the dependence of $\rho_{00}$ on the anisotropy parameter $\xi$ for quarkonium states at rest in the medium with $C = 1.0$ fm. For small anisotropies ($\xi < 0.2$), the spin alignment of J/$\psi$ decreases, whereas $\psi$(2S) exhibits only a weak enhancement. At larger anisotropies ($\xi > 0.2$), $\rho_{00}$ for J/$\psi$ increases, while for $\psi$(2S) it first decreases and then tends toward saturation. In contrast, the bottomonium states, $\Upsilon$(1S) and $\Upsilon$(2S), display almost no dependence on $\xi$, indicating that their spin alignment remains largely insensitive to momentum-space anisotropy. The lower right panel of Fig. 6.4 shows $\rho_{00}$ as a function of $p_{\rm T}$ for different quarkonium states at $C = 1.0$ fm. The solid lines correspond to an anisotropic medium with $\xi = 1.0$, while the dashed lines represent the isotropic case ($\xi = 0$). The results demonstrate a clear state dependence of the anisotropy effect. For J/$\psi$, the deviation of $\rho_{00}$ from the isotropic baseline value of 1/3 increases over the entire $p_{\rm T}$ range in the anisotropic medium, whereas for $\psi$(2S), the deviation slightly decreases at low $p_{\rm T}$. The $\Upsilon$(1S) state remains nearly insensitive to both anisotropy and transverse momentum, while $\Upsilon$(2S) ex-

hibits only a small but systematic shift in $\rho_{00}$ in the anisotropic medium. These observations highlight the role of momentum-space anisotropy in modifying the spin alignment of lighter quarkonium states. Although the effects are relatively small, they may provide useful information about the early-time dynamics of the quark-gluon plasma. In contrast, the heavier bottomonium states appear less sensitive to anisotropic medium effects, making their spin alignment a comparatively robust observable.

### 6.2.2 Off-diagonal elements of the spin density matrix

In addition to the diagonal spin density matrix element $\rho_{00}$, the off-diagonal elements of the spin density matrix also carry important information about the dynamics of the medium created in heavy-ion collisions. In particular, the off-diagonal elements can distinguish the local spin alignment of vector mesons from the global spin alignment. As discussed in Chapter 2, the off-diagonal matrix elements appear as coefficients of the angular distribution of the decay daughter in the mother particle's rest frame. The investigation of these observables provides valuable insights into the spin-hydrodynamic evolution of the system as well as the freeze-out dynamics [142, 255–257]. Additionally, the off-diagonal spin density matrix elements encode information about medium-induced spin correlations, long-range correlations, quantum coherence, local spin structure, and non-equilibrium QCD dynamics [258]. Using Eq. 6.31, the off-diagonal matrix elements of the spin−density matrix in a rotating frame, such as $\rho_{1,-1}$, $\rho_{-1,0}$, and $\rho_{1,0}$ can be expressed as follows;

1. $\rho^r_{1,-1}$ :

$$\rho^{\rm r}_{1,-1} = \frac{\sin^2\theta_{\rm r}}{4}\left(\rho_{1,1} + {\rm e}^{-2{\rm i}\phi_{\rm r}}\rho_{-1,-1} + 2{\rm e}^{-{\rm i}\phi_{\rm r}}\rho_{0,0}\right) \tag{6.34}$$

At $\phi_r = 0$, gives

$$\mathrm{Re}[\rho^{\rm r}_{1,-1}] = \frac{\sin^2\theta_{\rm r}}{4}\left(\rho_{1,1} + \rho_{-1,-1} + 2\rho_{0,0}\right) \tag{6.35}$$

Using the relation, $\rho_{1,1} + \rho_{0,0} + \rho_{-1,-1} = 1$, reduces to

$$\mathrm{Re}[\rho^{\mathrm{r}}_{1,-1}] = \frac{\sin^2\theta_{\mathrm{r}}}{4}\,(1+\rho_{0,0}) \tag{6.36}$$

2. $\rho^{r}_{-1,0}$ :

$$\rho^{\mathrm{r}}_{-1,0} = \frac{\sin\theta_{\mathrm{r}}}{2\sqrt{2}}\left[(1-\cos\theta_{\mathrm{r}})\mathrm{e}^{2\mathrm{i}\phi_{\mathrm{r}}}\rho_{1,1} + 2\cos\theta_{\mathrm{r}}\mathrm{e}^{\mathrm{i}\phi_{\mathrm{r}}}\rho_{0,0} + (1+\cos\theta_{\mathrm{r}})\rho_{-1,-1}\right] \tag{6.37}$$

At $\phi_r = 0$, gives

$$\mathrm{Re}[\rho^{\mathrm{r}}_{-1,0}] = \frac{\sin\theta_{\mathrm{r}}}{2\sqrt{2}}\left[(1-\cos\theta_{\mathrm{r}})\rho_{1,1} + 2\cos\theta_{\mathrm{r}}\rho_{0,0} - (1+\cos\theta_{\mathrm{r}})\rho_{-1,-1}\right] \tag{6.38}$$

3. $\rho^{r}_{1,0}$ :

$$\rho^{\mathrm{r}}_{1,0} = \frac{\sin\theta_{\mathrm{r}}}{2\sqrt{2}}\left[(1+\cos\theta_{\mathrm{r}})\rho_{1,1} - 2\cos\theta_{\mathrm{r}}\mathrm{e}^{\mathrm{i}\phi_{\mathrm{r}}}\rho_{0,0} - (1-\cos\theta_{\mathrm{r}})\mathrm{e}^{-2\mathrm{i}\phi_{\mathrm{r}}}\rho_{-1,-1}\right] \tag{6.39}$$

At $\phi_r = 0$, gives

$$\mathrm{Re}[\rho^{\mathrm{r}}_{1,0}] = \frac{\sin\theta_{\mathrm{r}}}{2\sqrt{2}}\left[(1+\cos\theta_{\mathrm{r}})\ \rho_{1,1} - 2\cos\theta_{\mathrm{r}}\rho_{0,0} - (1-\cos\theta_{\mathrm{r}})\rho_{-1,-1}\right] \tag{6.40}$$

The left panels of Fig. 6.5 present the real parts of the off-diagonal spin density matrix elements, $\mathrm{Re}[\rho_{1,-1}]$, $\mathrm{Re}[\rho_{-1,0}]$, and $\mathrm{Re}[\rho_{1,0}]$, as functions of $p_{\mathrm{T}}$ for J/$\psi$, $\psi$(2S), $\Upsilon$(1S), and $\Upsilon$(2S) in Pb+Pb collisions at $\sqrt{s_{\mathrm{NN}}} = 5.02$ TeV at mid-rapidity in the (30–40)% centrality class. The non-zero values of these matrix elements indicate a mixed quantum state with quantum superposition and possible decoherence effects in the medium. Overall, all three matrix elements exhibit similar qualitative $p_{\mathrm{T}}$ dependence, differing mainly in magnitude. $\mathrm{Re}[\rho_{1,-1}]$ remains positive, whereas $\mathrm{Re}[\rho_{-1,0}]$ and $\mathrm{Re}[\rho_{1,0}]$ are negative for all quarkonium states. Similar to $\rho_{00}$, the $\Upsilon$(1S) and $\Upsilon$(2S) states show only a weak dependence on $p_{\mathrm{T}}$, while for J/$\psi$ and $\psi$(2S), the magnitudes of the off-diagonal elements decrease at higher $p_{\mathrm{T}}$. These off-diagonal elements reflect correlations among different spin projections.

The middle and right panels of Fig. 6.5 show the real parts of the off-diagonal spin density matrix elements, $\mathrm{Re}[\rho_{1,-1}]$, $\mathrm{Re}[\rho_{-1,0}]$, and $\mathrm{Re}[\rho_{1,0}]$, as functions of temperature $T$ and circulation parameter $C$, respectively, for J/$\psi$, $\psi$(2S), $\Upsilon$(1S), and $\Upsilon$(2S) states.

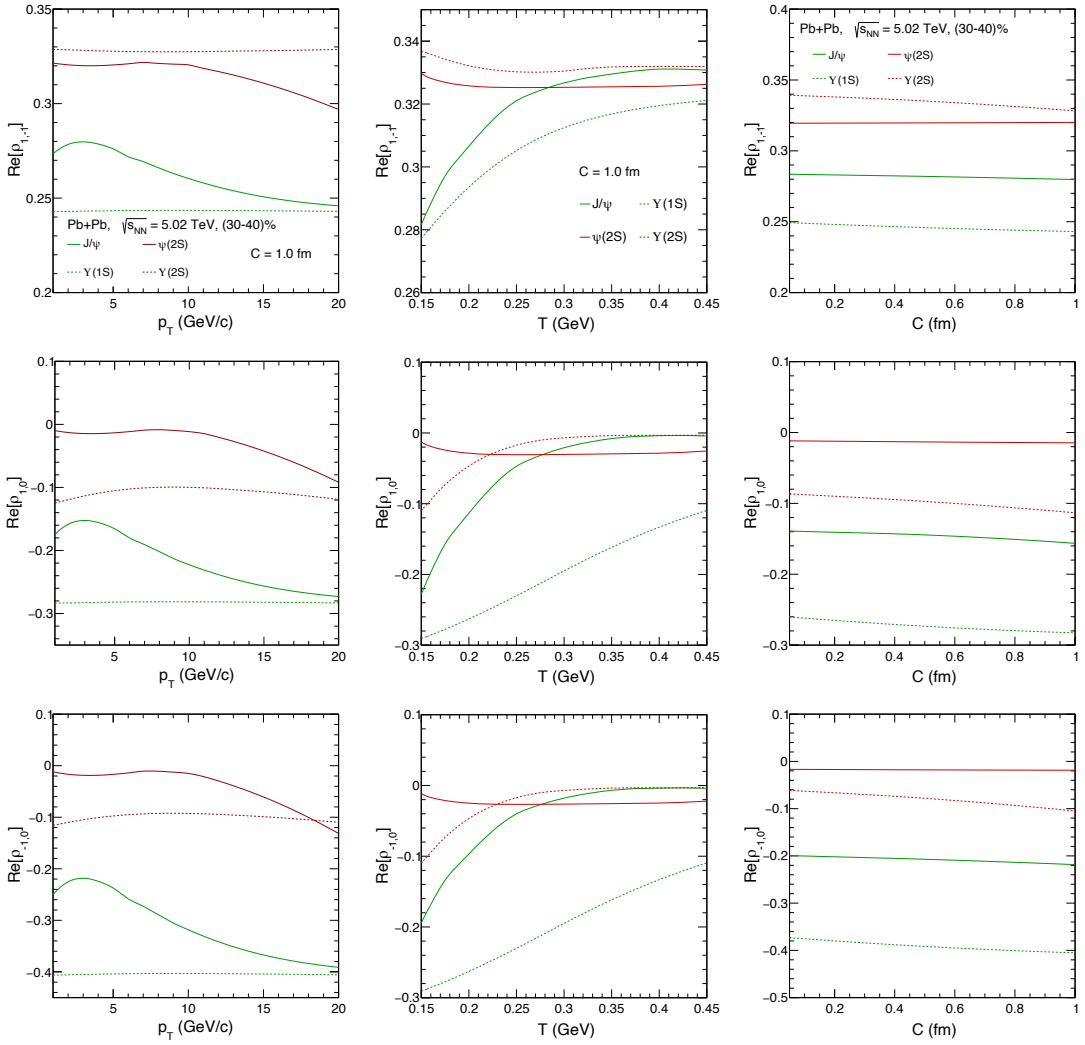



Figure 6.5: The off-diagonal elements of the spin density matrix, such as, $\mathrm{Re}[\rho_{1,-1}]$ (top), $\mathrm{Re}[\rho_{-1,0}]$ (middle), and $\mathrm{Re}[\rho_{1,0}]$ (bottom) as a functions of $p_{\mathrm{T}}$ (left), $T$ (middle), $C$(right) for Pb+Pb collisions at $\sqrt{s_{\mathrm{NN}}} = 5.02$ TeV calculated at mid-rapidity [163].

The temperature and vorticity dependence of these observables demonstrates the

influence of thermal and rotational properties of the medium on spin coherence. In particular, Re[$\rho_{-1,0}$] and Re[$\rho_{1,0}$] tend toward zero with increasing temperature, indicating suppression of quantum coherence at high temperatures. In contrast, increasing the circulation parameter $C$ enhances the magnitudes of the off-diagonal elements for $\Upsilon$(1S) (from an initially vanishing baseline), while the charmonium states and $\Upsilon$(2S) remain only weakly affected. These results suggest that rotational effects enhance quantum coherence among spin states, leading to stronger spin alignment in a thermo-vortical medium.

Using a similar methodology, we now calculate the spin alignment observable within an alternative framework. In the following, the spin alignment of quarkonia is evaluated by considering dissociation mechanisms such as collisional damping and gluon dissociation.

## 6.3 Spin alignment of quarkonia due to dissociation mechanisms

Quarkonium suppression and spin alignment provide complementary probes of the interaction between heavy quark–antiquark pairs and the QGP. In this context, we investigate how different dissociation mechanisms affect the spin alignment factor $\rho_{00}$ for J/$\psi$, $\psi$(2S), $\Upsilon$(1S), and $\Upsilon$(2S) states. The calculations are based on numerical solutions of the Schrödinger equation, which yield temperature-, vorticity-, and spin-projection-dependent eigenvalues and wave functions.

### 6.3.1 Collisional damping

The collisional energy loss of quarkonium in the QGP is commonly referred to as collisional damping, which arises due to the interactions of the bound heavy quark pair with the thermal partons in the medium. This effect leads to a finite in-medium width of the quarkonium state, reflecting its partial decoherence and

eventual dissociation. The dissociation rate associated with this mechanism can be evaluated using the imaginary part of the potential, $V(r, m_D)$, which encodes the medium-induced damping effect.

The collisional damping width, $\Gamma_{\rm damp,nl}$, quantifies the in-medium decay rate of quarkonium due to the imaginary part of the potential. It is computed using first-order perturbation theory as an expectation value of Im($V$) with the radial wave function of the bound state:

$$\Gamma_{\rm damp,}{}_{nlm}(\tau, p_{\rm T}) = \int [g_{nlm}(r)^{\dagger}\,[{\rm Im(V)}]\,g_{nlm}(r)]dr, \tag{6.41}$$

here $g_{nlm}(r)$ is the quarkonium singlet wave function. The spin-dependent wave functions for J/$\psi$, $\psi$(2S), $\Upsilon$(1S) and $\Upsilon$(2S) are obtained by solving the Schrödinger equation Eq. (6.11) in the presence of rotation, as described in the preceding section.

### 6.3.2 Gluonic dissociation

The gluon-induced dissociation (or gluonic dissociation) of quarkonia in the QGP medium is another dissociation mechanism. This process arises when a thermal gluon interacts inelastically with a color-singlet quarkonium state, leading to a transition to a color-octet state, which subsequently breaks apart. The corresponding dissociation cross-section depends on the gluon energy spectrum and temperature profile of the medium. Following the formalism introduced by Peskin and Bhanot [259, 260] and extended to finite-temperature QCD [235, 236, 261, 262], the gluon-dissociation cross section for a quarkonium state is given by,

$$\sigma_{\rm d,}{}_{nlm}(E_g) = \frac{\pi^2\alpha_s^u E_g}{N_c^2}\sqrt{\frac{m_q}{E_g + E_{nlm}}}\left(\frac{l|J_{nlm}^{q,l-1}|^2 + (l+1)|J_{nlm}^{q,l+1}|^2}{2l+1}\right) \tag{6.42}$$

where, $\alpha_s^u \simeq 0.76$ for bottom quark, and, $\alpha_s^u \simeq 0.87$ for charm quark. Here, $E_g$ is the incident gluon energy, and $E_{nlm}$ denotes the energy eigenvalue of the quarkonium state. The $g_{nlm}(r)$ and $h_{ql'}(r)$ are the color-singlet and color-octet

wave functions with orbital angular momenta $l$ and $l'$, respectively. The octet wave function $h_{\mathrm{q}l'}(r)$ has been obtained by solving the Schrödinger equation with the octet potential $V_8 = \alpha_{\mathrm{eff}}/8r$. For a given value of $n$ and $l$, the color-octet wave function and the corresponding energy eigenvalue are identical for all three spin projection states $m$. The value of $q$ is determined by using the conservation of energy, $q = \sqrt{m_q(E_g + E_{nlm})}$.

The probability density $J^{ql'}_{nlm}$ encodes the overlap between the initial bound and final continuum states and is computed using the in-medium singlet and octet wave functions,

$$J^{ql'}_{nlm} = \int_0^\infty dr\ r\ g^*_{nlm}(r)\ h_{ql'}(r) \tag{6.43}$$

As quarkonium moves with a finite velocity relative to the medium, the gluon distribution in the quarkonium rest frame gets modified due to the relativistic Doppler shift of gluon energies. Under a Lorentz transformation, the gluon energy in the quarkonium rest frame is modified as $E'_g = \gamma E_g(1 + v_Q \cos\theta)$, where $\gamma$ is the Lorentz factor, and $\theta$ is the angle between the quarkonium velocity vector and the incoming gluon momentum. Consequently, the modified gluon distribution function in the quarkonium frame is expressed as,

$$f_g = \left[\exp\left(\frac{E_g}{T_{\mathrm{eff}}}\,\gamma(1 + v_Q\cos\theta)\right) - 1\right]^{-1}. \tag{6.44}$$

This modified distribution plays an essential role in determining the gluonic dissociation rate and, consequently, the momentum-dependent dissociation of quarkonia in the QGP. The thermal-averaged gluonic dissociation, $\Gamma_{\mathrm{gd},nlm}$, can then be obtained by folding the cross section with this modified Bose–Einstein distribution of thermal gluons in the particle rest frame [235, 236], as given by;

$$\Gamma_{\mathrm{gd},nlm}(\tau, p_{\mathrm{T}}, b) = \frac{g_d}{4\pi^2}\int_0^\infty\int_0^\pi \frac{dp_g\, d\theta\, \sin\theta\, p_g^2 \sigma_{\mathrm{d},nlm}(E_g)}{e^{\{\frac{\gamma E_g}{T_{\mathrm{eff}}}(1+v_Q\cos\theta)\}} - 1} \tag{6.45}$$

here, $p_T$ is the transverse momentum of the quarkonium, and $g_d = 16$ represents the degeneracy factor for the gluons. Furthermore, the net decay width $\Gamma_{\mathrm{D}}$ for

quarkonia in-medium is obtained via taking the sum over Eq. (6.41), and (6.45), given as;

$$\Gamma_{\mathrm{D},nlm} = \Gamma_{\mathrm{damp},nlm} + \Gamma_{\mathrm{gd},nlm} \tag{6.46}$$

Notably, the collisional damping width is determined from the imaginary part of the potential and the quarkonium wave function, while the gluon-dissociation width depends on the binding energy extracted from the eigenvalues. Consistent with earlier studies [237, 238], collisional damping is found to dominate over gluonic dissociation throughout the medium evolution. The combined effects of collisional damping and gluonic dissociation are subsequently incorporated into the computation of the spin alignment observable $\rho_{00}$, allowing us to explore the role of medium-induced spin–vorticity coupling of quarkonia within a rotating QGP. Before studying the spin alignment of quarkonium states, we first examine the dependence of the decay width on temperature and $p_{\mathrm{T}}$.

Figure 6.6 shows the $p_{\mathrm{T}}$ dependence net decay width $\Gamma_D$ for J/$\psi$ (upper left), $\psi$(2S) (upper right), $\Upsilon$(1S) (lower left), and $\Upsilon$(2S) (lower right) in Pb–Pb collisions at $\sqrt{s_{\mathrm{NN}}} = 5.02$ TeV in the absence in-medium rotation ($C = 0$ fm) at $T =$ 175, 300, and 400 MeV. The results indicate a strong sensitivity of the dissociation rate to both temperature and momentum. At $T = 400$ MeV, the J/$\psi$ exhibits an enhanced dissociation rate, which gradually decreases with increasing $p_{\mathrm{T}}$. The sudden drop in $\Gamma_{\mathrm{D}}$ around $p_{\mathrm{T}} \sim 10$ GeV/c reflects that $T_{\mathrm{eff}} \ll T = 400$ MeV. Further, at $T = 300$, and 175 MeV, the effect of $T_{\mathrm{eff}}$ significantly diminishes and $\Gamma_{\mathrm{D}}$ decreases as a function of $p_{\mathrm{T}}$. A similar trend is evident for other quarkonium states, including $\psi$(2S), $\Upsilon$(1S), and $\Upsilon$(2S). In particular, at temperatures of 300 and 175 MeV, $\psi$(2S) exhibits a higher dissociation probability than J/$\psi$ across the entire $p_{\mathrm{T}}$ range. This can be attributed to the comparatively lower binding energy of $\psi$(2S) relative to J/$\psi$.

Consequently, the reduced survival probability of $\psi$(2S) further supports the sequential melting scenario in the QGP medium. Furthermore, due to the higher

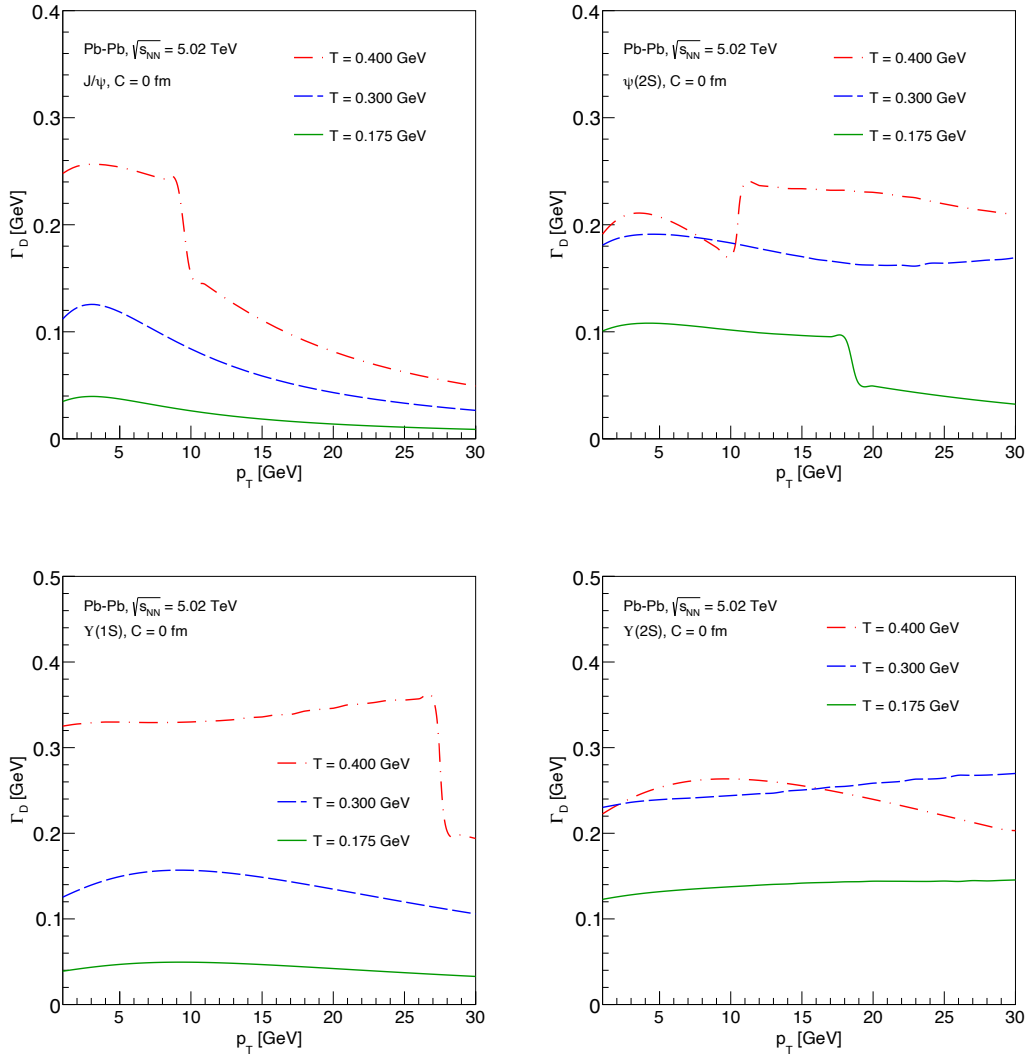



Figure 6.6: The total decay width $\Gamma_{\rm D}$ as a function of transverse momentum ($p_{\rm T}$) for J/$\psi$ (upper left), $\psi$(2S) (upper right), $\Upsilon$(1S) (lower left), and $\Upsilon$(2S) (lower right) in Pb–Pb collisions at $\sqrt{s_{\rm NN}}$ = 5.02 TeV. Results are presented for three different temperatures, such as $T$ = 0.400 GeV (red dotted dashed line), $T$ = 0.300 GeV (blue dashed line), and $T$ = 0.175 GeV (green solid line), with the circulation parameter $C$ = 0 fm [161].

mass of $\Upsilon$(1S) and $\Upsilon$(2S) states, which experience relatively stable effective temperatures as they traverse through the medium, as illustrated in Fig. 6.1. As a result, the dissociation probability for $\Upsilon$(1S) exhibits a modest decreasing trend towards higher $p_{\rm T}$. In contrast, for $\Upsilon$(2S), a slight increase in dissociation probability is observed with rising $p_{\rm T}$. Overall $p_{\rm T}$ dependence of $\Gamma_{\rm D}$ reflects the combined effects of the quarkonium decay width and its effective in-medium temperature. These contrasting behaviors offer important insights into the interplay between quarkonium binding energy and medium effects in heavy-ion collisions. Further, Fig. 6.7 and Fig. 6.8 demonstrate the impact of medium rotation on the $\Gamma_{\rm D}$, as a function of $p_{\rm T}$ for charmonium and bottomonium states, respectively. In the presence of a vortical background, the degeneracy in a quarkonium state is caused by spin-vorticity coupling. This implies that for $m_j = \pm 1$ state, the change in net $\Gamma_{\rm D}$ is prominent, which is an artifact of the term ($\sim m_j C/r^2$) appearing in the effective Hamiltonian. The spin–vorticity coupling alters the eigen energies and radial wave functions in a manner that depends on the sign of $m_j$. The spin-vorticity coupling term ($\sim m_j C/r^2$) is expected to alter the short-distance ($r \to 0$ ) behavior of quarkonium wave functions. At large distances, the behavior of quarkonium wave functions is negligible. For the QCD vacuum potential with $m_j = +1$, the additional term due to spin-orbit coupling lowers the effective potential barrier, thereby increasing the spatial extent of the wave function, or making it more peaked at short distances. Consequently, the dissociation probability rises, leading to a noticeably larger total decay width $\Gamma_{\rm D}$ compared to the non-rotating case. In contrast, for $m_j = -1$, the rotational term carries the opposite sign, effectively making the potential slightly more confining. This suppresses the sensitivity of the quarkonium wave function at short distances. For the $m_j = 0$ state, the quarkonium wave function is not affected due to the direct coupling to the rotation term, and naturally follows a trend similar to hydrogen atom wave functions. However, with the medium-modified color-singlet potential for quarkonia, the nature of the quarkonium wave function strongly

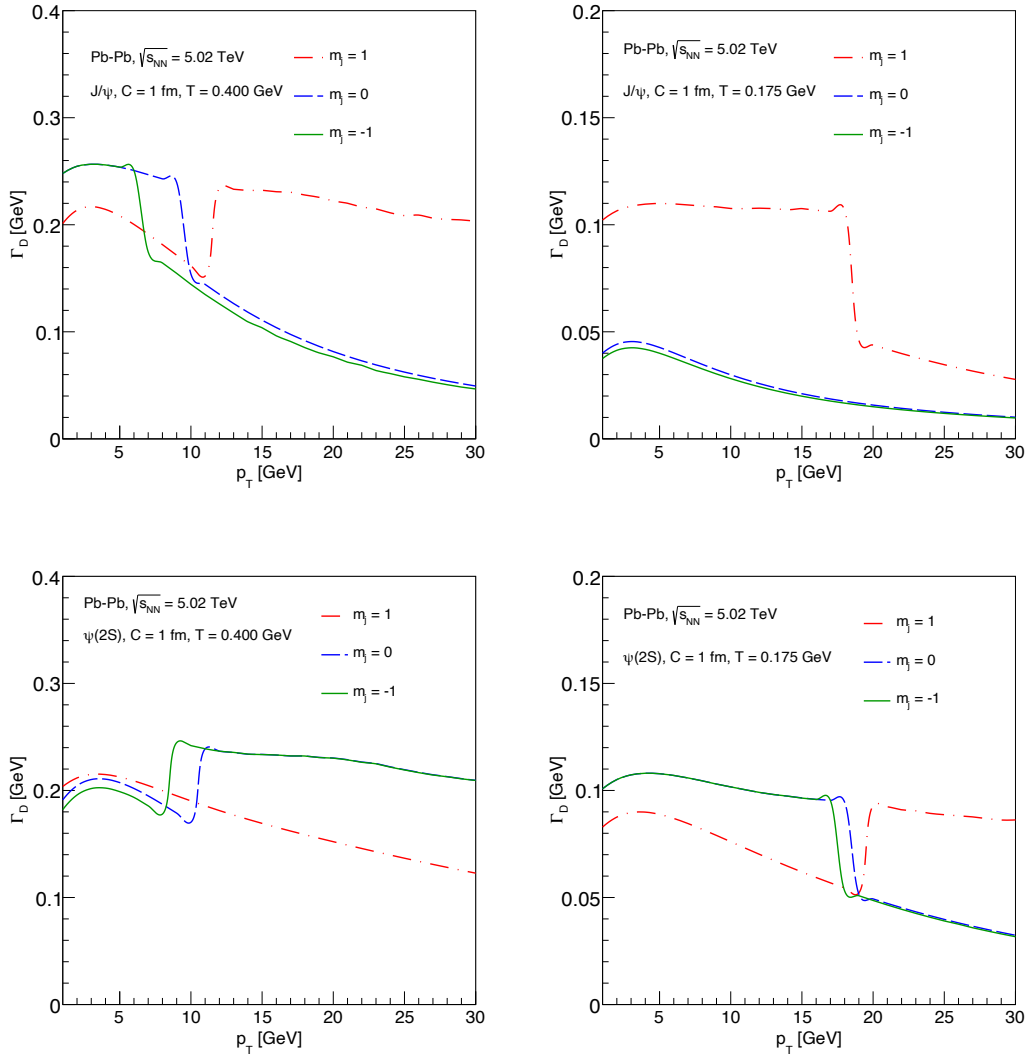



Figure 6.7: The total decay width $\Gamma_{\rm D}$ as a function of transverse momentum ($p_{\rm T}$) for J/$\psi$ (upper), and $\psi$(2S) (lower) in Pb–Pb collisions at $\sqrt{s_{\rm NN}} = 5.02$ TeV for three different spin projections $m_j = 1$ (red dotted dashed line), $m_j = 1$ (blue dashed line), $m_j = 1$ (green solid line) states with the circulation parameter $C = 1$ fm. The upper (lower) left and right panels present the J/$\psi$ ($\psi$(2S)) decay width for two different temperatures: $T = 0.400$ GeV and 0.175 GeV, respectively [161].

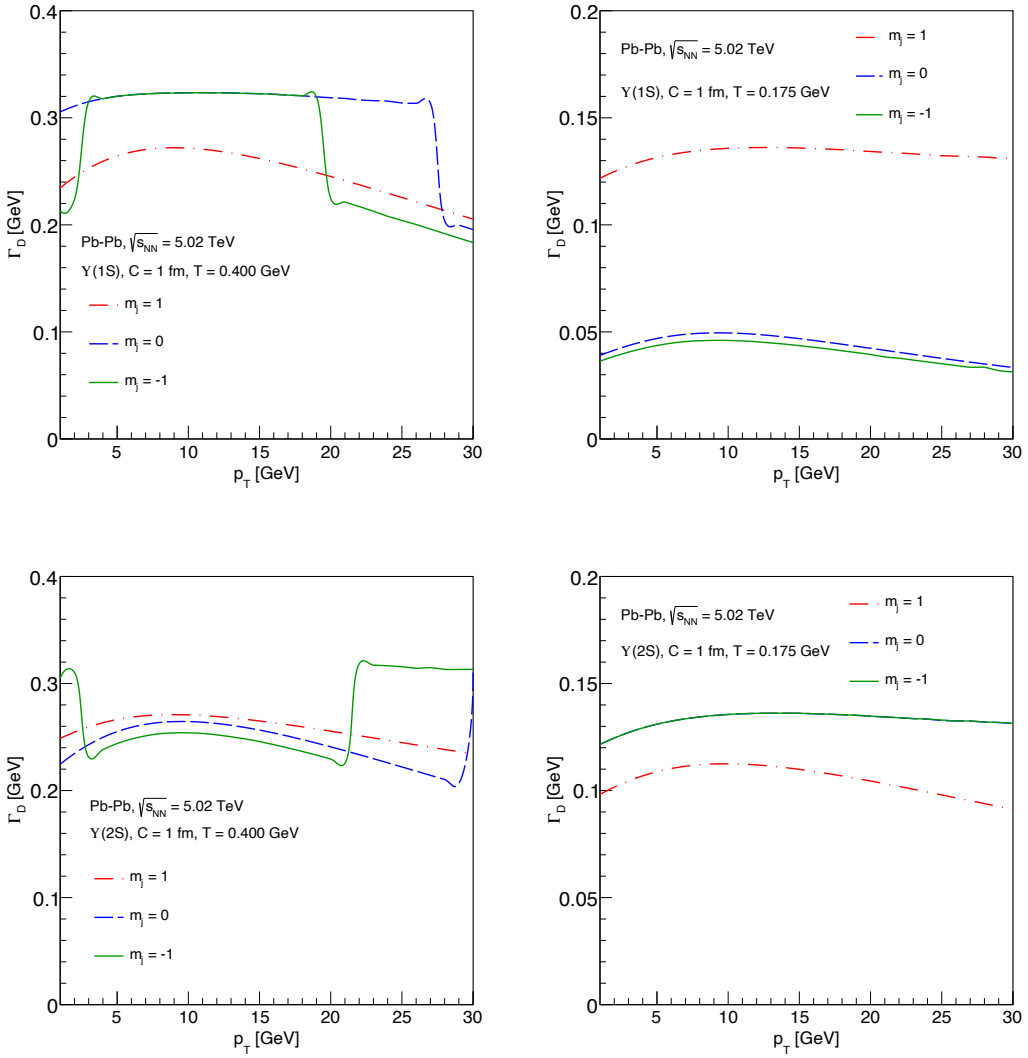



Figure 6.8: The total decay width $\Gamma_{\mathrm{D}}$ as a function of transverse momentum ($p_{\mathrm{T}}$) for $\Upsilon$(1S) (upper), and $\Upsilon$(2S) (lower) in Pb–Pb collisions at $\sqrt{s_{\mathrm{NN}}} = 5.02$ TeV for three different spin projections $m_j = 1$ (red dotted dashed line), $m_j = 1$ (blue dashed line), $m_j = 1$ (green solid line) states with the circulation parameter $C = 1$ fm. The upper (lower) left and right panels present the $\Upsilon$(1S) ($\Upsilon$(2S)) decay width for two different temperatures: $T = 0.400$ GeV and 0.175 GeV, respectively [161].

depends on temperature and the effective coupling constant. Further, the dissociation of the quarkonium state in medium is led by the imaginary part of the potential, which induces the Landau damping. Therefore, the net decay width of a quarkonium state is a complex interplay between the temperature-dependent quarkonium wave function and the imaginary part of the complex potential. It is observed that the behavior of the quarkonium wave function at $m_j = -1$ and $m_j = 0$ is almost similar. As a result, the net decay widths for the $m_j = 0$ and $m_j = -1$ states remain closely aligned for both charmonium and bottomonium. Meanwhile, the splitting between the $m_j = +1$ and the other two spin projections for $\Gamma_{\rm D}$ reflects the intrinsic asymmetry introduced by the $m_j C$ term in a rotating medium. This rotational effect is more pronounced for charmonium than bottomonium because the latter has a stronger binding, which reduces the relative impact of rotational distortions of the wave function. Nonetheless, for most cases, medium rotation preferentially enhances the dissociation of the $m_j = +1$ state in comparison with $m_j = 0$ and $m_j = -1$ states. Furthermore, the change in the $\Gamma_{\rm D}$ pattern with $p_{\rm T}$ in Fig. 6.7 and Fig. 6.8 is arises due to the additional contribution of $T_{\rm eff}$ as function of $p_{\rm T}$, which follows the similar explanation as Fig. 6.6.

### 6.3.3 Spin alignment of quarkonia

The dissociation probability of $m^{\rm th}$ spin state in the presence of rotation is given by;

$$\mathcal{P}_m = \exp\left[-\int_{\tau_0}^{\tau_f} \Gamma_{{\rm D},nlm}(\tau, p_{\rm T})\, d\tau\right]. \tag{6.47}$$

Here $m$ takes on the values $0, +1, -1$, representing the three distinct spin projections corresponding to the states 0, +1, and −1, respectively. The $\tau_0$ and $\tau_f$ are the proper times corresponding to the initial temperature $T_0$ and freeze-out temperature $T_f$ for the QGP medium. The dissociation rate, denoted as $\Gamma_{{\rm D},nlm}$, is

intricately linked to both the rotational dynamics and the specific spin projection states, $m$.

The spin alignment of vector mesons is measured via the elements of the spin density matrix $\rho_{m,m'}$, where $m$ and $m'$ denote the spin projections along a chosen quantization axis. For a vector meson with spin 1, the spin density matrix is defined as;

$$\rho_{m,m'} = \frac{\langle A_m A^*_{m'} \rangle}{\sum_{k=-1}^{k=+1} \langle |A_k|^2 \rangle} \tag{6.48}$$

where $A_m$ denotes the production amplitude for the spin projection $m$, and the denominator ensures proper normalization. The density matrix satisfies the normalization condition

$$\mathrm{Tr}(\rho) = \sum_{k=-1}^{k=+1} \rho_{m,m} = 1 \tag{6.49}$$

The diagonal elements of the spin density matrix are given by

$$\rho_{m,m} = \frac{\langle |A_m|^2 \rangle}{\sum_{k=-1}^{k=+1} \langle |A_k|^2 \rangle} \tag{6.50}$$

The production amplitude $A_m$ for the spin projection $m$, is related to the dissociation probability $\mathcal{P}_m$ via the relation

$$\mathcal{P}_m \equiv \langle |A_m|^2 \rangle \tag{6.51}$$

The $00^{\mathrm{th}}$ element of the $3 \times 3$ spin density matrix is defined in terms of the $\Gamma_{\mathrm{D},nlm}$;

$$\rho_{00} = \frac{\mathcal{P}_0}{\mathcal{P}_+ + \mathcal{P}_0 + \mathcal{P}_-} \tag{6.52}$$

Therefore, the spin alignment observable, i.e., $\rho_{00}$, is obtained using Eq. 6.52. With the above theoretical foundations, the discussion now focuses on the results obtained through this study.

Figure 6.9 shows $\rho_{00}$ as a function of charged-particle multiplicity, $\langle dN_{\mathrm{ch}}/d\eta \rangle$, for J/$\psi$ (upper left), $\psi$(2S) (upper right), $\Upsilon$(1S) (lower left), and $\Upsilon$(2S) (lower right)

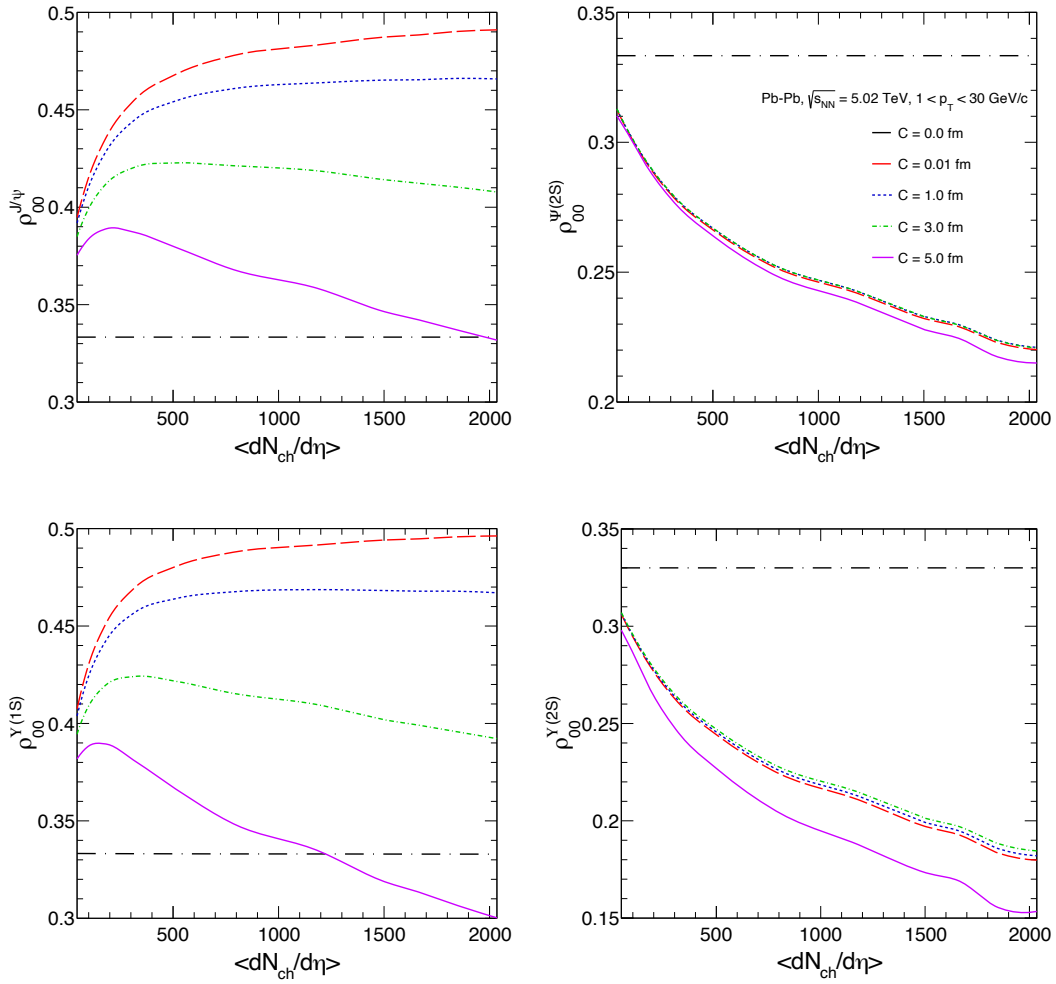



Figure 6.9: The spin alignment observable $\rho_{00}$ as a function of charged particle multiplicity ($\langle dN_{\rm ch}/d\eta \rangle$) for J/$\psi$ (upper left), $\psi$(2S) (upper right), $\Upsilon$(1S) (lower left), and $\Upsilon$(2S) (lower right) in Pb–Pb collisions at $\sqrt{s_{\rm NN}} = 5.02$ TeV integrated in the transverse momentum range 1< $p_{\rm T}$ < 30 GeV/c for different values of the circulation parameter, $C$ [161].

in Pb–Pb collisions at $\sqrt{s_{\rm NN}} = 5.02$ TeV at mid-rapidity. The charged particle multiplicity classes for Pb+Pb collisions at $\sqrt{s_{\rm NN}} = 5.02$ TeV are taken from ALICE experimental data [263] and reported in Table 6.1. The multiplicity-dependent $\rho_{00}$ is obtained by averaging over the transverse momentum range $1 \leq p_{\rm T} \leq 30$ GeV/$c$ using the weighting function $1/E_{\rm T}^4$ [236]. The resulting $p_{\rm T}$-integrated multiplicity-dependent spin alignment is expressed as;

$$\rho_{00}(b) = \frac{\int_{p_{\rm Tmin}}^{p_{\rm Tmax}} dp_{\rm T}\ \rho_{00}(p_{\rm T}, b)/(p_{\rm T}^2 + M_{nl}^2)^2}{\int_{p_{\rm Tmin}}^{p_{\rm Tmax}} dp_{\rm T}/(p_{\rm T}^2 + M_{nl}^2)^2} \tag{6.53}$$

| Multiplicity Class | Centrality Class | $\langle \frac{dN_{\rm ch}}{d\eta} \rangle$ |
|---|---|---|
| Mult. Class - 1 | (70-80)% | 44.9 ± 3.4 |
| Mult. Class - 2 | (60-70)% | 96.3 ± 5.8 |
| Mult. Class - 3 | (50-60)% | 183 ± 8 |
| Mult. Class - 4 | (40-50)% | 318 ± 12 |
| Mult. Class - 5 | (30-40)% | 512 ± 15 |
| Mult. Class - 6 | (20-30)% | 786 ± 20 |
| Mult. Class - 7 | (10-20)% | 1180 ± 31 |
| Mult. Class - 8 | (7.5-10)% | 1505 ± 44 |
| Mult. Class - 9 | (5.0-7.5)% | 1666 ± 48 |
| Mult. Class - 10 | (2.5-5.0)% | 1850 ± 55 |
| Mult. Class - 11 | (0-2.5)% | 2035 ± 52 |

Table 6.1: The $\langle \frac{dN_{\rm ch}}{d\eta} \rangle$ values measured for Pb+Pb collisions at $\sqrt{s_{\rm NN}} = 5.02$ TeV in $|\eta| < 0.5$ for 11 centrality classes are taken from ALICE experimental data [263].

The results for the spin alignment observable $\rho_{00}$ are presented for different values of the circulation parameter $C$, which characterizes the rotational strength of the medium. In the absence of experimental constraints on $C$, values ranging from

0.01 fm to 5.0 fm are considered to estimate the theoretical uncertainty in the prediction of $\rho_{00}$. The dashed horizontal line at $\rho_{00} = 1/3$ corresponds to the unpolarized limit and serves as the reference baseline. For the irrotational case ($C = 0$), all quarkonium states yield $\rho_{00} = 1/3$, independent of charged-particle multiplicity, reflecting the absence of spin–vorticity coupling.

For finite $C$, clear deviations from the baseline are observed, indicating that medium rotation induces spin-dependent dissociation and consequently generates spin alignment. In particular, the 1S states, J/$\psi$ and $\Upsilon$(1S), exhibit $\rho_{00} > 1/3$ over the full multiplicity range for small and intermediate values of $C$, suggesting comparatively weaker dissociation of the $m_j = 0$ state. At low multiplicities, where the medium temperature is smaller, vorticity effects are more pronounced, leading to an increase of $\rho_{00}$ with $\langle dN_{\rm ch}/d\eta \rangle$. With increasing multiplicity, the higher medium temperature enhances the dissociation of the degenerate $m_j = \pm 1$ states, while the spin–vorticity coupling associated with small $C$ becomes less effective. The interplay between spin-dependent dissociation and rotational effects therefore leads to a saturation of $\rho_{00}$ at high multiplicities. For larger values of $C$, the increased splitting of spin-dependent decay widths enhances the dissociation of the $m_j = 0$ state, driving $\rho_{00}$ toward the unpolarized limit for J/$\psi$ and producing a change in the spin-alignment orientation for $\Upsilon$(1S) at high multiplicities.

Figure 6.9 further shows that the quarkonium 2S states, $\psi$(2S) and $\Upsilon$(2S), exhibit $\rho_{00} < 1/3$ over the entire multiplicity range for all nonzero values of $C$. Owing to their relatively small binding energies, these states are more sensitive to thermal dissociation than to rotational effects. As a result, medium temperature dominates the spin-alignment dynamics, except possibly at very large values of $C$, leading to enhanced dissociation of the $m_j = 0$ state relative to the $m_j = \pm 1$ components. Consequently, $\rho_{00}$ for the 2S states decreases monotonically with increasing charged-particle multiplicity, indicating transverse spin alignment, while exhibiting only weak sensitivity to $C$. Overall, Fig. 6.9 demonstrates that the

multiplicity dependence of $\rho_{00}$ originates from the interplay between medium vorticity and temperature-driven dissociation. Rotational spin splitting significantly affects the tightly bound 1S states, whereas thermal effects dominate the more weakly bound 2S states. This state-dependent behavior highlights the sensitivity of quarkonium spin alignment to both quarkonium binding energy and the vortical structure of the QGP.

Figure 6.10 presents the $p_{\mathrm{T}}$ dependence of $\rho_{00}$ for J/$\psi$ (left panels) and $\psi$(2S) (right panels) in two multiplicity classes for Pb–Pb collisions at $\sqrt{s_{\mathrm{NN}}} = 5.02$ TeV. For the low-multiplicity class (upper panels), $\rho_{00}$ for J/$\psi$ remains above the unpolarized limit and exhibits a non-monotonic dependence on $p_{\mathrm{T}}$, increasing up to $p_{\mathrm{T}} \sim 15$ GeV/$c$ before gradually approaching $\rho_{00} = 1/3$ at higher $p_{\mathrm{T}}$. This behavior follows the $p_{\mathrm{T}}$ dependence of the net decay width $\Gamma_{\mathrm{D}}$, governed by the interplay between collisional damping, gluonic dissociation, and the effective temperature $T_{\mathrm{eff}}$. At higher multiplicities (lower panels), $\rho_{00}$ initially decreases up to $p_{\mathrm{T}} \sim 3$ GeV/$c$ and then increases at intermediate and high $p_{\mathrm{T}}$, reflecting the non-monotonic behavior of $T_{\mathrm{eff}}$ and its influence on the in-medium dissociation dynamics. For a fixed multiplicity class, increasing the circulation parameter $C$ systematically decreases $\rho_{00}$ without altering the overall $p_{\mathrm{T}}$ dependence, indicating that spin–vorticity coupling mainly modifies the relative dissociation probabilities of spin states, while the dominant momentum dependence remains controlled by $T_{\mathrm{eff}}$ and $\Gamma_{\mathrm{D}}$. The effect of vorticity is relatively weak for $C \lesssim 1$ fm and becomes more noticeable only at larger $C$ values. The $\psi$(2S) state exhibits $\rho_{00} < 1/3$ over the full $p_{\mathrm{T}}$ range for all multiplicity classes, indicating enhanced dissociation of the $m_j = 0$ component. Its $p_{\mathrm{T}}$ dependence also shows a non-monotonic structure, particularly at high multiplicities, where $\rho_{00}$ decreases up to $p_{\mathrm{T}} \sim$ 10–15 GeV/$c$ and rises at higher $p_{\mathrm{T}}$.

Owing to the weaker binding energy of $\psi$(2S), temperature-driven dissociation dominates over rotational effects, making the state highly sensitive to $T_{\mathrm{eff}}$. Consequently, the influence of the circulation parameter $C$ remains weak across the

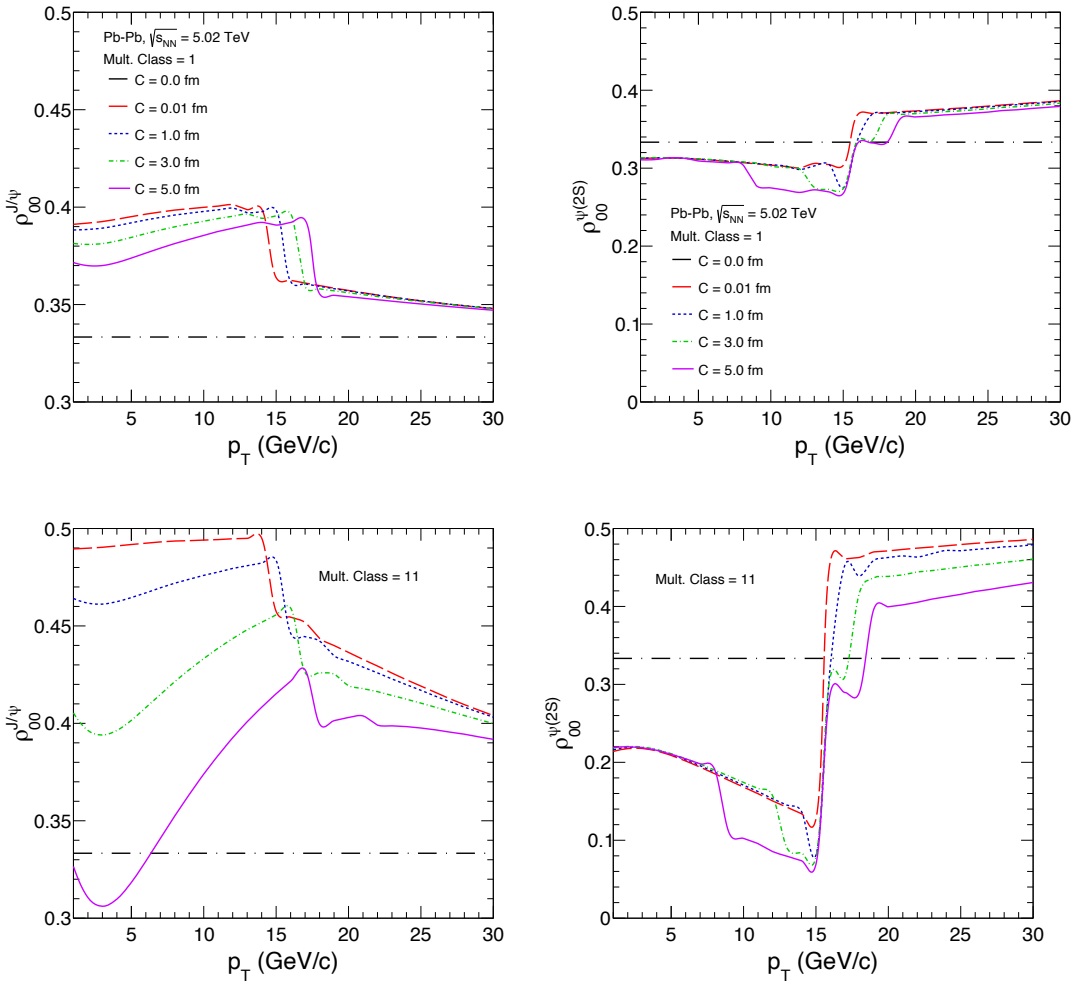



Figure 6.10: The spin alignment observable $\rho_{00}$ as a function of transverse momentum ($p_{\mathrm{T}}$) for J/$\psi$(1S) (left panel) and $\psi$(2S) (right panel) in Pb–Pb collisions at $\sqrt{s_{\mathrm{NN}}}$ = 5.02 TeV for various values of the circulation parameter, $C$, in two extreme multiplicity classes[161].

entire $p_{\mathrm{T}}$ range, indicating that spin–vorticity coupling provides only a subleading correction to the dominant thermal dissociation mechanism.

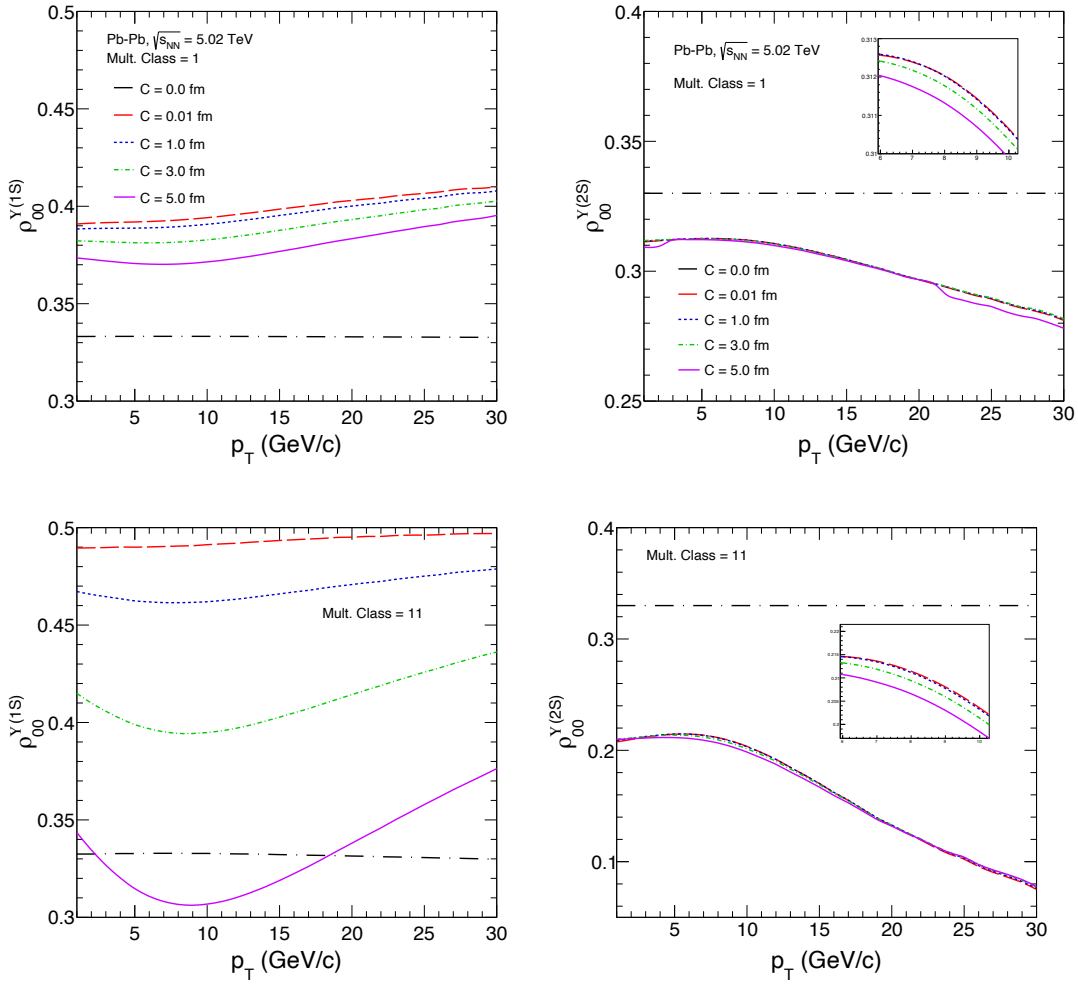



Figure 6.11: The spin alignment observable $\rho_{00}$ as a function of transverse momentum ($p_{\mathrm{T}}$) for $\Upsilon$(1S) (left panel) and $\Upsilon$(2S) (right panel) in Pb–Pb collisions at $\sqrt{s_{\mathrm{NN}}} = 5.02$ TeV for various values of the circulation parameter, $C$, in two extreme multiplicity classes [161].

Figure 6.11 presents the spin alignment of $\Upsilon$(1S) and $\Upsilon$(2S) as functions of $p_{\mathrm{T}}$ for different circulation parameters $C$ and multiplicity classes in Pb–Pb collisions at $\sqrt{s_{\mathrm{NN}}} = 5.02$ TeV. For $\Upsilon$(1S), $\rho_{00}$ generally increases with $p_{\mathrm{T}}$ at low multiplic-

ity due to the reduction of the net decay width $\Gamma_{\rm D}$ as the effective temperature $T_{\rm eff}$ decreases. At high multiplicity, $\rho_{00}$ decreases up to $p_{\rm T} \lesssim 10$ GeV/$c$ and then gradually rises at higher $p_{\rm T}$, reflecting the non-monotonic behavior of $T_{\rm eff}$. The systematic increase of $\rho_{00}$ with increasing $C$ across all multiplicity classes indicates a significant role of spin–vorticity coupling for the tightly bound $\Upsilon$(1S) state. In contrast, the $\Upsilon$(2S) state exhibits $\rho_{00} < 1/3$ over the entire $p_{\rm T}$ range, with only weak dependence on both $p_{\rm T}$ and $C$. Owing to its smaller binding energy, thermal dissociation dominates over rotational effects, leading to stronger suppression of the $m_j = 0$ component. As a result, the spin alignment of $\Upsilon$(2S) is governed mainly by thermal effects, while vorticity-induced modifications remain marginal. Overall, the observed $p_{\rm T}$ dependence of bottomonium spin alignment reflects the interplay between temperature-driven dissociation and rotational effects in the medium.

*In summary, the spin alignment of charmonium [J/$\psi$ and $\psi$(2S)] and bottomonium [$\Upsilon$(1S) and $\Upsilon$(2S)] states are estimated by obtaining the energy eigenvalues, total decay width, and quarkonium wavefunction in a thermal rotating medium. Both the diagonal and off-diagonal elements of the spin density matrix are calculated within a framework that incorporates the essential features of quarkonia evolution in an expanding vortical quark-gluon plasma. The diagonal spin density matrix element, $\rho_{00}$, is a sensitive probe of the thermalization of the medium, while the off-diagonal elements encode information about the quantum coherence of the system. The spin-dependent dissociation of quarkonium states is proposed as a viable microscopic mechanism contributing to quarkonium spin alignment. These findings deepen our understanding of quarkonium spin alignment in an anisotropic magneto-vortical thermal medium, shedding light on spin transport phenomena in heavy-ion collisions.*

# Chapter 7

## Spin polarization of hyperons and vector mesons

Based on:

1. "Impact of vorticity and viscosity on the hydrodynamic evolution of hot QCD medium", **B. Sahoo**, C. R. Singh, D. Sahu, R. Sahoo, and J. e. Alam, Eur. Phys. J. C **83**, 873 (2023).

2. "Probing rotational dynamics of quark gluon plasma via global vorticity", **B. Sahoo**, C. R. Singh, and R. Sahoo, Phys. Lett. B **880**, 140714 (2026).

3. "Global polarization of $\Lambda$ hyperons in hot QCD matter at TeV energies", **B. Sahoo**, C. R. Singh, and R. Sahoo, arXiv:2604.13701

4. "Impact of strong magnetic field, baryon chemical potential, and medium anisotropy on polarization and spin alignment of hadrons", **B. Sahoo**, C. R. Singh and R. Sahoo, Eur. Phys. J. C **85**, 580 (2025).

5. "Estimating Longitudinal Polarization of $\Lambda$ and $\bar{\Lambda}$ Hyperons at Relativistic Energies using Hydrodynamic and Transport models", **B. Sahoo**, C. R. Singh, and R. Sahoo, Phys. Scr. **100**, 065310 (2025).

---

This chapter begins with a brief discussion of the hydrodynamic evolution of the medium formed in ultrarelativistic heavy-ion collisions. The fundamental hydrodynamic equations governing the evolution of ideal, viscous, rotating viscous, and

magnetized rotating viscous fluids are systematically discussed. Subsequently, based on the properties of the medium at the freeze-out hypersurface, the spin polarization of hyperons and the spin alignment of vector mesons are calculated using the developed framework.

## 7.1 Hydrodynamic medium evolution

The strongly interacting transient state of the QGP medium created in ultra-relativistic collisions survives for a duration of a few fm/c. The spacetime evolution of QGP crucially depends on the EoS, vorticity, viscosity, and external magnetic field. The lifetime of a vortical QGP fluid is obtained within the ambit of relativistic second-order viscous hydrodynamics. To establish the theoretical framework, the hydrodynamic evolution of an ideal fluid is first presented before discussing the evolution of a vortical QGP fluid.

### 7.1.1 Ideal fluid

For an ideal fluid, the energy-momentum tensor ($T^{\mu\nu}$) does not contain a gradient of the hydrodynamic fields. This is called a $0^{\text{th}}$ order hydrodynamic model. The energy-momentum tensor for relativistic ideal hydrodynamics is

$$T^{\mu\nu}_{\text{Ideal}} = (\epsilon + P)u^{\mu}u^{\nu} - g^{\mu\nu}P \tag{7.1}$$

where $\epsilon$ is energy density, $P$ is pressure, $u^{\mu} = \gamma(1, \vec{v})$ is the four-velocity vector, with $\gamma = \frac{1}{\sqrt{1-\vec{v}^2}}$ being the Lorentz factor, and $g^{\mu\nu} = diag(1, -1, -1, -1)$ is the metric tensor. The conservation of energy-momentum (in the absence of an external field) is given by

$$\partial_{\mu}T^{\mu\nu} = 0 \tag{7.2}$$

Projecting Eq. (7.2) in the direction parallel to the fluid velocity, one obtains;

$$u_{\nu}\partial_{\mu}T^{\mu\nu} = 0 \tag{7.3}$$

Simplification of Eq. (7.3) leads to,

$$\partial_\mu((\epsilon + P)u^\mu) = u_\nu g^{\mu\nu}\partial_\mu P \tag{7.4}$$

Using the relation $D \equiv u^\mu\partial_\mu = \gamma\frac{d}{d\tau}$ in Eq. (7.4), the energy density evolution is given by

$$\frac{d\epsilon}{d\tau} = -\frac{1}{\gamma}(\epsilon + P)\ \partial_\mu u^\mu \tag{7.5}$$

For this study, a simple EoS is used to describe an ideal plasma of massless u, d, s quarks, and gluons. The pressure is given by $P = \epsilon/3 = aT^4$ with zero baryon chemical potential, where $a$ is the constant, defined as [264, 265]

$$a = \frac{\pi^2}{90}\left[16 + \frac{21}{2}N_f\right]$$

where $N_f = 3$, is the number of flavors. Using the EoS mentioned above, the equation governing the cooling rate can be obtained as,

$$\frac{dT}{d\tau} = -\frac{T}{3\gamma}\ \partial_\mu u^\mu \tag{7.6}$$

Equation 7.6 represents the cooling rate in $0^{\text{th}}$ order hydrodynamics (or for an ideal fluid).

### 7.1.2 Viscous fluid

The viscosity in a medium originates from the velocity gradient between fluid cells, which slows down the flow. Therefore, considering QGP as a viscous fluid modifies the medium evolution. The dissipative term ($\Pi^{\mu\nu}$) needs to be added to the energy-momentum tensor ($T^{\mu\nu}_{\text{Ideal}}$) representing the ideal fluid such that the total energy-momentum tensor is given by:

$$T^{\mu\nu} = T^{\mu\nu}_{\text{Ideal}} + \Pi^{\mu\nu} \tag{7.7}$$

where $\Pi^{\mu\nu}$ is the viscous stress tensor, expressed as,

$$\Pi^{\mu\nu} = \pi^{\mu\nu} + \Delta^{\mu\nu}\Pi$$

where $\Delta^{\mu\nu} = g^{\mu\nu} - u^{\mu}u^{\nu}$ is the projection operator, such that $\Delta^{\mu\nu}u_{\mu} = \Delta^{\mu\nu}u_{\nu} = 0$. The $\Pi^{\mu\nu}$ contains two parts; $\pi^{\mu\nu}$ accounts for the shear viscosity, and $\Delta^{\mu\nu}\Pi$ accounts for the bulk viscosity. For conformal fluids, the bulk viscous pressure does not contribute ($\Pi = 0$); therefore, it is neglected in the present study [266]. For first-order hydrodynamic theory, the $\pi^{\mu\nu}$ has the form;

$$\pi^{\mu\nu} = 2\eta_s \bigtriangledown^{<\mu} u^{\nu>} \tag{7.8}$$

where $\eta_s$ is the shear viscosity, with:

$$\bigtriangledown^{<\mu}u^{\nu>} \equiv \bigtriangledown^{(\mu}u^{\nu)} - \frac{1}{3}\Delta^{\mu\nu}\bigtriangledown^{\alpha}u_{\alpha}$$

where $\bigtriangledown^{(\mu}u^{\nu)}$ is defined as $A^{(\mu}B^{\nu)} = \frac{1}{2}\left(A^{\mu}B^{\nu} + A^{\nu}B^{\mu}\right)$. The space like derivative $\nabla^{\alpha} = \Delta^{\mu\nu}\partial_{\mu}$ is called as gradient operator.

For second-order hydrodynamic theory, the $T^{\mu\nu}$ contains both the first- and second-order gradients of the hydrodynamic fields. In Müller-Israel-Stewart (MIS) second-order theory, the $\pi^{\mu\nu}$ is given by [267],

$$\pi^{\mu\nu} = \eta_s \bigtriangledown^{<\mu} u^{\nu>} + \tau_{\pi}\left[\Delta^{\mu}_{\alpha}\Delta^{\nu}_{\beta}D\pi^{\alpha\beta}....\right] + O(\delta^2) \tag{7.9}$$

where $\tau_{\pi}$ is the relaxation time. Inclusion of the viscous term in energy density evolution changes Eq. (7.5) to the following form [264, 265];

$$\frac{d\epsilon}{d\tau} = -\frac{1}{\gamma}(\epsilon + P - \Phi)\,\partial_{\mu}u^{\mu} \tag{7.10}$$

Here $\Phi = \pi^{00} - \pi^{zz}$ is the difference between temporal and spatial components of the shear stress tensor representing the viscous term. For first-order theory, the shear stress term $\Phi = \frac{4\eta_s}{3\tau}$. The second-order MIS relaxation equation using Grad's 14-moment method for shear stress has the following form [264, 265];

$$D\pi^{\mu\nu} = -\frac{1}{\tau_{\pi}}\pi^{\mu\nu} - \frac{1}{2\beta_2}\pi^{\mu\nu}\left[\beta_2\theta + TD\left(\frac{\beta_2}{T}\right)\right] + \frac{1}{\beta_2}\bigtriangledown^{<\mu}u^{\nu>} \tag{7.11}$$

where $\theta \equiv \partial_{\mu}u^{\mu}$ represents the expansion of the system, $\tau_{\pi} = 2\eta_s\beta_2$ is the relaxation time, $\beta_2$ is the relaxation coefficient given as; $\beta_2 = 3/4P$. The shear

viscosity $\eta_s = bT^3$, where $b$ is defined as;

$$b = (1 + 1.70N_f)\frac{0.342}{(1 + N_f/6)\alpha_s^2 \ln(\alpha_s^{-1})}$$

Here, $N_f$ is the number of quark flavors, taken to be 3, and $\alpha_s$ is the strong coupling constant, taken to be 0.5.

Using the definition of $\Phi$, the evolution of viscous stress can be simplified to,

$$\frac{d\Phi}{d\tau} = -\frac{\Phi}{\gamma\tau_\pi} - \frac{\Phi}{2\gamma}\left(\partial_\mu u^\mu + \frac{\gamma}{\beta_2}T\frac{d}{d\tau}\left(\frac{\beta_2}{T}\right)\right) + \frac{1}{\gamma\beta_2}\left(\nabla^{<0}u^{0>} - \nabla^{<z}u^{z>}\right) \quad (7.12)$$

Using the EoS, $P = \epsilon/3 = aT^4$, the above equations can be written as;

$$\frac{dT}{d\tau} = -\frac{1}{\gamma}\left(\frac{T}{3} - \frac{T^{-3}\Phi}{12a}\right)\partial_\mu u^\mu \quad (7.13)$$

$$\frac{d\Phi}{d\tau} = -\frac{2aT\Phi}{3b\gamma} - \frac{\Phi}{2\gamma}\left(\partial_\mu u^\mu - \frac{5\gamma}{T}\frac{dT}{d\tau}\right) + \frac{4aT^4}{3\gamma}\left(\nabla^{<0}u^{0>} - \nabla^{<z}u^{z>}\right) \quad (7.14)$$

Thus, Eq. (7.13) and Eq. (7.14) represent the evolution of temperature and viscous term ($\Phi$) with the proper time, which cumulatively affects the temperature evolution in the second-order theory. Furthermore, with $\Phi = 0$ in Eq. (7.13) and Eq. (7.14), one gets the equation of motion for the ideal fluid.

### 7.1.3 Rotational viscous fluid

The discovery of global spin polarization of $\Lambda$ and $\bar{\Lambda}$ hyperons in non-central heavy-ion collisions provides compelling evidence that the medium produced in these collisions is the hottest, least viscous, and most vortical fluid ever created in the laboratory [52]. The resulting vorticity plays a central role in the phenomenology of heavy-ion collisions, affecting QCD thermodynamics [268], transport properties [269], phase transition [268], and spin polarization of produced hadrons [161, 163]. Moreover, the hydrodynamic evolution of the medium is significantly modified due to vorticity, slowing down the QGP lifetime [270].

In the non-relativistic system, the vorticity is defined as the curl of the velocity field of the fluid $\left(\boldsymbol{\omega} = \frac{1}{2}\boldsymbol{\nabla} \times \mathbf{v}\right)$. However, in relativistic hydrodynamics, several

other definitions of vorticity exist in the literature. These are useful in different physical contexts and are discussed in detail below [101, 271];

- **Kinematic vorticity**: The *kinematic vorticity* is defined as:

$$\omega^K_{\mu\nu} = -\frac{1}{2}\left(\partial_\mu u_\nu - \partial_\nu u_\mu\right) \tag{7.15}$$

  with $u_\mu$ being the four-velocity of the fluid. It is a natural generalization of the non-relativistic fluid, as its spatial components recover the non-relativistic form of the vorticity.

- **Temperature vorticity**: The *temperature vorticity* is defined as:

$$\omega^T_{\mu\nu} = \frac{1}{2}[\partial_\mu(Tu_\nu) - \partial_\nu(Tu_\mu)] \tag{7.16}$$

  Here, $T$ is the temperature of the fluid. The temperature vorticity for ideal uncharged fluids is relevant to the relativistic version of the Helmholtz–Kelvin theorem and helicity conservation equation.

- **Thermal vorticity:** The *thermal vorticity* is defined as:

$$\omega^\beta_{\mu\nu} = -\frac{1}{2}\left(\partial_\mu\beta_\nu - \partial_\nu\beta_\mu\right) \tag{7.17}$$

  where $\beta_\mu = \frac{u_\mu}{T}$ is the temperature four vector. The thermal vorticity characterizes the global equilibrium of the fluid, which is responsible for global and local spin polarization of particles in a fluid at global equilibrium, will be discussed in detail in the next section.

- **Enthalpy vorticity**: The *enthalpy vorticity* is defined as:

$$\omega^w_{\mu\nu} = -\frac{1}{2}\left[\partial_\mu\left(wu_\nu\right) - \partial_\nu\left(wu_\mu\right)\right] \tag{7.18}$$

where, $w = \frac{\epsilon+P}{n}$ is the enthalpy per particle, and $n$ is the number density. The enthalpy vorticity is the charged-fluid counterpart of the temperature vorticity.

In global equilibrium scenario, the thermal vorticity $\omega^{\beta}_{\mu\nu}$ is equivalent to the spin polarization tensor $\omega_{\mu\nu}$, which can be decomposed in the following way [187]:

$$\omega_{\mu\nu} = k_{\mu}u_{\nu} - k_{\nu}u_{\mu} + \epsilon_{\mu\nu\alpha\beta}u^{\alpha}\omega^{\beta} \tag{7.19}$$

where, $k_{\mu}$ and $\omega_{\mu}$ are defined in terms of spin polarization tensor;

$$k_{\mu} = \omega_{\mu\nu}u^{\nu}, \qquad \omega_{\mu} = \frac{1}{2}\epsilon_{\mu\nu\alpha\beta}\omega^{\nu\alpha}u^{\beta} \tag{7.20}$$

To hold the relation $k^{\mu}u_{\mu} = \omega^{\mu}u_{\mu} = 0$, the $\omega_{\mu}$ and $k_{\mu}$ are set to orthogonal to the fluid velocity $u_{\mu}$. Here $\epsilon_{\mu\nu\alpha\beta}$ is the Levi Civita antisymmetric four tensor, $\epsilon^{0123} = -\epsilon_{0123} = 1$. Considering the rotation in the $x$-$z$ plane, i.e. $\omega_{\mu} = (0, 0, \omega, 0)$, one needs to solve Eq. (7.19) and Eq. (7.20) self-consistently to obtain the spin polarization tensor, $\omega_{\mu\nu}$;

$$\omega_{\mu\nu} = \begin{pmatrix} 0 & 0 & 0 & 0 \\ 0 & 0 & 0 & \frac{\omega}{T} \\ 0 & 0 & 0 & 0 \\ 0 & -\frac{\omega}{T} & 0 & 0 \end{pmatrix}, \tag{7.21}$$

The rotational dynamics of the medium strongly depend on the choice of velocity profile. The velocity profile considered in the present study is given by $u^{\mu} = \gamma(1, v_x, 0, v_z)$. The $(v_x)$ and $(v_z)$ are given below;

$$v_x = \frac{\omega z}{2}, \quad v_z = \frac{z}{\tau} - \frac{\omega x}{2} \tag{7.22}$$

In Eq. 7.22, $x, z$ are the position coordinates, and $\tau$ is the proper time; $\omega$ denotes the vorticity of the system. Velocity along the rotation axis is considered to be zero, i.e., $v_y = 0$. The velocity profile is chosen in such a way that the transverse component of velocity $(v_x)$ depends on the longitudinal coordinates and the longitudinal component of velocity $(v_z)$ on the transverse coordinates [270, 272]. Both of these velocities lead to a 2+1D expansion of the fireball, while preserving the symmetry of the collision geometry. The velocity profiles used

here are the simplest parameterizations that capture the key physics of angular momentum transfer and vorticity generation in heavy-ion collisions. Specifically, the substantial initial orbital angular momentum of the colliding nuclei leads to shear flow development in the reaction plane, typically the $x$-$z$ plane. When $\omega = 0$, the velocity profile reduces to the 1+1D Bjorken flow.

The vorticity of the system is incorporated through the modified Euler's thermodynamic relation [187, 272, 273];

$$\epsilon + P = Ts + \mu n + \Omega \mathrm{w} \tag{7.23}$$

Here, $\Omega$ is the chemical potential corresponding to rotation, and w is the angular momentum (or spin) density. Furthermore, one can define $\Omega = \frac{T}{2\sqrt{2}}\sqrt{\omega_{\mu\nu}\omega^{\mu\nu}}$ and $\mathrm{w} = 4\frac{\mathrm{T}^3}{\pi^2}\cosh(\frac{\omega}{2\mathrm{T}})$. The detailed derivation of $\Omega$ and w are given in Refs [187, 272]. With the above inputs, at zero chemical potential, Eq. (7.23) reduces to;

$$\epsilon + P = Ts + \frac{2\omega T^3}{\pi^2}\cosh\left(\frac{\omega}{2T}\right) \tag{7.24}$$

Under the ideal massless limit, $\epsilon = 3P$, the above equation becomes,

$$\epsilon = \frac{3}{4}\left[Ts + \frac{2\omega T^3}{\pi^2}\cosh\left(\frac{\omega}{2T}\right)\right] \tag{7.25}$$

Differentiating the above equation with respect to proper time $\tau$,

$$\frac{d\epsilon}{d\tau} = \frac{3}{4}\left[\frac{Tds}{d\tau} + \frac{sdT}{d\tau} + \frac{2}{\pi^2}\frac{d}{d\tau}\left(\omega T^3\cosh\left(\frac{\omega}{2T}\right)\right)\right] \tag{7.26}$$

We use the standard form of entropy, $s = c + dT^3$, here c and d are the constant parameters and taken to be 0.00482 GeV$^2$, and 16.46, respectively [236]

$$\frac{d\epsilon}{d\tau} = \frac{3}{4}\left[\left(s + 3dT^3 + \frac{2F}{\pi^2}\right)\frac{dT}{d\tau} + \frac{2G}{\pi^2}\frac{d\omega}{d\tau}\right] \tag{7.27}$$

where, $F = 3T^2\omega\cosh\left(\frac{\omega}{2T}\right) - \frac{1}{2}\omega^2 T\sinh\left(\frac{\omega}{2T}\right)$ and $G = T^3\cosh\left(\frac{\omega}{2T}\right) + \frac{1}{2}\omega T^2\sinh\left(\frac{\omega}{2T}\right)$. Now, using Eq. (7.24) in Eq. (7.10), one obtains

$$\frac{d\epsilon}{d\tau} = -\frac{1}{\gamma}\left(Ts + \frac{2\omega T^3}{\pi^2}\cosh\left(\frac{\omega}{2T}\right) - \Phi\right)\partial_\mu u^\mu \tag{7.28}$$

Comparing Eq. (7.27) and Eq. (7.28), leads to

$$\frac{d\omega}{d\tau} = \frac{-\pi^2}{2G}\left[\frac{4T}{3\gamma}\left(s + \frac{2T^2\omega}{\pi^2}\cosh\left(\frac{\omega}{2\mathrm{T}}\right) - \frac{\Phi}{\mathrm{T}}\right)\partial_\mu \mathrm{u}^\mu + \left(\mathrm{s} + 3\mathrm{dT}^3 + \frac{2\mathrm{F}}{\pi^2}\right)\frac{\mathrm{dT}}{\mathrm{d}\tau}\right] \tag{7.29}$$

The temperature evolution equation can be obtained from the energy evolution Eq. (7.28) using the above EoS. The modified cooling rate is given by;

$$\frac{dT}{d\tau} = \frac{1}{\gamma}\left[-\frac{T}{3}\left(1 + \frac{2\omega T^2}{s\pi^2}\cosh\left(\frac{\omega}{2\mathrm{T}}\right)\right) + \frac{\Phi \mathrm{T}^{-3}}{12a}\right]\partial_\mu u^\mu \tag{7.30}$$

For the mentioned velocity profile, the detailed expressions for $u^\mu\partial_\mu$, $\partial_\mu u^\mu$, and $\bigtriangledown^{<0}u^{0>} - \bigtriangledown^{<z}u^{z>}$ are given in Ref. [270]. Finally, the three coupled non-linear differential equations (7.30), (7.14), and (7.29) are used to describe the medium evolution in terms of temperature, viscous term, and vorticity, respectively. For $\omega = 0$, these equations reduce to the second-order viscous hydrodynamics, and further, with $\Phi = 0$, it gives the solution corresponding to the ideal fluid.

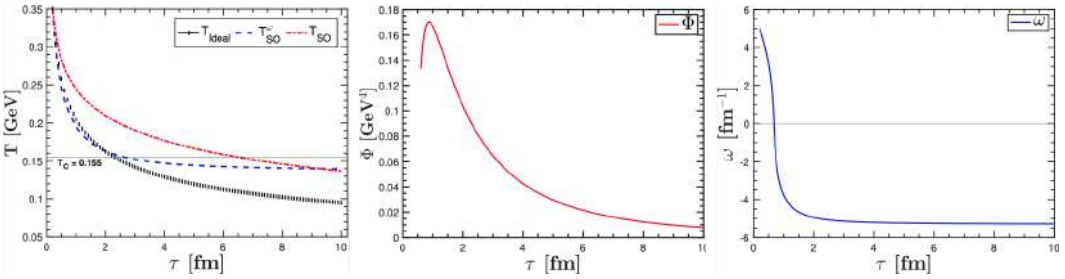



Figure 7.1: Temperature T (left), viscous term $\Phi$ (middle) and vorticity $\omega$ (right) as a function of time $\tau$ with the initial conditions: T = 0.35 GeV, $\tau_0$ = 0.2 fm, $\omega_0$ = 5.0 fm$^{-1}$. For $\mathrm{T_{Ideal}}$; $\omega = 0$ and $\Phi = 0$. For $\mathrm{T_{SO}}$; $\omega = 0$ but $\Phi \neq 0$. For $\mathrm{T}^{\omega}_{SO}$; $\omega \neq 0$ but $\Phi = 0$. In $\Phi$ plot, $\omega = 0$ and in $\omega$ plot, $\Phi = 0$ [270]. The notations used in this figure are the same as in Ref. [270].

Using the developed hydrodynamic framework, the following discussion focuses on the individual and combined effects of vorticity and the shear stress term on the medium evolution. The solution of these coupled differential equations is obtained with the initial conditions, i.e., $T_0$, $\tau_0$, $\omega_0$, and $\Phi_0$. The initial viscosity

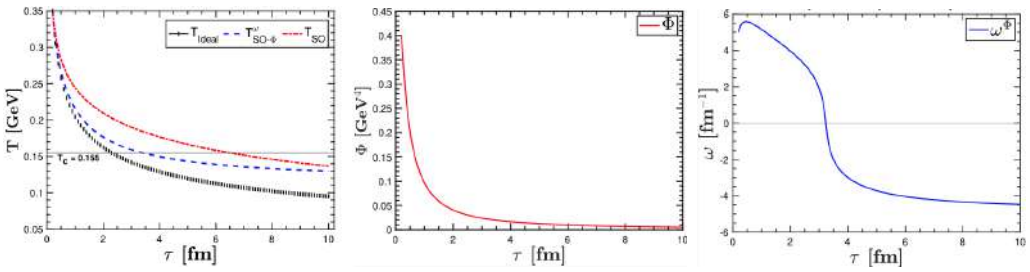



Figure 7.2: Temperature T (left), viscous term Φ (middle) and vorticity $\omega$ (right) as a function of time $\tau$ with the same initial conditions as Fig. 7.1 [164].

is given by; $\Phi_0 = \frac{1}{3\pi}\frac{s_0}{\tau_0}$ at $\tau = \tau_0$, where $s_0 = c + dT_0^3$ is the initial entropy density [236]. The initial condition for vorticity is chosen in such a way that the speed of rotation does not violate causality. On the other hand, the values of the position coordinates and pseudo-rapidity are chosen in such a way that it preserves causality. Given these conditions, the initial conditions are $T_0 = 0.35$ GeV, $\tau_0 = 0.2$ fm, and $\omega_0 = 5.0$ fm$^{-1}$. Figure 7.1 shows the medium evolution in terms of temperature (left), shear stress term (middle), and vorticity (right), where the vorticity and viscous term are not in a coupled framework. A rapid cooling is observed for an ideal fluid in the absence of any dissipation. In the presence of viscosity, additional heat production reduces the cooling. Similar to viscosity, vorticity also affects the cooling. Vortical motion present in the QGP medium imposes a constraint on the medium cooling.

During the first moments of evolution, the rotation speed is almost equal to the medium evolution rate; due to this, it does not affect the cooling rate much. Therefore, as shown in Fig. 7.1, initially upto $\tau \sim 2$ fm the cooling rate of $T^{\omega}_{SO}$ $\approx$ $T_{Ideal}$. Afterward, the system tries to hold back the evolution process when the rotation speed becomes smaller than the fluid velocity. The Φ dissipation and $\omega$ diffusion with time are plotted in the middle and right panels of Fig. 7.1. Initially, $\omega$ changes at a high rate, but at a later stage, it becomes almost constant in the absence of any other external force, while Φ approaches zero at large $\tau$. The negative value of $\omega$ in the plot depicts the change in the direction of the

rotation. This change in the rotation happens due to the initial fast expansion of the medium and the restriction imposed on it by the rotational motion of the fluid. This means medium evolution induces the rotation opposite to the initial vorticity. As time increases, vorticity also grows/diffuses in the opposite direction and gets saturated when the medium evolution becomes static.

Figure 7.2 shows the combined effect of vorticity and viscosity for large initial vorticity and a small thermalization time. In this case, $\mathrm{T}^{\omega}_{SO-\Phi}$ cools down slightly faster than $\mathrm{T}_{SO}$ due to the opposition of viscosity to changes in vorticity direction. Positive initial vorticity results in faster cooling, almost following the ideal rate. However, the presence of viscosity in the rotating fluid slows down $\mathrm{T}^{\omega}_{SO-\Phi}$ cooling compared to $\mathrm{T}_{\mathrm{Ideal}}$. The impact of viscosity on vorticity change can be observed in the variation of $\omega^{\Phi}$ as shown in the right panel of Fig. 7.2. The $\Phi$ evolution shown in the middle panel of Fig. 7.2 follows a similar pattern to the corresponding result shown in Fig. 7.2. The sensitivity of different initial conditions on medium evolution is studied in Ref. [270]. It is observed that the medium evolution is very sensitive to the initial temperature ($T$), the viscous term ($\Phi$) as well as on vorticity ($\omega$). These initial conditions significantly modify the medium evolution and QGP lifetime. Medium evolution becomes more complex with the coupling of vorticity and viscosity.

With this, the discussion now turns to the hydrodynamic evolution of the rotating viscous medium in the presence of a magnetic field.

### 7.1.4 Rotational viscous fluid in the presence of a magnetic field

Similar to the vorticity field, a strong magnetic field is produced in peripheral heavy-ion collisions. The magnetic field is expected to affect QCD thermodynamics [274], transport properties [275], phase transition [276], and spin polarization of produced hadrons [116, 125]. Moreover, the hydrodynamic evolution of the

medium is significantly modified due to the magnetic field by slowing down the QGP lifetime [270].

The hydrodynamic evolution of a rotating charged fluid in the presence of viscosity and a strong magnetic field is governed by the following energy–momentum tensor [277, 278];

$$T^{\mu\nu} = \left(\epsilon + P + B^2\right) u^\mu u^\nu - g^{\mu\nu}\left(P + \frac{B^2}{2}\right) - B^\mu B^\nu + \pi^{\mu\nu} \tag{7.31}$$

where $B^\mu = \frac{1}{2}\epsilon^{\mu\nu\alpha\beta}F_{\nu\alpha}u_\beta$ is the magnetic field in the fluid, $F_{\mu\nu}$ is the field strength tensor. The magnetic field four vector $B^\mu$ is space-like four vector with modulus $B^\mu B_\mu = -B^2$ and orthogonal to $u^\mu$ that is $B^\mu u_\mu = 0$, where $B = |\vec{\mathbf{B}}|$, and $|\vec{\mathbf{B}}|$ is the magnetic three vector.

The energy density evolution equation for a viscous medium in the presence of a magnetic field can be obtained from the energy-momentum conservation (Eq. (7.2)), and have the following form [277, 279];

$$\frac{d\epsilon}{d\tau} = -\frac{1}{\gamma}\left(\epsilon + P + B^2 - \Phi\right)\,\partial_\mu u^\mu - B\frac{dB}{d\tau} \tag{7.32}$$

Proceeding in the same way as Sec. 7.1.3, using the modified Euler equation $\epsilon + P = Ts + \mu n + \Omega \mathrm{w} + \mathrm{eBM}$, where $M = \chi_m B$ is the magnetization of the fluid, $\chi_m$ being the magnetic susceptibility, one obtains;

$$\begin{aligned}\frac{d\omega}{d\tau} = \frac{-\pi^2}{2G}\Bigg[&\left(s + 3dT^3 + \frac{2F}{\pi^2}\right)\frac{dT}{d\tau} + \left(\frac{4}{3} + 2e\chi_m\right)B\frac{dB}{d\tau} \\ &+ \frac{4T}{3\gamma}\left(s + \frac{2T^2\omega}{\pi^2}\cosh(\frac{\omega}{2\mathrm{T}}) + (1 + \mathrm{e}\chi_\mathrm{m})\frac{\mathrm{B}^2}{\mathrm{T}} - \frac{\Phi}{\mathrm{T}}\right)\partial_\mu \mathrm{u}^\mu\Bigg]\end{aligned} \tag{7.33}$$

The cooling rate in the presence of vorticity and a magnetic field is given by,

$$\frac{dT}{d\tau} = -\frac{T}{3\gamma}\left(1 + \frac{2\omega T^2}{s\pi^2}\cosh\left(\frac{\omega}{2T}\right) + \frac{\chi_m e B^2}{Ts}\right)\partial_\mu u^\mu + \frac{\Phi T^{-3}}{12a\gamma}\partial_\mu u^\mu \tag{7.34}$$

Moreover, Eq. (7.14) is used to include the viscous effect in this case as well. Finally, Eqs. (7.34), (7.14), and (7.33) describe the evolution of the medium in terms of temperature, viscous term, and vorticity, respectively, in the presence

of an external magnetic field. The changing magnetic field induces the electric field, making the medium evolution more complex. However, for simplicity, the induced electric field is neglected in this study. A time-dependent magnetic field is considered with a decay profile given by $B(\tau) = B_0(\tau_0/\tau)$. Here, $\tau_0$ denotes the thermalization time. In the numerical calculations, the value of $\chi_m$, $B_0$, and $\tau_0$ is taken to be 0.003, order of $m_\pi^2$ ($\approx 0.02$ GeV$^2$), and 0.3 fm, respectively. Using the above hydrodynamic framework, the following discussion moves towards the results obtained using the interplay among temperature, vorticity, shear stress term, and magnetic field.

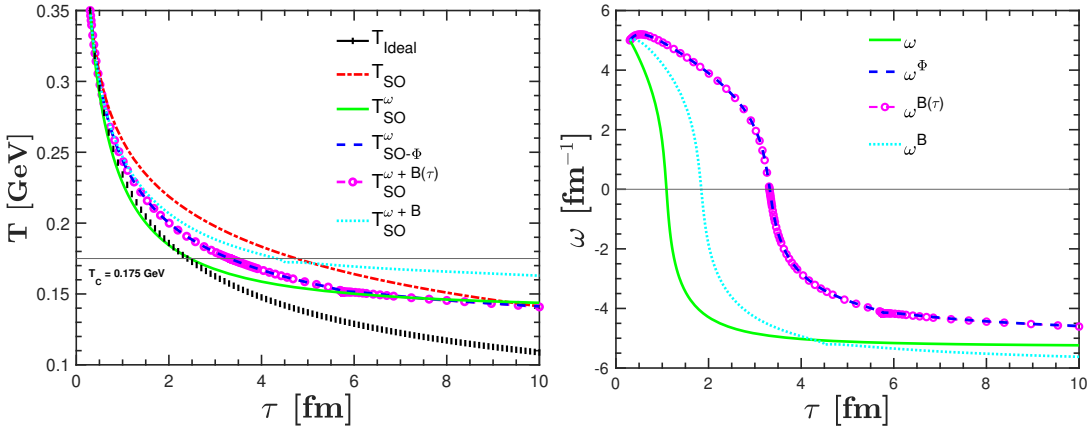



Figure 7.3: The temperature (T), and vorticity ($\omega$) are plotted as a function of time $\tau$ in the left and right panel, respectively, with the initial conditions: **T = 0.35 GeV, $\tau_0$ = 0.3 fm, $\omega_0$ = 5.0 fm$^{-1}$, $\Phi_0$ = 0.053 GeV$^4$**. In temperature plot, For $T_{Ideal}$; $\omega = 0$, $\Phi = 0$, $B = 0$. For $T_{SO}$; $\omega = 0$, $\Phi \neq 0$, $B = 0$. For $T^{\omega}_{SO}$; $\omega \neq 0$, $\Phi = 0$, $B = 0$. For $T^{\omega}_{SO-\Phi}$; $\omega \neq 0$, $\Phi \neq 0$, $B = 0$. For $T^{\omega+B(\tau)}_{SO}$; $\omega \neq 0$, $\Phi \neq 0$, and magnetic field is changing with time, B($\tau$). For $T^{\omega+B}_{SO}$; $\omega \neq 0$, $\Phi \neq 0$, and magnetic field is constant. In $\omega$ plot have the same meaning of notations as temperature plot [164].

Figure 7.3 shows the cooling rate (left) and vorticity dissipation rate (right), obtained by solving the coupled non-linear differential equations for $T$, $\omega$, and $\Phi$ in the presence of a magnetic field with the chosen initial conditions. The nota-

tions used in Fig. 7.3 are similar to Fig. 7.1 and 7.2. Additionally, $T^{\omega+B(\tau)}_{\mathrm{SO}-\Phi}$ and $T^{\omega+B}_{\mathrm{SO}-\Phi}$ correspond to cases with time-dependent and constant magnetic fields, respectively. The presence of a time-dependent magnetic field produces only a small modification to the cooling rate, whereas a constant magnetic field further suppresses cooling and delays freeze-out. The right panel of Fig. 7.3 presents the corresponding evolution of vorticity. Similar to the cooling rate, only small differences are observed between the rotating viscous case and the case including a time-dependent magnetic field, for one set of values of position and rapidity coordinates. However, a rapid initial decrease in vorticity is seen for the non-viscous rotating medium and for the rotating viscous medium with a constant magnetic field. The evolution of temperature, vorticity, viscosity, and magnetic fields at the freeze-out hypersurface is expected to strongly influence experimentally observable quantities, including hadron spin polarization.

Traditionally, the magnitude of vorticity and magnetic field produced in relativistic heavy ion collision laboratory is estimated from the experimental spin polarization measurement of $\Lambda$ and $\bar{\Lambda}$ hyperons. This is obtained under the assumption that the spin polarization phenomena primarily arises due to the combined effects of thermal vorticity and the magnetic field. Thus, in the thermal model in the non-relativistic limit, the spin polarization of $\Lambda$ and $\bar{\Lambda}$ hyperons can be expressed as:

$$\mathscr{P}_{\Lambda} = \frac{\hbar\,\omega}{2k_B T} + \frac{\mu_{\Lambda} B}{T} \tag{7.35}$$

$$\bar{\mathscr{P}}_{\Lambda} = \frac{\hbar\,\omega}{2k_B T} - \frac{\mu_{\bar{\Lambda}} B}{T} \tag{7.36}$$

From the above relations, the vorticity and magnetic field can be obtained as

$$\omega = \frac{(\mathscr{P}_{\Lambda} + \bar{\mathscr{P}}_{\bar{\Lambda}})k_B T}{\hbar}, \qquad B = \frac{(\mathscr{P}_{\Lambda} - \bar{\mathscr{P}}_{\bar{\Lambda}})T}{(\mu_{\Lambda} + \mu_{\bar{\Lambda}})} \tag{7.37}$$

However, in Ref. [280], an alternative method is proposed for extracting the magnitude of the global vorticity from the transverse momentum spectra of the hyperons and vector mesons. For instance, the left panel of Fig. 7.4 presents the global

vorticity $\Omega$ as a function of collision centrality for $\Lambda$, $\Xi^-$, $\bar{\Xi}^+$, $\Omega^-$, and $\bar{\Omega}^+$ obtained by analyzing the corresponding transverse momentum spectra in Pb+Pb collisions at mid-rapidity ($|y| < 0.5$) for $\sqrt{s_{\rm NN}} = 2.76$ TeV. It is observed that, for a given centrality class, the extracted vorticity differs among $\Lambda$, $\Xi^-$, and $\Omega^-$ hyperons, indicating a clear particle-species dependence of spin–vorticity coupling at freeze-out. This differential response arises from the distinct intrinsic properties of the hyperons, including mass, spin, and quark content, which influence their coupling to the rotating medium and shape their momentum spectra.

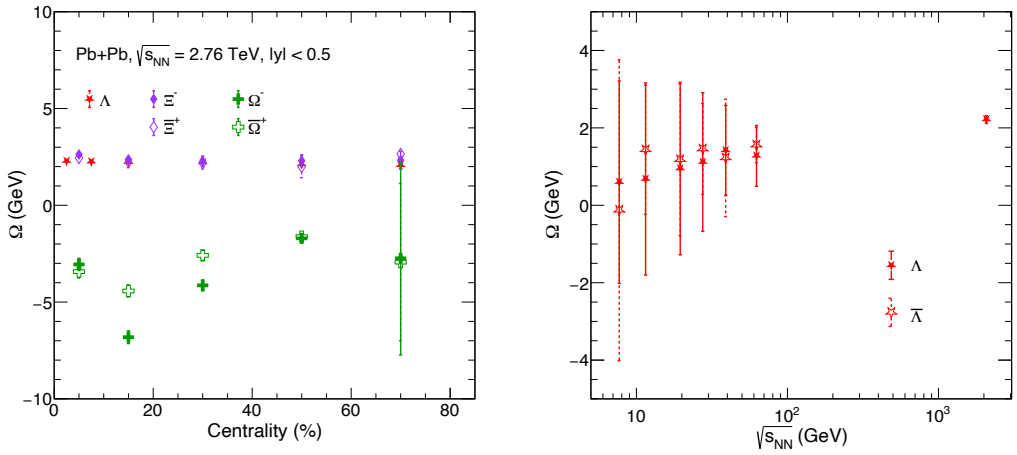



Figure 7.4: (Left) The global vorticity $\Omega$ as a function of collision centrality for $\Lambda$, $\Xi^-$, $\bar{\Xi}^+$, $\Omega^-$, and $\bar{\Omega}^+$ obtained in Pb+Pb collisions at mid-rapidity ($|y| < 0.5$) for $\sqrt{s_{\rm NN}} = 2.76$ TeV. (Right) $\Omega$ as a function of center of mass energies $\sqrt{s_{\rm NN}}$ for $\Lambda$, and $\bar{\Lambda}$ obtained in Au+Au and Pb+Pb collisions at mid-rapidity ($|y| < 0.5$) for 30-40% and 20-40% centrality classes, respectively [280].

Notably, the magnitude of $\Omega$ obtained from this spectral analysis is consistent, within uncertainties, with values inferred from $\Lambda$ and $\bar{\Lambda}$ spin polarization measurements using statistical thermal models in the non-relativistic limit [52]. The right panel of Fig. 7.4 illustrates the variation of global vorticity $\Omega$ as a function of center-of-mass energies $\sqrt{s_{\rm NN}}$ for $\Lambda$ and $\bar{\Lambda}$, indicating the same rotational alignment in hyperons and anti-hyperons. This observation indicates that the

spin-vorticity coupling acts identically on particles and antiparticles in all collision energies. It is worth mentioning that, although the vorticity field originates from the collective conversion of the initial orbital angular momentum of the system, its manifestation in rotational alignment varies among hadrons. Heavier particles couple more strongly to the vortical field and therefore exhibit a more pronounced rotational alignment than lighter ones. This mass-dependent behavior closely parallels the observed particle-species dependence of anisotropic flow coefficients, such as directed, elliptic, and triangular flow, in which a common collective background yields different magnitudes depending on hadron mass, quark content, and hadronization dynamics. Similarly, in the presence of a shared vortical medium, the resulting rotational alignment reflects the intrinsic properties of the produced hadrons.

Nevertheless, with a brief idea about the vorticity field, the magnetic field, and its effect on hydrodynamic evolution, the discussion now turns to the study of their effect on the spin polarization of hyperons.

## 7.2 Global spin polarization of hyperons

The physics motivation behind the global spin polarization of hyperons in ultrarelativistic heavy-ion collisions is discussed in Chapter 2. The study of spin polarization of $\Lambda$ hyperons in ultrarelativistic heavy-ion collisions provides insights into the angular momentum and vortical structure of the possible existence of QGP. Using the developed framework discussed in the above section, employing the vorticity and temperature profiles evaluated at the freeze-out hypersurface, the spin polarization of $\Lambda$ hyperons is determined in the following section. The contributions of thermal vorticity and magnetic field to the global spin polarization of $\Lambda$ hyperons are quantified, offering new insights into the magneto-vortical structure of the QCD matter.

### 7.2.1 Spin polarization due to thermal vorticity and magnetic field

The mean spin vector of a spin-1/2 particle, for example $\Lambda$ hyperon, with four-momentum $p_\delta$, arising from thermal vorticity and electromagnetic fields at leading order, is given by [116, 125],

$$\begin{aligned} S^\mu(x,p) &= -\frac{1}{8m_\Lambda}(1-f(x,p))\epsilon^{\mu\rho\sigma\delta}p_\delta\left[\bar{\omega}_{\rho\sigma} - \frac{2\mu_\Lambda F_{\rho\sigma}}{T}\right] \\ &= -\frac{1}{8}(1-f(x,p))\epsilon^{\mu\rho\sigma\delta}u_\delta\left[\bar{\omega}_{\rho\sigma} - \frac{2\mu_\Lambda F_{\rho\sigma}}{T}\right] \end{aligned} \tag{7.38}$$

where $m_\Lambda$ is the mass of $\Lambda$ hyperons, $\mu_\Lambda$ is the magnetic moment for $\Lambda$ hyperons, $\mu_\Lambda \approx -0.61\mu_N \approx -\frac{0.61e}{2m_p}$. The $\bar{\omega}_{\rho\sigma}$ is the thermal vorticity (defined in Eq. 7.17), $n_F$ is the covariant Fermi-Dirac phase space distribution, given by,

$$n_F = \frac{1}{\exp\left[\beta.p - \sum_j \mu_j q_j/T\right] + 1} \tag{7.39}$$

Equation 7.38 has an interesting physical interpretation. The mean spin vector is proportional to the axial thermal vorticity vector measured in the co-moving frame of the particle. In general, an antisymmetric tensor can be decomposed into two space-like vectors, namely an axial vector and a polar vector, with respect to an observer moving with four-velocity $u^\mu$:

$$\omega^\mu = \frac{1}{2}\epsilon^{\mu\rho\sigma\delta}\omega_{\rho\sigma}u_\delta, \qquad k^\mu = \omega^{\mu\nu}u_\nu. \tag{7.40}$$

Similarly, the electromagnetic field strength tensor $F^{\mu\nu}$ can be decomposed into electric and magnetic components as:

$$B^\mu = \frac{1}{2}\epsilon^{\mu\rho\sigma\delta}F_{\rho\sigma}u_\delta, \qquad E^\mu = F^{\mu\nu}u_\nu. \tag{7.41}$$

Now, using the co-moving axial thermal vorticity and co-moving magnetic field, the spin polarization vector in Eq. 7.38 can be rewritten as

$$S^\mu(x,p) = \frac{1}{4}(1-n_F)\left[\bar{\omega}^\mu - \frac{2\mu_\Lambda B^\mu}{T}\right] \tag{7.42}$$

Below, the mean spin vector is obtained by integrating Eq. 7.42 over the decoupling freeze-out hypersurface $\Sigma$,

$$S^{\mu}(p) = \frac{\int_{\Sigma} d\Sigma_{\lambda} p^{\lambda}\, n_F S^{\mu}(x,p)}{\int_{\Sigma} d\Sigma_{\lambda} p^{\lambda}\, n_F}, \tag{7.43}$$

Equation 7.43 can be further expanded as follows:

$$S^{\mu}(p) = \frac{1}{4}\frac{\int_{\Sigma} d\Sigma_{\lambda} p^{\lambda}\, n_F(1-n_F)\left[\bar{\omega}^{\mu} - \frac{2\mu_{\Lambda}B^{\mu}}{T}\right]}{\int_{\Sigma} d\Sigma_{\lambda} p^{\lambda}\, n_F}, \tag{7.44}$$

Integrals of Eq. 7.44 can be solved using cylindrical coordinates and given by;

$$S_y = \frac{1}{4\,T_{\rm dec}}\frac{\int \tau r \sum_{n=1}^{\infty} (\omega_y - 2\mu_{\Lambda}B_y) m_T I_0(O_1) K_1(O_2)\, dr}{\int \tau r \sum_{n=1}^{\infty} m_T I_0(O_1) K_1(O_2)\, dr} \tag{7.45}$$

where I's, K's are Bessel functions and $O_1 = n\frac{p_T}{T}\sinh y_T$, $O_2 = n\frac{m_T}{T}\cosh y_T$. The above Eq. 7.45 is obtained by assuming that hadronization happens at the decoupling hypersurface with a constant proper time $\tau$ and a temperature $T = T_{\rm dec}$. A detailed derivation of Eq. 7.45 is provided in Ref. [164]. In the rest frame of the particle, the spin vector is $S^{*\mu} = (0, \mathbf{S}^*)$, which is obtained by using the Lorentz transformation, given as:

$$\mathbf{S}^* = \mathbf{S}(\mathbf{p}) - \frac{\mathbf{S}\cdot\mathbf{p}}{E(E+m)}\mathbf{p} \tag{7.46}$$

Finally, the net spin polarization is defined as;

$$\mathbf{P} = 2\mathbf{S^*} \tag{7.47}$$

Figure 7.5 presents the global spin polarization of $\Lambda$ hyperons as a function of $p_{\rm T}$, obtained within the coupled hydrodynamic framework described in the previous section. In contrast to conventional hydrodynamic approaches, where the vorticity profile arises from the solution of the Israel–Stewart equations, the present framework explicitly incorporates vorticity both in the hydrodynamic evolution equations and in the velocity profile.

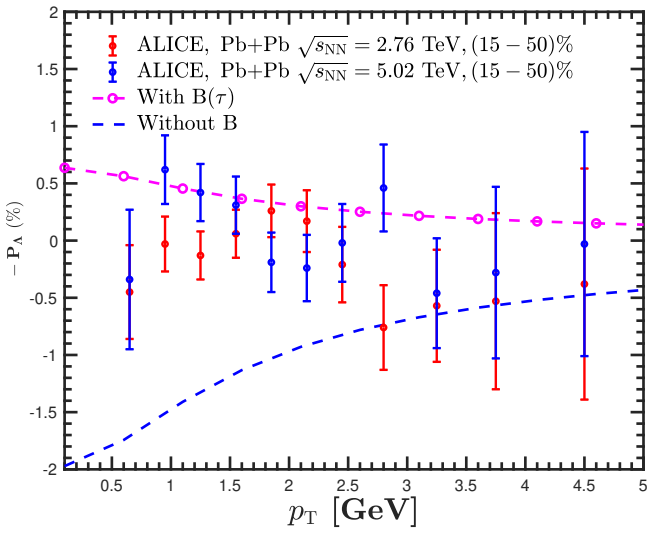



Figure 7.5: The global spin polarization of Λ hyperons as a function of transverse momentum ($p_{\rm T}$) for a rotating viscous medium with a time-varying magnetic field (magenta), and without a magnetic field (blue) [164]. The theoretical results are compared with the ALICE experimental measurement in Pb+Pb collisions at $\sqrt{s_{\rm NN}} = 2.76$ and 5.02 TeV at (15-50)% collision centrality [69].

We derive a dissipation-rate equation for vorticity in the presence of a magnetic field and use it to study the spin polarization of Λ hyperons under two scenarios: a rotating viscous medium with a time-dependent magnetic field (magenta line in Fig. 7.5) and a rotating viscous medium without a magnetic field (blue line). The results are compared with recent ALICE measurements in Pb+Pb collisions at $\sqrt{s_{\rm NN}} = 2.76$ and 5.02 TeV for the (15–50)% centrality class [69]. The hydrodynamic calculations employ initial conditions according to the considered collision system, energy, and centrality. A qualitative agreement between the model predictions and experimental data is observed. The spread between the two scenarios may be interpreted as an estimate of the theoretical uncertainty arising from different initial conditions. Overall, this study provides a novel framework for describing vorticity evolution and the resulting spin polarization of Λ hyperons in relativistic heavy-ion collisions.

The following section presents an alternative approach to calculating the spin polarization of various hyperons. In this approach, the global spin polarization of hyperons is determined from the global polarization of quarks.

### 7.2.2 Spin polarization due to Debye mass

The global quark polarization is obtained through parton elastic scattering within the framework of an effective static potential model. This model uses an effective mass, or Debye mass, to incorporate the parton scattering, which induces the quark polarization [79, 80, 82, 83], given as,

$$P_q = -\frac{\pi}{2}\frac{m_D p}{E(E+m_q)} \tag{7.48}$$

where $E = \sqrt{p^2+m_q^2}$, $p$ and $m_q$ are the energy, momentum, and mass of the quark in the center of mass frame of the parton scattering, $m_D$ is the Debye mass. This global quark polarization leads to the global hyperons' spin polarization at the hadronization stage. The spin polarization of hyperons under recombination and fragmentation processes is explicitly reported in the literature [79, 117]. The global spin polarization due to exclusive recombination process for $\Lambda$, $\Sigma^{\pm}$, $\Xi^{-}$, $\Omega^{-}$, and $\Delta^{++}$ hyperons are given as [79, 117];

$$P_{\Lambda}^{rec} = P_s, \quad P_{\Xi^-}^{rec} = \frac{4P_s - P_d - 3P_dP_s^2}{3-4P_dP_s+P_s^2}, \quad P_{\Sigma^+}^{rec} = \frac{4P_u - P_s - 3P_sP_u}{3-4P_uP_s+P_u^2} \tag{7.49}$$

$$P_{\Sigma^-}^{rec} = \frac{4P_d - P_s - 3P_sP_d}{3-4P_dP_s+P_d^2}, \quad P_{\Delta^{++}}^{rec} = \frac{P_u(5+P_u^2)}{3(1+P_u^2)}, \quad P_{\Omega^-}^{rec} = \frac{P_s(5+P_s^2)}{3(1+P_s^2)} \tag{7.50}$$

The hyperon spin polarization from inclusive recombination is difficult to estimate. However, at the extreme limit of inclusive recombination (i.e., fragmentation), the hyperon spin polarization due to polarized quarks is estimated in Ref. [79]. The spin-polarization due to fragmentation process for $\Lambda$, $\Sigma^{\pm}$, $\Xi^{-}$, $\Omega^{-}$,

and $\Delta^{++}$ hyperons are given as;

$$P_{\Lambda}^{frag} = \frac{n_s P_s}{n_s + 2f_s}, \quad P_{\Xi^-}^{frag} = \frac{4n_s P_s - f_s P_d}{3(2n_s + f_s)}, \quad P_{\Sigma^+}^{frag} = \frac{4f_s P_u - n_s P_s}{3(n_s + 2f_s)} \tag{7.51}$$

$$P_{\Sigma^-}^{frag} = \frac{4f_s P_d - n_s P_s}{3(n_s + 2f_s)}, \quad P_{\Omega^-}^{frag} = \frac{P_s}{3}, \; P_{\Delta^{++}}^{frag} = \frac{P_u}{3} \tag{7.52}$$

In the presence of the magnetic field, the global quark polarization defined in Eq. 7.48 is modified into

$$P_q = -\frac{\pi}{2} \sum_l \frac{m_D p}{E_z(E_z + m_q)} \tag{7.53}$$

and,

$$E_z = \sqrt{p_z^2 + m_q^2 + 2l|Q_i eB|}$$

where $p_z$ is the momentum component along the z direction, $l = 0, 1, 2 \ldots$ denotes the order of Landau levels, and $Q_i e$ is the fractional charge of the quark. The detailed derivation of Eq. 7.53 is given in Ref. [159].

### Debye Mass with Baryon Chemical Potential

Finite $\mu_B$ dictates the dominance of the number of quarks over anti-quarks; such an imbalance affects the final production yield of hadrons. In nature, any order parameter or disparity ultimately leads to the polarization of the system. Likewise, a non-zero baryon chemical potential can be the source of a polarized QGP medium. Any change brought to the QGP affects its effective mass; as a consequence, $\mu_B$ is incorporated in the Debye mass. In a hot and high baryon density medium (T, $\mu_B \gg m_q$, with $m_q$ as the light quark mass), the leading-order HTL/HDL calculation predicts a resultant Debye mass which has the following form [281–284];

$$m_D^2(T, \mu_B) = 4\pi\alpha_s(\Lambda^2)\left[T^2\left(\frac{N_c}{3} + \frac{N_f}{6}\right) + \sum_f \frac{\mu_B^2}{18\pi^2}\right] \tag{7.54}$$

Here, the strong coupling constant $\alpha_s(\Lambda^2)$ takes the form given in Eq. 6.16, and in the presence of baryon chemical potential, the renormalization scale is modified

to

$$\Lambda = 2\pi\sqrt{T^2 + \frac{\mu_B^2}{\pi^2}} \tag{7.55}$$

The Debye mass at zero baryon chemical potential can be obtained by setting $\mu_B = 0$ in Eq. 7.54.

The effect of the magnetic field and medium anisotropy on the Debye mass is discussed in Chapter 6.

## Net Debye Mass

The combine effect of $eB$, $\mu_B$, and $\xi$ on Debye mass can be obtained using the following relation [245];

$$m_D(T, \mu_B, eB, \xi) = m_D(T, \mu_B, eB)\Big[f_1(\xi)\cos^2\theta + f_2(\xi)\Big]^{-\frac{1}{4}} \tag{7.56}$$

and $m_D(T, \mu_B, eB)$ is the Debye mass in the presence of both magnetic field and baryon chemical potential calculated from the gluon self-energy tensor in Ref. [285]. It has the following form;

$$m_D(T, \mu_B, eB) = \sqrt{4\pi\alpha_s(\Lambda^2, |eB|)}\ \times \sqrt{\left[T^2\frac{N_c}{3} + \sum_f \frac{|q_f eB|}{4\pi^2 T}\int_0^\infty dp_z\{n^+(E_z)(1-n^+(E_z)) + n^-(E_z)(1-n^-(E_z))\}\right]} \tag{7.57}$$

with

$$n^\pm(E_z) = \left[\exp\frac{(E_z \mp \mu_B)}{T} + 1\right]^{-1} \tag{7.58}$$

The $n^+(E_z)$ and $n^-(E_z)$ are the phase-space distribution functions of quarks and anti-quarks, respectively. Furthermore, it is important to mention that the Debye mass at the leading order has the same form in the absence of a magnetic field, $\mu_B \to 0$, and $\xi \to 0$ limit.

With the established theoretical framework, the following discussion presents the results obtained on the spin polarization of various hadrons due to the magnetic field ($eB$), baryon chemical potential ($\mu_B$), and anisotropy parameter ($\xi$).

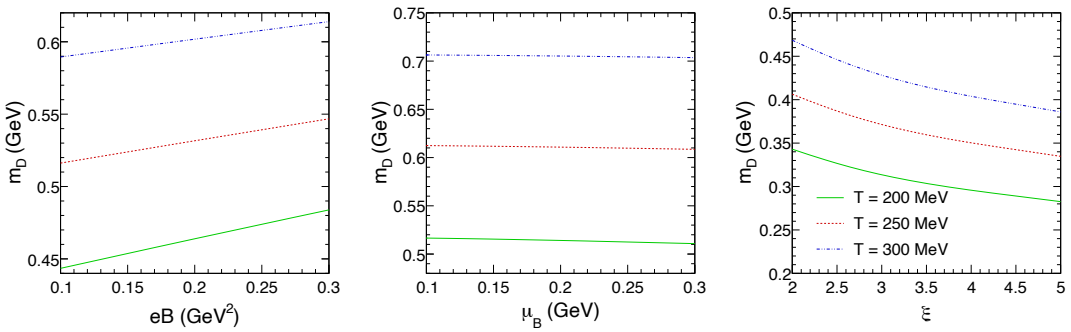



Figure 7.6: The variation of Debye mass ($m_D$) as a function of magnetic field ($eB$) (left panel), baryon chemical potential ($\mu_B$) (middle panel), and anisotropic parameter ($\xi$) (right panel) for three different values of temperatures, i.e T = 200 MeV, T=250 MeV, and T = 300 MeV [159].

Before presenting the spin polarization observables, Fig. 7.6 illustrates the modifications of the effective Debye mass due to the magnetic field, baryon chemical potential, and anisotropy parameter to validate the consistency of the framework. The left, middle, and right panels of Fig. 7.6 show the dependence of the effective Debye mass on $eB$, $\mu_B$, and $\xi$, respectively, for temperatures $T$ = 200, 250, and 300 MeV.

The influence of the external magnetic field on the Debye mass is found to be more pronounced at lower temperatures. The middle panel of Fig. 7.6 indicates a modest decrease in the Debye mass with increasing baryon chemical potential in a baryon-rich medium. Although the overall effect remains small, it becomes relatively more noticeable at lower temperatures. The right panel of Fig. 7.6 demonstrates that the Debye mass decreases significantly with increasing anisotropy parameter. Based on these observations, it can be inferred that medium effects are effectively encoded in the Debye mass, which appears to be more sensitive to the anisotropy parameter than to the magnetic field or baryon chemical potential. The Debye mass characterizes the effective degrees of freedom in the medium: a smaller Debye mass indicates a transition from partonic to hadronic degrees of

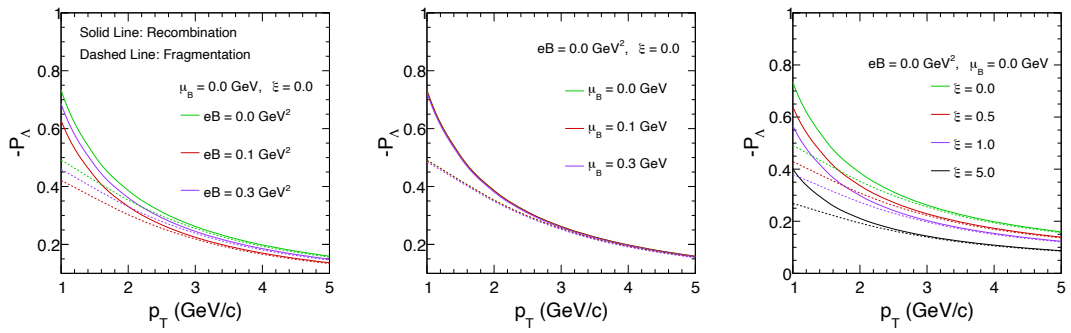



Figure 7.7: The variation of $\Lambda$ hyperon polarization ($P_\Lambda$) as a function of transverse momentum ($p_\mathrm{T}$) due to recombination (solid line) and the fragmentation (dashed line) process of hadronization in the presence of a magnetic field ($eB$) (left panel), baryon chemical potential ($\mu_B$) (middle panel), and anisotropic parameter ($\xi$) (right panel) at temperature T = 200 MeV [159].

freedom. Since the Debye mass depends on both the medium temperature and the coupling strength, external magnetic fields enhance the medium energy scale and strengthen the coupling constant, leading to an increase in the Debye mass, as observed in the left panel of Fig. 7.6. In contrast, a finite baryon chemical potential introduces additional energy into the medium while simultaneously reducing the coupling strength, resulting in a slight decrease in the Debye mass with increasing $\mu_B$. On the other hand, momentum-space anisotropy does not directly modify the coupling strength; instead, the non-uniform partonic distribution characterized by $\xi$ reduces the effective screening mass. Consequently, a significant suppression of the Debye mass is observed for larger values of $\xi$. Although the combined effects of magnetic field, baryon chemical potential, and anisotropy on the Debye mass can be evaluated using Eq. 7.57, they are not explicitly shown here. Nevertheless, their overall influence can be qualitatively inferred from Fig. 7.6.

Understanding how polarized quarks recombine to form polarized hyperons is essential for describing the final-state spin polarization. The spin polarization of

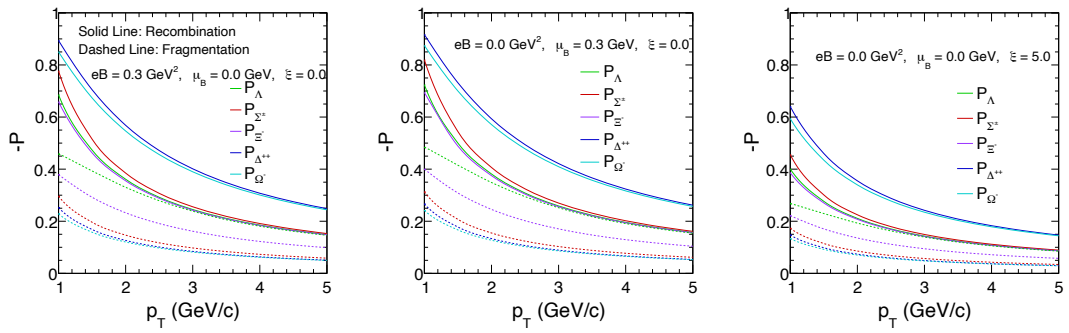



Figure 7.8: The variation of baryon polarization as a function of transverse momentum ($p_{\mathrm{T}}$) in the recombination (solid line) and fragmentation (dashed line) processes of hadronization due to the magnetic field ($eB$) (left panel), baryon chemical potential ($\mu_B$) (middle panel), and anisotropic parameter ($\xi$) (right panel) at temperature T = 200 MeV [159].

hyperons strongly depends on the hadronization mechanism. The spin polarization of $\Lambda$, $\Sigma^{\pm}$, $\Xi^{-}$, $\Delta^{++}$, and $\Omega^{-}$ hyperons is studied for two different hadronization mechanisms: (i) recombination and (ii) fragmentation. The recombination results are obtained using Eqs. 7.49 and 7.50, while the fragmentation results are calculated using Eqs. 7.51 and 7.52. The solid and dashed curves in Fig. 7.7 and Fig. 7.8 represent the hyperon spin polarization as a function of $p_{\mathrm{T}}$ for recombination and fragmentation hadronization mechanisms, respectively. The left panel of Fig. 7.7 shows the $p_{\mathrm{T}}$ dependence of $\Lambda$ polarization in the presence of magnetic fields at $\mu_B = 0$ and $\xi = 0$. Two finite magnetic-field strengths, $eB = 0.1$ and 0.3 GeV$^2$, are considered to investigate the influence of strong magnetic fields. The results indicate that the $\Lambda$ spin polarization decreases with increasing $p_{\mathrm{T}}$ for both hadronization mechanisms. The fragmentation scenario follows a trend similar to recombination, although a different slope is observed at low $p_{\mathrm{T}}$. The enhancement of $\Lambda$ polarization with increasing magnetic field can be attributed to the corresponding increase in the Debye mass.

The spin polarization of the $\Lambda$ hyperon is found to closely follow the polariza-

tion of the initial strange quark in the recombination process of hadronization. Strange quarks with lower momentum produce larger $\Lambda$ polarization after recombination, whereas higher-momentum strange quarks lead to smaller polarization. The middle panel of Fig. 7.7 shows the dependence of $\Lambda$ spin polarization on $p_{\rm T}$ for different values of $\mu_B$ in both recombination and fragmentation scenarios. Two finite values of $\mu_B = 0.1$ and 0.3 GeV are considered. The results indicate that the effect of $\mu_B$ on $\Lambda$ polarization is very small, consistent with the corresponding Debye-mass behavior shown in Fig. 7.6. For the chosen values of $\mu_B$, the temperature-dependent contribution in Eq. 7.54 dominates over the chemical-potential-dependent term, resulting in only a marginal modification of the polarization. The right panel of Fig. 7.7 presents $\Lambda$ spin polarization with $p_{\rm T}$ for different values of the anisotropy parameter $\xi$. Medium anisotropy induces a preferred spin orientation in the system. In this study, anisotropic cases with $\xi = 0.5$, 1.0, and 5.0 are compared with the isotropic case $\xi = 0$. The results show that the $\Lambda$ spin polarization decreases with increasing anisotropy parameter, indicating that momentum-space anisotropy plays a significant role in modifying the spin polarization of $\Lambda$ hyperons.

Figure 7.8 presents the $p_{\rm T}$ dependence of the spin polarization of $\Lambda$, $\Sigma^{\pm}$, $\Xi^{-}$, $\Delta^{++}$, and $\Omega^{-}$ hyperons for recombination and fragmentation hadronization mechanisms. The left panel shows the polarization results at $eB = 0.3$ GeV$^2$ with $\mu_B = 0$ and $\xi = 0$, while the middle and right panels correspond to $\mu_B = 0.3$ GeV and $\xi = 5$, respectively. The effect of $\mu_B$ on spin polarization is found to be qualitatively similar to that of the magnetic field. The results indicate that the spin polarization of all considered hyperons is more pronounced at low $p_{\rm T}$ in the recombination scenario. In the fragmentation mechanism, the polarization of $\Delta^{++}$ and $\Omega^{-}$ is approximately one-third of the corresponding polarization of the constituent $u$ and $s$ quarks, respectively. This reflects that, for baryons composed of identical quark flavors, each quark contributes equally to the final-state baryon polarization, whereas mixed-flavor baryons involve linear combinations of

different flavor contributions. Consequently, the spin polarization of $\Delta^{++}$ and $\Omega^{-}$ is significantly smaller than that of $\Lambda$, $\Sigma^{\pm}$, and $\Xi^{-}$. Although the magnetic field, baryon chemical potential, and anisotropy modify the polarization in both hadronization scenarios in a similar manner, the fragmentation contribution remains consistently smaller than the recombination contribution for all hyperons. Figure 7.8 further suggests a flavor-dependent structure in hyperon spin polarization. A grouping behavior is observed between baryon-octet states with spin-1/2 and baryon-decuplet states with spin-3/2 during spin–orbit coupling. Hyperons composed of identical quark flavors, such as $\Omega^{-}(sss)$ and $\Delta^{++}(uuu)$, exhibit similar spin orientations along the orbital angular momentum direction, whereas mixed-flavor hyperons such as $\Lambda(uds)$, $\Sigma^{\pm}(uus/dds)$, and $\Xi^{-}(dss)$ show different behavior. This may indicate the existence of flavor correlations that influence the polarization dynamics, similar to observations recently reported for the $\phi$ meson [152]. In addition, spin-3/2 baryon-decuplet states exhibit larger polarization than spin-1/2 baryon-octet states, implying that the particle spin itself also affects the polarization strength. Theoretically, it has been shown that, in local thermodynamic equilibrium, the mean spin vector at leading order in thermal vorticity is proportional to the particle spin and inversely proportional to its mass [96, 107, 116]. Therefore, lighter particles with larger spin are expected to polarize more efficiently in a vortical fluid. Although the detailed polarization pattern differs among hadron species, the overall agreement between hydrodynamic calculations and experimental observations suggests that the dominant origin of spin polarization is governed by collective hydrodynamic fields [126, 135]. This indicates that spin polarization is primarily driven by the collective dynamics of the medium rather than by purely flavor-dependent interactions [154]. Therefore, systematic measurements of the global polarization of particles with different spin, flavor composition, and magnetic moments are essential for clarifying the underlying spin-polarization mechanisms in relativistic heavy-ion collisions.

Figure 7.9 illustrates the combined influence of the magnetic field, baryon chem-

ical potential, and medium anisotropy on hyperon spin polarization. The left panel presents the resulting spin polarization of $\Lambda$ hyperons and compares the calculations with the STAR experimental measurements for Au+Au collisions at $\sqrt{s_{\rm NN}}$ = 200 GeV in the (20–60)% centrality class [54]. This comparison highlights the contribution of the Debye mass to hadron spin polarization in relativistic heavy-ion collisions. It is important to note that the comparison is not one-to-one, since the present theoretical framework does not explicitly incorporate detector acceptance, collision geometry, center-of-mass energy dependence, event-plane resolution, feed-down corrections, and related experimental effects. The present model predicts comparatively larger $\Lambda$ spin polarization as a function of $p_T$ than the measured values. This discrepancy likely arises because the current calculation considers only the modification of the medium Debye mass. In contrast, several additional mechanisms have been proposed in the literature to contribute to hyperon spin polarization, including thermal vorticity, thermal shear, gradients of baryon chemical potential over temperature (spin Hall effect), fluid acceleration, and electromagnetic fields [173, 286]. Therefore, the present results should be regarded as a qualitative or preliminary estimate rather than a complete quantitative description. Nevertheless, the polarization generated through Debye mass modifications is independent of these other mechanisms, and a unified treatment including all relevant sources may lead to better agreement with experimental observations. The right panel of Fig. 7.9 shows the spin polarization of $\Lambda$, $\Sigma^{\pm}$, $\Xi^{-}$, $\Omega^{-}$, and $\Delta^{++}$ baryons under the combined effects of $eB$, $\mu_B$, and $\xi$. The results are compared with the STAR measurements of $\Lambda$ hyperons and the averaged global spin polarization of $\Xi$ and $\Omega$ hyperons in Au+Au collisions at $\sqrt{s_{\rm NN}}$ = 200 GeV for the (20–80)% centrality class [59]. Experimentally, the polarization of $\Xi$ hyperons was obtained both directly and through polarization transfer to decay daughters, whereas the $\Omega$ polarization was extracted through decay transfer measurements [59]. Owing to the absence of differential $p_T$ measurements for $\Xi$ and $\Omega$ polarization, the comparison is performed

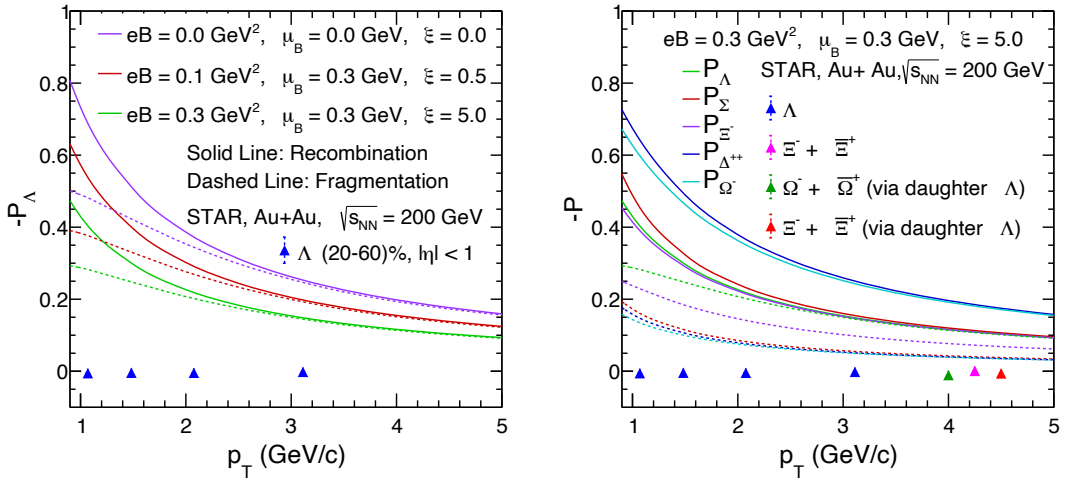



Figure 7.9: The variation of hyperon polarization as a function of transverse momentum due to magnetic field (left panel), baryon chemical potential (middle panel), and anisotropic parameter (right panel) at temperature T = 200 MeV [159]. The results are compared with STAR measurements taken from Refs. [54, 59]. The statistical and systematic uncertainties of the experimental data points are within the marker size.

using $p_T$-integrated values. Among the considered medium effects, momentum-space anisotropy is found to have the strongest influence on the spin polarization observable compared to the magnetic field and baryon chemical potential. This dominant role of anisotropy originates from its substantial impact on the Debye mass. The results therefore indicate that medium anisotropy plays a crucial role in determining hyperon spin polarization and warrants further detailed theoretical investigation.

Having discussed the global spin polarization of various hyperons induced by thermal vorticity, magnetic fields, baryon chemical potential, and medium anisotropy, the discussion now turns to the local spin polarization of hyperons.

## 7.3 Local spin polarization of $\Lambda$ hyperons

The physics motivation behind the local (or longitudinal) spin polarization of $\Lambda$ hyperons in ultrarelativistic heavy ion collisions is discussed in Chapter 2. The following section explores the local spin polarization due to the thermal shear tensor and thermal vorticity for an ideal uncharged fluid with a temperature that depends only on the Bjorken time. An analytical expression relating the longitudinal mean spin vector to the elliptic flow due to the thermal shear and thermal vorticity is derived. To obtain the local $\Lambda$-hyperon polarization under the developed formulation, hydrodynamic and multiphase transport models are used.

The total mean spin vector of a spin $\frac{1}{2}$ particle at local thermodynamic equilibrium is the sum of the contributions arising due to the thermal vorticity and thermal shear [179–181].

$$S^{\mu}(p) = S^{\mu}_{\bar{\omega}}(p) + S^{\mu}_{\xi}(p) \tag{7.59}$$

where, $S^{\mu}_{\bar{\omega}}(p)$ is the mean spin vector due to the thermal vorticity $\bar{\omega}$ and $S^{\mu}_{\xi}(p)$ is the mean spin vector due to the thermal shear $\xi$. The analytical expression for the longitudinal polarization for an ideal uncharged fluid due to the thermal vorticity and thermal shear is calculated in subsections 7.3.1 and 7.3.2, respectively.

### 7.3.1 Thermal vorticity

As discussed previously, the mean spin vector of a spin $\frac{1}{2}$ particle is intricately linked to the thermal vorticity at leading order [96, 107], and is given by;

$$S^{\mu}_{\bar{\omega}}(p) = -\frac{1}{8m}\epsilon^{\mu\rho\sigma\tau}p_{\tau}\frac{\int_{\Sigma} d\Sigma_{\lambda}p^{\lambda}\, n_F(1-n_F)\bar{\omega}_{\rho\sigma}}{\int_{\Sigma} d\Sigma_{\lambda}p^{\lambda}\, n_F}, \tag{7.60}$$

where $\bar{\omega}$ is the thermal vorticity. $n_F$ is the Fermi-Dirac distribution function.

Further, it is assumed that in the vicinity of the ideal uncharged fluid, the temperature vorticity is conserved along the velocity, i.e $\omega^{T}_{\mu\nu}u^{\nu} = 0$ [101, 118] and

satisfies the relativistic Kelvin circulation theorem. As a consequence, if $\omega^{T}_{\mu\nu}$ vanishes at the initial time, it remains absent during the whole evolution of the ideal uncharged fluid. Thus, by using this condition, one can obtain the thermal vorticity, $\bar{\omega}$, given as [101, 118];

$$\bar{\omega}_{\mu\nu} = \frac{1}{T}(A_\mu u_\nu - A_\nu u_\mu) \tag{7.61}$$

Here, A is the four-acceleration field. Now, using Eq. (7.61) in Eq. (7.60), one can obtain the modified form of the spin vector for spin $\frac{1}{2}$ particles, which is given as;

$$S^{\mu}_{\bar{\omega}}(p) = -\frac{1}{4m}\epsilon^{\mu\rho\sigma\tau}p_\tau \frac{\int_\Sigma d\Sigma_\lambda p^\lambda\, A_\rho \beta_\sigma n_F(1-n_F)}{\int_\Sigma d\Sigma_\lambda p^\lambda\, n_F}, \tag{7.62}$$

For the ideal uncharged fluid, the equation of motion is defined as,

$$A_\rho = \frac{1}{T}\nabla_\rho T = \frac{1}{T}(\partial_\rho - u_\rho u\cdot\partial)T. \tag{7.63}$$

Replacing Eq. (7.63) in Eq. (7.62), leads to;

$$\begin{aligned} S^{\mu}_{\bar{\omega}}(p) = -\frac{1}{4mT}\epsilon^{\mu\rho\sigma\tau}p_\tau \Bigg[ & \frac{\int_\Sigma d\Sigma_\lambda p^\lambda\, \partial_\rho T \beta_\sigma n_F(1-n_F)}{\int_\Sigma d\Sigma_\lambda p^\lambda\, n_F} \\ & - \frac{\int_\Sigma d\Sigma_\lambda p^\lambda\, \beta_\sigma u_\rho u.\partial T n_F(1-n_F)}{\int_\Sigma d\Sigma_\lambda p^\lambda\, n_F}\Bigg] \end{aligned} \tag{7.64}$$

It must be noted that the inclusion of the term $\epsilon^{\mu\rho\sigma\tau}\beta_\sigma u_\rho$ in the second part of Eq. (7.64) results in this part becoming zero. Therefore, the spin polarization tensor is solely determined by the first term.

Now, using the relation $\frac{\partial}{\partial p^\sigma}n_F = -\beta_\sigma n_F(1-n_F)$, Eq. (7.64) can be rewritten as;

$$S^{\mu}_{\bar{\omega}}(p) = \frac{1}{4mT}\epsilon^{\mu\rho\sigma\tau}p_\tau \frac{\int_\Sigma d\Sigma_\lambda p^\lambda\, \frac{\partial n_F}{\partial p^\sigma}\partial_\rho T}{\int_\Sigma d\Sigma_\lambda p^\lambda\, n_F}, \tag{7.65}$$

By first solving the numerator of the above Eq. (7.65), reduces to

$$\int_\Sigma d\Sigma_\lambda p^\lambda \frac{\partial n_F}{\partial p^\sigma}\partial_\rho T \;=\; \frac{\partial}{\partial p^\sigma}\int_\Sigma d\Sigma_\lambda p^\lambda n_F \partial_\rho T - \int_\Sigma d\Sigma_\sigma n_F \partial_\rho T.$$

In the relativistic limit, it is assumed that the decoupling hypersurface happens at $T = T_c$, where $T_c$ is the critical temperature. This entails that the normal vector to the hypersurface is the gradient of temperature, which forces the second integral of the above expression to vanish. Then, the final expression for the mean spin vector is given by

$$S^{\mu}_{\varpi}(p) = \frac{1}{4mT}\epsilon^{\mu\rho\sigma\tau}p_{\tau}\frac{\frac{\partial}{\partial p^{\sigma}}\int_{\Sigma} d\Sigma_{\lambda}p^{\lambda}\, n_F\, \partial_{\rho}T}{\int_{\Sigma} d\Sigma_{\lambda}p^{\lambda}\, n_F} \tag{7.66}$$

Here, an isochronous decoupling hypersurface is considered, with a temperature field only dependent on the Bjorken time, $\tau$. Further, the decoupling hypersurface is described by the coordinates x, y, $\eta$, with $\tau$ as a constant.

Let us calculate the numerator of Eq. (7.66) putting $\rho = 0$, one obtains;

$$\int_{\Sigma} d\Sigma_{\lambda}p^{\lambda}\, n_F\, \frac{dT}{d\tau}\cosh\eta. \tag{7.67}$$

Re-evaluating Eq. (7.66), at $Y = 0$, gives

$$S^{z}_{\varpi}(\mathbf{p}_T, Y = 0)\hat{\mathbf{k}} \simeq -\frac{dT}{d\tau}\frac{1}{4mT}\hat{\mathbf{k}}\frac{\partial}{\partial\phi}\log\int_{\Sigma} d\Sigma_{\lambda}p^{\lambda}n_F \tag{7.68}$$

where $\phi$ is the azimuthal angle of the emitted particle in the transverse plane. Expanding the Eq. (7.68) in Fourier series in $\phi$ and keeping only the elliptic flow term produces a simplified form of the longitudinal component of the mean spin vector;

$$\begin{aligned} S^{z}_{\varpi}(\mathbf{p}_T, Y = 0) &\simeq -\frac{dT}{d\tau}\frac{1}{4mT}\frac{\partial}{\partial\phi}2v_2(p_{\mathrm{T}})\cos 2\phi \\ &= \frac{dT}{d\tau}\frac{1}{mT}\, v_2(p_{\mathrm{T}})\sin 2\phi \end{aligned} \tag{7.69}$$

In the rest frame of the particle, the longitudinal polarization vector $P^*_z$ can be calculated from the longitudinal mean spin vector $S^*_z$ by using the relation,

$$P^*_z = 2S^*_z \tag{7.70}$$

At the midrapidity, $S^*_z = S_z$. Eq. (7.69) implies that the degree of longitudinal polarization depends on the temperature cooling rate, the second-order anisotropic

flow coefficient, and the azimuthal angle of the emitted particles. In peripheral heavy-ion collisions, the initial spatial anisotropy of the overlap region is converted into an anisotropic azimuthal distribution in the momentum space of the final state particles. This anisotropy can be characterized in terms of Fourier coefficients,

$$v_2 \equiv \langle \cos[2(\phi - \Psi_2)] \rangle \tag{7.71}$$

where $\Psi_2$ is the azimuthal angle of the event plane for the second-order harmonics.

### 7.3.2 Thermal shear

The mean spin vector of a spin $\frac{1}{2}$ particle due to the symmetric thermal shear tensor at leading order is given by [179, 180];

$$S^{\mu}_{\xi}(p) = -\frac{1}{4m}\epsilon^{\mu\rho\sigma\tau}p_{\tau}\frac{\int_{\Sigma} d\Sigma \cdot p \;\; n_F(1-n_F) \;\; \hat{t}_{\rho}\frac{p^{\lambda}}{\varepsilon}\xi_{\lambda\sigma}}{\int_{\Sigma} d\Sigma \cdot p \, n_F}, \tag{7.72}$$

where $\xi$ is the thermal shear, defined in terms of the symmetric derivative of four temperature fields, given by;

$$\xi_{\mu\nu} = \frac{1}{2}(\partial_{\mu}\beta_{\nu} + \partial_{\nu}\beta_{\mu}) \tag{7.73}$$

Here $\hat{t}_{\rho}$ is the direction of QGP in the center of mass frame; $\varepsilon = \hat{t}_{\rho} \cdot p = \sqrt{p^2 + m^2}$ is the energy, and $n_F$ is the Fermi Dirac distribution function.

Following these, the thermal shear tensor can be written as;

$$\xi_{\mu\nu} = \frac{1}{2}(\partial_{\mu}\beta_{\nu} + \partial_{\nu}\beta_{\mu}) = \frac{1}{T}\left[\frac{1}{2}(\partial_{\mu}u_{\nu} + \partial_{\nu}u_{\mu})\right] - \frac{1}{T^2}\left[\frac{1}{2}(u_{\nu}\partial_{\mu}T + u_{\mu}\partial_{\nu}T)\right] \tag{7.74}$$

The symmetric shear tensor ($\Xi_{\mu\nu}$) can be decomposed as [179],

$$\Xi_{\mu\nu} = \frac{1}{2}(\partial_{\mu}u_{\nu} + \partial_{\nu}u_{\mu}) = \frac{1}{2}(A_{\mu}u_{\nu} + A_{\nu}u_{\mu}) + \sigma_{\mu\nu} + \frac{1}{3}\theta\Delta_{\mu\nu} \tag{7.75}$$

where A is the four-acceleration field.

The shear stress tensor ($\sigma_{\mu\nu}$) in Eq. 7.75 can be written as;

$$\sigma_{\mu\nu} = \frac{1}{2}(\nabla_\mu u_\nu + \nabla_\nu u_\mu) - \frac{1}{3}\theta\Delta_{\mu\nu} \tag{7.76}$$

where $\theta = \partial_\mu u^\mu$ is the expansion rate, $\Delta^{\mu\nu} = g^{\mu\nu} - u^\mu u^\nu$ is the transverse projector operator, and defining the orthogonal derivative $\nabla_\mu = \Delta_{\mu\nu}\partial^\nu = \partial_\mu - u_\mu u\cdot\partial$

Further, the analytical expression for $\xi_{\mu\nu}$ from Eq. 7.74 is obtained as;

$$\xi_{\mu\nu} = \frac{1}{2T}\left[(A_\mu u_\nu + A_\nu u_\mu) + (\nabla_\mu u_\nu + \nabla_\nu u_\mu)\right] - \frac{1}{2T^2}\left[(u_\nu\partial_\mu T + u_\mu\partial_\nu T)\right] \tag{7.77}$$

Substituting the value of $\xi_{\lambda\sigma}$ in Eq. 7.72, the mean spin vector is proportional to;

$$S^\mu_\xi(p) \propto \epsilon^{\mu\rho\sigma\tau}\frac{\hat{t}_\rho}{\varepsilon}p_\tau p^\lambda\left[\frac{1}{2T}\left[(A_\lambda u_\sigma + A_\sigma u_\lambda) + (\nabla_\lambda u_\sigma + \nabla_\sigma u_\lambda)\right] - \frac{1}{2T^2}\left[(u_\sigma\partial_\lambda T + u_\lambda\partial_\sigma T)\right]\right] \tag{7.78}$$

Now, expanding the orthogonal derivative term in Eq. 7.78, one obtains;

$$S^\mu_\xi(p) \propto \epsilon^{\mu\rho\sigma\tau}\frac{\hat{t}_\rho}{\varepsilon}p_\tau p^\lambda\left[\frac{1}{2T}\Big((A_\lambda u_\sigma + A_\sigma u_\lambda) + (\partial_\lambda u_\sigma - u_\lambda u\cdot\partial\, u_\sigma) + (\partial_\sigma u_\lambda - u_\sigma u\cdot\partial\, u_\lambda)\Big) - \frac{1}{2T^2}(u_\sigma\partial_\lambda T + u_\lambda\partial_\sigma T)\right] \tag{7.79}$$

Further simplification of the above equation gives,

$$S^\mu_\xi(p) \propto \epsilon^{\mu\rho\sigma\tau}\frac{\hat{t}_\rho}{\varepsilon}p_\tau\left[\frac{1}{2T}\Big((p\cdot A)u_\sigma + A_\sigma(p\cdot u) + ((p\cdot\partial)\,u_\sigma - (p\cdot u)(u\cdot\partial)\,u_\sigma) + (p^\lambda\partial_\sigma u_\lambda - p^\lambda u_\sigma u\cdot\partial\, u_\lambda)\Big) - \frac{1}{2T^2}\left[(u_\sigma(p\cdot\partial)T + (p\cdot u)\partial_\sigma T)\right]\right] \tag{7.80}$$

Replacing the four-acceleration vector $A$, defined in Eq. 7.63, into Eq. 7.80, one obtains;

$$S^\mu_\xi(p) \propto \epsilon^{\mu\rho\sigma\tau}\frac{\hat{t}_\rho}{\varepsilon}p_\tau\left[\frac{1}{2T^2}\left[(p^\alpha(\partial_\alpha - u_\alpha u\cdot\partial)T)u_\sigma + (\partial_\sigma - u_\sigma u\cdot\partial)T\ \ (p\cdot u)\right] + \frac{1}{2T}\left[((p\cdot\partial)\,u_\sigma - (p\cdot u)(u\cdot\partial)\,u_\sigma) + (p^\lambda\partial_\sigma u_\lambda - p^\lambda u_\sigma u\cdot\partial\, u_\lambda)\right] - \frac{1}{2T^2}\left[(u_\sigma(p\cdot\partial)T + (p\cdot u)\partial_\sigma T)\right]\right] \tag{7.81}$$

Using the relation between four momentum and four velocity $p^\mu = mu^\mu$, and $p \cdot u = m$, the above Eq. 7.81 reduces to

$$S^\mu_\xi(p) \propto \epsilon^{\mu\rho\sigma\tau}\frac{\hat{t}_\rho}{\varepsilon}p_\tau\left[\frac{1}{2T^2}\Big[(p\cdot\partial T - p\cdot\partial T)u_\sigma + (\partial_\sigma - u_\sigma u\cdot\partial)T\ \ (p\cdot u)\Big]\right.$$
$$+\frac{1}{2T}\left[((p\cdot\partial)\ u_\sigma - (p\cdot\partial)\ u_\sigma) + (p^\lambda\partial_\sigma u_\lambda - p^\lambda u_\sigma u\cdot\partial\ u_\lambda)\right]$$
$$\left.-\frac{1}{2T^2}\left[(u_\sigma(p\cdot\partial)T + (p\cdot u)\partial_\sigma T)\right]\right] \tag{7.82}$$

With the help of the identity $u^\lambda\partial_\sigma u_\lambda = 0$; Eq. 7.82, reduces to;

$$S^\mu_\xi(p) \propto \frac{\hat{t}_\rho\epsilon^{\mu\rho\sigma\tau}p_\tau}{2T^2\varepsilon}\left[(\partial_\sigma T - u_\sigma u\cdot\partial T)\ (p\cdot u) - [(u_\sigma(p\cdot\partial)T + (p\cdot u)\partial_\sigma T)]\right] \tag{7.83}$$

Since the temperature field is considered for Bjorken flow, the $\partial_\sigma T \longrightarrow 0$. Hence Eq. 7.83, reduces to;

$$S^\mu_\xi(p) \propto \epsilon^{\mu\rho\sigma\tau}\frac{\hat{t}_\rho}{2T^2\varepsilon}p_\tau\left[-u_\sigma u\cdot\partial T\ \ (p\cdot u) - u_\sigma(p\cdot\partial)T\right] \tag{7.84}$$

On further simplification of $p\cdot u$ term, leads to;

$$S^\mu_\xi(p) \propto -\epsilon^{\mu\rho\sigma\tau}\frac{\hat{t}_\rho}{T\varepsilon}p_\tau(p\cdot\partial T)\beta_\sigma \tag{7.85}$$

Substituting Eq. 7.85 in the Eq. 7.72, the mean spin vector can be written as,

$$S^\mu_\xi(p) = \frac{1}{4mT}\epsilon^{\mu\rho\sigma\tau}p_\tau\frac{\hat{t}_\rho}{\varepsilon}\frac{\int_\Sigma d\Sigma\cdot p\ (p\cdot\partial T)\ n_F(1-n_F)\beta_\sigma}{\int_\Sigma d\Sigma\cdot p\ n_F}, \tag{7.86}$$

Using the relation $\frac{\partial}{\partial p^\sigma}n_F = -\beta_\sigma n_F(1-n_F)$, Eq. (7.86) is rewritten as;

$$S^\mu_\xi(p) = \frac{-1}{4mT}\epsilon^{\mu\rho\sigma\tau}p_\tau\frac{\hat{t}_\rho}{\varepsilon}\frac{\int_\Sigma d\Sigma\cdot p\ (p\cdot\partial T)\ \frac{\partial}{\partial p^\sigma}n_F}{\int_\Sigma d\Sigma\cdot p\ n_F}, \tag{7.87}$$

Solving the numerator of the above Eq. 7.87 yields

$$\int_\Sigma d\Sigma\cdot p\frac{\partial n_F}{\partial p^\sigma}(p\cdot\partial T)\ =\ \frac{\partial}{\partial p^\sigma}\int_\Sigma d\Sigma\cdot p\ n_F(p\cdot\partial T)$$
$$-\int_\Sigma d\Sigma\cdot p\ n_F\ \partial_\sigma T - \int_\Sigma d\Sigma_\sigma n_F(p\cdot\partial T) \tag{7.88}$$

The second and third integral of the above equation vanishes with a similar argument as discussed above. Thus, Eq. 7.87, becomes;

$$S^{\mu}_{\xi}(p) = \frac{-1}{4mT}\epsilon^{\mu\rho\sigma\tau}p_{\tau}\frac{\hat{t}_{\rho}}{\varepsilon}\frac{\frac{\partial}{\partial p^{\sigma}}\int_{\Sigma}d\Sigma\cdot p\, n_F(p\cdot\partial T)}{\int_{\Sigma}d\Sigma\cdot p\, n_F}, \tag{7.89}$$

At $\rho = 0$, the numerator of Eq. 7.89, is given as;

$$\int_{\Sigma}d\Sigma\cdot p\, n_F\, \varepsilon\frac{dT}{d\tau}\cosh\eta. \tag{7.90}$$

Hence, at $Y = 0$, the $\cosh\eta \approx 1$.

$$S^{\mu}_{\xi}(p) = \frac{-1}{4mT}\epsilon^{\mu\rho\sigma\tau}p_{\tau}\frac{\frac{\partial}{\partial p^{\sigma}}\int_{\Sigma}d\Sigma\cdot p\, n_F\frac{dT}{d\tau}}{\int_{\Sigma}d\Sigma\cdot p\, n_F}, \tag{7.91}$$

Eq. 7.91 follows the same form as Eq. 7.66. Hence, the net contribution to the mean spin vector due to the thermal shear term is obtained as;

$$S^{z}_{\xi}(\mathbf{p}_T, Y=0)\hat{\mathbf{k}} \simeq \frac{1}{4mT}\frac{dT}{d\tau}\hat{\mathbf{k}}\frac{\partial}{\partial\phi}\log\int_{\Sigma}d\Sigma_{\lambda}p^{\lambda}n_F \tag{7.92}$$

Expanding the Eq. (7.92) in Fourier series in $\phi$ and keeping only the elliptic flow term produces a simplified form of the longitudinal component of the mean spin vector;

$$\begin{aligned} S^{z}_{\xi}(\mathbf{p}_T, Y=0) &\simeq \frac{1}{4mT}\frac{dT}{d\tau}\frac{\partial}{\partial\phi}2v_2(p_{\mathrm{T}})\cos 2\phi \\ &= \frac{-1}{mT}\frac{dT}{d\tau}v_2(p_{\mathrm{T}})\sin 2\phi \end{aligned} \tag{7.93}$$

It is observed that the contribution of thermal shear to the mean spin vector is exactly equal but with an opposite sign for an ideal uncharged fluid, assuming the temperature evolves only with the Bjorken time. The second-order anisotropic flow coefficient (elliptic flow) is obtained using ECHO-QGP, EPOS4, and the AMPT model. The hydrodynamic temperature evolution is obtained using the (3+1)D relativistic hydrodynamic model. The elliptic flow coefficient is obtained using the event plane method [287]. A brief description of the ECHO-QGP, EPOS4, and AMPT and of event generation using these models is provided in Ref [160].

The longitudinal mean spin vectors arising from thermal vorticity and thermal shear are given by Eqs. 7.69 and 7.93, respectively. The longitudinal polarization is sensitive to the freeze-out temperature, temperature gradients at hadronization, the elliptic flow coefficient, particle mass, and the azimuthal angular distribution of emitted Λ ($\bar{\Lambda}$) hyperons. The elliptic flow and azimuthal distributions of emitted Λ ($\bar{\Lambda}$) hyperons are extracted from these models, while the temperature evolution at hadronization is obtained from ECHO-QGP. In EPOS4, the elliptic flow coefficient is evaluated using Eq. 7.71. In contrast, AMPT and ECHO-QGP allow the reaction plane angle to be fixed at $\Psi_2 = 0$, enabling the elliptic flow to be calculated as $v_2 = \langle \cos 2\phi \rangle$, where the average is taken over all produced Λ hyperons in an event. The centrality classes in ECHO-QGP are determined using fixed impact parameters based on Monte-Carlo Glauber model estimates [288], whereas in EPOS4 and AMPT the centrality selection is performed through geometrical slicing of the impact-parameter distribution.

The upper left panel of Fig. 7.10 presents the longitudinal polarization $P_z$ of Λ hyperons as a function of the azimuthal angle $\phi$, obtained using the ECHO-QGP hydrodynamic model. The green solid and dashed curves correspond to the contributions from thermal vorticity and thermal shear, respectively, in Pb+Pb collisions at $\sqrt{s_{\rm NN}} = 5.02$ TeV for the (30–50)% centrality class within $0.15 < p_{\rm T} < 3.0$ GeV/$c$. The red solid and dashed curves represent the corresponding results for Au+Au collisions at $\sqrt{s_{\rm NN}} = 200$ GeV in the same centrality and $p_{\rm T}$ ranges. The results exhibit a clear sinusoidal modulation of $P_z$ with $\phi$. Furthermore, the contributions from thermal vorticity and thermal shear are found to have nearly identical magnitudes but opposite signs, consistent with earlier studies [183, 186]. Notably, thermal shear reproduces the experimentally observed sign of the longitudinal polarization modulation measured by the STAR Collaboration [55]. The upper right panel of Fig. 7.10 compares the $\phi$ dependence of $P_z$ obtained from the three different models for Pb+Pb collisions in the (30–50)% centrality class and $0.15 < p_{\rm T} < 3.0$ GeV/$c$. Only marginal differences are observed between the

hydrodynamic and transport model predictions.

It is important to note that the contributions of thermal shear and thermal vorticity to the longitudinal mean spin vector become exactly equal in magnitude and opposite in sign only under the assumption of an ideal uncharged fluid. This simplified relation between the longitudinal mean spin vector and elliptic flow is obtained by considering temperature evolution solely through the Bjorken expansion time. However, when additional effects such as temperature gradients, chemical-potential gradients, and electromagnetic fields are included in the mean spin vector, a finite longitudinal polarization is expected.

The lower left panel of Fig. 7.10 shows the centrality dependence of the longitudinal polarization $P_z$ of $\Lambda$ hyperons obtained from hydrodynamic and transport models for $0.15 < p_{\rm T} < 3.0$ GeV/$c$ in Au+Au collisions at $\sqrt{s_{\rm NN}} = 200$ GeV and Pb+Pb collisions at $\sqrt{s_{\rm NN}} = 5.02$ TeV. The positive values of $P_z$ arise from the two negative contributions appearing in Eq. (11), namely the temperature cooling rate and the $\sin 2\phi$ term. Here, the $\sin 2\phi$ contribution in Eq. 7.69 is evaluated using the event-averaged azimuthal distribution of produced $\Lambda$ hyperons. The magnitude of longitudinal polarization is found to increase from central to mid-central collisions, which can be attributed to the stronger elliptic flow developed in more peripheral collisions. In the most-central collisions, the polarization signal nearly vanishes, although residual elliptic flow may still arise from initial-state density fluctuations. Further, the $P_z$ obtained from these models is compared with the corresponding experimental data for Au+Au $\sqrt{s_{\rm NN}} = 200$ GeV at STAR [55] and Pb+Pb $\sqrt{s_{\rm NN}} = 5.02$ TeV at ALICE [68].

The ECHO-QGP model predicts a slightly higher value of $P_z$ in the most-central (0–30)% Au+Au collisions at $\sqrt{s_{\rm NN}} = 200$ GeV compared to Pb+Pb collisions at $\sqrt{s_{\rm NN}} = 5.02$ TeV. In contrast, for mid-central (30–50)% collisions, the longitudinal polarization obtained from ECHO-QGP is larger for Pb+Pb collisions. The AMPT model consistently predicts slightly higher values of $P_z$ for Pb+Pb collisions at $\sqrt{s_{\rm NN}} = 5.02$ TeV than for Au+Au collisions at $\sqrt{s_{\rm NN}} = 200$ GeV across

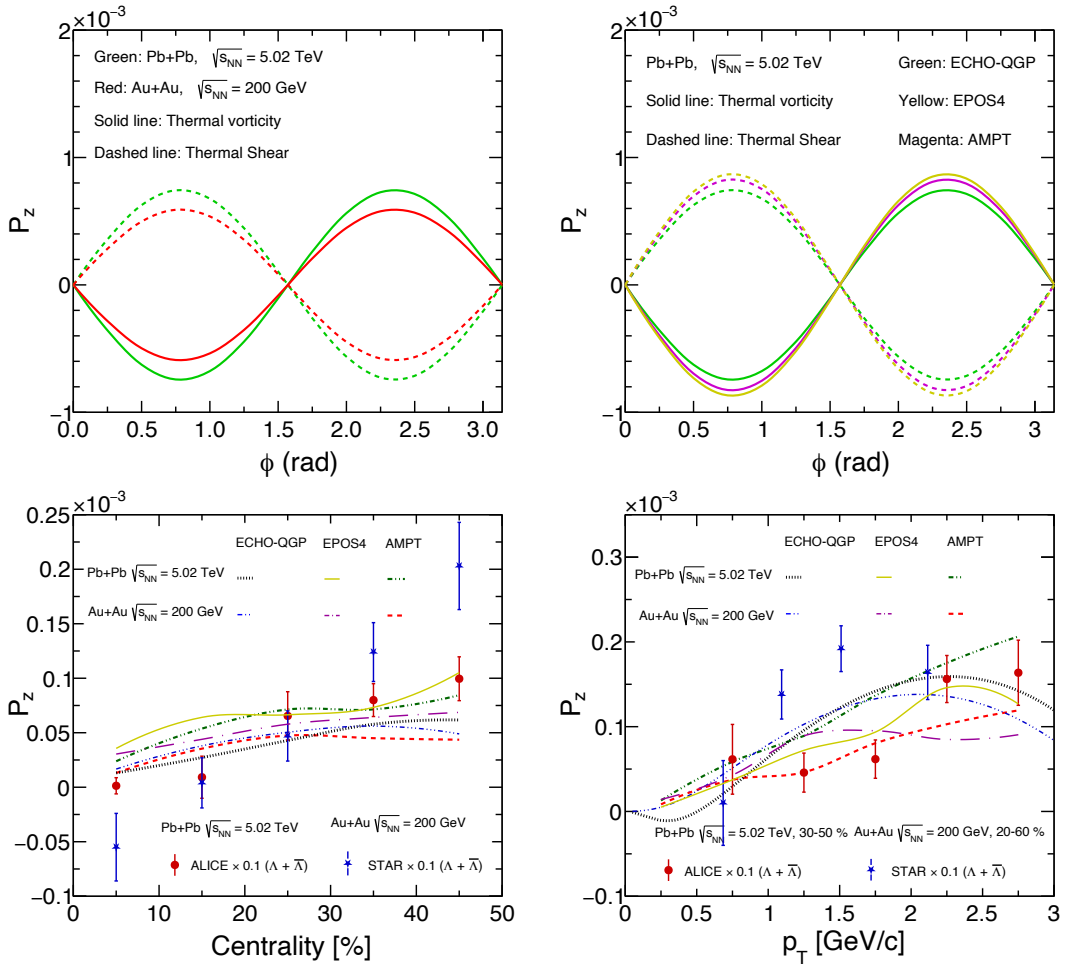



Figure 7.10: The upper left panel shows the longitudinal component of Λ and $\bar{\Lambda}$ polarization ($P_z$) as a function of azimuthal angle ($\phi$) obtained from ECHO-QGP model simulation for $\sqrt{s_{\rm NN}}$ = 5.02 TeV and $\sqrt{s_{\rm NN}}$ = 200 GeV in Pb+Pb and Au+Au collisions, respectively [160]. The upper right panel shows $P_z$ as a function of $\phi$ obtained from ECHO-QGP, EPOS4, AMPT model simulation for $\sqrt{s_{\rm NN}}$ = 5.02 TeV in Pb+Pb collisions [160]. The lower left and right panel shows $P_z$ as a function of collision centrality and transverse momentum ($p_{\rm T}$) obtained from ECHO-QGP, EPOS4, and AMPT model.

all centralities. A similar centrality dependence is observed in EPOS4, despite its different underlying formulation. Within the present framework, both AMPT and

EPOS4 indicate a collision-energy dependence of the longitudinal polarization for $\Lambda$ and $\bar{\Lambda}$ hyperons, whereas the ECHO-QGP results show only weak sensitivity to $\sqrt{s_{\rm NN}}$. The modest differences between hydrodynamic and transport models originate from their distinct medium evolution and hadronization dynamics. Overall, the beam-direction polarization induced by elliptic flow exhibits a much weaker collision-energy dependence than the global spin polarization reported in Ref. [52].

Since elliptic flow depends on both centrality and $p_{\rm T}$, the longitudinal polarization also exhibits a characteristic $p_{\rm T}$ dependence. The lower panel of Fig. 7.10 shows the $p_{\rm T}$ dependence of the elliptic flow-induced polarization for $\Lambda$ ($\bar{\Lambda}$) hyperons in the (30–50)% centrality class. In ECHO-QGP, the longitudinal polarization increases up to $p_{\rm T} \lesssim 2.0$ GeV/$c$ and decreases at higher $p_{\rm T}$. The model also predicts negative polarization at low $p_{\rm T}$ for Pb+Pb collisions, reflecting the negative elliptic flow values of $\Lambda$ ($\bar{\Lambda}$) hyperons in this region. In contrast, the AMPT model predicts a monotonic increase of $P_z$ with $p_{\rm T}$, following the corresponding behavior of elliptic flow. For EPOS4, the longitudinal polarization exhibits a non-monotonic dependence on $p_{\rm T}$ for both $\Lambda$ and $\bar{\Lambda}$ hyperons.

With a brief discussion on the local spin polarization of $\Lambda$ hyperons induced by thermal vorticity and thermal shear, the discussion now turns to the spin alignment of vector mesons.

## 7.4 Spin alignment of vector mesons

The physics motivation and the fundamental concepts of the spin density matrix underlying the spin alignment of vector mesons in ultrarelativistic heavy-ion collisions are discussed in Chapter 2. The following section describes the spin alignment of a vector meson, which is quantified by the $00^{\rm th}$ element of the spin density matrix, i.e., $\rho_{00}$. The global spin polarization of quarks (anti-quarks) can give rise to spin alignment of vector mesons in the recombination and fragmenta-

tion processes of hadronization [80]. The $00^{\text{th}}$ element of spin density matrix for $\rho$, $\phi$ and $K^*$ mesons for recombination and fragmentation processes are given as,

$$\rho_{00}^{\rho(rec)} = \frac{1-P_q^2}{3+P_q^2},\ \rho_{00}^{\phi(rec)} = \frac{1-P_s^2}{3+P_s^2},\ \rho_{00}^{K^{*(rec)}} = \frac{1-P_qP_s}{3+P_qP_s} \tag{7.94}$$

$$\rho_{00}^{\rho(frag)} = \frac{1+\beta P_q^2}{3-\beta P_q^2},\ \rho_{00}^{\phi(frag)} = \frac{1+\beta P_s^2}{3-\beta P_s^2} \tag{7.95}$$

$$\rho_{00}^{K^{*(frag)}} = \frac{f_s}{n_s+f_s}\frac{1+\beta P_q^2}{3-\beta P_q^2} + \frac{n_s}{n_s+f_s}\frac{1+\beta P_s^2}{3-\beta P_s^2} \tag{7.96}$$

where $\beta \simeq 0.5$, $n_s$ and $f_s$ are the strange quark abundances relative to up and down quarks in QGP and quark fragmentation, respectively.

The upper panel of Fig. 7.11 shows the effect of the magnetic field $eB$ (left) and the momentum-space anisotropy $\xi$ (right) on $\rho_{00}$ for the $\phi$ in two hadronization mechanisms. The curves below $\rho_{00} = 1/3$ correspond to recombination, while above $\rho_{00} = 1/3$ represent fragmentation. The predictions are compared with STAR data for Au+Au collisions in the (20–60)% centrality class [62]. As the magnetic field increases, the deviation from the unpolarized limit, $|\rho_{00} - 1/3|$, becomes larger for both mechanisms, indicating enhanced spin alignment. Similarly, the medium anisotropy can also significantly influence the spin alignment of the $\phi$ meson. Furthermore, the lower panel of Fig. 7.11 shows study of $\rho_{00}$ extended to $\phi$, $K^*$, and $\rho$ mesons at fixed $eB = 0.3$ GeV$^2$ (left), and $\xi = 5$ (right) The results indicate that the absolute deviation of $\rho_{00}$ from the unpolarized limit 1/3 is larger at low $p_{\mathrm{T}}$ for the recombination scenario compared to fragmentation. This suggests stronger spin alignment at low transverse momentum for $\phi$, $K^*$, and $\rho$ mesons produced via recombination. At higher $p_{\mathrm{T}}$, $\rho_{00}$ approaches 1/3, indicating a vanishing spin alignment for all three vector mesons. Within the quark polarization framework, quark polarization scales inversely with the square of the quark mass, leading to a characteristic mass ordering in vector-meson spin alignment. Consistent with this expectation, Fig. 7.11 shows the hierarchy $\rho_{00}^{\rho} > \rho_{00}^{K^*} > \rho_{00}^{\phi}$ at low $p_{\mathrm{T}}$ in the recombination scenario.

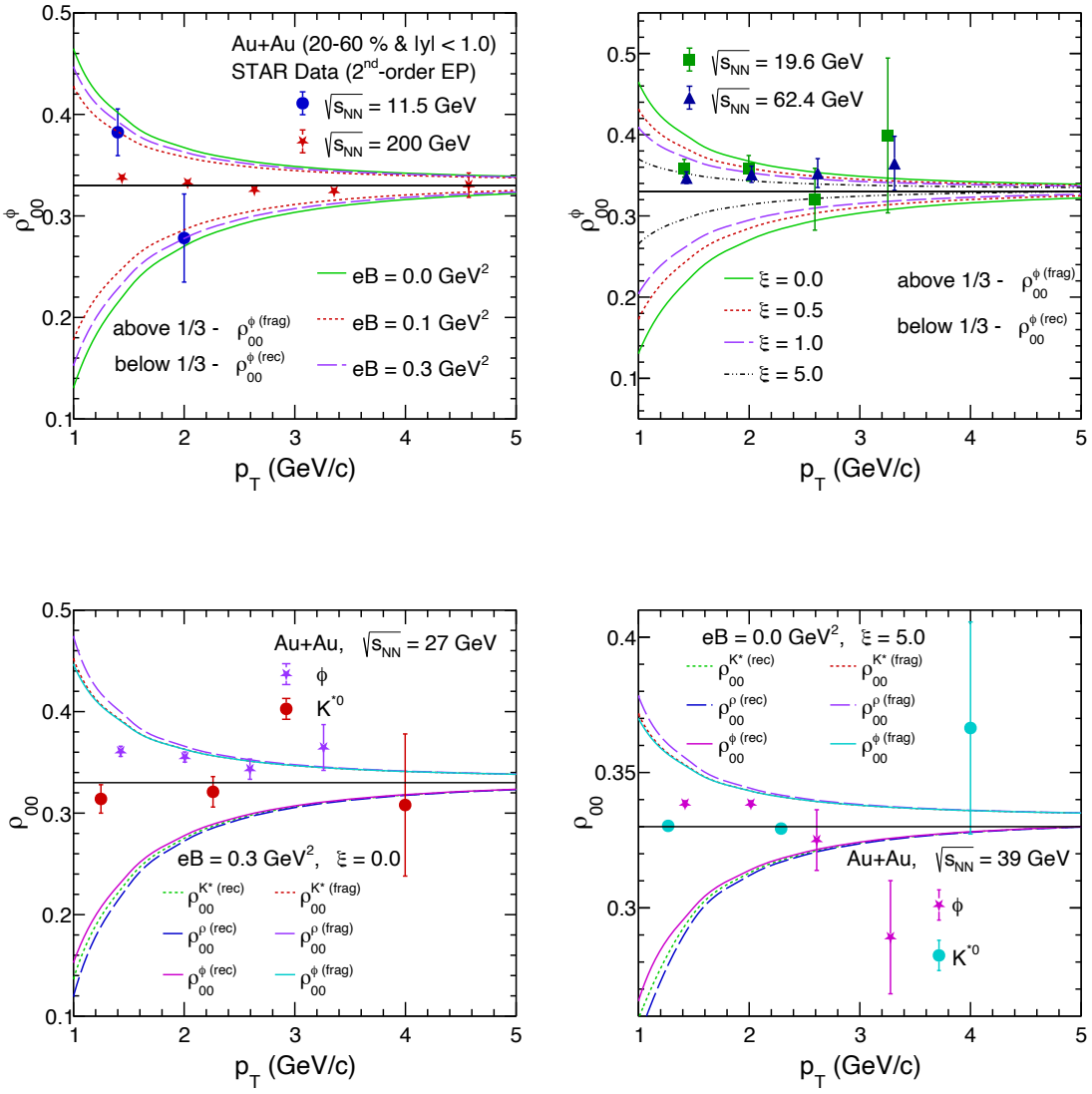



Figure 7.11: The upper panel shows the variation of spin alignment of the $\phi$ vector meson as a function of transverse momentum due to the magnetic field (left panel) and the anisotropic parameter (right panel) at temperature T = 200 MeV [159]. The lower panel shows the variation of spin alignment of $\phi$, $K^{*0}$, and $\rho$ vector mesons. The results are compared with STAR measurements taken from Ref. [62].

# Chapter 8

## Summary

In summary, this thesis presents both experimental and phenomenological studies on spin polarization of various hadrons at LHC energies. The experimental part focuses on the measurement of inclusive $J/\psi$ spin polarization in proton-proton ($pp$) and Oxygen-Oxygen (OO) collisions as a function of transverse momentum ($p_{\mathrm{T}}$) in helicity and Collins-Soper reference frames. These measurements are performed at forward rapidity ($2.5 < y < 4.0$) via their dimuon decay channel using the muon spectrometer of the upgraded ALICE detector. Using the high-statistics Run 3 $pp$ data samples, a more precise and differential measurement of the polarization parameters is obtained as a function of $p_{\mathrm{T}}$ at $\sqrt{s} =$ 13.6 TeV, extending down to zero $p_{\mathrm{T}}$ for the first time. The light-ion collision data of Run 3 allow the first measurement of J/$\psi$ polarization parameters as a function of $p_{\mathrm{T}}$ in OO collisions at $\sqrt{s_{\mathrm{NN}}} = 5.36$ TeV. The J/$\psi$ polarization measured in hadronic and light-ion collisions provides a powerful probe for understanding its production mechanism. Furthermore, quarkonium polarization is sensitive to the environment in which the bound state is formed, offering a unique opportunity to investigate the influence of the deconfined medium on the evolution of heavy-quark pairs and the formation of quarkonia. Moreover, in OO collisions, quarkonium polarization may be particularly sensitive to the presence of initial magnetic and vorticity fields. Thus, studying the J/$\psi$ polarization at

LHC energies in nuclear collisions sheds light on the structure and implications of the initially created orbital angular momentum and magnetic field. Hence, in this context, the spin polarization of quarkonia serves as an important and novel probe in understanding the hot QCD medium formed in ultrarelativistic collisions. It is observed that the $\lambda_\theta, \lambda_\phi$ and $\lambda_{\theta\phi}$ polarization parameters in *pp* collisions are close to zero for all $p_{\rm T}$ bins, within the statistical and systematic uncertainty. The important $\lambda_\theta$ parameter shows a maximum deviation of $1.8\sigma$ (helicity) and $2.2\sigma$ (Collins-Soper) for $8 < p_{\rm T} < 10$ GeV/c with respect to the no-polarization hypothesis. The results obtained in the analyses of *pp* collisions at $\sqrt{s} = 13.6$ TeV are compared with existing ALICE and LHCb measurements for lower energies in *pp* collisions at $\sqrt{s} = 7$ and 8 TeV, showing consistency ($\leq 2\sigma$) with respect to the previous measurements within the uncertainties. The results obtained in the analyses of OO collisions are compared with existing measurements in Pb–Pb collisions at $\sqrt{s_{\rm NN}} = 5.02$ TeV. A hint of polarization signal at low-$p_{\rm T}$ ($2 < p_{\rm T} < 4$ GeV/c) is observed with a significance of $1.8\sigma$ and $2.6\sigma$ in helicity and Collins-Soper frames, respectively. Furthermore, the measurements are confronted with several available theoretical frameworks, including NRQCD, CSM, ICEM, and the CGC-based NRQCD approach. Additionally, a charged-particle multiplicity and rapidity differential study of J/$\psi$ and $\psi(2S)$ polarization in *pp* collisions is presented using a Monte Carlo model for various center-of-mass energies. In conclusion, the quarkonium polarization measurements presented in this thesis in hadronic and nuclear collisions at LHC energies can provide a stringent test of theoretical models and contribute significantly to the understanding of quarkonium spin polarization and production mechanisms.

The phenomenological studies presented in this thesis complement the experimental investigations by exploring the spin polarization of hyperons and the spin alignment of vector mesons at LHC energies. To understand the observed spin alignment of quarkonium states, the diagonal and off-diagonal elements of the spin density matrix are calculated for charmonium [J/$\psi$, $\psi(2S)$] and bot-

tomonium [$\Upsilon(1S)$, $\Upsilon(2S)$] states in the presence of rotation, finite temperature, magnetic fields, and momentum-space anisotropy. The dynamics of quarkonium states are described by constructing an effective Hamiltonian including the spin–vorticity and spin–magnetic interactions in a thermal rotating medium with a temperature-dependent quarkonium potential. The space-time evolution of the medium is modeled using second-order relativistic viscous hydrodynamics with vorticity. The spin density matrix elements are calculated by evaluating the spin projection-dependent eigenenergies from the time-independent Schrödinger equation for Pb+Pb collisions at $\sqrt{s_{\rm NN}} = 5.02$ TeV at mid-rapidity. It is observed that the binding energy (mass) and melting temperature (width) of quarkonium states are sensitive to the medium temperature, rotation, magnetic field, and anisotropy parameters, and hence to the spin alignment observables. The magnetic field and medium anisotropies affect the quarkonium states in a state-dependent manner. The shape of the angular distribution depends strongly on the medium rotation, temperature, and equilibration time of the quark-gluon plasma. Thus, the spin alignment of the quarkonium state may serve as a probe of thermalization at LHC energies. Further, using the developed framework, the quarkonium decay width due to the collisional damping and gluon dissociation processes is estimated. The spin-dependent dissociation of quarkonium states, governed by their binding energies and sizes, is proposed as a potential mechanism underlying the spin alignment. The results provide a unified interpretation of the observed state-, momentum-, and multiplicity-dependent behavior of $\rho_{00}$, highlighting quarkonium spin alignment observables as sensitive probes of both the thermal and vortical properties of deconfined QCD matter.

Moreover, phenomenological studies further include the global and local spin polarization of hyperons obtained in a hydrodynamic and transport-model framework. The global spin polarization of $\Lambda$ hyperons is obtained by determining the lifetime of the vortical QGP and by developing a unified hydrodynamic framework within the ambit of second-order Müller-Israel-Stewart (MIS) based relativistic

viscous hydrodynamics. The medium viscosity, vorticity, and magnetic field are coupled in the hydrodynamic equations, and the interplay of spin-vorticity and spin-magnetic coupling is observed via the global spin polarization $\Lambda$ hyperons at LHC energies. Furthermore, the local spin polarization of $\Lambda$ hyperons due to thermal vorticity and thermal shear is obtained in an ideal uncharged fluid using hydrodynamic and transport model simulations. In another approach, the hyperons' spin polarization and vector meson spin alignment are explored through quark spin polarization in two hadronization scenarios: recombination and fragmentation. The spin polarization of baryons including $\Lambda$, $\Xi^-$, $\Omega^-$, $\Delta^{++}$ and $\Sigma^{\pm}$, and spin alignment of vector mesons $K^{*0}$, $\phi$, and $\rho$ are calculated through partonic elastic scattering within the framework of an effective static potential model. In this approach, the quark polarization is driven by the Debye mass. Hence, any change brought to the Debye mass due to external perturbations like magnetic field and anisotropy, in principle, affects the global quark polarization and thus the spin polarization of hadrons. The global baryon spin polarization and vector mesons' spin alignment show sensitivity to magnetic field, baryonic chemical potential, and medium anisotropy. The degree of spin polarization is found to be flavor-dependent for hyperons, while vector meson spin alignment depends on the hadronization mechanisms. The phenomenological predictions for spin polarization and spin alignment are compared with the corresponding experimental measurements, wherever available, at RHIC and LHC energies. The overall qualitative agreement between the model predictions and the data supports the validity of the phenomenological framework.

*In conclusion, this thesis advances the current understanding of hadron spin polarization at LHC energies from both experimental and theoretical perspectives, providing new insights into the mechanisms governing spin dynamics in high-energy nuclear and hadronic collisions.*

# Bibliography

[1] S. Navas *et al.* [Particle Data Group], Phys. Rev. D **110**, 030001 (2024).

[2] S. Acharya *et al.* [ALICE], Eur. Phys. J. C **84**, 813 (2024).

[3] P. de Forcrand, PoS **LAT2009**, 010 (2009).

[4] R. Gavai, S. Gupta and R. Ray, Prog. Theor. Phys. Suppl. **153**, 270 (2004).

[5] M. D'Elia and M. P. Lombardo, Phys. Rev. D **67**, 014505 (2003).

[6] R. V. Gavai and S. Gupta, Phys. Rev. D **71**, 114014 (2005).

[7] M. A. Stephanov, Prog. Theor. Phys. Suppl. **153**, 139 (2004).

[8] J. Adam *et al.* [ALICE], Phys. Lett. B **754**, 235 (2016).

[9] S. S. Adler *et al.* [PHENIX], Phys. Rev. Lett. **94**, 232301 (2005).

[10] A. Adare *et al.* [PHENIX], Phys. Rev. Lett. **104**, 132301 (2010).

[11] B. Abelev *et al.* [ALICE], Phys. Rev. C **88**, 044910 (2013).

[12] B. B. Abelev *et al.* [ALICE], Phys. Rev. Lett. **111**, 222301 (2013).

[13] B. B. Abelev *et al.* [ALICE], Phys. Rev. C **91**, 024609 (2015).

[14] J. Rafelski and B. Muller, Phys. Rev. Lett. **48**, 1066 (1982).

[15] P. Koch, B. Muller and J. Rafelski, Phys. Rept. **142**, 167 (1986).

[16] J. Rafelski, Phys. Lett. B **262**, 333 (1991).

[17] B. B.Abelev, *et al.* [ALICE], Phys. Lett. B **728**, 216 (2014); **734**, 409(E) (2014).

[18] A. Andronic, *et al.*, Phys. Lett. B **673**, 142 (2009); **678**, 516(E) (2009).

[19] J. Cleymans, *et al.*, Phys. Rev. C **74**, 034903 (2006)

[20] S. Acharya *et al.* [ALICE], JHEP **09**, 006 (2018).

[21] T. Matsui and H. Satz, Phys. Lett. B **178**, 416 (1986).

[22] S. Acharya *et al.* [ALICE], Phys. Rev. Lett. **132**, 042301 (2024).

[23] X. Du and R. Rapp, Nucl. Phys. A **943**, 147 (2015).

[24] A. Andronic, *et al.* Phys. Lett. B **797**, 134836 (2019).

[25] A. M. Sirunyan *et al.* [CMS], Eur. Phys. J. C **78**, 509 (2018).

[26] S. Acharya *et al.* [ALICE], Eur. Phys. J. C **80**, 693 (2020).

[27] S. Acharya *et al.* [ALICE], Nature Commun. **17**, 2585 (2026).

[28] R. Sahoo, AAPPS Bull. **29**, 16 (2019).

[29] R. Sahoo and T. K. Nayak, Curr. Sci. **121**, 1403 (2021).

[30] V. Khachatryan *et al.* [CMS], Phys. Lett. B **765**, 193 (2017).

[31] A. Ortiz Velasquez, *et al.*, Phys. Rev. Lett. **111**, 042001 (2013).

[32] C. Zhang, *et al.*, Phys. Lett. B **822**, 136702 (2021).

[33] T. Affolder *et al.*, [CDF], Phys. Rev. Lett. **85**, 2886 (2000).

[34] C. N. Brown *et al.*, [NuSea], Phys. Rev. Lett. **86**, 2529 (2001).

[35] D. Acosta *et al.*, [CDF], Phys. Rev. Lett. **88**, 161802 (2002).

[36] T. H. Chang *et al.*, [NuSea], Phys. Rev. Lett. **91**, 211801 (2003).

[37] A. Abulencia *et al.*, [CDF], Phys. Rev. Lett. **99**, 132001 (2007).

[38] B. I. Abelev *et al.* [STAR], Phys. Rev. C **76**, 024915 (2007).

[39] V. M. Abazov *et al.*, [D0], Phys. Rev. Lett. **101**, 182004 (2008).

[40] B. I. Abelev *et al.* [STAR], Phys. Rev. C **77**, 061902 (2008).

[41] E. Etzion *et al.*, [ATLAS], Nucl. Phys. B Proc. Suppl. **187**, 136 (2009).

[42] I. Abt *et al.*, [HERA-B], Eur. Phys. J. C **60**, 517 (2009).

[43] A. Adare *et al.*, [PHENIX], Phys. Rev. D **82**, 012001 (2010).

[44] T. Aaltonen *et al.*, [CDF], Phys. Rev. Lett. **108**, 151802 (2012).

[45] B. Abelev *et al.*, [ALICE], Phys. Rev. Lett. **108**, 082001 (2012).

[46] S. Chatrchyan *et al.*, [CMS], Phys. Lett. B **727**, 381 (2013).

[47] S. Chatrchyan *et al.*, [CMS], Phys. Rev. Lett. **110**, 081802 (2013).

[48] R. Aaij *et al.*, [LHCb], Eur. Phys. J. C **73**, 2631 (2013).

[49] R. Aaij *et al.* [LHCb], Eur. Phys. J. C **74**, 2872 (2014).

[50] L. Adamczyk *et al.*, [STAR], Phys. Lett. B **739**, 180 (2014).

[51] V. Khachatryan *et al.*, [CMS], Phys. Lett. B **761**, 31 (2016).

[52] L. Adamczyk *et al.* [STAR], Nature **548** 62 (2017).

[53] S. Acharya *et al.*, [ALICE], Eur. Phys. J. C **78**, 562 (2018).

[54] J. Adam *et al.* [STAR], Phys. Rev. C **98**, 014910 (2018).

[55] J. Adam *et al.* [STAR], Phys. Rev. Lett. **123**, 132301 (2019).

[56] J. Adam *et al.*, [STAR], Phys. Rev. D **102**, 092009 (2020).

[57] U. Acharya *et al.* [PHENIX], Phys. Rev. D **102**, 072008 (2020).

[58] M. S. Abdallah *et al.* [STAR], Phys. Rev. C **104**, L061901 (2021).

[59] J. Adam *et al.* [STAR], Phys. Rev. Lett. **126**, 162301 (2021).

[60] M. I. Abdulhamid *et al.* [STAR], Phys. Rev. C **108**, 014910 (2023).

[61] M. Abdulhamid *et al.* [STAR], Phys. Rev. Lett. **131**, 202301 (2023).

[62] M. S. Abdallah *et al.* [STAR], Nature **614** 244 (2023).

[63] S. Acharya *et al.* [ALICE], Phys. Rev. Lett. **131**, 042303 (2023).

[64] A. Hayrapetyan *et al.* [CMS], Phys. Lett. B **858**, 139044 (2024).

[65] B. E. Aboona *et al.* [STAR], JHEP **06**, 050 (2026).

[66] S. Acharya *et al.* [ALICE], Phys. Rev. Lett. **125**, 012301 (2020).

[67] S. Acharya *et al.*, [ALICE], Phys. Lett. B **815**, 136146 (2021).

[68] S. Acharya *et al.* [ALICE], Phys. Rev. Lett. **128**, 172005 (2022).

[69] S. Acharya *et al.* [ALICE], Phys. Rev. C **101**, 044611 (2020); **105**, 029902(E) (2022).

[70] R. Abou Yassine *et al.* [HADES], Phys. Lett. B **835**, 137506 (2022).

[71] S. Acharya *et al.*, [ALICE], Phys. Rev. Lett. **131**, 042303 (2023).

[72] S. Acharya *et al.* [ALICE], JHEP **10**, 094 (2025).

[73] R. Aaij *et al.* [LHCb], Phys. Rev. D **112**, 112022 (2025).

[74] A. K. Leibovich, Phys. Rev. D **56**, 4412 (1997).

[75] M. Beneke and M. Krämer, Phys. Rev. D **55**, 5269 (1997).

[76] M. Beneke, *et al.*, Phys. Rev. D **57**, 4258 (1998).

[77] E. Braaten, B. A. Kniehl and J. Lee, Phys. Rev. D **62**, 094005 (2000).

[78] B. A. Kniehl and J. Lee, Phys. Rev. D **62**, 114027 (2000).

[79] Z. T. Liang, *et al.*, Phys. Rev. Lett. **94**, 102301 (2005); **96** 039901(E) (2006).

[80] Z. T. Liang and X. N. Wang, Phys. Lett. B **629**, 20 (2005).

[81] B. Betz, M. Gyulassy and G. Torrieri, Phys. Rev. C **76**, 044901 (2007).

[82] Z. t. Liang, J. Phys. G **34**, S323-330 (2007).

[83] J. H. Gao, *et al.*, Phys. Rev. C **77**, 044902 (2008).

[84] F. Becattini, F. Piccinini and J. Rizzo, Phys. Rev. C **77**, 024906 (2008).

[85] B. Gong and J. X. Wang, Phys. Rev. Lett. **100**, 232001 (2008).

[86] H. Haberzettl and J. P. Lansberg, Phys. Rev. Lett. **100**, 032006 (2008).

[87] P. Faccioli, *et al.*, Phys. Rev. Lett. **102**, 151802 (2009).

[88] P. Faccioli, *et al.*, Eur. Phys. J. C **69**, 657 (2010).

[89] P. Faccioli, C. Lourenço and J. Seixas, Phys. Rev. D **81**, 111502 (2010).

[90] P. Faccioli, C. Lourenço and J. Seixas, Phys. Rev. Lett. **105**, 061601 (2010).

[91] H. S. Chung, C. Yu, S. Kim and J. Lee, Phys. Rev. D **81**, 014020 (2010).

[92] J. H. Gao, *et al.*, Phys. Rev. Lett. **109**, 232301 (2012).

[93] M. Butenschoen and B. A. Kniehl, Phys. Rev. Lett. **108**, 172002 (2012).

[94] K. T. Chao, *et al.*, Phys. Rev. Lett. **108**, 242004 (2012).

[95] L. P. Csernai, *et al.*, Phys. Rev. C **87**, 034906 (2013).

[96] F. Becattini, *et al.*, Annals Phys. **338** 32 (2013).

[97] B. Gong, *et al.*, Phys. Rev. Lett. **110**, 042002 (2013).

[98] H. S. Shao and K. T. Chao, Phys. Rev. D **90**, 014002 (2014).

[99] P. Faccioli, *et al.*, Phys. Lett. B **736**, 98 (2014).

[100] L. P. Csernai, *et al.*, Phys. Rev. C **90**, 021904 (2014).

[101] F. Becattini, et al., Eur. Phys. J. C **75**, 406 (2015); **78**, 354(E) (2018).

[102] H. S. Shao, *et al.*, JHEP **05**, 103 (2015).

[103] L. G. Pang, *et al.*, Phys. Rev. Lett. **117**, 192301 (2016).

[104] W. T. Deng and X. G. Huang, Phys. Rev. C **93**, 064907 (2016).

[105] Y. L. Xie, *et al.*, Phys. Rev. C **94**, 054907 (2016).

[106] F. Becattini, *et al.*, Phys. Rev. C **88**, 034905 (2013); **93**, 069901(E) (2016).

[107] R. H. Fang, *et al.*, Phys. Rev. C **94**, 024904 (2016).

[108] Y. Jiang, *et al.*, Phys. Rev. C **94**, 044910 (2016); **95**, 049904(E) (2017).

[109] O. V. Teryaev and V. I. Zakharov, Phys. Rev. D **96**, 096023 (2017).

[110] I. Karpenko and F. Becattini, Eur. Phys. J. C **77**, 213 (2017).

[111] H. Li, L. G. Pang, Q. Wang and X. L. Xia, Phys. Rev. C **96**, 054908 (2017).

[112] Y. Xie, D. Wang and L. P. Csernai, Phys. Rev. C **95**, 031901 (2017).

[113] H. Li, *et al.*, Nucl. Phys. A **967**, 772 (2017).

[114] I. Karpenko and F. Becattini, Nucl. Phys. A **967**, 764 (2017).

[115] Y. Sun and C. M. Ko, Phys. Rev. C **96**, 024906 (2017).

[116] F. Becattini, *et al.*, Phys. Rev. C **95**, 054902 (2017).

[117] Y. G. Yang, *et al.*, Phys. Rev. C **97**, 034917 (2018).

[118] F. Becattini and I. Karpenko, Phys. Rev. Lett. **120**, 012302 (2018).

[119] X. L. Xia, H. Li, Z. B. Tang and Q. Wang, Phys. Rev. C **98**, 024905 (2018).

[120] Z. Z. Han and J. Xu, Phys. Lett. B **786**, 255 (2018).

[121] Y. Q. Ma, *et al.*, JHEP **12**, 057 (2018).

[122] V. Cheung and R. Vogt, Phys. Rev. D **98**, 114029 (2018).

[123] E. E. Kolomeitsev, *et al.*, Phys. Rev. C **97**, 064902 (2018).

[124] L. P. Csernai, J. I. Kapusta and T. Welle, Phys. Rev. C **99**, 021901 (2019).

[125] Y. Guo, S. Shi, S. Feng and J. Liao, Phys. Lett. B **798**, 134929 (2019).

[126] D. X. Wei, *et al.*, Phys. Rev. C **99**, 014905 (2019).

[127] Y. B. Ivanov, *et al.*, Phys. Rev. C **100**, 014908 (2019).

[128] V. Cheung and R. Vogt, Phys. Rev. D **99**, 034007 (2019).

[129] R. Vogt, Nucl. Phys. A **982**, 751 (2019).

[130] F. Becattini, G. Cao and E. Speranza, Eur. Phys. J. C **79**, 741 (2019).

[131] X. L. Sheng, *et al.*, Phys. Rev. D **101**, 096005 (2020); **105**, 099903(E) (2022).

[132] X. L. Sheng, Q. Wang and X. N. Wang, Phys. Rev. D **102**, 056013 (2020).

[133] A. Ayala, *et al.* Phys. Lett. B **810**, 135818 (2020).

[134] X. G. Deng, *et al.*, Phys. Rev. C **101**, 064908 (2020).

[135] O. Vitiuk, *et al.*, Phys. Lett. B **803**, 135298 (2020).

[136] Xie, Y., Wang, D. and Csernai, L.P., Eur. Phys. J. C **80**, 39 (2020).

[137] F. Becattini and M. A. Lisa, Ann. Rev. Nucl. Part. Sci. **70**, 395 (2020).

[138] Y. Guo, *et al.*, Phys. Rev. C **104**, L041902 (2021).

[139] T. Stebel and K. Watanabe, Phys. Rev. D **104**, 034004 (2021).

[140] B. Fu, K. Xu, X. G. Huang and H. Song, Phys. Rev. C **103**, 024903 (2021).

[141] B. Mohanty, *et al.*, Mod. Phys. Lett. A **36**, 2130026 (2021).

[142] X. L. Xia, *et al.*, Phys. Lett. B **817**, 136325 (2021).

[143] V. Cheung and R. Vogt, Phys. Rev. D **104**, 094026 (2021).

[144] V. Cheung and R. Vogt, Phys. Rev. C **105**, 055202 (2022).

[145] S. Alzhrani, S. Ryu and C. Shen, Phys. Rev. C **106**, 014905 (2022).

[146] F. Becattini, Rept. Prog. Phys. **85**, 122301 (2022).

[147] P. Faccioli and C. Lourenço, Lect. Notes Phys. 1002 (2022).

[148] Y. Hidaka, *et al.*, Prog. Part. Nucl. Phys. **127**, 103989 (2022).

[149] Y. B. Ivanov and A. A. Soldatov, Phys. Rev. C **105**, 034915 (2022).

[150] K. Xu, F. Lin, A. Huang and M. Huang, Phys. Rev. D **106**, L071502 (2022).

[151] S. Wu and Y. Xie, Eur. Phys. J. A **59**, 108 (2023).

[152] X. L. Sheng, *et al.*, Phys. Rev. Lett. **131**, 042304 (2023).

[153] X. L. Sheng, S. Pu and Q. Wang, Phys. Rev. C **108**, 054902 (2023).

[154] F. Becattini, *et al.*, Int. J. Mod. Phys. E **33**, 2430006 (2024).

[155] X. L. Sheng, *et al.*u, Phys. Rev. D **110**, 056047 (2024).

[156] J. p. Lv, *et al.*, Phys. Rev. D **109**, 114003 (2024).

[157] B. Sahoo, *et al.*, Phys. Rev. C **109**, 034910 (2024).

[158] V. Voronyuk, *et al.*, Phys. Rev. C **111**, 034907 (2025).

[159] B. Sahoo, C. R. Singh and R. Sahoo, Eur. Phys. J. C **85**, 580 (2025).

[160] B. Sahoo, C. R. Singh and R. Sahoo, Phys. Scripta **100**, 065310 (2025).

[161] B. Sahoo, C. R. Singh and R. Sahoo, Phys. Rev. D **113**, 054023 (2026).

[162] S. Dey and A. Jaiswal, Phys. Lett. B **873**, 140202 (2026).

[163] B. Sahoo, C. R. Singh and R. Sahoo, Eur. Phys. J. C. (2026) [In Press]

[164] B. Sahoo, C. R. Singh and R. Sahoo, [arXiv:2604.13701].

[165] V. Skokov, *et al.*, Int. J. Mod. Phys. A **24**, 5925 (2009).

[166] G. Bunce, *et al.* Phys. Rev. Lett. **36**, 1113 (1976).

[167] K. Schilling, *et al.*, Nucl. Phys. B **15**, 397 (1970); **18**, 332 (E) (1970).

[168] M. A. Lisa, *et al.*, Phys. Rev. C **104**, 011901 (2021).

[169] W. M. Serenone, *et al.*, Phys. Lett. B **820**, 136500 (2021).

[170] Y. B. Ivanov, Phys. Rev. C **107**, L021902 (2023).

[171] V. H. Ribeiro, *et al.*, Phys. Rev. C **109**, 014905 (2024).

[172] J. H. Gao, Phys. Rev. D **104**, 076016 (2021).

[173] C. Yi, S. Pu, J. H. Gao and D. L. Yang, Phys. Rev. C **105**, 044911 (2022).

[174] V. E. Ambrus and M. N. Chernodub, Eur. Phys. J. C **82**, 61 (2022).

[175] B. E. Aboona *et al.* [STAR], Nature **650**, 65 (2026).

[176] X. L. Sheng, *et al.* Phys. Rev. Lett. **136**, 082301 (2026).

[177] S. Ryu, V. Jupic and C. Shen, Phys. Rev. C **104**, 054908 (2021).

[178] B. Fu, *et al.*, Phys. Rev. Lett. **127**, 142301 (2021).

[179] F. Becattini, *et al.*, Phys. Lett. B **820**, 136519 (2021).

[180] F. Becattini, *et al.*, Phys. Rev. Lett. **127**, 272302 (2021).

[181] A. Palermo, *et al.*, Eur. Phys. J. C **84**, 920 (2024).

[182] S. Y. F. Liu and Y. Yin, JHEP **07**, 188 (2021).

[183] W. Florkowski,*et al.*, Phys. Rev. C **105**, 064901 (2022).

[184] W. Florkowski, *et al.*, Phys. Rev. C **100**, 054907 (2019).

[185] H. Z. Wu, *et al.*, Phys. Rev. Research. **1**, 033058 (2019).

[186] C. Yi, S. Pu and D. L. Yang, Phys. Rev. C **104**, 064901 (2021).

[187] W. Florkowski,*et al.*, Phys. Rev. C **97**, 041901 (2018).

[188] W. Florkowski, *et al.*, Phys. Rev. D **97**, 116017 (2018).

[189] S. Bhadury, *et al.*, Phys. Lett. B **814**, 136096 (2021).

[190] S. Bhadury, *et al.*, Phys. Rev. D **103**, 014030 (2021).

[191] S. Y. F. Liu and Y. Yin, Phys. Rev. D **104**, 054043 (2021).

[192] M. Buzzegoli, Phys. Rev. C **105**, 044907 (2022).

[193] Y. Sun and C. M. Ko, Phys. Rev. C **99**, 011903 (2019).

[194] B. Müller *et al.*, Phys. Rev. D **105**, L011901 (2022); **106**, 039904(E) (2022).

[195] A. Kumar, B. Müller and D. L. Yang, Phys. Rev. D **108**, 016020 (2023).

[196] S. K. Das, *et al.*, Phys. Lett. B **768**, 260 (2017).

[197] Esma Mobs. "The CERN Accelerator Complex". In: Open-Pho-Accel-2016-009, Open-Pho-a (2018).

[198] G. Apollinari, et al., CERN Yellow Rep., 1-19 (2015).

[199] G. Aad *et al.* [ATLAS], JINST **3**, S08003 (2008).

[200] S. Chatrchyan *et al.* [CMS], JINST **3**, S08004 (2008).

[201] A. A. Alves, Jr. *et al.* [LHCb], JINST **3**, S08005 (2008).

[202] K. Aamodt *et al.* [ALICE], JINST **3**, S08002 (2008).

[203] S. Upadhyaya, Int. J. Mod. Phys. A **40**, 2444006 (2025).

[204] G. Dellacasa *et al.* [ALICE], CERN-LHCC-99-05.

[205] W. H. Trzaska [ALICE], Nucl. Instrum. Meth. A **845**, 463 (2017).

[206] P. Cortese *et al.* [ALICE], CERN-LHCC-2008-014.

[207] J. Allen, *et al.* CERN-LHCC-2010-011.

[208] G. Dellacasa *et al.* [ALICE], CERN-LHCC-99-04.

[209] G. Volpe [ALICE], Nucl. Instrum. Meth. A **876**, 133 (2017).

[210] A. Akindinov, *et al.* Eur. Phys. J. Plus **128**, 44 (2013).

[211] S. Acharya *et al.* [ALICE], Nucl. Instrum. Meth. A **881**, 88 (2018).

[212] A. L. Gera, PoS **EPS-HEP2019**, 102 (2020).

[213] J. Adolfsson *et al.* [ALICE TPC], JINST **16**, P03022 (2021).

[214] B. Abelev *et al.* [ALICE], J. Phys. G **41**, 087002 (2014).

[215] C. Finck [ALICE Muon Spectrometer], J. Phys. Conf. Ser. **50**, 397 (2006).

[216] G. Garcia *et al.* [ALICE], CERN-LHCC-2013-014.

[217] M. Tarhini, HAL-tel-01691725 [Ph.D. Thesis].

[218] R. Sadek, CERN-THESIS-2022-319.

[219] M. Coquet, tel-04337446.

[220] D.Brinkand, G.Stachler, Angular momentum, Clarendon Press. (1993).

[221] A. Batista Camejo, NNT : 2017CLFAC004.

[222] J. C. Collins and D. E. Soper, Phys. Rev. D **16**, 2219 (1977).

[223] K. Gottfried and J. D. Jackson, Nuovo Cim. **33**, 309 (1964).

[224] S. Li, tel-01294986.

[225] B. Sahoo, and R. Sahoo, AN: alice-notes.web.cern.ch/node/1668

[226] L. Mattei, et al., AN: alice-notes.web.cern.ch/node/1478

[227] [ALICE], ALICE-PUBLIC-2015-006.

[228] L. M. Massacrier, et al., AN: alice-notes.web.cern.ch/node/941

[229] B. Sahoo, and R. Sahoo, AN: alice-notes.web.cern.ch/node/1691

[230] L. Micheletti et al., AN: alice-notes.web.cern.ch/node/889

[231] D. Kumar et al., AN: alice-notes.web.cern.ch/node/1386

[232] R. Cerri, et al., AN: alice-notes.web.cern.ch/node/1743

[233] B. Sahoo, and R. Sahoo, AN: alice-notes.web.cern.ch/node/1698

[234] S. Deb, D. Thakur, S. De and R. Sahoo, Eur. Phys. J. A **56**, 134 (2020).

[235] C. R. Singh, S. Ganesh and M. Mishra, Eur. Phys. J. C **79**, 147 (2019).

[236] C. R. Singh, *et al.*, Eur. Phys. J. C **82**, 542 (2022).

[237] C. R. Singh, *et al.*, Phys. Rev. D **112**, 014017 (2025).

[238] C. R. Singh, *et al.*, Phys. Rev. C **92**, 034916 (2015).

[239] S. Ganesh, C. R. Singh and M. Mishra, J. Phys. G **45**, 035003 (2018).

[240] N. Hatwar, *et al.*, Phys. Rev. C **104**, 034905 (2021).

[241] Anandan, J., Suzuki, J. (n.d.). Quantum Mechanics in a Rotating Frame. doi.org/arxiv.org/pdf/quant-ph/0305081.pdf

[242] Gordan Baym, Lectures on Quantum Mechanics (1969). archive.org/details/lecturesonquantu0000baym/page/n611/mode/2up

[243] David J. Griffiths, Introduction to Quantum Mechanics. www.fisica.net/mecanica-quantica/Griffiths%20-%20Introduction%20to%20quantum%20mechanics.pdf

[244] F. Nendzig and G. Wolschin, Phys. Rev. C **87**, 024911 (2013).

[245] L. Dong, *et al.*, Phys. Rev. D **104**, 096017 (2021).

[246] L. Dong, *et al.*, JHEP **09**, 200 (2022).

[247] M. Strickland and D. Bazow, Nucl. Phys. A **879**, 25 (2012).

[248] P. Romatschke and M. Strickland, Phys. Rev. D **68**, 036004 (2003).

[249] P. Romatschke and M. Strickland, Phys. Rev. D **70**, 116006 (2004).

[250] M. Strickland, Acta Phys. Pol. B **45**, 2355 (2014).

[251] B. Karmakar, *et al.*, Eur. Phys. J. C **79**, 658 (2019).

[252] H. X. Zhang, J. W. Kang and B. W. Zhang, Eur. Phys. J. C **81**, 623 (2021).

[253] A. Bandyopadhyay, *et al.*, Phys. Rev. D **100**, 034031 (2019).

[254] B. Singh, L. Thakur and H. Mishra, Phys. Rev. D **97**, 096011 (2018).

[255] P. H. De Moura, *et al.*, Phys. Rev. D **108**, 034032 (2023).

[256] K. J. Gonçalves and G. Torrieri, Phys. Rev. C **105**, 034913 (2022).

[257] K. J. Gonçalves, *et al.*, Phys. Rev. C **112**, 014901 (2025).

[258] M. Anselmino, P. Kroll and B. Pire, Z. Phys. C **29**, 135 (1985).

[259] M.E. Peskin, Nucl. Phys. B **156**, 365 (1979).

[260] G. Bhanot, M.E. Peskin, Nucl. Phys. B **156**, 391 (1979).

[261] L. Grandchamp, R. Rapp, Nucl. Phys. A **709**, 415 (2002).

[262] N. Brambilla, *et al.*, Phys. Rev. D **78**, 014017 (2008).

[263] J. Adam *et al.* [ALICE], Phys. Rev. Lett. **116**, 222302 (2016).

[264] A. Muronga, Phys. Rev. Lett. **88**, 062302 (2002); **89**, 159901(E) (2002).

[265] A. Muronga, Phys. Rev. C **69**, 034903 (2004).

[266] S. Weinberg, Gravitation and Cosmology: Principles and Applications of the General Theory of Relativity (J. Wiley and Sons, New York, 1972).

[267] P. Romatschke, Int. J. Mod. Phys. E **19**, 53 (2010).

[268] K. K. Pradhan, *et al.*, Eur. Phys. J. C **84**, 936 (2024).

[269] C. W. Aung, *et al.*, Phys. Rev. C **109** 034913 (2024).

[270] B. Sahoo, *et al.*, Eur. Phys. J. C **83**, 873 (2023).

[271] X. G. Huang, *et al.*, Lecture Notes in Physics **987**, 281 (2021).

[272] B. Singh, J. R. Bhatt and H. Mishra, Phys. Rev. D **100**, 014016 (2019).

[273] F. Becattini and L. Tinti, Ann. Phys. **325**, 1566 (2010).

[274] B. Sahoo, *et al.*, Phys. Rev. D **108**, 074028 (2023).

[275] K. Singh, J. Dey, R. Sahoo and S. Ghosh, Phys. Rev. D **108**, 094007 (2023).

[276] M. D'Elia, S. Mukherjee and F. Sanfilippo, Phys. Rev. D **82**, 051501 (2010).

[277] V. Roy, S. Pu, L. Rezzolla and D. Rischke, Phys. Lett. B **750**, 45 (2015).

[278] R. Biswas, *et al.*, JHEP **10**, 171 (2020).

[279] S. Pu, *et al.*, Phys. Rev. D **93**, 074022 (2016).

[280] B. Sahoo, C. R. Singh and R. Sahoo, Phys. Lett. B **880**, 140714 (2026).

[281] J. Zhao and B. Chen, Phys. Rev. C **107**, 044909 (2023).

[282] D. Lafferty and A. Rothkopf, Phys. Rev. D **101**, 056010 (2020).

[283] G. Huang and P. Zhuang, Phys. Rev. D **104**, 074001 (2021).

[284] M. Le Bellac, Thermal Field Theory (1996).

[285] S. A. Khan, M. Hasan and B. K. Patra, Nucl. Phys. A **1034**, 122643 (2023).

[286] X. Y. Wu, *et al.*, Phys. Rev. C **105**, 064909 (2022).

[287] M. Masera, *et al.*, Phys. Rev. C **79**, 064909 (2009).

[288] C. Loizides, *et al.*, Phys. Rev. C **97**, 054910 (2018); **99**, 019901(E) (2019).

# Appendix

## A.1: $\cos\theta$ differential signal extraction in $pp$ collisions

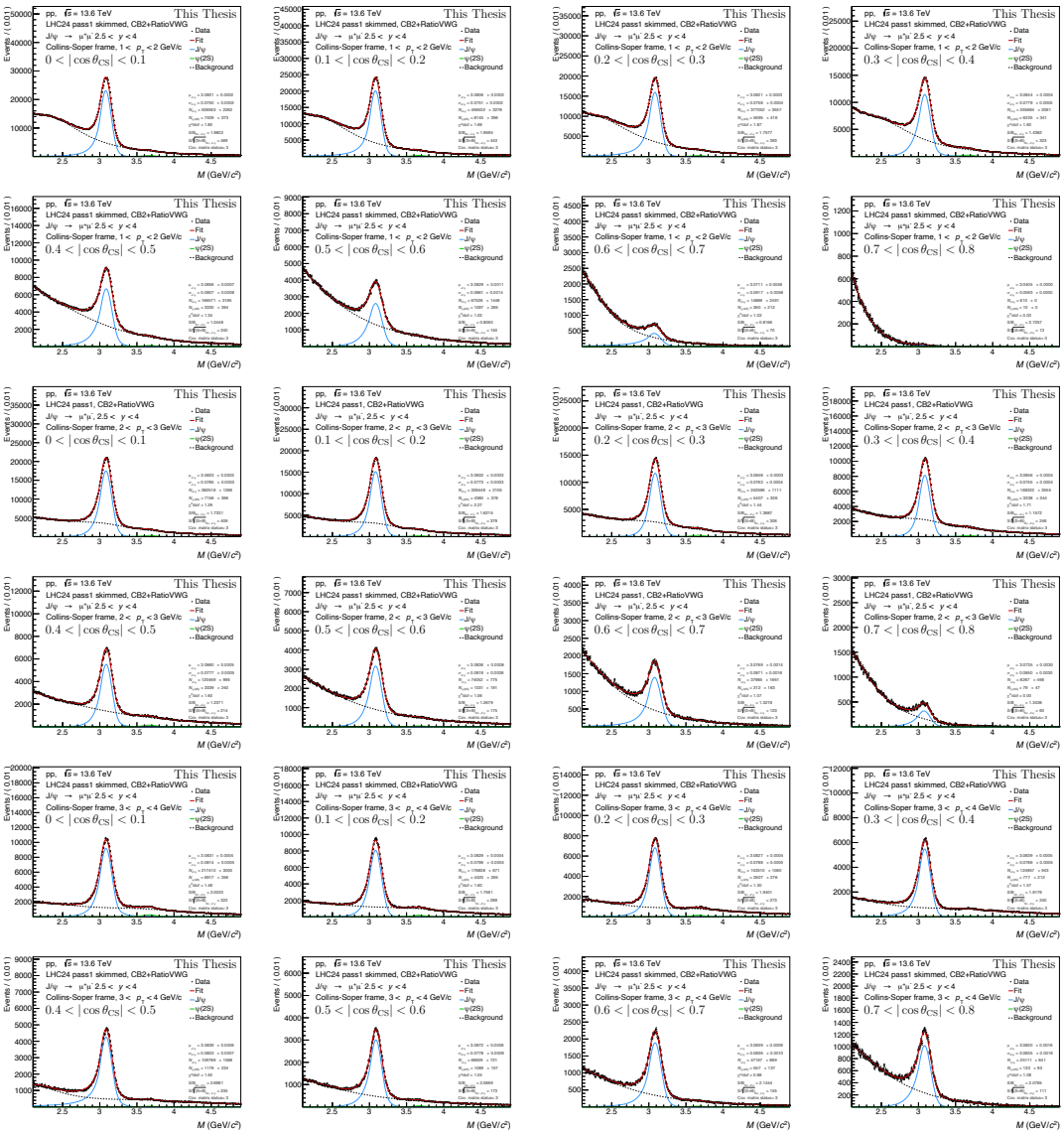


Figure 1: cos$\theta$ differential signal extraction for J/$\psi$ using CB2+RatioVWG function for $1 < p_{\mathrm{T}} < 4$ GeV/c in Collins-Soper reference frame [229].

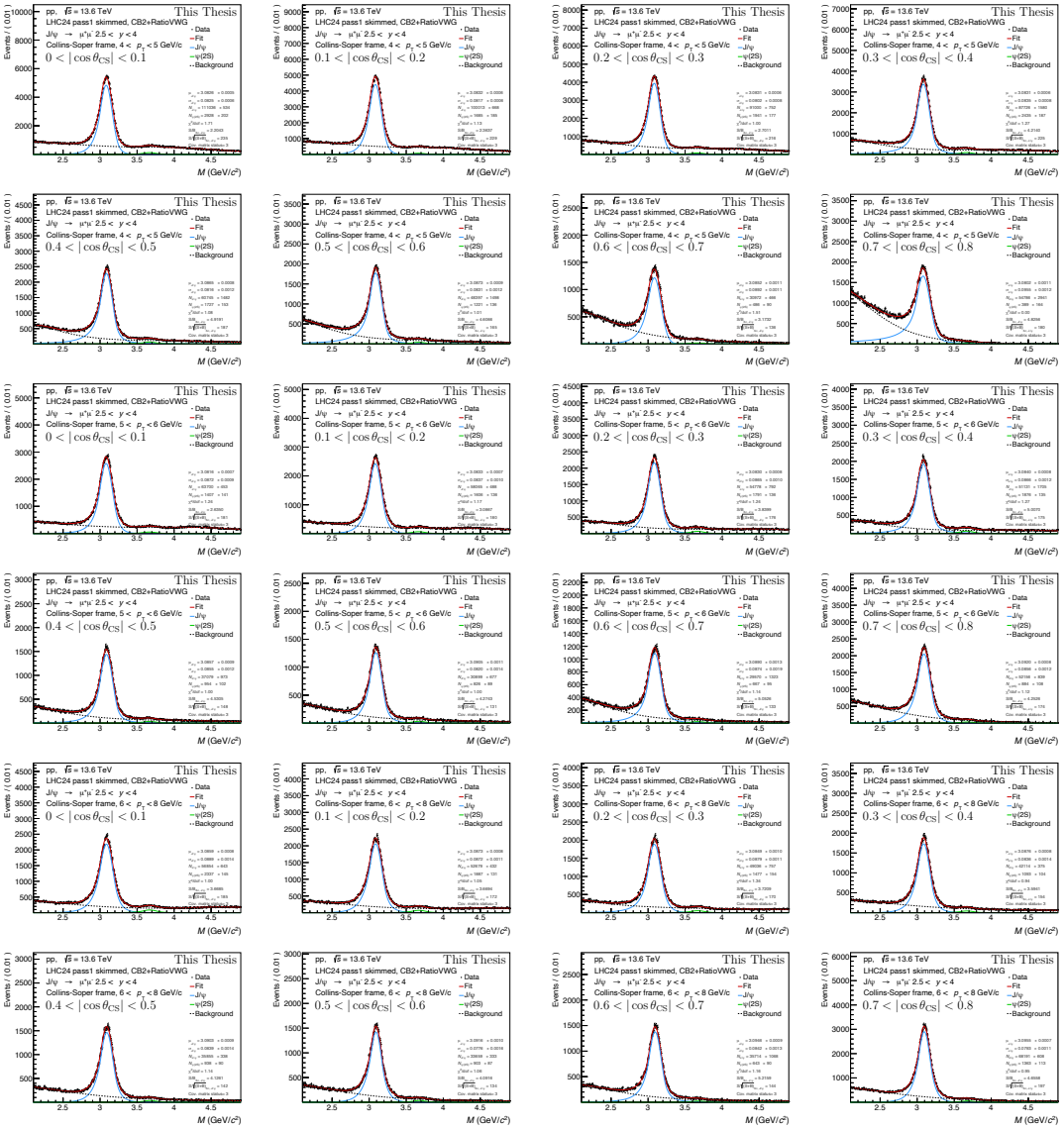



Figure 2: $\cos\theta$ differential signal extraction for J/$\psi$ using CB2+RatioVWG function for $4 < p_{\mathrm{T}} < 8$ GeV/c in Collins-Soper reference frame [229].

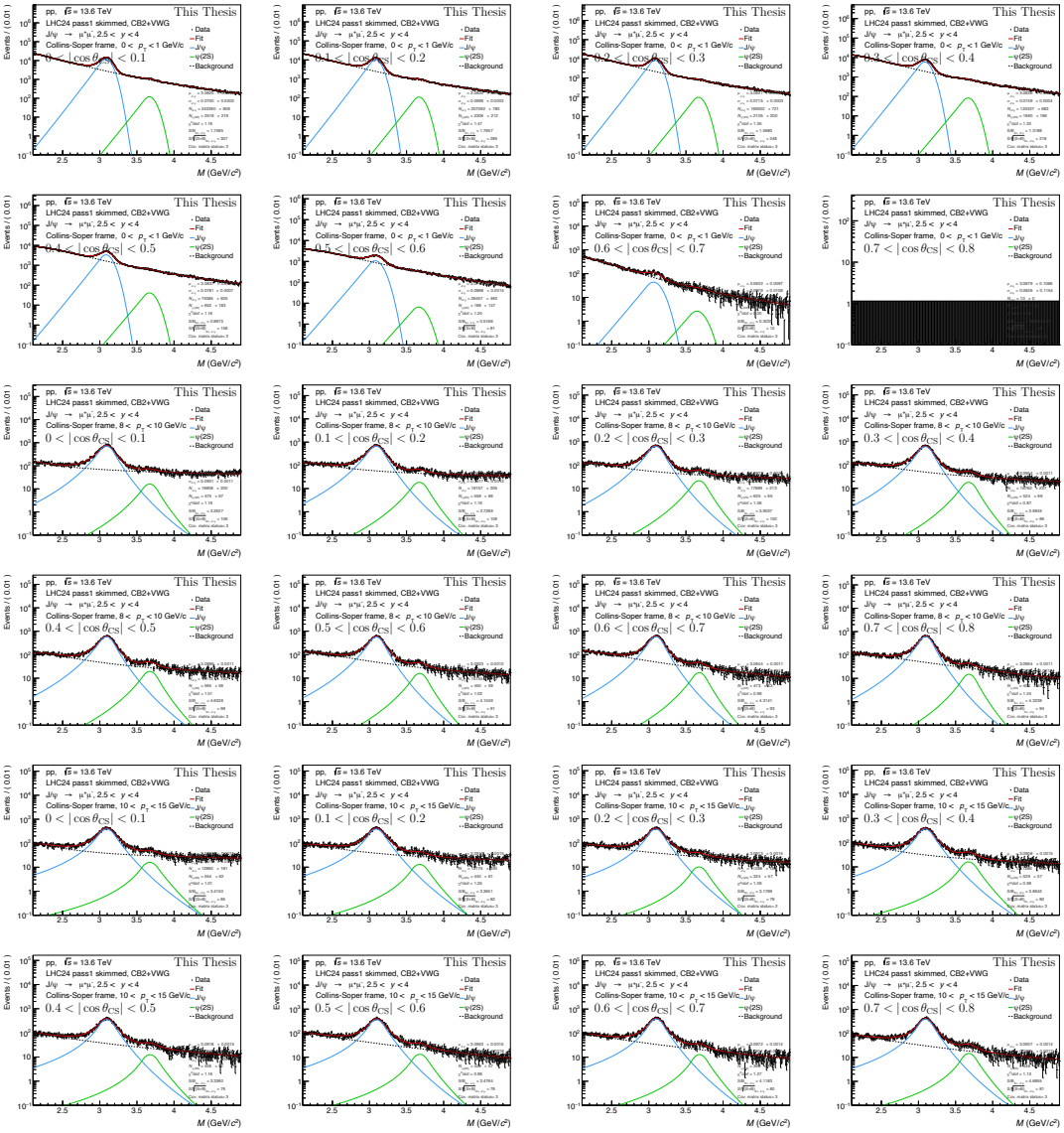


Figure 3: cos$\theta$ differential signal extraction for J/$\psi$ using CB2+VDW function for $0 < p_{\mathrm{T}} < 1$ GeV/c (top two rows), and $8 < p_{\mathrm{T}} < 15$ GeV/c (bottom four rows) in Collins-Soper reference frame [229].

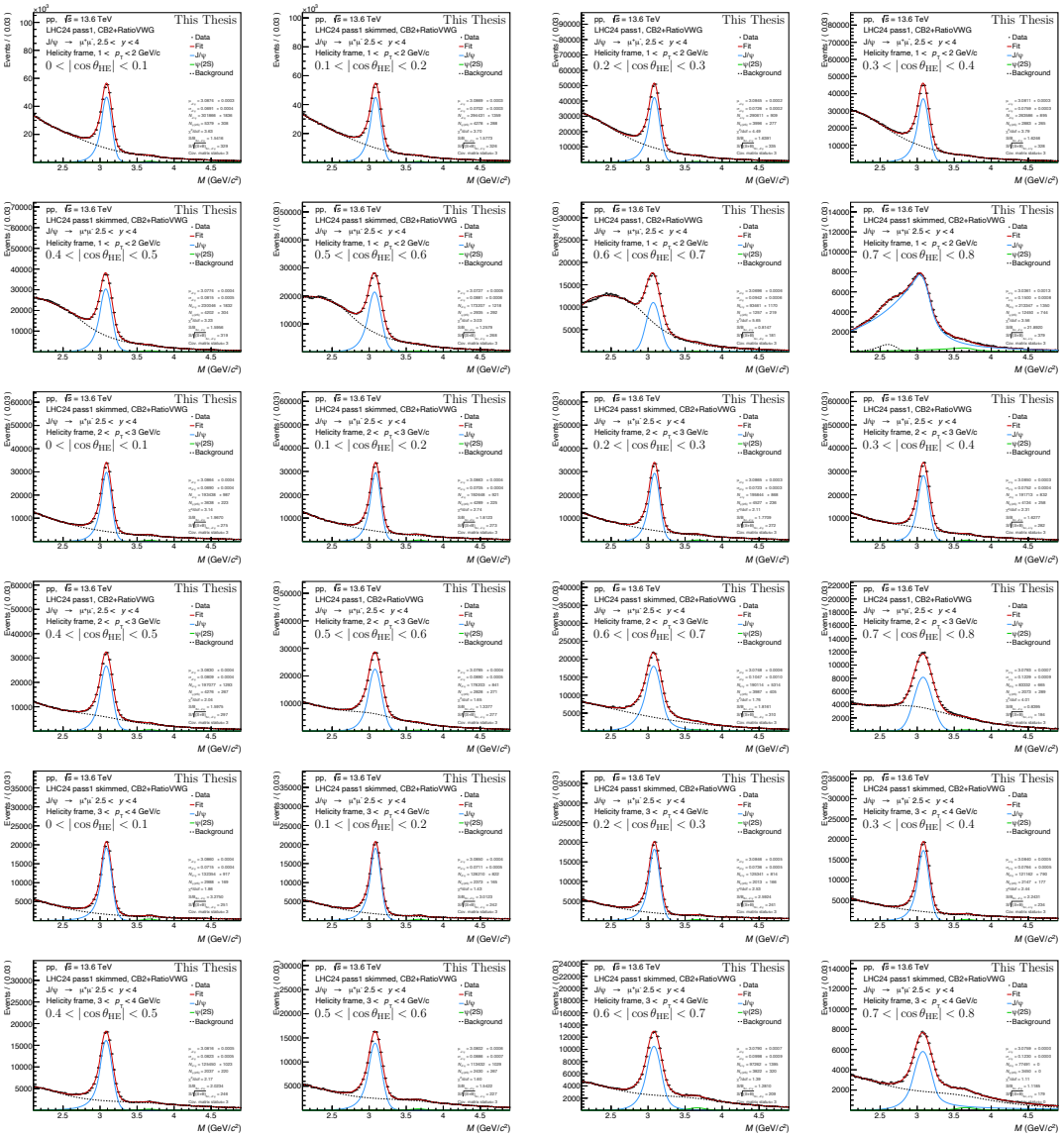



Figure 4: $\cos\theta$ differential signal extraction for J/$\psi$ using CB2+RatioVWG function for $1 < p_{\mathrm{T}} < 4$ GeV/c in helicity reference frame [229].

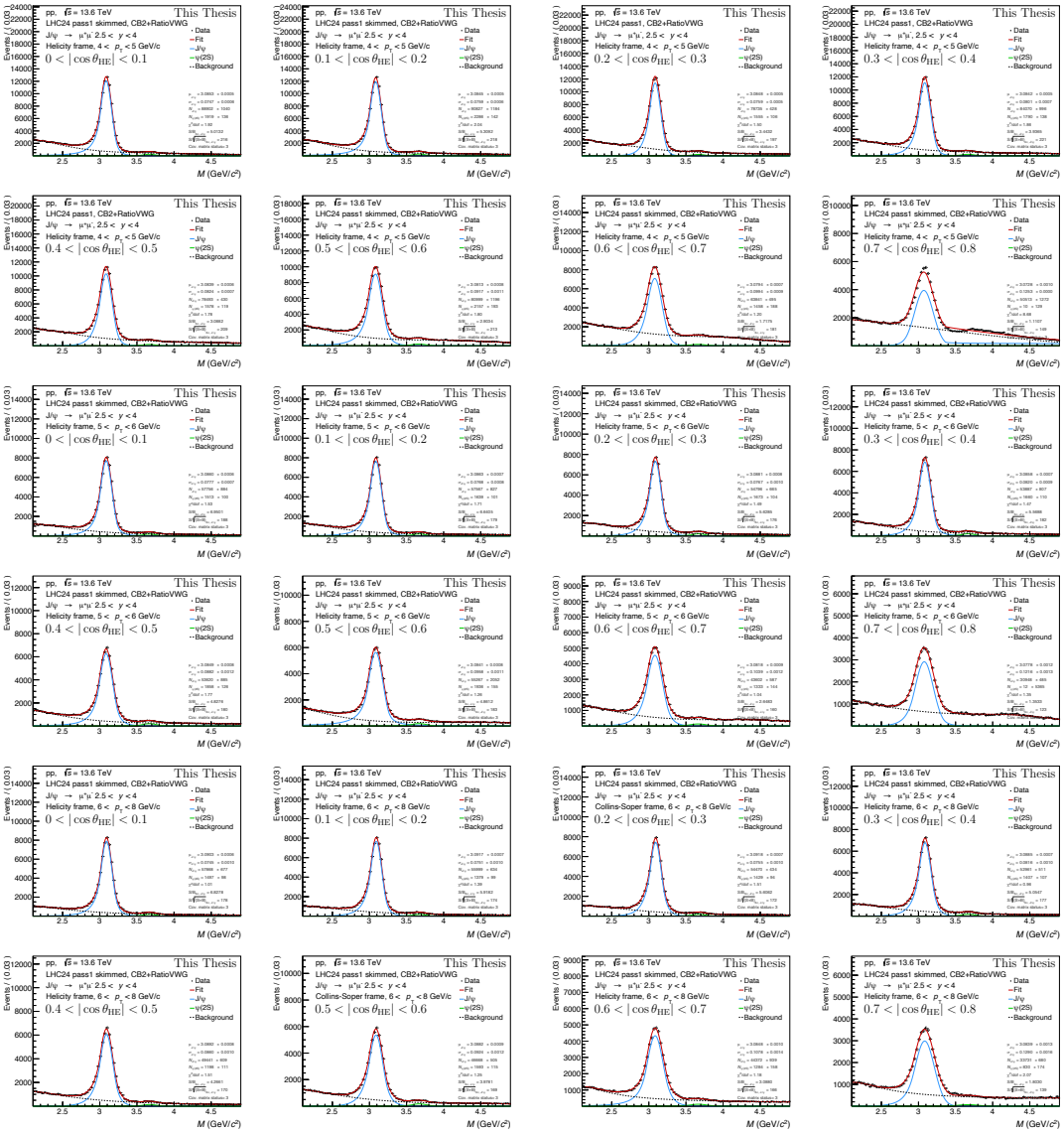



Figure 5: $\cos\theta$ differential signal extraction for J/$\psi$ using CB2+RatioVWG function for $4 < p_{\mathrm{T}} < 8$ GeV/c in helicity reference frame [229].

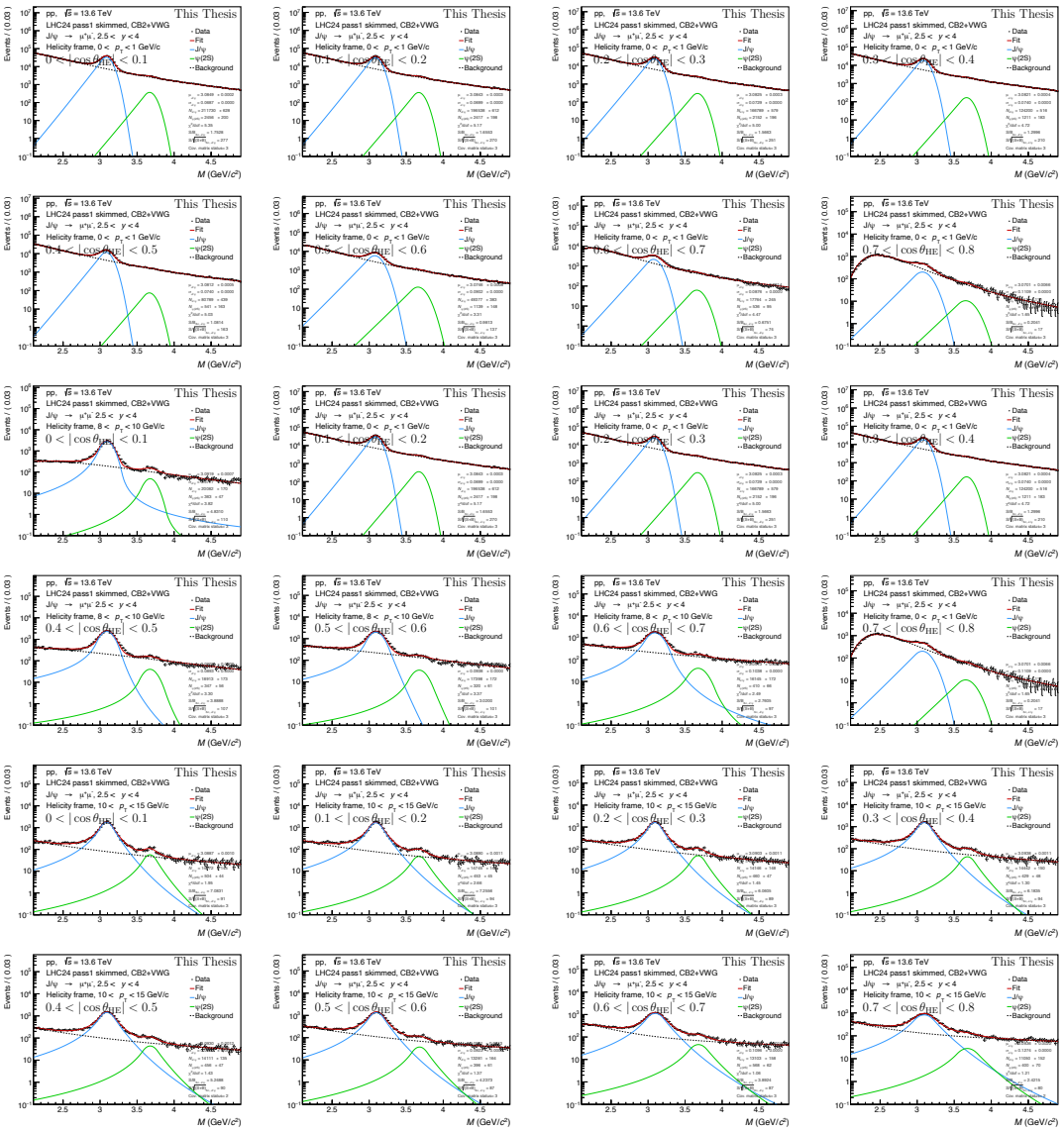



Figure 6: cos$\theta$ differential signal extraction for J/$\psi$ using CB2+VWG function for $0 < p_{\mathrm{T}} < 1$ GeV/c (top two rows), and $8 < p_{\mathrm{T}} < 15$ GeV/c (bottom four rows) in helicity reference frame [229].

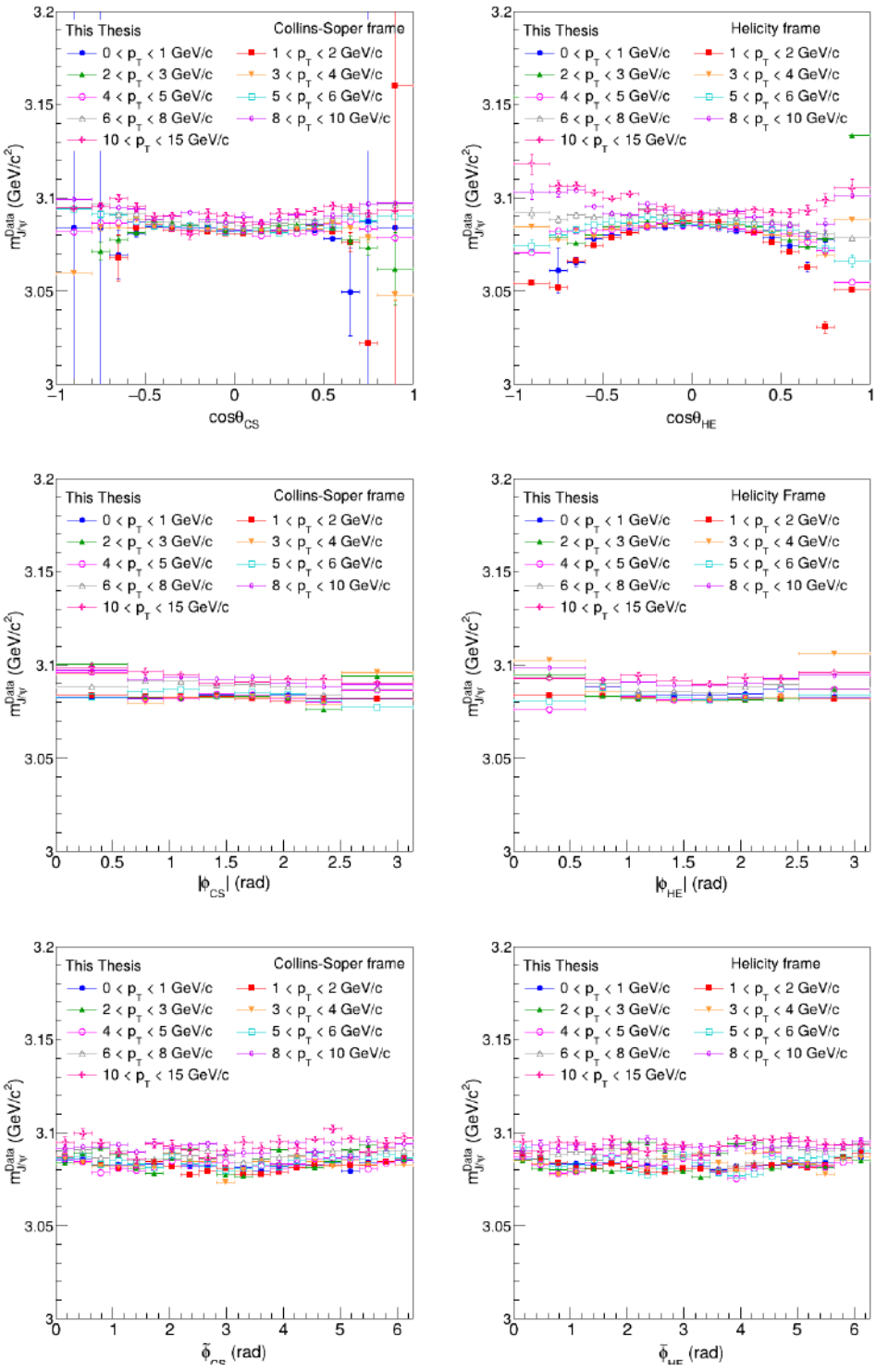



Figure 7: J/$\psi$ mass as a function of $\cos\theta$ (top), $|\phi|$ (middle), and $\tilde{\phi}$ (bottom) in Collins-Soper (left) and helicity (right) frames for $0 < p_{\mathrm{T}} < 15$ GeV/c [229].

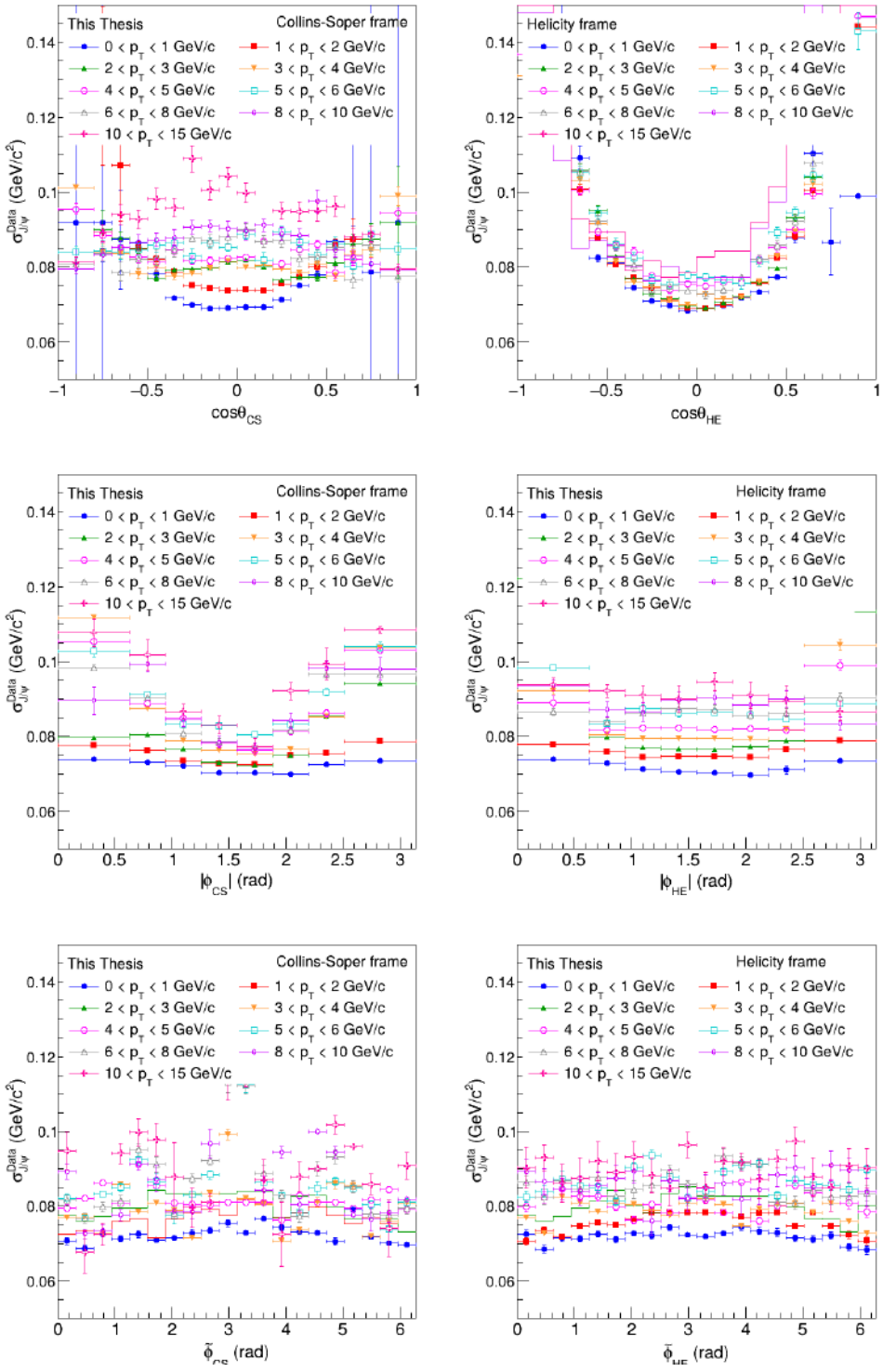



Figure 8: J/$\psi$ width as a function of $\cos\theta$ (top), $|\phi|$ (middle), and $\tilde{\phi}$ (bottom) in Collins-Soper (left) and helicity (right) frames for $0 < p_{\mathrm{T}} < 15$ GeV/c [229].

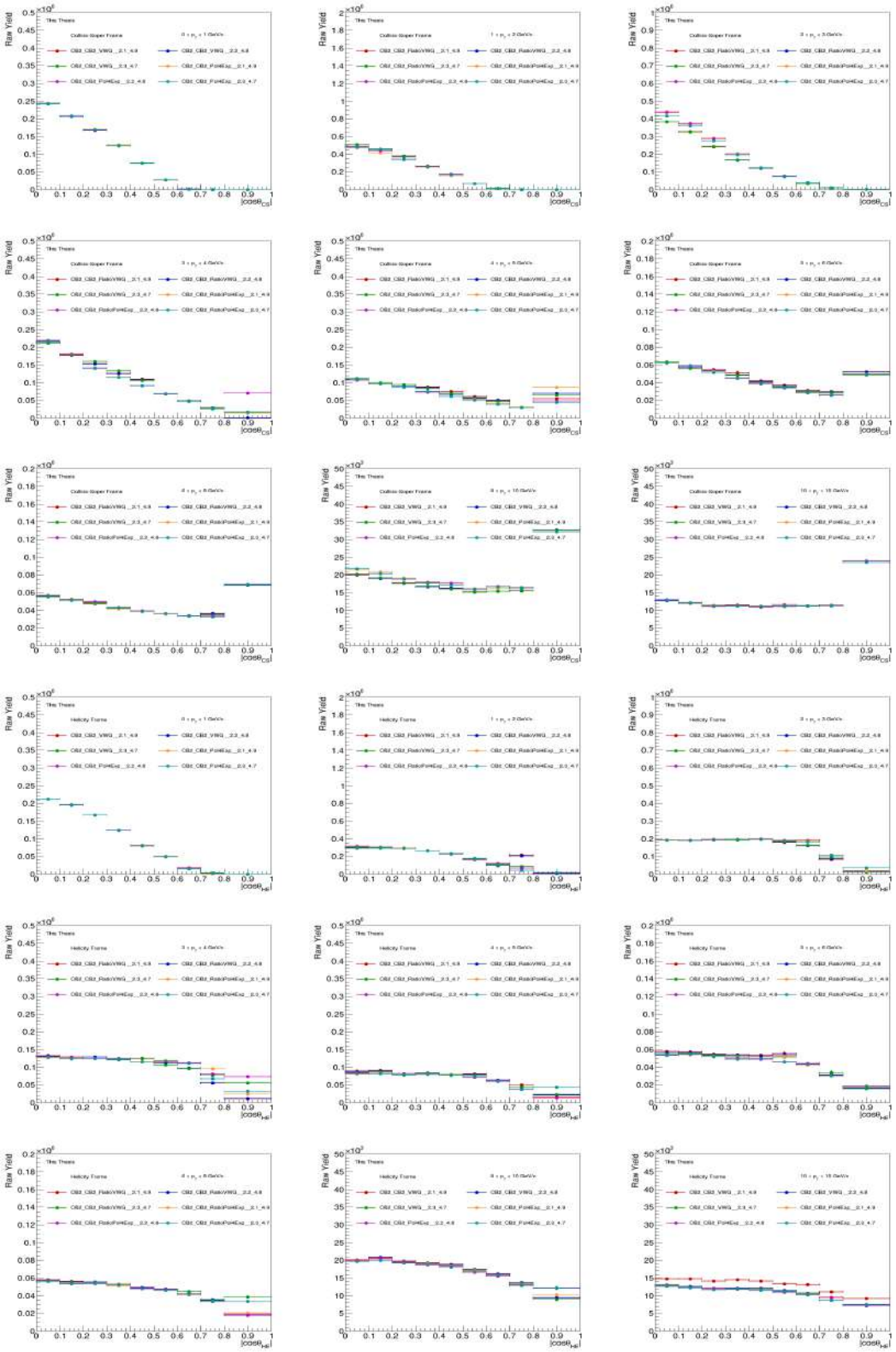


Figure 9: J/$\psi$ raw yield as a function of cos$\theta$ in CS and HE frame.

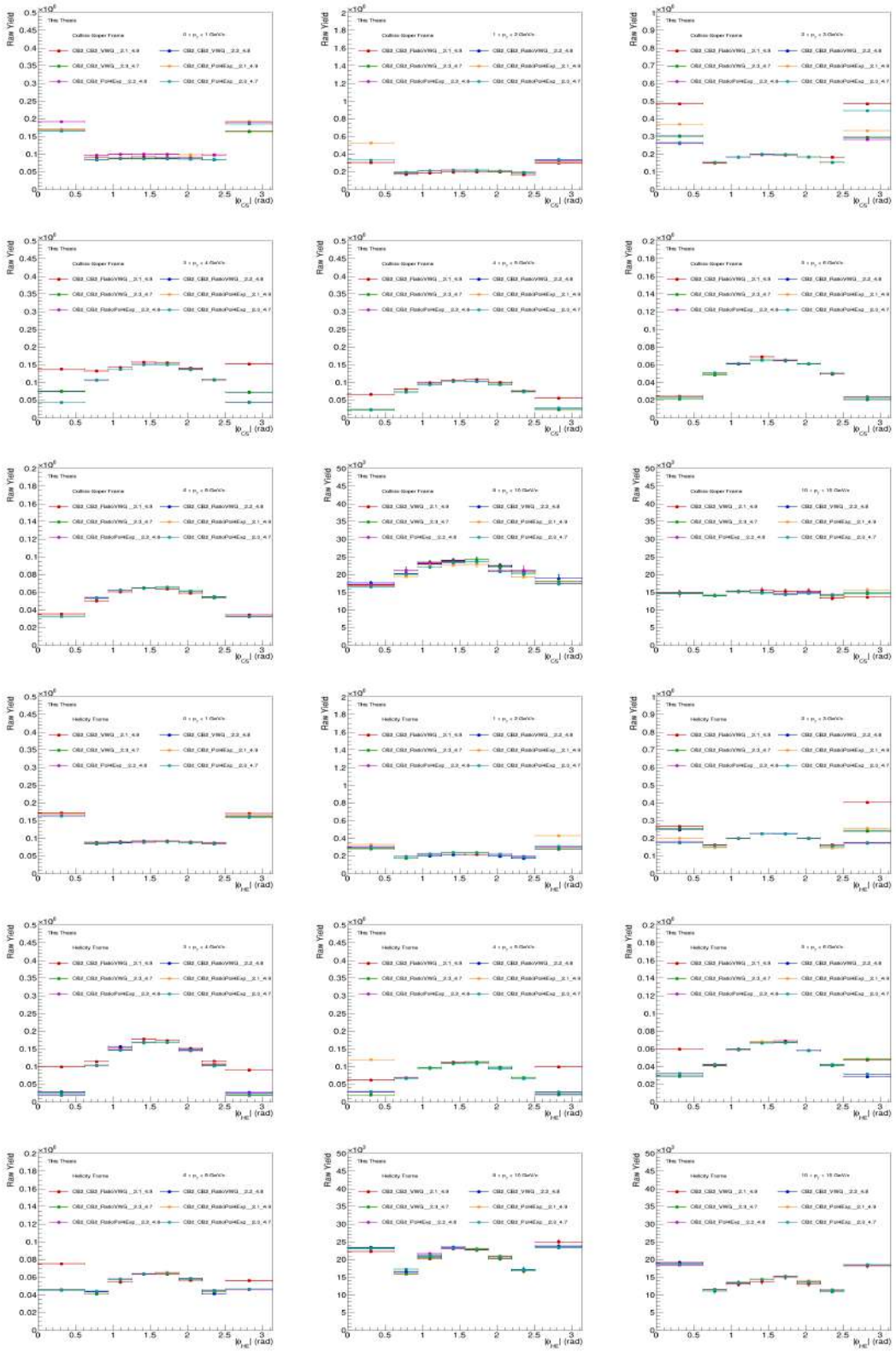


Figure 10: J/$\psi$ raw yield as a function of $\phi$ in CS and HE frame.

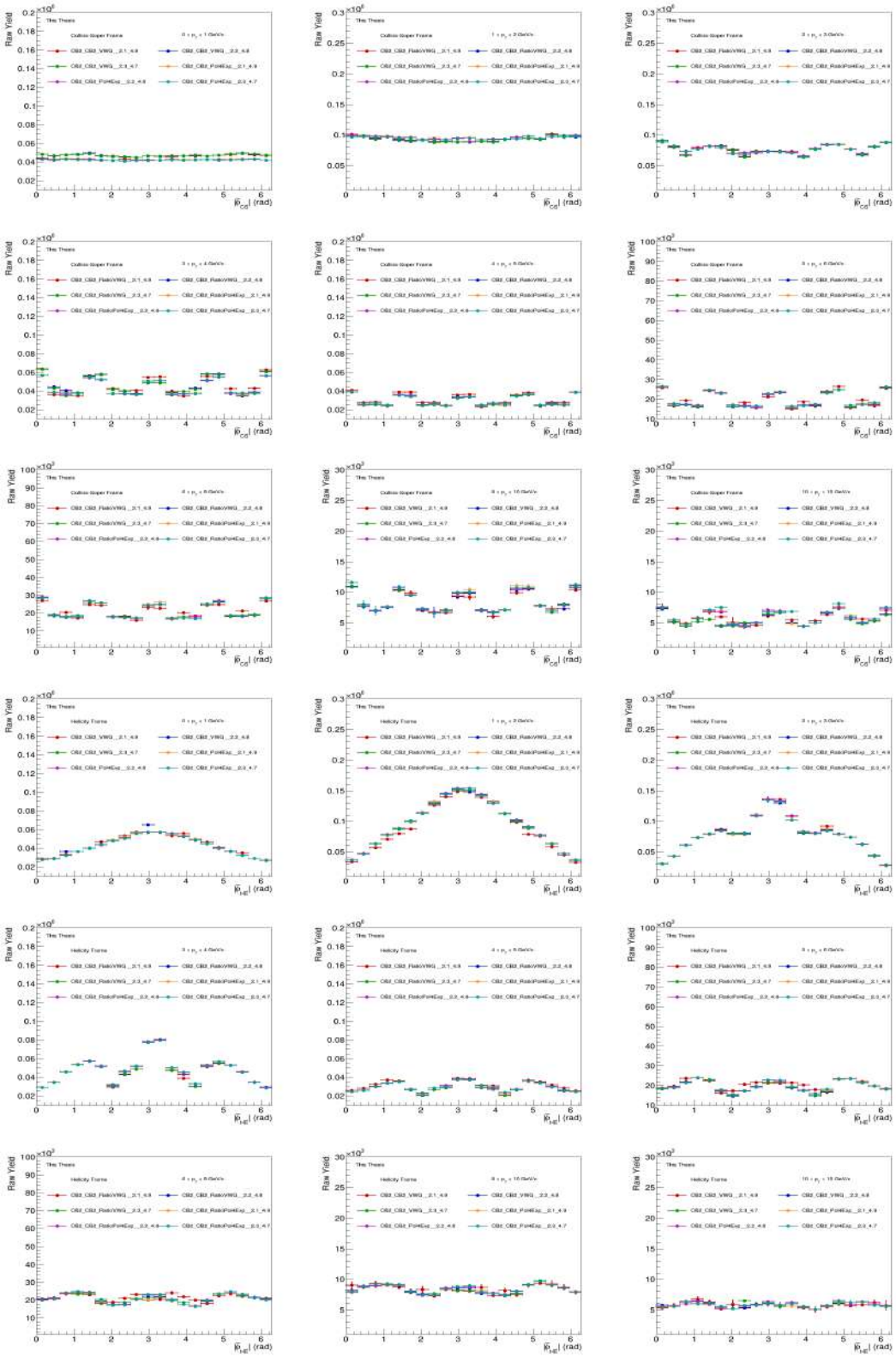


Figure 11: J/$\psi$ raw yield as a function of $\tilde{\phi}$ in CS and HE frame.

## B.1: $\cos\theta$ differential signal extraction in O–O collisions

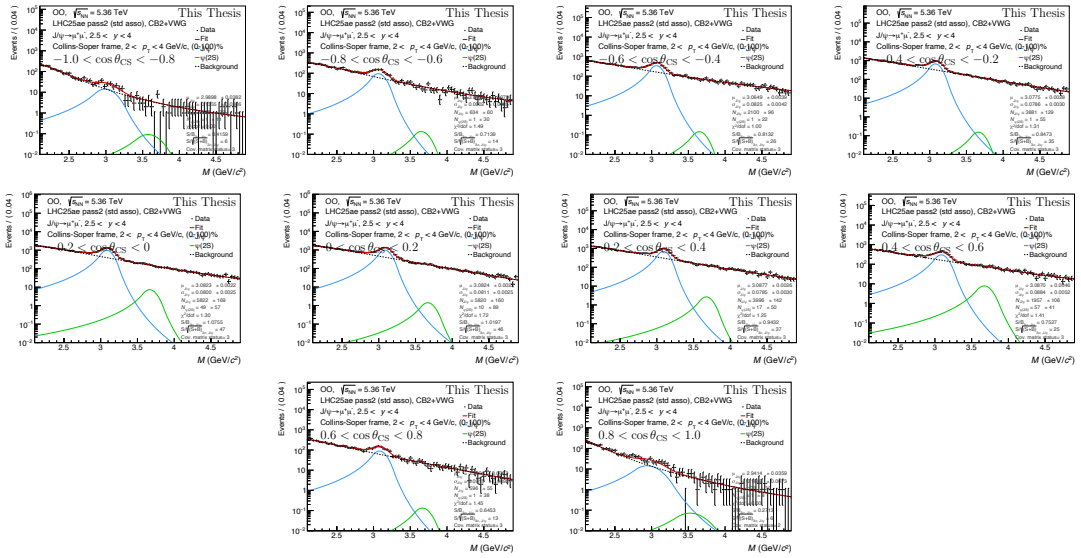



Figure 12: cos$\theta$ differential signal extraction for $2 < p_{\mathrm{T}} < 4$ GeV/c in CS [233].

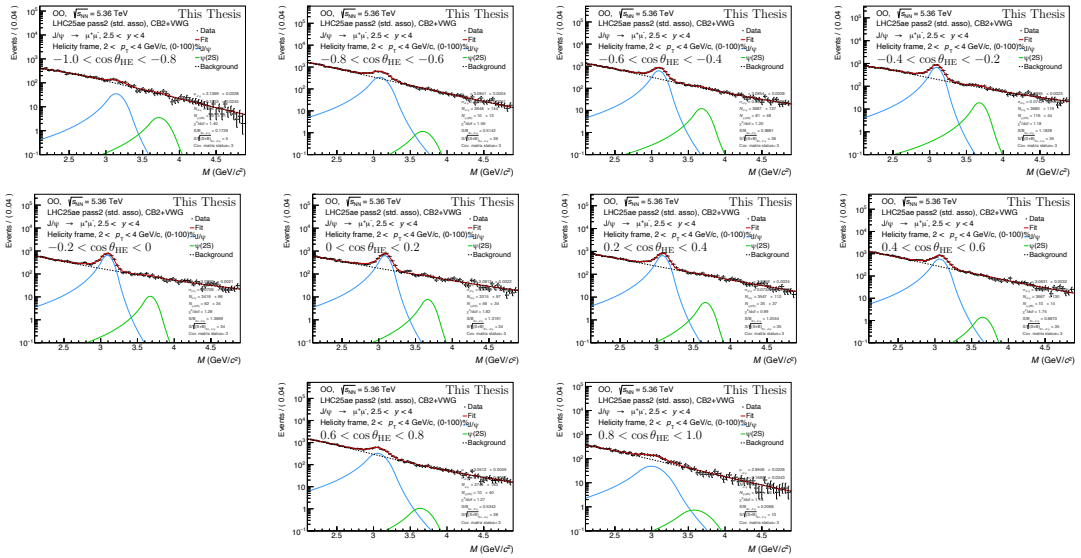



Figure 13: cos$\theta$ differential signal extraction for $2 < p_{\mathrm{T}} < 4$ GeV/c in HE [233].

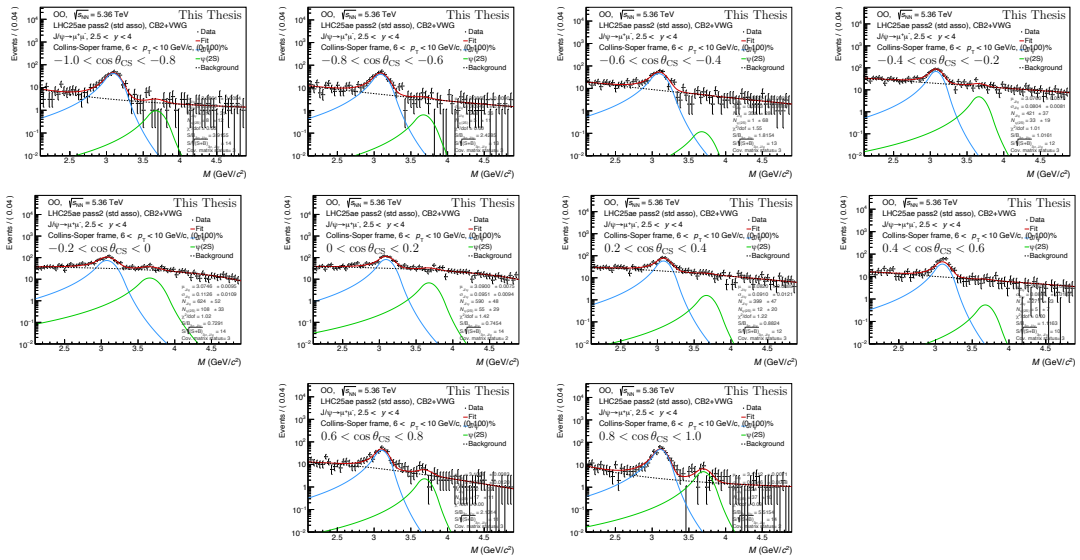



Figure 14: cos$\theta$ differential signal extraction for $6 < p_{\mathrm{T}} < 10$ GeV/c in CS [233].

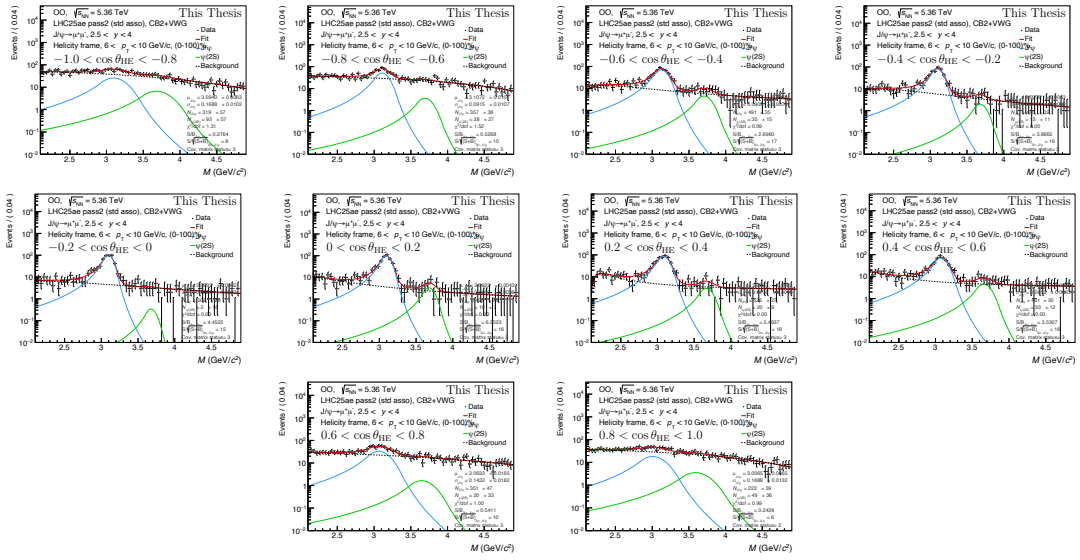



Figure 15: cos$\theta$ differential signal extraction for $6 < p_{\mathrm{T}} < 10$ GeV/c in HE [233].

## B.2: $\phi$ differential signal extraction in O–O collisions

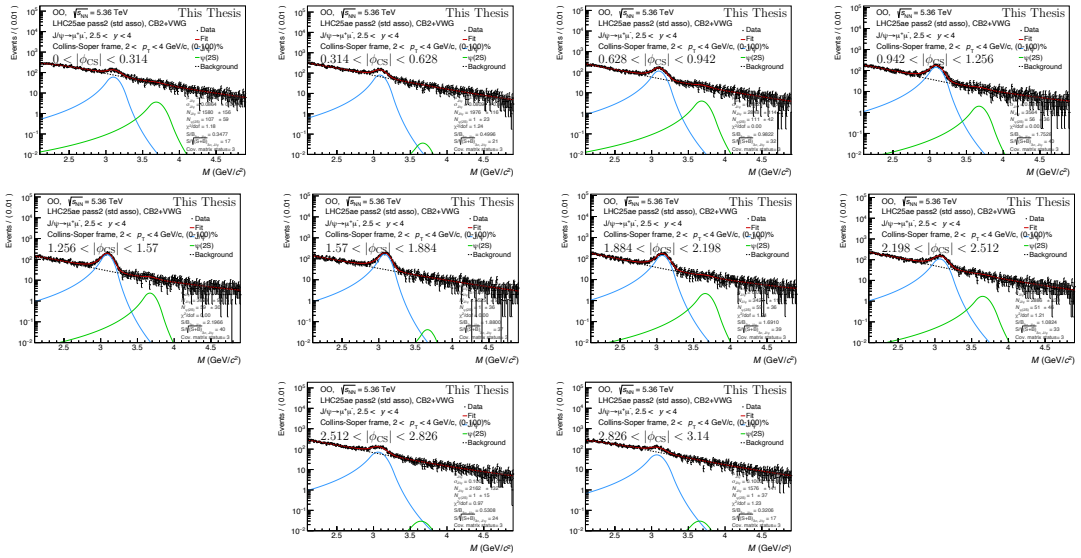



Figure 16: $\phi$ differential signal extraction for $2 < p_{\mathrm{T}} < 4$ GeV/c in CS [233].

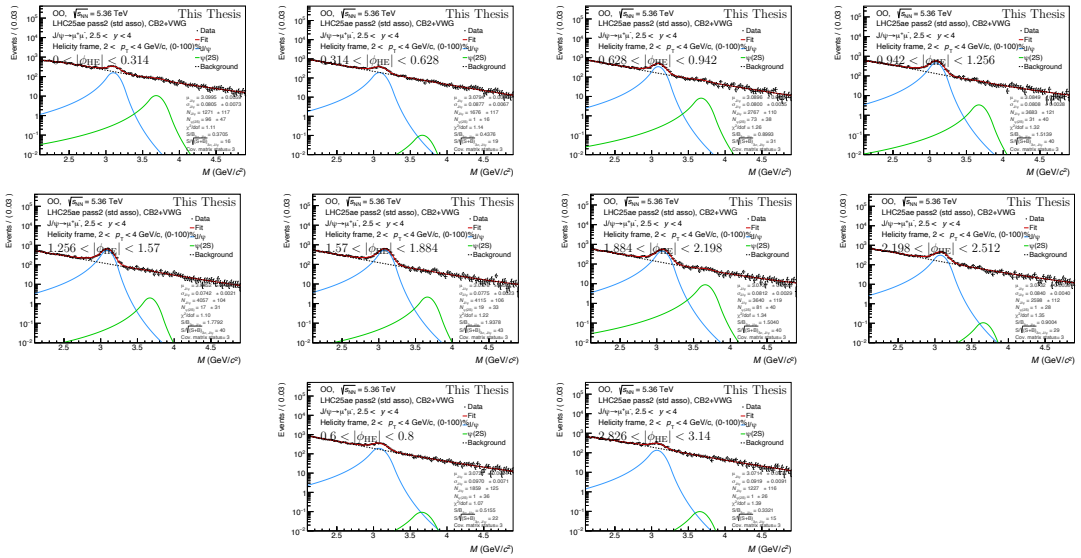



Figure 17: $\phi$ differential signal extraction for $2 < p_{\mathrm{T}} < 4$ GeV/c in HE [233].

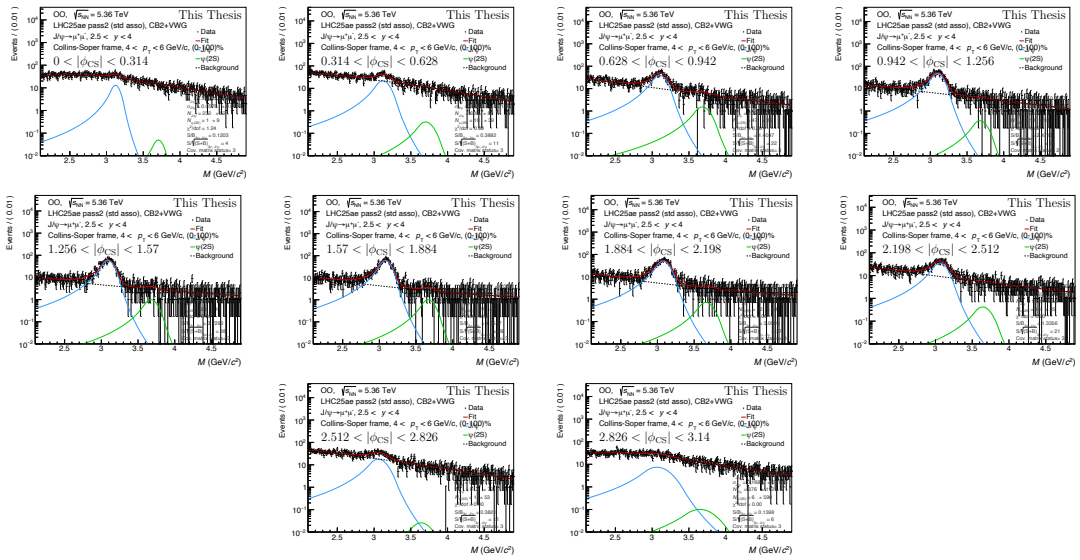



Figure 18: $\phi$ differential signal extraction for $4 < p_{\mathrm{T}} < 6$ GeV/c in CS [233].

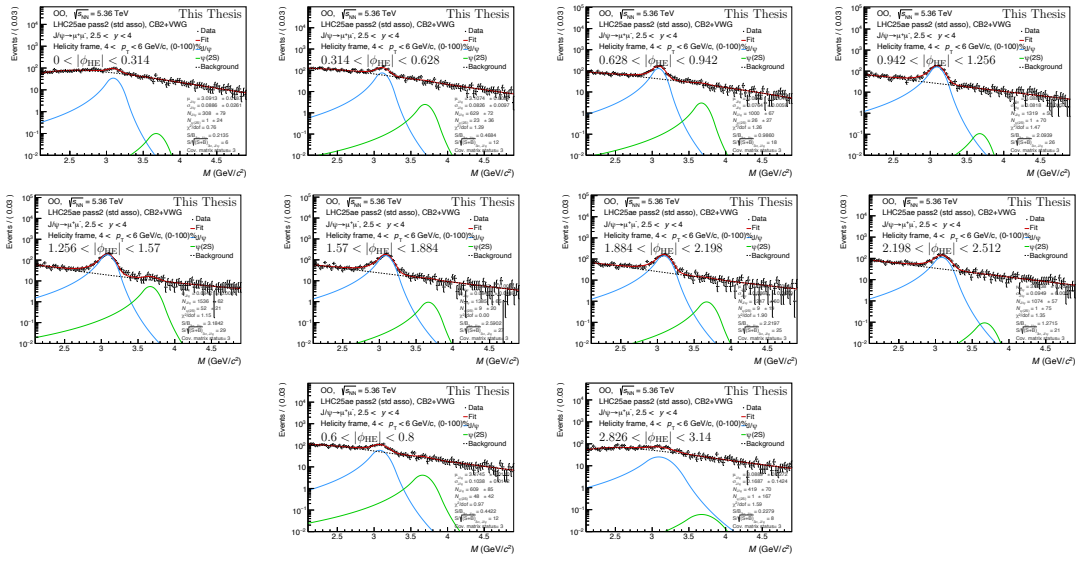



Figure 19: $\phi$ differential signal extraction for $4 < p_{\mathrm{T}} < 6$ GeV/c in HE [233].

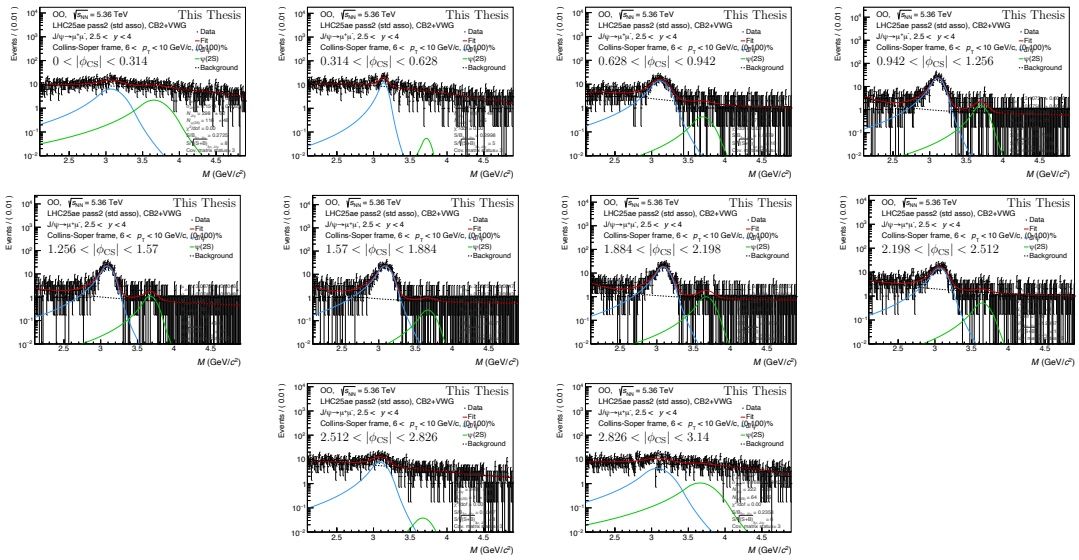



Figure 20: $\phi$ differential signal extraction for $6 < p_{\mathrm{T}} < 10$ GeV/c in CS [233].

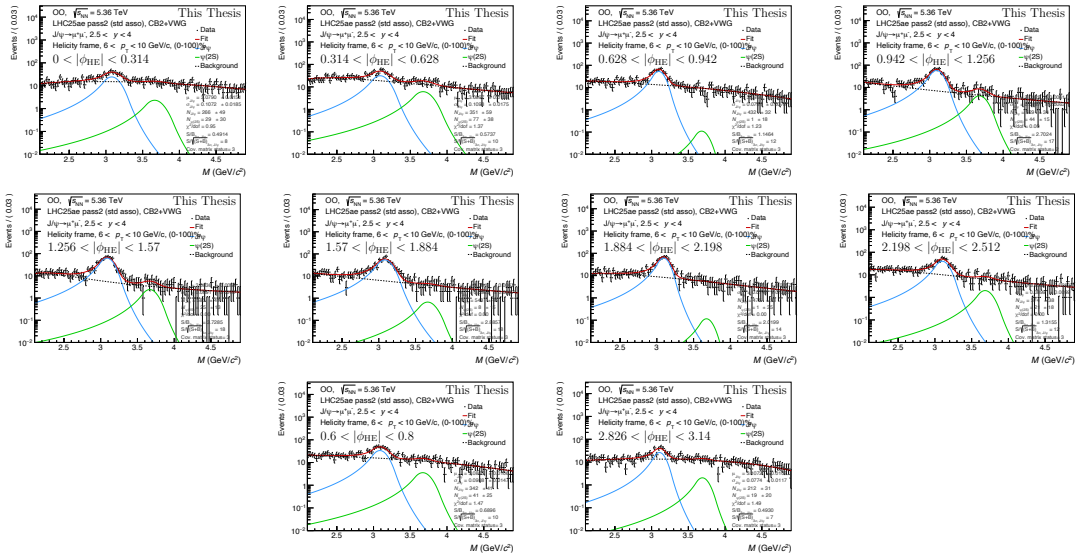



Figure 21: $\phi$ differential signal extraction for $6 < p_{\mathrm{T}} < 10$ GeV/c in HE [233].

## B.3: $\tilde{\phi}$ differential signal extraction in O–O collisions

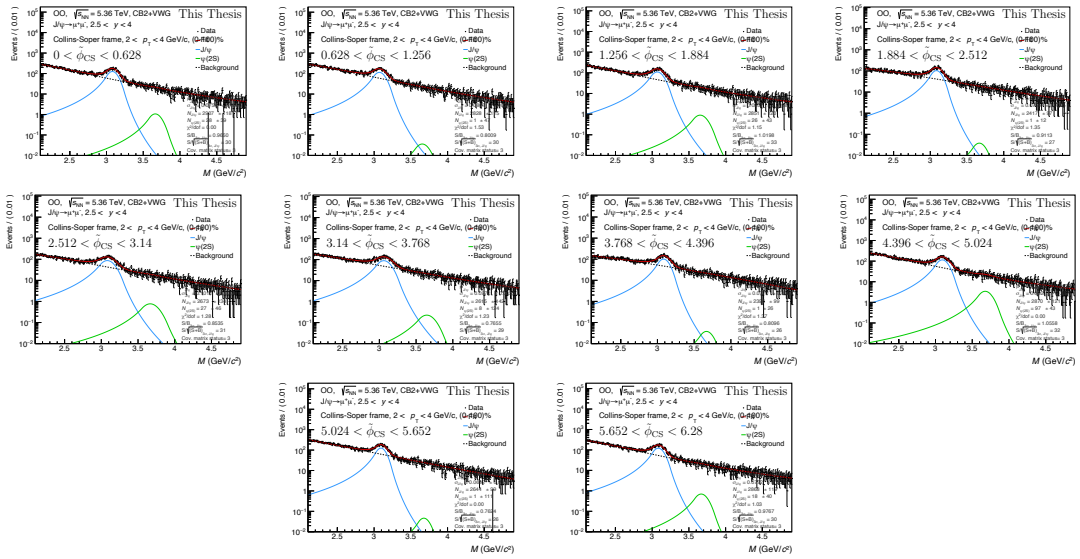



Figure 22: $\tilde{\phi}$ differential signal extraction for $2 < p_{\mathrm{T}} < 4$ GeV/c in CS [233].

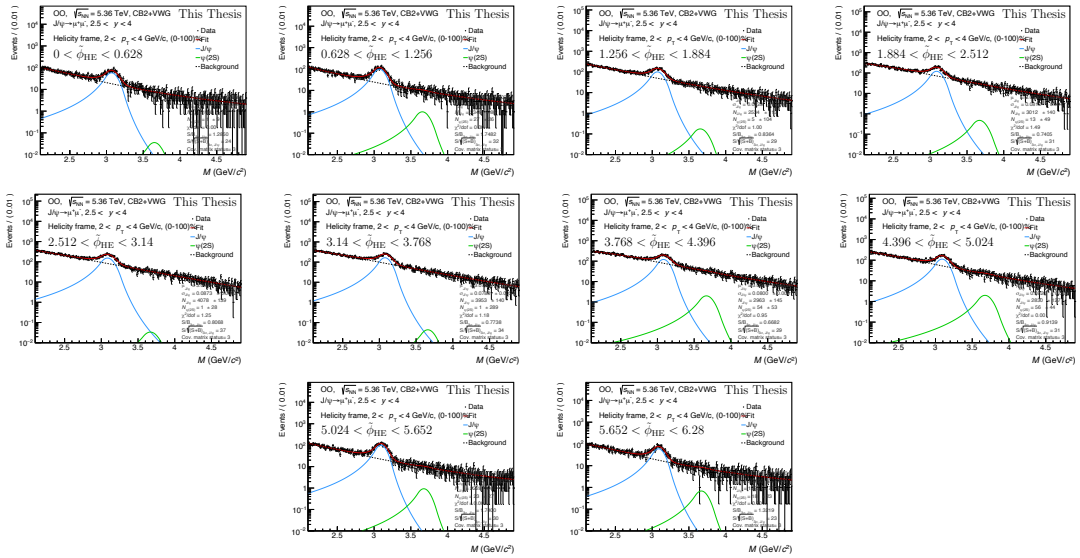



Figure 23: $\tilde{\phi}$ differential signal extraction for $2 < p_{\mathrm{T}} < 4$ GeV/c in HE [233].

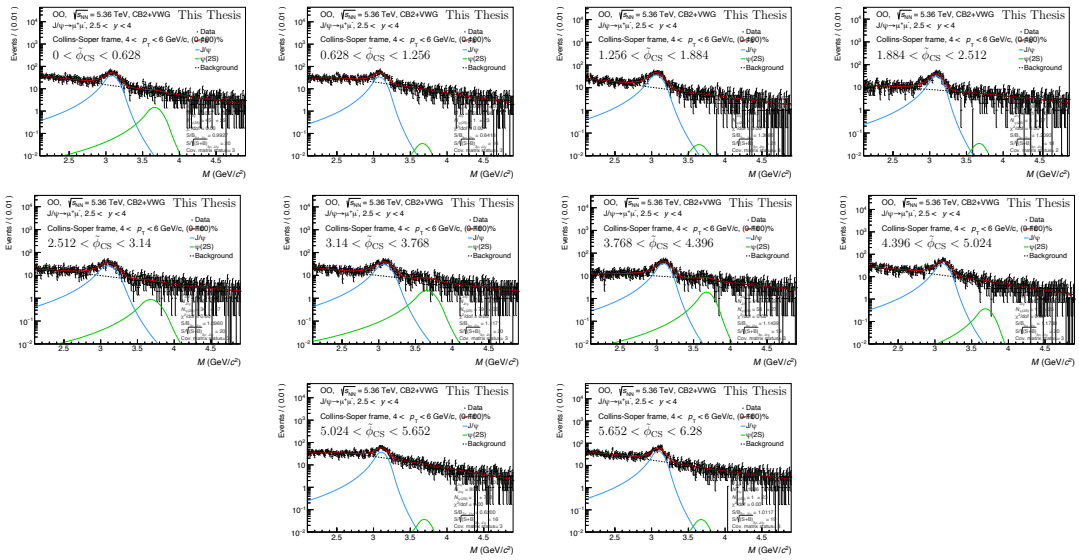



Figure 24: $\tilde{\phi}$ differential signal extraction for $4 < p_{\mathrm{T}} < 6$ GeV/c in CS [233].

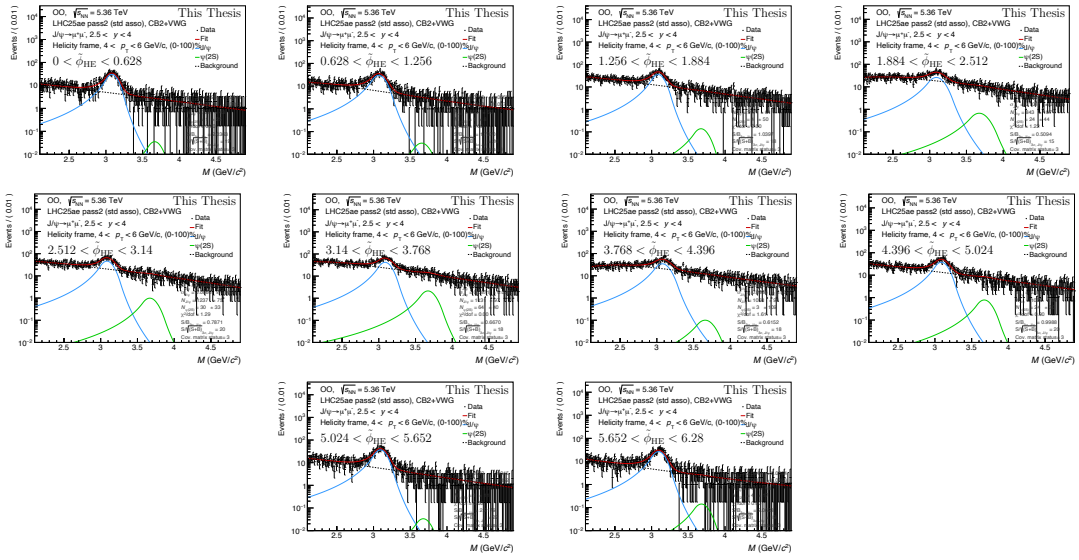



Figure 25: $\tilde{\phi}$ differential signal extraction for $4 < p_{\mathrm{T}} < 6$ GeV/c in HE [233].

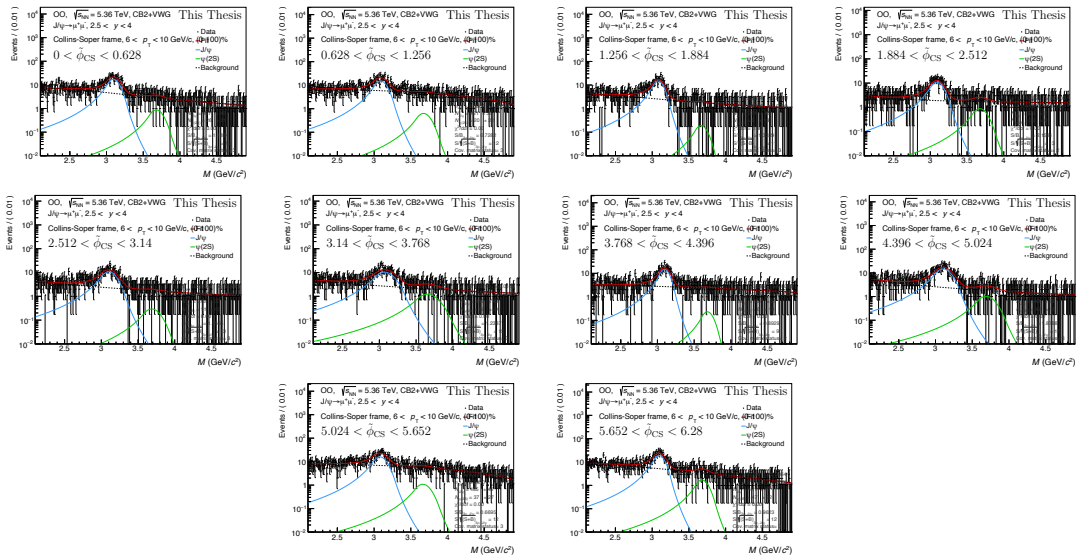



Figure 26: $\tilde{\phi}$ differential signal extraction for $6 < p_{\mathrm{T}} < 10$ GeV/c in CS [233].

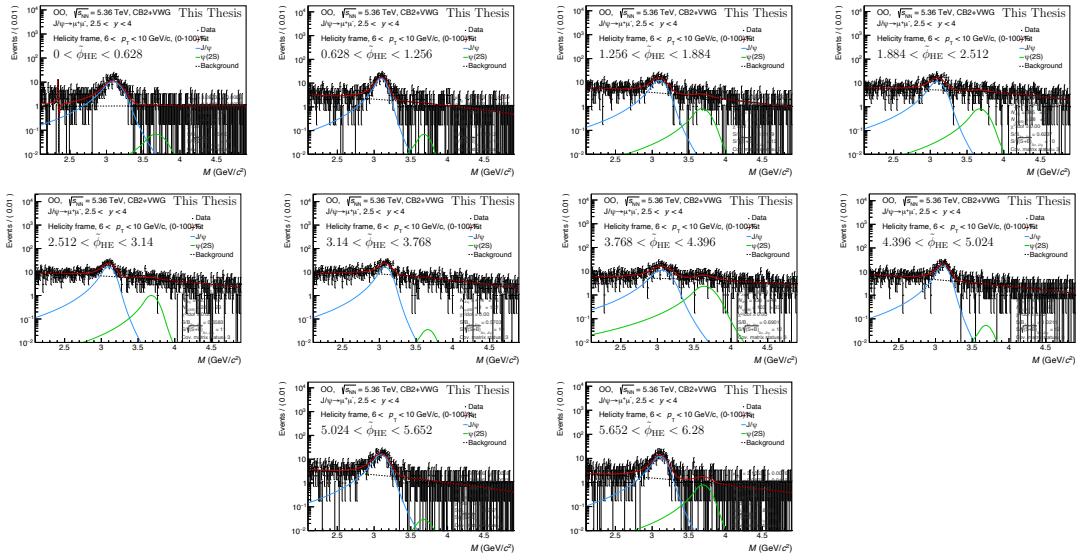



Figure 27: $\tilde{\phi}$ differential signal extraction for $6 < p_{\mathrm{T}} < 10$ GeV/c in HE [233].

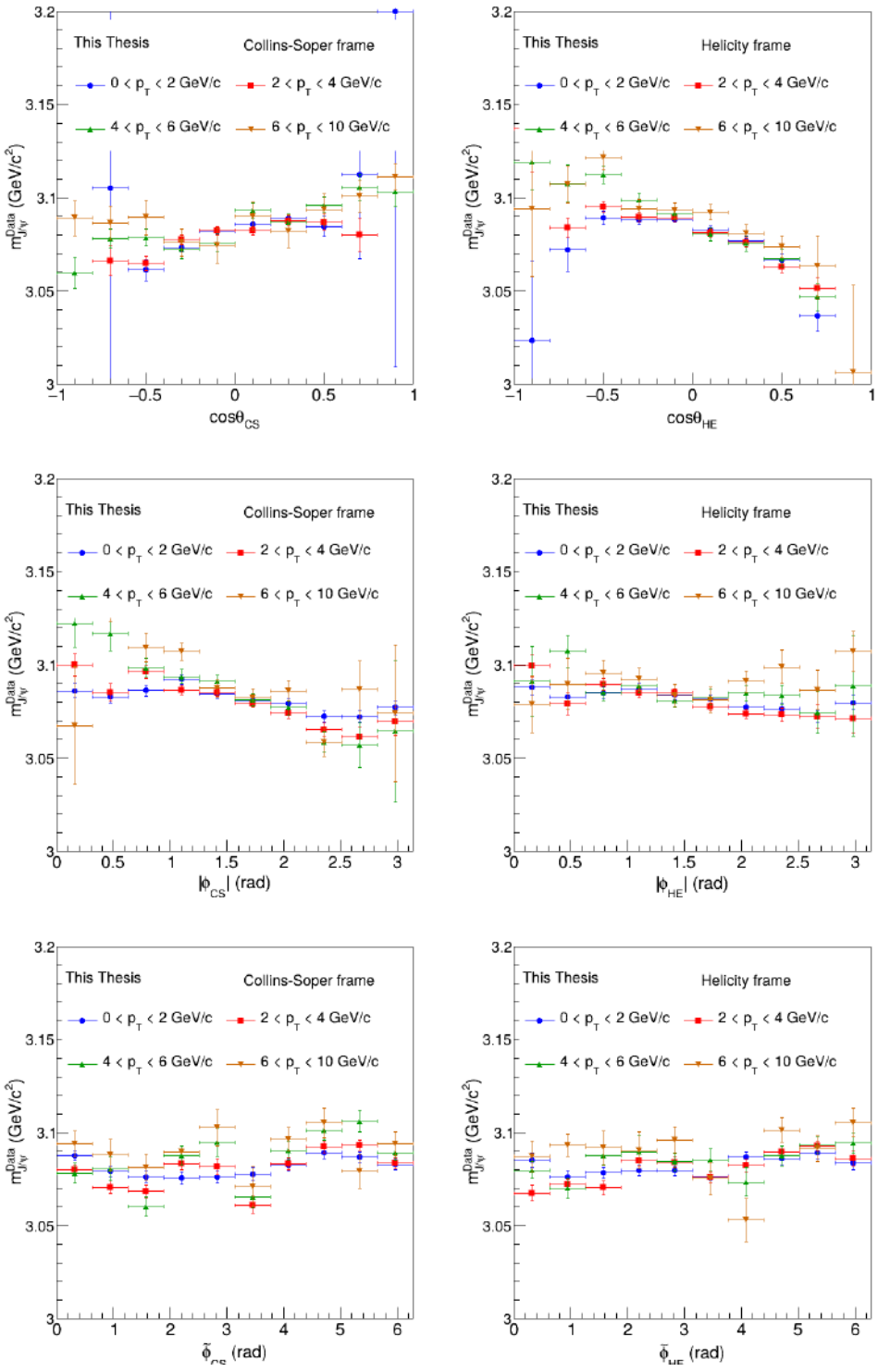



Figure 28: J/$\psi$ mass as a function of $\cos\theta$ (top), $|\phi|$ (middle), and $\tilde{\phi}$ (bottom) in Collins-Soper (left) and helicity (right) frames for $0 < p_{\mathrm{T}} < 15$ GeV/c [233].

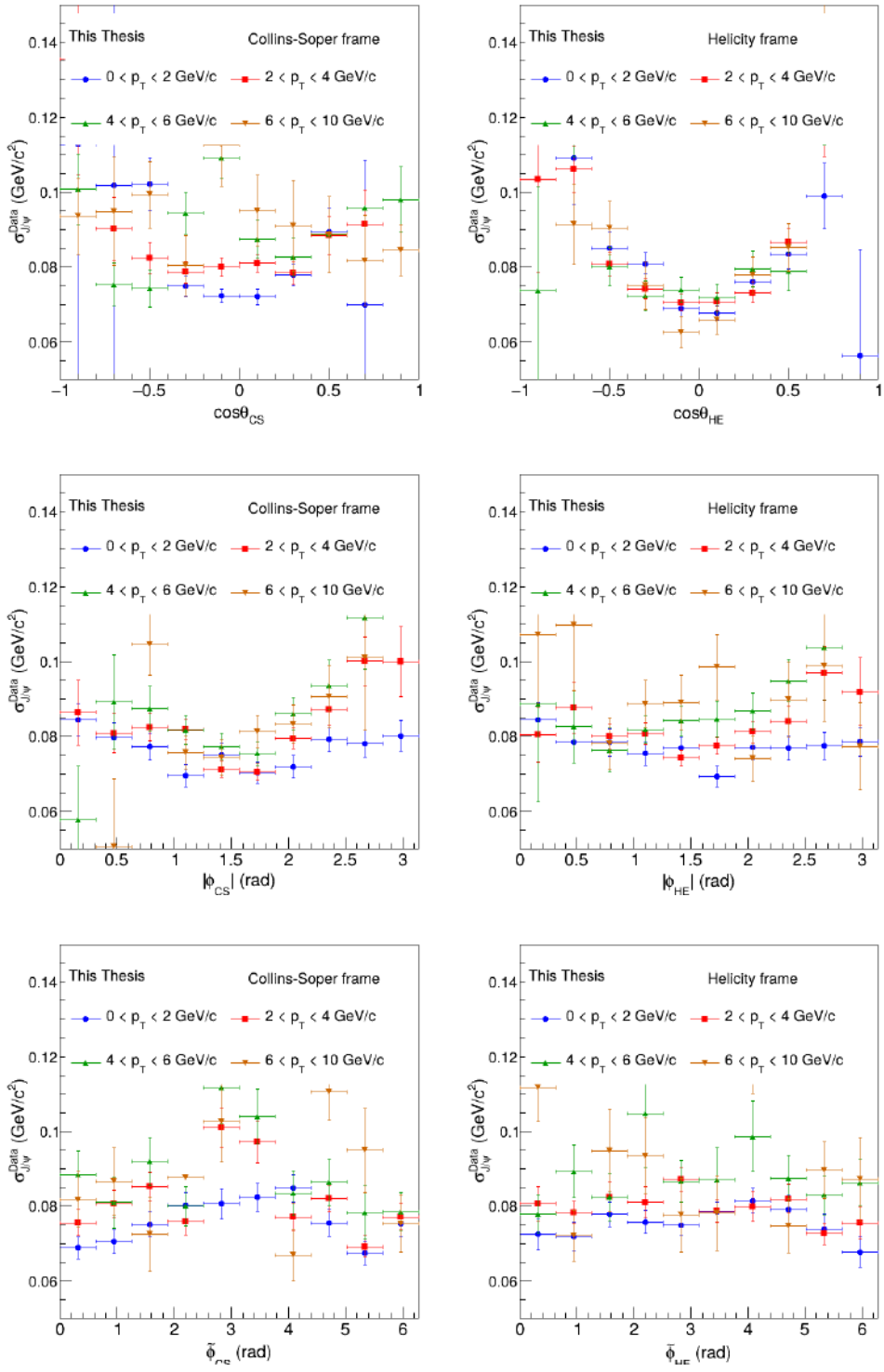



Figure 29: J/$\psi$ width as a function of $\cos\theta$ (top), $|\phi|$ (middle), and $\tilde{\phi}$ (bottom) in Collins-Soper (left) and helicity (right) frames for $0 < p_{\mathrm{T}} < 10$ GeV/c [233].

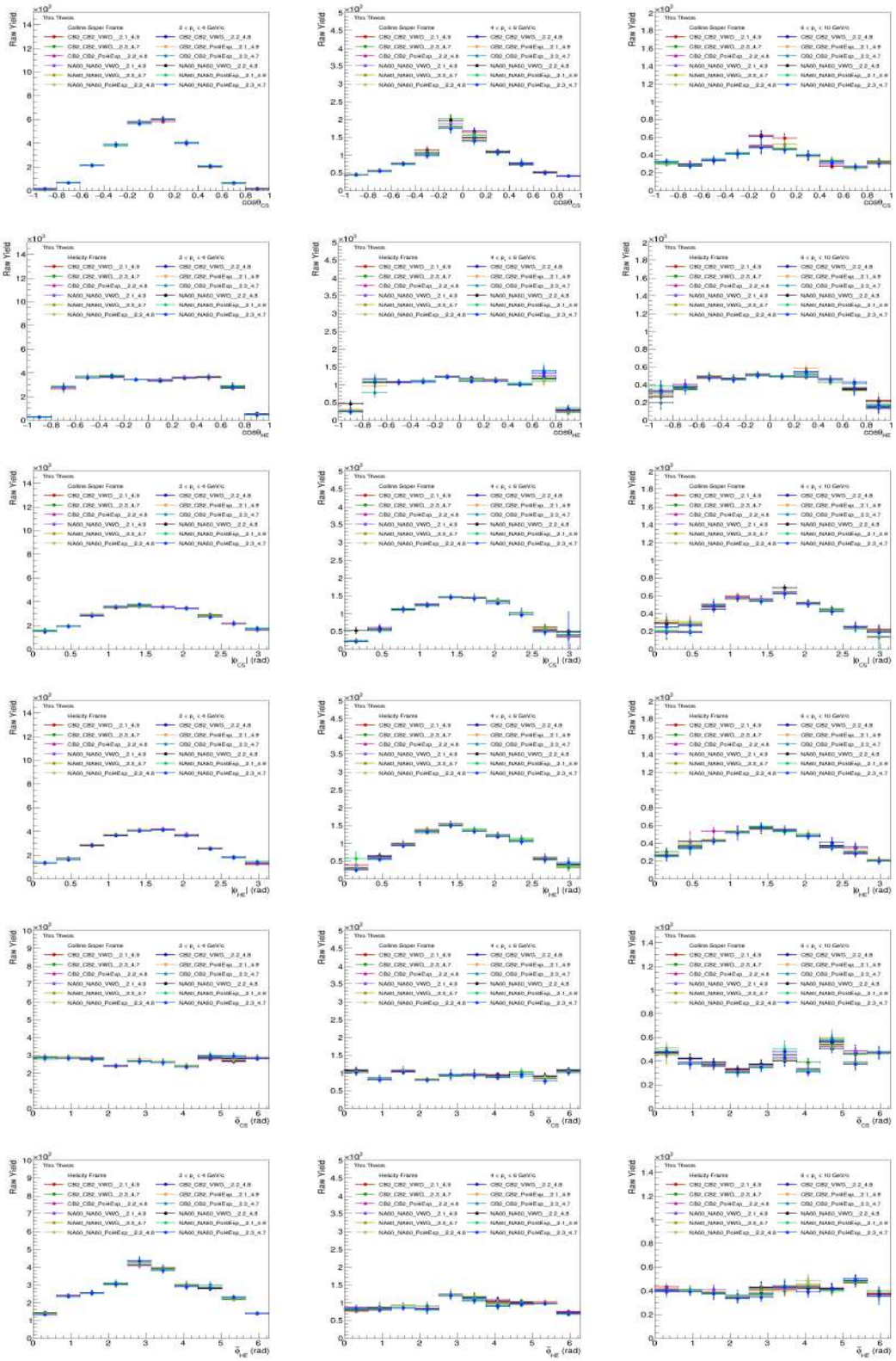


Figure 30: J/$\psi$ raw yield as a function of cos$\theta$, $\phi$, and $\tilde{\phi}$ in CS and HE frame.